Does the SARS-CoV-2 lab leak theory hold up? p. 1072

Fall books roundup p. 1078

Translation problems in Charcot-Marie-Tooth disease pp. 1089, 1156, & 1161

Science

$15
3 SEPTEMBER 2021
sciencemag.org

AAAS



ARCTIC REACH

Polar vortex shakes up weather pp. 1091 & 1116

THE NORWEGIAN ACADEMY OF SCIENCE AND LETTERS ANNOUNCES

THE KAVLI PRIZE

CALL FOR NOMINATIONS

September 1 - December 1, 2021

ANYONE CAN NOMINATE

- **Diversity in nominations encouraged**
- **Multiple nominations welcomed**

The Kavli Prize honors scientists worldwide for breakthroughs in **astrophysics, nanoscience and neuroscience** – transforming our understanding of the very big, the very small and the very complex.

$1,000,000 Prizes Announced June 1, 2022



KAVLIPRIZE.ORG

The Kavli Prize is a partnership among
The Norwegian Academy of Science and Letters,
The Norwegian Ministry of Education and Research,
and The Kavli Foundation (USA).



3 SEPTEMBER 2021 • VOLUME 373 • ISSUE 6559

NEWS

IN BRIEF

1064 News at a glance

IN DEPTH

1066 **U.S. astronomers weigh fate of giant telescopes**
"Decadal survey" could recommend bailout for struggling projects
By D. Clery

1067 **SARS-CoV-2 infection confers greater immunity than shots**
Study from Israel, the largest of its kind, also finds infection combined with a single jab is highly protective
By M. Wadman

1068 **Using mirrors to tame the savage x-ray laser**
Scheme that harkens back to ordinary lasers could open new research avenues
By A. Cho

1070 **Confederate ties knock ocean science pioneer from pedestals**
Institutions move to drop Matthew Fontaine Maury's name
By P. Voosen

1071 **Molecular cleanup crew moves outside the cell**
Drug candidates now target extracellular proteins, broadening diseases they may treat
By R. F. Service

FEATURES

1072 **Call of the wild**
Why most scientists say it's unlikely that SARS-CoV-2 originated from a "lab leak"
By J. Cohen

1076 **The hunt for SARS-CoV-2's ancestors heats up**
By J. Cohen
PODCAST

INSIGHTS

BOOKS *ET AL.*

1078 **A sampling of seasonal science books**

PERSPECTIVES

1084 **A quantum vortex made of atoms**
Vortex states seen for photons and electrons have been created in rare gas atoms and dimers *By O. Kornilov*
RESEARCH ARTICLE p. 1105

1085 **Transformational ecology and climate change**
Management of imminent ecosystem shifts demands adaptive, translational approaches
By S. T. Jackson

1086 **Lipid-mediated regulation of flowering time**
An anionic phospholipid tells plants when to flower according to ambient temperature
By Y. Jaillais and F. Parcy
REPORT p. 1137

1088 **Enabling oncogenes**
Melanoma can arise only from cells with a permissive chromatin landscape
By D. W. Vredevoogd and D. S. Peeper
RESEARCH ARTICLE p. 1104

1089 **Stressing out translation**
Integrated stress response activation drives neuropathy in Charcot-Marie-Tooth disease *By W. Mellado and D. E. Willis*
REPORTS pp. 1156 & 1161

1091 **Stratospheric winds trigger cold spells**
Changes in Arctic sea ice and snow cover can alter wind patterns at high altitudes
By D. Coumou
REPORT p. 1116

1092 **Steven Weinberg (1933–2021)**
Titan of theoretical physics *By J. Preskill*

POLICY FORUM

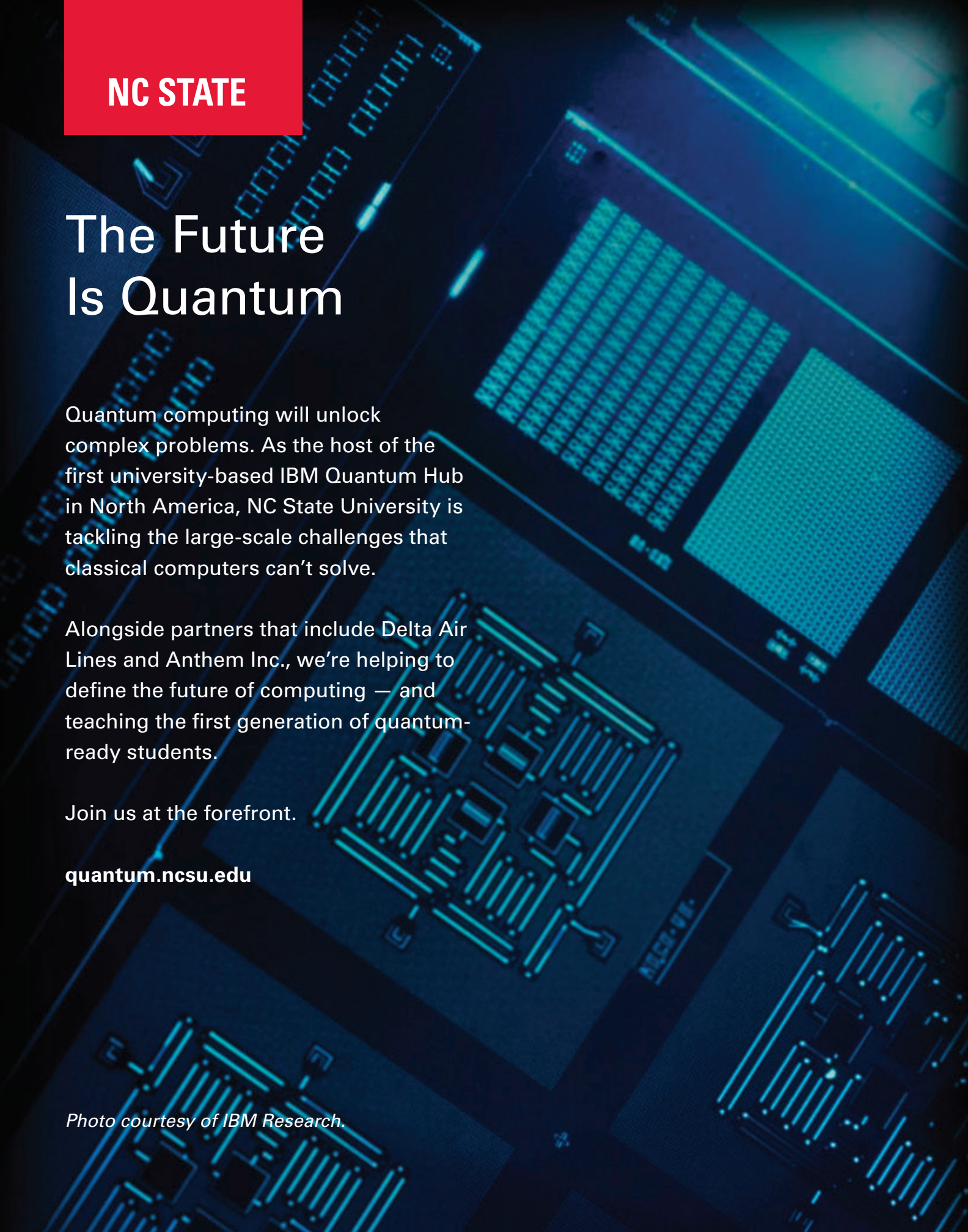
1093 **Do we need a new science-policy interface for food systems?**
Credibility, legitimacy, and diversity of knowledge are critical *By E. Turnhout* et al.

LETTERS

1097 **Animal welfare's role in human-wildlife conflict**
By J. V. López-Bao and P. Mateo-Tomás

1097 **Disability innovation strengthens STEM**
By I. S. Daehn and P. L. Croxson

ILLUSTRATION: GABY D'ALESSANDRO



NC STATE

The Future Is Quantum

Quantum computing will unlock complex problems. As the host of the first university-based IBM Quantum Hub in North America, NC State University is tackling the large-scale challenges that classical computers can't solve.

Alongside partners that include Delta Air Lines and Anthem Inc., we're helping to define the future of computing — and teaching the first generation of quantum-ready students.

Join us at the forefront.

quantum.ncsu.edu

Photo courtesy of IBM Research.

1099 Collective agency transforms societies
By Y. Namer and O. Razum

RESEARCH

IN BRIEF

1100 From *Science* and other journals

REVIEW

1103 Neuroscience
Architectures of neuronal circuits
L. Luo et al.
REVIEW SUMMARY; FOR FULL TEXT: DOI.ORG/10.1126/SCIENCE.ABG7285

RESEARCH ARTICLES

1104 Melanoma
Developmental chromatin programs determine oncogenic competence in melanoma *A. Baggiolini* et al.
RESEARCH ARTICLE SUMMARY; FOR FULL TEXT: DOI.ORG/10.1126/SCIENCE.ABC1048
PERSPECTIVE p. 1088

1105 Quantum physics
Vortex beams of atoms and molecules
A. Luski et al.
PERSPECTIVE p. 1084; PODCAST

1109 Coronavirus
Broad betacoronavirus neutralization by a stem helix–specific human antibody
D. Pinto et al.

REPORTS

1116 Climate dynamics
Linking Arctic variability and change with extreme winter weather in the United States
J. Cohen et al.
PERSPECTIVE p. 1091

1122 Superconductivity
Discovery of mesoscopic nematicity wave in iron-based superconductors
T. Shimojima et al.

1125 Supernovae
A transient radio source consistent with a merger-triggered core collapse supernova
D. Z. Dong et al.

1129 Quantum gases
Generalized hydrodynamics in strongly interacting 1D Bose gases
N. Malvania et al.

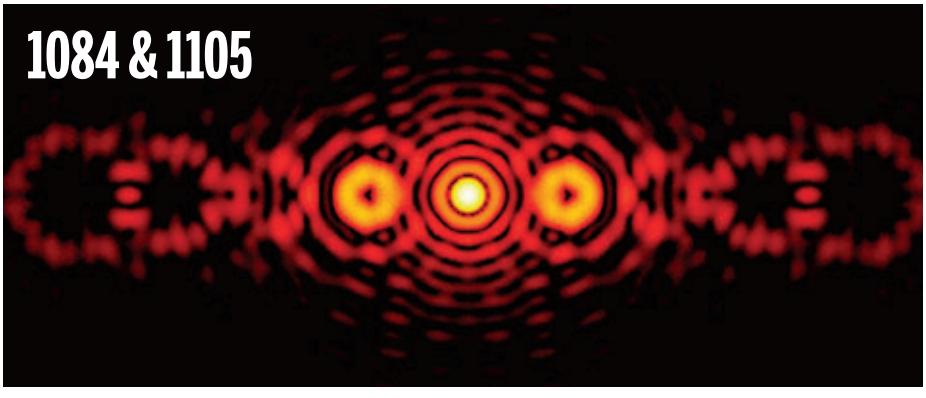
1133 Metasurfaces
Plasmonic topological metasurface by encircling an exceptional point
Q. Song et al.

1137 Plant science
Florigen sequestration in cellular membranes modulates temperature-responsive flowering
H. Susila et al.
PERSPECTIVE p. 1086

1142 Coronavirus
Structural basis of mismatch recognition by a SARS-CoV-2 proofreading enzyme
C. Liu et al.

1146 CRISPR techonology
MIC-Drop: A platform for large-scale in vivo CRISPR screens
S. Parvez et al.

1151 Structural biology
Three-megadalton complex of methanogenic electron-bifurcating and CO_2-fixing enzymes
T. Watanabe et al.



CREDITS (FROM LEFT): A. LUSKI *ET AL.*; ROBERT NEUBECKER

Neuroscience

1156 The integrated stress response contributes to tRNA synthetase–associated peripheral neuropathy
E. L. Spaulding et al.

1161 tRNA overexpression rescues peripheral neuropathy caused by mutations in tRNA synthetase
A. Zuko et al.
PERSPECTIVE p. 1089



DEPARTMENTS

1063 Editorial
The will to fight *By Scott Atran*

1170 Working Life
Writing my way through *By A. Rani Elwy*

ON THE COVER

Snow blankets the ground in Dallas, Texas, on 18 February 2021. The cold wave of February 2021 was one of the costliest weather disasters in the United States, especially for Texas, owing to the intersection of energy regulation decisions and exceptionally severe winter weather. New research combines machine learning analysis of observations with numerical modeling to demonstrate that Arctic climate change has modified polar vortex behavior to increase the likelihood of such extreme events. See pages 1091 and 1116. *Photo: Nitashia Johnson/The New York Times/Redux*



Science Staff 1062
New Products 1167
Science Careers 1168

SCIENCE (ISSN 0036-8075) is published weekly on Friday, except last week in December, by the American Association for the Advancement of Science, 1200 New York Avenue, NW, Washington, DC 20005. Periodicals mail postage (publication No. 484460) paid at Washington, DC, and additional mailing offices. Copyright © 2021 by the American Association for the Advancement of Science. The title SCIENCE is a registered trademark of the AAAS. Domestic individual membership, including subscription (12 months): $165 ($74 allocated to subscription). Domestic institutional subscription (51 issues): $2148; Foreign postage extra: Air assist delivery: $98. First class, airmail, student, and emeritus rates on request. Canadian rates with GST available upon request, GST #125488122. Publications Mail Agreement Number 1069624. **Printed in the U.S.A.**
Change of address: Allow 4 weeks, giving old and new addresses and 8-digit account number. **Postmaster:** Send change of address to AAAS, P.O. Box 96178, Washington, DC 20090–6178. **Single-copy sales:** $15 each plus shipping and handling available from backissues.sciencemag.org; bulk rate on request. **Authorization to reproduce** material for internal or personal use under circumstances not falling within the fair use provisions of the Copyright Act can be obtained through the Copyright Clearance Center (CCC), www.copyright.com. The identification code for *Science* is 0036-8075. *Science* is indexed in the *Reader's Guide to Periodical Literature* and in several specialized indexes.

Science AAAS

Editor-in-Chief Holden Thorp, hthorp@aaas.org

Executive Editor Monica M. Bradford

Editors, Research Valda Vinson, Jake S. Yeston **Editor, Insights** Lisa D. Chong

DEPUTY EDITORS Julia Fahrenkamp-Uppenbrink (UK), Stella M. Hurtley (UK), Phillip D. Szuromi, Sacha Vignieri **SR. EDITORIAL FELLOW** Andrew M. Sugden (UK) **SR. EDITORS** Gemma Alderton (UK), Caroline Ash (UK), Brent Grocholski, Pamela J. Hines, Di Jiang, Marc S. Lavine (Canada), Yevgeniya Nusinovich, Ian S. Osborne (UK), Beverly A. Purnell, L. Bryan Ray, H. Jesse Smith, Keith T. Smith (UK), Jelena Stajic, Peter Stern (UK), Valerie B. Thompson, Brad Wible, Yuen Yiu, Laura M. Zahn **ASSOCIATE EDITORS** Michael A. Funk, Priscilla N. Kelly, Tage S. Rai, Seth Thomas Scanlon (UK), Yury V. Suleymanov **LETTERS EDITOR** Jennifer Sills **LEAD CONTENT PRODUCTION EDITORS** Harry Jach, Lauren Kmec **CONTENT PRODUCTION EDITORS** Amelia Beyna, Jeffrey E. Cook, Chris Filiatreau, Julia Katris, Nida Masiulis, Abigail Shashikanth, Suzanne M. White **SR. EDITORIAL COORDINATORS** Carolyn Kyle, Beverly Shields **EDITORIAL COORDINATORS** Aneera Dobbins, Joi S. Granger, Jeffrey Hearn, Lisa Johnson, Maryrose Madrid, Ope Martins, Shannon McMahon, Jerry Richardson, Hilary Stewart (UK), Alana Warnke, Alice Whaley (UK), Anita Wynn **PUBLICATIONS ASSISTANTS** Jeremy Dow, Alexander Kief, Ronmel Navas, Brian White **EXECUTIVE ASSISTANT** Jessica Slater **ASI DIRECTOR, OPERATIONS** Janet Clements (UK) **ASI SR. OFFICE ADMINISTRATOR** Jessica Waldock (UK)

News Editor Tim Appenzeller

NEWS MANAGING EDITOR John Travis **INTERNATIONAL EDITOR** Martin Enserink **DEPUTY NEWS EDITORS** Elizabeth Culotta, Lila Guterman, David Grimm, Eric Hand (Europe), David Malakoff **SR. CORRESPONDENTS** Daniel Clery (UK), Jon Cohen, Jeffrey Mervis, Elizabeth Pennisi **ASSOCIATE EDITORS** Jeffrey Brainard, Kelly Servick, Catherine Matacic **NEWS REPORTERS** Adrian Cho, Jennifer Couzin-Frankel, Jocelyn Kaiser, Rodrigo Pérez Ortega (Mexico City), Robert F. Service, Erik Stokstad, Paul Voosen, Meredith Wadman **INTERNS** Menna Ibrahim, Sofia Moutinho, Anil Oza, Alex Viveros **CONTRIBUTING CORRESPONDENTS** Warren Cornwall, Andrew Curry (Berlin), Ann Gibbons, Sam Kean, Eli Kintisch, Kai Kupferschmidt (Berlin), Andrew Lawler, Mitch Leslie, Eliot Marshall, Virginia Morell, Dennis Normile (Tokyo), Elisabeth Pain (Careers), Charles Piller, Michael Price, Tania Rabesandratana (Barcelona), Joshua Sokol, Emily Underwood, Gretchen Vogel (Berlin), Lizzie Wade (Mexico City) **CAREERS** Rachel Bernstein (Editor), Katie Langin (Associate Editor) **COPY EDITORS** Julia Cole (Senior Copy Editor), Morgan Everett, Cyra Master (Copy Chief) **ADMINISTRATIVE SUPPORT** Meagan Weiland

Creative Director Beth Rakouskas

DESIGN MANAGING EDITOR Marcy Atarod **GRAPHICS MANAGING EDITOR** Alberto Cuadra **PHOTOGRAPHY MANAGING EDITOR** William Douthitt **WEB STRATEGY MANAGER** Kara Estelle-Powers **MULTIMEDIA MANAGING PRODUCER** Joel Goldberg **DESIGN EDITOR** Chrystal Smith **DESIGNER** Christina Aycock **GRAPHICS EDITOR** Nirja Desai **INTERACTIVE GRAPHICS EDITOR** Kelly Franklin **SENIOR GRAPHICS SPECIALISTS** Holly Bishop, Nathalie Cary **SENIOR SCIENTIFIC ILLUSTRATORS** Valerie Altounian, Chris Bickel **SCIENTIFIC ILLUSTRATOR** Ashley Mastin **SENIOR PHOTO EDITOR** Emily Petersen **PHOTO EDITOR** Kaitlyn Dolan **SOCIAL MEDIA STRATEGIST** Jessica Hubbard **SOCIAL MEDIA PRODUCER** Sabrina Jenkins **WEB DESIGNER** Jennie Pajerowski **SENIOR PODCAST PRODUCER** Sarah Crespi **VIDEO PRODUCER** Meagan Cantwell **INTERN** Claire Hogan

Chief Executive Officer and Executive Publisher Sudip Parikh

Publisher, Science Family of Journals Bill Moran

DIRECTOR, BUSINESS SYSTEMS AND FINANCIAL ANALYSIS Randy Yi **DIRECTOR, BUSINESS OPERATIONS & ANALYSIS** Eric Knott **DIRECTOR OF ANALYTICS** Enrique Gonzales **MANAGER, BUSINESS OPERATIONS** Jessica Tierney **SENIOR BUSINESS ANALYST** Cory Lipman **FINANCIAL ANALYST** Isacco Fusi **ADVERTISING SYSTEM ADMINISTRATOR** Tina Burks **DIGITAL/PRINT STRATEGY MANAGER** Jason Hillman **SENIOR MANAGER, PUBLISHING AND CONTENT SYSTEMS** Marcus Spiegler **ASSISTANT MANAGER DIGITAL/PRINT** Rebecca Doshi **SENIOR CONTENT AND PUBLISHING SYSTEMS SPECIALIST** Jacob Hedrick **SENIOR CONTENT SPECIALISTS** Steve Forrester, Antoinette Hodal, Lori Murphy **PRODUCTION SPECIALIST** Kristin Wowk **DIGITAL PRODUCTION MANAGER** Lisa Stanford **CONTENT SPECIALIST** Kimberley Oster **ADVERTISING PRODUCTION OPERATIONS MANAGER** Deborah Tompkins **DESIGNER, CUSTOM PUBLISHING** Jeremy Huntsinger **SR. TRAFFIC ASSOCIATE** Christine Hall **SPECIAL PROJECTS ASSOCIATE** Sarah Dhere

ASSOCIATE DIRECTOR, BUSINESS DEVELOPMENT Justin Sawyers **GLOBAL MARKETING MANAGER** Allison Pritchard **DIGITAL MARKETING MANAGER** Aimee Aponte **JOURNALS MARKETING MANAGER** Shawana Arnold **MARKETING ASSOCIATES** Ashley Hylton, Mike Romano, Tori Velasquez, Jenna Voris, Justin Wood **SENIOR DESIGNER** Kim Huynh

DIRECTOR AND SENIOR EDITOR, CUSTOM PUBLISHING Sean Sanders **ASSISTANT EDITOR, CUSTOM PUBLISHING** Jackie Oberst

DIRECTOR, PRODUCT & PUBLISHING DEVELOPMENT Chris Reid **DIRECTOR, BUSINESS STRATEGY AND PORTFOLIO MANAGEMENT** Sarah Whalen **ASSOCIATE DIRECTOR, PRODUCT MANAGMENT** Kris Bishop **PRODUCT DEVELOPMENT MANAGER** Scott Chernoff **PUBLISHING TECHNOLOGY MANAGER** Michael Di Natale **SR. PRODUCT ASSOCIATE** Robert Koepke **PRODUCT ASSOCIATE** Anne Mason **SPJ ASSOCIATE MANAGER** Samantha Bruno Fuller **SPJ ASSOCIATE** Casey Buchta

DIRECTOR, INSTITUTIONAL LICENSING Iquo Edim **MARKETING MANAGER** Kess Knight **BUSINESS DEVELOPMENT MANAGER** Rasmus Andersen **SENIOR INSTITUTIONAL LICENSING MANAGER** Ryan Rexroth **INSTITUTIONAL LICENSING MANAGER** Marco Castellan, Claudia Paulsen-Young **CUSTOMER SUCCESS MANAGER** Judy Lillibridge **SENIOR OPERATIONS ANALYST** Lana Guz **FULFILLMENT COORDINATOR** Melody Stringer

DIRECTOR, GLOBAL SALES Tracy Holmes **US EAST COAST AND MID WEST SALES** Stephanie O'Connor **US MID WEST, MID ATLANTIC AND SOUTH EAST SALES** Chris Hoag **US WEST COAST SALES** Lynne Stickrod **ASSOCIATE DIRECTOR, ROW** Roger Goncalves **SALES REP, ROW** Sarah Lelarge **SALES ADMIN ASSISTANT, ROW** Victoria Glasbey **DIRECTOR OF GLOBAL COLLABORATION AND ACADEMIC PUBLISHING RELATIONS, ASIA** Xiaoying Chu **ASSOCIATE DIRECTOR, INTERNATIONAL COLLABORATION** Grace Yao **SALES MANAGER** Danny Zhao **MARKETING MANAGER** Kilo Lan **ASCA CORPORATION, JAPAN** Yoshimi Toda (Tokyo), Miyuki Tani (Osaka)

DIRECTOR, COPYRIGHT, LICENSING AND SPECIAL PROJECTS Emilie David **RIGHTS AND LICENSING COORDINATOR** Jessica Adams **RIGHTS AND PERMISSIONS ASSOCIATE** Elizabeth Sandler **LICENSING ASSOCIATE** Virginia Warren

---

MAIN HEADQUARTERS
Science/AAAS
1200 New York Ave. NW
Washington, DC 20005

SCIENCE INTERNATIONAL
Clarendon House
Clarendon Road
Cambridge, CB2 8FH, UK

SCIENCE CHINA
Room 1004, Culture Square
No. 59 Zhongguancun St.
Haidian District, Beijing, 100872

SCIENCE JAPAN
ASCA Corporation
Sibaura TY Bldg. 4F, 1-14-5
Shibaura Minato-ku
Tokyo, 108-0073 Japan

EDITORIAL
science_editors@aaas.org

NEWS
science_news@aaas.org

INFORMATION FOR AUTHORS
sciencemag.org/authors/science-information-authors

REPRINTS AND PERMISSIONS
sciencemag.org/help/reprints-and-permissions

MEDIA CONTACTS
scipak@aaas.org

MULTIMEDIA CONTACTS
SciencePodcast@aaas.org
ScienceVideo@aaas.org

INSTITUTIONAL SALES AND SITE LICENSES
sciencemag.org/librarian

PRODUCT ADVERTISING & CUSTOM PUBLISHING
advertising.sciencemag.org/products-services
science_advertising@aaas.org

CLASSIFIED ADVERTISING
advertising.sciencemag.org/science-careers
advertise@sciencecareers.org

JOB POSTING CUSTOMER SERVICE
employers.sciencecareers.org
support@sciencecareers.org

MEMBERSHIP AND INDIVIDUAL SUBSCRIPTIONS
sciencemag.org/subscriptions

MEMBER BENEFITS
aaas.org/membership/benefits

AAAS BOARD OF DIRECTORS
CHAIR Claire M. Fraser
PRESIDENT Susan G. Amara
PRESIDENT-ELECT Gilda A. Barabino
TREASURER Carolyn N. Ainslie
CHIEF EXECUTIVE OFFICER Sudip Parikh
BOARD Cynthia M. Beall, Rosina M. Bierbaum, Ann Bostrom, Janine Austin Clayton, Laura H. Greene, Kaye Husbands Fealing, Maria M. Klawe, Robert B. Millard, William D. Provine

Science serves as a forum for discussion of important issues related to the advancement of science by publishing material on which a consensus has been reached as well as including the presentation of minority or conflicting points of view. Accordingly, all articles published in *Science*—including editorials, news and comment, and book reviews—are signed and reflect the individual views of the authors and not official points of view adopted by AAAS or the institutions with which the authors are affiliated.

BOARD OF REVIEWING EDITORS (Statistics board members indicated with **S**)

Erin Adams, *U. of Chicago*
Takuzo Aida, *U. of Tokyo*
Leslie Aiello, *Wenner-Gren Fdn.*
Deji Akinwande, *UT Austin*
Judith Allen, *U. of Manchester*
Marcella Alsan, *Harvard U.*
Sebastian Amigorena, *Inst. Curie*
James Analytis, *UC Berkeley*
Trevor Archer, *NIEHS, NIH*
Paola Arlotta, *Harvard U.*
David Awschalom, *U. of Chicago*
Clare Baker, *U. of Cambridge*
Delia Baldassarri, *NYU*
Nenad Ban, *ETH Zürich*
Nandita Basu, *U. of Waterloo*
Franz Bauer, *Pontificia U. Católica de Chile*
Ray H. Baughman, *UT Dallas*
Carlo Beenakker, *Leiden U.*
Yasmine Belkaid, *NIAID, NIH*
Philip Benfey, *Duke U.*
Kiros T. Berhane, *Columbia U.*
Joseph J. Berry, *NREL*
Alessandra Biffi, *Harvard Med.*
Chris Bowler, *École Normale Supérieure*
Ian Boyd, *U. of St. Andrews*
Emily Brodsky, *UC Santa Cruz*
Ron Brookmeyer, *UCLA* (**S**)
Christian Büchel, *UKE Hamburg*
Dennis Burton, *Scripps Res.*
Carter Tribley Butts, *UC Irvine*
György Buzsáki, *NYU School of Med.*
Mariana Byndloss, *Vanderbilt U. Med. Ctr.*
Annmarie Carlton, *UC Irvine*
Simon Cauchemez, *Inst. Pasteur*
Ling-Ling Chen, *SIBCB, CAS*
M. Keith Chen, *UCLA*
Zhijian Chen, *UT Southwestern Med. Ctr.*
Ib Chorkendorff, *Denmark TU*
Amander Clark, *UCLA*
James J. Collins, *MIT*
Robert Cook-Deegan, *Arizona State U.*
Virginia Cornish *Columbia U.*
Carolyn Coyne, *Duke U.*
Roberta Croce, *VU Amsterdam*
Ismaila Dabo, *Penn State U.*
Jeff L. Dangl, *UNC*
Chiara Daraio, *Caltech*
Nicolas Dauphas, *U. of Chicago*
Christian Davenport, *U. of Michigan*
Frans de Waal, *Emory U.*
Claude Desplan, *NYU*
Sandra Díaz, *U. Nacional de Córdoba*
Ulrike Diebold, *TU Wien*
Stefanie Dimmeler, *Goethe-U. Frankfurt*
Hong Ding, *Inst. of Physics, CAS*
Dennis Discher, *UPenn*
Jennifer A. Doudna, *UC Berkeley*
Ruth Drdla-Schutting, *Med. U. Vienna*
Raissa M. D'Souza, *UC Davis*
Bruce Dunn, *UCLA*
William Dunphy, *Caltech*
Scott Edwards, *Harvard U.*
Todd Ehlers, *U. of Tübingen*
Andrea Encalada, *U. San Francisco de Quito*
Nader Engheta, *UPenn*
Karen Ersche, *U. of Cambridge*
Beate Escher, *UFZ & U. of Tübingen*
Barry Everitt, *U. of Cambridge*
Vanessa Ezenwa, *U. of Georgia*
Michael Feuer, *GWU*
Toren Finkel, *U. of Pitt. Med. Ctr.*
Gwenn Flowers, *Simon Fraser U.*
Peter Fratzl, *Max Planck Inst. Potsdam*
Elaine Fuchs, *Rockefeller U.*
Jay Gallagher, *U. of Wisconsin*
Daniel Geschwind, *UCLA*
Ramon Gonzalez, *U. of South Florida*
Sandra González-Bailón, *UPenn*
Nicolas Gruber, *ETH Zürich*
Hua Guo, *U. of New Mexico*
Taekjip Ha, *Johns Hopkins U.*
Sharon Hammes-Schiffer, *Yale U.*
Wolf-Dietrich Hardt, *ETH Zürich*
Louise Harra, *U. Coll. London*
Jian He, *Clemson U.*
Carl-Philipp Heisenberg, *IST Austria*
Ykä Helariutta, *U. of Cambridge*
Janet G. Hering, *Eawag*
Heather Hickman, *NIAID, NIH*
Hans Hilgenkamp, *U. of Twente*
Kai-Uwe Hinrichs, *U. of Bremen*
Deirdre Hollingsworth, *U. of Oxford*
Randall Hulet, *Rice U.*
Auke Ijspeert, *EPFL*
Akiko Iwasaki, *Yale U.*
Stephen Jackson, *USGS & U. of Arizona*
Erich Jarvis, *Rockefeller U.*
Peter Jonas, *IST Austria*
Matt Kaeberlein, *U. of Wash.*
William Kaelin Jr., *Dana-Farber Cancer Inst.*
Daniel Kammen, *UC Berkeley*
Kisuk Kang, *Seoul Nat. U.*
Sabine Kastner, *Princeton U.*
V. Narry Kim, *Seoul Nat. U.*
Robert Kingston, *Harvard Med.*
Nancy Knowlton, *Smithsonian Institution*
Etienne Koechlin, *École Normale Supérieure*
Alex L. Kolodkin, *Johns Hopkins U.*
Julija Krupic, *U. of Cambridge*
Paul Kubes, *U. of Calgary*
Gabriel Lander, *Scripps Res.* (**S**)
Mitchell A. Lazar, *UPenn*
Wendell Lim, *UCSF*
Luis Liz-Marzán, *CIC biomaGUNE*
Omar Lizardo, *UCLA*
Jonathan Losos, *Wash. U. in St. Louis*
Ke Lu, *Inst. of Metal Res., CAS*
Christian Lüscher, *U. of Geneva*
Jean Lynch-Stieglitz, *Georgia Inst. of Tech.*
David Lyons, *U. of Edinburgh*
Fabienne Mackay, *QIMR Berghofer*
Anne Magurran, *U. of St. Andrews*
Asifa Majid, *U. of York*
Oscar Marín, *King's Coll. London*
Charles Marshall, *UC Berkeley*
Christopher Marx, *U. of Idaho*
David Masopust, *U. of Minnesota*
Geraldine Masson, *CNRS*
Jason Matheny, *Georgetown U.*
Heidi McBride, *McGill U.*
C. Robertson McClung, *Dartmouth*
Rodrigo Medellín, *U. Nacional Autónoma de México*
Jane Memmott, *U. of Bristol*
C. Jessica Metcalf, *Princeton U.*
Baoxia Mi, *UC Berkeley*
Tom Misteli, *NCI, NIH*
Alison Motsinger-Reif, *NIEHS, NIH* (**S**)
Suresh Naidu, *Columbia U.*
Danielle Navarro, *U. of New South Wales*
Daniel Nettle, *Newcastle U.*
Daniel Neumark, *UC Berkeley*
Beatriz Noheda, *U. of Groningen*
Helga Nowotny, *Vienna Sci. & Tech. Fund*
Rachel O'Reilly, *U. of Birmingham*
Pilar Ossorio, *U. of Wisconsin*
Andrew Oswald, *U. of Warwick*
Isabella Pagano, *Istituto Nazionale di Astrofisica*
Elizabeth Levy Paluck, *Princeton U.*
Jane Parker, *Max Planck Inst. Cologne*
Giovanni Parmigiani, *Dana-Farber Cancer Inst.* (**S**)
Daniel Pauly, *U. of British Columbia*
Ana Pêgo, *U. do Porto*
Samuel Pfaff, *Salk Inst.*
Julie Pfeiffer, *UT Southwestern Med. Ctr.*
Philip Phillips, *UIUC*
Matthieu Piel, *Inst. Curie*
Kathrin Plath, *UCLA*
Martin Plenio, *Ulm U.*
Katherine Pollard, *UCSF*
Elvira Poloczanska, *Alfred-Wegener-Inst.*
Julia Pongratz, *Ludwig Maximilians U.*
Philippe Poulin, *CNRS*
Jonathan Pritchard, *Stanford U.*
Lei Stanley Qi, *Stanford U.*
Trevor Robbins, *U. of Cambridge*
Joeri Rogelj, *Imperial Coll. London*
Amy Rosenzweig, *Northwestern U.*
Mike Ryan, *UT Austin*
Miquel Salmeron, *Lawrence Berkeley Nat. Lab*
Nitin Samarth, *Penn State U.*
Erica Ollmann Saphire, *La Jolla Inst.*
Joachim Saur, *U. zu Köln*
Alexander Schier, *Harvard U.*
Wolfram Schlenker, *Columbia U.*
Susannah Scott, *UC Santa Barbara*
Anuj Shah, *U. of Chicago*
Vladimir Shalaev, *Purdue U.*
Jie Shan, *Cornell U.*
Beth Shapiro, *UC Santa Cruz*
Jay Shendure, *U. of Wash.*
Steve Sherwood, *U. of New South Wales*
Brian Shoichet, *UCSF*
Robert Siliciano, *JHU School of Med.*
Lucia Sivilotti, *U. Coll. London*
Alison Smith, *John Innes Ctr.*
Richard Smith, *UNC* (**S**)
Mark Smyth, *QIMR Berghofer*
John Speakman, *U. of Aberdeen*
Tara Spires-Jones, *U. of Edinburgh*
Allan C. Spradling, *Carnegie Institution for Sci.*
V. S. Subrahmanian, *Dartmouth*
Ira Tabas, *Columbia U.*
Eriko Takano, *U. of Manchester*
Patrick Tan, *Duke-NUS Med. School*
Sarah Teichmann, *Wellcome Sanger Inst.*
Rocio Titiunik, *Princeton U.*
Shubha Tole, *Tata Inst. of Fundamental Res.*
Maria-Elena Torres Padilla, *Helmholtz Zentrum München*
Kimani Toussaint, *Brown U.*
Barbara Treutlein, *ETH Zürich*
Wim van der Putten, *Netherlands Inst. of Ecology*
Henrique Veiga-Fernandes, *Champalimaud Fdn.*
Reinhilde Veugelers, *KU Leuven*
Bert Vogelstein, *Johns Hopkins U.*
David Wallach, *Weizmann Inst.*
Jane-Ling Wang, *UC Davis* (**S**)
Jessica Ware, *Amer. Mus. of Natural Hist.*
David Waxman, *Fudan U.*
Chris Wikle, *U. of Missouri* (**S**)
Terrie Williams, *UC Santa Cruz*
Ian A. Wilson, *Scripps Res.* (**S**)
Hao Wu, *Harvard U.*
Wei Xie, *Tsinghua U.*
Yu Xie, *Princeton U.*
Jan Zaanen, *Leiden U.*
Kenneth Zaret, *UPenn School of Med.*
Bing Zhu, *Inst. of Biophysics, CAS*
Xiaowei Zhuang, *Harvard U.*
Maria Zuber, *MIT*

EDITORIAL

The will to fight

As the Taliban rapidly crushed US-backed Afghan forces, many politicians, pundits, and military leaders expressed surprise at having overestimated an ally's will to fight and underestimated the enemy's. Similarly in 2014, after the Islamic State (ISIS) routed US-backed Iraqi forces, President Obama endorsed the intelligence assessment that "predicting the will to fight…is an imponderable." That attitude reflects political and military leaders' continual discounting of research, supported and known by many of those leaders, on the importance of sacred values and spiritual strength to the will to fight. It may remain "imponderable"—and attendant security challenges seemingly intractable—so long as it continues to be viewed through a narrow lens of instrumental, utilitarian rationality.

Throughout history, revolutionaries willing to sustain extreme conflict have been "Devoted Actors" fused together by faith in defending or advancing non-negotiable "sacred values," whether religious or secular, like God or country. Insurgents willing to sacrifice for their cause have often prevailed with far less firepower and manpower than opposing state forces that mainly relied on material incentives such as pay and punishment.

One ongoing effort to understand willingness to sacrifice in contexts of conflict is a partnership between Artis International, the University of Oxford's Changing Character of War Centre, and Spain's Universidad de Educación a Distancia and Universitat Autònoma de Barcelona. Supported by the US National Science Foundation and the US Department of Defense's Minerva Initiative, this research has shown that willingness to fight and die among frontline combatants in Iraq from 2015 to 2016 was greatest for those who fought for sacred values and who perceived "spiritual strength" (*ruhi bi ghiyrat*) as more important than material strength (manpower, firepower). From 2017 to 2018, young Sunni Arab men in Iraq's Mosul region who professed belief in core ISIS values of strict Sharia and a Sunni Arab homeland expressed greater willingness to fight and die than did supporters of a democratic or unified Iraq. In Europe, neuroimaging of supporters of armed jihad revealed that willingness to sacrifice for sacred values corresponds to inhibiting brain activity in areas associated with deliberative, cost-benefit reasoning while activating areas involved in rapid, rule-bound moral judgments.

Research indicates that the Taliban and their supporters believe it's worth dying for establishment of an Islamic Emirate—not global jihad—involving territorial sovereignty under Sharia law. Motivation and strength can be found on both sides of conflict. Research found that US Air Force Academy cadets' perception of spiritual strength, tied to group loyalty, was more strongly associated with willingness to fight than was physical formidability. Yet, however strong the esprit du corps of American fighters, no amount of arms or training could ensure its transference to other forces and cultures.

The findings are clear, but uptake by decision-makers is constrained by fear of sunken costs (lives and treasure spent in vain) and reliance on programs with tangible costs, fungible options, and short time horizons—everything the sacred and spiritual are not. Adversaries' and allies' core values must be faced as they are, not as some might wish them to be (and generally not be denigrated, which tends only to backfire). Only then might commonalities and conflicts across cultures, values, and interests be effectively navigated. For example, few outside Afghanistan's urban minority value democracy and women's rights—however worthy of foreign support—and most Afghans oppose the imposing of such values by foreign forces. But most Afghans also consider their homeland sacrosanct and oppose foreign jihadis using Afghanistan to attack other countries. Taliban leadership never consented to Al-Qaeda's 9/11 attack, so the United States might realize a security goal if the Taliban abide by their long-standing offer to prevent Afghanistan from becoming a base of operations against the West.

> "…core values must be faced as they are…"

By failing to recognize limits on the ability to impose on other cultures values that have taken many years to attain gradually in its own culture, the United States and its partners will continue the unsound habit of approaching problems by building up the wrong kinds of allies and armies—weakly modeled in America's image but devoid of the spirit that can only arise from one's own values and cultures. To honor Western democratic values by example, advancing them through financial, media, and moral alliances, and using force only to defend rather than dispense, is a surer way forward.

–Scott Atran



PHOTO: MARION FREGAC

Scott Atran
is an emeritus director of research at the French National Center for Scientific Research, Paris, France; a senior research associate at the Changing Character of War Centre, University of Oxford, Oxford, UK; and adjunct professor at the Ford School of Public Policy, University of Michigan, Ann Arbor, MI, USA. satran@umich.edu

10.1126/science.abl9949

NEWS

IN BRIEF

Edited by **Jeffrey Brainard**



CLIMATE SCIENCE

As the planet dries, species may need escape routes

Eastern Siberia, home to the Char Sands (above), is among the world's regions in which arid areas are forecast to grow substantially by midcentury.

Earth's arid areas will be expanding by the mid–21st century, and the trend could imperil plans to conserve vulnerable species, a forecast says. Ecologist Hanqin Tian of Auburn University and colleagues used data on precipitation and plant water use to calculate the speed and direction of changes in aridity from 1979 to 2016, then projected how rising carbon dioxide levels would affect those trends going forward. By 2050, arid areas may advance at an average of 750 meters annually in most places, and by more than 8 kilometers per year in the driest, his team reported this week in the *Proceedings of the National Academy of Sciences*. Tian says conservationists should study his group's maps of the projected spread to plan corridors that allow vulnerable species, such as amphibians, to migrate to wetter areas.

Researchers faulted over remains

RESEARCH ETHICS | Although anthropologists affiliated with the University of Pennsylvania (UPenn) didn't violate professional ethics, they showed "extremely poor judgment" and "gross insensitivity" in their treatment of the remains of a victim of the 1985 MOVE bombing in Philadelphia, according to an independent report by a law firm released last week. That year, city police bombed the home of MOVE, a Black activist group, killing 11 people. After authorities could not conclusively identify one victim's remains, they sent them in 1986 to Alan Mann, then a physical anthropologist at UPenn. No identification was made, and the remains stayed at the university for decades. According to the investigation, commissioned by UPenn, Janet Monge, a curator at the Penn Museum and Mann's former student, eventually made efforts to return the remains. But she also displayed and discussed them in an online course at Princeton University in 2019, which sparked outrage earlier this year. The remains were returned to the MOVE community in July.

Another AIDS vaccine fails

CLINICAL RESEARCH | An AIDS vaccine approach developed by Johnson & Johnson has joined the long list of candidates that over the past 2 decades failed to prove themselves in large-scale efficacy trials. The company said this week that a placebo-controlled study of its strategy,

PHOTO: PARSHINA OLGA/ISTOCKPHOTO.COM

which combines two different vaccines, in 2600 women in five sub-Saharan African countries found a low level of efficacy. Researchers hope to investigate the limited immune responses elicited, which could help them design better vaccines. A separate efficacy study of a similar strategy designed by Johnson & Johnson is underway in the Americas and Europe in transgender people and men who have sex with men.

Iran replaces nuclear dealmaker

NONPROLIFERATION | Injecting fresh uncertainty into stalled efforts to restore the Iran nuclear deal, the country's new president this week appointed an engineer who has been sanctioned by the International Atomic Energy Agency (IAEA) as the nation's atomic czar. Mohammad Eslami replaces Ali Akbar Salehi, an MIT-trained nuclear scientist and a chief architect of the 2015 agreement, which restrained Iran's nuclear program in return for relief from economic sanctions. "Salehi was such a crucial figure in getting the deal done that I can't see any upside in his departure," says Jeffrey Lewis of the Middlebury Institute of International Studies. In contrast, in 2008 IAEA linked Eslami, then a defense official, to "proliferation-sensitive" activities that could support the development of nuclear weapons.

Afghan wheat researchers escape

WAR | A perilous journey to safety has ended well for 23 Afghan scientists and staff members affiliated with Michigan State University's esteemed Grain Research and Innovation (GRAIN) Project. Late last week, they and their families—75 people altogether—made it onto a flight out of Kabul to Albania, where they are applying for U.S. visas. Representative Elissa Slotkin (D–MI), whose district includes the university's East Lansing campus, worked with Albanian officials and the U.S. ambassador to Albania, Yuri Kim, to ensure the refugees's admission, says GRAIN project director Kurt Richter. "It's a miracle we got them out," says Richter, who worked around the clock for 10 days on logistics. But the success is bittersweet, he says, as they were unable to secure passage for an additional 22 Afghan scientists and staff members associated with GRAIN.

North Korea makes plutonium

NONPROLIFERATION | North Korea appears to be processing plutonium again after a 5-year hiatus. In a 27 August report that calls North Korea's actions "deeply regrettable," the International Atomic Energy Agency noted that a reprocessing lab at the Yongbyon site operated from mid-February to early July. That's long enough to extract three bombs' worth of plutonium from spent fuel generated at Yongbyon's research reactor. The agency believes the reactor came back online in early July after a shutdown of more than 2 years.

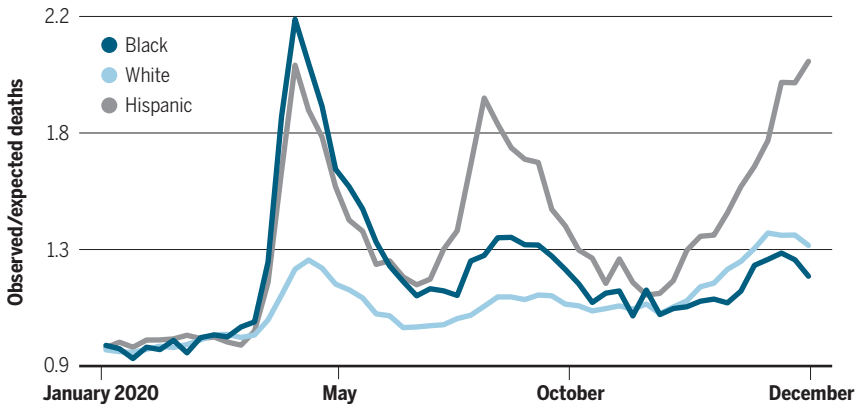
PUBLIC HEALTH

Surge in COVID-19 deaths among older Blacks subsides

A measure of mortality among U.S. Black people ages 65 and over spiked in early 2020 and then declined substantially, researchers reported last month. During the pandemic's first wave, in spring 2020, older Black people had a higher rate of "excess deaths"—those from all causes beyond what would be expected from historical trends—than people of the same age from other ethnic groups. Researchers suspected COVID-19 was the cause. But by the pandemic's third wave, in late 2020, Black people had the lowest rate of excess deaths, lower even than among white people; at the same time, the figures for Hispanic and Asian people had risen, according to research published on 20 August in the *Morbidity and Mortality Weekly Report*. Why older Black people were spared another rise in excess deaths is not clear, but this especially vulnerable population group must have taken effective coronavirus countermeasures, perhaps in response to targeted public health messages, says co-author Jeremy Faust of Brigham and Women's Hospital. He and his colleagues did not present data for 2021.

A respite for one group

Black people aged 65 and older experienced an early, pandemic-driven spike, then a big drop, in rates of "excess deaths" from all causes in 2020.



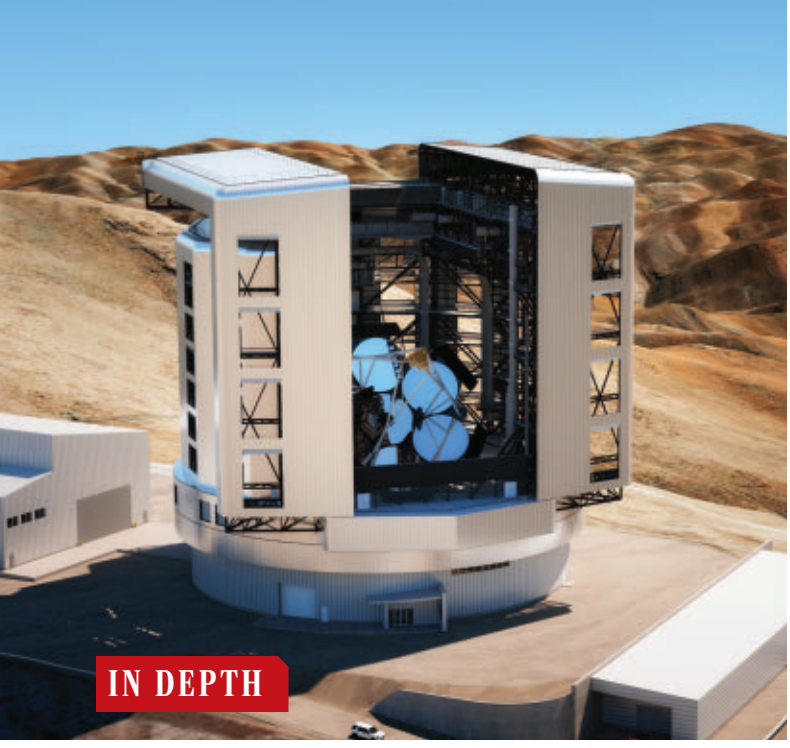
U.S. tackles climate-health nexus

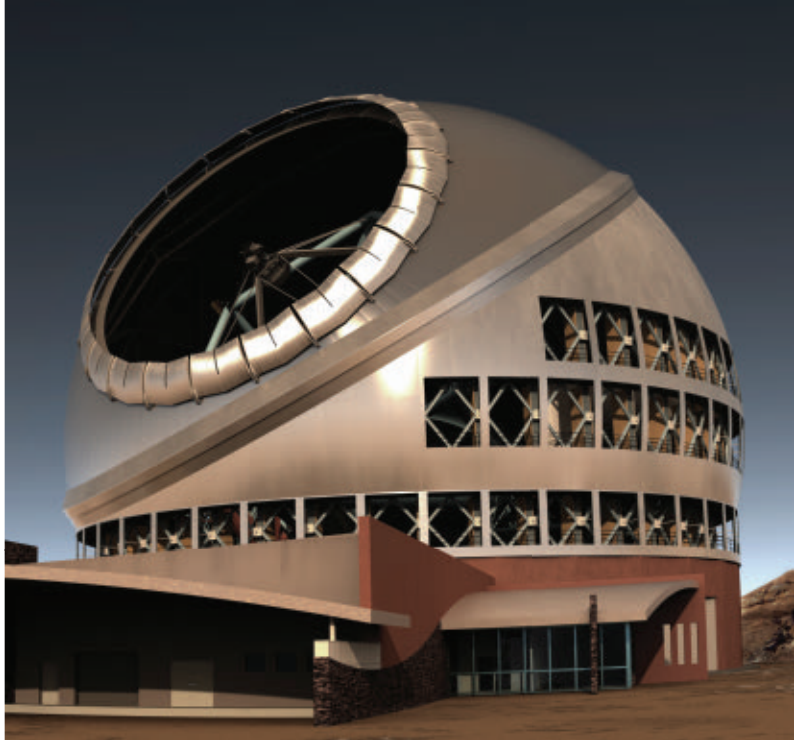
OVERSIGHT | The U.S. Department of Health and Human Services said this week it will establish an Office of Climate Change and Health Equity. It will be the first U.S. government office with a mission to protect the health of people in vulnerable and disadvantaged communities that disproportionately bear the burden of pollution and of natural disasters, such as drought and wildfires, that are worsened by climate change.

Penn apologizes for prison studies

BIOETHICS | The University of Pennsylvania (UPenn) on 20 August apologized for controversial prison experiments carried out by Albert Kligman, a former dermatology researcher on its faculty. To develop medications against acne and other conditions, Kligman, who died in 2010, performed experiments on incarcerated people—many of them Black men—in Philadelphia's Holmesburg Prison between 1951 and 1974. Critics have challenged the work, arguing that research subjects were permanently injured, did not properly consent, and were not adequately compensated. In a statement, medical school Dean Larry Jameson acknowledged the "pain Dr. Kligman's work caused." He promised UPenn would sunset a lectureship and retitle a professorship, both named for Kligman, who was white. UPenn also pledged to finance fellowships for the study of skin disorders among patients of color.

CREDITS: (GRAPHIC) J. BRAINARD/*SCIENCE*; (DATA) *MORBIDITY AND MORTALITY WEEKLY REPORT*





The Giant Magellan Telescope (left) and the Thirty Meter Telescope, shown in artists' concepts, are making a joint pitch for federal funding.

ASTRONOMY

U.S. astronomers weigh fate of giant telescopes

"Decadal survey" could recommend bailout for struggling projects

By **Daniel Clery**

Roughly every 10 years since the 1960s, U.S. astronomers have provided a valuable show of consensus to U.S. funding agencies and Congress by agreeing on which questions and new facilities are critical to the field. But the current "decadal survey," known as Astro2020 and scheduled to be published at any time, faces a particularly knotty question, one that could settle whether the United States stays in the front rank of ground-based observing. Should the National Science Foundation (NSF) come to the rescue of two struggling private projects to build giant optical telescopes in exchange for a chunk of observing time?

The future of the Giant Magellan Telescope (GMT) and the Thirty Meter Telescope (TMT) likely depends on whether the survey recommends that NSF spend what sources put at $1.8 billion to support a recently forged partnership between the projects. If it does, other proposals could lose out, such as a continent-spanning radio array and detectors for neutrinos and other cosmic particles. (Space missions are ranked separately.)

Understandably, astronomers are divided. The GMT-TMT proposal "is critical for the field to thrive," says John O'Meara, chief scientist of the W. M. Keck Observatory. With Europe pushing ahead with its own giant telescope, "If a federal partnership does not happen, I believe that the U.S., which has been the international leader in the field of astronomy for a century, will pass that role on to Europe," says Wendy Freedman of the University of Chicago. But Richard Ellis of University College London, former director of the Palomar Observatory, believes rescuing both telescopes would cost "too much money and would eclipse so many other things."

For ground-based optical astronomers, giant telescopes with mirrors about 30 meters across are the obvious next step after the huge advances made with today's 10-meter scopes. O'Meara says there is no other way to image an Earth-like planet around a red dwarf star, for example. "No matter how tricky you get, the laws of physics overrule you," he says. "Aperture is king."

Telescope designers have been planning such behemoths since the 1990s, and the European Southern Observatory is laying the foundations for its 39-meter Extremely Large Telescope (ELT) on the summit of Cerro Armazones in Chile, with first light due in 2027. But divisions over technology and funding have hampered the two U.S.-led projects. The TMT, to be built in Hawaii by the California Institute of Technology and the University of California (UC), will have a honeycomb mirror built of 492 hexagonal segments. In contrast, the GMT, led by the Carnegie Institution for Science, will arrange six 8.4-meter mirrors around a seventh, giving the Chile-based telescope an aperture of 24.5 meters. The projects had early talks about joining forces, but "there was no desire to abandon their telescopes," Ellis says. "Once money started flowing, it was impossible to merge."

The 2000 decadal survey rated a giant segmented-mirror telescope (essentially the TMT) as the No. 1 U.S. priority in ground-based projects. NSF started discussions with the TMT about partnership in the project, but backed away after the GMT objected. In the 2010 decadal a giant ground-based scope dropped to No. 3, behind a large survey telescope and an instrument innovation program—a decision that essentially killed federal involvement for another 10 years. "That really damaged the momentum of the project," says Garth Illingworth of UC Santa Cruz.

Both projects set out to raise their own funds, but neither has sufficient money so far. The TMT has also faced continued opposition, including legal challenges, from Native Hawaiians to building such a large structure on Mauna Kea, which they consider sacred.

For the current decadal, the projects have finally united into a two-telescope package that would give all U.S. astronomers access to at least 25% of the observing time in exchange for the $1.8 billion (a figure that is

PHOTOS: (LEFT TO RIGHT) GIANT MAGELLAN TELESCOPE/GMTO CORPORATION; TMT INTERNATIONAL OBSERVATORY

not officially confirmed). This deal, dubbed US-ELT, would give U.S. astronomers an advantage over Europeans: front rank telescopes in both the Northern and Southern hemispheres. "The U.S. really does need [giant telescopes] to follow up on other investments on the ground and in space," Illingworth says.

Those include the James Webb Space Telescope (JWST), set for launch later this year. The JWST should revolutionize astronomy by picking out objects including the earliest galaxies with its pin-sharp infrared eyes, but fine-grained spectrometers on the ground will be needed to follow up on some discoveries. Then there is NSF's Vera C. Rubin Observatory in Chile, a survey telescope that from 2023 will carry out a census of the sky nearly every night, identifying thousands of objects demanding closer investigation. "It would be an admission of defeat to let Europe take over this area," Illingworth says.

Others say the U.S. giants are too far behind to avoid that outcome, and the costs are prohibitive. "How can you make a sales pitch for two telescopes when the rest of the world has one?" Ellis asks. Astronomers also worry about the consequences of funding US-ELT for projects such as a next-generation upgrade of the Very Large Array Radio Telescope (ngVLA) in New Mexico into a continent-spanning network of 263 dishes. "The ngVLA is no silly idea, it's something we must do," O'Meara says. The science cases behind upgrading the IceCube Neutrino Observatory at the South Pole and building a next-generation detector for the cosmic microwave background radiation are similarly compelling.

The decadal may also decide that U.S. astronomy doesn't need to pursue an endless quest for ever-greater expanses of glass on the ground. Some astronomers think the greatest potential for discovery lies in modest new telescopes, or upgrades of older ones, with multiobject spectrographs that can scrutinize thousands of objects at once. "It's a different vision," says Ray Carlberg of the University of Toronto, and one that requires a team-based approach more familiar to particle physicists. "So much more science can be done with large groups of collaborators working together on a range of projects," says Jennifer Marshall of Texas A&M University, College Station, project scientist of the proposed Maunakea Spectroscopic Explorer.

The 20-strong decadal committee, after a delay of more than 6 months because of the COVID-19 pandemic, should soon deliver its verdict, bringing joy to some and misery to others. "You need really big pockets" to build giant telescopes, Carlberg says. "The only people who can build them now are nations or consortia of nations." ■

COVID-19

SARS-CoV-2 infection confers greater immunity than shots

Study from Israel, the largest of its kind, also finds infection combined with a single jab is highly protective

By **Meredith Wadman**

The natural immune protection that develops after a SARS-CoV-2 infection is a stouter shield against the Delta variant of the pandemic coronavirus than two doses of the Pfizer-BioNTech vaccine, according to a large Israeli study that some scientists wish came with a "Don't try this at home" label. The newly released data, which have not been peer reviewed, show people who once had a SARS-CoV-2 infection are much less likely than never-infected, vaccinated people to get Delta, develop symptoms from it, or become hospitalized with serious COVID-19.

The study, which examined the medical records of tens of thousands of Israelis from late spring through the first half of August, demonstrates the power of the human immune system and confirms findings from some laboratory studies. But infectious disease experts emphasize that vaccination remains highly protective against severe disease and death. And they caution that whatever its immunological legacy, SARS-CoV-2 infection is extremely risky. "What we don't want people to say is: 'All right, I should go out and get infected, I should have an infection party,'" says Michel Nussenzweig, an immunologist at Rockefeller University who was not involved in the study. "Because somebody could die."

> **"What we don't want people to say is: 'All right, I should go out and get infected.'"**
> **Michel Nussenzweig**, Rockefeller University

The researchers also found that vaccination plus infection yields even stronger protection. People who were infected and received one dose of the Pfizer-BioNTech messenger RNA (mRNA) vaccine were half as likely to become reinfected as those who had the virus and were still unvaccinated. That finding could inform discussion of whether previously infected people need to receive both doses of the Pfizer-BioNTech vaccine or the similar mRNA vaccine from Moderna, as the United States currently recommends. Countries including Germany, France, Italy, and Israel administer just one vaccine dose to previously infected people.

The research impresses Nussenzweig and other scientists who have reviewed the results, posted last week on medRxiv. "It's a textbook example of how natural immunity is really better than vaccination," says Charlotte Thålin, a physician and immunology researcher at Danderyd Hospital and the Karolinska Institute. "To my knowledge, it's the first time [this] has really been shown in the context of COVID-19."

Still, Thålin, who cares for gravely ill COVID-19 patients, most of them unvaccinated, cautions that although showing the benefits of natural immunity, the study doesn't reveal the physical toll of infection. Adds Marion Pepper, an immunologist at the University of Washington, Seattle: "[It] doesn't take into account what this virus does to the body to get to that point." COVID-19 has killed 4.5 million people and left some survivors with the lingering symptoms known as Long Covid.

The new study uses the database of Maccabi Healthcare Services, which enrolls about 2.5 million Israelis. Led by Tal Patalon and Sivan Gazit at KSM, the system's research arm, it found that never-infected people who were vaccinated in January and February were, in June, July, and the first half of August, six to 13 times more likely to get infected than unvaccinated people who were previously infected with the coronavirus. In one analysis involving more than 32,000 people, the risk of developing symptomatic illness was 27 times higher among the vaccinated, and the risk of hospitalization eight times higher. All of these findings were statistically significant.

"The differences are huge but the numbers are small," Thålin cautions. For instance, the higher hospitalization rate in the 32,000-person analysis was based on just eight hospitalizations in the vaccinated group of more than 16,000 people. And the 13-fold increased risk of infection was based on just 238 infections in the vaccinated population—less than 1.5% of that group. There were no COVID-19–related deaths



A Jerusalem health care worker in January prepares a dose of the Pfizer-BioNTech vaccine.

in any of the people studied—a clear sign that vaccines still offer a formidable shield against serious disease.

In another analysis, the researchers compared more than 14,000 people who had a confirmed SARS-CoV-2 infection and were still unvaccinated with an equivalent number of previously infected people who received one dose of the Pfizer-BioNTech vaccine, most of them after being infected rather than before. The team found that the unvaccinated group was twice as likely to be reinfected as the singly vaccinated. (The protection from reinfection did not reach statistical significance when only the infected-then-vaccinated group was considered.)

"We continue to underestimate the importance of natural infection immunity … especially when [infection] is recent," says Eric Topol, a physician-scientist at Scripps Research. "And when you bolster that with one dose of vaccine, you take it to levels you can't possibly match with any vaccine in the world right now."

Nussenzweig says the results in people who have been both infected and vaccinated confirm laboratory findings by his group, his Rockefeller colleague Paul Bieniasz, and others. They've shown that the immune systems of people who develop natural immunity to SARS-CoV-2 and then get vaccinated produce exceptionally broad and potent antibodies against the coronavirus. A preprint posted last month by Bieniasz and his team, for example, reported that people who were previously infected and then vaccinated with an mRNA vaccine had antibodies in their blood that neutralized the infectivity of another virus, harmless to humans, that was engineered to express a version of the coronavirus spike protein containing 20 concerning mutations. Sera from vaccinated and naturally infected people couldn't do this.

Still, says Natalie Dean, a biostatistician at Emory University, "It will be important to see [the Israeli] findings replicated or refuted." She, Topol, and others note important limitations in the study such as the inherent weakness of a retrospective analysis compared with a prospective study that regularly tests all participants to identify new cases and tracks symptomatic infections, hospitalizations, and deaths.

"The biggest limitation in the study is that testing [for SARS-CoV-2 infection] is still a voluntary thing—it's not part of the study design," Dean says. That means, she says, that comparisons could be confounded if, for example, previously infected people who developed mild symptoms were less likely to get tested than vaccinated people because they believed they were immune.

Thålin, for her part, notes the study doesn't involve one crucial group: never-infected, never-vaccinated people. The researchers "are comparing [vaccination] to [natural] immunity but they should be comparing it to no immunity." Given the risks for that group, she says, "The most important thing now is that we vaccinate as many people as possible." ■

PHYSICS

Using mirrors to tame the savage x-ray laser

Scheme that harkens back to ordinary lasers could open new research avenues

By **Adrian Cho**

Twelve years ago, physicists turned on the first x-ray laser, and since then it and several others around the world have proved themselves revolutionary probes of materials and molecules. But the devices, called x-ray free-electron lasers (XFELs), are only partially laserlike. In contrast to the pure, single-wavelength light emitted by conventional lasers, they produce noisy, chaotic beams. Now, physicists are developing a scheme that would enlist perfect diamond mirrors to make the x-ray pulses much more like ordinary laser beams and even more useful.

With two facilities now racing to stage proof-of-principle experiments as early as 2023, would-be users are taking notice. "I'm excited about the potential of this," says Serena DeBeer, a chemist at the Max Planck Institute for Chemical Energy Conversion, who says the beams could be used to study the inner workings of enzymes as they catalyze reactions. But realizing such sophisticated XFELs may take 10 years and won't be easy, warns Harald Sinn, an x-ray physicist at the European XFEL: "There are nightmares ahead."

A conventional laser consists of a light-emitting material sitting between two mirrors. The carefully spaced mirrors form a cavity that resonates with light of the desired wavelength, just as an organ pipe rings with sound of a specific pitch. As the light passes back and forth through the material, it stimulates the stuff to produce more photons of the same wavelength, amplifying the light until a wave of identical photons marching in quantum mechanical lockstep—a laser beam—shines through one mirror, designed to be only partly reflective.

This scheme won't work for x-rays. Physicists lack both an obvious radiating material and, until recently, mirrors able to

PHOTO: AHMAD GHARABLI/AFP/GETTY IMAGES

reflect x-rays at large enough angles to form a resonating cavity. So they use a particle accelerator to fire a bunch of electrons down a vacuum pipe and through long trains of magnets called undulators, which shake the electrons side to side so they radiate x-ray photons. The light then travels along with the electrons and pushes them into microbunches, which wiggle in unison and radiate far more strongly, producing a burst of x-rays just femtoseconds long.

The first free-electron laser flicked on in the 1970s, producing much longer wavelength microwaves. It was not until 2009 that physicists at SLAC National Accelerator Laboratory achieved the feat for "hard" x-rays, when they used the lab's 3-kilometer-long linear accelerator to fire up the world's first XFEL, the Linac Coherent Light Source (LCLS). Other countries have since built a half-dozen XFELs.

As with ordinary laser beams, x-rays from an XFEL arrive in smooth fronts, like ocean waves across a beach. A single XFEL pulse can scatter off a nanometer-size crystal and reveal its atomic structure, even as it blows the crystal to bits. Biologists have used XFELs to determine the structures of myriad proteins and other molecules that won't form crystals big enough to be studied at less intense x-ray sources. But because an XFEL uses fluctuations in the density of the electron beam to begin to generate x-rays, one pulse varies from another in intensity, and each pulse has a wide and randomly distributed spectrum of wavelengths.

To squelch such noise, physicists have turned to an idea kicked around for decades, says Kwang-Je Kim, an accelerator physicist at Argonne National Laboratory. "People talked about it from time to time over drinks, but it was party conversation," he says. "Nobody did any serious calculations" until Kim, SLAC's Zhirong Huang, and others tackled the issues in the 2000s.

The idea is to extract part of the x-ray pulse generated by one bunch of electrons and feed it back to the entrance of the undulators just in time to overlap with the next bunch of electrons. The recirculated x-rays would serve as a seed that causes the electrons to radiate more predictably. In repeated cycles, the x-ray pulses should become very pure and smooth, with a spread of wavelengths only 1/1000th as wide as ordinary XFEL pulses.

The plan requires very special mirrors, however. X-rays blast through most material, but for 100 years, physicists have known that a perfect crystal should reflect x-rays at certain angles, depending on the x-rays' energy and the crystal's structure and orientation, as the x-rays diffract off parallel planes of atoms in the crystal. The crystal also acts as a filter, because it reflects x-rays only in a narrow range of wavelengths. Such crystal mirrors remained an aspiration until 2010, when Yuri Shvyd'ko, an x-ray physicist at Argonne, and colleagues showed small synthetic diamonds can reflect x-rays with 99% efficiency. Fortunately, an XFEL's beam is less than 100 micrometers wide. "You don't need a large crystal," Shvyd'ko says. "You need a perfect crystal of small size."

The scheme also requires a linear accelerator with a high repetition rate, to ensure the x-ray beam encounters a fresh bunch of electrons each time it rounds its circuit of mirrors. SLAC's original accelerator is way too slow, firing 120 times a second. The European XFEL runs at 2.2 million cycles a second, so a cavity just 136 meters long would synchronize the x-rays with the electron bunches. SLAC is installing an accelerator that will run at 1 million cycles per second starting in 2022.

To test the essential elements for a cavity-based XFEL, physicists from Argonne, SLAC, and the Japanese lab Spring-8 plan to use four crystal mirrors to build a 66-meter-long cavity around seven LCLS undulators. By fiddling with SLAC's current accelerator, they will shoot two bunches of electrons separated by 220 nanoseconds through the undulators and hope to show that recirculating x-rays from the first bunch make the second bunch radiate more efficiently. The system should be up and running in 2023, says Gabriel Marcus, an accelerator physicist at SLAC. Researchers at the European XFEL plan to implement a slightly different design by 2024. They hope to send up to 2700 electron bunches through the undulators and watch the laser beam grow stronger and smoother with each pass.

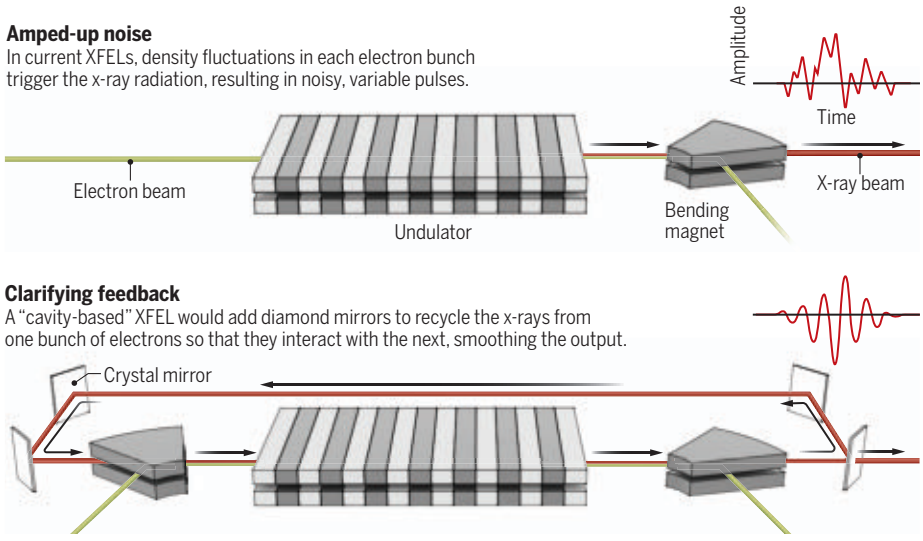
Patrick Rauer, an x-ray physicist at the University of Hamburg who has modeled the European XFEL project on a computer, cautions that the scheme will require extraordinary precision, with the millimeter-size diamonds aligned to a few millionths of a degree. "It's a major problem," Rauer says. "This is going to very difficult." Ilya Agapov, an accelerator physicist at the German Electron Synchrotron laboratory, says that maintaining the alignment will become even harder as circulating x-rays heat the mirrors.

Still, potential users foresee major benefits. For example, Christian Gutt of the University of Siegen has used the European XFEL to study how proteins in solution diffuse and cluster on time scales as short as nanoseconds by studying correlations in the patterns of x-rays diffracted by the proteins. Those patterns would be far sharper with a cavity-based XFEL, he says. "That would be a game changer for us."

With its extremely narrow spectrum, a cavity-based XFEL might even serve to control the quantum states of atomic nuclei much as atomic physicists now control the states of atoms with visible light, says Linda Young, an atomic physicist at Argonne. "It's very wild," she says. All it will take is a few mirrors—and a lot of hard work. ■

The harmony of the mirrors

In an x-ray free-electron laser (XFEL), an undulator magnet shakes a bunch of energetic electrons sideways so they emit x-rays. The x-rays push the electrons into subbunches that, radiating in concert, generate a noisy tsunami of x-rays. A scheme involving x-ray mirrors could produce more consistent, smoother x-ray pulses.



GRAPHIC: V. ALTOUNIAN/*SCIENCE*



Workers removed a statue of Matthew Fontaine Maury from the streets of Richmond, Virginia, in July 2020.

PHOTO: AP PHOTO/STEVE HELBER

SOCIAL JUSTICE

Confederate ties knock ocean science pioneer from pedestals

Institutions move to drop Matthew Fontaine Maury's name

By **Paul Voosen**

Matthew Fontaine Maury simply couldn't give up the fight for slavery. In 1861, the pioneering ocean researcher and former superintendent of the U.S. Naval Observatory joined many others from his rebellious home state of Virginia in the Confederate navy, battling then-President Abraham Lincoln's Union. Sent to the United Kingdom, he developed mines and bought warships. And after the Confederacy lost the war in 1865, Maury remained abroad, seeking to create a "New Virginia" in Mexico, where former Confederates could continue to enslave people.

Despite Maury's racism and avid support for slavery, he remained an honored figure in U.S. oceanography. The U.S. Navy has put his name on a research building, a library, and at least six vessels. His bust welcomed visitors to the Woods Hole Oceanographic Institution (WHOI). His statue looked over Virginia's capital, Richmond, and his name was on lakes, roads, and leafy university campuses—and even programs designed to advance scientists from minority backgrounds.

Now, in the wake of protests against statues and other recognition of Confederate leaders, institutions are moving to stop publicly honoring Maury. Last week, a federal commission charged with renaming military assets that honor Confederates visited the U.S. Naval Academy, where campus leaders and members of Congress have called for the retitling of Maury Hall, a research building. The visit comes in the wake of decisions by numerous governments and institutions to remove Maury's name or likeness from their grounds. "It's all long due," says Rick Murray, deputy director of WHOI, which this year renamed "Maury Lane" after Marie Tharp, an oceanographer famed for mapping the Atlantic Ocean sea floor.

Maury was a controversial figure even in his own time. Many academics reviled him because of his influential books, which promoted often inaccurate ideas about ocean circulation. "Maury was really a popularizer," says Penelope Hardy, a science historian at the University of Wisconsin, La Crosse, and a graduate of the Naval Academy. "That was one thing serious scientists held against him."

After a leg injury derailed a life at sea, Maury became head of the Naval Observatory, where he coordinated the charts and instruments used by U.S. forces. He sought to wean them off dependence on U.K. maps, enlisting merchant ships and whalers to collect and share measurements of wind and currents, which he turned into state-of-the-art maps and visualizations. "He was instrumental in turning the Navy toward formal training and science," says Helen Rozwadowski, a science historian at the University of Connecticut, Avery Point.

In many ways, Maury was an early big data scientist. One notable accomplishment was helping persuade many U.S. allies to gather, standardize, and save ocean and weather measurements taken by ships. Now, those records tell some of the earliest stories about climate change, recording a world before fossil fuel emissions took hold.

Textbooks long described Maury as the first true oceanographer—with little account of his pro-slavery actions. That was a grave oversight, Rozwadowski says, because "his science was intimately tied to his racism and his beliefs in slavery." Although he did not own enslaved people, many of Maury's research initiatives were aimed at finding ways to expand U.S. commerce, and especially slavery, beyond the United States, Hardy and Rozwadowski wrote in an influential commentary published last year in *Oceanography*. He pushed for military explorations of South and Central America, for example, that were designed in part to probe their openness to slavery. "He was a Southern nationalist all the time," says John Grady, a retired journalist who wrote a 2014 biography of Maury.

During the Civil War, Confederate leaders sent Maury to the United Kingdom, where he used his prominence to urge U.K. support for the rebels. He tinkered with electrically actuated floating mines and bought ships for the Confederate navy; one, the *CSS Georgia*, had a long run raiding Union merchants. He also corresponded with French shipyards on the design of Confederate ironclads. "He was sending as much data as he could back across the ocean," Grady says.

After the war ended, Maury appeared to become almost delusional, Rozwadowski says. "Some of his Southern compatriots had a hard time convincing him it was over." Eventually, Maury returned to the United States, serving at the Virginia Military Institute until his death in 1873. Later, Maury's scientific prominence made him "superuseful" to those wanting to downplay the role of slavery in the Civil War and recast it as a noble Lost Cause, says Duncan Agnew, a marine seismologist and historian at the Scripps Institution of Oceanography.

Maury also became "a bit of an icon" for the U.S. Navy, Agnew says. It is now one of the last institutions to operate facilities bearing his name, including a library in Mississippi and an oceanographic vessel launched in 2016. The renaming commission's report is due in October 2022, and those names seem likely to change, Hardy says, if only because "celebrating traitors seems inappropriate" in places used "for training future naval officers." ■

DRUG DEVELOPMENT

Molecular cleanup crew moves outside the cell

Drug candidates now target extracellular proteins, broadening diseases they may treat

By **Robert F. Service**

A hot drug strategy gets cells to dispose of disease-causing proteins with their garbage. But this concept, which involves tagging the troublemakers with a molecule that directs them to the cell's trash compactor, has only worked on undesirable proteins *inside* cells. Now, researchers have developed a trio of closely related techniques to mark damaging extracellular proteins so they are brought inside and similarly eliminated. This twist could lead to new therapies for conditions ranging from autoimmune diseases to bacterial infections. And companies are lining up to pursue outside-in protein disposal.

Protein degradation "has really captured the hearts and minds of people in biopharma," says Carolyn Bertozzi, a chemist at Stanford University. Her group came up with one of the new approaches, and she is a founder of Lycia Therapeutics, a startup pursuing drugs that use the strategy. The latest advances, she adds, "open up new doors to targeting different compounds."

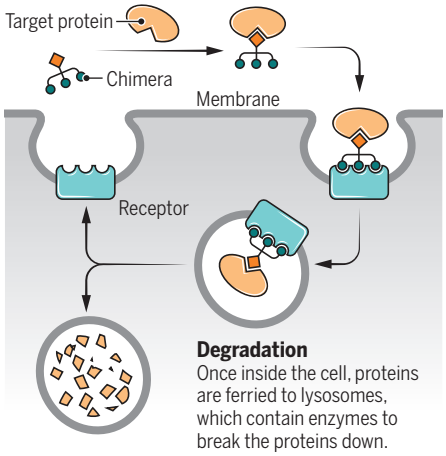
The first doors, for intracellular proteins, opened in 2001. Researchers led by Craig Crews, a Yale University biochemist, reported designing two-part molecules called chimeras, with one end that latches onto an intracellular cancer protein called METAP2. The other end summons a protein called E3 ubiquitin ligase, which adds a chemical tag to METAP2, marking it for destruction by the proteasome, the cell's primary protein recycler. Crews's technique, known as proteolysis-targeting chimeras, or PROTACs, along with offshoots have exploded in popularity, with billions of dollars in investments from pharmaceutical companies hoping to degrade intracellular proteins involved in a wide array of diseases. Eighteen such protein degraders are in or nearing clinical trials, according to an April analysis in *Nature Reviews Drug Discovery*. A few already approved drugs, such as thalidomide, have turned out to work the same way.

Unlike conventional medicines that gum up a disease protein's active site, explains Alessio Ciulli, a biochemist at the University of Dundee, PROTAC drugs remove proteins altogether. That can give degraders longer lasting impact and potentially allow them to disable "undruggable" proteins by binding anywhere on the molecule, rather than having to target an active site.

Still, PROTACs have limitations. Importantly, Bertozzi says, about 40% of proteins in the body work outside cells—on their surface, in the bloodstream, or in the extracellular matrix. With the new methods, those proteins, too, are becoming viable targets for degraders. In August 2020 in *Nature*, Bertozzi and her colleagues reported on LYTACs, or lysosome-targeting chimeras. These molecules bind an extracellular target protein and a cell-surface receptor that pulls the protein into a cell and delivers it to the lysosome, a trash compactor responsible for degrading extracellular proteins.

Two-headed molecule

A molecular chimera helps direct a disease-related protein to a receptor that guides the bundle into a liver cell, where the protein gets chewed up.



But LYTACs, like PROTACs, operate in all tissues, not specific ones, raising the risk of side effects. New refinements make it possible to limit their activity to the liver, the body's main organ for breaking down proteins. In summer 2020, within a few weeks, groups led by Bertozzi, synthetic chemist David Spiegel of Yale, and Weiping Tang, a medicinal chemist at the University of Wisconsin, Madison, all posted preprints on liver-targeted extracellular protein degraders. "It's not an accident that multiple labs converged on the same idea," Bertozzi says.

Bertozzi's and Tang's peer-reviewed papers appeared this spring. On 4 March, in *ACS Central Science*, Tang reported developing chimeras that bind to a growth factor cell-surface receptor that's commonly mutated and overexpressed in tumors. The chimera ferries those proteins to a second binding partner, the asialoglycoprotein receptor (ASGPR), which is abundant on liver cells. The snagged receptors shuttle into the cell and get sent to the lysosome.

On 25 March in *Nature Chemical Biology* online, Bertozzi and her colleagues published a nearly identical strategy. The chimeras developed by both groups rely on a highly specific antibody to snare target proteins. Bertozzi's group also targets extracellular proteins with protein fragments called peptides. The other part of the chimera consists of a trio of sugar molecules that bind ASGPR.

Antibodies are large molecules that are typically expensive to produce and must be delivered intravenously. Peptides also need to be delivered by IV, and enzymes in the body can quickly destroy them. Spiegel's group has devised chimeras that get around those problems. On 19 August in *Nature Chemical Biology* online, the team reports latching onto a target protein using much smaller, druglike molecules while using the sugar group to bind the ASGPR receptor. The researchers then showed, in both cells and mice, that such chimeras could selectively degrade antibodies or cytokines, extracellular proteins known to trigger unwanted inflammation.

Ciulli says extracellular protein degradation is ideally suited to treating autoimmune diseases and amyloid diseases, such as Alzheimer's, where rogue proteins clump together outside cells. Spiegel's paper, he adds, is "a nice addition to the new approach."

Extracellular degradation is taking off, as PROTACs did before it. In June, Lycia raised $50 million to target extracellular disease proteins, and last week, it inked a deal with Eli Lilly and Company worth $35 million up front, with a promise of another $1.6 billion in royalty payments should the drugs meet key milestones. Spiegel has licensed his technology to Biohaven Pharmaceuticals. And Tang says he has been in discussions with biotech and pharma companies about licensing his technology. Getting rid of the cell's trash may have a big payoff in more ways than one. ■

GRAPHIC: D. CAIANIELLO *ET AL.*, *NATURE CHEMICAL BIOLOGY*, 17, HTTPS://DOI.ORG/10.1038/S41589-021-00851-1 (2021). ADAPTED BY C. BICKEL/*SCIENCE*



CALL OF THE WILD

Why most scientists say it's unlikely that SARS-CoV-2 originated from a "lab leak"

By **Jon Cohen**

During the first year of the COVID-19 pandemic, the "lab leak" theory gained little traction. Sure, U.S. President Donald Trump suggested SARS-CoV-2 originated in a laboratory in Wuhan, China—and called it "the China virus"—but he never presented evidence, and few in the scientific community took him seriously. In fact, early in the pandemic, a group of prominent researchers dismissed lab-origin notions as "conspiracy theories" in a letter in *The Lancet*. A report from a World Health Organization (WHO) "joint mission," which sent a scientific team to China in January to explore possible origins with Chinese colleagues, described a lab accident as "extremely unlikely."

But this spring, views began to shift. Suddenly it seemed that the lab-leak hypothesis had been too blithely dismissed. In a widely read piece, fueled by a "smoking gun" quote from a Nobel laureate, a veteran science journalist accused scientists and the mainstream media of ignoring "substantial evidence" for the scenario. The head of WHO openly pushed back against the joint mission's conclusion, and U.S. President Joe Biden ordered the intelligence community to reassess the lab-leak possibility. Eighteen scientists, including leaders in virology and evolutionary biology, signed a letter published in *Science* in May that called for a more balanced appraisal of the "laboratory incident" hypothesis.

Yet behind the clamor, little had changed. No breakthrough studies have been published. The highly anticipated U.S. intelligence review, delivered to Biden on 24 August, reached no firm conclusions, but leaned toward the theory that the virus has a natural origin.

Fresh evidence that would resolve the question may not emerge anytime soon. China remains the best place to hunt for clues, but its relative openness to collaboration during the joint mission seems to have evaporated. Chinese officials have scoffed at calls from Biden and WHO Director-General Tedros

PHOTO: ADAM DEAN/PANOS PICTURES



Scientists have found a distant relative of SARS-CoV-2 in a horseshoe bat they sampled in the countryside in Thailand.

Adhanom Ghebreyesus for an independent audit of key Wuhan labs, which some say should include an investigation of notebooks, computers, and freezers. Chinese vice health minister Zeng Yixin said such demands show "disrespect toward common sense and arrogance toward science." In response to the increasing pressure, China has also blocked the "phase 2" studies outlined in the joint mission's March report, which could reveal a natural jump between species.

Despite the impasse, many scientists say the existing evidence—including early epidemiological patterns, SARS-CoV-2's genomic makeup, and a recent paper about animal markets in Wuhan—makes it far more probable that the virus, like many emerging pathogens, made a natural "zoonotic" jump from animals to humans.

Some of those clues have led Michael Worobey, an evolutionary biologist at the University of Arizona, away from the lab-origin theory. Worobey, who has done groundbreaking work on the origins of HIV and the 1918 flu pandemic, says he was previously neutral, and he co-signed the *Science* letter calling for a more thorough investigation of the lab-leak hypothesis. But like at least one other signatory, he now has second thoughts about that plea, in part because it heightened political tensions. "I think it probably did more harm than good in terms of actually having relevant information flow out of China," he says.

Jesse Bloom, an evolutionary biologist at the Fred Hutchinson Cancer Research Center who spearheaded the *Science* letter, says the lab-origin theory will continue to thrive until the Chinese government becomes more cooperative. "I don't think Chinese scientists are less trustworthy," says Bloom, who has sharply criticized China for attempting to "obscure" data about early COVID-19 cases. "But it's clear that, at least in relation to this topic, they are operating under strong constraints imposed by the government."

"Accidents can only happen when you already have a live virus in culture that *can* leak."

Linfa Wang, Duke-NUS Medical School

AT ITS CORE, the lab-origin hypothesis rests on proximity. A novel coronavirus, genetically linked to bats, surfaced in a city that's home to the Wuhan Institute of Virology (WIV), which has long specialized in studying bat coronaviruses, and two smaller labs that also handle those viruses. One or more lab workers could have become infected by accident, then passed the virus to others. Lab accidents are not unheard of, after all: SARS-CoV, the coronavirus that causes severe acute respiratory syndrome (SARS), has infected researchers as many as six times after the global outbreak of that disease ended in July 2003.

A researcher's infection with SARS-CoV-2 needn't have happened in Wuhan itself. Alina Chan, a gene therapy researcher at the Broad Institute who also co-signed the *Science* letter, cites a study by WIV researchers, published in 2015, that sampled blood from 218 people who lived 1000 kilometers from the city near caves that were home to coronavirus-infected bats. Six of these people had antibodies that suggested prior infections by SARS-related bat coronaviruses, a branch of the family tree that includes SARS-CoV, SARS-CoV-2, and close cousins. Wuhan researchers have visited that area repeatedly and "easily could have picked up something from a human who already carried a human-adapted form of a SARS-related virus," Chan says.

Shi Zhengli, the lead bat coronavirus scientist at WIV, denies that anyone at the lab fell ill around the time SARS-CoV-2 emerged. In an email interview with *Science* in July 2020, she wrote that "all staff and students in the lab" were tested for SARS-CoV-2 and related coronaviruses and were negative.

Still, in January, days before Trump left office, the U.S. Department of State said the "government has reason to believe that several researchers inside the WIV became sick in autumn 2019." And on 23 May, *The Wall Street Journal* reported the existence of an "undisclosed U.S. Intelligence report" that said three WIV researchers "sought hospital care" in November 2019. The story had no details about their illnesses, and some have noted that Chinese hospitals provide care for all ailments, including minor ones.

Virologist Robert Garry of Tulane University finds it improbable that a Wuhan lab worker picked up SARS-CoV-2 from a bat and then brought it back to the city, sparking the pandemic. As the WIV study of people living near bat caves shows, transmission of related bat coronaviruses occurs routinely. "Why would the virus first have infected a few dozen lab researchers?" he asks. The virus may also have moved from bats into other species before jumping to humans, as happened with SARS. But again, why would it have infected a lab worker first? "There are hundreds of millions of people who come in contact with wildlife."

Another data point argues against infected researchers playing a role, Garry says. As the WHO joint mission report spells out, clusters of early COVID-19 cases had links to multiple Wuhan markets around the same time, which Garry says supports the idea of infected animals or animal traders bringing the virus to the city. A lab worker with COVID-19 would have had to make "a beeline not just to one market, but to several different markets," he says. "You can't rule it out, but then why the markets? Why not a soccer game or a concert or 100 other different scenarios?"

But David Relman, a Stanford University microbiome researcher who also co-signed the *Science* letter, questions the "hopelessly impoverished" data on the earliest COVID-19 cases. "I just don't think we have enough right now to say anything with great confidence," Relman says.



A worker processes skins at a fur market in Tongxiang, China. Three species commonly farmed for fur—foxes, raccoon dogs, and minks—can be infected with SARS-CoV-2.

PHOTO: FEATURE CHINA/BARCROFT MEDIA/GETTY IMAGES

Linfa Wang, a molecular virologist at the Programme in Emerging Infectious Diseases at Duke-NUS Medical School in Singapore who has collaborated extensively with WIV on bat coronavirus studies, has a simpler reason for dismissing the lab-leak hypothesis. "Accidents can only happen when you already have a live virus in culture that *can* leak," Wang says. Bat coronaviruses are notoriously hard to grow. Shi told *Science* last year that her lab had more than 2000 bat fecal samples and anal and oral swabs that tested positive for coronaviruses. But the lab had only isolated and grown three viruses over 15 years, Shi said, and none closely resembled SARS-CoV-2. Some have questioned Shi's veracity—she may well be under pressure from the Chinese government—and noted inconsistencies in her statements, but several scientific collaborators outside China have high regard for her integrity.

Wang also discounts reports that WIV has live bats. "Many years back" the lab conducted immune studies on live bats, Wang says, but these were not of the genus *Rhinolophus*—the only one found to harbor SARS-related coronaviruses—which no lab has ever been able to keep alive in captivity.

A great deal of speculation about the pandemic's origin has centered on six men who developed severe respiratory illnesses in 2012 after clearing bat feces from a copper mine in Mojiang, in China's Yunnan province. Three of them died. Lab-origin proponents have suggested the men were infected with a coronavirus, a belief fed by a 2013 master's thesis that provided no direct evidence. That bat virus, they argue, either was SARS-CoV-2 or was turned into it through genetic engineering.

When the miners fell ill, Shi and co-workers were asked to sample bats at the mine, which they did on several occasions. They discovered nine new SARS-related viruses (see sidebar, p. 1076). One of these, dubbed RaTG13, is 96.2% genetically identical to SARS-CoV-2, the closest overall similarity yet found. A loose-knit group whose members call themselves DRASTIC—for the Decentralized Radical Autonomous Search Team Investigating COVID-19—has driven a heated discussion about possible links between RaTG13 and SARS-CoV-2.

Shi has reported that her lab tested blood from the miners and did not find evidence of coronaviruses or antibodies to them. Wang, who helped with these analyses, finds the assertion that the team suppressed evidence of SARS-CoV-2's link to the Mojiang mine preposterous. "We wanted to prove that a coronavirus caused the deaths," says Wang, who grew up in Shanghai but is now an Australian citizen. "If we proved that another SARS-like virus was in humans in China that would have been scientifically brilliant," he says. "It's a *Science* or *Nature* paper. No scientist is going to wait for this to leak."

Even Bloom agrees with that logic. "That's one of the strongest arguments you can make against a lab accident," he says. "On the other hand, I feel like a lot of these questions could be resolved pretty easily by enhanced transparency."

IN THE MOST ELABORATE lab-leak scenarios, SARS-CoV-2 is not a naturally occurring virus, but was created at WIV. That would bring worldwide condemnation on China, but it would also devastate the field of virology. There has been an intense debate over the past decade about the scientific value of "gain-of-function" (GOF) studies, which deliberately create pathogens that are more virulent or more transmissible to humans—or both—than their natural cousins. Some say GOF studies can help identify and thwart future threats, but critics argue the potential benefits don't outweigh the risk of creating and unleashing pandemic pathogens.

Shi has created chimeric viruses in the past to get around the difficulty of growing coronaviruses isolated from bats. In work with Peter Daszak of the EcoHealth Alliance and Wang, described in a 2017 paper in *PLOS Pathogens*, WIV made chi-

meras using the genetic "backbone" of one of the bat coronaviruses her lab could culture and genes that coded for the surface protein, called spike, from newly found coronaviruses.

Scientists disagree about whether this was GOF research. Shi says it was not, because the hybrid viruses her group created were not expected to be more dangerous than the original strains. Anthony Fauci, head of the U.S. National Institute of Allergy and Infectious Diseases, which helped fund the study, told Congress it does not qualify as GOF research under NIAID's guidelines. Relman finds the GOF label "vague and confusing" and instead describes this as "unnecessarily risky research."

Definitions aside, if Shi was creating chimeric viruses, SARS-CoV-2 may have been one of them, lab-leak proponents say. They also note biosecurity measures at the lab were relaxed. In her 2020 *Science* interview, Shi denied conducting chimeric virus experiments beyond those reported in the 2017 paper, but she acknowledged doing some coronavirus studies in biosafety level 2 facilities. That's one level lower than even Ralph Baric, a coronavirus researcher at Duke University who has collaborated with Shi, thinks is appropriate. Shi stressed that the work complied with all Chinese regulations.

Still, many scientists contend that SARS-CoV-2 can't be a lab concoction because no known virus is close enough to have served as its starting material. Some have countered that RaTG13, the virus found in the Mojiang mine, could have been that backbone. That makes no sense, asserts a "critical review" by Garry, Worobey, and 19 other scientists that *Cell* published online on 19 August. More than 1100 nucleotides, the building blocks of RNA, separate the genomes of the two viruses, and the differences are scattered in a way that doesn't suggest deliberate engineering.

"Nobody has the sort of insight into viral pathogenesis to design something as really devious as SARS-CoV-2," Garry says. Three other bat viruses more similar to SARS-CoV-2 than RaTG13 in some key genomic regions are also unlikely to have been used as a template for the pandemic virus, according to the paper.

The "smoking gun" evidence that SARS-CoV-2 was engineered, in the words of virologist and Nobel laureate David Baltimore, has not held up either. Spike has a cleavage site, a spot where a human enzyme named furin cuts the protein, which helps SARS-CoV-2 infect cells. Since early in the pandemic, lab-origin proponents have claimed that no SARS-related bat coronaviruses have this feature, leading to speculation that a lab added the site to a virus so it could infect humans. When retired *New York Times* writer Nicholas Wade made the case for a lab leak this spring, the furin cleavage site, buttressed by Baltimore's provocative words, was an essential part of the argument.

But it's dead wrong, say many coronavirus specialists and evolutionary biologists. The SARS-related coronaviruses are in the beta genus, one of four in the Coronaviridae family. Several members of that genus feature furin cleavage sites, which appear to have evolved repeatedly. And one SARS-CoV-2–related virus, described in a *Current Biology* paper last year by a team led by Shi Weifeng of Shandong First Medical University, has three of the four amino acids that constitute the furin cleavage site, which is "strongly suggestive of a natural zoonotic origin" for SARS-CoV-2, the authors concluded.

Baltimore has backpedaled the statement. He did not know several bat beta coronaviruses have the furin cleavage site, he acknowledged in an email to *Science*. "[T]here is more to this story than I am aware of," he wrote. "The furin cleavage is the most ridiculous stuff," Wang says.

Instead of genetically manipulating a virus, a lab could also have created SARS-CoV-2 by passaging, a technique in which researchers grow a virus in a lab dish or an animal, harvest it, and repeat the process again and again, allowing mutations to accrue. But again, they would have needed to start with a close relative of SARS-CoV-2. There's no evidence that this precursor existed in any lab. And passaging in cell cultures often deletes the furin cleavage site or makes viruses weaker.

Even the U.S. intelligence community during the Trump administration discounted the suggestion that SARS-CoV-2 was "humanmade." The report requested by Biden, which sought input from several groups in the intelligence community, similarly concludes that the virus "was probably not genetically engineered." (It also said there was "broad agreement" that it "was not developed as a biological weapon.")

THE JOINT MISSION REPORT from WHO, which runs more than 300 pages and delves into everything from the viral sequences of the earliest cases to pharmacy sales, has several little-noticed findings that make a natural origin appear more likely than a lab leak, says Kristian Andersen, an evolutionary biologist at Scripps Research who co-authored the recent *Cell* paper with Garry and Worobey. "It wasn't the perfect report," he says, but it was "a great start to a collaborative study on understanding the origin of SARS-CoV-2."

The earliest official announcement about the pandemic came on 31 December 2019, when Wuhan's Municipal Health Commission reported a cluster of unexplained pneumonia cases linked to the city's Huanan seafood market. The WHO report devotes much attention to details about Huanan and other Wuhan markets, but also cautions that their role remains "unclear" because several early cases had no link to any market. But after reading the report, Andersen became more convinced that the Huanan market played a critical role.

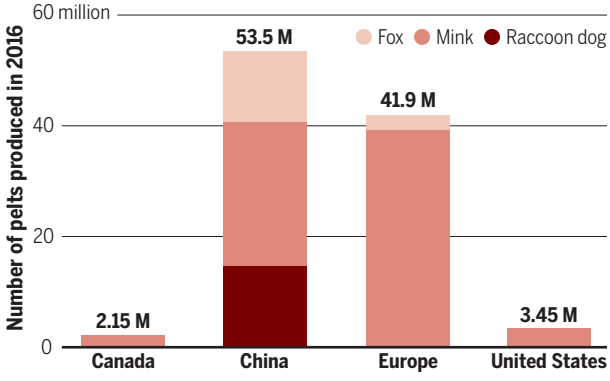
One specific finding bolsters that case, Wang says. The report describes how scientists took many samples from floors, walls, and other surfaces at Wuhan markets and were able to culture two viruses isolated from Huanan. That shows the market was bursting with virus, Wan says: "In my career, I have never been able to isolate a coronavirus from an environmental sample."

The report also contained a major error: It claimed there were "no verified reports of live mammals being sold around 2019" at Huanan and other markets linked to early cases. A surprising study published in June by Zhou Zhao-Min of China West Normal University and colleagues challenged that view. It found nearly 50,000 animals from 38 species, most alive, for sale at 17 shops at Huanan and three other Wuhan markets between May 2017 and November 2019. (The researchers had surveyed the markets as part of a study of a tick-borne disease afflicting animals.)

Live animals can more easily transmit a respiratory virus than meat from a butchered one, and the animals included masked palm civets, the main species that transmitted

Could fur farms be part of the origin story?

China's fur industry, the biggest in the world, processes animals that are potential hosts for SARS-CoV-2.



GRAPHIC: K. FRANKLIN/*SCIENCE*

SARS-CoV to humans, and raccoon dogs, which also naturally harbored that virus and have been infected with SARS-CoV-2 in lab experiments. Minks—a species farmed for fur that has acquired SARS-CoV-2 infections from humans in many countries—were also abundant. "None of the 17 shops posted an origin certificate or quarantine certificate, so all wildlife trade was fundamentally illegal," Zhou and his colleagues wrote in their paper. (Zhou did not respond to emails from *Science*.)

It's unclear why the international members of the WHO joint mission were not told about the live market mammals by their Chinese counterparts. "I'm really disappointed that came out after [the report]," says WHO's Maria Van Kerkhove, who acknowledges contributing to the oversight herself because she mistakenly ignored a draft of the paper that the authors sent her when they first submitted it in October 2020.

Worobey says the paper played a key role in tilting his thinking away from the lab-origin hypothesis. "The fact that early [COVID-19] cases were linked to the market, and that the market was selling what were very likely intermediate hosts?" he says. "All of that is probably trying to tell us something."



Speculation about a lab leak has focused on the Wuhan Institute of Virology, which has studied bat coronaviruses for years.

PHOTO: NG HAN GUAN/AP IMAGES

Worobey suspects that after a SARS-CoV-2 progenitor jumped from animals to humans, it pingponged back and forth, steadily adapting to its new host. This could have happened at the market and gone unnoticed for weeks, as the outbreak only surfaced when several people became severely ill, a relatively rare outcome of a SARS-CoV-2 infection. Or the virus could have first infected animal farmers in remote villages. "If this happened in a small town, it's quite probable it would never have taken off," says William Hanage, an evolutionary biologist at Harvard University. Then animal traders might have brought the virus to markets in Wuhan, a city of 11 million.

Linda Saif, a veterinarian at Ohio State University, Wooster, says China's enormous fur industry is at the top of her list of places to hunt for SARS-CoV-2's precursors. Saif cites a report showing the vast majority of the world's pelts from raccoon dogs and foxes—both canids, a family readily infected with SARS-CoV-2—are from animals farmed or trapped in China (see graphic, p. 1075). The country produces half of the world's mink pelts, too.

SO WHERE TO NOW? Bloom would like more details about the earliest human cases of COVID-19 and says WIV should share bat coronavirus sequences in a database it removed from the internet in September

The hunt for SARS-CoV-2's ancestors heats up

Whether SARS-CoV-2 jumped into humans by way of a lab accident or a natural infection from animals, something close to the virus likely still circulates in an unidentified host. Bats harbor its closest known relatives, but those viruses differ so much from SARS-CoV-2 that many researchers suspect an additional species, or maybe several, served as way stations en route to a human-adapted virus. Scientists are now hunting for these links in the viral chain.

The chain likely begins with *Rhinolophus*, or horseshoe bats, which are infected with a plethora of coronaviruses and are widespread in Asia. "We have an equal chance to find the progenitor virus inside southern China or outside in Southeast Asia, because the bats are similar in the region," says Linfa Wang, an emerging disease specialist at the Duke-NUS Medical School in Singapore.

One widely discussed virus is RaTG13, found in 2013 in an *R. affinis* bat in a Yunnan province mine by Shi Zhengli and colleagues at the Wuhan Institute of Virology (see main story, p. 1072). RaTG13 is closer to SARS-CoV-2 than any virus found to date, but differences in their genetic sequences suggest they're separated by decades of viral evolution.

In the same mine, Shi's group in 2015 discovered eight close cousins of RaTG13—one in *R. affinis* and seven in *R. stheno*—described in a May preprint. In a paper published in *Cell* on 19 August, evolutionary biologist Edward Holmes from the University of Sydney and Shi Weifeng of Shandong First Medical University described two viruses that are closer to SARS-CoV-2 in several genes, but not overall. They were found in bat species elsewhere in Yunnan named *R. malayanus* and *R. pusillus*.

Researchers keep returning to Yunnan for a reason. A 2019 review published by Shi Zhengli's team noted that bat coronaviruses had been found in more than a dozen Chinese provinces, but only the ones from Yunnan could attach to the angiotensin-converting enzyme 2 (ACE2) receptor on human cells, which both SARS-CoV-2 and SARS-CoV—the virus that caused the 2003 outbreak of severe acute respiratory syndrome—depend on to establish infections. "Certain areas in Yunnan province are hot spots for spillover," the authors warned.

Other teams are hunting for origin clues outside China. In Cambodia, investigators found two SARS-CoV-2–related sequences in *R. shameli* bats sampled in 2010. Veasna Duong of the Pasteur Institute of Cambodia has blood, tissue swabs, and fecal samples from other wild mammals in protected areas and the rangers who work there, as well as from people who collect bat guano, which is sold as fertilizer. He's awaiting official permission to study them. Other groups have found SARS-CoV-2–like bat viruses in Thailand and even Japan.

Scientists remain fascinated by the role of pangolins. Studies have found intriguing relatives of SARS-CoV-2 in these ant-eating mammals, which are prized in traditional Chinese medicine for their leathery scales and, as a result, trafficked and endangered. Pangolins confiscated by Chinese customs had viruses that showed up to 92.4% similarity to SARS-CoV-2, and one peculiarity jumped out: Their viral surface proteins have a section, the receptor-binding domain, that strongly attaches to human ACE2 receptors and more closely matches the same area in SARS-CoV-2 than in related bat viruses.

It's unclear whether the pangolins became infected in the wild or by other animals

2019, claiming the site had been hacked. "That could put a lot of this to rest," he says. Sales data from Wuhan markets could help, too. If researchers could trace who farmed or trapped the live animals sold there and who delivered them to the markets, those people could be interviewed and perhaps sampled for evidence of past infections.

In a letter published by *Nature* on 25 August, the international members of the joint mission warned it's time to get on with "phase 2" because the window for some studies is closing. But WHO is reconfiguring the team. It recently announced a new International Scientific Advisory Group for Origins of Novel Pathogens (SAGO) that will provide "rapid advice" to launch the follow-up studies described in the mission report, but also study the origins of future outbreaks. The Chinese government has shown no signs it will welcome SAGO members, but Wang is hopeful it will have a change of heart: "In an ideal world, we need a Chinese collaboration."

Chinese scientists are conducting their own studies into potential natural origins, but few outside the country know details. "Unfortunately, finding out what is being done is getting harder by the day because the lab-leak stuff has turned COVID origins into a major political weapon," says one Western researcher who asked not to be identified. "My colleagues in China are nervous and feeling great pressure."

China has been pushing the theory that the virus came from another country—maybe brought in on frozen food, or, according to baseless propaganda, concocted at a U.S. military lab. "It's comical," Worobey says. "The big picture here is China is doing everything it can to push the narrative that this pandemic started outside of China." He suspects that while rejecting the lab-leak theory, the Chinese government is also unenthusiastic about pursuing a natural origin, fearing that proof would expose China to further blame for a pandemic even if the discovery exonerated Chinese scientists. "I think at some point they thought, here's the strategy: We try to muddy the waters," he says.

But even without China's cooperation, there are ways to move ahead. Some studies elsewhere have already yielded intriguingleads.Researchershavefoundcoronaviruses in bats in neighboring countries that suggest evolutionary pathways from an ancestor of SARS-CoV-2 to the pandemic virus. More clues may come from studies in Southeast Asia of wild pangolins—the only other species to date found to harbor a close SARS-CoV-2 relative.

Researchers can also hunt for cases outside of China that predate the December 2019 outbreak. One possibility, Wang says, is to check the blood of Wuhan visitors or residents who were in the city in the months before, including the 9000 athletes from more than 100 countries who attended the Military World Games there in October 2019. (A new antibody assay from his lab, he says, can distinguish between SARS-CoV-2 and related viruses that may have preceded it.)

The search will never lead us to patient zero, the first person to be infected by SARS-CoV-2, Hanage says. "Humans are looking for a story," he says. "They want Columbo to come in and just somehow get somebody to confess or show what actually happened." Instead, there are "possible stories" about SARS-CoV-2's origin—some more probable than others—and stories that can be excluded, Hanage says. "And the space of possible stories in which there was a natural origin in or around the markets is much larger than the space of possible origins in which the Wuhan Institute of Virology is involved." ■

With reporting by Kai Kupferschmidt.

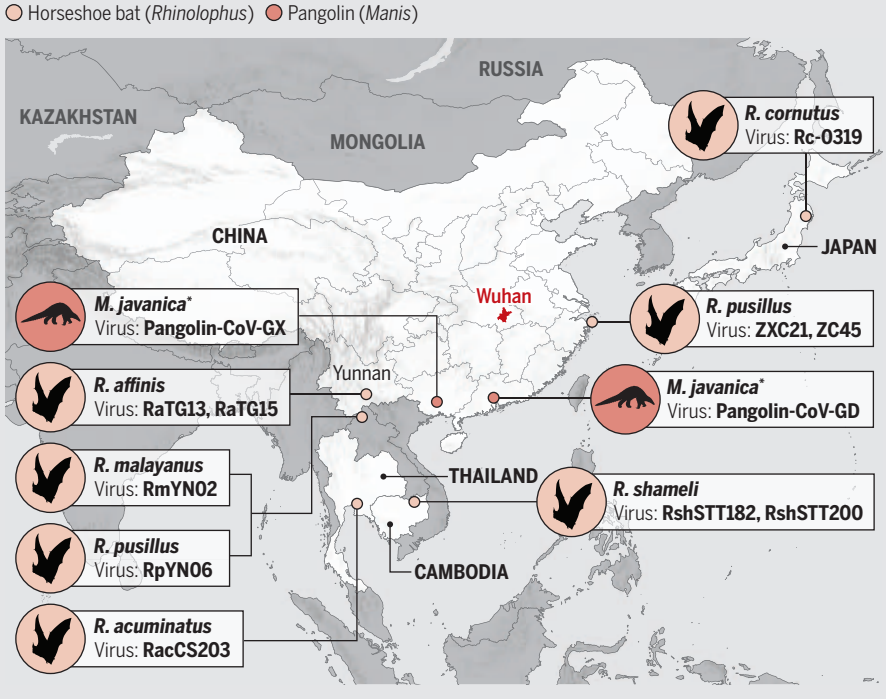
trafficked with them, says molecular virologist Tommy Lam of the University of Hong Kong, who helped identify some of these viruses. Lam suggests a bat coronavirus could have spread to pangolins, acquired mutations that made it a better fit for human ACE2, moved to other species, and then mutated into the precursor of the pandemic virus. A wide range of species, from raccoon dogs and minks to pigs, cows, and cats, can be infected with SARS-CoV-2 and could have been the host that infected humans.

Infectious disease epidemiologist Gregory Gray of Duke University has long-standing collaborations in China, Malaysia, and Vietnam that he hopes will start SARS-CoV-2 origin studies once the pandemic abates—and political sensitivities subside. He is most keen to find out whether people who have "intense exposure" to domestic or wild animals, including animal market workers, have telltale antibodies to novel coronaviruses. "Those are rare studies and they're hard to do," Gray says, because people are "afraid that we might find something that would harm their businesses."

None of these studies may uncover the origin of SARS-CoV-2 anytime soon, Lam says. But, he adds, "Those who are not patient are not really interested in the truth." —*J.C.*

Meet the relatives

Researchers have found a host of coronaviruses similar to SARS-CoV-2 in bats and pangolins in China and neighboring countries. The closest relative, RaTG13, was found in a bat living in a cave in Yunnan province.



*Pangolins were confiscated by customs officers in China but were captured elsewhere.

GRAPHIC: K. FRANKLIN/*SCIENCE*



BOOKS *et al.*

FALL BOOKS

A sampling of seasonal science books

A botanist's quest for new medicines takes her deep into the Amazon. A computer scientist and a sci-fi author peer into the future of artificial intelligence. An anthropologist confronts changing attitudes about death. From an ambitious road map for the future of physics to a whirlwind tour of animal outlaws, the books on this year's fall reading list—reviewed by alumni of the AAAS Science and Technology Policy Fellowship program—challenge readers to see the topics under consideration in a new light. Join a neurologist on a journey to understand the myriad causes of psychogenic illnesses, gain a better grasp of the origins of the climate crisis, and confront the ways ideas about gender have shaped innovation, all with the help of the books reviewed below. **—Valerie Thompson**

The Sleeping Beauties

Reviewed by **Susan Douglas**[1]

Psychosomatic illnesses, in which symptoms such as pain, tics, and seizures occur in the absence of a discernible physical cause, frequently originate from, and are sometimes aggravated by, emotional stress. In *The Sleeping Beauties*, neurologist Suzanne O'Sullivan compassionately explores the range of issues and attitudes that reinforce these peculiar phenomena, immersing herself in the cultural contexts of the cases she presents and describing factors, including family roles, cultural reactions, and traumatic experiences, that contribute to psychogenic illness.

O'Sullivan begins with a story from Sweden, where Sophie, a 9-year-old girl, has been in a psychosomatic coma for longer than a year. Sophie, an asylum seeker from Russia, had witnessed her parents' horrific encounters with the local mafia, so a psychosomatic response made a certain amount of sense to her physicians. When more than 200 other children succumbed to the same strange "sleeping sickness," later renamed "resignation syndrome," however, things became more difficult.

O'Sullivan eventually witnesses the syndrome herself in a pair of sisters, Nola and Helan, whose family, like Sophie's, is seeking asylum in Sweden. She describes not only the children's symptoms but also the circumstances of their lives and the behaviors of all persons involved, noting that "a whole lifetime had led Nola and Helan to this place."

Later, O'Sullivan travels to Port Arthur, Texas, to see another group of asylum seekers, members of the Miskito, an Indigenous tribe from the Mosquito Coast, which runs along the coast of Nicaragua and into Honduras. Here, she meets individuals suffering from a condition known as "grisi siknis," which manifests solely in

ILLUSTRATION: GABY D'ALESSANDRO



this community and begins "innocuously enough" but eventually leads to convulsions and a visual hallucination wherein sufferers report being "visited by a frightening stranger—a dark figure, usually wearing a hat—who [comes] to carry the victim away."

Near the end of the book, O'Sullivan describes her own experience treating psychogenic illness, relaying the story of Sienna, a young woman who was convinced that she was experiencing epileptic seizures even though there was no clinical evidence that she was suffering from a seizure disorder. O'Sullivan recounts how she attempted to help Sienna and her parents understand that there was no evidence for a seizure disorder and encouraged them to explore other stresses that might be contributing to the seizure-like episodes. Sienna eventually relents, accepting that her symptoms are the result of dissociation—a normal phenomenon regularly experienced by most people—and not seizures and agreeing to see a psychologist to help retrain her oversensitive nervous system, but not before asking O'Sullivan for a letter requesting that special academic accommodations be made for her condition.

Against her better judgment, O'Sullivan writes the letter, but she later wishes she had pushed back. "[T]he lines between behaviour and illness, normal and abnormal—even the demarcation between disease and health—have become so blurred that it is possible to give an illness category to almost any person," she notes. "Once that is done, a person becomes a patient."

The Sleeping Beauties and Other Stories of Mystery Illness, *Suzanne O'Sullivan*, Picador, 2021, 336 pp.

Fuzz

Reviewed by **Katherine E. Himes**[2]

In her latest book, *Fuzz: When Nature Breaks the Law*, Mary Roach seeks to answer a question that has confronted humankind for centuries and evades resolution: What is the proper course when wildlife breaks laws intended for people?

Over 2 years, Roach dutifully investigated the myriad dimensions of human–wildlife conflict, researching related science, law, history, and cultural practices and meeting with wildlife managers, conflict specialists, forensics gurus, attack experts, poison testers, and others in the US, Canada, India, New Zealand, and Vatican City. "Felony crimes," such as murder, assault, and robbery, committed by the likes of bears, elephants, leopards, monkeys, cougars, legumes, and trees encompass the first half of the book, with more commonplace violations—vandalism and jaywalking by birds and other lawbreaking species—revealed in the second half.

Each chapter is packed with the results of these detailed investigations. Roach uses footnotes to add both depth and lightness to the topic at hand by capturing misfit studies, asides, and hilarious tangents. Here, the reader learns the average weight of Asian elephant droppings (4 pounds), is introduced to a moose taser prototype, and more.

The book opens with the first records Roach can find of wildlife on trial. In 1545, vintners legally prosecuted weevils, while caterpillars were summoned to court in 1659 for trespassing and damaging orchards.

Having laid out a historical context for human–wildlife conflict, Roach's first stop is a forensics training seminar in a Reno casino conference room, taught by the British Columbia Conservation Officer Service and hosted by the Nevada Department of Wildlife, where the training manikins, meant to simulate bodies attacked by animals, are named after Canadian beers—an



Human encroachment on wild habitats can precipitate and exacerbate human–wildlife conflict.

effort on the part of the trainers to lighten the otherwise grim mood. In the classroom, she and other participants learn to identify species-specific attack patterns and integrate victim and animal evidence.

Later, in India, Roach discovers the difficulties of managing aggressive monkeys that, among other antics, enter hospitals and pull IVs out of patients to suck on the glucose. Government agencies debate jurisdiction (are the monkeys wild or not?), attempt to effectively sequester the offenders in a wildlife sanctuary, and grapple with accommodating religious beliefs (can fines be administered if monkeys are at a temple?).

Roach relates examples of how science has informed, and continues to inform, decision-making with respect to human–wildlife conflict. She elucidates how experts have found that translocating repeat offenders can increase rather than decrease an animal's aggressive behavior; the difficulty of addressing troublesome monkey populations owing to the complexity of administering birth control to such groups; and the importance of establishing guidelines for the use of CRISPR to control rodents. Rather than requiring nature to bend to human rule, peaceful coexistence may be possible, argues Roach.

Yet the book rarely steps back to examine larger factors at play, and some animal outlaws receive a great deal of attention while others receive none. The actions of avian offenders extend over three chapters, for example, while the various crimes of mosquitoes and ticks go unmentioned. That said, *Fuzz* is a refreshing addition to the nonfiction science genre, illuminating a historically niche topic for a broader audience and helping to bring it to the fore.

Fuzz: When Nature Breaks the Law, *Mary Roach*, Norton, 2021, 320 pp.

Our Biggest Experiment

Reviewed by **Gifford J. Wong**[3]

Alice Bell's *Our Biggest Experiment* reads like a "chocolate box of a book"—to borrow a phrase from the author—regaling readers with a curated history of the people, science, politics, and technology that have intersected with the current climate crisis. She deftly weaves subtle and lesser-known details about the brilliant (and sometimes eccentric) individuals who have worked out how to measure and describe what we, as a species, have wrought upon Earth. Bell's focus is on the complex human story of discovery and realization, ensuring that readers appreciate both the impressive intellectual achievements that have punctuated this story and the thorny threads of racism, sexism, and colonialism that are intertwined with them.

The book begins with American amateur scientist Eunice Newton Foote, who, in 1856, published the results of an elegant experiment involving two glass cylinders filled with various substances (dry air, moist air, and carbon dioxide), a sunny window, and a thermometer. The cylinder filled with carbon dioxide became noticeably warmer than either dry or moist air, leading Foote to conclude that "an atmosphere of that gas would give to our earth a high temperature." Although her work was presented at that year's annual meeting of the American Association for the Advancement of Science (AAAS) by Joseph Henry—3 years before John Tyndall's important work identifying the gases responsible for the greenhouse effect—her contribution to our overall understanding of the climate crisis has only recently been rediscovered.

A century after Foote's observations were made public, oceanographer Roger Revelle—seen now as one of the pioneering researchers in the study of human influence on the atmosphere and climate—testified before Congress regarding the issue of burning fossil fuels and increasing atmospheric carbon dioxide. "Here we are making perhaps the greatest geophysical experiment in history, an experiment which could not be made in the past because we didn't have an industrial civilization and which will be impossible to make in the future because all the fossil fuels will be gone," he observed at the 1956 hearing. At this point, notes Bell, Revelle and his colleagues were more interested in the intellectual opportunity presented by this planetary-level experiment than in mitigating it.

It took another researcher, and the note he wrote while in a cab heading to a congressional hearing, to help move the conversation toward a push for public action. Climate modeler James Hansen had been invited to testify before the Senate in 1988, a year experiencing "yet another heatwave in the USA, yet another 'worst drought since the dustbowl' summer." While the former NASA researcher's testimony was clear—he highlighted "a cause and effect relationship between the greenhouse effect and observed warming"—it was the contents of the note to himself that he used in response to a reporter's question that helped shape headlines: "It is time to stop waffling…the greenhouse effect is here and is affecting our climate now."

"The story of the climate crisis has always been a choose your own adventure and continues to be," notes Bell. As such, she remains optimistic that there is a feasible path forward, arguing that we must act now: "We owe it not just to future generations who'll inherit whatever we do to this Earth, but also to the memory of those who came before, who gave us something to work with."

Our Biggest Experiment: An Epic History of the Climate Crisis, *Alice Bell*, Counterpoint Press, 2021, 288 pp.

PHOTO: ISTOCK.COM/GODDARD_PHOTOGRAPHY

AI 2041

Reviewed by **Carolyn Wong Simpkins**[4]

AI 2041 builds a multilayered view of a future where artificial intelligence (AI)–enabled technologies become embedded in our lives, for good or ill. The book braids together a series of fictional short stories set in the year 2041 with essays that make explicit the warnings and prophecies illustrated in each story and provide an introduction to the underlying technologies for nonexperts. The book's coauthors split the writing duties according to their background, with Kai-Fu Lee, a Taiwanese-born American computer scientist with a long history of pioneering work in AI, writing the nonfiction essays, and Chen Qiufan, a prolific Chinese science fiction author, writing the stories.

The collection ranges broadly and imaginatively. In "The Golden Elephant," for example, Qiufan explores the perils of sharing one's entire digital existence with an algorithm in exchange for insurance discounts. In "Gods Behind the Masks," he probes deepfake technology and the power wielded by those who create misleading media. And in "The Holy Driver," he interrogates how AI will change human work, painting a vision of the future in which human rescue drivers must be deployed in emergency situations that cannot be handled by self-driving AI. If you read each story sequentially, you will find that Lee's accompanying essays build on one another to provide the reader with an accessible introduction to the various techniques, advances, and subfields that lie beneath the blanket term "AI"—from machine learning and deep learning to convolutional neural networks and generative adversarial networks and more.

As with any collection of short stories, some will likely resonate more than others. If, like me, you struggle to connect with one, skip ahead and circle back later. My personal favorites came later in the book, beginning with the fourth story, "Contactless Love," which imagines a future in which relationships are shaped by society's coevolution with a now-endemic COVID-19 crisis and we have become accustomed to dealing with ever-emerging variants. There was something strangely comforting and yet also discomfiting in the protagonist's extreme isolation from physical contact and in seeing how well this is enabled by future versions of some of the technologies that have been deployed over the past 18 months. In a future shaped by COVID-19, robots deliver packages, and other robots open and disinfect the contents. Real-time data track infection risk by neighborhood, block, and even at the individual level. New variants are identified and tracked, and new vaccines and treatments are continuously being developed. Against this intriguing backdrop, a well-crafted story takes the protagonist on a hero's journey, overcoming a series of obstacles in a quest for love.

For those who have worked in AI, or indeed in any field in which personal data are collected, analyzed, and put to use, it is likely that the moral issues and cautions presented throughout the book are ones that come up with some regularity. Regardless of one's professional engagement with the topic, however, this book serves as an imaginative invitation to consider the potential for harm that may arise from such projects, however unintended.

AI 2041: Ten Visions for Our Future, *Kai-Fu Lee and Chen Qiufan*, Currency, 2021, 480 pp.

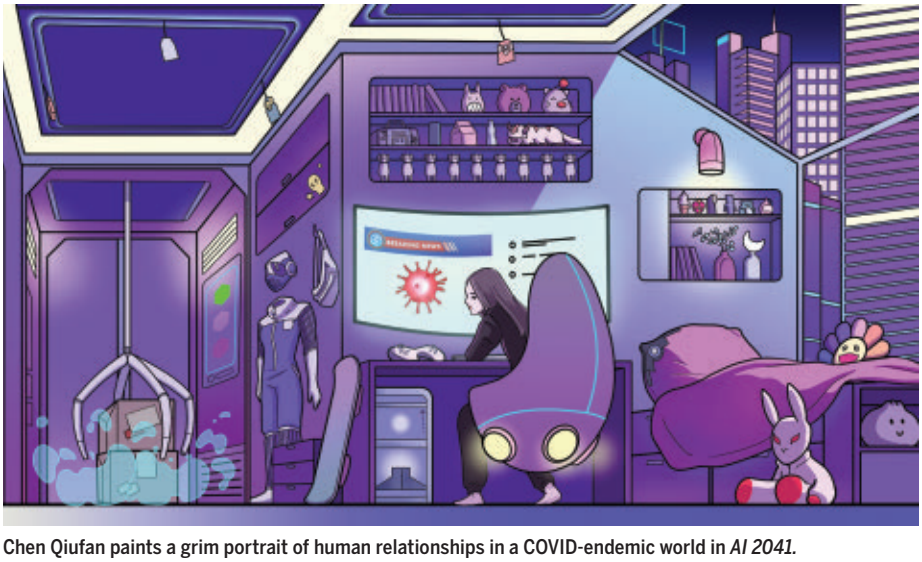


ILLUSTRATION: AVERY OTA/© RANDOM HOUSE

Chen Qiufan paints a grim portrait of human relationships in a COVID-endemic world in *AI 2041*.

American Afterlives

Reviewed by **Rosemarie Szostak**[5]

What do Americans want to be done with their bodies when they die? What do they think happens to an individual after death? These two questions open anthropologist Shannon Lee Dawdy's touching and beautifully written examination of American death practices in the 21st century.

Every society throughout history has developed rituals to deal with death. Deathcare for Americans, ritualized over the past 100 years, most often consists of some sort of preparation of the body, a scheduled viewing for family members and friends, and a final disposition in a concrete cemetery vault. Ritual specialists traditionally manage this process for the grieving family.

According to Dawdy, however, this practice is dying its own rapid death in the 21st century. Today, more than 60% of Americans say that they want to be cremated rather than embalmed and entombed. Death is being reinvented in the US on three levels: how human remains are disposed of, the types of rituals practiced by the living, and the ways people think about the afterlife. This book explores all three.

Natural burial practices are all the rage. Many people now request burial in a simple shroud or cardboard box or to be planted with a tree. Dawdy recounts how she allowed herself to be wrapped in a shroud and lowered into a grave to show the process of a natural burial as part of a recent documentary film (*1*). Others opt for a more theatrical exit, asking that their remains be mixed with fireworks and ignited during a memorial service.

Dawdy cites 9/11 as a pivotal moment in the evolution of death practices for those whose bodies are never recovered. In the aftermath of the terrorist attacks that claimed the lives of 2977 people, a makeshift memorial wall near the World Trade Center became a spontaneous reaction to the grief of the loss of so many lives, embodying a new way of memorializing the dead. More people today interact with the dead than before, she notes. Toys, coins, souvenirs, and even cans of beer are regularly left on graves or memorials visited by loved ones. The COVID-19 pandemic, which struck while Dawdy was writing this book, has likewise changed grief and death practices in ways that will undoubtedly be the focus of studies for many years to come.

Surprisingly, when it comes to what happens after death, Dawdy finds that Americans are moving toward a more spiritual attitude about the afterlife. Many no longer perceive a corpse as mere dead matter but feel that it contains an essence of the deceased person and a potential source of both spiritual and



Ethnobotanist Cassandra Quave (right) interviews a local woman in the Albanian village of Borje in 2019.

ecological regeneration. The most striking statement on this topic is made by a young man named Dakota whom Dawdy meets in a cemetery, where the teen is helping to tend a graveside garden. When asked about the afterlife, Dakota says, "I truly don't know, but I do hold the law of thermodynamics to be very true—that energy cannot be created nor destroyed, so our energy—our entity—itself lives forever after death."

REFERENCES AND NOTES

1. S. L. Dawdy, D. Zox, *I Like Dirt* (Zox Films, 2020).

American Afterlives: Reinventing Death in the Twenty-First Century, *Shannon Lee Dawdy*, Princeton University Press, 2021, 272 pp.

The Plant Hunter

Reviewed by **Erica C. Jonlin**[6]

Inspired by her interest in medicine, her love of the outdoors, and an undergraduate trip to the Peruvian Amazon that awoke in her a passion for medicinal plants, ethnobotanist Cassandra Leah Quave has dedicated her life to the search for novel, efficacious antibiotics. Working at the interface of anthropology, botany, and chemistry, Quave recalls the highs and lows of her unusual scientific career in her engaging new memoir, *The Plant Hunter*, recounting her childhood in rural southwest Florida, field studies in remote villages of Italy and the Balkans, and the health challenges she has faced that have helped motivate her research.

Quave's earliest discoveries began when she was a graduate student, working in the fertile soil of the extinct volcano Monte Vulture in Italy. Here, Quave collected the leaves of sweet chestnut trees (*Castanea sativa*), long used by local healers to treat infections. Like all of the plants Quave studies, chestnut leaves contain hundreds of compounds. Quave explains the many steps her lab takes to fractionate and investigate plant extracts, testing each for antimicrobial properties. With time, many painstaking experiments, and dogged determination, Quave's lab zeroed in on the anti-infective compounds that were indeed contained in the leaves.

Making friends and finding like-minded scientific collaborators is, in some ways, the easier part of Quave's career journey. The harder part has proven to be getting recognition and funding for her work. Stacked against Quave are grant reviewers' questions about the viability of finding plant-derived drugs, as well as the usual hurdles faced by female scientists. Writing about the latter challenge, Quave recounts her interactions with a number of characters who will be familiar to many who have pursued a career in academia, including "Professor Toad," a faculty member who cannot believe Quave is a principal investigator and who insists on mansplaining natural products chemistry, one of her areas of expertise; "Professor Creeper," an older male professor who makes a pass at her in a crowded room; and "Professor Snake," who makes it his mission to bully and harass women scientists, including Quave, via public confrontation and cruel reviews of their work. Throughout it all, Quave remains determined, resourceful, and cognizant of the alliances that have enabled her life's work, including her partnership with her remarkable husband, Marco—a man who shares her love of the natural world, who can and does fix any machine, and who quits his own job to stay at home with the couple's children while Quave works to get her career off the ground.

Quave exhibits a deep humanity and humility in her writing. This, along with her thrilling adventures—often with children in tow—spurs the reader on. In the end, she succeeds in demonstrating that plants are an underutilized resource for drug discovery and in communicating the many joys and challenges that accompany a career in science.

The Plant Hunter: A Scientist's Quest for Nature's Next Medicines, *Cassandra Leah Quave*, Viking, 2021, 384 pp.

Fear of a Black Universe

Reviewed by **Kanwal Singh**[7]

One of the great joys of modern physics for the expert and the novice alike is contemplating the common sense–shattering insights from relativity and quantum mechanics. As an artist friend of mine once said, "Who needs science fiction when the real stuff is so wild?" In *Fear of a Black Universe*, physicist Stephon Alexander contends that the world of research physics would do well to take a lesson from the art world's embrace of outsiders like Basquiat and Banksy. Beginning with Einstein's and Schrödinger's more fanciful thought experiments, he argues that free thinking is the way to make progress in our understanding of the Universe. Grinding out equations and applying logical principles to problems may give us a foundation of knowledge, he maintains, but such practices are not all there is to physics.

The book is divided into two sections. In the first part, Alexander attempts to do three things at once: explain the funda-

PHOTO: SUSANNE MASTERS

mental principles of invariance, quantum superposition, and emergence; illustrate the leaps in thinking that led to these three principles; and argue for greater diversity in the field. Along the way, he uses anecdotes from his own journey as a Black physicist to personalize and illustrate his major point: To successfully understand our mysterious Universe, we must not only accept but also embrace the wild, "far-out" ideas that come from those considered to be outsiders.

The second part of the book is, in Alexander's words, structured "like a jazz album." (Alexander is also a jazz musician.) In this section, he takes the reader through many of the central phenomena in cosmology, including the Big Bang, the cosmic microwave background, and loop quantum gravity, explaining the models themselves and the histories of their development. Throughout this section, he touches on a recurring metaphysical theme: the potential connection between consciousness and the existence of the Universe.

Fear of a Black Universe packs in a lot of information and moves quickly from illustrative analogies to complex explanations of some of the most sophisticated models in cosmology and quantum physics. For example, the chapter "The Zen of Quantum Fields," despite its soothing title, contains a dense description of how individual particles arise from quantum fields. As do several other chapters, this one begins casually but may ultimately be difficult to comprehend without some fundamental understanding of quantum principles.

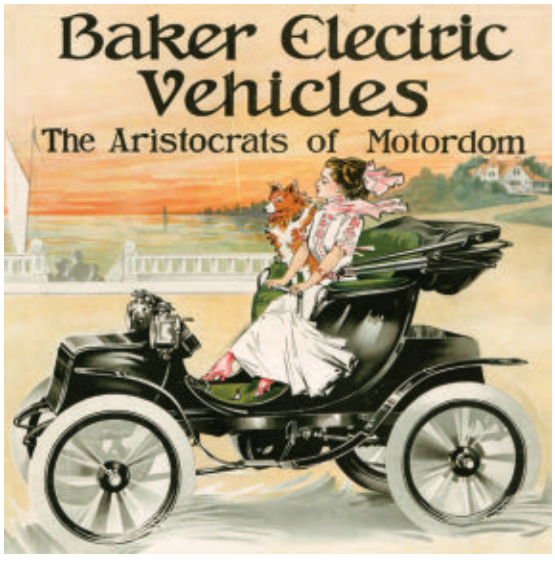
This book is very ambitious—perhaps overly so. Alexander has a vast intellect, and his attempt to construct a framework that incorporates both the development of fundamental principles of physics and a case for diversity, all while ruminating on the field's connections to consciousness, could have easily comprised multiple volumes. Readers with a strong background in physics and an appetite for connecting the physical world to sociological and metaphysical questions, however, will find much to appreciate in this book.

Fear of a Black Universe: An Outsider's Guide to the Future of Physics, *Stephon Alexander*, Basic Books, 2021, 256 pp.

Mother of Invention

Reviewed by **Ilana G. Goldberg**[8]

In the United Kingdom, less than 1% of venture capital goes to start-ups founded exclusively by women. In Sweden, just over 1% of venture capital is invested in companies founded by women. In the United States, nearly 40% of all businesses are owned by women, but less than 3% of venture funding goes to businesses with all female founders. This imbalance is the result of an economy built for men, argues Swedish author Katrine Marçal in *Mother of Invention*. Throughout the book, Marçal uses lessons in the history of technological developments to make the case that gender bias has been a crucial factor in determining which innovations are embraced and which are rejected, arguing that it still hampers innovation today.



The accessibility of early electric cars paradoxically destroyed their market appeal, argues Katrine Marçal in *Mother of Invention*.

One timely analysis she presents centers on the origins and evolution of the electric car. "At the turn of the [20th] century," Marçal notes, "one-third of all of Europe's cars were electric." She goes on to show how, according to one frustrated member of the board of an electric car company, gas car dealers successfully "branded the electric as a car for the aged and infirm and for the women," which effectively destroyed their market appeal. Eventually, the strengths of the electric car—most notably, its automatic ignition—were adapted to the gas car as concessions to female drivers. But why, wonders Marçal, "was comfort so long considered a feminine frill as opposed to a cutting-edge technological innovation?"

Likewise, fields such as artificial intelligence and robotics began by focusing on problems that Marçal points out "were interchangeable with the activities that we had learned to view as 'male,'" such as playing chess and complex algebra. Motor skills, meanwhile, which are essential to tasks such as cleaning and caretaking—work performed primarily by women—were a secondary consideration.

"We [incorrectly] thought that if machines could simply learn to succeed in the 'difficult' things (like beating Garry Kasparov at chess), then they would almost automatically be able to take on the 'easy' things, like sorting laundry," she observes, musing, "Had the early AI pioneers not been a narrow group of white male professors, would research have started to see cleaning as an equally legitimate problem as chess?"

The book's central theme of understanding technology through the lens of masculinity transcends recent history. "We don't know what came first," writes Marçal, "the [masculine] spear or the [feminine] digging stick. What's interesting is that we assume the spear." This perspective, she notes, is even ingrained in our educational systems, where students are "taught that the Bronze Age was followed by the Iron Age." "We could just as easily have called them the 'Pottery Age,' or the 'Flax Age,'" she observes.

The joy of the book is how it manages to weave in stories of women influencing innovation in masculine spaces. Marçal highlights, for example, how the space suits worn by Neil Armstrong and Buzz Aldrin were developed by Playtex, a women's bra company, which "understood that sewing was a technology…[and] managed to build an organization that reflected this." Innovation may have been stifled by gender bias in the past, but *Mother of Invention* shows that we can choose a different future. ■

Mother of Invention: How Good Ideas Get Ignored in an Economy Built for Men, *Katrine Marçal*, Abrams Press, 2021, 304 pp.

10.1126/science.abl8018

[1]The reviewer is at the Department of Neurology, UCLA Medical Center, Los Angeles, CA, USA. Email: susandouglas.md@cox.net [2]The reviewer is director of the McClure Center for Public Policy Research, University of Idaho, Boise, ID, USA. Email: katherinehimes@uidaho.edu [3]The reviewer is at the IDA Science and Technology Policy Institute, Washington, DC, USA. Email: gwong@ida.org [4]The reviewer is a physician and molecular biologist in Chevy Chase, MD, USA, who consults on health systems and data for technology and health care organizations. Email: carolyndca@gmail.com [5]The reviewer is a senior analyst at Nerac Inc., Tolland, CT, USA. Email: rszostak@nerac.com [6]The reviewer is at the Institute for Stem Cell and Regenerative Medicine, University of Washington, Seattle, WA, USA. Email: ejonlin@u.washington.edu [7]The reviewer is provost and dean of faculty at Sarah Lawrence College, Bronxville, NY, USA. Email: ksingh@sarahlawrence.edu [8]The reviewer is currently a program officer in Bethesda, MD, USA, and formerly served as a AAAS Science and Technology Policy Fellow and a Fulbright Scholar. Email: ilana.goldberg@outlook.com

IMAGE: © THE ADVERTISING ARCHIVES/BRIDGEMAN IMAGES

PERSPECTIVES

QUANTUM PHYSICS

A quantum vortex made of atoms

Vortex states seen for photons and electrons have been created in rare gas atoms and dimers

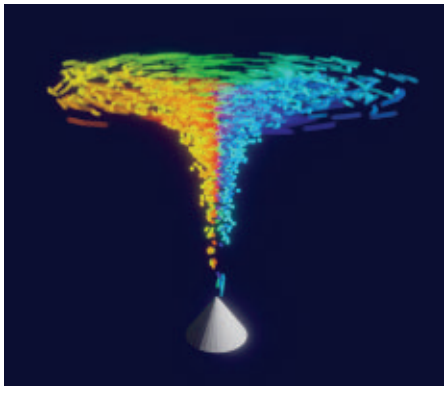
By **Oleg Kornilov**

Vortices have attracted the attention of physicists in part because of their exceptional stability. Vortices can occur naturally as whirlpools and tornadoes on Earth and as gravitational vortices around black holes in space. In quantum physics, vortices usually are found in particle ensembles such as superfluids, superconductors, and Bose-Einstein condensates. However, whether movement of a single particle could represent a vortex was not addressed until 1992, when Allen *et al.* (*1*) suggested that photons in a laser beam can carry orbital angular momentum (OAM) like a vortex. Several methods for generation and detection of optical vortex beams have since been developed and applied in many scientific areas, and vortex beams of another elementary particle, the electron, have also been generated (*2*). On page 1105 of this issue, Luski *et al.* (*3*) present a technique that generates vortex beams of larger composite particles: atoms and molecules.

The stability of vortices is the manifestation of the conservation of angular momentum and follows from application of Noether's theorem to isotropic space. Stated in simple terms, in an isotropic medium (one that has the same properties in all directions), conservation of angular momentum in the vortex keeps it swirling, like a tornado or a whirlpool. In classical physics, vortices can be observed in fluids, but individual free particles move along straight trajectories and a vortex-like spiral motion is impossible. The situation is different in the quantum world, where all particles can be represented by wave functions, as suggested by de Broglie in 1924. The center-of-mass part of the wave functions can actually carry angular momentum, which is conserved in the absence of external interactions, as dictated by Noether's theorem.

In the demonstration by Allen *et al.* (*1*) of a photon particle vortex, a laser beam carried OAM because the phase of the wave circled around the axis of propagation. The number of turns defines the quantized OAM of a photon. In the center of the beam, the phase remains undefined (a so-called dislocation point), and so there is a hole in the center of the beam. Several ways of producing OAM beams have been developed, such as applying circular phase masks or using gratings with a dislocation, and applications include optical tweezers, direct observation of extraterrestrial planets, and telecommunication (*4*).

Electrons can also be represented by waves and free-electron wave functions can also be shaped to carry OAM. Vortex beams were produced in 2010 by Uchida and Tonomura (*2*) by passing a beam of electrons through a phase mask made of graphite thin films. This study confirmed the correspondence between optical and matter waves and inspired fundamental research using electron vortex beams.



Particles must interact to form a vortex in classical physics, but single particles can form a vortex in quantum physics. Luski *et al.* extend quantum vortex formation to helium atoms (colored dots).

Both photons and electrons are elementary particles with no internal structure, unlike protons, atoms, and molecules. The wave functions of such particles, in addition to the center-of-mass part, also have a part describing their internal structure. If a measurement can couple the center-of-mass part of the wave function with the internal one, then the vortex beams can give experimenters an additional control of the total angular momentum and reveal the properties of the internal structure.

Composite particles are heavier than electrons, and their de Broglie wavelengths are typically shorter. The shorter wavelengths make it more difficult to realize coherent (wave-like) beams. This problem was overcome with the development of nanotechnologies that allowed transmission gratings with very small periods (down to tens of nanometers) to be fabricated that are suitable for diffraction of matter waves. These diffraction experiments were demonstrated by Keith *et al.* (*5*) and Schöllkopf and Toennies (*6*) and were subsequently applied in experiments with atoms, molecules, and clusters, experiments such as those by Kunitski *et al.* that used such gratings to separate elusive Efimov trimers of helium (*7*).

Luski *et al.* also produced well-collimated beams of helium atoms, but in a metastable state, and sent them through a nanograting containing a dislocation. Such grating dislocations can induce a circular phase in a diffracted beam, and the diffracted beams they detected were vortex beams. Similar to the optical vortex beam and classical vortices, the beams have a hole in the center and the phase of the wave function revolves around the dislocation axis (see the figure). The method of Luski *et al.* is general and could be applied to all particles that can be shaped in beams with a sufficiently well-defined velocity, because the velocity determines the de Broglie wavelength. The authors not only demonstrated vortex beams of metastable helium atoms but also detected vortex beams of neon atoms and helium dimers.

Luski *et al.*'s method for generating atomic and molecular vortex beams can be used for fundamental experiments. They propose an exciting fundamental test—the investigation of the internal structure of protons (*3*, *8*). Vortex beams of protons could be generated by applying the present method to hydrogen atoms (a proton and an electron) followed by ionization. The internal structure could then be revealed in experiments that are sensitive both to the center-of-mass and internal parts of the proton's wave function. ■

Max Born Institute, Max-Born-Strasse 2A, 12489 Berlin, Germany. Email: kornilov@mbi-berlin.de

REFERENCES AND NOTES

1. L. Allen, M. W. Beijersbergen, R. J. C. Spreeuw, J. P. Woerdman, *Phys. Rev. A* **45**, 8185 (1992).
2. M. Uchida, A. Tonomura, *Nature* **464**, 737 (2010).
3. A. Luski *et al.*, *Science* **373**, 1105 (2021).
4. Y. Shen *et al.*, *Light Sci. Appl.* **8**, 90 (2019).
5. D. W. Keith, M. L. Schattenburg, H. I. Smith, D. E. Pritchard, *Phys. Rev. Lett.* **61**, 1580 (1988).
6. W. Schöllkopf, J. P. Toennies, *Science* **266**, 1345 (1994).
7. M. Kunitski *et al.*, *Science* **348**, 551 (2015).
8. G. M. Vanacore *et al.*, *Nat. Mater.* **18**, 573 (2019).

ACKNOWLEDGMENTS

I thank C. Granados and L. Drescher for their valuable suggestions. The illustration was created using the Blender software package.

10.1126/science.abk1565

ILLUSTRATION: OLEG KORNILOV

ECOLOGY

Transformational ecology and climate change

Management of imminent ecosystem shifts demands adaptive, translational approaches

By **Stephen T. Jackson**[1,2]

Ecosystem transformation is emerging as a global threat under climate change (*1*–*3*). Conversion of conifer forest to shrubland, steppe, and other ecosystems is underway from Mexico to Alaska (*1*, *3*). Shrub steppe and chaparral are giving way to non-native annual grassland in the western United States. Floodplain forests are yielding to savanna in Amazonia, shrubs and trees are invading Arctic tundra, reef corals are being replaced by macroalgae, and geographic shifts in pelagic marine species are creating unprecedented combinations. Climate change is a primary driver of these transformations. Rapid ecological change is receiving increased scientific attention (*4*), much of which is focused on identifying tipping points between alternative stable states, tying into powerful theoretical and conceptual frameworks. However, ecological transformation can occur gradually, as incremental changes in dominant species populations accumulate and species ranges shift under changing climate. Developing a science of transformational ecology is timely in view of ongoing and imminent changes.

In the face of transformation, natural-resource managers have three options (*5*–*7*). They can resist change, intervening to restore original ecosystem states after disturbances, prevent severe disturbances where they have not already happened, and forestall gradual processes that may lead ultimately to transformation. Alternatively, managers may abide whatever new ecosystem states arise on their own. Or, managers may intervene to direct successional trajectories and other processes toward a desirable or acceptable new ecosystem state. Each of these options is fraught with scientific uncertainties and conflicting values. Scientific knowledge is necessary to inform these choices, but curiosity-driven research is insufficient. Transformational ecology will only be effective if it adopts translational approaches and practices, including deep and sustained engagement with decision-makers, understanding of decision contexts and constraints, and participation of managers in research conception and design (*8*).

Decision-makers will benefit from transformation-vulnerability assessments that identify the likelihood and consequences of ecological transformation and explore the viability of various management choices. Although resistance confers short-term benefits and buys time to explore alternatives, it may be prohibitively expensive and doomed to eventual failure under continuing climate change. Managers may often be forced to accept spontaneously emergent ecosystems, but they will need clear understanding of impacts on biodiversity and ecosystem services. Directing change toward new ecosystem states requires identification of those states, understanding of their properties, assessment of their sustainability, and determination of intervention pathways to attain them. Choosing among these alternatives entails trade-offs among diverse values and opportunity costs (*9*) and is laced with uncertainties.

A particular challenge comes from uncertainties at time scales intermediate between seasonal climate forecasting (about 6 months) and long-range climate scenarios (25 years and beyond). Annual to decadal climate variability is dominated by interactions among the atmosphere, oceans, land surface, and cryosphere and will interact with greenhouse-gas impacts. Robust forecasting at these time scales is lacking, but success or failure of management actions may depend on annual to decadal climate behavior (*10*). For example, success of a post-disturbance intervention depends on recruitment and growth of specific species populations, which can be contingent on whether the years immediately after the disturbance are hot or cool, wet or dry. Ecological legacies of climate events can constrain future ecological states as climate continues to change. Thus, even by resisting or accepting change, managers must confront the possibility of multiple, alternative future states, differing by path-dependent processes, with paths determined by annual to decadal climate realizations.



Natural-resource managers must adapt to ecosystem transformations that can arise after severe fires and other disturbances as climate becomes hotter and drier. The 2020 Creek Fire in California destroyed about 380,000 acres.

These scientific uncertainties amplify existing cultural, political, and institutional barriers to adaptation (*9*, *11*). Constraints, resource limitations, and institutional inertia can lead to default options, either business-as-usual resistance or acceptance of emerging ecosystems. These may often be the most viable choices, but they must be considered in context of directed-change alternatives, which can range from minor redirections to wholesale ecosystem engineering that uses translocated species, new functional dominants, and altered disturbance or herbivore regimes (*7*). Directed changes represent intentional departures from historical states toward locally or even universally new states. Although acceptance may also result in unprecedented states, the intentionality and design of directed change imposes ethical burdens on decision-makers; they assume responsibility for consequences of their interventions. Even in the knowledge that resistance will fail, and that acceptance will yield undesirable new states, managers may be paralyzed by risks of unintended consequences or failure resulting from intentional intervention.

Historical norms are deeply embedded in conservation practice and resource management, so barriers to acceptance or creation of change are particularly high. Barriers can be lowered through awareness that ecological change is natural, that most

[1]US Geological Survey, Southwest and South Central Climate Adaptation Science Centers, Tucson, AZ 85721, USA. [2]Department of Geosciences, University of Arizona, Tucson, AZ 85721, USA. Email: stjackson@usgs.gov

PHOTO: DAVID MCNEW/GETTY IMAGES

in situ ecosystems are relatively young, and that ecosystem states are often contingent on past events (*2*, *12*). Although directed change may appear new and intimidating, humans have centuries to millennia of experience in managing directed change (*13*). Outcomes and impacts of past ecosystem manipulations—inferred from paleoenvironmental, archeological, and historical records—can be instructive, as can examination of the role of indigenous practices (such as cultural burning) in creating and maintaining particular ecosystems. Much can also be learned from successes and failures of nearly two centuries of scientific management of fisheries, wildlife, forests, grazing lands, and other ecosystems.

Long-term outcomes should be sought that our descendants in coming decades will be grateful for. However, it is not always clear which actions taken today will lead to those outcomes. A few principles can guide decisions. Minimizing biodiversity loss—Aldo Leopold's "saving all the parts"—is important (*5*, *9*). Paleoecology indicates that some of today's dominant or keystone species were rare under different climates just a few thousand years ago (*2*, *12*). By analogy, now-obscure species may become important under future climates. Maximizing decision options for future managers is also important; today's decisions may foreclose tomorrow's choices. And systematic knowledge gain, including advancement of ecological knowledge and practical understanding of what works and what does not, is critical.

Adaptive learning, creative approaches, and close partnerships between communities of research and practice are needed to address the challenges posed by compounded uncertainties, path dependencies, and alternative future states (*8*, *9*). Numerous decision-support tools—including adaptive management, climate-smart conservation, scenario planning, state-and-transition models, and the resist/accept/direct trichotomy—are available. These and other aids can be deployed systematically in broadly framed, experimental adaptive-management portfolios (*5*, *14*). For a given region, landscape, or ecosystem type, experimental treatments may include acceptance (intervention-free "controls"), a suite of resistance strategies, and another suite of directed-change interventions. Treatments should be developed in anticipation of realistic alternative climate events or trajectories (*10*). As the experiments proceed, failing approaches can be abandoned or redirected, with new treatments introduced as more is learned and as circumstances continue to unfold. In much of the United States, undeveloped lands comprise mosaics managed by multiple federal, state, and local agencies; Native Nations; conservation nongovernmental organizations; and private owners. Each has its own management priorities and constraints. Although such jurisdictional patchworks have been viewed historically as barriers to comprehensive management, they present an opportunity. Jurisdictional mosaics can be incorporated into the overall design because certain treatments will be possible in some jurisdictions but not others (*5*).

Diversified, experimental management portfolios have a dual advantage of fostering adaptive learning and bet-hedging under uncertainty (*5*, *14*). Depending on the setting, leadership might come from government agencies, professional organizations, conservation nongovernmental organizations, or universities. Processes and governance will need to be emplaced to ensure that core activities—including design, manipulations, monitoring, analysis, synthesis, and products—are driven primarily by management and policy questions. In view of the ambitious scale, large costs, and high stakes, design and monitoring should be directed to provide "good enough" answers, with less precision and detail than research scientists might find ideal (*14*).

Ecosystem transformation will characterize the globe for the foreseeable future, and many ecosystems emerging today will be transient, yielding to further transformation as climate change continues and ecological processes at different temporal scales keep pace. Implementing effective, adaptive approaches to understanding and managing those transformations is an urgent challenge for the scientific, management, and policy communities. Development of innovative, adaptive initiatives is especially timely with inception of the United Nations Decade on Ecosystem Restoration (*15*). ■

REFERENCES AND NOTES

1. C. I. Millar, N. L. Stephenson, *Science* **349**, 823 (2015).
2. C. Nolan *et al.*, *Science* **361**, 920 (2018).
3. J. D. Coop *et al.*, *Bioscience* **70**, 659 (2020).
4. M. G. Turner *et al.*, *Philos. Trans. R. Soc. Lond. B Biol. Sci.* **375**, 20190105 (2020).
5. G. H. Aplet, P. S. McKinley, *Ecosyst. Health Sustain.* **3**, e01261 (2017).
6. G. W. Schuurman *et al.*, *BioScience* 10.1093/biosci/biab067 (2021).
7. L. M. Thompson *et al.*, *Fisheries* **46**, 8 (2021).
8. C. A. F. Enquist *et al.*, *Front. Ecol. Environ.* **15**, 541 (2017).
9. B. G. Norton, *Sustainable Values, Sustainable Change: A Guide to Environmental Decision Making* (Univ. Chicago Press, 2015).
10. J. B. Bradford, J. L. Betancourt, B. J. Butterfield, S. M. Munson, T. E. Wood, *Front. Ecol. Environ.* **16**, 295 (2018).
11. L. Shi, S. Moser, *Science* **372**, eabc8054 (2021).
12. D. A. Fordham *et al.*, *Science* **369**, eabc5654 (2020).
13. L. Stephens *et al.*, *Science* **365**, 897 (2019).
14. C. J. Walters, C. S. Holling, *Ecology* **71**, 2060 (1990).
15. www.decadeonrestoration.org.

10.1126/science.abj6777

PLANT SCIENCE

Lipid-mediated regulation of flowering time

An anionic phospholipid tells plants when to flower according to ambient temperature

By **Yvon Jaillais**[1] *and* **François Parcy**[2]

FLOWERING LOCUS T (FT) is a mobile protein, known as florigen, that causes flowering in plants. In *Arabidopsis thaliana*, *FT* transcription is activated in the leaf vascular tissues (phloem) when days become longer (*1*). FT protein then moves long distances through the phloem to reach the shoot apical meristem, where it induces floral transitions by regulating nuclear transcription complexes (*1*, *2*). FT has homologies with characterized lipid-binding proteins in animals and belongs to the phosphatidylethanolamine-binding protein (PEBP) family (*2*). Although conserved throughout flowering plants, the function of FT lipid-binding capacity has remained enigmatic. On page 1137 of this issue, Susila *et al.* (*3*) show that FT binds to the anionic phospholipid phosphatidylglycerol, which sequesters FT in membrane compartments of phloem cells at low temperature, thereby delaying flowering in cold conditions. Thus, a temperature-dependent regulation of FT translocation by a membrane phospholipid tunes the plant response to ambient temperature.

Susila *et al.* found that FT binds to the anionic phospholipid phosphatidylglycerol in vitro and in phloem cells in vivo. Anionic phospholipids modulate the physicochemical properties of membranes, notably their electrostatic field, and provide docking platforms for proteins (*4*). Each anionic phospholipid species localizes to precise compartments within plant cells, thereby regulating the membrane identity of these organelles (*4*). Phosphatidyl-

[1]Laboratoire Reproduction et Développement des Plantes, Université de Lyon, ENS de Lyon, CNRS, INRAE, Lyon, France. [2]Laboratoire Physiologie Cellulaire et Végétale, Université Grenoble Alpes, CNRS, CEA, INRAE, IRIG-DBSCI-LPCV, Grenoble, France. Email: yvon.jaillais@ens-lyon.fr

glycerol mostly accumulates in chloroplasts and mitochondria (*5*) but has also been found in various compartments of the endomembrane system (*6*). However, its precise localization is largely unknown, raising the question of where FT interacts with phosphatidylglycerol.

Susila *et al.* found that in *A. thaliana* protoplasts (plant cells without a cell wall), FT associates with various membranes that contain phosphatidylglycerol: the plasma membrane, Golgi apparatus, trans-Golgi network, endoplasmic reticulum, and chloroplast envelope. Low temperature (i.e., a long day at 16°C) induced the interaction between FT and cellular membranes in a phosphatidylglycerol-dependent manner.

Differentiated phloem tissues consist of conducting cells, called the sieve elements, and specialized parenchymal cells, called companion cells (see the figure). Sieve elements are enucleated cells responsible for transporting sugars, metabolites, and some proteins throughout the plants. Companion cells are nucleated cells responsible for the metabolic functioning of sieve elements. They are closely associated with sieve elements through specialized cell-to-cell connections called plasmodesmata. FT is expressed in phloem companion cells and then moves to the sieve elements via the cytoplasmic canal of the plasmodesmata (*1*, *7*). Low temperature promotes the phosphatidylglycerol-dependent retention of FT in cellular membranes of companion cells, which delays flowering by reducing FT movement toward the sieve elements and thus the shoot meristem. In phosphatidylglycerol biosynthetic mutants, this temperature-dependent retention is reduced, leading to an early flowering phenotype and temperature insensitivity. During long days at 23°C, FT is not sequestered within companion cell membranes and moves into phloem sieve elements to reach the shoot apical meristem and accelerate flowering.

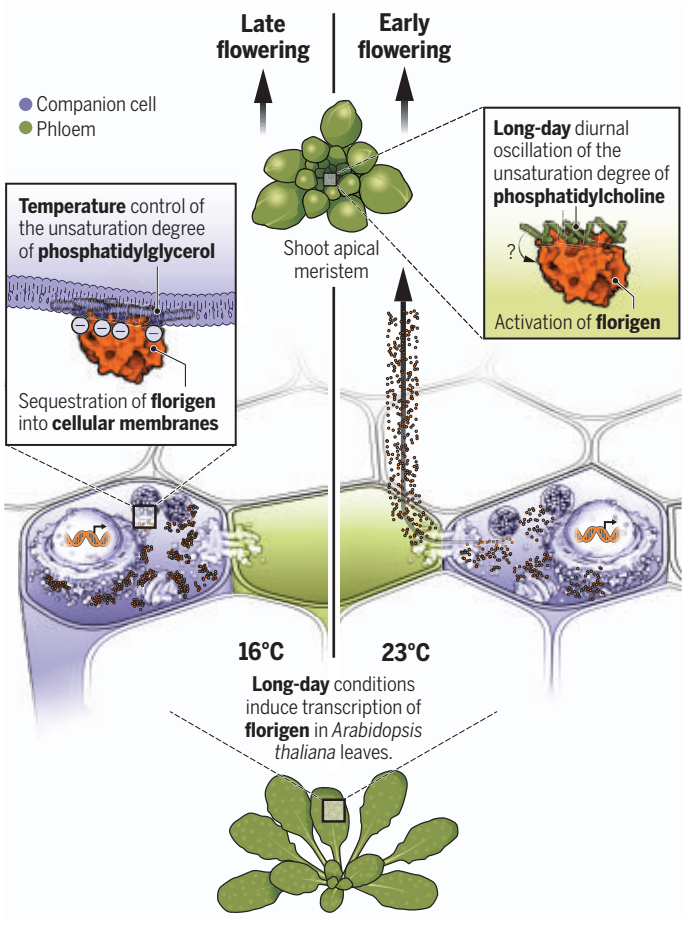
Once in the meristem, FT binds to another phospholipid, phosphatidylcholine, to induce flowering (*5*, *8*). FT preferentially interacts with phosphatidylcholine species with low saturation (i.e., few numbers of carbon-carbon double bonds in their fatty acid chains), which are more abundant under long-day conditions. However, it remains unclear how ambient temperature modulates FT-phosphatidylglycerol interaction and thus the mobility of FT. Lipidomic analyses by Susila *et al.* suggest that the overall amounts of phosphatidylglycerol do not vary with temperature. Yet, consistent with the intense temperature-dependent remodeling of lipids in plants (*6*, *9*, *10*), the abundance of polyunsaturated phosphatidylglycerol species increases at 16°C compared with 23°C. Because FT interaction with phosphatidylcholine is dependent on its unsaturation degree (*8*), this could also be the case for FT-phosphatidylglycerol interaction. As such, the membrane network, through changes in lipid unsaturation, could catch or release PEBP proteins, thereby regulating plant architecture in response to environmental cues, notably temperature variations. However, such a model will require further investigation.

A major step toward understanding how different phospholipid molecular species could regulate FT will be to characterize this interaction at the atomic level. High-resolution crystal structures suggest possible lipid-binding sites (*11*), but the next step will be to analyze FT structure in complex with its lipid ligands or even directly inserted into membranes. Dissecting this interaction should allow the identification of FT variants specifically defective in lipid binding with intact transcriptional activity, thus allowing the uncoupling of temperature-sensing capacity from the flowering-inducing functions of FT. It will be particularly interesting to analyze whether such FT variants may already exist in nature, for example in plant species with temperature-insensitive flowering transitions.

The results of Susila *et al.* provide a likely explanation for why florigen retained its capacity to bind membrane lipids when it functions as a transcriptional coactivator in the nucleus of meristem cells. Susila *et al.* found that FT also localizes to TERMINAL FLOWER 1 (TFL1)–containing vesicles (*12*). TFL1 is a homolog of FT that belongs to the PEBP family (*2*, *7*) and also binds to phosphatidylglycerol in vitro (*3*). It acts as a flowering repressor and may be involved in vacuolar trafficking (*12*) as well as transcriptional regulation (*2*). It will be interesting to analyze the importance of TFL1 lipid binding and potential temperature sensitivity in regulating meristem functions antagonistically with FT. Similarly, the potential relevance of temperature-sensitive membrane interaction for members of the PEBP family involved in bud release or tuber formation in other plants will be worth exploring (*2*, *7*). ■

Regulation of florigen by lipids

Florigen transcription is induced in leaf vascular tissues when days become longer. Its movement through the phloem to the meristem, where it promotes flowering, is regulated by binding to phospholipids, which are altered by temperature. Thus, regulation of florigen by temperature and photoperiod influences flowering time.



GRAPHIC: V. ALTOUNIAN/*SCIENCE*

REFERENCES AND NOTES

1. L. Corbesier *et al.*, *Science* **316**, 1030 (2007).
2. Y. Zhu, S. Klasfeld, D. Wagner, *J. Exp. Bot.* **72**, 2301 (2021).
3. H. Susila *et al.*, *Science* **373**, 1137 (2021).
4. L. C. Noack, Y. Jaillais, *Annu. Rev. Plant Biol.* **71**, 71 (2020).
5. L. A. Colin, Y. Jaillais, *Curr. Opin. Plant Biol.* **53**, 1 (2020).
6. M. Uemura, R. A. Joseph, P. L. Steponkus, *Plant Physiol.* **109**, 15 (1995).
7. S. Jin, Z. Nasim, H. Susila, J. H. Ahn, *Semin. Cell Dev. Biol.* **109**, 20 (2021).
8. Y. Nakamura *et al.*, *Nat. Commun.* **5**, 3553 (2014).
9. D. L. Falcone, J. P. Ogas, C. R. Somerville, *BMC Plant Biol.* **4**, 17 (2004).
10. Q. Li *et al.*, *Plant Cell* **27**, 86 (2015).
11. Y. Nakamura *et al.*, *iScience* **21**, 577 (2019).
12. E. J. Sohn *et al.*, *Proc. Natl. Acad. Sci. U.S.A.* **104**, 18801 (2007).

10.1126/science.abl4883

CANCER

Enabling oncogenes

Melanoma can arise only from cells with a permissive chromatin landscape

By **David W. Vredevoogd** *and* **Daniel S. Peeper**

Melanoma is a cancer that arises from the neural crest–derived melanocytic lineage. Melanocytes are responsible for pigmentation of the skin, serving to protect epidermal keratinocytes in particular against DNA damage through ultraviolet (UV) irradiation. Melanoma typically resides in the skin but can also occur at other sites, such as the eye or mucosal surfaces. It is largely accepted that for melanomagenesis, a founder mutation is required to spur uncontrolled proliferation of the affected cells (*1*). Intriguingly, such alterations, called driver mutations, are also detected in normal, healthy skin (*2*, *3*). This raises the question of why some cells, upon acquiring an oncogenic driver mutation, have the capacity to form tumors, whereas others remain largely dormant. On page 1104 of this issue, Baggiolini *et al.* (*4*) present evidence for the concept of oncogenic competence: that a permissive chromatin landscape is a prerequisite to enable oncogenes to transform cells.

The generation of melanocytes occurs in a highly structured fashion, evolving from SOX10^{+} neural crest precursor cells into an intermediate microphthalmia-associated transcription factor (MITF)$^{+}$ melanoblast population before eventually differentiating into mature, pigment-producing melanocytes (*5*). To give rise to cancer, cells from this melanocytic lineage require the acquisition of driver mutations. For melanoma, such mutations frequently occur in proteins of the mitogen-activated protein kinase (MAPK) pathway, with the BRAF^{V600E} mutation (in which Val^{600} is replaced with Glu) being most prevalent (*6*).

Human skin contains many individual melanocytes harboring potentially oncogenic driver mutations (*2*). However, what determines which of those cells can evolve to produce melanoma has remained largely unclear. Baggiolini *et al.* used genetically engineered zebrafish deficient for the tumor suppressor *p53* to drive expression of the BRAF^{V600E} oncoprotein in each stage of melanocyte differentiation. They found that both neural crest cells and melanoblasts were capable of giving rise to melanomas but, unexpectedly, that melanocytes were relatively resistant. These findings from zebrafish were recapitulated in human pluripotent stem cells (hPSCs) rendered deficient for the tumor suppressors retinoblastoma (RB), p53, and p16 and in which BRAF^{V600E} was induced at different stages of melanocytic differentiation: Melanocytes, but not neural crest cells or melanoblasts, were largely incapable of forming tumors when subcutaneously transplanted into immunodeficient mice.

By comparing hPSC-derived melanoblasts to hPSC-derived melanocytes, the authors observed a different chromatin landscape. Through integration of these data with analyses from human melanomas, it was inferred that this chromatin landscape was at least partially shaped by the epigenetic regulator ATAD2 (adenosine triphosphatase family AAA domain–containing protein 2). ATAD2 overexpression in hPSC-derived melanocytes increased the chromatin accessibility of neural crest–associated genes in particular. This was accompanied by a decline in pigmentation, suggesting dedifferentiation. In some zebrafish, overexpression of ATAD2 was sufficient for melanocytes to progress to melanomas. ATAD2 binds to the transcription factors SOX10 and Myc to induce their gene expression programs and activates extracellular regulated kinase (ERK) signaling. These findings indicate that the ATAD2-induced chromatin landscape is more permissive to tumor formation, endowing a previously oncogenically incompetent cell type with the ability to undergo oncogenic transformation.

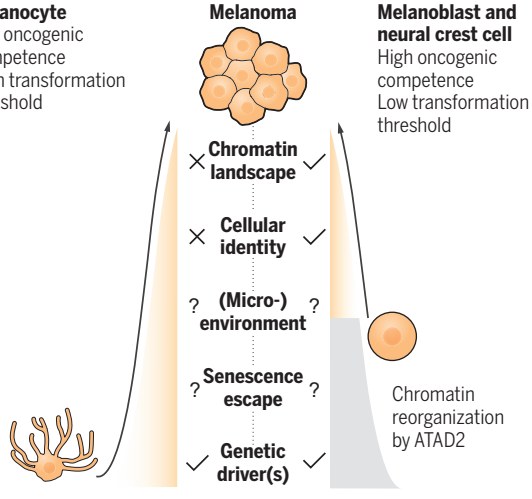
These findings have important ramifications for at least two facets of melanomagenesis: the identity of the cell of origin (a long-debated issue) and the competence of a given driver mutation to initiate disease. A key factor contributing to competence is the cancer-enabling genetic context. Baggiolini *et al.* demonstrate that whereas the expression of BRAF^{V600E} in the context of the loss of *p53* is insufficient to drive melanomagenesis from melanocytes in zebrafish, the additional loss of the tumor suppressor phosphatase and tensin homolog (PTEN) can result in at least some degree of melanoma formation from the same cell type. This implies that for oncogenic competence, the driver mutation needs to mechanistically "match" the collaborating oncogenic alterations (such as the prototypic HRAS + MYC combination), or that a threshold of oncogenic activity needs to be surpassed, or both. Whether this activity of PTEN relates to chromatin regulation is for future exploration. Such oncogenic collaboration is also observed in mouse models of melanomagenesis, in which BRAF^{V600E} expression in the context of *Pten* loss results in the formation of melanomas from melanocytes (*7*, *8*).

Baggiolini *et al.* highlight an important and increasingly appreciated role for epigenetic regulation. Although it has been shown that melanoma cells are plastic and that dedifferentiation can occur during expansion, invasion, and upon treatment (*8*–*10*), it was unknown that this may facilitate oncogenic competence. Albeit speculative, this may offer an explanation as to why some driver mutations, especially weaker ones, do not always result in the oncogenic transformation of affected cells (*2*, *3*): The chromatin architecture may not permit sufficient signaling required to fuel neoplastic growth.

It will be interesting to determine any

Oncogenic competence in melanoma

Despite the presence of a driver mutation such as BRAF^{V600E}, in which Val600 is replaced with Glu, there is a high threshold for melanocytes to progress to melanoma. The chromatin-modifying enzyme ATAD2 (adenosine triphosphatase family AAA domain-containing protein 2), expressed at lower amounts in melanocytes than in melanoblasts and neural crest cells, generates a permissive chromatin landscape that enables melanomagenesis.



GRAPHIC: N. DESAI/*SCIENCE*

Division of Molecular Oncology and Immunology, Oncode Institute, Netherlands Cancer Institute, Plesmanlaan 121, 1066CX, Amsterdam, Netherlands. Email: d.peeper@nki.nl

mechanistic link between ATAD2-dependent chromatin regulation and the cellular microenvironment, which contributes to melanomagenesis. In mice, fully differentiated pigmented melanocytes can form melanoma upon loss of *Pten* and expression of $BRAF^{V600E}$ (*8*). In that model, microenvironmental cues rather than cell-intrinsic differences dictate melanoma predisposition. Although a possible explanation for this difference is the exact nature of the models, together the data suggest that both cellular identity (coupled with a specific chromatin state) and microenvironmental cues dictate melanoma predisposition. Future investigations should delineate any involvement of the epigenetic architecture in integrating environmental signals.

Other factors also likely affect oncogenic competence. For example, melanomas at different sites of the body, specifically sun-exposed and non–sun-exposed skin, generate molecularly distinguishable tumors (*1*). This implies that there may be different requirements for oncogenic competence in these locations. Additionally, $BRAF^{V600E}$ mutations occur in healthy human skin and are prevalent in melanocytic nevi (moles) (*11*). However, in isolation they rarely promote melanomagenesis; instead, nevi typically remain durably arrested with hallmarks of oncogene-induced senescence, a tumor-suppressive mechanism that halts the expansion of cells carrying an oncogenic lesion (*12*). Nevi would thus seem to be oncogenically incompetent, and this can be reversed through ablation of tumor suppressors, including PTEN (*13*). Notably, chromatin reorganization contributes to senescence (*14*).

The findings of Baggiolini *et al.* suggest that there is considerable cross-talk between different facets of melanomagenesis (the cell of origin, the driver mutation or mutations, the epigenetic state, the microenvironmental context, and possibly senescence), each of which may influence oncogenic competence (see the figure). Whether such oncogenic competence factors play a role in other cancers as well will be an interesting area for future exploration. ■

REFERENCES AND NOTES

1. A. H. Shain, B. C. Bastian, *Nat. Rev. Cancer* **16**, 345 (2016).
2. J. Tang *et al.*, *Nature* **586**, 600 (2020).
3. I. Martincorena *et al.*, *Science* **348**, 880 (2015).
4. A. Baggiolini *et al.*, *Science* **373**, eabc1048 (2021).
5. J. Diener, L. Sommer, *Stem Cells Transl. Med.* **10**, 522 (2021).
6. H. Davies *et al.*, *Nature* **417**, 949 (2002).
7. D. Dankort *et al.*, *Nat. Genet.* **41**, 544 (2009).
8. C. Köhler *et al.*, *Cell Stem Cell* **21**, 679 (2017).
9. J. Tsoi *et al.*, *Cancer Cell* **33**, 890 (2018).
10. K. S. Hoek *et al.*, *Cancer Res.* **68**, 650 (2008).
11. P. M. Pollock *et al.*, *Nat. Genet.* **33**, 19 (2003).
12. C. Michaloglou *et al.*, *Nature* **436**, 720 (2005).
13. L. C. W. Vredeveld *et al.*, *Genes Dev.* **26**, 1055 (2012).
14. M. Narita *et al.*, *Cell* **113**, 703 (2003).

10.1126/science.abl4510

CELL BIOLOGY

Stressing out translation

Integrated stress response activation drives neuropathy in Charcot-Marie-Tooth disease

By **Wilfredo Mellado**[1] *and* **Dianna E. Willis**[1,2]

Many Charcot-Marie-Tooth (CMT) disease–causing mutations occur in the genes encoding aminoacyl–transfer RNA (tRNA) synthetases (AARSs), leading to peripheral sensory and motor neuropathy. AARSs are responsible for implementing the genetic code: They catalyze the initial reaction of protein translation, charging the tRNA with its respective amino acid (*1*). One of the putative causes of this disease is the inhibition of global protein synthesis; however, the underlying mechanism or mechanisms are unknown, although studies suggest that it is independent of aminoacylation activity. On pages 1156 and 1161 of this issue, Spaulding *et al.* (*2*) and Zuko *et al.* (*3*), respectively, demonstrate that CMT neurons have altered translational profiles and aberrant AARS-tRNA binding, which causes depletion of available aminoacyl tRNAs, resulting in activation of the integrated stress response (ISR) and leading to neuropathy. Taken together, these results point to a compelling model that can explain how dominantly inherited mutations in multiple AARSs result in similar CMT disease.

Given their critical role in protein synthesis, it is no surprise that mutations in these AARSs are implicated in human disease. The most common of these falls into the class of CMT neuropathies. CMT is the most common inherited neuromuscular disorder, with a prevalence of 1 in 2500 and mutations in at least 70 genes identified. Although clinically and genetically heterogeneous, these mutations result in a common disease phenotype characterized by progressive muscle weakening, muscle atrophy, and sensory dysfunction caused by degeneration of peripheral sensory and motor axons (*4*). The molecular mechanisms by which such a large number of mutations cause similar peripheral neuropathy is not known.

Mutations in six different AARSs cause CMT, and these mutations are predominantly localized within the catalytic domains. Therefore, many studies have focused on how these mutations affect tRNA aminoacylation (*5*, *6*). This catalytic activity of the AARSs is the process by which an amino acid is attached to its corresponding tRNA, resulting in a "charged" tRNA ready to deliver its amino acid to a growing polypeptide. In this way, the AARSs act to maintain the genetic code by properly pairing amino acids with their cognate tRNAs. Although it was initially hypothesized that these AARS mutations caused disease owing to the loss or impairment of tRNA aminoacylation function, and indeed many AARS mutant proteins exhibit such a defect, not all mutations show a loss of function. This has led to the search for alternative disease mechanisms. Most notably, some mutations in glycyl-tRNA synthetase (GlyRS) and tyrosyl-tRNA synthetase (TyrRS) do not alter aminoacylation, and where aminoacylation is affected, there is no correlation between the degree of the defect and the severity of disease (*7*–*10*). Instead, these mutations impart toxic gain-of-function effects.

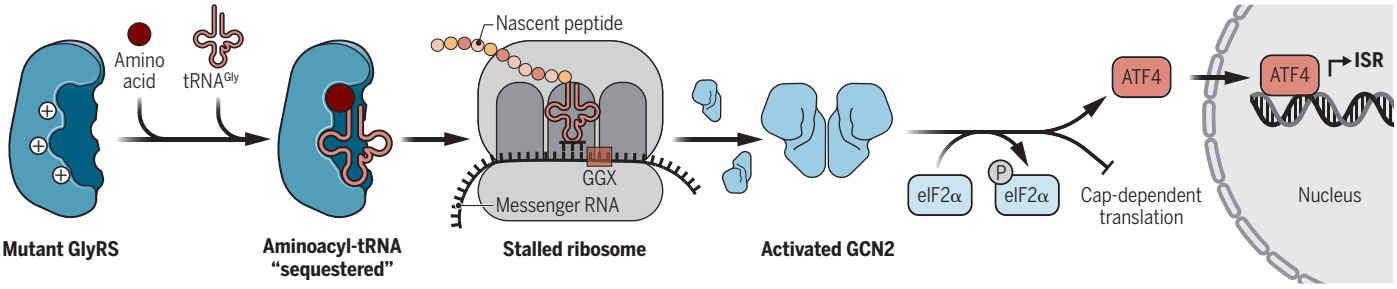
Many of the proposed gain-of-function disease mechanisms have focused on the interaction between the AARS and its tRNA. When amino acids associated with CMT mutations are mapped onto structural models of the AARS-tRNA complexes, they tend to reside near tRNA contact sites (*11*). This region is critical for both the recognition of the correct tRNA as well as for the kinetics of charging and release of the tRNA. The strength of the interaction between the AARS and tRNA is largely driven by the interaction between the positively charged basic amino acids on the AARS and the negatively charged phosphate groups on the tRNA. The AARS mutations associated with CMT almost exclusively result in an increase in the positive charge, which would predict a strengthening of the binding between the AARS and the tRNA.

Zuko *et al.* show that overexpression of $tRNA^{Gly}$ can rescue protein synthesis levels and attenuate peripheral neuropathy in both fly and mouse models of CMT caused by GlyRS mutations. The relative efficiency of this rescue was dependent on the type of $tRNA^{Gly}$ that was overexpressed as well as the specific GlyRS mutation. This is at least in part explained by the relative $tRNA^{Gly}$ binding and release rates, which demonstrate that GlyRS mutants display mark-

[1]Burke Neurological Institute, White Plains, NY, USA. [2]Feil Family Brain & Mind Research Institute, Weill Cornell Medicine, New York, NY, USA. Email: diw2004@med.cornell.edu; wim2007@med.cornell.edu

Charcot-Marie-Tooth disease pathogenesis

Mutation in the aminoacyl–transfer RNA (tRNA) synthetases, such as glycyl-tRNA synthetase (GlyRS), results in increased positive charge and enhanced binding between GlyRS and $tRNA^{Gly}$. This sequesters $tRNA^{Gly}$ and leads to ribosome stalling and translational repression. These stressors activate general control nondepressible 2 (GCN2), resulting in the phosphorylation (P) of eukaryotic translation initiation factor 2α (eIF2α) and inhibition of global cap-dependent translation. Concurrently, activating transcription factor 4 (ATF4) translocates to the nucleus to induce the integrated stress response (ISR). Chronic activation of the ISR likely contributes to pathophysiology.



edly slow release rates that are indicative of strengthened binding between the AARS and the tRNA. The subsequent reduction in the available pool of $tRNA^{Gly}$ results in ribosome stalling and reduced translation. This insufficiency is relieved by overexpression of $tRNA^{Gly}$, explaining why this results in the rescue of protein synthesis and attenuation of peripheral neuropathy in mice and flies. Further supporting this putative mechanism of $tRNA^{Gly}$ sequestration-induced ribosome stalling as the cause of disease pathology, inactivation of the ribosome rescue factor guanosine-5′-triphosphate–binding protein 2 (GTPBP2) further enhances peripheral neuropathy in mice. These results provide mechanistic support to the idea that the change in charge caused by the AARS CMT-associated mutations enhances the binding with its tRNA, leading to downstream reduction in protein synthesis as a result of ribosome stalling.

Although the results of Zuko *et al.* help to explain the potential mechanism that links certain gain-of-function AARS mutations with an effect on protein synthesis, the biological ramification of these changes and how they result in CMT neuropathy are unclear. Spaulding *et al.* identify an altered translational profile in affected neurons from two mouse models of CMT caused by dominant mutations in GlyRS that points to activation of ISR. The ISR acts to protect cells from a diverse set of stressors by temporarily halting or decreasing global protein synthesis while allowing translation of select messenger RNAs (mRNAs) to restore cellular homeostasis and survival. They show that the ISR occurs through the general control nondepressible 2 (GCN2) sensor kinase. GCN2 is one of the kinases that phosphorylates eukaryotic translation initiation factor 2α (eIF2α) to initiate ISR. eIF2α is a critical component of the rate-limiting translation initiation step, and phosphorylation leads to limiting amounts of the ternary initiating complex and inhibits global protein synthesis.

ISR activation through GCN2-dependent pathways has previously been shown to occur in the context of protein synthesis impairments and with ribosome stalling (*12*, *13*). Supporting this mechanistic role for GCN2 in CMT, *Gcn2* deletion in a mouse model of CMT results in a reduction in neuropathy progression, and the use of a GCN2 inhibitor reduced ISR activation in a GlyRS mouse model of CMT. Zuko *et al.* further demonstrate that $tRNA^{Gly}$ overexpression suppresses this ISR activation. The studies of Zuko *et al.* and Spaulding *et al.* support the compelling hypothesis that GlyRS mutations cause ribosome stalling and reduced translation. They further cause activation of the ISR through GCN2-dependent mechanisms, ultimately resulting in the peripheral neuropathy of CMT (see the figure). Such chronic activation of the ISR would prevent the cell from making the proteins needed for the normal biological functions of neurons. Indeed, activation of ISR has been demonstrated in several neurodegenerative disorders, so understanding the underlying mechanisms may have broad implications.

Clarity is beginning to develop around the role of mutation in AARSs in driving CMT disease. The idea that these mutations do not simply result in reduced tRNA aminoacylation has long been discussed; however, the evidence supporting alternative disease mechanisms has been limited. Zuko *et al.* and Spaulding *et al.* provide compelling support for one potential mechanism. Additional questions remain, however. For instance, GlyRS is one of only two dual-localized AARSs, being targeted to both the cytoplasm and to the mitochondria (*14*). Many neurodegenerative diseases have been associated with mitochondrial dysfunction, and axons are especially susceptible to deficient mitochondrial activity. Might $tRNA^{Gly}$ sequestration be especially detrimental to mitochondrial function, resulting in axonal degeneration? Perhaps more integral to the question of CMT disease phenotype is the lack of apparent effect of AARS mutations in non-neuronal tissue. The sequestration of $tRNA^{Gly}$ would be expected to occur in all cell types, yet the disease primarily manifests as peripheral sensory and motor neuron degeneration. Spaulding *et al.* allude to cell-type specificity of GCN2-mediated ISR activation; however, linkage between this response, altered translation, and subsequent neuronal deficits remains to be established.

Given this new mechanism and the demonstration that $tRNA^{Gly}$ overexpression suppresses ISR activation and improves disease phenotype in mice and flies, can therapeutic approaches be designed to overexpress a specific tRNA in accordance with the underlying AARS mutation, or, can pharmacological approaches to inhibit components of the ISR be used (*15*)? Although these questions must still be answered, the studies of Zuko *et al.* and Spaulding *et al.* provide better understanding of the disease mechanism of CMT and, excitingly, point toward the promise of therapeutics aimed at preventing the initiation of the ISR caused by translation inhibition. ■

REFERENCES AND NOTES

1. M. A. Rubio Gomez, M. Ibba, *RNA* **26**, 910 (2020).
2. E. L. Spaulding *et al.*, *Science* **373**, 1156 (2021).
3. A. Zuko *et al.*, *Science* **373**, 1161 (2021).
4. L. C. Barreto *et al.*, *Neuroepidemiology* **46**, 157 (2016).
5. E. Storkebaum, *BioEssays* **38**, 818 (2016).
6. R. C. Wallen, A. Antonellis, *Curr. Opin. Genet. Dev.* **23**, 302 (2013).
7. A. Antonellis *et al.*, *J. Neurosci.* **26**, 10397 (2006).
8. C. A. Froelich, E. A. First, *Biochemistry* **50**, 7132 (2011).
9. L. A. Nangle, W. Zhang, W. Xie, X. L. Yang, P. Schimmel, *Proc. Natl. Acad. Sci. U.S.A.* **104**, 11239 (2007).
10. E. Storkebaum *et al.*, *Proc. Natl. Acad. Sci. U.S.A.* **106**, 11782 (2009).
11. N. Wei, Q. Zhang, X. L. Yang, *J. Biol. Chem.* **294**, 5321 (2019).
12. A. J. Inglis *et al.*, *Proc. Natl. Acad. Sci. U.S.A.* **116**, 4946 (2019).
13. R. Ishimura, G. Nagy, I. Dotu, J. H. Chuang, S. L. Ackerman, *eLife* **5**, e14295 (2016).
14. J. Alexandrova, C. Paulus, J. Rudinger-Thirion, F. Jossinet, M. Frugier, *RNA Biol.* **12**, 1301 (2015).
15. W. Costa-Mattioli, P. Walter, *Science* **368**, eaat5314 (2020).

10.1126/science.abk3261

GRAPHIC: V. ALTOUNIAN/*SCIENCE*

ATMOSPHERIC SCIENCE

Stratospheric winds trigger cold spells

Changes in Arctic sea ice and snow cover can alter wind patterns at high altitudes

By **Dim Coumou**[1,2]

In February 2021, Canada, the United States, and parts of northern Mexico experienced an extreme cold spell caused by the southerly migration of cold air from the Arctic. Texas was especially hard hit, with at least 111 reported fatalities. Frozen pipelines and power grid failures across the state led to record damages amounting to nearly $200 billion, substantially more than losses from recent high-impact hurricanes (*1*). The potential role of global warming in the occurrence of such winter extremes is an area of active scientific debate (*2*). On pages 1116 of this issue, Cohen *et al.* (*3*) provide new evidence that changes to stratospheric winds might play a role.

Simple thermodynamics imply that with warming temperatures, winters will get milder. Over the past 30 years, the Arctic has warmed at more than twice the rate as the planet overall, a phenomenon known as Arctic amplification. Given that the air in the Arctic is now substantially warmer than it was several decades ago, northerly winds coming from the Arctic are a lot less cold, too (*4*). These thermodynamic effects of global warming are strong, and therefore cold waves throughout the mid-latitudes have become milder (*5*). Still, possible changes in atmospheric dynamics (the large-scale atmospheric flow patterns such as jet streams) act on top of these thermodynamic changes and might cause a change in the frequency or persistence of specific winter extremes.

A central role of potential dynamical changes in winter weather involves the stratospheric polar vortex. This vortex is a band of fast-blowing westerly winds that circle the Arctic during the cold season at altitudes between 10 and 50 km. As the circling winds become stronger, the enclosed air becomes more isolated, inhibiting mixing with warmer air masses at lower latitudes. Variability in the stratospheric polar vortex can have a strong effect on mid-latitude weather conditions (*6*). During so-called sudden stratospheric warmings, the Arctic stratosphere rapidly warms by several tens of degrees. This is associated with a reversal of the wind direction, and sudden stratospheric warmings are often followed by cold spells in mid-latitude regions, especially Eurasia. Yet, the different anomalous states of the stratospheric polar vortex and the influence that these states might have on surface weather conditions are poorly understood. Moreover, the extent to which Arctic amplification influences specific vortex states, including sudden stratospheric warmings, is strongly debated (*7*).

Cohen *et al.* build upon earlier work that identified a "stretched" stratospheric polar vortex state that is important for cold spells over the United States (*8*). During stretched states, the vortex weakens and the wind pattern deviates from the normal circular flow. Instead, the wind flow makes stronger southward excursions above the American and Eurasian continents. Cohen *et al.* report that the frequency of these stretched vortex states has increased over recent decades, with the number of autumn and winter days in this regime almost doubling between 1980 and 2020. Furthermore, using regression analyses, the authors show that there is likely a link between stretched stratospheric polar vortex states and abnormal states of Arctic sea ice and Eurasian snow cover. To establish the causal direction of these links, Cohen *et al.* conducted climate modeling experiments whereby the model was run with two specific conditions. One was increased surface albedo over Eurasia—that is, an increase in the reflectivity of the incoming sunlight due to the observed increase in snow cover. The other condition was additional atmospheric heating over the Barents–Kara Seas (which are an extension of the Arctic Ocean north of Siberia). This represented reduced sea ice conditions in autumn and early winter. The atmospheric response to these surface forcings resembles a stretched stratospheric polar vortex state, thus providing evidence that the combination of increasing Eurasian snow cover and decreasing Barents–Kara sea ice favors the occurrence of the stretched states.

> **"...relatively minor changes in dynamics can have important consequences for extremes..."**

A key strength of the study by Cohen *et al.* is that it combines careful observational analyses with new modeling experiments. Thus far, observational studies tend to support a role for Arctic amplification in spurring winter cold spells, whereas most model experiments show little or no connections between Arctic sea ice or snow cover and mid-latitude winter extremes. Also, the study of Cohen *et al.* indicates that the influence of the Arctic on lower latitudes is likely to be rather subtle. The effects of sea ice and snow cover changes on the stratosphere are likely small relative to internal variability (*9*). Yet, given the marked changes in Arctic sea ice and snow cover, even small effects can have important consequences for the stratospheric polar vortex. The frequency of only some stratospheric polar vortex states changes, which thus has little influence on the total variability. Nevertheless, such relatively minor changes in dynamics can have important consequences for extremes, with impacts on society. Thus, from a societal risk perspective, it is imperative to understand these dynamical changes in detail, also to improve predictability and early warning. The thermodynamics of global warming push toward milder winter weather, but changes to atmosphere dynamics could still present risks for society—as illustrated by the extraordinary events in Texas.

Future work should aim at further disentangling causal Arctic teleconnections for the cold and warm seasons in the mid-latitude regions, paying specific attention to high-impact extremes. Arguably, the societal risks are larger with summertime heat waves in which dynamic and thermodynamic drivers can act in the same direction, i.e., toward very intense heat waves (*10*). It will be important to more tightly merge careful observational analyses with modeling experiments. This presents an opportunity to apply new machine learning tools to bridge observation-based and model-based studies and thereby hopefully overcome the typical discrepancies between the two approaches (*11*, *12*). ■

[1]Institute for Environmental Studies (IVM), Vrije Universiteit Amsterdam, Amsterdam, Netherlands. [2]Royal Netherlands Meteorological Institute (KNMI), De Bilt, Netherlands.
Email: d.coumou@vu.nl

REFERENCES AND NOTES

1. J. Doss-Gollin *et al.*, *Environ. Res. Lett.* **16**, 064056 (2021).
2. J. Cohen *et al.*, *Nat. Clim. Chang.* **10**, 20 (2020).
3. J. Cohen *et al.*, *Science* **373**, 1116 (2021).
4. J. A. Screen *et al.*, *Nat. Clim. Chang.* **4**, 577 (2014).
5. G. J. van Oldenborgh *et al.*, *Environ. Res. Lett.* **14**, 114004 (2019).
6. B. Baldwin *et al.*, *Rev. Geophys.* **59**, 1 (2021).
7. T. G. Shepherd, *Science* **353**, 989 (2016).
8. M. Kretschmer *et al.*, *npj Clim. Atmos. Sci.* **1**, 44 (2018).
9. M. Kretschmer *et al.*, *Weather Clim. Dyn.* **1**, 715 (2020).
10. D. Coumou *et al.*, *Nat. Commun.* **9**, 2959 (2018).
11. J. Runge *et al.*, *Nat. Commun.* **10**, 2553 (2019).
12. M. Reichstein *et al.*, *Nature* **566**, 195 (2019).

10.1126/science.abl9792

RETROSPECTIVE

Steven Weinberg (1933–2021)

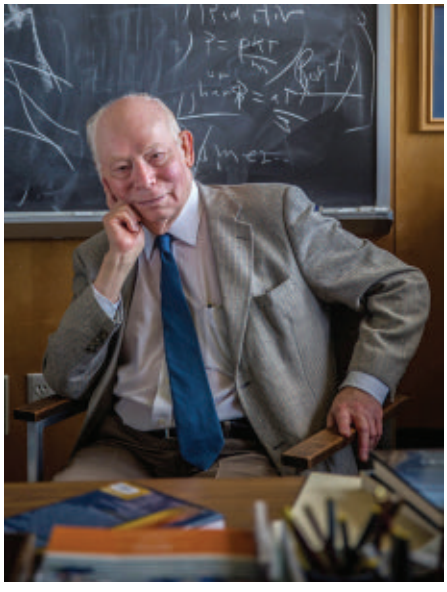
Titan of theoretical physics

By **John Preskill**

Steven Weinberg, widely regarded as the preeminent theoretical particle physicist of his era, passed away on 23 July at age 88. Steve took a pivotal step toward establishing what came to be known as the standard model of the fundamental particles and their interactions, for which he shared the 1979 Nobel Prize in Physics with Sheldon Glashow and Abdus Salam. That contribution was just one highlight in a career studded with major accomplishments. In later years, Steve authored a series of highly influential physics textbooks, as well as eloquent books and essays for the general public expounding on societal and scientific issues. He remained scientifically active up to his final days.

Born in New York City on 3 May 1933, Steve attended the Bronx High School of Science, which claims seven physics Nobel laureates among its alumni, including Steve's classmate Sheldon Glashow. He graduated from Cornell University in 1954 with a BA and received his PhD in physics from Princeton University in 1957, under the supervision of theoretical physicist Sam Treiman. After postdoctoral appointments at Columbia University and the University of California, Berkeley, Steve held faculty positions at Berkeley and the Massachusetts Institute of Technology before moving to Harvard University, where he was hired to fill the shoes of the departing Julian Schwinger. At the time of his death, he was the Jack S. Josey-Welch Foundation Chair in Science and Regental Professor at the University of Texas at Austin, where he had been director of the Theory Group since 1982.

At the start of Steve's career, particle physics was awash in new data, but theoretical understanding lagged behind. Twenty years later, the situation had changed completely. By then, all of nature's known fundamental forces, apart from gravitation, had been woven into a common framework, the standard model, which agrees with experiments in exquisite detail. A crucial step was Steve's "model of leptons," which provided a mathematically sensible description of how electrons interact with neutrinos. What makes that model work is an idea Steve "fell in love with" when he first encountered it in 1960: Nature respects exact symmetries that are hidden from our view because the physical states we encounter (including the vacuum state) are less symmetrical than the underlying physical laws. Steve's model predicted a kind of weak nuclear force never before seen, associated with a previously unknown fundamental particle called the Z boson. By the late 1970s, the existence of this new force had been firmly established experimentally, setting the stage for the Nobel Prize.



It is ironic that Steve's most famous contribution to physics is a concrete model. Constructing models was not his usual style—he preferred robust general arguments expressing solid truths that might survive even as particular models are found wanting and cast aside. Much more in character was another of Steve's groundbreaking achievements, formulating and advancing the idea known as effective field theory. A truly complete theory of fundamental physics would need to include massive particles and short-distance interactions that are still unknown because they are beyond the reach of currently feasible experiments. Steve exhorted physicists to write down an "effective theory" that incorporates all the essential principles, such as locality in space and time, conservation of probability, and all relevant symmetries that apply. Surprisingly, our ignorance about the more complete theory does not prevent us from making precise quantitative predictions about experiments performed at accessible energies. The success of this framework, in particle physics and beyond, is a vindication of Steve's credo that we should build our understanding of nature on the most general and trusted fundamental principles. While the roots of the effective field theory concept came from Kenneth Wilson, it was Steve who masterfully developed it into an efficient computational scheme and convinced other physicists of its power.

Steve had many distinctive qualities as a researcher. For one, he was not a visual thinker at all—Steve believed in the explanatory power of equations, not pictures. His otherwise lucid textbook *Gravitation and Cosmology*, published in 1972, contains hardly any figures, even though most physicists appreciate drawings that convey the geometry of spacetime. When MS-DOS was superseded by Windows, Steve migrated to the new operating system reluctantly, because he was much more comfortable typing on the command line than clicking an icon.

With a few exceptions, Steve was the sole author of his best-known papers, and he almost never collaborated directly with students. He usually worked at home, where only his wife, Louise, could interrupt him. Oddly, he kept a television on his desk, which was often turned on while he worked; he explained that this made it easier to resume the task at hand after taking a break. As my PhD adviser during the late 1970s, Steve was a fount of inspiration more than a source of concrete guidance (which was fine with me). My explorations of the very early Universe and of particle physics beyond the standard model followed in his footsteps.

Although he never stopped conducting high-quality original research, Steve also excelled at writing physics textbooks that blended uncommon insight with meticulous attention to detail. His extensive writings for the lay public often staked out controversial positions on subjects such as nuclear proliferation, religion, the history of science, and funding for big science projects. Whatever the topic, his clear arguments and deep scholarship never failed to impress and edify.

Steve believed in the power of the human mind to understand the world. He sometimes mused about how astonishing it is that a theorist's "squiggles" on paper can align with physical reality. And yet they can. Few squiggles have captured nature's hidden secrets better than those written by the hand of Steven Weinberg. ■

Division of Physics, Mathematics, and Astronomy, California Institute of Technology, Pasadena, CA 91125, USA. Email: preskill@caltech.edu

10.1126/science.abl8187

PHOTO: TAMIR KALIFA/*THE NEW YORK TIMES*/REDUX

POLICY FORUM

FOOD

Do we need a new science-policy interface for food systems?

Credibility, legitimacy, and diversity of knowledge are critical

By **Esther Turnhout[1,2], Jessica Duncan[3], Jeroen Candel[4], Timo Y. Maas[5], Anna M. Roodhof[3], Fabrice DeClerck[6,7], Robert T. Watson[8]**

Food systems require urgent transformations to meet multiple demands of food and nutrition security, justice, livelihoods, biodiversity conservation, and climate change mitigation and adaptation. These transformations require knowledge on the multiple dimensions of food systems (e.g., production, trade, consumption, culture, human and animal health, livelihoods and employment, food waste, and environmental sustainability), as well as a mechanism to translate these insights and analyses into governance processes. Drawing on the role of the Intergovernmental Panel on Climate Change (IPCC) in global climate policy, an equivalent platform has been proposed to support food system transformations (*1*). These calls have gained momentum in the context of the upcoming United Nations Food Systems Summit (FSS) (*2*). We reflect on the science-policy landscape for food systems and discuss requirements for and challenges of a science-policy platform, focused on addressing social, cultural, and political dimensions of food and challenges in food systems governance.

Our analysis is relevant for the current processes around the FSS, where critical voices have pointed to risks of undue corporate influence of the Summit and a dominance of techno-optimist approaches and solutions (*3, 4*). These concerns demonstrate the need to ensure equity and justice in the inclusion of scientific, local, and Indigenous knowledge systems and in the participation of actors from civil society, the private sector, and governments.

[1]Section of Science, Technology, and Policy Studies, University of Twente, Enschede, Netherlands. [2]Forest and Nature Conservation Policy Group, Wageningen University, Wageningen, Netherlands. [3]Rural Sociology Group, Wageningen University, Wageningen, Netherlands. [4]Public Administration and Policy Group, Wageningen University, Wageningen, Netherlands. [5]PBL Netherlands Environmental Assessment Agency, The Hague, Netherlands. [6]OneCGIAR, Montpellier, France. [7]EAT Forum, Montpellier, France. [8]Department of Environment, University of East Anglia, Norwich, UK. Email: e.turnhout@utwente.nl

THE GLOBAL FOOD SYSTEMS SCIENCE-POLICY LANDSCAPE

There is no shortage of organizations and initiatives dedicated to the synthesis and assessment of knowledge around food systems for policy purposes. These include applied research organizations such as the reformed One CGIAR, assessment processes such as the International Assessment of Agricultural Knowledge, Science and Technology for Development (IAASTD), the EAT-Lancet Commission, and the High-Level Panel of Experts (HLPE) to the UN Committee on World Food Security (CFS). Moreover, aspects of food systems are covered by the Intergovernmental Platform on Biodiversity and Ecosystem Services (IPBES), the IPCC, and the expert bodies of the Codex Alimentarius Commission.

A recent report commissioned by the European Commission reviewed the global food systems landscape and concluded that current organizations and initiatives provide valuable contributions to bridging gaps between knowledge and policy-making (*5*). Nonetheless, it identified a need for integration and coordination, in addition to filling gaps in knowledge related to, for example, the political economy and sustainability dimensions of food, as well as options for transforming food systems (*5*). By underscoring the importance of global knowledge synthesis for food systems transformations, the report illustrates a mode of reasoning identified in other policy domains where the science-policy interface is put forward as a solution to improve governance (*6*). Although this reasoning can be intuitively appealing, we raise two critical questions to consider as part of any decision-making process about whether and how to improve the food systems science-policy interface: How can a food systems platform ensure legitimate and credible knowledge?; and how will it be able to support actual improvements in food systems governance?

ENSURING CREDIBLE AND LEGITIMATE KNOWLEDGE

There is increasing consensus that inclusive and participatory approaches to knowledge production can support the credibility and legitimacy of knowledge. This is particularly important for the case of food systems science and knowledge. Although science can provide clarity on global guardrails to guide policy on health, climate, and environment, the IAASTD has made evident that food systems science and knowledge involve tensions and contestations, among others, about the potential contributions and risks of technologies like genetically modified organisms, pesticides, trade agreements, agroecology, and organic farming to desired food system outcomes (*7*). It is important to recognize that these contestations are characterized by competing understandings not only of what policy options are effective and legitimate but also of what knowledge is seen as relevant and credible. That is, they are not simply controversies over competing values or interests; they are knowledge controversies (*8*).

Although there is no doubt about the value of science, the persistence of knowledge controversies underscores the importance of including plural forms of knowledge from natural science, social science, and humanities disciplines, as well as from Indigenous and local knowledge systems. A key task of global platforms lies in organizing the rigorous, independent, and expert-led synthesis and assessment of this knowledge without a priori privileging science. Put differently: We need a knowledge-policy interface, not just a science-policy interface.

However, ensuring pluralism is not an easy task in view of current inequities between knowledge holders, particularly geographical differences in scientific capacities, access, and resources, and differences between industry-funded versus civil society–oriented research efforts. In this regard, IPBES is often seen as an example of a mechanism that has taken explicit steps to ensure this inclusion and diverse participation (*9*), and this has been of key importance to the authority and relevance of its assessments. The HLPE, which develops evidence-based analyses and advice at the request of the CFS, similarly calls for the representation of diverse knowledges (*10*). Notably, the HLPE pays explicit attention to controversies to explore how diverse knowledges can enrich understanding of problems, solutions, tensions, and trade-offs (*10*). The HLPE's Global Narratives report offers an example that explicitly discusses controversial areas, such as sustainable intensification and Climate Smart Agriculture, and identifies and assesses diverse knowledge claims from plural knowledge systems (*11*).

SUPPORTING IMPROVED FOOD SYSTEMS GOVERNANCE

Improving the knowledge-policy interface only makes sense if it can actually contribute to the needed transformations in food systems. This is an urgent issue in view of the challenges of global food governance, which include a lack of coordination, conflicting interests between stakeholders and member states, and a general failure to ensure equitable access to sufficient and healthy diets, improve livelihood opportunities for food producers and processors, and contribute to sustainability (*12*).

Experiences from IPBES and IPCC show that political buy-in and uptake are facilitated by the joint negotiation by governments of the assessments' summaries for policy-makers. The 2019 IPBES Global Assessment made global headlines, and the IPCC's repeated messages over many years have contributed to raising awareness and changing discourse and policy. However, challenges remain in informing and supporting concrete actions by public and private decision-makers across levels and scales (*13*). The pluralist approach suggested in the previous section is key to securing relevance for and uptake by a diversity of actors in government, civil society, and the private sector, all of whom play vital roles in food systems governance (*14*). In other words, and expanding further on the notion of the knowledge-policy interface, what is needed might be better called a knowledge-governance interface.

The CFS and the HLPE offer an example with procedures comparable to those of IPBES and the IPCC in the sense that HLPE reports form the basis for the joint negotiation of policy recommendations. Notably, the CFS has offered participation rights to relevant stakeholder groups, including from civil society and the private sector. This means that member states and participants are active in negotiations, including those concerning knowledge and assessment, and, with varying degrees of influence, in the contextualization of policy outcomes (*11*). Analysis of the ongoing national food system dialogues of the FSS could illuminate whether this other model can effectively engage diverse actors and enhance the credibility, legitimacy, and actionability of options and pathways.

Moreover, the IPCC and IPBES inform specific multilateral conventions and also address specific requests from these conventions. This adds weight to the assessments that are produced and pushes the scientific community to produce "demand-driven" research that has specific value to decision-making. Apart from binding regulations related to the trade of food mediated through the World Trade Organization (WTO), there is no dedicated global convention for food systems.

Improving the knowledge-governance interface requires not just improving science and knowledge, but also improved coordination of governance. This can involve coordination between international organizations such as the CFS and WTO, as well as the development of dedicated international food systems regulations (*15*). For example, the UN Framework Convention on Climate Change and the Convention on Biological Diversity could include targets and actions to promote food systems sustainability. The fragmentation of food systems governance means that it is currently unclear what governance processes a food systems platform will inform and how governments and other intended policy and societal audiences will be engaged. If there is no real perspective on improved governance, this will ultimately undermine the utility and effectiveness of a food systems platform.



ALFREDO CALIZ/PANOS PICTURES/PANOS PICTURES/REDUX

AN IPCC FOR FOOD?

As we have discussed so far, efforts to strengthen the food systems knowledge-governance interface require improved coordination of knowledge as well as governance, and a participatory and pluralist approach to both.

Creating a new food systems platform following the models of the IPCC and IPBES is a potential option to meet these objectives. However, this model involves considerable challenges. For one, it will likely take several years of intergovernmental negotiations before assessment work could start, and the costs of such a platform are also substantial: an estimated USD 5 to 8 million per year. Second, close engagement with governments and stakeholders will be needed to ensure that the platform is demand-driven; supports the interaction between knowledge, policy, and action; and maintains independence, legitimacy, and credibility.

Despite the tremendous efforts of IPCC and IPBES in accomplishing these goals, there is also a potential limitation per-



Food systems touch on many aspects of human life, such as this market in Saint-Louis, Senegal, and require aligned actions to achieve global goals.

taining to pluralism and legitimacy. The experience of IPCC and IPBES shows that governments have been restrictive in allowing the participation of stakeholders from science, the private sector, or civil society in decision-making roles in the platform, including decisions about what assessments will be undertaken and other components of the program of work, or the negotiation of platform products. Governments thus have a deciding role in what and whose knowledge needs will be met and how. If repeated in a new food systems platform, this may affect the credibility and legitimacy of assessments, as well as their relevance for and uptake in governance processes.

In this respect, the participatory mechanisms of the CFS and the HLPE provide alternative models to enhance pluralism in the production of assessments, as well as in their use and uptake (*4*). Both are not without challenges and limitations of their own. Intergovernmental negotiations are often frustrating and lengthy, and the open and participatory approach of the CFS can contribute to this. Recent policy negotiations have left many actors questioning its effectiveness. Moreover, the HLPE relies on a much smaller number of scientists than IPBES or IPCC and needs increased funding and capacity to integrate available knowledge.

Another option, and a potential way to make progress on this issue, is the organization of a food systems assessment. This would contribute to the coordination and synthesis of knowledge without the high costs and lengthy negotiations involved in creating a new platform. To ensure relevance and uptake, the assessment could be called for and overseen by an existing intergovernmental body such as the UN General Assembly or the FAO Council and could create organizational roles for the CFS and HLPE. In this option, care must be taken to ensure participation and inclusion of diverse stakeholders and forms of knowledge. Throughout the process, a clearer picture could emerge on what further institutional steps can be taken, whether to create a new platform, strengthen the HLPE and the CFS, or take some other approach.

NO SILVER BULLET

There is no silver-bullet solution that will be able to address current challenges in food systems knowledge and governance. Efforts to coordinate knowledge can be valuable, but only if these efforts ensure the legitimacy and credibility of knowledge, and when they can contribute to urgently needed improved global food governance. Although creating a new platform can be appealing, we offer three issues for careful consideration.

First, we have to consider what is already in place. In many ways, the CFS and the HLPE are well positioned to fulfill the role of a food systems knowledge-governance interface. We need to consider what challenges they face and why, and how these challenges can be overcome. Without such reflection, a new platform or assessment will likely reproduce these same challenges.

Second, if pluralism, equitable participation, and inclusion of diverse forms of knowledge cannot be ensured, a new platform could do more harm than good. In this scenario, a new platform would risk promoting a narrow and regressive understanding of food systems issues and knowledge and risk acting as an obstacle for the needed transformations.

Third, we must recognize that effective governance cannot be reduced to scientific input. Fostering a just and sustainable global food system requires commitment, political will, and the participation of governments and stakeholders. The implicit suggestion in many science-policy interface initiatives that the synthesis, assessment, and communication of knowledge will strengthen governance in and of itself is misguided and overly simplistic, and it risks detracting attention away from actual policy action. Any existing or new science-policy platform will have to carefully navigate these political dimensions by putting inclusion, justice, and equity center stage. ■

REFERENCES AND NOTES

1. J. Von Braun, M. Kalkuhl, "International science and policy interaction for improved food and nutrition security: Toward an International Panel on Food and Nutrition (IPFN)," ZEF working paper series nr 142, University of Bonn, Center for Development Research (ZEF), Bonn (2015). www.econstor.eu/bitstream/10419/142725/1/837872839.pdf.
2. L. Fresco, "To feed a growing world, we need to change our food systems now," World Economic Forum (2020). www.weforum.org/agenda/2020/11/how-to-create-sustainable-food-systems/.
3. M. Canfield, M. D. Anderson, P. McMichael, *Front. Sustain. Food Syst.* **5**, 1 (2021).
4. B.Burlingame et al. Open Letter: Food systems science-policy interface: don't reinvent the wheel, strengthen it! HLPE, Rome (2021). http://www.fao.org/fileadmin/templates/cfs/Docs2021/Documents/SPI_for_Food_Systems_-_No_need_to_reinvent_the_wheel__HLPE_Open_Letter_20_May_2021.pdf?fbclid=IwAR2el_qnbcxHsutjS0cRsV4UrhCArlpvdx-i7qttmAAWpSzVJaKgJGDYlhrQ.
5. European Commission, "Recommendations to the United Nations' Food Systems Summit Scientific Group from the European Commission's High-Level Expert Group to assess needs and options to strengthen the international Science Policy Interface for Food Systems Governance" (2021). https://ec.europa.eu/info/sites/default/files/research_and_innovation/research_by_area/documents/hleg_recommendation_to_the_unfss_scientific_group_web.pdf.
6. E. Turnhout, K. Neves, E. de Lijster, *Environ. Plan. A.* **46**, 581 (2014).
7. IAASTD 2008a. "Executive summary of the synthesis report" (IAASTD, 2008), https://www.globalagriculture.org/fileadmin/files/weltagrarbericht/IAASTDBerichte/IAASTDExecutiveSummarySynthesisReport.pdf.
8. E. Turnhout, W. Tuinstra, W. Halffman, Environmental Expertise: Connecting Science, Policy and Society (Cambridge Univ. Press, 2019).
9. I. Díaz-Reviriego, E. Turnhout, S. Beck, *Nat. Sustain.* **2**, 457 (2019).
10. J. Duncan, P. Claeys, *Food Secur.* **10**, 1411 (2018).
11. HLPE, "Food security and nutrition: Building a global narrative towards 2030," a report by the High Level Panel of Experts on Food Security and Nutrition of the Committee on World Food Security, Rome (2020). http://www.fao.org/3/ca9731en/ca9731en.pdf.
12. J. J. L. Candel, *Food Secur.* **6**, 585 (2014).
13. T. Y. Maas *et al.*, *Environ. Sci. Policy* **123**, 210 (2021).
14. W. Pearce, M. Mahony, S. Raman, *Environ. Sci. Policy* **80**, 125 (2018).
15. R. Vos, "Thought for food: Strengthening global governance of food security," Committee for Development Policy, CDP background paper nr. 29, New York (2015). https://www.un.org/en/development/desa/policy/cdp/cdp_background_papers/bp2015_29.pdf.

ACKNOWLEDGMENTS

The authors declare ongoing and past engagements with several of the science-policy platforms mentioned. These include the study and analysis of CFS and HLPE (J.D.) and IPBES (E.T.), and expert and other roles in EAT-Lancet (F.D.C.), IAASTD (R.T.W.), IPCC (R.T.W.), IPBES (F.D.C., R.T.W., E.T.), CFS (J.D., F.D.C.), and the UNFSS (F.D.C.).

10.1126/science.abj5263

CALL FOR NOMINATIONS

Mechthild Esser Nemmers Prize in Medical Science

Northwestern University Feinberg School of Medicine invites nominations for the Mechthild Esser Nemmers Prize in Medical Science. This prize includes a cash award of $200,000. Candidacy for the 2022 Nemmers Prize is open to physician-scientists whose body of research exhibits outstanding achievement in their disciplines as demonstrated by works of lasting significance. Individuals of all nationalities and institutional affiliations are eligible except current or recent members of the Northwestern University faculty and recipients of the Nobel Prize.

The 2022 recipient of the Nemmers Prize will deliver a public lecture and participate in other scholarly activities at Northwestern University. Nominations for the Prize will be accepted until November 1, 2021.

For further information, and to submit a nomination, please visit feinberg.northwestern.edu/nemmers

Northwestern Medicine®
Feinberg School of Medicine

The Nemmers Prize in Medical Science | Northwestern University Feinberg School of Medicine | Chicago, IL 60611
nemmersmedicine@northwestern.edu

1848 SOCIETY
AAAS

Your Legacy to Science

AN ESTATE GIFT TO THE AMERICAN ASSOCIATION FOR THE ADVANCEMENT OF SCIENCE

AAAS is deeply committed to advancing science, engineering and innovation around the world for the benefit of all people. **You can help us.**

By making AAAS a beneficiary of your will, trust, retirement plan, or life insurance policy, you will become a member of our 1848 Society, joining Thomas Edison, Alexander Graham Bell and the many distinguished individuals whose vision led to the creation of AAAS and our world-renowned journal, *Science*, so many years ago.

Unlike many of its peers, *Science* is not for-profit. Your estate gift would provide long-term financial stability and durable annual income that will support operations and competitive innovation for years to come.

If you plan to include AAAS in your estate plans, provide this information to your lawyer or financial adviser:

Legal Name: American Association for the Advancement of Science
Federal Tax ID Number: 53-0196568
Address: 1200 New York Avenue, NW, Washington, DC 20005

For more information or to let us know you are including AAAS in your future giving plans, contact the AAAS Office of Philanthropy and Strategic Partnerships at **1-800-215-1969** or **philanthropy@aaas.org.**

Additional details online at **www.aaas.org/1848Society.**

LETTERS



Ensuring livestock welfare could help reduce predator attacks.

PHOTO: MAURITIUS IMAGES GMBH/ALAMY STOCK PHOTO

Edited by **Jennifer Sills**

Animal welfare's role in human-wildlife conflict

Human-wildlife conflicts threaten biodiversity conservation, food security, and human well-being. As recently highlighted in the Perspective "Human-wildlife conflict under climate change" (B. Abrahms, 30 July, p. 484), climate change is causing this threat to escalate. To mitigate human-wildlife conflicts, there have been calls for better integration of social, economic, political, ecological, and even historical factors. However, one factor of paramount importance is often overlooked: the responsibility of farmers and competent authorities to ensure livestock welfare.

Livestock welfare has been declared a priority by the World Organisation for Animal Health (OIE), an intergovernmental body with 180 member nations. OIE provides standards for the improvement of the welfare of farm animals, including recommendations for protecting them from wildlife attacks. Wildlife attacks impinge on an animal's right to live without discomfort, fear, distress, pain, or injuries (*1*). As Abrahms explains, wildlife attacks on livestock may intensify in some regions as climate change forces predators and livestock to increase their spatial overlap and interactions (*2*). Climate-driven changes may also increase livestock vulnerability as diseases become more prevalent or decreased resources lead to poor nutrition (*3*, *4*).

Enforcing livestock welfare will serve to further reduce livestock vulnerability to predation. Efforts to secure animal welfare can also buffer the impact of climate change on these human-wildlife conflicts worldwide by reducing both wildlife attacks on healthy unprotected livestock and those mediated by livestock's poor condition. Governments should enact regulations that integrate livestock welfare duties and hold livestock owners accountable for providing adequate resources and protection to farm animals. For example, European Directive 98/58/EC states that "animals not kept in buildings shall where necessary and possible be given protection from adverse weather conditions, predators, and risks to their health" (*5*). Strengthening livestock protection by, for example, guarding, fencing, using nonlethal deterrents (*6*), and requiring farmers to inspect livestock frequently would reduce wildlife attacks while allowing proper attention to sick or injured livestock.

The integration of animal welfare into human-wildlife conflict mitigation strategies makes clear that the responsibility for alleviating conflict lies with everyone involved, not just conservation professionals.

José Vicente López-Bao* and Patricia Mateo-Tomás
Biodiversity Research Institute (Consejo Superior de Investigaciones Científicas–Oviedo University–Principality of Asturias), Oviedo University, E-33600 Mieres, Spain.
*Corresponding author.
Email: jv.lopezbao@gmail.com

REFERENCES AND NOTES

1. Farm Animal Welfare Council, "Farm animal welfare in Great Britain: Past, present, and future" (2009).
2. A. Aryal *et al*., *Theor. Appl. Climatol.* **115**, 517 (2014).
3. L. Musemwa *et al*., *Asian J. Agric. Rural Dev.* **2**, 621 (2012).
4. D. Grace *et al*., "Climate and livestock disease: Assessing the vulnerability of agricultural systems to livestock pests under climate change scenarios," CCAFS Working Paper no. 116 (CGIAR Research Program on Climate Change, Agriculture, and Food Security, Copenhagen, Denmark, 2015).
5. European Commission, "Directive 98/58/EC of 20 July 1998 concerning the protection of animals kept for farming purposes" (OJ L 221, 8/8/1998) (1998).
6. L. M. Van Eeden *et al*., *Plos Biol*. **16**, e2005577 (2018).

10.1126/science.abl8293

Disability innovation strengthens STEM

Individuals with disabilities face many barriers to pursuing careers in science, technology, engineering, and mathematics



Pushing the Boundaries of Knowledge

As AAAS's first multidisciplinary, open access journal, *Science Advances* publishes research that reflects the selectivity of high impact, innovative research you expect from the *Science* family of journals, published in an open access format to serve a vast and growing global audience. Check out the latest findings or learn how to submit your research: **ScienceAdvances.org**

Science Advances
AAAS

GOLD OPEN ACCESS, DIGITAL, AND FREE TO ALL READERS

(STEM). In an effort to contribute fully, they have called for accommodations such as flexible schedules, remote work options, and a supportive work culture. Meanwhile, they created technologies that would allow them to work more effectively. During the COVID-19 pandemic lockdowns, many in STEM who had never needed such accommodations before came to rely on them (*1*). Going forward, we must remember that accommodating people with disabilities in STEM benefits us all.

People with disabilities are hindered by limited understanding by employers (*2*), lack of role-models (*3*), and limited encouragement to pursue a career and participate in STEM-related activities (*4*). Students with disabilities are less likely to receive financial aid and to be enrolled full time (*5*). Women with disabilities are more likely to be unemployed and hold lower status occupations compared to men with disabilities (*6*). Barriers to inclusion go beyond a lack of access to accommodations; culturally informed biases, stigma, and even self-doubt relating to disability contribute to underrepresentation and inequity.

Diversity drives innovation. Despite the challenges they have faced, people with disabilities pioneered technologies that eased the transition to a work-from-home culture. The background-blurring feature in video conference calls was developed by a deaf software engineer to facilitate lip-reading (*7*). This tool now offers privacy to people juggling working from home and childcare or messy home settings. An engineering graduate student with carpal tunnel syndrome developed the transformative touchscreen and multi-finger gesture technology (such as two-finger scrolling) that underlies the touchscreens used on iPads and iPhones (*8, 9*).

As we dealt with upheaval in schedules and adjusted to home workspaces, many in STEM have leveraged mental health tools to manage pandemic anxiety (*10*). This experience has made us all more aware of what it's like to live and work under conditions that are not optimal. As people with disabilities have argued, we need to be flexible, to adjust our work expectations (*11*), and to be kind to ourselves. Now is the time to acknowledge that individuals with disabilities are strong and innovative contributors to society. By valuing traits such as compassion, empathy, and humility, we can empower all people in STEM, making our field better, not weaker.

We call on our institutions to harness the strengths that true diversity of ability brings, to work together toward a fully inclusive culture, to raise awareness of disability as an essential part of diversity, and to actively work toward an environment free from bias and discrimination. This requires that we unlearn harmful assumptions and learn new concepts, such as Universal Design principles (*12*). It will require continuous self-education and reflection as well as persistence, concrete actions, funding, and, above all, accountability. Individuals with disabilities can and should lead these efforts, which will benefit the scientific community and humanity as a whole.

Ilse S. Daehn[1]* and Paula L. Croxson[2,3]
[1]Department of Medicine–Nephrology, Icahn School of Medicine at Mount Sinai, New York, NY 10029, USA. [2]Mortimer B. Zuckerman Mind Brain Behavior Institute, Columbia University, New York, NY 10027, USA. [3]Department of Neuroscience, Icahn School of Medicine at Mount Sinai, New York, NY 10029, USA.
*Corresponding author.
Email: ilse.daehn@mssm.edu

REFERENCES AND NOTES

1. A. Shew, *Nature* **581**, 9 (2020).
2. C. Dunn, K. S. Rabren, S. L. Taylor, C. K. Dotson, *Intervent. School Clinic* **48**, 47 (2012).
3. H. Lee, R. Templeton, *Theor. Pract.* **47**, 212 (2008).
4. L. Eriksson, J. Welander, M. Granlund, *J. Dev. Phys. Disabil.* **19**, 485 (2007).
5. National Science Foundation, "Women, minorities, and persons with disabilities in science and engineering" (2019); www.nsf.gov/statistics/2017/nsf17310/.
6. S. Lindsay *et al., Disabil. Rehabil.* **41**, 319 (2019).
7. S. Ray, "Empathy and innovation: How Microsoft's cultural shift is leading to new product development" (Microsoft, 2019); https://news.microsoft.com/innovation-stories/empathy-innovation-accessibility/.
8. W. Westerman, *Hand Tracking, Finger Identification, and Chordic Manipulation on a Multi-touch Surface* (University of Delaware, 1999).
9. S. McGrane, "No press, no stress: When fingers fly," *The New York Times* (2002).
10. O. Lahtinen, J. Aaltonen, J. Kaakinen, L. Franklin, J. Hyönä, *Curr. Psychol.* 10.1007/s12144-021-01762-z (2021).
11. K. Ljuslinder *et al., Scand. J. Disabil. Res.* **22**, 35 (2020).
12. S. Burgstahler, "Universal Design in postsecondary education: Process, principles, and applications," Disabilities, Opportunities, Internetworking, and Technology (2008).

10.1126/science.abk2631

Collective agency transforms societies

Human agency may provide the lens through which COVID-19's legacy will be viewed, according to J. Couzin-Frankel's historical account of pandemics ("Will COVID-19 change science? Past pandemics offer clues," News, 13 July, https://scim.ag/2W7ZtD2). She uses the legacy of the HIV pandemic as one example, celebrating the patient-activists who had to fight for access to then-experimental HIV treatment and whose efforts ultimately transformed treatment approval policies. HIV activists' transformative legacy is larger than this, however: It was collective agency that fought marginalization, exclusion, and stigma attached to HIV-affected communities. This legacy of fighting stigma should also shape the lessons societies learn in the wake of COVID-19.

Stigmatization is a dynamic social process that discredits certain types of knowledge and lived experience (*1*). Stigma is a form of symbolic power that intends to keep people either down (e.g., by shaming) or away (e.g., by excluding). Stigmatization contributes to the marginalization of groups and maintains racialized and gendered inequalities in societies (*2*). Stigmatization is thus a threat to societal cohesion and an obstacle to sharing knowledge in a way that transforms societies.

The lived experiences of a pandemic are discredited when the affected community is already stigmatized, as was the case for LGBTQI+ people during the HIV epidemic. Thus, many experiences learned in the HIV epidemic, such as how to increase acceptance of barrier methods (e.g., condoms for HIV and now face masks for COVID-19) (*3*), were lost and had to be relearned for the societal response to COVID-19. Marginalized communities who have suffered disproportionately from COVID-19 have developed forms of collective agency as well (*4*). Yet collective agency–based perspectives remain under-explored (*5*) or under-heard in health research. Learning from the collective agency of marginalized communities in pandemics would benefit societies as a whole and promote cohesion, provided it is combined with actively fighting marginalization and stigma.

Transformative learning inspired by health activism research could take many shapes (*6*). The memories of collective agency should be kept alive and accessible to all members of the society. Lived experience of marginalized communities should be acknowledged as expert knowledge. Creating equitable, cohesive, and participatory spaces will allow the transfer of community knowledge and collective agency.

Yudit Namer* and Oliver Razum
Department of Epidemiology and International Public Health, School of Public Health, Bielefeld University, Bielefeld, Germany, and Research Institute Social Cohesion, Bielefeld, Germany.
*Corresponding author.
Email: yudit.namer@uni-bielefeld.de

REFERENCES AND NOTES

1. E. Goffman, *Stigma: Notes on the Management of a Spoiled Identity* (Simon & Schuster, 1963).
2. B. G. Link, J. Phelan, *Soc. Sci. Med.* **103**, 24 (2014).
3. R. O. Valdiserri, D. R. Holtgrave, S. C. Kalichman, *AIDS Behav.* **24**, 3283 (2020).
4. C. H. Logie *et al., Glob. Public Health*, 10.1080/17441692.2021.1934061 (2021).
5. I. Duque Franco *et al., Environ. Urban.* **32**, 523 (2020).
6. S. Chown, L. H. Malcoe, in *Critical Inquiries for Social Justice in Mental Health*, M. Morrow, L. H. Malcoe, Eds. (University of Toronto Press, 2017), pp. 443–474.

10.1126/science.abl7621

RESEARCH

IN *SCIENCE* JOURNALS

Edited by
Michael Funk



An electron microscopy structure of a complex involved in methanogenesis reveals electron bifurcation and transport pathways.

IMAGE: WATANABE *ET AL.*

STRUCTURAL BIOLOGY

Methanogenesis megacomplex

An important first step in methanogenesis is the conversion of carbon dioxide to a reduced one-carbon formyl unit that is a substrate for downstream steps. This reaction is catalyzed by a complex of enzymes, including components for oxidizing hydrogen or formate and splitting two electrons along different energetic paths. Watanabe *et al.* carefully purified and prepared anaerobic cryo–electron microscopy samples of the enzyme complex responsible, resulting in a three-megadalton hexameric structure at 3- to 3.5-angstrom resolution. The arrangement of iron–sulfur cofactors provides an explanation for how electron bifurcation is coupled to large protein motions, which are expected from the multiple conformational states present. —MAF *Science,* abg5550, this issue p. 1151

SCIENTIFIC COMMUNITY

Gender disparities in authorship practices

Authorship is the professional capital of scientists. Ni *et al.* revealed the underlying mechanisms of gender differences in authorship naming and ordering practices by surveying more than 5500 scientists worldwide and statistically analyzing the responses. More than half of the respondents had experienced authorship disagreements, but women were more likely than men to encounter them. Communication can mitigate disagreements. Women were more likely to discuss authorship with their collaborators, to do so early in the process, and to feel uncomfortable discussing authorship issues. Because of disagreements, women were more likely to observe hostility and limit future collaborations, whereas men were more likely to observe fraud and engage in retribution. Addressing fairness disparities in authorship matters is necessary for closing the gender gap in science. —JD

Sci. Adv. 10.1126/sciadv.abe4639 (2021).

CRISPR TECHNOLOGY

Screen time for CRISPR

CRISPR-Cas9 has been used to edit the genomes of organisms ranging from fruit flies to primates, but it has not been used in large-scale genetic screens in animals because generating, validating, and keeping track of large numbers of mutant animals is prohibitively laborious. Parvez *et al*. developed Multiplexed Intermixed CRISPR Droplets, or MIC-Drop, a platform combining droplet microfluidics, en masse CRISPR injections, and barcoding, to enable large-scale genetic screens. In pilot phenotypic screens in zebrafish, MIC-Drop enabled rapid identification of the target of a small molecule and discovery of several new genes governing cardiovascular development. MIC-Drop is potentially scalable to thousands of targets and adaptable to diverse organisms and experiments. —DJ

Science, abi8870, this issue p. 1146

SUPERCONDUCTIVITY

Patterned nematics

Electrons in solids can break rotational symmetry, resulting in electronic nematicity. This phenomenon has been observed in both cuprate-based and iron-based high-temperature superconductors, and its relationship to superconductivity remains a subject of debate. Shimojima *et al*. used linear dichroism measurements to image nematicity in two iron-based superconductors. Unexpectedly, the researchers found periodic patterns with very long wavelengths. The findings could be described with a phenomenological model assuming a train of nematic domain walls. —JS

Science, abd6701, this issue p. 1122

CORONAVIRUS

A proofreader in SARS-CoV-2

Although vaccines provide protection against severe acute respiratory syndrome coronavirus 2 (SARS-CoV-2), there remains a need for antivirals to treat COVID-19. Nucleotide analog drugs such as remdesivir, which target the viral RNA polymerase, have potential but are compromised by exoribonuclease (ExoN) activity that removes incorrect nucleotides from newly synthesized RNA. Liu *et al*. determined the structure of the complex that harbors the ExoN activity (nsp10–nsp-14) bound to a mimic of RNA that has incorporated an incorrect nucleotide. The structure shows how the RNA is recognized and suggests how ExoN specifically removes mismatched nucleotides. It also provides clues for designing nucleotide analogs that may evade excision. —VV

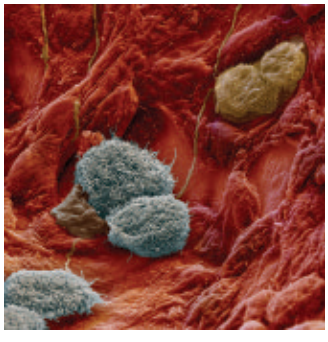
Science, abi9310, this issue p. 1142

IMMUNOLOGY

Fine-tuning macrophage function

Dysregulation of alveolar macrophages in the lung results in the accumulation of surfactant and respiratory failure if left untreated. Shoger *et al*. found that the amount of the suppressor of cytokine signaling family protein CISH was increased in response to the homeostatic cytokine granulocyte-macrophage colony-stimulating factor (GM-CSF). Loss of CISH led to increased GM-CSF signaling, increased activity of the transcription factor GATA2, and dysregulation of the genes responsible for alveolar macrophage function. Thus, the fine-tuning of cytokine signaling is required to regulate tissue-specific pathways that maintain alveolar macrophage function. —JFF

Sci. Signal. **14**, eabe5137 (2021).



Alveolar macrophages, seen here by false-color scanning electron microscopy, rely on cytokine signaling to function properly in tissues such as the lung.

PHOTOS: (LEFT TO RIGHT) EYE OF SCIENCE/SCIENCE SOURCE; CHRIS ROBBINS/ALAMY STOCK PHOTO

CLIMATE DYNAMICS

Cold weather disruptions

Despite the rapid warming that is the cardinal signature of global climate change, especially in the Arctic, where temperatures are rising much more than elsewhere in the world, the United States and other regions of the Northern Hemisphere have experienced a conspicuous and increasingly frequent number of episodes of extremely cold winter weather over the past four decades. Cohen *et al*. combined observations and models to demonstrate that Arctic change is likely an important cause of a chain of processes involving what they call a stratospheric polar vortex disruption, which ultimately results in periods of extreme cold in northern midlatitudes (see the Perspective by Coumou). —HJS

Science, abi9167, this issue p. 1116; see also abl9792, p. 1091

METASURFACES

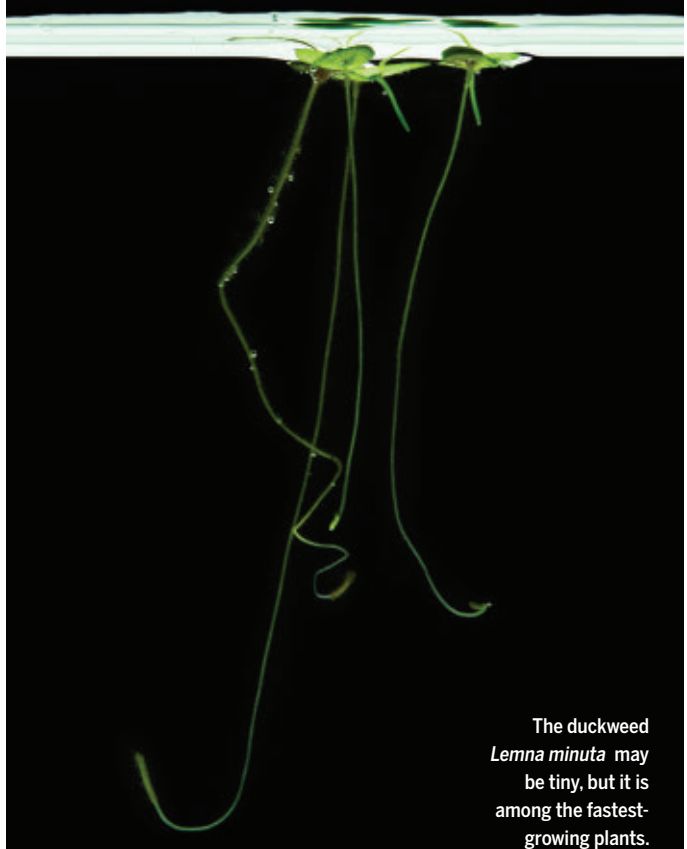
Upon reflection, modulate phase

Metasurfaces provide a platform to fabricate optical devices in a compact form much thinner than their corresponding bulk optical components. Recognizing that metasurfaces are also open systems interacting with their environment, Song *et al*. designed a metasurface that exploits those non-Hermitian properties such that they can encircle an exceptional point. Subsequent scattering from such an exceptional point was shown to be polarization dependent, thus providing an additional control knob in designing metasurfaces for wave front engineering. —ISO

Science, abj3179, this issue p. 1133

IN OTHER JOURNALS

Edited by **Caroline Ash** *and* **Jesse Smith**



The duckweed *Lemna minuta* may be tiny, but it is among the fastest-growing plants.

PLANT ECOLOGY

Doubling duckweed

Despite their diminutive size, duckweeds in the aquatic family Lemnaceae are among the fastest-growing plants. Usually consisting of a single floating leaf and a small root, they grow clonally, with biomass doubling in as little as a day under favorable conditions. Ishizawa *et al.* have characterized the traits that underpin this growth pattern. They found that the duckweed resource use strategy is among the most acquisitive of all plant species, fueled by traits including small leaf mass per unit area of leaf and high photosynthetic rate per unit area. These results not only help to explain why duckweeds rapidly clog domestic ponds but also inform research into the use of duckweeds for biomass production and wastewater treatment. —AMS *J. Ecol.* **109**, 2950 (2021).

INFECTIOUS DISEASE

A possible cause of microcephaly

Zika virus infection during pregnancy causes microcephaly (small head circumference) in children. Pang *et al*. examined mouse brains infected with Zika virus and found alterations in the nicotinamde adenine dinucleotide (NAD^+) metabolic pathways, including oxidative phosphorylation and the Kreb's cycle. Indeed, supplementation of Zika virus–infected pregnant mice and their neonates with nicotinamide riboside (a



PERMAFROST CARBON

Taking up the challenge

One of the biggest wildcards related to how global warming will affect future climate is the fate of carbon in melting permafrost. How much of the huge amount of carbon stored there winds up in the atmosphere depends in large measure on the magnitude of plant uptake of the carbon dioxide released as the permafrost melts. Wei *et al.* report that on the Tibetan Plateau, which contains the largest area of alpine permafrost on Earth, fixation of carbon dioxide by plants exceeds its loss from permafrost. Thus, there exists a plant-dominated negative feedback to climate warming in that region. —HJS

Proc. Natl. Acad. Sci. U.S.A. **118**, e2015283118 (2021).

Melting permafrost on the Tibetan Plateau

precursor of NAD^+) reduced cell death in mouse brains, increased brain and body weight, and improved survival. Thus, dysregulated metabolic pathways may cause neuronal cell death and consequent microcephaly in offspring, but exactly how Zika virus induces these metabolic changes is unknown. —GKA

Nat. Metab. **3**, 1109 (2021).

INDUCED SEISMICITY

Managing triggered earthquakes

Human-induced earthquakes have become a growing problem over the past decade. Because this type of seismicity is mostly tied to fluid injection, mitigating it should be possible through oil field management. Hagar *et al.* showed that induced seismicity could be accurately forecasted in the Val d'Agri oil field in Italy. This required coupling a large number of geophysical observations with fluid modeling and earthquake source physics to determine the impact of fluid injections. The results suggest a path for a more refined reservoir management strategy that may avoid triggering large and damaging earthquakes. —BG

Nature **595**, 684 (2021).

PLANT SCIENCE

A new floral carnivore

When nutrients are sparse, plants sometimes resort to eating animals. A monocot with sticky flower stalks found in the poorly nutritious bogs of western Canada is an unexpected addition to the list of carnivorous vegetables. *Triantha occidentalis*, or false asphodel, has lost a gene encoding a ferredoxin plastoquinone reductase, a signature of carnivory among other plant carnivores. Lin *et al.* show that the sticky flower stalks of *Triantha* are covered in red glands containing digestive enzymes, including phosphatase, and can entrap a variety of tiny flies and beetles. The modest white flowers also attract larger pollinators but they are strong enough to avoid getting caught. In experiments, *Drosophila* fed ^{15}N were used as prey to find out how much nutrient the plants were gaining from insects. The N label was initially concentrated in the stem and fruit, but the authors estimated that 64% of leaf N comes from a lifetime of carnivory. —CA

Proc. Natl. Acad. Sci. U.S.A. **118**, e2022724118 (2021).

QUANTUM SENSING

Setting a trap for particle detection

The trapping of single electrons and ions with electromagnetic fields has provided a platform for high-precision metrology studies. Such trapped charged species are also finding applications as the basic building blocks in quantum information processing. Carney *et al.* propose that trapped electrons and ions could be used as ultrasensitive particle detectors. Their calculations show that the energy dissipated by a passing charged particle should result in a positional disturbance of a trapped electron or ion. Measurable changes in the electromagnetic forces required to restore its position then provides a measure of a particle's energy. The authors show that such a setup could be used to probe a wide range of interactions, including possible dark matter candidates. —ISO

Phys. Rev. Lett. **127**, 61804 (2021).

BIOCHEMISTRY

A check on glycolysis

Cancer cells shift their metabolism away from oxidative phosphorylation toward glycolysis for their energy supply, a phenomenon known as the Warburg effect. A central enzyme in glycolysis is lactate dehydrogenase A (LDHA). Woodford *et al.* show that in normal cells, LDHA is inhibited by binding to the tumor suppressor protein folliculin (FLCN). Biochemistry experiments showed that inhibition occurs, not through binding to the enzyme's active site, but rather by controlling the movement of a loop involved in enzyme activity. In cancer cells, FLCN is not seen bound to LDHA, indicating that there is another level of regulation of this interaction. Interestingly, FLCN-derived peptide can bind and inhibit LDHA in cancer cells, leading to cell death. —VV

Nat. Struct. Mol. Biol. **28**, 662 (2021).

PHOTO: GERTRUD & HELMUT DENZAU/MINDEN PICTURES

ALSO IN *SCIENCE* JOURNALS

Edited by **Michael Funk**

NEUROSCIENCE

Defeating peripheral neuropathy

The mechanisms underlying peripheral neuropathies are not well understood. Spaulding *et al*. studied mouse models of the inherited Charcot-Marie-Tooth (CMT) disease, which is caused by mutations in transfer RNA (tRNA) synthetases. Changes in gene expression and the rate of protein synthesis in neurons in the spinal cord triggered the cell stress response activated by the protein sensor GCN2. When GCN2 was genetically deleted or inhibited with drugs, the stress response was blocked and the neuropathy was much milder. Zuko *et al*. found that mutant glycyl-tRNA synthetases bind $tRNA^{Gly}$ but fail to release it, thus depleting the cellular $tRNA^{Gly}$ pool. This process caused stalling of translating ribosomes on glycine codons and activated the integrated stress response. Transgenic $tRNA^{Gly}$ overexpression prevented peripheral neuropathy and protein synthesis defects in mouse and fruit fly models. Thus, elevating $tRNA^{Gly}$ levels or targeting GCN2 may have therapeutic potential for this currently untreatable disease (see the Perspective by Mellado and Willis). —SMH

Science, abb3414, abb3356, this issue p. 1156, 1161; see also abk3261, p. 1089

QUANTUM PHYSICS

Vortex beams of nonelementary particles

The discovery of photon and electron vortex beams carrying orbital angular momentum (as a result of a twisting wave front) has led to appreciable advances in optical imaging, optical and electron microscopy, communications, quantum optics and micromanipulation, and more advances are expected. In an effort to extend this progress to other types of beams, Luski *et al*. demonstrate the production of vortex beams of helium atoms and dimers formed from supersonic beams with large coherence lengths diffracted off of specifically nanofabricated gratings with fork dislocations (see the Perspective by Kornilov). Vortex beams made of nonelementary particles with internal degrees of freedom represent a direct manifestation of quantum mechanics on macroscopic scale, and their production paves the way for many long-awaited applications. —YS

Science, abj2451, this issue p. 1105; see also abk1565, p. 1084

SUPERNOVAE

Radio evidence of a stellar merger

Core collapse supernovae occur when a massive star exhausts its fuel and explodes. Theorists have predicted that a similar explosion could occur if an evolved massive star were to merge with a compact companion such as a neutron star. Dong *et al*. identified a radio source not present in earlier radio surveys. Follow-up radio and optical spectroscopy showed that it is an expanding supernova remnant slamming into surrounding material, probably ejected from the star centuries before it exploded. An unidentified x-ray transient occurred at a consistent location in 2014, suggesting that an explosion at that time produced a jet. The authors suggest that the most likely explanation is a merger-triggered supernova. —KTS

Science, abg6037, this issue p. 1125

QUANTUM GASES

Monitoring quantum dynamics

Reducing the dimensionality of a quantum system of interacting particles can simplify its physics. Such reduction is possible in ultracold atomic gases, where a lattice of one-dimensional (1D) gases can be generated using optical potentials. Malvania *et al*. studied the dynamics of 1D rubidium-87 atomic gases after a sudden increase in the axial trapping potential. Normally, these dynamics would be difficult to describe theoretically, but the researchers found that a theory called generalized hydrodynamics captured the behavior of their 1D system over a long time evolution. —JS

Science, abf0147, this issue p. 1129

MELANOMA

Chromatin state and oncogenic competence

Although specific DNA mutations can lead to tumor generation, they are not transforming in all cellular contexts. This may be due to the intrinsic transcriptional program present in the cell of origin. Using zebrafish and human pluripotent stem cell cancer models, Baggiolini *et al*. report that neural crest cells and melanoblasts (precursors to melanocytes) are susceptible to specific mutation of the *BRAF* gene, whereas melanocytes are relatively resistant (see the Perspective by Vredevoogd and Peeper). The competent cells display higher levels of chromatin factors such as the protein ATAD2 compared with the less competent ones. ATAD2 forms a complex with the neural crest transcription factor SOX10 and establishes a chromatin state that makes them permissive to BRAF mutagenesis. These data indicate that developmental chromatin programs are a determinant of how cells respond to DNA mutations. —BAP

Science, abc1048, this issue p. 1104; see also abl4510, p. 1088

CORONAVIRUS

Targeting a range of betacoranaviruses

In the past 20 years, three highly pathogenic β-coronaviruses have crossed from animals to humans, including the most recent: severe acute respiratory syndrome coronavirus 2 (SARS-CoV-2). A spike protein that decorates these viruses has an S1 domain that binds host cell receptors and an S2 domain that fuses the viral and cell membranes to allow cell entry. The S1 domain is the target of many neutralizing antibodies but is more genetically variable than S2, and antibodies can exert selective pressure, leading to resistant variants. Pinto *et al*. identified five monoclonal antibodies that interact with a helix in the S2 domain. The most broadly neutralizing antibody inhibited all β-coronavirus subgenera and reduced viral burden in hamsters infected with SARS-CoV-2. —VV

Science, abj3321, this issue p. 1109

PLANT SCIENCE

Linking flowering to ambient temperature

In the small mustard plant *Arabidopsis*, the florigen FLOWERING LOCUS T (FT) mobilizes to initiate flowering at the shoot apical meristem. Susila *et al*. now show that FT, which is produced in leaf cells, can be held in reserve if ambient temperatures are not favorable (see the Perspective by Jaillais and Parcy). At low temperatures, FT binds a membrane phospholipid and is thus restricted in mobility. At higher temperatures, such binding is less favored, and FT is released to mobilize into the shoot apical meristem to drive flowering. Thus, temperature-sensitive lipid binding helps the plant time flowering with favorable ambient temperatures. —PJH

Science, abh4054, this issue p. 1137; see also abl4883, p. 1086

T CELLS

T_{regs} potentiate skin inflammation

Regulatory T cells (T_{regs}) regulate various immune responses all

over the body, with their specific roles differing between anatomical locations. In the skin, T_{regs} help to control wound healing, but the details of their role in this process are unclear. Moreau *et al.* used transcriptomics and engineered mouse models to show that T_{regs} in the skin have heightened transforming growth factor-β (TGF-β) signaling and αvβ8 integrin expression, which contributes to delayed epidermal repair after inducing skin injury. Specifically, αvβ8 expression in skin T_{regs} helps to activate TGF-β in neighboring keratinocytes, leading to innate immune influx and protection from *Staphylococcus aureus* infection. These data provide a better understanding of the interactions between T_{regs} and epithelial cells in the skin during skin injury and bacterial infection. —DAE

Sci. Immunol. **6**, eabg2329 (2021).

NEUROSCIENCE

General principles of neuronal communication

The explosion of modern technologies over the past years has produced vast amounts of knowledge about the molecular, anatomical, and physiological properties of individual neurons. However, individual neurons do not function in isolation; they interact with each other in circuits to process information. Luo attempted to synthesize different types of investigations to extract generalized principles underlying how neurons communicate with each other through specific patterns of synaptic connectivity. Although different elements of the projection motifs and architectural plans have been discussed separately in the past, these motifs and architectures can now be brought together in the same intellectual framework. —PRS

Science, abg7285, this issue p. 1103

WOUND REPAIR

Scar wars

Scars developing after skin wounds can cause important functional, aesthetic, psychological, and social consequences. The mechanisms mediating scar formation after a skin wound remain to be completely elucidated. Griffin *et al.* show that pathological scarring induced by overexpressing the transcription factor JUN in mice is mediated by fibroblast modulation dependent on the cell surface receptor CD36, which results in increased fibrosis at the site of injury. Pharmacological CD36 inhibition with salvianolic acid B reduced the fibrosis process in human fibroblasts and scar formation in *Jun*-overexpressing mice. These results suggest that targeting CD36 might be effective in reducing hypertrophic scar formation during skin wound healing. —MM

Sci. Transl. Med. **13**, eabb3312 (2021).

REVIEW SUMMARY

NEUROSCIENCE

Architectures of neuronal circuits

Liqun Luo

BACKGROUND: The human brain contains about 100 billion neurons, each of which makes thousands of synaptic connections. Although individual neurons can themselves be sophisticated information-processing units, it is their synaptic connection patterns that enable neurons to form specialized circuits for specific functions, making the brain a powerful computational device. Decades of research using anatomical tracing, physiological recording, functional perturbation, and computational modeling in diverse organisms have detailed the connection patterns of neurons and their functions at scales ranging from microcircuits of a few neurons to global organization of millions of neurons. Here, I synthesize these findings from the perspective of circuit architectures and discuss how these architectures might emerge during development and evolution.

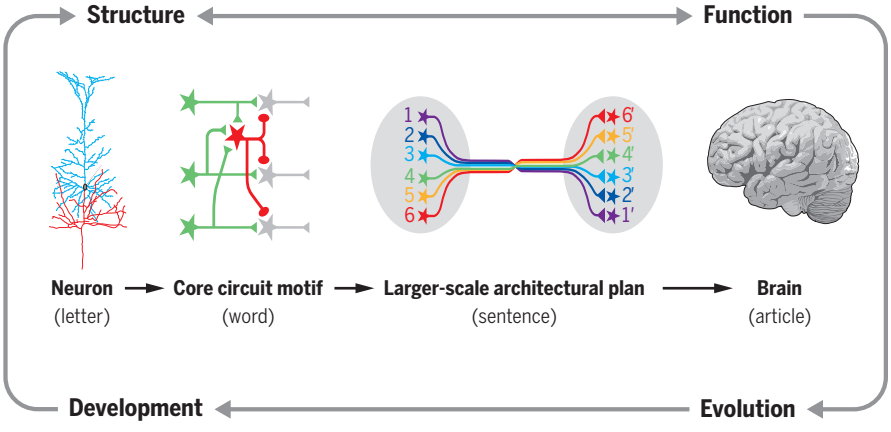
ADVANCE: Suppose individual neurons are to the brain what letters are to an article. We can then consider microcircuit motifs as words and larger-scale architectural plans as sentences. At the level of words and microcircuits, specific patterns of connections between excitatory and inhibitory neurons confer elementary information-processing functions. For example, feedforward excitation allows information to propagate across neural regions, with convergent and divergent excitation to integrate signals from multiple upstream sources and disseminate signals to diverse downstream targets, respectively. Feedforward inhibition and feedback inhibition regulate the duration and magnitude of incoming excitatory signals and often work together to control gain and dynamic range of input signals as well as facilitate synchronous and oscillatory firing. Lateral inhibition selects information to be propagated to downstream circuits by amplifying differences in activity between parallel pathways. Mutual inhibition can produce rhythmic outputs and regulate brain states. These core circuit motifs are almost always used in concert to build up complex signal-processing units.

The next level of organization, the sentences, is more heterogeneous in scale and configuration. Continuous topographic mapping, in which neighboring input neurons connect to neighboring target neurons through orderly axonal projections, provides a way to organize information at successive stages of processing, minimizes wiring length, and can facilitate extraction of local contrast through lateral inhibition. Discrete parallel processing allows signals to be represented and processed in parallel, reducing computational depth and increasing processing speed. Dimensionality expansion enables output neurons to represent different combinations of inputs, facilitating pattern separation by downstream neurons. Biased input and segregated output divide neuromodulatory systems with broad projections into subsystems, each serving distinct behavioral functions and being differentially regulated by different stimuli. Recurrent loops are abundant in nervous systems and support rich neural activity dynamics. Architectures of many neuronal circuits at this level are awaiting discovery.

Unlike computer circuits, which are products of top-down design, neuronal circuits are products of hundreds of millions of years of evolution. Some circuit motifs may have originated long ago, having since been conserved across diverse clades and passed on to more recently evolved neural regions. Other architectures have evolved independently in different clades. Duplication and divergence of neuron types and brain regions play important roles in brain evolution and may result in the modularity of brain connections.

Neuronal circuits are also products of development over an individual's life span. Molecular cues hardwire the nervous system using genetic instructions selected by evolution, and neuronal activity and experience fine-tune connectivity. Continuous topographic maps can be constructed by molecular gradients, whereas discrete parallel processing often requires combinatorial cell surface protein codes. These strategies enable a small number of proteins to specify a much larger number of connections.

OUTLOOK: Application of circuit-mapping tools such as serial electron microscopy and transsynaptic tracing to diverse neural regions in different species will generate a wealth of data from which we can distill common principles of neuronal circuit architectures. Activity recording and perturbation of key elements in a circuit can establish their functions in information processing and animal behavior. A key challenge is to investigate how different motifs and architectures operate across scales. A deliberate effort to investigate how letters and words are assembled into sentences in key circuit architectures across species could yield valuable insights. Integrating studies of the structure, function, development, and evolution of neuronal circuits will enable a deeper understanding of nervous system organization beyond the level of individual neurons. Exploration of neuronal circuit architectures will also continue to inspire important advances in artificial intelligence. ■



Between neurons and the brain. Core circuit motifs, such as lateral inhibition depicted here, enable elementary signal processing. Larger-scale architectural plans, such as continuous topographic mapping also depicted here, enable specialized functions. Interrogating the structure and function of neuronal circuits is a central goal of neuroscience; investigating their evolution and development likewise provides crucial insights.

The list of author affiliations is available in the full article online.
Department of Biology and Howard Hughes Medical Institute, Stanford University, Stanford, CA 94305, USA.
Email: lluo@stanford.edu
Cite this article as L. Luo, *Science* 373, eabg7285 (2021).
DOI: 10.1126/science.abg7285

READ THE FULL ARTICLE AT
https://doi.org/10.1126/science.abg7285

REVIEW

NEUROSCIENCE

Architectures of neuronal circuits

Liqun Luo

Although individual neurons are the basic unit of the nervous system, they process information by working together in neuronal circuits with specific patterns of synaptic connectivity. Here, I review common circuit motifs and architectural plans used in diverse brain regions and animal species. I also consider how these circuit architectures assemble during development and might have evolved. Understanding how specific patterns of synaptic connectivity can implement specific neural computations will help to bridge the huge gap between the biology of the individual neuron and the function of the entire brain, allow us to better understand the neural basis of behavior, and may inspire new advances in artificial intelligence.

Over a century ago, Santiago Ramón y Cajal and his contemporaries proposed that individual neurons are the basic unit of the nervous system. Ramón y Cajal further proposed that information flows from dendrites to cell bodies to axons within individual neurons (Fig. 1) (*1*). Given that dendrites and axons of most vertebrate neurons are readily distinguishable morphologically, systematic studies of isolated neurons labeled by Golgi staining (*2*) provided the first overview of how information flows within vertebrate nervous systems (*1*).

With the advent of modern technologies (Box 1), we have accumulated vast amounts of knowledge of the anatomical, physiological, and functional properties of individual neurons. However, individual neurons do not work in isolation; they work together in neuronal circuits to process information. What is less clear is whether there are generalizable principles about the structural organization of neuronal circuits across different brain regions and animal species. Here, I discuss principles underlying how neurons communicate with each other through specific patterns of synaptic connectivity. Although the importance of activity dynamics in neuronal populations has been increasingly recognized in information processing in diverse systems from invertebrates to mammals (*3*, *4*), synaptic connectivity patterns provide the physical bases on which neuronal dynamics execute their functions. Understanding how these connectivity patterns implement specific computations will allow us to decipher information-processing principles in the nervous system and should inspire new advances in artificial intelligence.

Department of Biology and Howard Hughes Medical Institute, Stanford University, Stanford, CA 94305, USA.
Email: lluo@stanford.edu

Commonly used circuit motifs

If individual neurons are seen as the letters in an alphabet used to write an article that is a brain, then what are the intermediates? In this section, I focus on circuit motifs used across diverse brain regions and animal species (*5*) (Fig. 2), which can be considered the "words." In the next section, I explore circuit architectures that might operate at the level of "sentences." Here, I discuss the most commonly used circuit motifs involving excitatory and inhibitory neurons. Some of these motifs apply not only to neuronal circuits but also to gene-regulatory circuits (*6*). Architectures based on some of these motifs have also been used in artificial intelligence to great effect (*7*).

Feedforward excitation

The primary means by which signals flow from one neural region to another is through feedforward excitation, a series of connections between excitatory neurons (Fig. 2A). At each stage, a neuron often receives input from multiple presynaptic partners (convergent excitation) and sends output through branched axons to multiple postsynaptic partners (divergent excitation). Convergent excitation can enable postsynaptic neurons to respond selectively to features not solely or explicitly present in any of the presynaptic neurons. It can also increase the signal-to-noise ratio if multiple input neurons carry the same signal but uncorrelated noise. Divergent excitation allows the same signal to be processed by multiple downstream pathways.

One of the best characterized examples of feedforward excitation is the mammalian visual system, where signals flow from photoreceptors → bipolar cells → retinal ganglion cells → lateral geniculate nucleus (LGN) relay neurons → layer 4 primary visual cortical (V1) neurons → V1 neurons in other layers → neurons in higher cortical areas (*1*, *8*, *9*). (Note that whereas the discussion here focuses on individual neurons and their synaptic connections, feedforward excitation can also be applied to neural regions in broad strokes, such as retina → LGN → V1.) Along these feedforward pathways, representations of visual information are transformed from light intensity to contrasts, edges, objects, and motion. The feedforward architecture of the mammalian visual system inspired the development of the "perceptron" (*10*) and

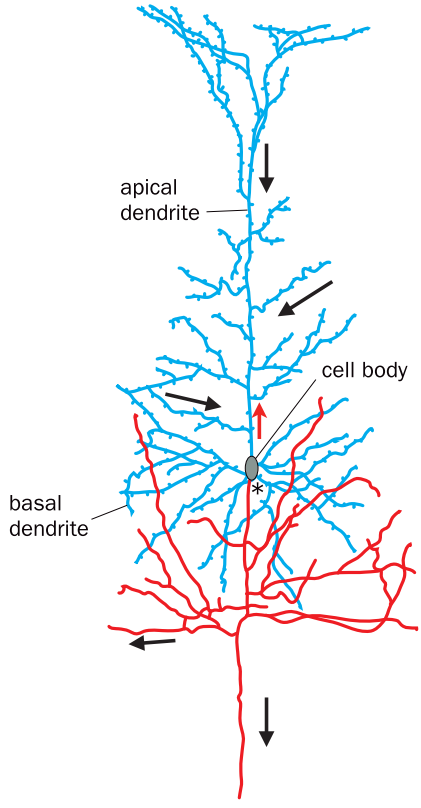


Fig. 1. Information flow within a vertebrate neuron. A pyramidal neuron from rabbit cerebral cortex. Neurons generally use dendrites (blue) to receive information from their presynaptic partners and the axon (red) to send information to their postsynaptic partners. Thus, information flows from dendrites to cell bodies to the axon (black arrows). Asterisk indicates an axon initial segment, where action potentials are generated. Red arrow indicates back-propagating action potentials that can interact with synaptic inputs in complex ways for dendritic computation (*115*). Whereas axons and dendrites are readily distinguishable by morphological criteria in most vertebrate neurons, most invertebrate central nervous system neurons extend a single process from the cell body that gives rise to both dendrites and the axon. Thus, in invertebrate neurons, information flow is less easily deciphered from morphological criteria alone. Figure was modified and used with permission from (*1*, *5*).

Box 1. Tools for mapping neuronal circuit architecture.

Diverse tools have been used to study the structural organization of the nervous system (*94*, *95*).

Single-neuron tracing

In this approach, a dense library of single neurons within a neural region is created by sparse labeling in individual animals using Golgi staining (*2*), intracellular dye filling (*8*), or genetic methods (*96*–*100*), such that dendritic morphology and axonal projections are clearly resolved using light microscopy. One can infer that neuron *A* synapses onto neuron *B* when *A*'s axon overlaps with *B*'s dendrites. Ramón y Cajal used this approach to chart the coarse organization of the vertebrate nervous system (*1*). Genetic methods for sparse labeling now allow researchers to infer connectivity between neurons of specific types. A key limitation of this method is that spatial overlap visualized with light microscopy between dendrites and axons is necessary but insufficient to confidently classify two neurons as synaptic partners. Thus, it is only useful for inferring possible connectivity at a coarse level.

Serial electron microscopic reconstruction

Serial electron microscopic (EM) reconstruction is the most comprehensive way of deciphering synaptic wiring diagrams, because it is the only method able to unambiguously visualize synapses. All synapses can be visualized in the same specimen, with the potential of producing a complete wiring diagram. Serial EM reconstruction has been used to decipher the synaptic wiring diagram of the entire *Caenorhabditis elegans* nervous system (*101*). Recent years have seen rapid progress in the acquisition and partial reconstruction of EM volumes of neural regions from multiple organisms (*89*, *102*–*105*). A densely reconstructed *Drosophila* hemibrain has been achieved (*106*), and the entire mouse brain has been proposed as the next ambitious target (*107*). Limitations include the extensive labor needed to accurately reconstruct connections from EM volumes, especially across large distances, and the difficulty of deciphering cell types or connection signs (excitatory versus inhibitory) unless the region is also well characterized by other means.

Trans-synaptic tracing

Trans-synaptic tracing relies on an event such as gene expression or viral transduction occurring in one neuron to trigger the labeling of its presynaptic partners (retrograde trans-synaptic labeling) or postsynaptic partners (anterograde trans-synaptic labeling). The most widely used methods in mammals use viruses that naturally transduce neurons across synapses, particularly rabies virus for retrograde trans-synaptic tracing from a defined neuron type in a specific location (*108*, *109*). Axon terminal–initiated rabies tracing can reveal inputs to neuronal populations that project to specific targets, allowing inference of input-output architecture (Fig. 4). Anterograde methods have also been reported (*110*–*113*). Limitations include poor understanding of trans-synaptic transmission mechanisms, potential biases due to cell type and subcellular locations of synapses, and incomplete characterization of false negatives (synaptic partners not labeled) and false positives (labeling of nonsynaptic partners) for most methods.

Electrophysiological and optical methods

Simultaneous intracellular recordings can reveal synaptic connections between multiple neurons, as well as their sign and strength. This method is mostly limited to in vitro preparations and is therefore mostly used to map local connectivity. However, channelrhodopsin (ChR2)–assisted circuit mapping (*114*) can map long-range connections between a specific input population (expressing ChR2) and its target neurons in a brain slice, because photostimulating $ChR2^+$ axon terminals can often elicit responses in postsynaptic neurons. Because of their low throughput, these electrophysiological and optical methods are mostly used to validate connections suggested by other methods and for detailed analysis of synaptic properties rather than to reveal connectivity within or between neural regions de novo.

"deep neural network" (*11*) for image recognition and categorization; deep neural networks have also been used in artificial intelligence to solve problems far beyond image analysis (*7*).

Feedforward and feedback inhibition

Although long-range signals in the nervous system are mostly delivered by excitatory neurons (notable exceptions include basal ganglia and cerebellum circuits), inhibitory interneurons play key roles in sculpting such signals locally (*12*–*14*). Two widely used motifs are feedforward and feedback inhibition (Fig. 2B). In feedforward inhibition, an inhibitory neuron receives input from a presynaptic excitatory neuron, and both inhibitory and presynaptic excitatory inputs converge onto a postsynaptic neuron. In feedback inhibition, an inhibitory neuron receives input from and projects back onto an excitatory neuron, often at its presynaptic terminals. Almost every excitatory connection in the visual pathway described above is accompanied by feedforward inhibition, feedback inhibition, or both. For example, LGN neurons directly excite V1 GABA-releasing neurons to provide feedforward inhibition to layer 4 excitatory neurons, and layer 4 excitatory neurons also activate V1 GABA-releasing neurons to provide feedback inhibition onto themselves (*15*, *16*).

Feedforward inhibition acts more rapidly than feedback inhibition because it reaches the postsynaptic target cell with only one synaptic delay after excitatory signals, whereas feedback inhibition has two synaptic delays (Fig. 2B). Feedforward inhibition is proportional to the strength of the input, whereas feedback inhibition is proportional to the strength of the output; both are used to regulate the duration and magnitude of incoming excitatory signals. For example, limiting the duration of activation in response to sensory input allows circuits to quickly return to their baseline activity levels to maximize their sensitivity to future inputs that signal changes in the environment. Networks of feedforward and feedback inhibitory neurons often act in concert and can perform many interesting functions, such as regulating the gain and dynamic range of input signals and facilitating synchronous or oscillatory firing (*14*, *17*). Feedforward and feedback inhibition also play an essential role in maintaining a "balance" between excitation and inhibition (e.g., strong excitation is accompanied by strong inhibition) to prevent overly excited or inhibited states. Such balanced networks can enhance the speed and signal-to-noise ratio of information processing (*18*, *19*).

Lateral inhibition

Lateral inhibition (Fig. 2C) is a widely occurring circuit motif. It selects information to be propagated to downstream circuits by amplifying differences in activity between parallel pathways. For example, photoreceptor neurons in the vertebrate retina activate horizontal cells, which provide feedback inhibition to many photoreceptor neurons nearby. This action is a major contributor to the classic center-surround receptive field in downstream ganglion cells (*20*, *21*), conferring on these neurons the ability to extract information about spatial or color contrast. Lateral inhibition is also used in other sensory systems (*3*, *22*, *23*), with the general purpose of sharpening representations of ethologically relevant information to be processed by downstream circuits.

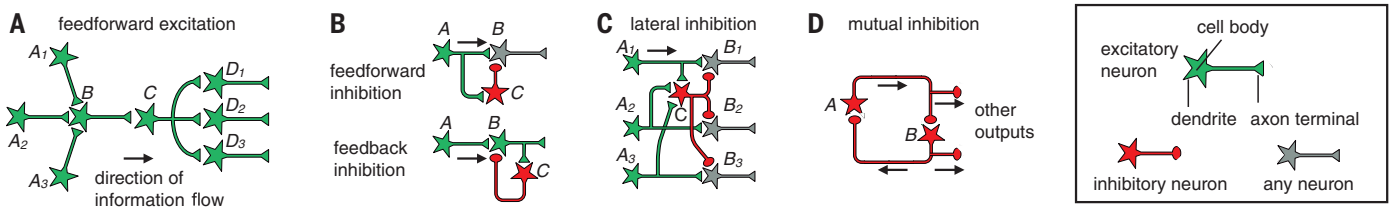


Fig. 2. Commonly used circuit motifs. (**A**) Feedforward excitation. Information flows through a series of excitatory neurons, *A* to *D*. Three different *A* neurons synapse onto *B*, exemplifying convergent excitation. *C* synapses onto three distinct *D* neurons, exemplifying divergent excitation. (**B**) In feedforward inhibition (top), inhibitory neuron *C* receives input from presynaptic excitatory neuron *A* and sends inhibitory output to postsynaptic neuron *B*; in feedback inhibition (bottom), inhibitory neuron *C* receives input from and sends inhibitory output to postsynaptic excitatory neuron *B*. (**C**) In lateral inhibition, parallel pathways ($A_n \rightarrow B_n$; three are shown) each excite inhibitory neuron *C*, which in turn sends inhibitory output to all pathways. (**D**) In mutual inhibition, two inhibitory neurons form reciprocal connections and also provide outputs through branched axons to broadcast their activity states. The inhibitory neurons can also act through intermediary excitatory neurons to inhibit each other (not shown). See box on the right for a key to symbols. Figures in (A) to (C) were modified and used with permission from (*5*).

Mutual inhibition

Communication between inhibitory neurons can confer circuits with interesting properties. For example, if inhibitory neuron *A* directly inhibits inhibitory neuron *B*, then activation of *A* would disinhibit target neurons of *B*. If *B* also inhibits *A*, then they form the mutual (reciprocal) inhibition motif (Fig. 2D). Mutual inhibition is widely used in circuits that exhibit rhythmic activity, such as those involved in locomotion (*24*). A classic example is the crustacean stomatogastric ganglion (*25*). Operating on a longer time scale, mutual inhibition can also be used to regulate brain states such as the sleep–wake cycle (*26*, *27*).

So far, our discussion has involved an alphabet comprising just two letters: excitatory and inhibitory neurons. In reality, the neuronal alphabet is far richer. Both excitatory and inhibitory neurons have many variations because of the heterogeneity in their dendrite morphology, ion channel composition, spiking properties, and the subcellular distribution and strength of their input and output synapses. For example, in the mammalian neocortex, three classes of inhibitory neurons, the Martinotti, basket, and chandelier cells, target their presynaptic terminals to distal dendrites, cell bodies, and axon initial segments of excitatory pyramidal neurons, respectively, and thus control different aspects of how pyramidal neurons integrate synaptic inputs and produce spikes (*28*, *29*). In the stomatogastric ganglion, mutually inhibiting neurons have distinct ion channel compositions and input-output synaptic strengths, which underlie their sequential firing patterns within each rhythmic cycle (*30*). Finally, the neuronal alphabet also includes many modulatory neuron types to be discussed later.

At the level of core motifs, there are also many variations. For example, the mutual inhibition motif often includes intermediary neurons (e.g., inhibitory neuron *A* inhibits an excitatory neuron that excites inhibitory neuron *B*). It is important to note that the core motifs discussed above are almost always used in concert. Indeed, the large-scale architectural patterns discussed in the next section always contain these motifs.

In summary, a rich alphabet of neurons with diverse intrinsic properties can be used to compose words using a set of core motifs and their variations. These words are often used in concert to produce phrases, which together form the basis for sentences, as I discuss next.

Specialized architectures for specific functions

The next level of organization is more heterogeneous in scale and configuration and less readily generalizable. Nevertheless, I attempt here to extract some high-order circuit architectural patterns that have been found in multiple neural regions and diverse species.

Continuous topographic mapping

Continuous topographic mapping is a common organizational scheme for representing information in the nervous system. Neighboring input neurons connect to neighboring target neurons through orderly axonal projections (Fig. 3A). A prime example is retinotopy, in which neighboring retinal ganglion cells synapse onto neighboring LGN neurons, which then connect to neighboring V1 neurons, which in turn connect to neighboring higher-order visual cortical neurons. Retinotopy enables spatial relationships in the outside world captured by the retina to be recapitulated in V1 and higher visual cortical areas. Continuous topographic mapping is also used elsewhere. In the sensory and motor homunculi, somatosensory stimuli from neighboring body parts are coarsely represented in neighboring areas of the primary somatosensory cortex, and motor outputs to neighboring body parts are coarsely controlled by neighboring areas of the motor cortex (*31*).

Topographic maps provide a convenient way to organize information at successive stages of processing and can be constructed by robust developmental mechanisms (see below). They have a variety of computational advantages. For example, retinotopy facilitates the extraction of local contrast through lateral inhibition for object recognition. Furthermore, by placing circuit elements that are more often functionally connected nearby each other, topographic maps save energy by minimizing wiring length (*32*). The design of "convolutional neural networks" (*7*) takes a page from topographic mapping to greatly reduce the number of variables needed to tune an artificial neural network and thus speed up computation.

Discrete parallel processing

Discrete parallel processing (Fig. 3B) allows signals to be represented and processed in parallel by discrete information channels. A prime example is the glomerular organization of the vertebrate olfactory bulb and insect antennal lobe: Olfactory receptor neurons expressing the same odorant receptors send their axons to the same glomerulus to synapse onto the dendrites of their corresponding second-order projection neurons, forming discrete olfactory processing channels (*33*, *34*). Tens to thousands of individual olfactory receptor neurons expressing the same odorant receptor converge their axons onto the same glomerulus, thus enhancing the signal-to-noise ratio. Rather than representing continuous values, different glomeruli represent signals from discrete olfactory receptor neuron types and thus the nature of the chemicals that activate those odorant receptors. Discrete parallel processing also characterizes the mammalian taste system (*35*).

Discrete parallel processing is often used in conjunction with continuous topographic mapping. In the retina, for example, superimposed on the continuous retinotopy are discrete layers where different bipolar and ganglion cell types

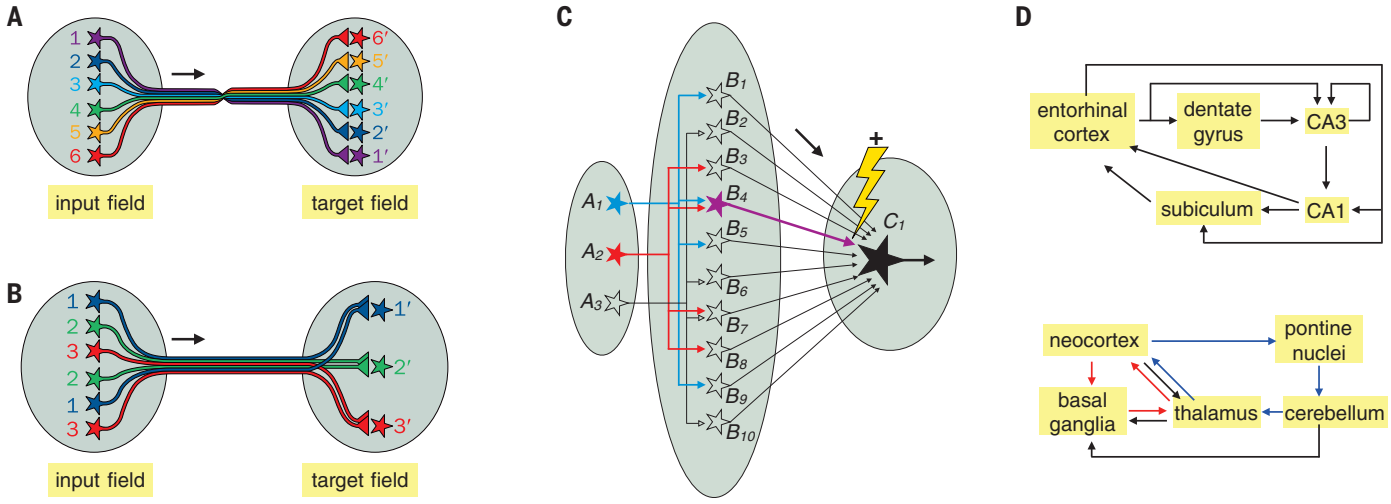


Fig. 3. Specialized architectures for specific functions. (**A**) Continuous topographic mapping. Neighboring neurons in the input field project their axons in an orderly fashion to connect to neighboring neurons in the target field, preserving their spatial relationships. A prime example is the retinotopic map. (**B**) Discrete parallel processing. Neurons of a specific type (same color) in the input field, regardless of their spatial locations, connect to the corresponding neuron type in the target field. A prime example is the olfactory glomerular map. Target neurons do not need to be spatially ordered as shown; they could extend their dendrites to connect specifically with the axons of specific input neuron types. (**C**) Dimensionality expansion. Signals represented by a small number of neurons in field *A* are represented by a much larger number of neurons in field *B*, such that activation of *B* neurons can represent specific combinations of *A* neurons (e.g., B_4 represents coactivation of A_1 and A_2). Furthermore, the synaptic connections between *B* and *C* can be altered by coactivation of a teaching signal (the lightning and plus sign signals strengthening) and a specific *B* neuron to modify the synaptic strength between that particular *B* and *C*. Thus, only after training would coactivation of A_1 and A_2 reaches the threshold (thick arrow for B_4) for activating C_1. Likewise, a C_2 neuron (not shown) can be trained to respond to the coactivation of A_2 and A_3 by modifying the strength of $B_7 \rightarrow C_2$. Filled and open symbols represent active and inactive neurons, respectively. (**D**) Two examples of recurrent loops. In the entorhinal–hippocampal loop (top), arrows indicate direct connections between neurons within the indicated regions. Many connections within these regions are topographically organized (*116*). In the neocortex–basal ganglia–thalamus (red) and neocortex–pons–cerebellum–thalamus loops (blue), arrows represent connections between these brain regions but not necessarily direct synaptic connections between specific neuron types. Within the basal ganglia and cerebellum, for example, inputs are transformed at intermediary stages to produce outputs. Figures in (A) and (B) were modified and used with permission from (*117*).

form specific connections to process different types of visual signals such as luminance, color, and motion in parallel. Compared with serial processing, parallel processing reduces computational depth, thus decreasing error rate and increasing processing speed. Indeed, massively parallel processing is a salient feature of complex nervous systems with large numbers of neurons and large numbers of connections per neuron (*5*). This architecture is increasingly being adopted in computer systems design (*11*).

Dimensionality expansion

In the dimensionality expansion architecture, signals from a relatively small number of input neurons diverge onto a much larger number of output neurons (Fig. 3C), allowing output neurons to represent distinct combinations of inputs. Similar signals at the input level are more readily distinguished at the output level, facilitating pattern separation by downstream neurons (*36*–*39*). Two prime examples are the insect mushroom body (olfactory projection neurons → mushroom body Kenyon cells → mushroom body output neurons) and the vertebrate cerebellum (mossy fibers → cerebellar granule cells → Purkinje cells). In both cases, a relatively small number of inputs (projection neurons or mossy fibers, respectively) synapse onto a much larger number of output neurons (Kenyon cells or granule cells, respectively). Information at the level of the output neurons can thus be represented in a much higher dimensional space, with each dimension representing the firing rate of one cell. Small differences in input firing patterns (e.g., different projection neuron populations representing different odor combinations) can more readily be distinguished by the population firing patterns of their postsynaptic partners. This architecture allows for learning by adjusting the synaptic strengths of the output neurons through "teaching" signals from dopamine neurons in the mushroom body (*40*, *41*) and climbing fibers in the cerebellum (*42*). After training, the same input can produce different output patterns (Fig. 3C).

Another example of dimensionality expansion is the entorhinal cortex → dentate gyrus granule cell → CA3 pyramidal neuron circuit (Fig. 3D, top). The large number of dentate gyrus granule cells can perform pattern separation for information from the entorhinal cortex regarding space and objects for further processing by the downstream hippocampal circuit (*43*, *44*). Unlike in the mushroom body and cerebellar cortex, teaching neurons have not been identified here. This may be because the hippocampal circuit uses unsupervised learning, whereas the cerebellar and mushroom body circuits implement algorithms akin to supervised and reinforcement learning.

Recurrent loops

Nervous systems are full of recurrent loops in which neurons connect back onto themselves, often through intermediary neurons. These recurrent loops are heterogeneous in scale, ranging from within a particular neural region (e.g., mutual inhibition used in the crustacean stomatogastric circuit) to spanning large parts of the brain. In the mammalian visual system, for example, in addition to "bottom-up" projections from LGN → V1 → higher cortical areas, "top-down" projections from higher cortical areas → V1 → LGN serve several functions such as attentional control. Long-range recurrent loops may incorporate continuous topographic mapping or discrete parallel processing architectures. Figure 3D illustrates two examples in the mammalian brain at the level of neuronal populations (top) and brain regions (bottom). Recurrent loops generally

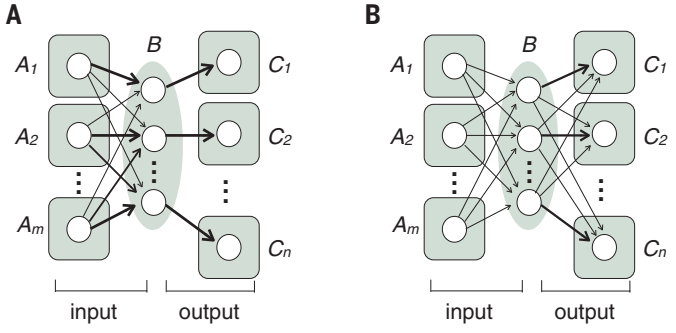


Fig. 4. Input–output organization of neuromodulatory circuits with broad projections. Modulatory neurons in region *B* collectively receive inputs from regions A_1–A_m and send broad output to regions C_1–C_n. (**A**) Biased input–segregated output architecture. This architecture applies to several neuromodulatory systems, including midbrain dopamine neurons, dorsal raphe serotonin neurons, and preoptic area galanin neurons. Arrows of different thicknesses represent different input strengths. (**B**) Integration-and-broadcast architecture. Neuronal populations in region *B* that project to a specific output region also send output to other output regions, with the possibility of a quantitative bias; these populations also receive similar inputs. Locus coeruleus norepinephrine neurons approximate this architecture. Each circle symbolizes a neuronal population rather than an individual neuron, as the input–output organization summarized here is based on studies at the population level rather than at the level of individual neurons. Figure was modified and used with permission from (*48*, *49*).

support rich neural activity dynamics, but their exact computational roles are not clear in most cases and are likely to differ on a case-by-case basis. Understanding the general principles of information processing in recurrent loops is a major challenge in modern neuroscience.

Biased input–segregated output

The above discussions have focused on circuits comprising excitatory and inhibitory neurons. Nervous systems also use modulatory neurons for important functions. Modulatory neurons use neurotransmitters such as monoamines and neuropeptides that primarily engage G protein–coupled receptors; therefore, their actions on postsynaptic neurons are slower and last between tens of milliseconds to seconds, in contrast to fast excitatory and inhibitory neurotransmitters, which engage ionotropic receptors and act within a few milliseconds. In addition to acting across the synaptic cleft, modulatory neurotransmitters can also be released at sites without postsynaptic specializations, so-called "volume release," and can thus influence targets at distances greater than that of a typical synaptic cleft.

Some modulatory neurons in the mammalian brain have cell bodies clustered in small regions but project axons broadly and receive diverse inputs. Viral-genetic tracing in the mouse (Box 1) revealed that midbrain dopamine, dorsal raphe serotonin, and hypothalamic neuropeptide galanin systems all adopt a "biased input–segregated output" architecture at the population level (*45*–*48*) (Fig. 4A). Each system can be divided into parallel subsystems defined based on their segregated output projections to distinct target regions that serve different behavioral functions. Each output subsystem receives inputs from similar regions with quantitative biases, allowing these subsystems to be differentially regulated by external and internal stimuli. One exception is the locus coeruleus norepinephrine system. At the population level, locus coeruleus norepinephrine axons projecting to one brain region also project broadly to other regions, even though branching patterns of individual neurons can be idiosyncratic (*49*, *50*). These observations suggest that the locus coeruleus norepinephrine system adopts an integration-and-broadcast architecture (Fig. 4B) that may suit its role in regulating global brain states such as arousal.

Nervous systems also use architectures not discussed above. A prominent architecture in bilaterians is interconnected bilateral symmetry (*51*), which formal network analysis identified as the top-level organization in forebrain connectivity maps (*52*). The architectures of many neuronal circuits, such as those of the canonical mammalian neocortex (*53*) and basal ganglia (*54*) circuits, do not fit neatly into the categories described above even though they use the aforementioned core circuit motifs and can participate as parts of other architectures such as topographic maps (*55*) and recurrent loops (Fig. 3D bottom). This may be because we have not yet dug deeply enough into these specific circuits to decipher their computational principles or because our understanding of the nervous system is not broad enough to identify shared architectures. We expect ample future opportunities to explore both the depth and breadth of neural circuit architectures by collecting greater amounts of data with increasingly sophisticated tools (Box 1). Only when we know more about these "sentences" and their numerous variations and complex interactions will we have a deeper understanding of how they constitute "paragraphs" (e.g., brain regions) and eventually the "article": the overall organization of an entire nervous system.

Evolutionary and developmental perspectives

Whereas computer circuits are products of top-down design, complex neuronal circuits have evolved over hundreds of millions of years. Neuronal circuits also self-assemble during development using evolutionarily selected genetic instructions and are fine-tuned by experience. Thus, existing neuronal circuit architectures are likely a selection of those that can be readily evolved and assembled during development. Looking at a neuronal circuit in isolation may not tell us what elements are functionally important. Seeing what has been evolutionarily selected, expanded, shrunken, eliminated, or repeatedly produced through convergent evolution can, however, suggest what elements to focus on in functional studies.

Evolution of neuronal circuits

Extant bilaterian nervous systems (including all vertebrate and most invertebrate phyla) likely derived from ancestors through progressive sophistication: those with only myocytes, followed by the sequential evolution of sensorimotor neurons, separate sensory and motor neurons, interneurons, and centralized interneuron networks that gave rise to the central nervous system and brain (*51*, *56*). The ubiquity of some core motifs, such as feedforward excitation and feedforward and feedback inhibition, may have originated early in animals with interneurons and a central nervous system and have since been conserved across diverse species and spread across neural regions within each species because of their utility. Other architectures have evolved independently. The glomerular organization of the insect and vertebrate olfactory systems is likely the result of convergent evolution, because many clades descended from their last common ancestor do not have this organization, and different types of molecules are used as odorant receptors. Visual systems provide striking examples of convergent evolution of many fundamental features from retinotopy to motion detection algorithms in invertebrate and vertebrate lineages (*57*, *58*).

Progressive sophistication of the nervous system requires expansion of neuron numbers (*59*), neuron types and their connections (*60*), and brain regions (*61*). All of these processes must result from changes to DNA. A key mechanism of evolutionary innovation is the duplication and divergence of genes; for example, duplication and divergence of a cone opsin gene conferred trichromacy on some primates (*62*). Duplication and divergence is also used in the evolution of neuron types (*63*–*65*) and

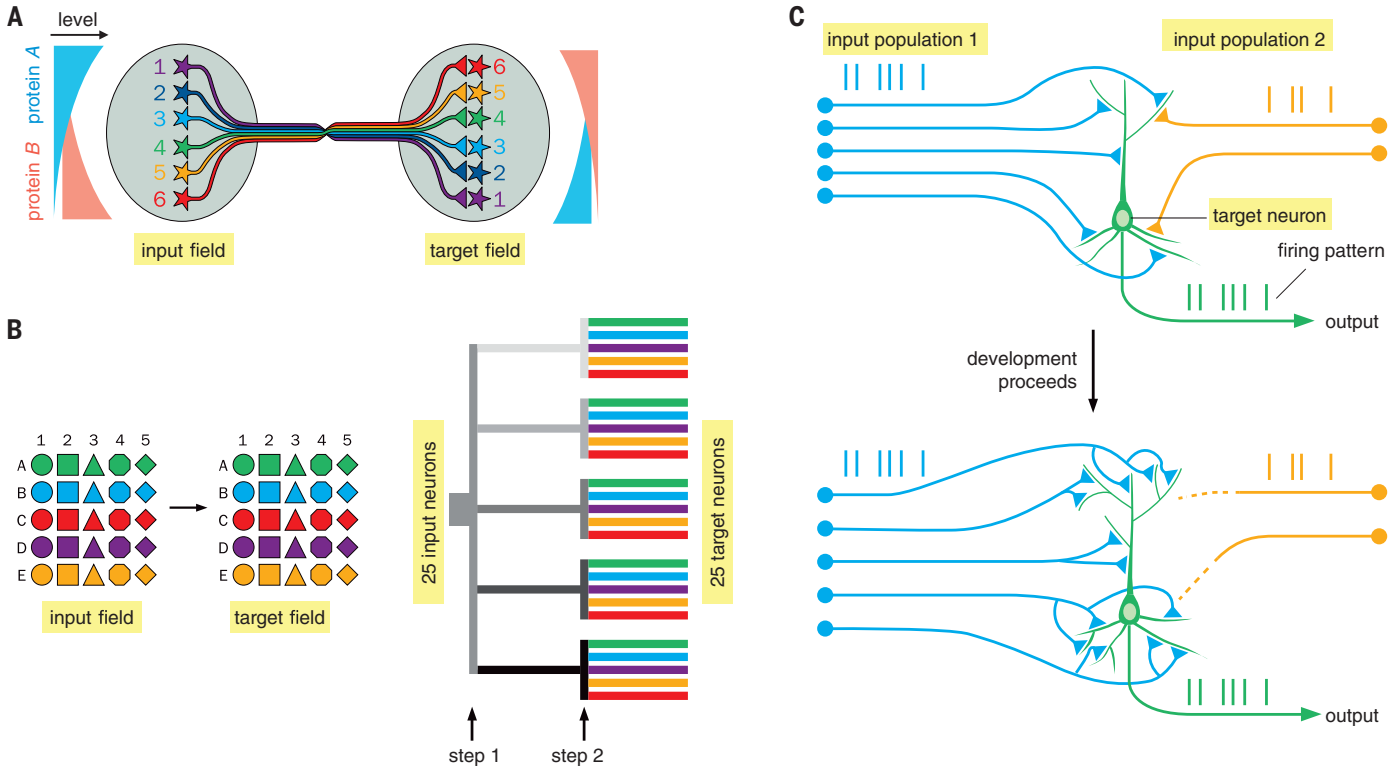


Fig. 5. Wiring up neuronal circuits. (**A**) Protein gradients can be used to construct continuous topographic maps. In this example, both input and target fields are patterned by opposing gradients of cell surface proteins *A* and *B*. Suppose that neuronal processes expressing protein *A* and protein *B* mutually repel each other. Because neuron 1 has the highest level of protein *A*, it seeks a target field with the lowest level of protein *B*; likewise, neuron 6 seeks a target field with the lowest level of protein *A*. (**B**) Illustration of combinatorial strategies to specify connections between 25 discrete cell types in the input and target fields. Left: Suppose that connection specificities between the input and target fields are mediated by homophilic attraction molecules. If each connection is specified by a single molecule, then 25 molecules are needed to specify 25 connections. If each connection is specified by a combination of two molecules (a letter and a number), then only 10 molecules are needed. Right: The combinatorial strategy is realized by dividing the wiring process into two steps. At step 1, five molecules (represented by different shades of gray) separate five input axons into five groups; at step 2, five more molecules (represented by different colors) are used in each of the five groups to specify the final connections. (**C**) Schematic illustration of Hebb's rule in instructing wiring. At an early developmental stage, the target neuron is connected to two groups of input neurons with distinct coincident firing patterns (blue and yellow vertical lines). Because stronger connections to the group 1 input drive the target neuron to fire in a pattern (green vertical lines) similar to that of group 1, their connections are strengthened. Synaptic connections between group 2 input and the target neuron weaken because of their dissimilar firing patterns. Eventually, the target neuron is only connected with group 1 input. Figure was modified and used with permission from (*5*).

brain regions (*66*). Duplication and divergence for brain region evolution should in principle make neuronal circuits modular: rich connections within a duplicated unit and sparse connections between units (as opposed to all-to-all nonmodular architectures used as the starting conditions in many artificial neural networks). In turn, the modular nature of neuronal circuits might speed up evolution (*6*) because different modules can evolve independently of each other.

Development of neuronal circuits

Evolution exerts its influence on neuronal circuits primarily by modifying genes involved in circuit wiring during development. A key question is how a limited number of genes (~20,000 across many animal species) can construct nervous systems with much larger numbers of synaptic connections (~10^7 in fruit flies, ~10^{11} in mice, and >10^{14} in humans) with specific motifs and architectures.

Extracellular cues and their cell surface receptors enable recognition of specific targets by axonal and dendritic growth cones. These molecules are the predominant force for establishing a coarse organization of the nervous system and can also specify synaptic connectivity with great precision in certain circuits and organisms (*67*–*69*). One strategy to establish specificity of a large number of connections with a limited number of genes is to use different expression levels of the same protein to specify different connections. This strategy is readily used in constructing continuous topographic maps (*70*, *71*) (Fig. 5A), perhaps contributing to the prevalence of this circuit architecture (Fig. 3A). Graded expression of cell surface molecules is also used in the early steps of constructing discrete maps (*72*, *73*). However, discrete parallel processing (Fig. 3B) requires distinguishing between discrete cell types and often uses combinatorial cell surface protein codes such that a small number of proteins can specify many more connections (Fig. 5B, left). An efficient way to implement combinatorial coding is to divide the wiring process into distinct spatiotemporal steps (Fig. 5B, right); in addition to conserving molecules, this strategy can also enhance robustness because growth cones are faced with few simultaneous choices at each step. The same wiring molecules can be used at different times and places, sometimes in different parts of the same circuit, through elaborate spatiotemporal regulation of their expression patterns (*74*–*76*).

Neuronal activity, both spontaneous and experience driven, refines synaptic wiring diagrams. Activity-dependent wiring, often through competition between neurons with

different activity levels, has been well documented (*77*–*81*). A prominent mechanism by which neuronal activity influences wiring is by implementing Hebb's rule: Synapses at which firing of presynaptic neurons causes firing of postsynaptic neurons are strengthened, or colloquially, "fire together, wire together" (*82*, *83*) (Fig. 5C). Non-Hebbian mechanisms such as homeostatic synaptic plasticity also contribute to activity-dependent circuit wiring (*84*). These activity-dependent mechanisms continue to operate in the adult nervous system, enabling animals to change their synaptic connectivity patterns as a consequence of experience throughout life.

Many synaptic connections are not completely specified. In vertebrate neuromuscular systems, for example, whereas the connections between motor neuron pools and muscles are precisely specified (*85*), the specific connection patterns between individual motor neurons and muscle fibers within a motor pool are highly variable (*86*). Likewise, in the fly olfactory circuit, synaptic connections between specific olfactory projection neuron types and mushroom body Kenyon cells (Fig. 3C) are mostly random (*87*–*89*). In both cases, it is not necessary, or even desirable, to have more stereotyped connectivity. As more synaptic connectomes are mapped (Box 1), more examples of wiring variability will surely emerge.

In summary, two broad kinds of mechanisms are used to establish wiring patterns of neuronal circuits: molecular cues hardwire the nervous system and neuronal activity and experience fine-tune connectivity. There is also interplay between neuronal activity and molecular cues; for example, neuronal activity can regulate the expression of molecular cues or complement their action (*90*, *91*). However, apart from the limited examples discussed above, most developmental studies have not focused on addressing how specific circuit motifs and architectures are established, and most investigations of circuit function have not considered developmental constraints. There is thus ample opportunity for cross-fertilization of developmental and functional studies of neuronal circuits.

Outlook

Applications of circuit-mapping tools such as serial electron microscopy and trans-synaptic tracing (Box 1) to diverse neural regions and organisms will surely generate a wealth of data from which we can distill common principles of structural organization of neuronal circuits. Relating structures to the functions they implement will be an important next step. This can be done by leveraging powerful tools that have been developed and applied to functionally interrogate neuronal circuits in the context of animal behavior (*92*–*94*). Such interrogation is essential for identifying the functions of each circuit elements. In addition, a key challenge is to investigate how these motifs and architectures interact with each other across scales. Understanding how different architectures cooperate in an individual nervous system should also inspire new artificial neural networks that might someday achieve general purpose artificial intelligence.

We are still only beginning to gain insights into the evolutionary and developmental processes that give rise to circuit architecture in complex nervous systems. We still do not know, for example, whether and to what degree algorithmic changes in the wiring process and operation of neuronal circuits can account for the increased complexity of the mammalian brain. A deliberate effort to investigate how letters are assembled into words and words into sentences in key circuit architectures across different species could yield valuable insights. Comparative study of neuron-type composition of homologous brain regions using single-cell transcriptomics (*63*–*66*) is a useful first step. This can be followed by investigation of the mechanisms that establish their connectivity patterns and that underlie their functional operations. Integrating studies of the structure, function, development, and evolution of neuronal circuits will enable a deeper understanding of nervous system organization beyond the level of individual neurons.

REFERENCES AND NOTES

1. S. R. Cajal, *Histology of the Nervous System of Man and Vertebrates* (Oxford Univ. Press, 1995).
2. C. Golgi, Sulla struttura della sostanza grigia del cervello. *Gazetta medica lombarda* **IV** (1873).
3. G. Laurent *et al*., Odor encoding as an active, dynamical process: Experiments, computation, and theory. *Annu. Rev. Neurosci.* **24**, 263–297 (2001). doi: 10.1146/annurev.neuro.24.1.263; pmid: 11283312
4. K. V. Shenoy, M. Sahani, M. M. Churchland, Cortical control of arm movements: A dynamical systems perspective. *Annu. Rev. Neurosci.* **36**, 337–359 (2013). doi: 10.1146/annurev-neuro-062111-150509; pmid: 23725001
5. L. Luo, *Principles of Neurobiology* (CRC Press/Garland Science, ed. 2, 2020).
6. U. Alon, *An Introduction to Systems Biology* (CRC Press, ed. 2, 2020).
7. Y. LeCun, Y. Bengio, G. Hinton, Deep learning. *Nature* **521**, 436–444 (2015). doi: 10.1038/nature14539; pmid: 26017442
8. C. D. Gilbert, T. N. Wiesel, Morphology and intracortical projections of functionally characterised neurones in the cat visual cortex. *Nature* **280**, 120–125 (1979). doi: 10.1038/280120a0; pmid: 552600
9. D. J. Felleman, D. C. Van Essen, Distributed hierarchical processing in the primate cerebral cortex. *Cereb. Cortex* **1**, 1–47 (1991). doi: 10.1093/cercor/1.1.1; pmid: 1822724
10. F. Rosenblatt, The perceptron: A probabilistic model for information storage and organization in the brain. *Psychol. Rev.* **65**, 386–408 (1958). doi: 10.1037/h0042519; pmid: 13602029
11. A. Krizhevsky, I. Sutskever, G. Hinton, Imagenet classification with deep convolutional neural networks. *In Proc. Adv. Neural Inf. Process. Syst.* **25**, 1090–1098 (2012).
12. C. S. Sherrington, Remarks on some aspects of reflex inhibition. *Proc. R. Soc. London Ser. B* **97**, 519–545 (1925). doi: 10.1098/rspb.1925.0017
13. J. S. Coombs, J. C. Eccles, P. Fatt, The inhibitory suppression of reflex discharges from motoneurones. *J. Physiol.* **130**, 396–413 (1955). doi: 10.1113/jphysiol.1955.sp005414; pmid: 13278907
14. J. S. Isaacson, M. Scanziani, How inhibition shapes cortical activity. *Neuron* **72**, 231–243 (2011). doi: 10.1016/j.neuron.2011.09.027; pmid: 22017986
15. K. A. Martin, P. Somogyi, D. Whitteridge, Physiological and morphological properties of identified basket cells in the cat's visual cortex. *Exp. Brain Res.* **50**, 193–200 (1983). doi: 10.1007/BF00239183; pmid: 6641854
16. X. Y. Ji *et al*., Thalamocortical innervation pattern in mouse auditory and visual cortex: Laminar and cell-type specificity. *Cereb. Cortex* **26**, 2612–2625 (2016). doi: 10.1093/cercor/bhv099; pmid: 25979090
17. L. Roux, G. Buzsáki, Tasks for inhibitory interneurons in intact brain circuits. *Neuropharmacology* **88**, 10–23 (2015). doi: 10.1016/j.neuropharm.2014.09.011; pmid: 25239808
18. C. van Vreeswijk, H. Sompolinsky, Chaos in neuronal networks with balanced excitatory and inhibitory activity. *Science* **274**, 1724–1726 (1996). doi: 10.1126/science.274.5293.1724; pmid: 8939866
19. M. N. Shadlen, W. T. Newsome, The variable discharge of cortical neurons: Implications for connectivity, computation, and information coding. *J. Neurosci.* **18**, 3870–3896 (1998). doi: 10.1523/JNEUROSCI.18-10-03870.1998; pmid: 9570816
20. S. W. Kuffler, Discharge patterns and functional organization of mammalian retina. *J. Neurophysiol.* **16**, 37–68 (1953). doi: 10.1152/jn.1953.16.1.37; pmid: 13035466
21. H. B. Barlow, Summation and inhibition in the frog's retina. *J. Physiol.* **119**, 69–88 (1953). doi: 10.1113/jphysiol.1953.sp004829; pmid: 13035718
22. V. B. Mountcastle, Modality and topographic properties of single neurons of cat's somatic sensory cortex. *J. Neurophysiol.* **20**, 408–434 (1957). doi: 10.1152/jn.1957.20.4.408; pmid: 13439410
23. G. M. Shepherd, W. R. Chen, C. A. Greer, "Olfactory bulb," in *The Synaptic Organization of the Brain*, G. M. Shepherd, Ed. (Oxford Univ. Press, 2004), pp. 165–216.
24. S. Grillner, Biological pattern generation: The cellular and computational logic of networks in motion. *Neuron* **52**, 751–766 (2006). doi: 10.1016/j.neuron.2006.11.008; pmid: 17145498
25. E. Marder, D. Bucher, Understanding circuit dynamics using the stomatogastric nervous system of lobsters and crabs. *Annu. Rev. Physiol.* **69**, 291–316 (2007). doi: 10.1146/annurev.physiol.69.031905.161516; pmid: 17009928
26. C. B. Saper, P. M. Fuller, N. P. Pedersen, J. Lu, T. E. Scammell, Sleep state switching. *Neuron* **68**, 1023–1042 (2010). doi: 10.1016/j.neuron.2010.11.032; pmid: 21172606
27. F. Weber, Y. Dan, Circuit-based interrogation of sleep control. *Nature* **538**, 51–59 (2016). doi: 10.1038/nature19773; pmid: 27708309
28. H. Markram *et al*., Interneurons of the neocortical inhibitory system. *Nat. Rev. Neurosci.* **5**, 793–807 (2004). doi: 10.1038/nrn1519; pmid: 15378039
29. Z. J. Huang, A. Paul, The diversity of GABAergic neurons and neural communication elements. *Nat. Rev. Neurosci.* **20**, 563–572 (2019). doi: 10.1038/s41583-019-0195-4; pmid: 31222186
30. A. A. Prinz, D. Bucher, E. Marder, Similar network activity from disparate circuit parameters. *Nat. Neurosci.* **7**, 1345–1352 (2004). doi: 10.1038/nn1352; pmid: 15558066
31. W. Penfield, T. Rasmussen, *The Cerebral Cortex of Man: A Clinical Study of Localization of Function* (Macmillan, 1950).
32. I. E. Wang, T. R. Clandinin, The influence of wiring economy on nervous system evolution. *Curr. Biol.* **26**, R1101–R1108 (2016). doi: 10.1016/j.cub.2016.08.053; pmid: 27780051
33. R. Axel, The molecular logic of smell. *Sci. Am.* **273**, 154–159 (1995). doi: 10.1038/scientificamerican1095-154; pmid: 7481719
34. L. B. Vosshall, R. F. Stocker, Molecular architecture of smell and taste in *Drosophila*. *Annu. Rev. Neurosci.* **30**, 505–533 (2007). doi: 10.1146/annurev.neuro.30.051606.094306; pmid: 17506643
35. D. A. Yarmolinsky, C. S. Zuker, N. J. Ryba, Common sense about taste: From mammals to insects. *Cell* **139**, 234–244 (2009). doi: 10.1016/j.cell.2009.10.001; pmid: 19837029
36. D. Marr, A theory of cerebellar cortex. *J. Physiol.* **202**, 437–470 (1969). doi: 10.1113/jphysiol.1969.sp008820; pmid: 5784296
37. J. S. Albus, A theory of cerebellar dunction. *Math. Biosci.* **10**, 25–61 (1971). doi: 10.1016/0025-5564(71)90051-4
38. A. Litwin-Kumar, K. D. Harris, R. Axel, H. Sompolinsky, L. F. Abbott, Optimal degrees of synaptic connectivity. *Neuron* **93**, 1153–1164.e7 (2017). doi: 10.1016/j.neuron.2017.01.030; pmid: 28215558
39. N. A. Cayco-Gajic, R. A. Silver, Re-evaluating circuit mechanisms underlying pattern separation. *Neuron* **101**, 584–602 (2019). doi: 10.1016/j.neuron.2019.01.044; pmid: 30790539

40. T. Hige, Y. Aso, M. N. Modi, G. M. Rubin, G. C. Turner, Heterosynaptic plasticity underlies aversive olfactory learning in *Drosophila*. *Neuron* **88**, 985–998 (2015). doi: 10.1016/j.neuron.2015.11.003; pmid: 26637800
41. R. Cohn, I. Morantte, V. Ruta, Coordinated and compartmentalized neuromodulation shapes sensory processing in *Drosophila*. *Cell* **163**, 1742–1755 (2015). doi: 10.1016/j.cell.2015.11.019; pmid: 26687359
42. C. I. De Zeeuw, S. G. Lisberger, J. L. Raymond, Diversity and dynamism in the cerebellum. *Nat. Neurosci.* **24**, 160–167 (2021). doi: 10.1038/s41593-020-00754-9; pmid: 33288911
43. D. Marr, Simple memory: A theory for archicortex. *Philos. Trans. R. Soc. Lond. B Biol. Sci.* **262**, 23–81 (1971). doi: 10.1098/rstb.1971.0078; pmid: 4399412
44. J. P. Neunuebel, J. J. Knierim, CA3 retrieves coherent representations from degraded input: Direct evidence for CA3 pattern completion and dentate gyrus pattern separation. *Neuron* **81**, 416–427 (2014). doi: 10.1016/j.neuron.2013.11.017; pmid: 24462102
45. K. T. Beier *et al*., Circuit architecture of VTA dopamine neurons revealed by systematic input-output mapping. *Cell* **162**, 622–634 (2015). doi: 10.1016/j.cell.2015.07.015; pmid: 26232228
46. T. N. Lerner *et al*., Intact-brain analyses reveal distinct information carried by SNC dopamine subcircuits. *Cell* **162**, 635–647 (2015). doi: 10.1016/j.cell.2015.07.014; pmid: 26232229
47. J. Ren *et al*., Anatomically defined and functionally distinct dorsal raphe serotonin sub-systems. *Cell* **175**, 472–487.e20 (2018). doi: 10.1016/j.cell.2018.07.043; pmid: 30146164
48. J. Kohl *et al*., Functional circuit architecture underlying parental behaviour. *Nature* **556**, 326–331 (2018). doi: 10.1038/s41586-018-0027-0; pmid: 29643503
49. L. A. Schwarz *et al*., Viral-genetic tracing of the input-output organization of a central noradrenaline circuit. *Nature* **524**, 88–92 (2015). doi: 10.1038/nature14600; pmid: 26131933
50. J. M. Kebschull *et al*., High-throughput mapping of single-neuron projections by sequencing of barcoded rna. *Neuron* **91**, 975–987 (2016). doi: 10.1016/j.neuron.2016.07.036; pmid: 27545715
51. L. W. Swanson, *Brain Architecture* (Oxford Univ. Press, ed. 2, 2012).
52. L. W. Swanson, J. D. Hahn, O. Sporns, Structure-function subsystem models of female and male forebrain networks integrating cognition, affect, behavior, and bodily functions. *Proc. Natl. Acad. Sci. U.S.A.* **117**, 31470–31481 (2020). doi: 10.1073/pnas.2017733117; pmid: 33229546
53. R. J. Douglas, K. A. Martin, Neuronal circuits of the neocortex. *Annu. Rev. Neurosci.* **27**, 419–451 (2004). doi: 10.1146/annurev.neuro.27.070203.144152; pmid: 15217339
54. C. R. Gerfen, D. J. Surmeier, Modulation of striatal projection systems by dopamine. *Annu. Rev. Neurosci.* **34**, 441–466 (2011). doi: 10.1146/annurev-neuro-061010-113641; pmid: 21469956
55. J. Lee, W. Wang, B. L. Sabatini, Anatomically segregated basal ganglia pathways allow parallel behavioral modulation. *Nat. Neurosci.* **23**, 1388–1398 (2020). doi: 10.1038/s41593-020-00712-5; pmid: 32989293
56. J. H. Kaas, *Evolutionary Neuroscience* (Elsevier, ed. 2, 2020).
57. L. V. Salvini-Plawen, E. Mayr, On the evolution of photoreceptors and eyes. *Evol. Biol.* **10**, 207–263 (1977).
58. D. A. Clark *et al*., Flies and humans share a motion estimation strategy that exploits natural scene statistics. *Nat. Neurosci.* **17**, 296–303 (2014). doi: 10.1038/nn.3600; pmid: 24390225
59. J. H. Lui, D. V. Hansen, A. R. Kriegstein, Development and evolution of the human neocortex. *Cell* **146**, 18–36 (2011). doi: 10.1016/j.cell.2011.06.030; pmid: 21729779
60. D. Arendt *et al*., The origin and evolution of cell types. *Nat. Rev. Genet.* **17**, 744–757 (2016). doi: 10.1038/nrg.2016.127; pmid: 27818507
61. M. Chakraborty, E. D. Jarvis, Brain evolution by brain pathway duplication. *Philos. Trans. R. Soc. Lond. B Biol. Sci.* **370**, 20150056 (2015). doi: 10.1098/rstb.2015.0056; pmid: 26554045
62. G. H. Jacobs, J. Nathans, The evolution of Primate color vision. *Sci. Am.* **300**, 56–63 (2009). doi: 10.1038/scientificamerican0409-56; pmid: 19363921
63. M. A. Tosches *et al*., Evolution of pallium, hippocampus, and cortical cell types revealed by single-cell transcriptomics in reptiles. *Science* **360**, 881–888 (2018). doi: 10.1126/science.aar4237; pmid: 29724907
64. Y. R. Peng *et al*., Molecular classification and comparative taxonomics of foveal and peripheral cells in primate retina. *Cell* **176**, 1222–1237.e22 (2019). doi: 10.1016/j.cell.2019.01.004; pmid: 30712875
65. R. D. Hodge *et al*., Conserved cell types with divergent features in human versus mouse cortex. *Nature* **573**, 61–68 (2019). doi: 10.1038/s41586-019-1506-7; pmid: 31435019
66. J. M. Kebschull *et al*., Cerebellar nuclei evolved by repeatedly duplicating a conserved cell-type set. *Science* **370**, eabd5059 (2020). pmid: 33335034
67. A. L. Kolodkin, M. Tessier-Lavigne, Mechanisms and molecules of neuronal wiring: A primer. *Cold Spring Harb. Perspect. Biol.* **3**, a001727 (2011). doi: 10.1101/cshperspect.a001727; pmid: 21123392
68. W. Hong, L. Luo, Genetic control of wiring specificity in the fly olfactory system. *Genetics* **196**, 17–29 (2014). doi: 10.1534/genetics.113.154336; pmid: 24395823
69. J. R. Sanes, S. L. Zipursky, Synaptic specificity, recognition molecules, and assembly of neural circuits. *Cell* **181**, 536–556 (2020). doi: 10.1016/j.cell.2020.04.008; pmid: 32359437
70. U. Drescher *et al*., In vitro guidance of retinal ganglion cell axons by RAGS, a 25 kDa tectal protein related to ligands for Eph receptor tyrosine kinases. *Cell* **82**, 359–370 (1995). doi: 10.1016/0092-8674(95)90425-5; pmid: 7634326
71. H.-J. Cheng, M. Nakamoto, A. D. Bergemann, J. G. Flanagan, Complementary gradients in expression and binding of ELF-1 and Mek4 in development of the topographic retinotectal projection map. *Cell* **82**, 371–381 (1995). doi: 10.1016/0092-8674(95)90426-3; pmid: 7634327
72. T. Imai, M. Suzuki, H. Sakano, Odorant receptor-derived cAMP signals direct axonal targeting. *Science* **314**, 657–661 (2006). doi: 10.1126/science.1131794; pmid: 16990513
73. T. Komiyama, L. B. Sweeney, O. Schuldiner, K. C. Garcia, L. Luo, Graded expression of semaphorin-1a cell-autonomously directs dendritic targeting of olfactory projection neurons. *Cell* **128**, 399–410 (2007). doi: 10.1016/j.cell.2006.12.028; pmid: 17254975
74. W. J. Joo, L. B. Sweeney, L. Liang, L. Luo, Linking cell fate, trajectory choice, and target selection: Genetic analysis of Sema-2b in olfactory axon targeting. *Neuron* **78**, 673–686 (2013). doi: 10.1016/j.neuron.2013.03.022; pmid: 23719164
75. J. Cang, D. A. Feldheim, Developmental mechanisms of topographic map formation and alignment. *Annu. Rev. Neurosci.* **36**, 51–77 (2013). doi: 10.1146/annurev-neuro-062012-170341; pmid: 23642132
76. D. T. Pederick *et al*., Reciprocal repulsions instruct the precise assembly of parallel hippocampal networks. *Science* **372**, 1068–1073 (2021). doi: 10.1126/science.abg1774; pmid: 34083484
77. T. N. Wiesel, D. H. Hubel, Single-cell responses in striate cortex of kittens deprived of vision in one eye. *J. Neurophysiol.* **26**, 1003–1017 (1963). doi: 10.1152/jn.1963.26.6.1003; pmid: 14084161
78. M. Constantine-Paton, M. I. Law, Eye-specific termination bands in tecta of three-eyed frogs. *Science* **202**, 639–641 (1978). doi: 10.1126/science.309179; pmid: 309179
79. M. P. Stryker, W. A. Harris, Binocular impulse blockade prevents the formation of ocular dominance columns in cat visual cortex. *J. Neurosci.* **6**, 2117–2133 (1986). doi: 10.1523/JNEUROSCI.06-08-02117.1986; pmid: 3746403
80. A. A. Penn, P. A. Riquelme, M. B. Feller, C. J. Shatz, Competition in retinogeniculate patterning driven by spontaneous activity. *Science* **279**, 2108–2112 (1998). doi: 10.1126/science.279.5359.2108; pmid: 9516112
81. M. Buffelli *et al*., Genetic evidence that relative synaptic efficacy biases the outcome of synaptic competition. *Nature* **424**, 430–434 (2003). doi: 10.1038/nature01844; pmid: 12879071
82. D. O. Hebb, *The Organization of Behavior* (Wiley, 1949).
83. G. S. Stent, A physiological mechanism for Hebb's postulate of learning. *Proc. Natl. Acad. Sci. U.S.A.* **70**, 997–1001 (1973). doi: 10.1073/pnas.70.4.997; pmid: 4352227
84. G. G. Turrigiano, The dialectic of Hebb and homeostasis. *Philos. Trans. R. Soc. London Ser. B* **372**, 20160258 (2017). doi: 10.1098/rstb.2016.0258; pmid: 28093556
85. C. Lance-Jones, L. Landmesser, Pathway selection by embryonic chick motoneurons in an experimentally altered environment. *Proc. R. Soc. London Ser. B* **214**, 19–52 (1981). doi: 10.1098/rspb.1981.0080; pmid: 6121329
86. J. Lu, J. C. Tapia, O. L. White, J. W. Lichtman, The interscutularis muscle connectome. *PLOS Biol.* **7**, e32 (2009). pmid: 19209956
87. S. J. Caron, V. Ruta, L. F. Abbott, R. Axel, Random convergence of olfactory inputs in the *Drosophila* mushroom body. *Nature* **497**, 113–117 (2013). doi: 10.1038/nature12063; pmid: 23615618
88. F. Li *et al*., The connectome of the adult *Drosophila* mushroom body provides insights into function. *eLife* **9**, e62576 (2020). doi: 10.7554/eLife.62576; pmid: 33315010
89. Z. Zheng *et al*., A complete electron microscopy volume of the brain of adult *Drosophila* melanogaster. *Cell* **174**, 730–743.e22 (2018). doi: 10.1016/j.cell.2018.06.019; pmid: 30033368
90. S. Serizawa *et al*., A neuronal identity code for the odorant receptor-specific and activity-dependent axon sorting. *Cell* **127**, 1057–1069 (2006). doi: 10.1016/j.cell.2006.10.031; pmid: 17129788
91. T. McLaughlin, C. L. Torborg, M. B. Feller, D. D. O'Leary, Retinotopic map refinement requires spontaneous retinal waves during a brief critical period of development. *Neuron* **40**, 1147–1160 (2003). doi: 10.1016/S0896-6273(03)00790-6; pmid: 14687549
92. M. Z. Lin, M. J. Schnitzer, Genetically encoded indicators of neuronal activity. *Nat. Neurosci.* **19**, 1142–1153 (2016). doi: 10.1038/nn.4359; pmid: 27571193
93. C. K. Kim, A. Adhikari, K. Deisseroth, Integration of optogenetics with complementary methodologies in systems neuroscience. *Nat. Rev. Neurosci.* **18**, 222–235 (2017). doi: 10.1038/nrn.2017.15; pmid: 28303019
94. L. Luo, E. M. Callaway, K. Svoboda, Genetic dissection of neural circuits: A decade of progress. *Neuron* **98**, 256–281 (2018). doi: 10.1016/j.neuron.2018.03.040; pmid: 29673479
95. W. M. Cowan, The emergence of modern neuroanatomy and developmental neurobiology. *Neuron* **20**, 413–426 (1998). doi: 10.1016/S0896-6273(00)80985-X; pmid: 9539119
96. T. Lee, L. Luo, Mosaic analysis with a repressible cell marker for studies of gene function in neuronal morphogenesis. *Neuron* **22**, 451–461 (1999). doi: 10.1016/S0896-6273(00)80701-1; pmid: 10197526
97. G. Feng *et al*., Imaging neuronal subsets in transgenic mice expressing multiple spectral variants of GFP. *Neuron* **28**, 41–51 (2000). doi: 10.1016/S0896-6273(00)00084-2; pmid: 11086982
98. H. Zong, J. S. Espinosa, H. H. Su, M. D. Muzumdar, L. Luo, Mosaic analysis with double markers in mice. *Cell* **121**, 479–492 (2005). doi: 10.1016/j.cell.2005.02.012; pmid: 15882628
99. J. Livet *et al*., Transgenic strategies for combinatorial expression of fluorescent proteins in the nervous system. *Nature* **450**, 56–62 (2007). doi: 10.1038/nature06293; pmid: 17972876
100. A. Nern, B. D. Pfeiffer, G. M. Rubin, Optimized tools for multicolor stochastic labeling reveal diverse stereotyped cell arrangements in the fly visual system. *Proc. Natl. Acad. Sci. U.S.A.* **112**, E2967–E2976 (2015). doi: 10.1073/pnas.1506763112; pmid: 25964354
101. J. G. White, E. Southgate, J. N. Thomson, S. Brenner, The structure of the nervous system of the nematode *Caenorhabditis elegans*. *Philos. Trans. R. Soc. London Ser. B* **314**, 1–340 (1986). doi: 10.1098/rstb.1986.0056; pmid: 22462104
102. S. Y. Takemura *et al*., A visual motion detection circuit suggested by *Drosophila* connectomics. *Nature* **500**, 175–181 (2013). doi: 10.1038/nature12450; pmid: 23925240
103. J. S. Kim *et al*., Space-time wiring specificity supports direction selectivity in the retina. *Nature* **509**, 331–336 (2014). doi: 10.1038/nature13240; pmid: 24805243
104. W. C. Lee *et al*., Anatomy and function of an excitatory network in the visual cortex. *Nature* **532**, 370–374 (2016). doi: 10.1038/nature17192; pmid: 27018655
105. D. G. C. Hildebrand *et al*., Whole-brain serial-section electron microscopy in larval zebrafish. *Nature* **545**, 345–349 (2017). doi: 10.1038/nature22356; pmid: 28489821
106. L. K. Scheffer *et al*., A connectome and analysis of the adult *Drosophila* central brain. *eLife* **9**, e57443 (2020). doi: 10.7554/eLife.57443; pmid: 32880371
107. L. F. Abbott *et al*., The mind of a mouse. *Cell* **182**, 1372–1376 (2020). doi: 10.1016/j.cell.2020.08.010; pmid: 32946777
108. I. R. Wickersham *et al*., Monosynaptic restriction of transsynaptic tracing from single, genetically targeted neurons. *Neuron* **53**, 639–647 (2007). doi: 10.1016/j.neuron.2007.01.033; pmid: 17329205
109. E. M. Callaway, L. Luo, Monosynaptic circuit tracing with glycoprotein-deleted rabies viruses. *J. Neurosci.* **35**, 8979–8985 (2015). doi: 10.1523/JNEUROSCI.0409-15.2015; pmid: 26085623

110. L. Lo, D. J. Anderson, A Cre-dependent, anterograde transsynaptic viral tracer for mapping output pathways of genetically marked neurons. *Neuron* **72**, 938–950 (2011). doi: 10.1016/j.neuron.2011.12.002; pmid: 22196330
111. B. Zingg *et al*., Aav-mediated anterograde transsynaptic tagging: Mapping corticocollicular input-defined neural pathways for defense behaviors. *Neuron* **93**, 33–47 (2017). doi: 10.1016/j.neuron.2016.11.045; pmid: 27989459
112. M. Talay *et al*., Transsynaptic mapping of second-order taste neurons in flies by trans-tango. *Neuron* **96**, 783–795.e4 (2017). doi: 10.1016/j.neuron.2017.10.011; pmid: 29107518
113. T. H. Huang *et al*., Tracing neuronal circuits in transgenic animals by transneuronal control of transcription (*TRACT*). *eLife* **6**, e32027 (2017). doi: 10.7554/eLife.32027; pmid: 29231171
114. L. Petreanu, D. Huber, A. Sobczyk, K. Svoboda, Channelrhodopsin-2-assisted circuit mapping of long-range callosal projections. *Nat. Neurosci.* **10**, 663–668 (2007). doi: 10.1038/nn1891; pmid: 17435752
115. M. London, M. Häusser, Dendritic computation. *Annu. Rev. Neurosci.* **28**, 503–532 (2005). doi: 10.1146/annurev.neuro.28.061604.135703; pmid: 16033324
116. N. M. van Strien, N. L. Cappaert, M. P. Witter, The anatomy of memory: An interactive overview of the parahippocampal-hippocampal network. *Nat. Rev. Neurosci.* **10**, 272–282 (2009). doi: 10.1038/nrn2614; pmid: 19300446
117. L. Luo, J. G. Flanagan, Development of continuous and discrete neural maps. *Neuron* **56**, 284–300 (2007). doi: 10.1016/j.neuron.2007.10.014; pmid: 17964246

ACKNOWLEDGMENTS

I thank W. Allen, T. Clandinin, L. Fei-Fei, M. Feller, J. Kebschull, J. Lui, J. Ren, M. Scanziani, A. Shuster, L. Stryer, and M. Wagner for helpful critiques and Taylor & Francis Group, LLC for granting permission to adapt figures from *Principles of Neurobiology* (*5*). **Funding:** This work was supported by the National Institutes of Health, the National Science Foundation, the Howard Hughes Medical Institute, and the Wu Tsai Neurosciences Institute at Stanford University. **Competing interests:** The author declares no competing interests.

10.1126/science.abg7285

ScienceImmunology.org



READY TO PUT THE SPOTLIGHT ON YOUR RESEARCH?

Submit your research:
cts.ScienceMag.org

Science Immunology
AAAS

Twitter: @SciImmunology
Facebook: @ScienceImmunology

RESEARCH ARTICLE SUMMARY

MELANOMA

Developmental chromatin programs determine oncogenic competence in melanoma

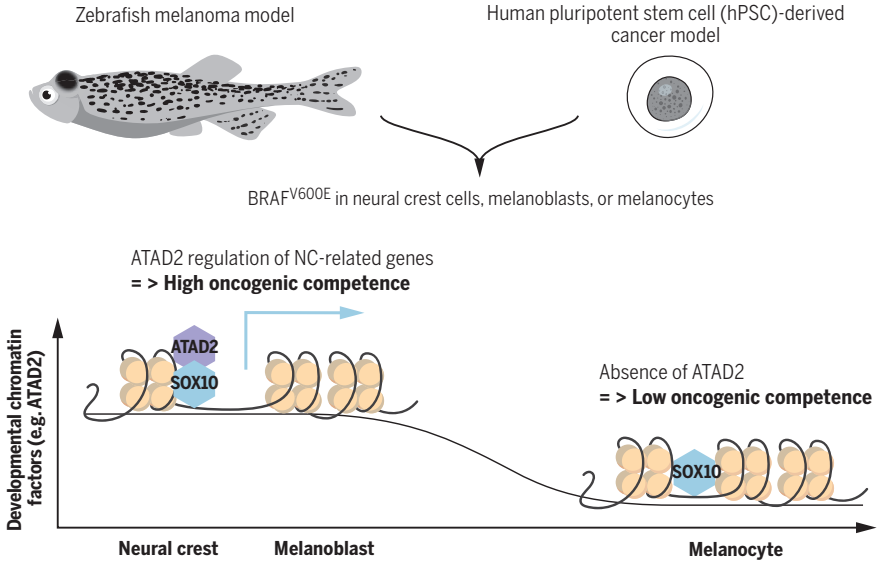
Arianna Baggiolini†, Scott J. Callahan†, Emily Montal, Joshua M. Weiss, Tuan Trieu, Mohita M. Tagore, Sam E. Tischfield, Ryan M. Walsh, Shruthy Suresh, Yujie Fan, Nathaniel R. Campbell, Sarah C. Perlee, Nathalie Saurat, Miranda V. Hunter, Theresa Simon-Vermot, Ting-Hsiang Huang, Yilun Ma, Travis Hollmann, Satish K. Tickoo, Barry S. Taylor, Ekta Khurana, Richard P. Koche, Lorenz Studer*‡, Richard M. White*‡,

INTRODUCTION: Tumor analyses have shown that DNA mutations can transform cells in some situations but not in others. In melanoma, $BRAF^{V600E}$ [serine/threonine-protein kinase B-raf (BRAF) in which valine at position 600 is replaced with glutamic acid] expression coincides with the aberrant expression of a developmental signature typical of the neural crest, suggesting that the neural crest state might be linked to oncogenic competence. The mechanisms by which this state is acquired and gives rise to oncogenic competence are unknown.

RATIONALE: During development, neural crest cells give rise to melanoblasts, which then further differentiate into melanocytes. Using a combination of zebrafish transgenesis and human pluripotent stem cell models, we assessed oncogenic response to $BRAF^{V600E}$ in each of these three cell states. We used these models to determine why certain cell states but not others were preferentially competent to form tumors.

RESULTS: We engineered zebrafish to drive $BRAF^{V600E}$ expression under the *sox10* promoter, the *mitfa* promoter, or the *tyrp1* promoter in the $p53^{-/-}$ background. This allows for oncogene activation at the neural crest, at the melanoblast, or melanocyte stage, respectively. Fish that received the oncogenic mutation during the neural crest and melanoblast stages efficiently developed tumors, whereas melanocytes were relatively resistant. To extend these findings to human cells, we developed a human pluripotent stem cell (hPSC)–derived tumor model. hPSCs can differentiate into neural crest cells, melanoblasts, and melanocytes. We used gene targeting to introduce oncogenic $BRAF^{V600E}$ and to inactivate the tumor suppressors RB1, TP53, and P16 in these cells. Analogous to what we found in the zebrafish, upon subcutaneous transplant into NSG mice, human melanocytes were relatively resistant to malignant transformation, whereas the neural crest cells and melanoblasts readily developed tumors. RNA-sequencing of these cells with or without $BRAF^{V600E}$ revealed a robust transcriptional response to the oncogene in the neural crest cells and melanoblasts, whereas melanocytes had little change despite equal activation of phosphorylated extracellular signal–regulated kinase (pERK). This suggested that there were intrinsic differences across these cells that determined how they responded to oncogenic insult. Pathway analysis revealed significant up-regulation of several chromatin-modifying enzymes in the more competent neural crest and melanoblast cells, including readers, writers, and erasers (ATAD2, BPTF, BAZ1A, EZH2, and others). This raised the hypothesis that the neural crest cells and melanoblasts had higher intrinsic transcriptional plasticity compared with that of melanocytes because of these chromatin modifiers. Further investigation demonstrated that one of these factors, ATAD2, is commonly amplified or overexpressed in melanoma patients and is correlated with a worse prognosis. In vitro, expression of ATAD2 in hPSC-derived melanocytes led to acquisition of a more progenitor-like phenotype, and inhibition of ATAD2 impaired neural crest differentiation. In vivo, ATAD2 is sufficient to endow oncogenic competence to the melanocytes and allows for formation of melanoma in these otherwise more resistant cells. We show that ATAD2 forms a protein complex with SOX10, a key transcription factor required for neural crest development. Analysis with ATAC-seq, RNA-seq, and Cut&Run demonstrate that ATAD2 facilitates expression of SOX10 developmental target genes as well as genes related to the mitogen-activated protein kinase (MAPK) pathway. Together, these allow for a robust transcriptional response to oncogenes such as $BRAF^{V600E}$.

CONCLUSION: Overall, these data suggest that oncogenic competence is mediated by a combination of oncogenes (such as $BRAF^{V600E}$), lineage-specific transcription factors (such as SOX10), and developmentally regulated chromatin factors (such as ATAD2). These data imply that there may not be a single cell of origin for melanoma but instead that melanoma origin may depend on the relative levels of these factors in different contexts or anatomic locations. Beyond melanoma, the specific combination of such factors is likely to be different in each type of tumor. Further investigation into the mechanisms regulating their expression opens up the possibility of therapeutically targeting competence factors. ■



Developmental chromatin factors allow for oncogenic competence and tumor formation. Both zebrafish and hPSC-derived cancer models show that neural crest cells and melanoblasts have oncogenic competence, whereas melanocytes are relatively resistant. Progenitor cells express a specific profile of epigenetic factors such as ATAD2, reexpression of which then endows melanocytes with oncogenic competence.

*Corresponding authors. Email: studerl@mskcc.org (L.S.); whiter@mskcc.org (R.M.W.)
†These authors contributed equally to this work.
‡These authors contributed equally to this work.
Cite this article as A. Baggiolini *et al.*, *Science* **373**, eabc1048 (2021). DOI: 10.1126/science.abc1048

READ THE FULL ARTICLE AT
https://doi.org/10.1126/science.abc1048

RESEARCH ARTICLE

MELANOMA

Developmental chromatin programs determine oncogenic competence in melanoma

Arianna Baggiolini[1]†, Scott J. Callahan[1,2,3]†, Emily Montal[2], Joshua M. Weiss[2,4], Tuan Trieu[5,6,7,8], Mohita M. Tagore[2], Sam E. Tischfield[9,10,11], Ryan M. Walsh[1], Shruthy Suresh[2], Yujie Fan[1,12], Nathaniel R. Campbell[2,4], Sarah C. Perlee[2,3], Nathalie Saurat[1], Miranda V. Hunter[2], Theresa Simon-Vermot[2], Ting-Hsiang Huang[2], Yilun Ma[2,4], Travis Hollmann[13], Satish K. Tickoo[13], Barry S. Taylor[9,10,11,14], Ekta Khurana[5,6,7,8], Richard P. Koche[15], Lorenz Studer[1]*‡, Richard M. White[2,12]*‡

Oncogenes only transform cells under certain cellular contexts, a phenomenon called oncogenic competence. Using a combination of a human pluripotent stem cell–derived cancer model along with zebrafish transgenesis, we demonstrate that the transforming ability of $BRAF^{V600E}$ along with additional mutations depends on the intrinsic transcriptional program present in the cell of origin. In both systems, melanocytes are less responsive to mutations, whereas both neural crest and melanoblast populations are readily transformed. Profiling reveals that progenitors have higher expression of chromatin-modifying enzymes such as ATAD2, a melanoma competence factor that forms a complex with SOX10 and allows for expression of downstream oncogenic and neural crest programs. These data suggest that oncogenic competence is mediated by regulation of developmental chromatin factors, which then allow for proper response to those oncogenes.

DNA mutations are tumorigenic depending on the preexisting transcriptional programs and only in certain cellular contexts (*1*), which we refer to as oncogenic competence. In the skin, $BRAF^{V600E}$ [serine/threonine-protein kinase B-raf (BRAF) in which valine at position 600 is replaced with glutamic acid] activates a neural crest lineage program to initiate tumor formation (*2*, *3*). In particular, *crestin*, a gene that in zebrafish is specifically expressed in neural crest cells, is reactivated in melanoma-initiating cells and maintained in the tumor (*2*). The activation of neural crest lineage–specific mechanisms (*2*–*6*) together with oncogene mutations such as $BRAF^{V600E}$ are fundamental for the acquisition of a malignant state (*7*). However, it is not known why a neural crest–like state is required and particularly susceptible to oncogenic transformation by BRAF or what factors regulate this state.

[1]Center for Stem Cell Biology and Developmental Biology Program, Memorial Sloan Kettering Cancer Center, New York, NY 10065, USA. [2]Department of Cancer Biology and Genetics, Memorial Sloan Kettering Cancer Center, New York, NY 10065, USA. [3]Gerstner Graduate School of Biomedical Sciences, Memorial Sloan Kettering Cancer Center, New York, NY 10065, USA. [4]Weill Cornell/Rockefeller/Sloan-Kettering Tri-Institutional MD-PhD Program, New York, NY 10065, USA. [5]Institute for Computational Biomedicine, Weill Cornell Medical College, New York, NY 10021, USA. [6]Department of Physiology and Biophysics, Weill Cornell Medicine, 1300 York Avenue, New York, NY 10065, USA. [7]Caryl and Israel Englander Institute for Precision Medicine, Weill Cornell Medicine, New York, NY, USA. [8]Meyer Cancer Center, Weill Cornell Medicine, New York, NY, USA. [9]Department of Epidemiology and Biostatistics, Memorial Sloan Kettering Cancer Center, New York, NY 10065, USA. [10]Human Oncology and Pathogenesis Program, Memorial Sloan Kettering Cancer Center, New York, NY 10065, USA. [11]Marie-Josée and Henry R. Kravis Center for Molecular Oncology, Memorial Sloan Kettering Cancer Center, New York, NY 10065, USA. [12]Weill Cornell Graduate School of Medical Sciences, Cornell University, New York, NY 10065, USA. [13]Department of Pathology, Memorial Sloan Kettering Cancer Center, New York, NY 10065, USA [14]Joan & Sanford I. Weill Medical College of Cornell University, Cornell University, New York, NY, USA. [15]Center for Epigenetics Research, Memorial Sloan Kettering Cancer Center, New York, NY 10065, USA.
***Corresponding authors. Email: studerl@mskcc.org (L.S.); whiter@mskcc.org (R.M.W.)**
†These authors contributed equally to this work.
‡These authors contributed equally to this work.

Neural crest and melanoblasts, but not melanocytes, are oncogenically competent in zebrafish

The melanocytic lineage develops as a hierarchy of cells that starts as undifferentiated neural crest cells, proceeding through a melanoblast stage and then finally differentiating into melanocytes. To understand which cells within this lineage are most sensitive to oncogenic insult, we engineered zebrafish to initiate tumors by using stage-specific promoters to drive $BRAF^{V600E}$ in neural crest cells (*sox10* promoter), melanoblasts (*mitfa* promoter), or melanocytes (*tyrp1* promoter). Fish with p53 mutations that expressed $BRAF^{V600E}$ in either the neural crest cells or the melanoblasts developed aggressive tumors (Fig. 1, A to D, and figs. S1 and S2, A and B). However, the *tyrp1*-$BRAF^{V600E}$ $p53^{-/-}$ transgenic animals failed to develop tumors and instead developed small patches of nevus-like cells (Fig. 1, B, E, H, and K, and fig. S2C). We analyzed both the neural crest and the melanoblast-derived tumors and found that they stained equally for $BRAF^{V600E}$ and phosphorylated extracellular signal–regulated kinase (pERK) (Fig. 1, F, G, I, and J). Hematoxylin and eosin (H&E) staining showed that the neural crest and melanoblast-derived tumors were histologically distinct (fig. S2, A and B). The neural crest–derived tumors appeared undifferentiated and were predominantly positive for the neuronal markers huc/hud and ncam and sparsely for sox10 (Fig. 1, L, N, and P), reflecting the multipotency of the neural crest (fig. S2D) (*8*). By contrast, the *mitfa*-driven tumors had an appearance characteristic of typical cutaneous melanoma and stained positive for sox10 and mlana (Fig. 1, M and Q, and fig. S2F), whereas they were negative for the neuronal markers huc or hud (Fig. 1O). RNA-sequencing (RNA-seq) analysis showed that these tumors were transcriptionally distinct (Fig. 1R, fig. S2E, and table S1) and confirmed that the neural crest–derived tumors expressed neuronal genes, whereas the melanoblast-derived melanomas expressed genes related to the melanocytic lineage (fig. S2F). Gene set association analysis (GSAA) showed that neural crest–derived tumors displayed a gene signature linked to poor survival in neuroblastoma (fig. S2G) (*9*).

These data suggested that competence to respond to $BRAF^{V600E}$ is biased toward cells of origin that exhibit progenitor gene programs and that those programs allow for formation of distinct tumors. However, because melanocytes have been shown to give rise to melanoma in mouse melanoma models through the *Tyrosinase*-Cre transgene (*10*, *11*), this raised the question of whether the melanocytes in our model were entirely impervious to melanoma formation. To test this, we used CRISPR to inactivate phosphatase and tensin homolog (*pten*) in the *tyrp1*-$BRAF^{V600E}$ $p53^{-/-}$ fish and observed that 11% of animals developed melanoma (fig. S3). This indicates that both melanoblasts and melanocytes can be competent to give rise to melanoma, but that the melanoblasts do so much more readily.

An hPSC-based cancer model recapitulates the zebrafish models

To mechanistically study oncogenic competence in the precise stages along the differentiation of a melanocyte, we built a human pluripotent stem cell (hPSC)–derived cancer model. We used gene targeting in hPSCs to introduce oncogenic $BRAF^{V600E}$ and to inactivate the tumor suppressors RB1, TP53 (P53), and P16 (referred to hereafter as 3xKO cells) (Fig. 2A). These 3xKO engineered cells were then differentiated into neural crest cells, melanoblasts, and mature melanocytes (Fig. 2A and fig. S4, A and B) (*12*), and $BRAF^{V600E}$ expression was induced by doxycycline (dox) (fig. S4C), which caused comparable phosphorylation of ERK (Fig. 2B). Upon subcutaneous injection in NSG mice, we found that similar to the zebrafish, both 3xKO dox neural crest cells and melanoblasts readily formed tumors

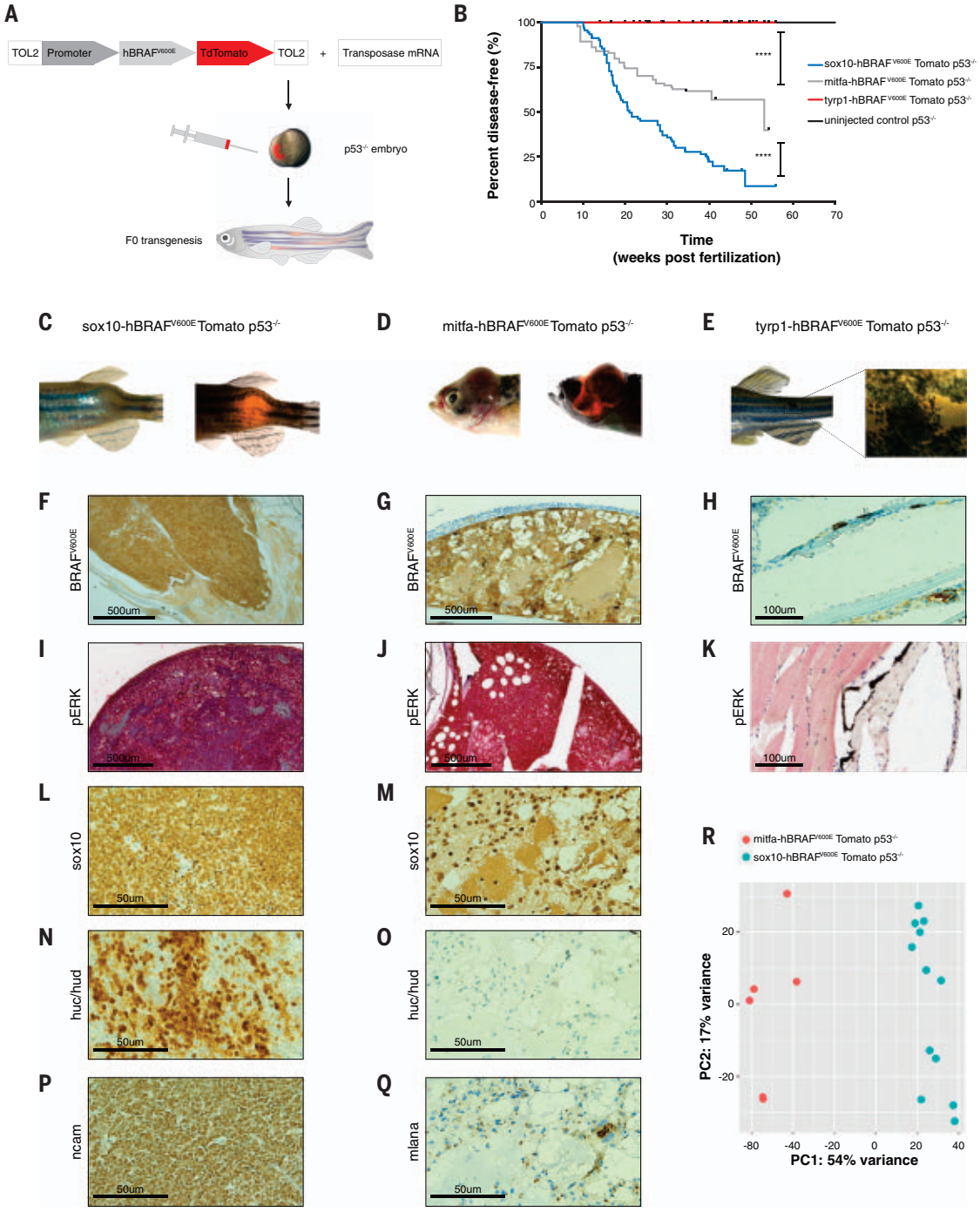


Fig. 1. Zebrafish models show that neural crest cells and melanoblasts, but not melanocytes, are cancer competent. (**A**) Schematic drawing of zebrafish F_0 transgenesis. F_0 zebrafish transgenic fish were engineered by means of injection of $p53^{-/-}$ single-cell embryos with transposase mRNA together with TOL2-flanked plasmids, which encoded a stage-specific promoter (*sox10*, *mitfa*, and *tyrp1*) driving $BRAF^{V600E}$ fused to TdTomato. (**B**) Kaplan-Meier curves of F_0 $p53^{-/-}$ transgenic zebrafish injected with plasmids driving $BRAF^{V600E}$ fused to TdTomato under either the neural crest–specific promoter *sox10* (n = 92 biological replicates), the melanoblast-specific promoter *mitfa* (n = 94 biological replicates), or the melanocyte-specific promoter *tyrp1* (n = 49 biological replicates) or uninjected control (n = 86 biological replicates). ****$P < 0.0001$ for the comparison of the tumor-free survival curves of fish with melanoblast-derived tumors and melanocyte-derived nevus-like structures; ****$P < 0.0001$ for the comparison of the tumor-free survival curves of fish with neural crest– and melanoblast-derived tumors; log-rank (Mantel-Cox) test. (**C**) Neural crest–derived tumor developed in the *sox10*-$BRAF^{V600E}$ $p53^{-/-}$ transgenic fish. (**D**) Melanoblast-derived tumor developed in the *mitfa*-$BRAF^{V600E}$ $p53^{-/-}$ transgenic fish. (**E**) Nevus-like structure developed in the *tyrp1*-$BRAF^{V600E}$ $p53^{-/-}$ transgenic fish. (**F** to **K**) Immunohistochemistry for $BRAF^{V600E}$ and pERK in the neural crest– and melanoblast-derived tumors and in the melanocyte-derived nevus-like structure. (**L** to **Q**) Immunohistochemistry staining for sox10, huc/hud, ncam, and mlana. Neural crest–derived tumors were positive for the neuronal marks huc/hud and ncam [(N) and (P)] and weakly positive for sox10 expression (L). MB-derived tumors were melanomas positive for sox10 (M), mlana (Q), and negative for the neuronal marks huc and hud (O). (**R**) Principal components analysis (PCA) plot of *mitfa*-driven tumors (n = 6, M, red) and *sox10*-driven tumors (n = 12, S, blue) for whole-genome RNA-seq shows a separation at the transcriptional level.

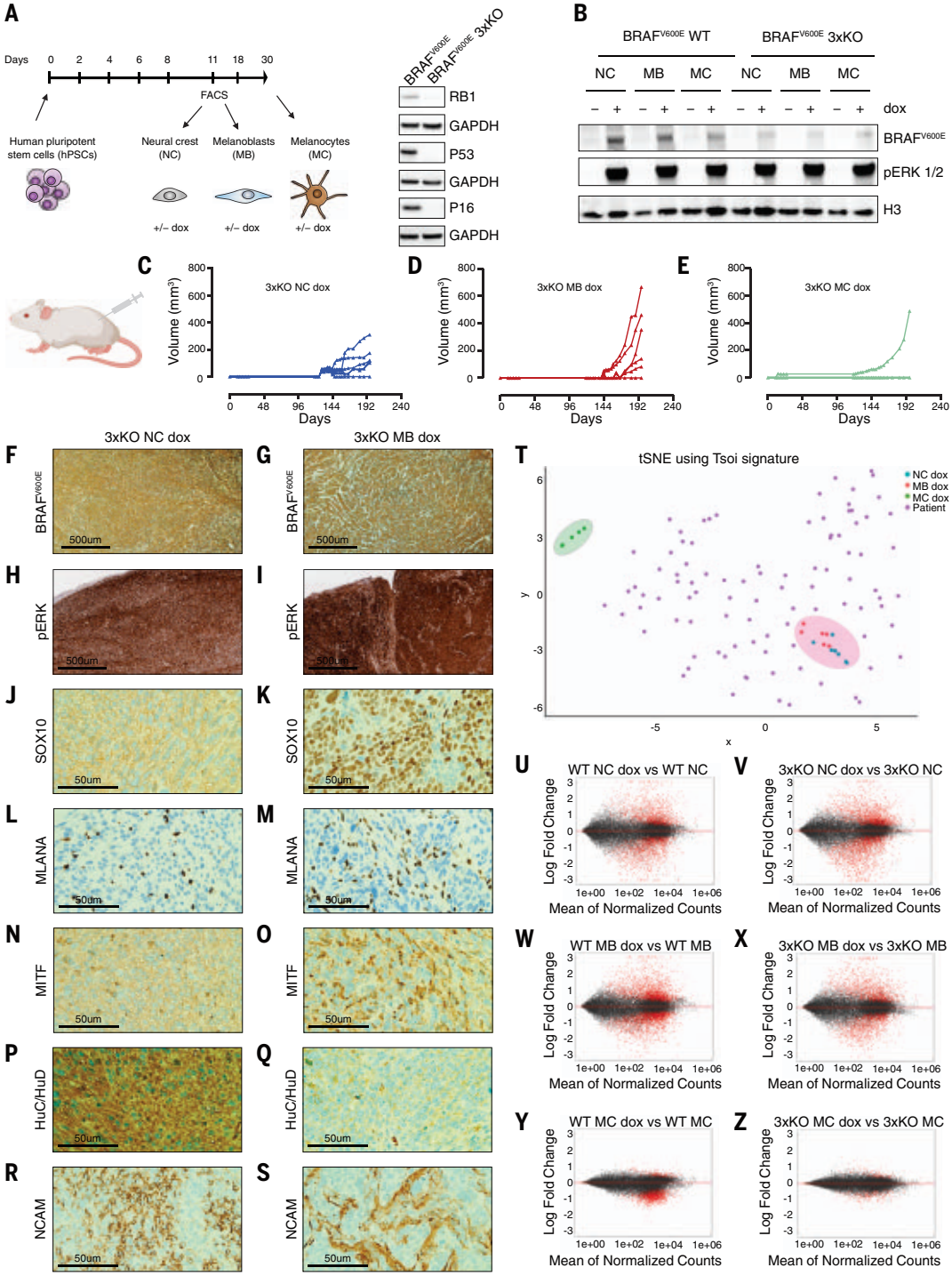


Fig. 2. A hPSC-based cancer model recapitulates the zebrafish models and demonstrates that human neural crest and melanoblast states are cancer competent, whereas the differentiated melanocyte state is not. (**A**) Schematic summary of hPSCs differentiation into neural crest cells, melanoblasts, and melanocytes and Western blot of the dox-inducible BRAF^{V600E} (iBRAF^{V600E}) hPSC line inactivation for RB1, P53, and P16 (3xKO) by using CRISPR/Cas9 technology. (**B**) Western blot of neural crest cells, melanoblasts, and melanocytes differentiated from either the iBRAF^{V600E} WT or the iBRAF^{V600E} 3xKO hPSCs. The cells were exposed to dox (1 μg/ml) for 72 hours. (**C** to **E**) In vivo growth curves of 3xKO neural crest cells + dox (n = 6 per group) (C); in vivo growth curves of 3xKO melanoblasts + dox (n = 6 per group) (D). 3xKO melanocytes + dox were not able to grow in vivo (n = 6 per group, 1 outlier) (E) but gave rise to nevus-like structures (fig. S4D). hPSCs-derived cells were injected subcutaneously in immunodeficient NSG mice exposed to a dox-containing diet. (**F** to **S**) Immunohistochemistry of neural crest–derived and melanoblast-derived tumors + dox treatment. Neural crest–derived tumors were undifferentiated and heterogeneous tumors, with strong neuronal features [(P) and (R)]. Melanoblast-derived tumors were diagnosed as melanomas and were positive for all the common melanocytic marks [(K), (M), and (O)]. (**T**) t-distributed stochastic neighbor embedding (t-SNE) of 3xKO + dox neural crest, melanoblast, and melanocyte samples and the TCGA melanoma samples by using the Tsoi signature for melanoma subtypes. (**U** to **Z**) MA plots of the RNA-seq of WT neural crest cells, melanoblasts, and melanocytes ± dox treatment and 3xKO neural crest cells, melanoblasts, and melanocytes ± dox treatment (n = 3 replicates per condition). The mean of normalized counts of each gene was plotted against the log fold change after dox-induced BRAF^{V600E} expression within that condition. Adjusted P value cut-off of 0.05 was used for significantly differentially expressed genes (red).

(Fig. 2, C and D), whereas the 3xKO dox melanocytes largely failed to do so, with only one single animal developing a tumor under this condition (Fig. 2E and fig. S4D). As a control, we also transplanted wild-type (WT) neural crest cells, melanoblasts, and melanocytes and found that these were unable to grow in vivo. Histological analysis of the neural crest– and melanoblast-derived tumors (Fig. 2, F to S, and fig. S4, E to L) showed a high level of BRAF^{V600E} and pERK expression in both (Fig. 2, F to I). Analogous to the zebrafish tumors, the hPSC-derived 3xKO dox neural crest cells gave rise to tumors that showed a strong preponderance of neuronal markers (Fig. 2, P and R). Previous work has shown that neural crest cells that differentiate into neuronal derivatives down-regulate SOX10

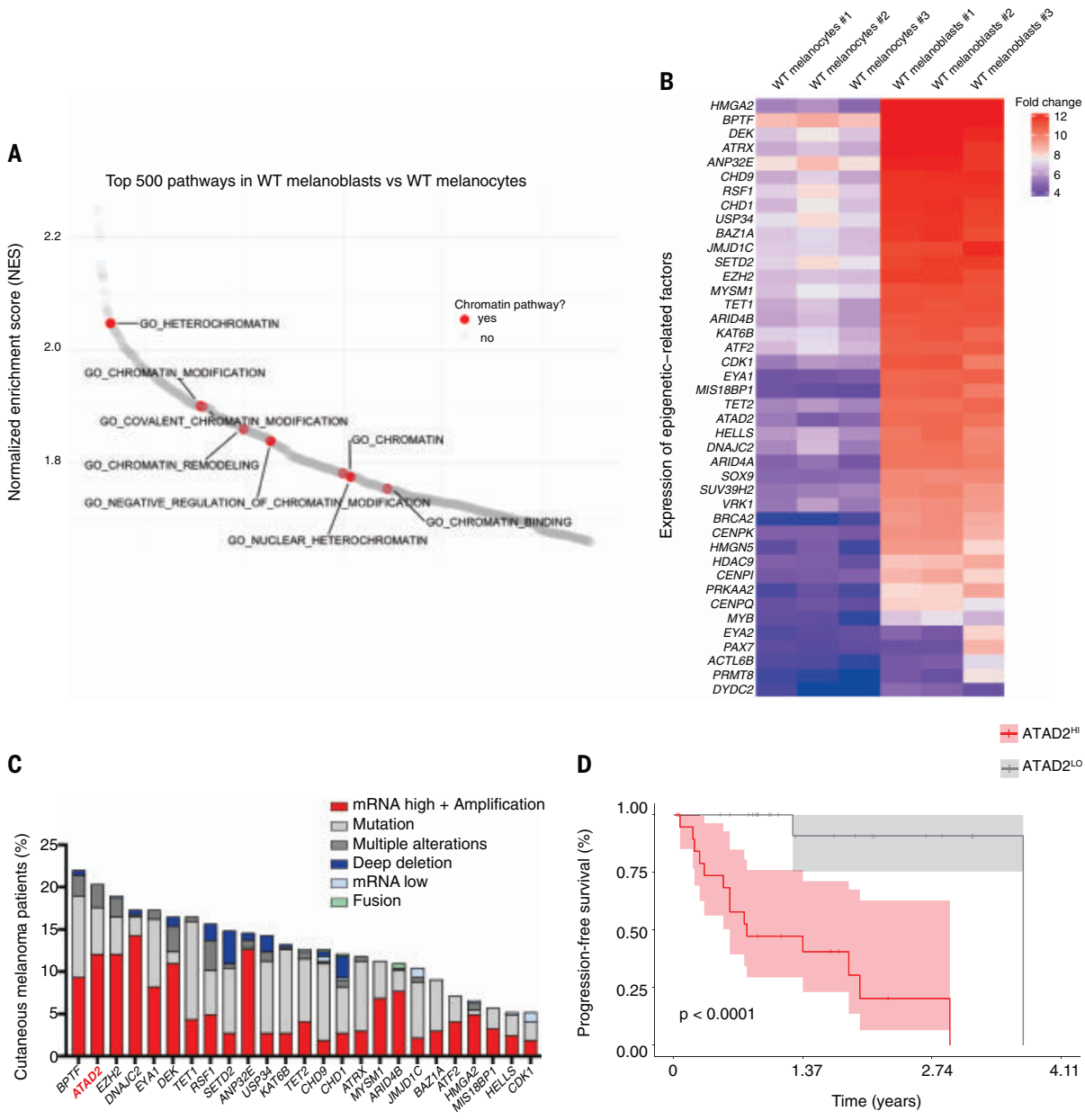


Fig. 3. Cancer competence is reflected by a distinct expression of chromatin-related genes, and ATAD2 is a key chromatin factor shared between hPSC-derived melanoblasts and patient melanoma cells. (**A**) Waterfall plot of the enriched pathways from the GSAA comparing WT melanoblasts with WT melanocytes. Chromatin-related pathways are indicated in red. (**B**) Heatmap depicting the differential expression of chromatin-related genes between WT melanoblasts and WT melanocytes. Normalized log2fold change. (**C**) Alteration frequency of the top 25 epigenetic-related factors overexpressed in WT melanoblasts in TCGA SKCM melanoma patient samples. (**D**) Kaplan-Meier overall survival curve of TCGA SKCM patients belonging either to the patients group with high levels of ATAD2 expression ($ATAD2^{HI}$) or with low expression levels ($ATAD2^{LO}$), log-rank *P* value reported.

expression (*13*), which is consistent with relatively little SOX10 being seen with immunohistochemistry at this time point. The 3xKO dox melanoblast–derived tumors were instead positive for all of the common markers of melanoma, whereas they were negative for HuC and HuD and were pathologically categorized as desmoplastic melanomas (Fig. 2, K, M, O, Q, and S). GSAA showed that neural crest cells were transcriptionally similar to the neural crest–derived tumors in the fish (fig. S5, A and B) and that melanoblasts were transcriptionally similar to the melanoblast-derived tumors in the fish (fig. S5C), which further corroborated the comparability between the two models. To ensure that our hPSC-derived tumors are relevant to human patients, we performed RNA-seq of the $BRAF^{V600E}$ 3xKO neural crest cells, melanoblasts, and melanocytes and compared their expression profiles with data from The Cancer Genome Atlas (TCGA), using a published signature for melanoma subgroups (*14*). We observed that the hPSC-derived 3xKO dox neural crest cells and 3xKO dox melanoblasts strongly clustered with the human melanoma patient samples (Fig. 2T), whereas the hPSC-derived 3xKO dox melanocytes did not. We found that the 3xKO melanoblasts, even without $BRAF^{V600E}$ induction, could form tumors in mice, indicating that loss of tumor suppressors alone gives these cells enough of a proliferative advantage to grow in this context (fig. S5D).

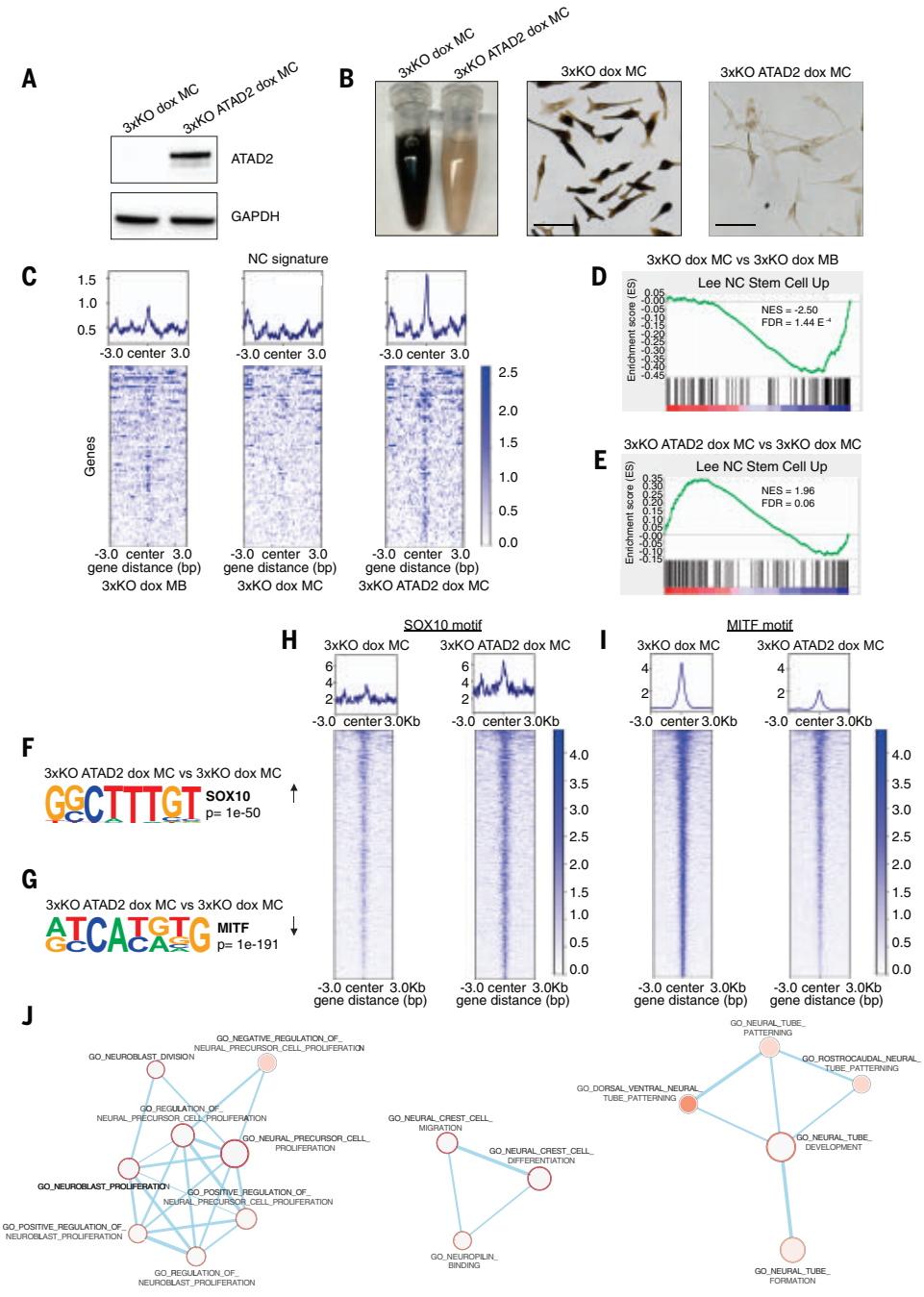


Fig. 4. ATAD2 expression in melanocytes reshapes the chromatin around neural crest and melanoblast loci and reactivates a developmental signature. (**A**) Western blot for lenti-induced ATAD2 expression in 3xKO dox melanocytes. (**B**) (Right) 3xKO dox melanocytes and (left) 3xKO ATAD2 dox melanocytes. Scale bars, 50 μm. (**C**) Tornado plots of the gene set enrichment analysis (GSEA) of the ATAC-seq showing genes belonging to Lee NC Stem Cell Up gene set in 3xKO dox melanoblasts, 3xKO dox melanocytes, and 3xKO ATAD2 dox melanocytes. (**D** and **E**) GSEA of (D) the ATAC-seq of 3xKO dox melanocytes compared with 3xKO dox melanoblasts for Lee NC Stem Cell Up [normalized enrichment score (NES) = −2.50, false discovery rate (FDR) = 1.44 E^{-4}] and (E) 3xKO ATAD2 dox melanocytes compared with 3xKO dox melanocytes for Lee NC Stem Cell Up (NES = 1.96, FDR = 0.06). (**F**) Homer motif discovery shows that the SOX10 motif is one of the most enriched motifs ($P < 1 \times 10^{-50}$) in 3xKO ATAD2 dox melanocytes compared with 3xKO dox melanocytes. (**G**) Homer motif discovery shows that the MITF motif is the most closed motif ($P < 1 \times 10^{-191}$) in 3xKO ATAD2 dox melanocytes compared with 3xKO dox melanocytes. (**H**) Tornado plots depict any dynamic ATAC peak that contains the SOX10 motif, regardless of genomic location or gene annotation. (**I**) Tornado plots depict any dynamic ATAC peak that contains the MITF motif, regardless of genomic location or gene annotation. (**J**) Network analysis of the genes with increased accessibility for the SOX10 binding motif in 3xKO ATAD2 dox melanocytes compared with 3xKO dox melanocytes.

Neural crest and melanoblasts have strong transcriptional responses to BRAF, in contrast to melanocytes

To gain insight into why these cells differed in oncogenic competence, we performed RNA-seq of neural crest cells, melanoblasts, and melanocytes ± $BRAF^{V600E}$ on both the WT and 3xKO background. We observed that dox-induced $BRAF^{V600E}$ expression caused dramatic transcriptional changes in both the neural crest cells and melanoblasts (Fig. 2, U to X, and fig. S5, A and E). By contrast, the transcriptional response to BRAF in melanocytes was nearly absent, with few genes being altered (Fig. 2, Y and Z; fig. S5, A and E; and table S2). Thus, despite equally robust activation of pERK (Fig. 2B), this indicates that the melanocyte state was refractory to eliciting a transcriptional response after oncogene activation. This raised the question of what was intrinsically different between these cell types. GSAA pathway analysis in WT melanoblasts and WT melanocytes (table S2) showed that multiple pathways related to chromatin modification were enriched in melanoblasts (Fig. 3A), and by examining individual genes, we found the enrichment of specific chromatin modifiers (Fig. 3B). This suggested that melanoblasts express epigenetic-related factors that enable rewiring of their chromatin state in response to $BRAF^{V600E}$, which renders them competent for melanoma initiation.

ATAD2 is a chromatin modifier shared between neural crest cells, melanoblasts, and melanoma cells

To identify which of these chromatin factors is likely most important in establishing competence, we analyzed the top 25 epigenetic-

related factors that are higher in melanoblasts as compared with melanocytes (Fig. 3B) and then asked which of these is most commonly amplified or overexpressed in the human melanoma TCGA cohort, which revealed BPTF (bromodomain PHD finger transcription factor), ATAD2 (ATPase family AAA domain containing 2), and EZH2 (histone methyltransferase enhancer of zeste homolog 2) at the top of this analysis (Fig. 3C). Although there are known associations between BPTF and EZH2 and melanoma (*15*, *16*), there is no information about ATAD2 in neural crest or melanoma development. ATAD2, an adenosine triphosphatase (ATPase)– and bromodomain-containing protein (*17*), is known to play roles in chromatin accessibility (*18*) and was negatively associated with survival in melanoma; patients in the highest 20% of expression had significantly worse survival as compared with the remaining patients (Fig. 3D and fig. S8A).

ATAD2 acts to reshape chromatin around key neural crest and melanoblast loci

We sought to determine whether ATAD2 was required for the establishment of a progenitor signature and subsequent tumorigenesis. We generated a lentivirus that induced ATAD2 expression in the 3xKO melanocytes (Fig. 4A) to a level comparable with what would be found in melanoblasts (fig. S6A). Although melanocytes without ATAD2 are deeply pigmented with melanin, reflecting their differentiated state, the 3xKO melanocytes expressing ATAD2 decreased their pigmentation (Fig. 4B), possibly because of dedifferentiation (*19*–*21*). To test this idea, we performed an assay for transposase-accessible chromatin with high-throughput sequencing (ATAC-seq) on 3xKO dox melanoblasts, 3xKO dox melanocytes, and 3xKO ATAD2 dox melanocytes to assess global changes in chromatin accessibility. Addition of ATAD2 to the 3xKO melanocytes did not lead to a global increase in open chromatin (fig. S6, B and C). Instead, overexpression of ATAD2 in melanocytes led to the specific increase in chromatin accessibility at neural crest–related loci (Fig. 4, C to E). To gain insight into the transcription factors that are binding to these newly opened chromatin regions, we performed HOMER (Hypergeometric Optimization of Motif Enrichment) analysis. This revealed that the top motif enriched by ATAD2 was SOX10 itself (Fig. 4, F and H), suggesting that ATAD2 was specifically allowing SOX10 to bind to its target genes. Analogously, we also asked which peaks became closed after expression of ATAD2 and found that these were most highly enriched for the MITF (melanocyte inducing transcription factor) motif (Fig. 4, G and I). Network analysis of the loci most affected by ATAD2 and that carried the SOX10 motif confirmed a strong enrichment for pathways associated with neural precursor proliferation and neural crest migration (Fig. 4J).

ATAD2 is necessary for neural crest induction

Because SOX10 is essential for proper neural crest induction, these data suggested that loss of ATAD2 might impair proper neural crest formation. To test this, we used an inducible Cas9 system (*22*) to inactivate ATAD2 during the differentiation of hPSCs into neural crest cells (fig. S7). We measured the percentage of neural crest cells and found ~50% reduction in neural crest formation upon loss of ATAD2 (fig. S7D). Overall, these data are consistent with the notion that ATAD2 facilitates access to an early neural crest state.

ATAD2 forms a complex with SOX10 and c-Myc, allowing for expression of neural crest genes and MAPK-related genes

Previous work has shown that ATAD2 is able to build a protein complex with Myc and in this way regulate a Myc-dependent signature in cancer (*23*). We hypothesized that ATAD2 might be acting in a similar way with SOX10, by directly binding to it and facilitating transcription of its target genes. In support of this idea, we analyzed genes differentially expressed in the $ATAD2^{HI}$ and $ATAD2^{LO}$ patients from the TCGA cohort (Fig. 5A and fig. S8A). Pathway analysis revealed a strong Myc signature in the $ATAD2^{HI}$ patients (Fig. 5, A and B, and fig. S8B), and motif analysis showed enrichment of the SOX motif (Fig. 5C). We confirmed with co-immunoprecipitation (co-IP) that ATAD2 forms a complex with Myc in the 3xKO ATAD2 dox melanocytes and found that it also does so with SOX10 (Fig. 5, D and E, and fig. S8C). On the basis of these findings, we hypothesized that ATAD2 might play a dual role and facilitate the expression of target genes of both Myc and SOX10 transcription factors. To test this, we performed CUT&RUN for ATAD2, SOX10, and Myc in the 3xKO ATAD2 dox melanocytes, comparing it with binding in the control 3xKO dox melanocytes. We created tornado plots to look at the overlap between these factors and revealed co-binding, in which ATAD2 and SOX10 co-bound 43.4% of the ATAD2 target genes (Fig. 5F), ATAD2 and Myc co-bound 6.4%, and 4.0% were co-bound by all three factors (Fig. 5G). To further confirm which of these genes are likely transcriptional targets of these complexes, we next performed RNA-seq of the 3xKO ATAD2 dox melanocytes compared with the control 3xKO dox melanocytes (Fig. 5H and table S3). We found significant enrichment for neural crest–related genes (*MEIS2*, *CDH2*, and *CDH11*) (*24*) that were co-bound by ATAD2 and SOX10 or co-bound by ATAD2, SOX10, or Myc and up-regulated in the RNA-seq dataset (Fig. 5, I, K, and L). Furthermore, we also discovered a significant up-regulation and binding of regulators of the mitogen-activated protein kinase (MAPK) pathway, including key upstream regulators [epidermal growth factor receptor (EGFR) and fibroblast growth factor receptor 2 (FGFR2)] (Fig. 5, J and L) and key downstream regulators of MAPK, including Myc target genes (*RPS6KA6*, *JUN*, and *E2F*) (Fig. 5L and fig S6D). Recent work has demonstrated that up-regulation of EGFR and FGF, which we found is facilitated by ATAD2, are key mechanisms of MAPK pathway activation in $BRAF^{V600E}$ mutant melanoma, especially in the setting of drug resistance (*25*, *26*). In the 3xKO ATAD2 dox melanocytes, it is possible that this increase in EGFR and FGF explains the increased phosphorylation of ERK1 and -2 (fig. S8E), and future studies will be required to investigate the potential link between ATAD2 expression, ERK activation, and EGFR and FGF in this context. Overall, our data indicate that ATAD2 directly binds to both SOX10 and Myc, facilitates the expression of their target genes, and leads to increased activity of two major tumorigenic mechanisms in melanoma: a neural crest lineage program and MAPK pathway activity.

ATAD2 promotes melanoma phenotypes

EdU incorporation assays showed that 3xKO ATAD2 ± dox melanocytes had a proliferation rate comparable with that of 3xKO dox melanoblasts and that they were significantly more proliferative than 3xKO dox melanocytes (fig. S8F). Both proliferation rates in 3xKO neural crest cells and melanoblasts increased upon $BRAF^{V600E}$ expression, whereas in the already highly proliferative 3xKO ATAD2 dox melanocytes, they did not. In vitro 3xKO melanocytes were not entering a senescent state upon $BRAF^{V600E}$ expression, and their proliferation rate did not change. 3xKO ATAD2 ± dox melanocytes were also more invasive, as measured with the invasion chamber analysis (fig. S9, A and B) and as supported by ATAC-seq gene signatures consistent with an epithelial-to-mesenchymal (EMT) program (fig. S9, C and D). We also assessed the metabolic profile of these hPSC-derived tumor lines and found evidence of substantial metabolic rewiring. We used Seahorse assays to measure mitochondrial bioenergetics and glycolysis by means of oxygen consumption rate (OCR) and the extracellular acidification rate (ECAR). The ratio between OCR and ECAR showed that 3xKO melanoblasts were mostly relying on glycolysis for energy production and that this trend was amplified by dox-induced oncogene expression (fig. S10A) (*27*). On the contrary, 3xKO melanocytes displayed a profoundly different metabolic profile, with sustained oxidative metabolism. Upon ATAD2 expression, the 3xKO ATAD2 dox melanocytes switched to a more glycolytic state, as evidenced by an increased ECAR/OCR ratio (fig. S10).

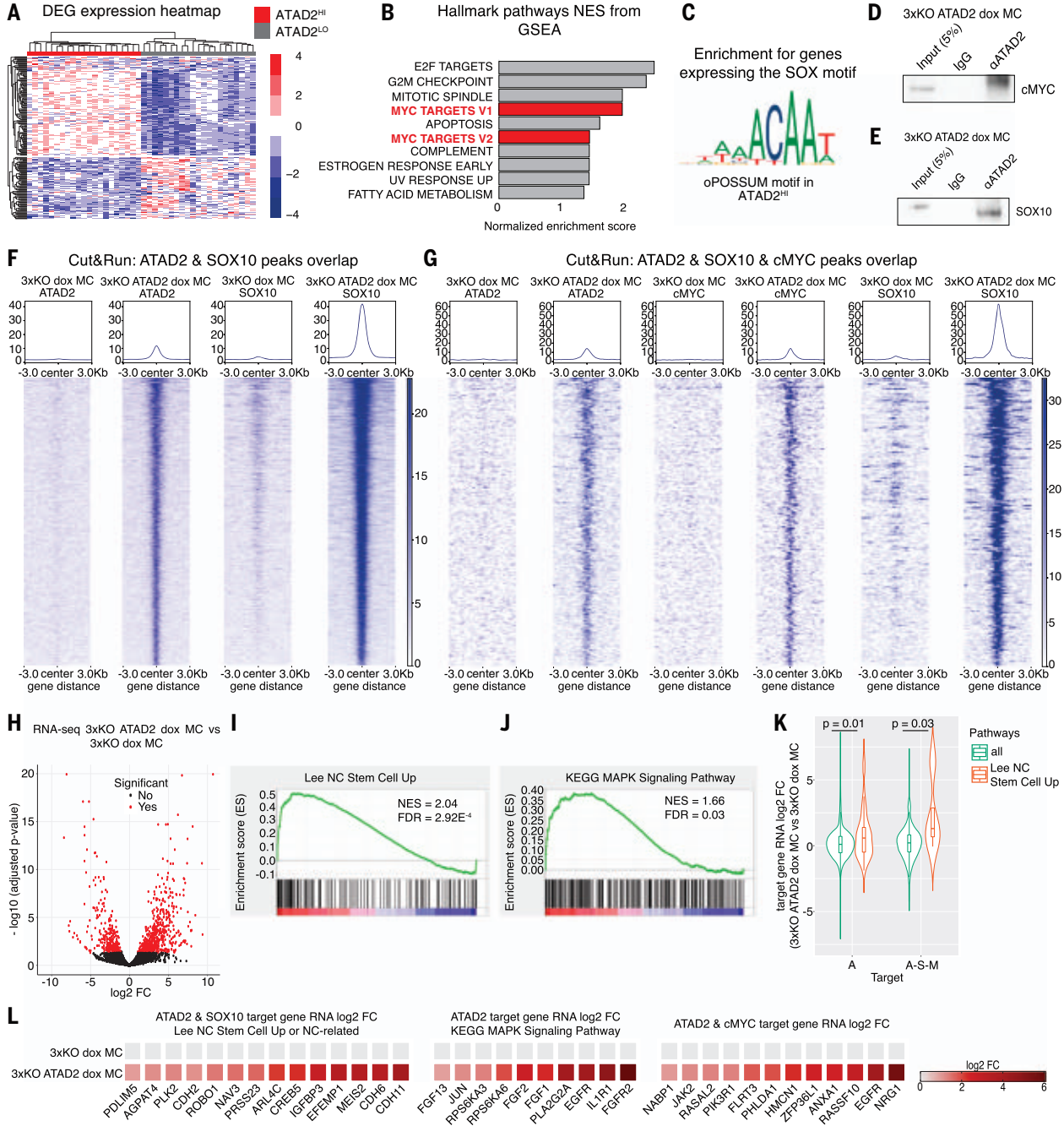


Fig. 5. ATAD2 promotes melanoma phenotypes through c-Myc and SOX10 in both clinical samples of cutaneous melanoma and in the hPSC-derived cancer model. (**A**) Heatmap plot of differentially expressed genes (DEGs) in the ATAD2^{HI} patient group versus the ATAD2^{LO} patient group. (**B**) Top 10 hallmark pathways from GSEA enriched in the ATAD2^{HI} patient group compared with the ATAD2^{LO} patient group. (**C**) Identification of the SOX binding motif on genes coexpressed in the ATAD2^{HI} patient groups, determined by means of analysis with the oPOSSUM software tool. (**D** and **E**) Co-IP analysis of protein lysates of 3xKO ATAD2 dox melanocytes by using either the ATAD2 or the control immunoglobulin G (IgG) antibody and then blotted against (D) c-Myc and (E) SOX10. (**F**) Tornado plots depict the Cut&Run peaks overlapping between ATAD2 and SOX10 in 3xKO dox melanocytes and 3xKO ATAD2 dox melanocytes. (**G**) Tornado plots depict the Cut&Run peaks overlapping between ATAD2, c-Myc, and SOX10 in 3xKO dox melanocytes and 3xKO ATAD2 dox melanocytes. (**H**) Volcano plot of the RNA-seq depicts the distribution of the transcriptional differences between 3xKO ATAD2 dox melanocytes over 3xKO dox melanocytes. (**I** and **J**) GSEA of the RNA-seq of 3xKO ATAD2 dox melanocytes compared with 3xKO dox melanocytes for (I) Lee NC Stem Cell Up (NES = 2.04, FDR = 2.92×10^{-4}) and (J)Kyoto Encyclopedia of Genes and Genomes (KEGG) MAPK Signaling Pathway (NES = 1.66, FDR = 0.03). (**K**) Violin plots showing the distribution of Cut&Run target genes that are also significantly up-regulated in the RNA-seq dataset. Genes bound by ATAD2 are enriched for RNA up-regulation of the Lee NC Stem Cell signature (left, Mann-Whitney U test, $P = 0.01$), as are genes cobound by ATAD2/SOX10/c-Myc (right, Mann-Whitney U test, $P = 0.03$). (**L**) Heatmap depicting expression changes of the ATAD2 and SOX10 co-bound Cut&Run target genes belonging to the Lee NC Stem Cell Up gene set (left). Heatmap depicting expression changes of the ATAD2 Cut&Run target genes belonging to the KEGG MAPK Signaling Pathway (middle). Heatmap depicting expression changes of selected ATAD2 and c-Myc co-bound Cut&Run target genes (right).

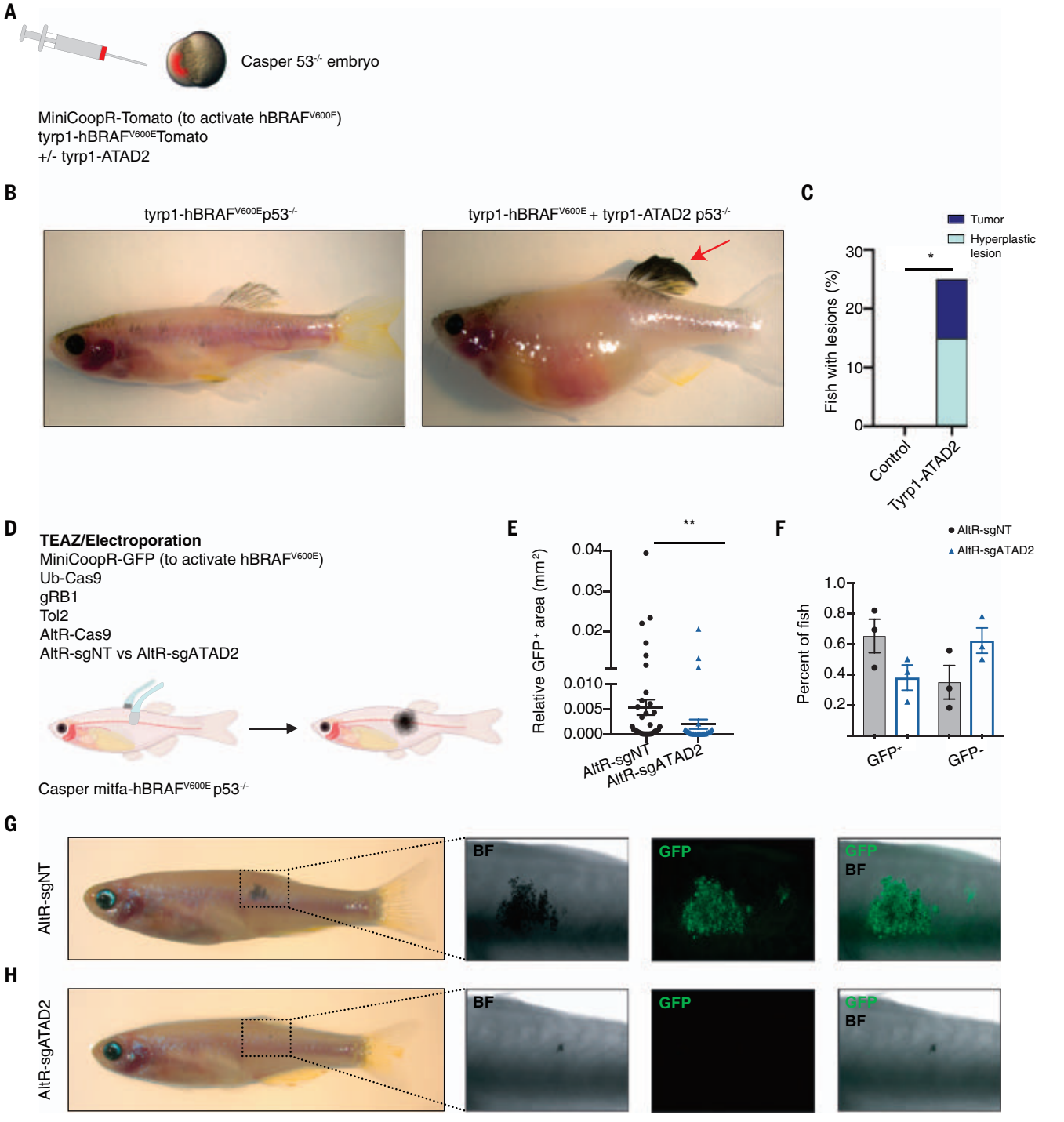


Fig. 6. ATAD2 is necessary and sufficient for melanoma initiation. (**A**) p53$^{-/-}$;casper single-cell embryos were injected with a plasmid that encoded the melanocyte-specific promoter *tyrp1* driving BRAF^{V600E} ± a plasmid that encoded *tyrp1* driving ATAD2, along with a MiniCoopR-tdTomato plasmid to rescue melanocytes in the casper background. (**B**) (Left) Transgenic control fish with *tyrp1* driving BRAF^{V600E} and (right) a transgenic fish expressing *tyrp1* driving both BRAF^{V600E} and ATAD2, which developed a pigmented tumor. (**C**) Percentage of fish that developed melanoma with the *tyrp1* driving BRAF^{V600E} ± ATAD2. Control fish expressing *tyrp1*-BRAF^{V600E} did not develop tumors (n = 0 of 23 fish), whereas fish expressing *tyrp1* driving BRAF^{V600E} + ATAD2 developed melanomas (n = 2 of 20 fish) and hyperplastic lesions (n = 3 of 20 fish). Fisher's exact test, *P < 0.05. (**D**) Schematic drawing for the TEAZ-electroporation experiment. Fish that were p53$^{-/-}$, casper;*mitfa*-BRAF^{V600E} were electroporated with MiniCoopR-GFP (*mitfa*-MITF and *mitfa*-GFP), Ub-Cas9, gRB1, Tol2, AltR-Cas9, and either AltR-sgNT or a pool of AltR-sgATAD2. The fish were then monitored and quantified for melanoma initiation. (**E**) Quantification of the GFP$^+$ area (square millimeters) in the transgenic fish 2 weeks after electroporation. Mann-Whitney test with **P = 0.01. (**F**) Percentage of fish that were either GFP$^+$ or GFP$^-$ depending on the electroporation of AltR-sgNT or AltR-sgATAD2. (**G**) Transgenic fish electroporated with AltR-sgNT, 4 weeks after electroporation. The images depict early lesions characterized by pigmentation and GFP expression. (**H**) Transgenic fish electroporated with AltR-sgATAD2, 4 weeks after electroporation.

ATAD2 endows melanocytes with oncogenic competence in vivo

To test whether ATAD2 was sufficient for melanoma initiation, we created transgenic zebrafish (Fig. 6A) in which we could overexpress $BRAF^{V600E}$ ± ATAD2 in the melanocytes using the *tyrp1* promoter, a cell type that we showed above (Fig. 1B) is refractory to develop melanoma. In the casper background (*28*) with rescued melanocytes, none of the *tyrp1*-$BRAF^{V600E}$ $p53^{-/-}$ animals developed hyperplasia or melanoma (0%, n = 0 of 23). By contrast, we found that 10% (n = 2 of 20) of *tyrp1*-$BRAF^{V600E}$ *tyrp1*-ATAD2 $p53^{-/-}$ animals developed melanomas and 15% (n = 3 of 20) developed hyperplastic lesions (Fig. 6, B and C, and fig. S11). Conversely, we next wanted to test whether loss of ATAD2 would prevent melanoma initiation. Using the electroporation-based TEAZ (transgene electroporation in adult zebrafish) approach (*29*) with nontargeting single-guide RNAs (sgRNAs), 65% of the fish developed a patch of green fluorescent protein–positive (GFP^+) melanocytes (Fig. 6, D to G), easily discernible from the surrounding normal skin. By contrast, in the animals that were electroporated with sgRNAs against ATAD2, we found that the majority was negative for any GFP (Fig. 6, E, F and H), and the quantification of the GFP^+ area revealed a significant decrease in overall tumor size in the ATAD2-deleted fish compared with the control fish (Fig. 6E). We further tested the role of ATAD2 in the context of PTEN deletion using the MASERATI vector (fig. S12A) (*30*), in which patches seen at 14 days gave rise to fully penetrant melanomas in 78.6% of animals by day 84 (fig. S12, B to H). Similar to the results above, ATAD2 sgRNA led to a significant reduction in melanoma size at day 14 (fig. S12I). Analogous to the CRISPR deletion of SOX10 (*2*), over time we observed selection for WT or in-frame ATAD2 clones (fig. S12, J and K). Taken together, our data support a model in which high levels of ATAD2 expression, which is found in neural crest cells and melanoblasts, allows for reexpression of a progenitor signature in melanocytes and supports the ability of BRAF to initiate tumors (fig. S13).

Discussion

These data show that the ability of a cell to respond to $BRAF^{V600E}$ depends on the preexisting transcriptional state of that cell. We found that both the neural crest and the melanoblast stages are able to respond to $BRAF^{V600E}$, and that ATAD2 is an oncogenic competence factor required for melanoma initiation in melanocytes.

One difference between our observations and data from using genetically engineered mouse models is that we found mature melanocytes (both zebrafish and hPSC-derived) to be relatively resistant to oncogenesis, although not impervious. The most commonly available mouse models of melanoma use a *tyrosinase*-Cre driver to activate $BRAF^{V600E}$ in combination with loss of various tumor suppressors (*10*, *11*). These animals can develop melanoma, although this can be accelerated through inactivation of tumor suppressors such as CDKN2A, TP53, or PTEN (*31*). Which cells within these mice act as the melanoma cell of origin has not been fully resolved (*32*–*34*), but our studies are not precisely comparable with the mouse studies because our zebrafish use *tyrp1*-driven $BRAF^{V600E}$. One possible explanation for this discrepancy is that in our system, the *tyrp1* promoter is actually driving expression in a more fully differentiated melanocyte compared with the *tyr* promoter used in mouse studies. Another explanation is that these differences may reflect different biological thresholds for tumorigenesis, in that a different number of DNA lesions may be required to transform melanocytes in human versus mice versus zebrafish.

We found that melanocytes can eventually be induced into melanoma formation with additional hits such as PTEN inactivation, albeit still much less efficiently than the melanoblasts. Given that melanocytes are likely more numerically frequent in patient skin compared with melanoblasts or neural crest–like cells, it is possible that these cells may serve as a cell of origin, but that they would need more genetic lesions compared with melanoblast-like cells.

Our study does not rule out other possible mechanisms that could regulate the response to pro-oncogenic signals, such as the timing or the specific order of acquiring mutations. Another aspect of oncogenic competence might be the particular microenvironment in which each of these cells reside. Previous studies have in fact suggested that microenvironmental cues might influence the ability of a cell to transform (*32*, *33*). It would be important to investigate how oncogenic competence might be modulated in each potential cell of origin depending on the local microenvironment.

Our data suggest a model in which there may not be a discrete cell of origin of melanoma. Instead, multiple cells along the spectrum from neural crest– and melanoblast-like cells to melanocytes may be competent to give rise to tumors (fig. S13). This competence appears dependent on three interrelated factors that cooperate to determine susceptibility: DNA mutations (such as $BRAF^{V600E}$, $p53^{-/-}$, $CDKN2A^{-/-}$, and $PTEN^{-/-}$); cell type–specific transcription factors (such as SOX10 and MITF); and the inherent levels of developmental chromatin modifiers, which allow for a permissive chromatin landscape (such as ATAD2).

Materials and methods summary

Zebrafish transgenesis

Zebrafish lines used in these studies includes the WT (AB), casper ($mitfa^{-/-}$;$mpv17^{-/-}$), *sox10*-$BRAF^{V600E}$ $p53^{-/-}$, *mitfa*-$BRAF^{V600E}$ $p53^{-/-}$, and *tyrp1*-$BRAF^{V600E}$ $p53^{-/-}$ lines. For TEAZ-based transgenics, the plasmids were electroporated directly into the skin of adult animals, as previously described (*29*).

hPSCs engineering and differentiation

To derive neural crest cells and melanoblasts, hPSCs were plated at day −1 on matrigel-coated dishes in E8 medium and 10 μM ROCKi. From day 0 to day 2, cells were cultured in E6 medium with 1 ng/ml BMP4, 10 μM SB, and 600 nM CHIR. From day 2 to day 4, cells were cultured in E6 medium with 10 μM SB + 1.5 μM CHIR. From day 4 to day 6, cells were cultured in E6 medium with 1.5 μM CHIR. From day 6 to day 11, cells were cultured in E6 medium with 1.5 μM CHIR, 5 ng/ml BMP4, and 100 nM EDN3. Cells were fluorescence-activated cell–sorted for cKIT and P75 expression, and double-positive cells were further differentiated into melanocytes by using melanocytes medium.

Detailed materials and methods are available in the supplementary materials.

REFERENCES AND NOTES

1. K. M. Haigis, K. Cichowski, S. J. Elledge, Tissue-specificity in cancer: The rule, not the exception. *Science* **363**, 1150–1151 (2019). doi: 10.1126/science.aaw3472; pmid: 30872507
2. C. K. Kaufman *et al*., A zebrafish melanoma model reveals emergence of neural crest identity during melanoma initiation. *Science* **351**, aad2197 (2016). doi: 10.1126/science.aad2197; pmid: 26823433
3. R. M. White *et al*., DHODH modulates transcriptional elongation in the neural crest and melanoma. *Nature* **471**, 518–522 (2011). doi: 10.1038/nature09882; pmid: 21430780
4. S. Varum *et al*., Yin Yang 1 orchestrates a metabolic program required for both neural crest development and melanoma formation. *Cell Stem Cell* **24**, 637–653.e9 (2019). doi: 10.1016/j.stem.2019.03.011; pmid: 30951662
5. M. V. Heppt *et al*., MSX1-induced neural crest-like reprogramming promotes melanoma progression. *J. Invest. Dermatol.* **138**, 141–149 (2018). doi: 10.1016/j.jid.2017.05.038; pmid: 28927893
6. O. Shakhova *et al*., Sox10 promotes the formation and maintenance of giant congenital naevi and melanoma. *Nat. Cell Biol.* **14**, 882–890 (2012). doi: 10.1038/ncb2535; pmid: 22772081
7. M. Kunz, Oncogenes in melanoma: An update. *Eur. J. Cell Biol.* **93**, 1–10 (2014). doi: 10.1016/j.ejcb.2013.12.002; pmid: 24468268
8. M. Bronner-Fraser, S. E. Fraser, Cell lineage analysis reveals multipotency of some avian neural crest cells. *Nature* **335**, 161–164 (1988). doi: 10.1038/335161a0; pmid: 2457813
9. S. Asgharzadeh *et al*., Prognostic significance of gene expression profiles of metastatic neuroblastomas lacking MYCN gene amplification. *J. Natl. Cancer Inst.* **98**, 1193–1203 (2006). doi: 10.1093/jnci/djj330; pmid: 16954472
10. D. Dankort *et al*., Braf(V600E) cooperates with Pten loss to induce metastatic melanoma. *Nat. Genet.* **41**, 544–552 (2009). doi: 10.1038/ng.356; pmid: 19282848
11. N. Dhomen *et al*., Oncogenic Braf induces melanocyte senescence and melanoma in mice. *Cancer Cell* **15**, 294–303 (2009). doi: 10.1016/j.ccr.2009.02.022; pmid: 19345328
12. Y. Mica, G. Lee, S. M. Chambers, M. J. Tomishima, L. Studer, Modeling neural crest induction, melanocyte specification, and disease-related pigmentation defects in hESCs and patient-specific iPSCs. *Cell Rep.* **3**, 1140–1152 (2013). doi: 10.1016/j.celrep.2013.03.025; pmid: 23583175
13. J. Kim, L. Lo, E. Dormand, D. J. Anderson, SOX10 maintains multipotency and inhibits neuronal differentiation of neural crest stem cells. *Neuron* **38**, 17–31 (2003). doi: 10.1016/S0896-6273(03)00163-6; pmid: 12691661
14. J. Tsoi *et al*., Multi-stage differentiation defines melanoma subtypes with differential vulnerability to drug-induced iron-dependent oxidative stress. *Cancer Cell* **33**, 890–904.e5 (2018). doi: 10.1016/j.ccell.2018.03.017; pmid: 29657129

15. A. A. Dar *et al*., The role of BPTF in melanoma progression and in response to BRAF-targeted therapy. *J. Natl. Cancer Inst.* **107**, djv034 (2015). doi: 10.1093/jnci/djv034; pmid: 25713167
16. D. Zingg *et al*., The epigenetic modifier EZH2 controls melanoma growth and metastasis through silencing of distinct tumour suppressors. *Nat. Commun.* **6**, 6051 (2015). doi: 10.1038/ncomms7051; pmid: 25609585
17. F. Boussouar, M. Jamshidikia, Y. Morozumi, S. Rousseaux, S. Khochbin, Malignant genome reprogramming by ATAD2. *Biochim. Biophys. Acta* **1829**, 1010–1014 (2013). doi: 10.1016/j.bbagrm.2013.06.003; pmid: 23831842
18. Y. Morozumi *et al*., Atad2 is a generalist facilitator of chromatin dynamics in embryonic stem cells. *J. Mol. Cell Biol.* **8**, 349–362 (2016). doi: 10.1093/jmcb/mjv060; pmid: 26459632
19. K. S. Hoek *et al*., In vivo switching of human melanoma cells between proliferative and invasive states. *Cancer Res.* **68**, 650–656 (2008). doi: 10.1158/0008-5472.CAN-07-2491; pmid: 18245463
20. D. J. Konieczkowski *et al*., A melanoma cell state distinction influences sensitivity to MAPK pathway inhibitors. *Cancer Discov.* **4**, 816–827 (2014). doi: 10.1158/2159-8290.CD-13-0424; pmid: 24771846
21. J. Müller *et al*., Low MITF/AXL ratio predicts early resistance to multiple targeted drugs in melanoma. *Nat. Commun.* **5**, 5712 (2014). doi: 10.1038/ncomms6712; pmid: 25502142
22. F. González *et al*., An iCRISPR platform for rapid, multiplexable, and inducible genome editing in human pluripotent stem cells. *Cell Stem Cell* **15**, 215–226 (2014). doi: 10.1016/j.stem.2014.05.018; pmid: 24931489
23. M. Ciró *et al*., ATAD2 is a novel cofactor for MYC, overexpressed and amplified in aggressive tumors. *Cancer Res.* **69**, 8491–8498 (2009). doi: 10.1158/0008-5472.CAN-09-2131; pmid: 19843847
24. R. M. Williams *et al*., Reconstruction of the global neural crest gene regulatory network in vivo. *Dev. Cell* **51**, 255–276.e7 (2019). doi: 10.1016/j.devcel.2019.10.003; pmid: 31639368
25. C. Sun *et al*., Reversible and adaptive resistance to BRAF (V600E) inhibition in melanoma. *Nature* **508**, 118–122 (2014). doi: 10.1038/nature13121; pmid: 24670642
26. V. E. Wang *et al*., Adaptive resistance to dual BRAF/MEK inhibition in BRAF-driven tumors through autocrine FGFR pathway activation. *Clin. Cancer Res.* **25**, 7202–7217 (2019). doi: 10.1158/1078-0432.CCR-18-2779; pmid: 31515463
27. A. Hall *et al*., Dysfunctional oxidative phosphorylation makes malignant melanoma cells addicted to glycolysis driven by the (V600E)BRAF oncogene. *Oncotarget* **4**, 584–599 (2013). doi: 10.18632/oncotarget.965; pmid: 23603840
28. R. M. White *et al*., Transparent adult zebrafish as a tool for in vivo transplantation analysis. *Cell Stem Cell* **2**, 183–189 (2008). doi: 10.1016/j.stem.2007.11.002; pmid: 18371439
29. S. J. Callahan *et al*., Cancer modeling by Transgene Electroporation in Adult Zebrafish (TEAZ). *Dis. Model. Mech.* **11**, dmm.034561 (2018). doi: 10.1242/dmm.034561; pmid: 30061297
30. J. Ablain, E. M. Durand, S. Yang, Y. Zhou, L. I. Zon, A CRISPR/Cas9 vector system for tissue-specific gene disruption in zebrafish. *Dev. Cell* **32**, 756–764 (2015). doi: 10.1016/j.devcel.2015.01.032; pmid: 25752963
31. E. Pérez-Guijarro, C. P. Day, G. Merlino, M. R. Zaidi, Genetically engineered mouse models of melanoma. *Cancer* **123** (S11), 2089–2103 (2017). doi: 10.1002/cncr.30684; pmid: 28543694
32. C. Köhler *et al*., Mouse cutaneous melanoma induced by mutant BRaf arises from expansion and dedifferentiation of mature pigmented melanocytes. *Cell Stem Cell* **21**, 679–693.e6 (2017). doi: 10.1016/j.stem.2017.08.003; pmid: 29033351
33. H. Moon *et al*., Melanocyte stem cell activation and translocation initiate cutaneous melanoma in response to UV exposure. *Cell Stem Cell* **21**, 665–678.e6 (2017). doi: 10.1016/j.stem.2017.09.001; pmid: 29033353
34. Q. Sun *et al*., A novel mouse model demonstrates that oncogenic melanocyte stem cells engender melanoma resembling human disease. *Nat. Commun.* **10**, 5023 (2019). doi: 10.1038/s41467-019-12733-1; pmid: 31685822

ACKNOWLEDGMENTS

We thank J. Ablain for the MASERATI vector. Figures 2 and 6 and fig. S12 contain images created with BioRender. **Funding:** This work was supported by awards from the Melanoma Research Alliance (to R.M.W. and L.S.); NIH Research Program Grant R01CA229215, NIH Director's New Innovator Award DP2CA186572, NIH Mentored Clinical Scientist Research Career Development Award K08AR055368, The Pershing Square Sohn Foundation, The Alan and Sandra Gerry Metastasis Research Initiative at the Memorial Sloan Kettering Cancer Center, The Harry J. Lloyd Foundation, Consano, and the Starr Cancer Consortium (to R.M.W.); NYSTEM award DOH01-STEM5-2016-00300 and the Starr Stem cell initiative (to L.S.); Kirschstein-NRSA predoctoral fellowship F31CA196305, Joanna M. Nicolay Melanoma Foundation Research Scholar Award, and the Robert B. Catell Fellowship (to S.J.C.); Kirschstein-NRSA predoctoral fellowship F30CA220954, Melanoma Research Foundation, and Medical Scientist Training Program T32GM007739 (to N.R.C.); NRSA (F32) 5F32MH116590-02 (to R.M.W.); Frank Lappin Horsfall, Jr. Fellowship (to Y.F.); Kirschstein-NRSA predoctoral fellowship F30CA236442, Molecular and Cell Biology Teaching Grant T32GM008539, and Medical Scientist Training Program T32GM007739 (to J.M.W.); Individual Predoctoral to Postdoctoral Fellow Transition Award (F99/K00) 5K00CA223016-04 (to E.M.); the Swiss National Science Foundation Postdoc.mobility fellowship P2ZHP3_171967 and P400PB_180672 (to A.B.); and P30 CA008748 (NCI Core Facility Grant). **Author contributions:** A.B., S.J.C., L.S., and R.M.W. developed the experiments and interpreted results. A.B. and S.J.C. performed most experiments and collected and analyzed data. E.M., J.M.W., M.M.T., S.S., and S.C.P. performed zebrafish-related experiments. T.T. and E.K. performed computational analyses. S.E.T. and B.S.T. performed TCGA-related analyses. N.R.C. and M.V.H. performed computational analyses. M.M.T. performed the ATAC-seq experiment. R.M.W., Y.F., and N.S. assisted with hPSCs-related experiments. T.S.-V., T.-H.H., and Y.M. assisted with zebrafish-related experiments. T.H. and S.K.T. assisted with the pathology analyses. R.P.K. performed computational analysis and assisted with the interpretation of the results. A.B., L.S., and R.M.W. wrote the manuscript. L.S. and R.M.W. acquired funding for the project. All authors read and edited the manuscript. **Competing interests:** L.S. is cofounder and consultant of BlueRock Therapeutics and is listed as inventor on a patent application by Memorial Sloan Kettering Cancer Center related to melanocyte differentiation from human pluripotent stem cells (WO2011149762A2). R.M.W. is a consultant to N-of-One, a subsidiary of Qiagen. All other authors declare no competing interests. **Data and materials availability:** Datasets are deposited at Gene Expression Omnibus (GEO) (RNA-seq, ATAC-seq, and Cut&Run): GSE172069. All zebrafish lines are available upon request from the authors or from the ZIRC zebrafish stock center (https://zebrafish.org/home/guide.php). WA-09 lines (NC, MB, MC, 3xKO NC, 3xKO MB, and 3xKO MC) will be made available upon request from the Studer laboratory at Memorial Sloan Kettering Cancer Center under a materials transfer agreement with the institute.

SUPPLEMENTARY MATERIALS

science.sciencemag.org/content/373/6559/eabc1048/suppl/DC1
Materials and Methods
Figs. S1 to S13
Tables S1 to S4
References (*35*–*62*)

6 April 2020; resubmitted 11 November 2020
Accepted 14 July 2021
10.1126/science.abc1048

RESEARCH ARTICLES

QUANTUM PHYSICS

Vortex beams of atoms and molecules

Alon Luski[1]†, Yair Segev[1]†‡, Rea David[1], Ora Bitton[1], Hila Nadler[1], A. Ronny Barnea[2], Alexey Gorlach[3], Ori Cheshnovsky[2], Ido Kaminer[3], Edvardas Narevicius[1]*

Angular momentum plays a central role in quantum mechanics, recurring in every length scale from the microscopic interactions of light and matter to the macroscopic behavior of superfluids. Vortex beams, carrying intrinsic orbital angular momentum (OAM), are now regularly generated with elementary particles such as photons and electrons. Thus far, the creation of a vortex beam of a nonelementary particle has never been demonstrated experimentally. We present vortex beams of atoms and molecules, formed by diffracting supersonic beams of helium atoms and dimers off transmission gratings. This method is general and could be applied to most atomic and molecular gases. Our results may open new frontiers in atomic physics, using the additional degree of freedom of OAM to probe collisions and alter fundamental interactions.

Vortices represent one of the clearest manifestations of angular momentum in nature, governing the hydrodynamics of the smallest insects, patterns of weather, and the motions of the stars in the galaxy. On all scales, vortices are characterized by the circulation of flux around an axis, whether the flux is composed of fluid mass in a classical eddy (*1*), magnetic field in a superconductor, or phase in a superfluid wave function (*2*). In quantum mechanics, a particle's angular momentum must have an integer value (*3*). Accordingly, the quantum manifestations of angular momentum are inherently different from the classical manifestations, contributing to selection rules in optical transitions, magnetic resonance spectroscopy, and the origins of the atomic fine structure. A particularly notable example of angular momentum is the quantized vortices often observed in a Bose-Einstein condensate (BEC) (*4*–*6*). In these, as well as in other vortices, the phase of the wave function varies around a singular point or axis, giving rise to a quantity called orbital angular momentum (OAM).

The quantization axis of the OAM in a vortex can also coincide with the propagation axis of a beam. Unlike vortices in a cold, confined BEC, which constitute an excitation of many atoms, a vortex beam consists of freely moving particles, each carrying intrinsic OAM that arises from the nontrivial shape of the single-particle wave function. Such vortex beams were first realized in experiments with photons (*7*), which have since found applications ranging from optical tweezers (*8*) to astrophysics (*9*), communication (*10*), and more (*11*, *12*). Electron vortex beams (*13*), first predicted and demonstrated two decades later (*14*), have been used, for example, to study chirality (*15*), magnetization mapping (*16*), and transfer of angular momentum to nanoparticles (*17*), and ongoing efforts include altering selection rules and controlling nuclear decay (*18*–*20*). Going beyond elementary particles such as the photon and electron, various proposals have been put forth for creating vortex beams of composite particles, such as neutrons (*21*), protons (*22*), and atoms (*23*, *24*), which are envisioned to alter the fundamental interactions of such particles and to enable probing of their internal structure. There have been experimental efforts to create neutron beams with OAM (*25*), which have been hindered by insufficient coherence lengths (*26*). Thus far, no experiment has created vortex beams of nonelementary particles.

Here, we present the first reported experimental demonstration of vortex beams with nonelementary particles, namely atoms and molecules of helium. Starting with a supersonic gas source, we created a beam of atoms with large transverse coherence lengths and diffracted them off a nanometric grating. The diffracted image revealed a series of ring-shaped patterns corresponding to nonzero OAM states of helium atoms. We further observed vortex beams of metastable helium dimers, a molecule formed in the supersonic expansion of the atomic gas after an electrical discharge. Although we used metastable helium beams for efficient and spatially resolved detection, our method could be generally applied to any supersonic beam of atoms or molecules and might be applicable to create vortices of ions and protons.

The common path to imparting OAM on particles in a beam is through waveform shaping—modifying an incoming plane wave's amplitude and phase to produce the desired wave. Before shaping, the wave function of a free particle propagating along the z axis can be described by $\psi'(r,z) = f'(r)e^{ikz}$, where $f'(r)$ is the transverse radial distribution and k is the particle's wave number. The characteristic dimension of the transverse distribution is defined by the coherence length Δ_c, a length scale dictated by the uncertainty in the transverse position of a particle. The phase of $\psi'(r,z)$ is uniform in each plane normal to the z axis and is modulated along z according to the wave number, $k = 2\pi/\lambda$. For a particle with mass m, $\lambda = h/mv$ is the de Broglie wavelength, where v is the propagation velocity and h is Planck's constant. Whereas the de Broglie wavelength can be only increased by reducing a particle's velocity, the coherence length can be manipulated by

[1]Faculty of Chemistry, Weizmann Institute of Science, Rehovot, Israel. [2]School of Chemistry, Sackler Faculty of Exact Sciences, Tel Aviv University, Tel Aviv, Israel. [3]Department of Electrical and Computer Engineering, Technion – Israel Institute of Technology, Haifa, Israel.
*Corresponding author. Email: edn@weizmann.ac.il
†These authors contributed equally to this work. ‡Present address: Department of Physics, University of California, Berkeley, Berkeley, CA, USA.

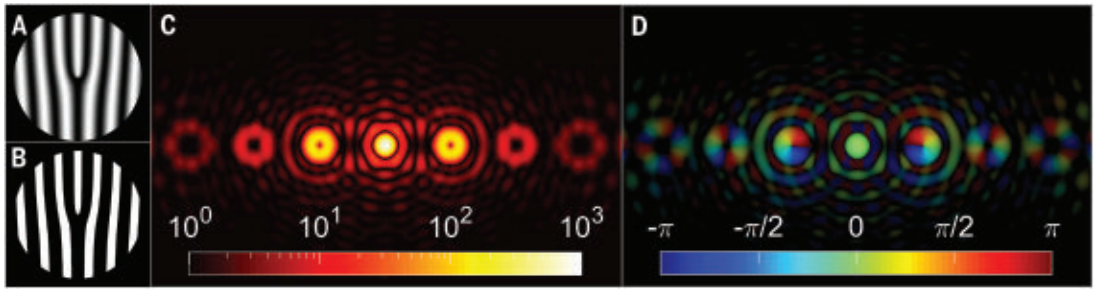


Fig. 1. Calculated diffraction image of vortex beams from a binary transmission grating. (**A** to **D**) The grating required to produce a vortex beam with a topological charge of $|l| = 1$, calculated from the interference between the target and reference wave, is shown in (A). For fabrication purposes, the calculated amplitude is binarized into slits with transmitting (white) and blocking (black) areas, with a forked edge dislocation in the center (B). This produces a series of vortices with topological charges $l = \pm1, \pm2, \ldots$, and in the far field, the intensity of the wave appears as a series of rings on either side of a central $l = 0$ spot (C). The hole in each ring coincides with a singularity in the phase of the function (D), around which the phase varies by $|2\pi l|$. The images were calculated for a grating with an open-to-blocked slit periodicity ratio of 40/60 and assuming that the coherence length of the beam is equal to the diameter of the circular aperture. Intensity in (C) is in arbitrary units.

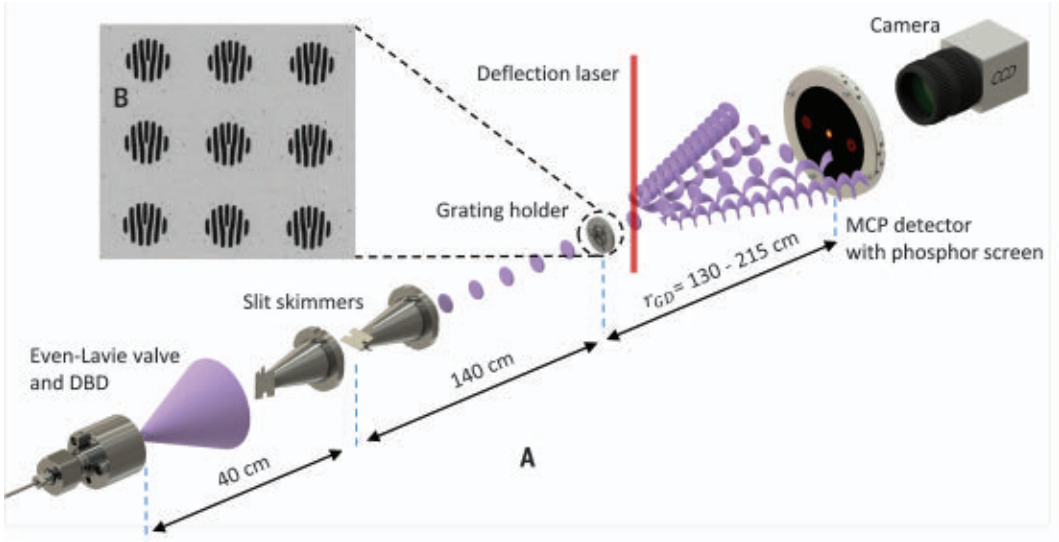


Fig. 2. Experimental setup for the production and detection of atomic and molecular vortex beams. (**A** and **B**) As shown in (A), a cooled Even-Lavie valve emits supersonic pulses of gas (purple cone), which are collimated by two slit skimmers to select the radial velocity spread and increase the transverse coherence length of the particles (purple disks). The beam impacts nanometric gratings, manufactured as an array of forked shapes (B), and is diffracted as vortex beams with different values of OAM (purple helixes). The metastable fraction of particles excited by the DBD in the valve decay upon interacting with the MCP, emitting light from a phosphor screen that is recorded on a camera. The impact point is localized in real time to high resolution, and the integrated image, assembled from hundreds of thousands of events, reveals the characteristic series of rings of OAM beams on either side of the central spot. When imaging the metastable dimers, a deflection laser beam resonant with an atomic transition of the triplet-state metastable atoms is crossed with the particles immediately after the grating (vertical red line), deflecting most of the detectable atoms to emphasize the dimer signal.

geometrical means. The desired outgoing vortex beam can be described by $\psi(r,z,\phi) = f(r)e^{ikz+il\phi}$, where ϕ is the azimuthal angle around the z axis and the integer l is termed the topological charge of the wave. Here, the constant phase wavefront is helical. Such a wave carries $l\hbar$ of OAM (*7*), where $\hbar = h/2\pi$. To achieve this shaping, several previous demonstrations of vortex beams of photons and electrons used spiral phase plates (*27*, *28*), which impart a single quanta $l\hbar$ of OAM on particles passing through them. However, fabricating such plates becomes challenging for beams of heavy particles with correspondingly shorter wavelengths, such as atoms and molecules, because of the required precision of the spiraling thickness profile. The spiral-plate method is further limited for atoms and molecules because of their low transmission probabilities through solid plates.

We followed an alternative approach, first demonstrated with vortices of light (*29*), and implemented transmission gratings designed by computer-generated holography. In this process, the required grating is designed by calculating the interference between the target wave—the vortex wavefunction—and a slightly tilted reference plane wave. The ideal theoretical grating contains a sinusoidal amplitude profile with an edge dislocation in the center, giving a "forked" shape (Fig. 1A). For fabrication, the amplitude profile was binarized, producing areas that either transmit or block the wave (Fig. 1B). The resulting binary gratings create a series of vortex beams with different topological charges with integer values $l = \pm n, \pm 2n, \ldots$. In a far-field plane parallel to the gratings, the intensity—or probability density, $|\psi|^2$—appears as a corresponding series of rings on either side of a central spot (Fig. 1C). The holes in these rings correspond to singularities in the phase of the wave function (Fig. 1D), with the phase changing by $|2\pi l|$ along a circle around a singularity with charge l. The number of edge dislocations, n, that fall within the transverse extent of an impacting particle's wave function (its coherence length) determines the spacing of the OAM values imparted into neighboring vortex beams, $n\hbar$.

Using such gratings, we have demonstrated the production of atomic vortex beams by gratings with one and two dislocations. We have also demonstrated molecular vortices produced by a single-edge dislocation grating with dimensions optimized for metastable helium dimers.

Experimental setup

We began by generating a supersonic beam of helium using a pulsed Even-Lavie valve (*30*). This source produces dense ensembles of particles with narrow velocity distributions. The longitudinal wavelength of the particles is controlled by changing the valve's temperature, where a lower temperature corresponds to a slower beam and thus a longer wavelength. We cooled the valve to 115 K to produce a beam with a mean velocity of v = 1090 m/s, corresponding to a de-Broglie wavelength of λ = 90 pm for helium atoms. We measured a longitudinal velocity spread of about 3% (full width at half-maximum), sufficiently low to avoid substantial chromatic aberrations in the diffraction image.

The pulse of atoms propagated until it diffracted off the transmission grating. Producing such diffraction gratings for beams of atoms or molecules requires fabrication of nanometric features, because the dimensions must correspond to the relatively small transverse coherence lengths associated with these particles (*31*–*35*). This coherence length is typically controlled by selecting the range of transverse velocities of the particles reaching the grating (*36*). In our experiment, we limited the radial spread by placing two perpendicular slit skimmers 40 cm downstream of the valve, allowing only a collimated beam to pass through their 150-μm apertures (Fig. 2A). The spread of the impacting particles was thus constrained by the solid angle covered by the skimmer apertures as viewed from the grating. For measurements aimed at imaging atoms, we set the distance between the skimmers and the grating to 140 cm to limit this divergence to a cone with a half-angle α = 55 μrad. For helium atoms, this corresponds to an average transverse coherence length of $\Delta_c = \lambda/2\alpha$ = 840 nm.

For our gratings, we constructed nanometric transmission holograms on 20-nm-thick silicon nitride membranes. The fabrication process is described in detail in the supplementary materials. Each hologram was etched in a circular area with a diameter a = 600 nm, and the grating slits were designed with a periodicity of d = 100 nm and approximately equal open and blocked areas, to give a diffraction angle of λ/d = 0.9 mrad for the l = ±1 orders. To increase the total intensity, the gratings repeated periodically every 1.2 μm over an area of 50 μm by 50 μm (Fig. 2B). The developed area was sufficiently small to avoid substantial incoherent blurring of the image in the far field, and the distance between holograms was chosen to be large enough to avoid coherent interference ("cross-talk") between paths through neighboring holograms. Details on the sources of blurring are given in the supplementary materials.

For detection, we used a dielectric-barrier discharge (*37*) (DBD) device installed in the

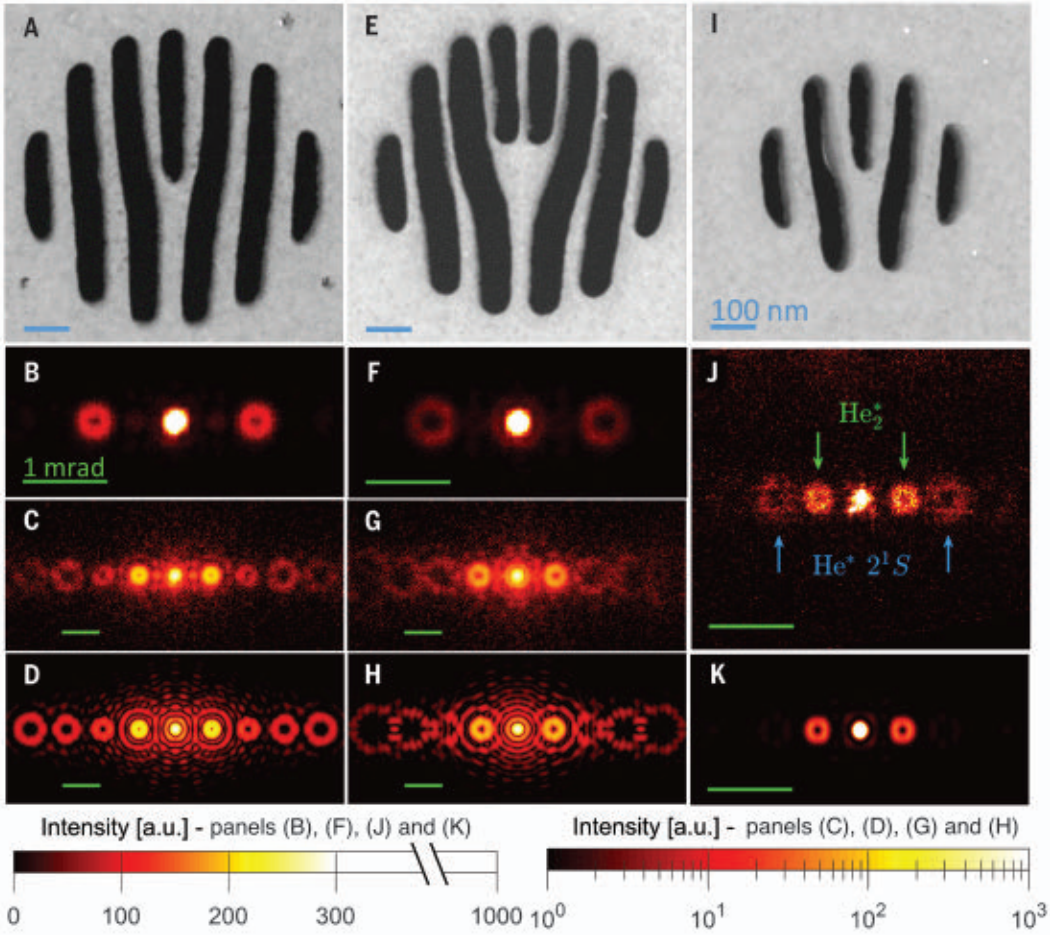


Fig. 3. Gratings and diffraction images of helium vortex beams. Experimental images were each assembled from 200,000 detected events. Theoretical images were calculated for a single grating. (**A** to **D**) A single-edge dislocation grating with a 600-nm diameter (A) produces clear rings (B) corresponding to atomic vortices with OAM of $\pm 1\hbar$ on either side of the central $l = 0$ spot. A logarithmic scale (C) reveals orders up to $l = \pm 4$ and gives a good quantitative fit to the calculated image (D). (**E** to **H**) A double-edge dislocation grating of the same size (E) produces larger diameter rings (F) with OAM of $\pm 2\hbar$, and the logarithmic scale (G) reveals the $l = \pm 4$ and ± 6 orders, as expected in the simulation (H). The logarithmic scale images [(C) and (G)] also reveal "half-order" spots resulting from metastable helium dimers, absent in the calculations [(D) and (H)]. (**I** to **K**) A smaller-diameter grating, 400 nm (I), reveals rings (J) associated with OAM-carrying dimer beams. To image the dimer vortices, the detector was distanced further from the gratings, and a resonant laser was used to deflect metastable atoms in the 2^3S state. The remaining metastable atoms in the 2^1S state appear as weak rings at twice the dimer $l = \pm 1$ diffraction angles, whereas the dimer rings give a good fit to the simulation (K). (A), (E), and (I) are scanning transmission electron microscope images. The color scale in all images is in arbitrary units. The color scale in (B), (F), (J), and (K) is saturated above 30% of the maximum intensity to emphasize the structure of the rings. The intensity in each pixel is evaluated by counting particle impacts over an area of about 900 μrad^2 in (B), (C), (F), and (G) and 400 μrad^2 in (J). Scale bars in (A), (E), and (I) are 100 nm; scale bars in (B) to (D), (F) to (H), and (J) and (K) are 1 mrad.

throat of the valve's nozzle, which applied high-voltage pulses to produce two different long-lived (metastable) excited states of atoms (*38*): 2^1S and 2^3S. These states have excess energy of about 20 eV, enabling efficient time and position-sensitive measurements using a microchannel plate (MCP) detector installed a distance $r_{GD} = 125$ cm downstream of the grating. Note that the DBD excites only a small fraction of the atoms, and therefore this method left most of the particles in the vortex beams undetected. The narrow collimation apertures and the low probability of excitation led to a recorded event rate on the order of 1 in every 50 valve pulses. The repetition rate of the experiment was set at 30 to 50 Hz, limited by the pumping speed in the source chamber and image processing.

Results

Figure 3 presents accumulated images of metastable particles impacting the detector, with comparison to simulated images for single gratings. In each measured image, about 200,000 events were recorded to reveal the far-field pattern corresponding to the probability density of the diffracted matter wave. Figure 3B presents the measured diffraction image from a forked grating with a single-edge dislocation (Fig. 3A). The image contains two clear rings on either side of a central spot. Additional rings can be seen in the logarithmic scale image (Fig. 3C). The image fits well with the simulated results for this grating (Fig. 3D), with the observed rings corresponding to vortex beams with topological charges of $l = -4$ to 4. Figure 3, E to H, presents a similar measurement and calculation for a grating with a double-edge dislocation. Here, the first two rings correspond to vortex beams with topological charges $l = \pm 2$ and are therefore larger than the first-order rings of the single-edge grating. Higher even-order OAM states, up to $l = \pm 6$, are observable in the logarithmic scale images (Fig. 3, G and H).

The diffraction patterns with helium beams revealed additional diffraction spots, located between the integer diffraction orders expected for atoms. We attributed these spots to metastable helium dimers (He_2^*) produced in the valve by the DBD, which had a corresponding de Broglie wavelength half that of the atoms. Such dimers are routinely created by discharges in supersonic valves at similar source conditions (*39*), especially at low temperatures and high pressures. We verified that these additional diffraction peaks were dimers through the strong dependence of their relative intensity on these source parameters and by observing that a laser locked to a transition of the metastable atoms only transferred momentum to particles in the integer-order beams. The verification methods, which were also tested on a regular slit diffraction grating, are detailed in the supplementary materials.

Figure 3J presents the diffraction image from smaller single-edge dislocation gratings (Fig. 3I) designed for imaging the dimers. The de Broglie wavelength of these particles was half that of the atoms owing to their mass, which would lead to a correspondingly smaller diffraction image. The angular expansion of each vortex is related to the Airy disk formula

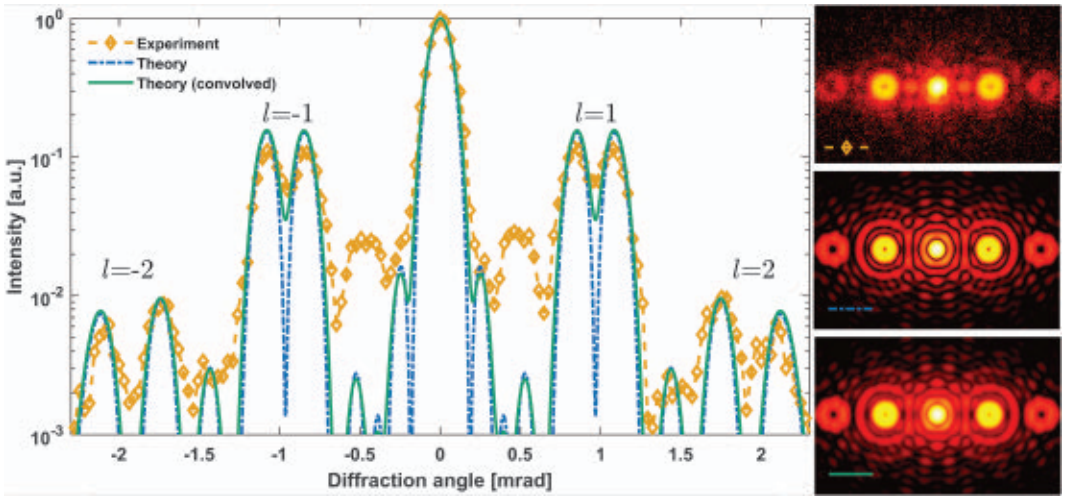


Fig. 4. Comparison of intensity measured in the experiment to theory, with simulated contribution of only the atoms. (**Left**) The intensity curves are plotted along a line crossing the helium vortex centers, shown in the range covering the l = −2 to 2 orders. Each point in the experimentally measured curve (orange) represents integration over an area 30 μrad wide (along the center line) by 90 μrad vertically. The ideal theoretical curve (blue), calculated for a monochromatic incoming wave of atoms diffracted from a single grating with an open-to-blocked slit periodicity ratio of 40/60, presents zero intensity at the center of nonzero OAM vortices. The green curve represents the ideal case with the convolution effects due to the velocity spread and the repeating grating pattern in the experiment. The latter curve shows a good fit to the experimentally measured data except for the lack of "half-order" peaks related to helium dimers. All values are given in arbitrary units normalized to the maximum intensity. (**Right**) Corresponding two-dimensional plots of the intensity for each of the three one-dimensional curves.

for the first minimum angle, $\theta \approx 1.22\lambda/a$. Therefore, we decreased the diameter of the gratings to a = 400 nm to partially compensate for the shorter wavelength. To compensate for the reduction in open area due to the smaller diameter, the gratings in this array repeated every 0.8 μm. We also installed narrower slit skimmers, with 75-μm apertures—half the value used for atoms. This was necessary to minimize incoherent blurring due to non–point source effects, also related to the divergence angle α, which become more pronounced for smaller diffraction angles. The reduction of α by half led to the same coherence length as with atoms, compensating for the doubled mass. In addition, we increased the free-flight distance from the grating to the detector to r_{GD} = 215 cm to allow for more expansion of the dimer vortex beams. Finally, the diffracted beam contains a substantial number of atoms, which would have obscured the dimer signal. One demonstrated technique for enhancing the relative contribution of dimers in a mixed beam uses another grating for mass selection (*40*). We followed an alternative method, demonstrated with sodium atoms and dimers (*41*), where a laser perpendicular to the gas beam was used to deflect the atoms out of the image. We applied a 1083-nm laser beam, resonant with the 2^3S-2^3P transition of the triplet-state metastable atoms (*42*), at 40 mW over a ~1-cm^2 spot size immediately after the grating (Fig. 2), thus scattering momentum off these atoms in the transverse direction. A small fraction of atoms, from the 2^1S state, remained in the image. Aside from this, the observed image fits well with a simulation for the dimers (Fig. 3K).

Figure 4 presents a quantitative comparison of the measurements with a single-edge dislocation grating to a calculation for helium atoms. The intensity distribution is shown along a line crossing in the transverse image plane through the centers of the rings of different orders. The most appreciable discrepancy arose from the odd-order peaks of diffracted dimers, absent in the theoretical curve. For the other peaks, we improved the fit by considering that the van der Waals interaction between the grating surface and the atoms narrowed the effective width of the slits. Indeed, studies of the interactions between atoms and surfaces made from similar materials showed that van der Waals forces extend to several nanometers away from the surfaces and reduce the effective width of slits (*43*). The effect is enhanced for species with higher polarizability and is especially strong in beams of metastable helium and neon (*44*). In our results, we found an optimal fit for an effective open (transmitting) slit width of 40 nm in place of the 55 nm estimated from the scanning transmission electron microscope image. The fit was further improved by adding the contributions of blurring due to pattern repetition of the holograms and of chromatic aberration from the measured beam velocity spread.

Outlook

We have demonstrated the generation of vortex beams of atoms and molecules with intrinsic OAM. To our knowledge, this is the first successful demonstration of vortices of nonelementary particles. The experiment was enabled by the production of beams with a relatively large coherence length, comparable to the dimensions of the nanometric grating. The method could be applied to most gaseous species owing to the generality of the supersonic valve apparatus (for example, see our measurement of neon vortices in the supplementary materials). Although heavy species require collimation with narrower skimmers to achieve sufficient transverse coherence length, and possibly the use of a carrier gas for efficient expansion cooling, there is no fundamental limit on the mass that can be used (*45*). Supersonic beams are also a convenient source for creating charged beams, through ionization of the atoms. In this manner, it would be possible to form a charged vortex beam of various particles, which could provide an extension to applications of electron vortex beams (*46*). A particularly interesting case would be to create OAM beams of protons by ionizing atomic hydrogen, a prospective path to studying the proton's internal structure through the coupling of the internal charge distribution with the twisting wavefunction of the center of mass (*22*).

The fabrication method we established can be used to design other holograms for wavefront shaping of matter waves, which could yield a broad range of potential applications; for example, matter waves may be shaped in such a manner that they will pull a collision target instead of pushing it (*47*). In low-energy scattering experiments between atoms and/or molecules, wavefront shaping would open an entirely new frontier. To date, in all such realizations with well-defined low collision energy (*38*, *48*, *49*), the scattering partners are well described by single momentum values, i.e., plane waves. There is often a certain variance of momenta value (transversely and longitudinally), but it is considered as an incoherent distribution rather than a coherent superposition as in our case. OAM beams would introduce helicity to these otherwise axisymmetric probes and may allow one to explore chiral interactions with various molecular partners.

Conversely, the vortex-generating mask itself may be used as a probe for OAM in scattering experiments. Here, particles exiting a collision are diffracted from a grating, and any preexisting OAM will lead to an asymmetric intensity

image, as demonstrated in OAM sorters of electron beams (*50*). In this manner, it would be possible to observe hitherto unexplored properties of reactions or other collisions between atoms or molecules. This concept of identifying OAM resulting from scattering experiments can be generalized beyond atomic physics: OAM sorters can be used in high-energy physics to extract new types of information from scattering processes, about chirality and generally regarding the role of transverse wave functions in altering fundamental interactions (*51*).

Finally, the OAM of matter waves may be used to try to modify selection rules in light-matter interactions. The probability of absorbing light through an atomic transition is dependent on the angular momentum of the photon and on the total angular momentum of the atomic state before and after the transition. Previous works have shown how creating vortex beams of photons can alter selection rules in transitions of trapped ions, with the intrinsic OAM of the photons contributing to the total angular momentum balance (*52*). Instead of the photons, we propose shaping the massive particles as vortices to examine the coupling strength of the matter wave OAM with other degrees of freedom. Experimental signatures of such an experiment would be, for example, the observation of an electronic transition that would otherwise be forbidden. This approach could be expanded by exciting the atoms to Rydberg states, where the vortex extent and the internal dimensions of the electron wave functions in the atoms are comparable. Taking these ideas to light-matter interactions of molecules could couple the OAM degree of freedom to the complexity of molecular rotations, creating hybrid rotational states that combine the quantum states of the nuclei and the center of mass.

REFERENCES AND NOTES

1. L. M. Milne-Thomson, *Theoretical Hydrodynamics* (Macmillan, 1968).
2. D. R. Tilley, J. Tilley, *Superfluidity and Superconductivity* (Adam Hilger, 1990).
3. R. N. Zare, *Angular Momentum: Understanding Spatial Aspects in Chemistry and Physics* (Wiley, 1988).
4. M. R. Matthews *et al*., *Phys. Rev. Lett.* **83**, 2498–2501 (1999).
5. K. W. Madison, F. Chevy, W. Wohlleben, J. Dalibard, *Phys. Rev. Lett.* **84**, 806–809 (2000).
6. J. R. Abo-Shaeer, C. Raman, J. M. Vogels, W. Ketterle, *Science* **292**, 476–479 (2001).
7. L. Allen, M. W. Beijersbergen, R. J. C. Spreeuw, J. P. Woerdman, *Phys. Rev. A* **45**, 8185–8189 (1992).
8. H. He, M. E. J. Friese, N. R. Heckenberg, H. Rubinsztein-Dunlop, *Phys. Rev. Lett.* **75**, 826–829 (1995).
9. G. C. G. Berkhout, M. W. Beijersbergen, *J. Opt. A Pure Appl. Opt.* **11**, 094021 (2009).
10. J. T. Barreiro, T. C. Wei, P. G. Kwiat, *Nat. Phys.* **4**, 282–286 (2008).
11. M. J. Padgett, *Opt. Express* **25**, 11265–11274 (2017).
12. Y. Shen *et al*., *Light Sci. Appl.* **8**, 90 (2019).
13. K. Y. Bliokh *et al*., *Phys. Rep.* **690**, 1–70 (2017).
14. M. Uchida, A. Tonomura, *Nature* **464**, 737–739 (2010).
15. J. Verbeeck, H. Tian, P. Schattschneider, *Nature* **467**, 301–304 (2010).
16. S. Lloyd, M. Babiker, J. Yuan, *Phys. Rev. Lett.* **108**, 074802 (2012).
17. J. Verbeeck, H. Tian, G. Van Tendeloo, *Adv. Mater.* **25**, 1114–1117 (2013).
18. J. Harris *et al*., *Nat. Phys.* **11**, 629–634 (2015).
19. S. M. Lloyd, M. Babiker, G. Thirunavukkarasu, J. Yuan, *Rev. Mod. Phys.* **89**, 035004 (2017).
20. S. Gargiulo, I. Madan, F. Carbone, Nuclear excitation by electron capture in excited ions. arXiv:2102.05718v1 [nucl-th] (2021).
21. H. Larocque, I. Kaminer, V. Grillo, R. W. Boyd, E. Karimi, *Nat. Phys.* **14**, 1–2 (2018).
22. G. M. Vanacore *et al*., *Nat. Mater.* **18**, 573–579 (2019).
23. V. E. Lembessis, D. Ellinas, M. Babiker, O. Al-Dossary, *Phys. Rev. A* **89**, 053616 (2014).
24. I. Madan, G. M. Vanacore, S. Gargiulo, T. LaGrange, F. Carbone, *Appl. Phys. Lett.* **116**, 230502 (2020).
25. C. W. Clark *et al*., *Nature* **525**, 504–506 (2015).
26. R. L. Cappelletti, T. Jach, J. Vinson, *Phys. Rev. Lett.* **120**, 090402 (2018).
27. S. S. R. Oemrawsingh *et al*., *Appl. Opt.* **43**, 688–694 (2004).
28. A. Béché, R. Winkler, H. Plank, F. Hofer, J. Verbeeck, *Micron* **80**, 34–38 (2016).
29. N. R. Heckenberg, R. McDuff, C. P. Smith, H. Rubinsztein-Dunlop, M. J. Wegener, *Opt. Quantum Electron.* **24**, S951–S962 (1992).
30. U. Even, J. Jortner, D. Noy, N. Lavie, C. Cossart-Magos, *J. Chem. Phys.* **112**, 8068–8071 (2000).
31. D. W. Keith, M. L. Schattenburg, H. I. Smith, D. E. Pritchard, *Phys. Rev. Lett.* **61**, 1580–1583 (1988).
32. J. Fujita *et al*., *Nature* **380**, 691–694 (1996).
33. M. Arndt *et al*., *Nature* **401**, 680–682 (1999).
34. C. Brand *et al*., *Nat. Nanotechnol.* **10**, 845–848 (2015).
35. A. R. Barnea, O. Cheshnovsky, U. Even, *Phys. Rev. A* **97**, 023601 (2018).
36. C. Keller, J. Schmiedmayer, A. Zeilinger, *Opt. Commun.* **179**, 129–135 (2000).
37. K. Luria, N. Lavie, U. Even, *Rev. Sci. Instrum.* **80**, 104102 (2009).
38. A. B. Henson, S. Gersten, Y. Shagam, J. Narevicius, E. Narevicius, *Science* **338**, 234–238 (2012).
39. M. Raunhardt, M. Schäfer, N. Vanhaecke, F. Merkt, *J. Chem. Phys.* **128**, 164310 (2008).
40. W. Schöllkopf, J. P. Toennies, *Science* **266**, 1345–1348 (1994).
41. M. S. Chapman *et al*., *Phys. Rev. Lett.* **74**, 4783–4786 (1995).
42. M. R. Wehr, *Phys. Rev.* **39**, 796–801 (1932).
43. R. E. Grisenti, W. Schöllkopf, J. P. Toennies, G. C. Hegerfeldt, T. Köhler, *Phys. Rev. Lett.* **83**, 1755–1758 (1999).
44. R. Brühl *et al*., *Europhys. Lett.* **59**, 357–363 (2002).
45. Y. Y. Fein *et al*., *Nat. Phys.* **15**, 1242–1245 (2019).
46. D. Karlovets, *New J. Phys.* **23**, 033048 (2021).
47. A. A. Gorlach, M. A. Gorlach, A. V. Lavrinenko, A. Novitsky, *Phys. Rev. Lett.* **118**, 180401 (2017).
48. S. N. Vogels *et al*., *Science* **350**, 787–790 (2015).
49. J. Jankunas, K. Jachymski, M. Hapka, A. Osterwalder, *J. Chem. Phys.* **142**, 164305 (2015).
50. A. H. Tavabi *et al*., *Phys. Rev. Lett.* **126**, 094802 (2021).
51. I. Kaminer *et al*., *Phys. Rev. X* **6**, 011006 (2016).
52. C. T. Schmiegelow *et al*., *Nat. Commun.* **7**, 12998 (2016).
53. A. Luski *et al*., Vortex beams of atoms and molecules. Zenodo (2021); https://doi.org/10.5281/zenodo.4917316.

ACKNOWLEDGMENTS

We acknowledge I. Kaplan-Ashiri for professional support in providing the STEM images. **Funding:** European Research Council H2020 Program and the Minerva Foundation. **Author contributions:** A.L., Y.S., R.D., and E.N. designed, constructed, and conducted the experiment and analyzed the results. A.R.B. provided designs for essential parts. O.B., H.N., A.R.B., and O.C. developed the fabrication process and prepared the gratings. O.C. contributed to the development of experimental methodology. A.L., Y.S., E.N., I.K., and A.G. contributed to the conception of the project. **Competing interests:** The authors declare that they have no competing interests. **Data and materials availability:** All data underlying the figures are deposited at Zenodo (*53*).

SUPPLEMENTARY MATERIALS

science.sciencemag.org/content/373/6559/1105/suppl/DC1
Materials and Methods
Supplementary Text
Figs. S1 to S6
Table S1

29 April 2021; accepted 24 June 2021
10.1126/science.abj2451

CORONAVIRUS

Broad betacoronavirus neutralization by a stem helix–specific human antibody

Dora Pinto[1]†, Maximilian M. Sauer[2]†, Nadine Czudnochowski[3]†, Jun Siong Low[4]†, M. Alejandra Tortorici[2], Michael P. Housley[3], Julia Noack[3], Alexandra C. Walls[2], John E. Bowen[2], Barbara Guarino[1], Laura E. Rosen[3], Julia di Iulio[3], Josipa Jerak[4], Hannah Kaiser[3], Saiful Islam[3], Stefano Jaconi[1], Nicole Sprugasci[1], Katja Culap[1], Rana Abdelnabi[5], Caroline Foo[5], Lotte Coelmont[5], Istvan Bartha[1], Siro Bianchi[1], Chiara Silacci-Fregni[1], Jessica Bassi[1], Roberta Marzi[1], Eneida Vetti[1], Antonino Cassotta[4], Alessandro Ceschi[6,7,8,9], Paolo Ferrari[9,10,11], Pietro E. Cippà[10,12], Olivier Giannini[9,10], Samuele Ceruti[13], Christian Garzoni[14], Agostino Riva[15], Fabio Benigni[1], Elisabetta Cameroni[1], Luca Piccoli[1], Matteo S. Pizzuto[1], Megan Smithey[3], David Hong[3], Amalio Telenti[3], Florian A. Lempp[3], Johan Neyts[5], Colin Havenar-Daughton[3], Antonio Lanzavecchia[1], Federica Sallusto[4,16], Gyorgy Snell[3], Herbert W. Virgin[3,17,18], Martina Beltramello[1], Davide Corti[1]*, David Veesler[2]*

The spillovers of betacoronaviruses in humans and the emergence of severe acute respiratory syndrome coronavirus 2 (SARS-CoV-2) variants highlight the need for broad coronavirus countermeasures. We describe five monoclonal antibodies (mAbs) cross-reacting with the stem helix of multiple betacoronavirus spike glycoproteins isolated from COVID-19 convalescent individuals. Using structural and functional studies, we show that the mAb with the greatest breadth (S2P6) neutralizes pseudotyped viruses from three different subgenera through the inhibition of membrane fusion, and we delineate the molecular basis for its cross-reactivity. S2P6 reduces viral burden in hamsters challenged with SARS-CoV-2 through viral neutralization and Fc-mediated effector functions. Stem helix antibodies are rare, oftentimes of narrow specificity, and can acquire neutralization breadth through somatic mutations. These data provide a framework for structure-guided design of pan-betacoronavirus vaccines eliciting broad protection.

Coronaviruses are zoonotic pathogens responsible for several epidemics and a pandemic in the past two decades. All three highly pathogenic coronaviruses belong to the betacoronavirus genus: Severe acute respiratory syndrome coronavirus 2 (SARS-CoV-2) and SARS-CoV cluster within the *sarbecovirus* subgenus and originated in bats, whereas Middle East respiratory syndrome coronavirus (MERS-CoV) belongs to the *merbecovirus* subgenus and is transmitted to humans through dromedary camels. Moreover, HCoV-HKU1 and HCoV-OC43 (*embecovirus* subgenus, betacoronaviruses) as well as NL63 and 229E (*setracovirus*

and *duvinacovirus* subgenera, alphacoronaviruses) are endemic and cause common colds in humans.

The coronavirus spike (S) glycoprotein promotes viral entry into host cells through an S_1 subunit that engages host receptors and an S_2 subunit mediating membrane fusion (*1*). The S_1 subunit is the major target of (neutralizing) antibodies (Abs) and is more genetically variable than the S_2 subunit (*2*–*5*). Accordingly, Abs binding to the S_1 subunit receptor-binding domain (RBD) and N-terminal domain (NTD) exert a selective pressure that results in the emergence of new variants (*5*–*10*). SARS-CoV-2 S comprises 22 N-linked glycans (13 and 9 of them in the S_1 and S_2 subunits, respectively) participating in folding as well as modulating access to host proteases and antibodies (*1*, *2*, *11*–*13*). Monoclonal antibodies (mAbs) binding to the S_2 fusion machinery can neutralize distantly related coronaviruses (*14*–*16*), as observed for other viruses such as influenza and HIV-1 (*17*, *18*).

Results

Isolation of a broadly neutralizing betacoronavirus mAb from a convalescent SARS-CoV-2–exposed individual

To identify mAbs targeting highly conserved regions of the S glycoprotein, we interrogated human immunoglobulin G^+ (IgG^+) memory B cells from three COVID-19 convalescent donors. Five mAbs bound to the prefusion-stabilized S ectodomain trimers of SARS-CoV and SARS-CoV-2 (*sarbecovirus*), MERS-CoV (*merbecovirus*), and OC43 and HKU1 (*embecovirus*), but not to the human alphacoronaviruses 229E and NL63 (Fig. 1, A to C, and fig. S1, A and B). S2P6 and S2S43 mAbs were each derived from a separate donor and use VH1-46*01 and D5-12*01 genes, whereas P34D10, P34G12, and P34E3 mAbs were derived from a third donor, are clonally related, and use the VH3-30 gene (fig. S1A). These five mAbs share nucleotide sequence identities with their respective germline genes ranging from 86 to 97% (fig. S1A), which correspond to a higher level of mutations than that observed for RBD- and NTD-specific mAbs isolated early after SARS-CoV-2 infection or vaccination (*5*, *19*–*21*). The mAbs bound to all prefusion-stabilized human-infecting betacoronavirus S trimers (Fig. 1, A to C, and fig. S1B), and they all neutralize SARS-CoV-2 S vesicular stomatitis virus (VSV) pseudotypes (fig. S1C).

S2P6 was selected for further in-depth characterization because it exhibited the overall greatest cross-reactivity and neutralization breadth. S2P6 bound both prefusion and post-fusion SARS-CoV-2 S with comparable avidities, which indicates that its epitope might be (at least partially) accessible in both conformational states (Fig. 1, A and B, and fig. S1D). S2P6 bound to all full-length SARS-CoV-2 S variants tested and to 25 S glycoproteins representative of all *sarbecovirus* clades (Fig. 1D and fig. S1, E and F). Using surface plasmon resonance (SPR), we found that the S2P6 Fab fragment had the highest affinity for SARS-CoV-2 S and SARS-CoV S followed by MERS-CoV S and OC43 S with equilibrium dissociation constants (K_D) of 7, 7, 12, and 16 nM, respectively (fig. S1, G and H). S2P6 also bound to HKU1 S, albeit with reduced affinity (K_D ~120 nM) (fig. S1G). Collectively, these data demonstrate that S2P6 cross-reacts with all human-infecting betacoronaviruses.

To evaluate the neutralization potency and breadth of S2P6, we investigated its ability to inhibit entry of authentic SARS-CoV-2 into Vero-E6 cells in the presence or absence of TMPRSS2, as this protease activates fusion with the cytoplasmic membrane in cultured lung cells (*22*–*24*). S2P6 completely neutralized infection of TMPRSS2-positive Vero-E6 cells but was less effective in inhibiting infection of Vero-E6 cells lacking TMPRSS2 (Fig. 1E), which suggests that S2P6 binding might be reduced at endosomal pH. The recognition of prefusion SARS-CoV-2 S by S2P6 is pH dependent, with higher binding affinity at pH 7, relative to pH 5, in both IgG and Fab formats (fig. S1H). We subsequently assessed S2P6-mediated neutralization of VSV (*25*) pseudotyped with SARS-CoV-2 S of several variants of concern (VOCs), including B.1.1.7 (Alpha), B.1.351 (Beta), P.1 (Gamma), and B1.617.1 (Kappa), and we observed similar potency to that found against the parental SARS-CoV-2 D614G S (Fig. 1F and fig. S1I). Moreover, S2P6 inhibited SARS-CoV S, Pangolin Guangdong 2019 (PANG/GD) S, MERS-CoV S, and OC43 S VSV pseudotypes with median inhibitory concentration (IC_{50}) values ranging from 0.02 to 17 μg/ml (Fig. 1G). S2P6 is therefore a broadly neutralizing betacoronavirus mAb with activity against SARS-CoV-2 and SARS-CoV–related viruses as well as members of the *merbecovirus* and *embecovirus* subgenera.

Peptide mapping experiments using 15-nucleotide oligomer linear overlapping peptides revealed that all five mAbs bound to peptides containing the SARS-CoV-2 motif F_{1148}KEELDKYF_{1156} located in the S_2 subunit stem helix (Fig. 1H and fig. S2A). This region is strictly conserved in SARS-CoV, is highly conserved among other betacoronaviruses, and overlaps with the epitopes of the B6 (Fig. 1I) and 28D9 mouse mAbs (*14*, *15*). S2P6 bound efficiently to the stem helix peptides of the five betacoronaviruses that infect humans (albeit with a faster off-rate for HKU1) as well as those of the MERS-CoV–related bat viruses (HKU4 and HKU5) and murine hepatitis virus (MHV) (Fig. 1J and fig. S2B). S2S43 exhibited similar overall binding to that of S2P6, with markedly weaker reactivity toward the HKU1, HKU4, and HKU5 peptides, whereas the three clonally related P34D10, P34G12, and P34E3 mAbs exhibited weaker or no binding to HKU4 and HKU5 peptides (fig. S2B).

Structural basis for S2P6 binding to the conserved S glycoprotein stem helix

To determine the molecular basis of the S2P6 neutralization breadth, we determined a cryo–electron microscopy (cryo-EM) structure of the SARS-CoV-2 S ectodomain trimer in complex with the Fab fragments of S2P6 and S2M11 [to lock the RBDs in the closed state (*21*)] at 4.2-Å overall resolution. The marked conformational dynamics of the region recognized by S2P6 limited the local resolution of the stem helix–Fab to ~12 Å, and three-dimensional classification of the cryo-EM data revealed incomplete Fab saturation (Fig. 2A; table S1; and fig. S3, A to F). Our cryo-EM structure confirms that S2P6 recognizes the stem helix and suggests that the mAb disrupts its quaternary structure, which is presumed to form a three-helix bundle in prefusion SARS-CoV-2 S (*2*, *3*, *14*). To overcome the limited resolution of the stem helix–Fab interface in the cryo-EM structure, we determined a crystal structure of the S2P6 Fab in complex with the SARS-CoV-2 S stem helix peptide (residues 1146 to 1159) at 2.67-Å resolution (Fig. 2, B to D; fig. S4A; and table S2). The peptide folds as an amphipathic α helix resolved for residues 1146 to 1159. S2P6 buries ~600 $Å^2$ upon binding to its epitope using shape-complementarity and hydrogen bonding involving complementarity-determining regions (CDRs) H1 to H3, L1, and L3. The light chain residues Y33, Y92, G93, S94, P96, P97, and F99 as well as heavy chain residues Y33, I50, H57, T58, S59, P101, K102, and G103 form a deep groove in which the hydrophobic side

[1]Humabs Biomed SA, a subsidiary of Vir Biotechnology, 6500 Bellinzona, Switzerland. [2]Department of Biochemistry, University of Washington, Seattle, WA 98195, USA. [3]Vir Biotechnology, San Francisco, CA 94158, USA. [4]Institute for Research in Biomedicine, Università della Svizzera italiana, 6500 Bellinzona, Switzerland. [5]Rega Institute for Medical Research, Laboratory of Virology and Chemotherapy, KU Leuven, 3000 Leuven, Belgium. [6]Clinical Trial Unit, Ente Ospedaliero Cantonale, 6900 Lugano, Switzerland. [7]Division of Clinical Pharmacology and Toxicology, Institute of Pharmacological Sciences of Southern Switzerland, Ente Ospedaliero Cantonale, 6900 Lugano, Switzerland. [8]Department of Clinical Pharmacology and Toxicology, University Hospital Zurich, 8091 Zurich, Switzerland. [9]Faculty of Biomedical Sciences, Università della Svizzera italiana, 6900 Lugano, Switzerland. [10]Department of Medicine, Ente Ospedaliero Cantonale, 6500 Bellinzona, Switzerland. [11]Clinical School, University of New South Wales, Sydney, NSW, 2052, Australia. [12]Faculty of Medicine, University of Zurich, 8057 Zurich, Switzerland. [13]Intensive Care Unit, Clinica Luganese Moncucco, 6900 Lugano, Switzerland. [14]Clinic of Internal Medicine and Infectious Diseases, Clinica Luganese Moncucco, 6900 Lugano, Switzerland. [15]III Division of Infectious Diseases, ASST Fatebenefratelli Sacco, Luigi Sacco Hospital, 20157 Milan, Italy. [16]Institute of Microbiology, ETH Zurich, 8093 Zurich, Switzerland. [17]UT Southwestern Medical Center, Dallas, TX 75390, USA. [18]Washington University School of Medicine, St. Louis, MO 63110, USA.

***Corresponding author. Email: dveesler@uw.edu (D.V.); dcorti@vir.bio (D.C.)**

†These authors contributed equally to this work.

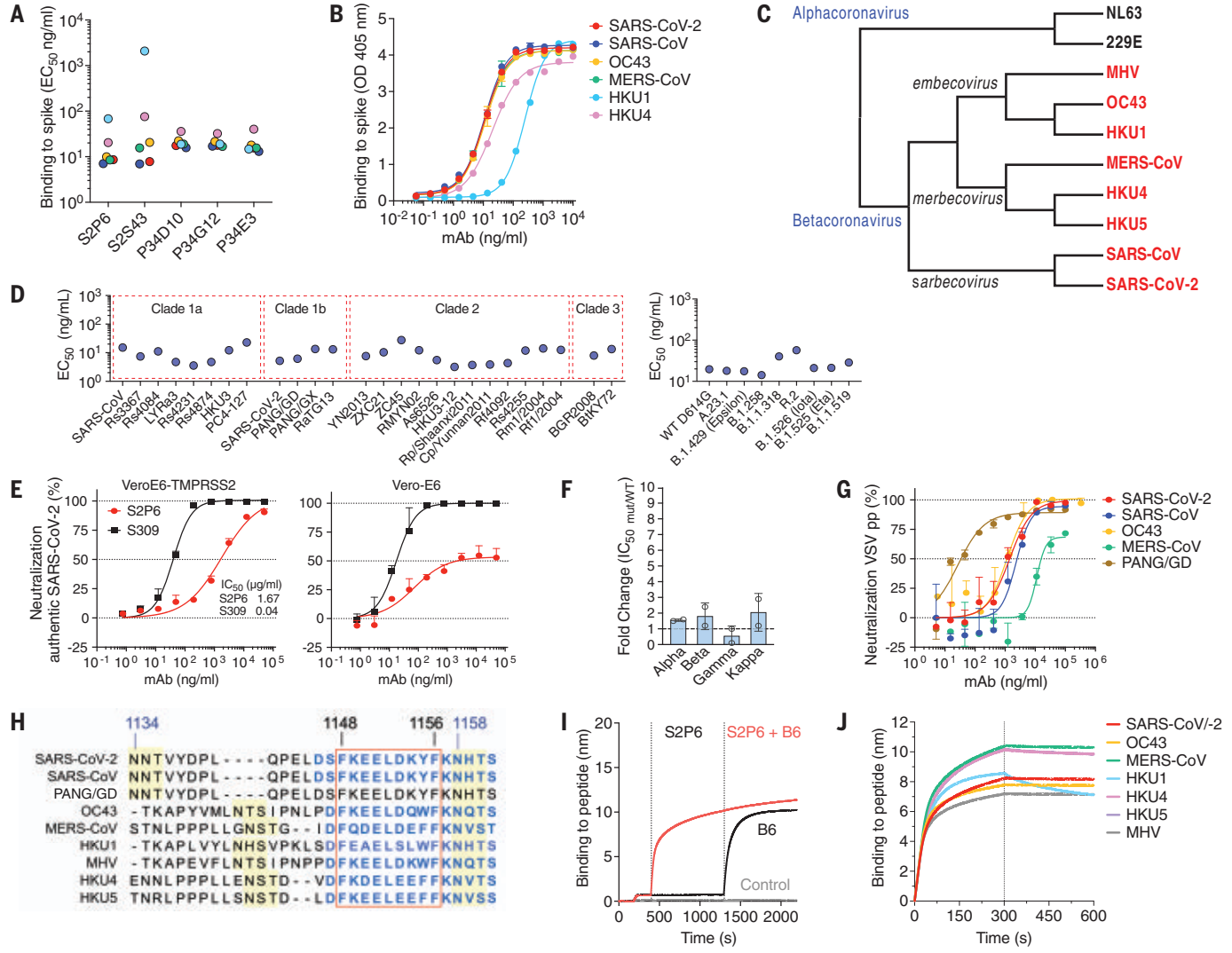


Fig. 1. The S2P6 cross-reactive mAb broadly neutralizes betacoronaviruses from three subgenera. (**A**) Binding avidity (EC_{50}) of five mAbs to prefusion coronavirus S trimer ectodomains as determined by ELISA. (**B**) S2P6 ELISA binding curves showing the full titration. One representative experiment out of two is shown. OD, optical density. (**C**) Cladogram of representative alpha- (black) and betacoronavirus (red) S glycoprotein amino acid sequences inferred through maximum likelihood analysis. (**D**) Flow cytometry analysis of S2P6 binding (from 10 to 0.22 μg/ml) to a panel of 26 S glycoproteins representative of all *sarbecovirus* clades (left) and eight SARS-CoV-2 variants (right) displayed as EC_{50} values. (**E**) Neutralization of authentic SARS-CoV-2 by S2P6 determined using VeroE6-TMPRSS2 (left) or Vero-E6 (right) cells. The S309 mAb that binds RBD site IV (*38*) is included for comparison. The mean ± SD of triplicates from one representative experiment out of three is shown. (**F**) S2P6-mediated neutralization of SARS-CoV-2 B.1.1.7 (Alpha) S, B.1.351 (Beta) S, P.1 (Gamma) S, and B1.617.1 (Kappa) S VSV pseudotypes (mut) represented as IC_{50} fold change relative to wild-type (WT) (D614G) S VSV pseudotype. Individual values for each of the two replicates are shown as open circles, the mean as a colored bar, and the SD as error bars. (**G**) S2P6-mediated neutralization of VSV pseudotyped with various betacoronavirus S glycoproteins. Error bars indicate standard deviation of triplicates. IC_{50} values are 2.4 μg/ml, 1.4 μg/ml, 17.1 μg/ml, 1.3 μg/ml, and 0.02 μg/ml for SARS-CoV, SARS-CoV-2, MERS-CoV, OC43, and PANG/GD, respectively. pp, pseudoparticles. (**H**) Alignment of betacoronavirus stem helix amino acid sequences with the S2P6 epitope boxed. Residue numbering is shown according to SARS-CoV-2 S. The sequences of the peptides used in this study are shown in blue, and N-linked glycosylation sequons are highlighted in yellow. (**I**) Competition assay for S2P6 or B6 binding to the SARS-CoV-2 or SARS-CoV stem helix peptide (herein defined as SARS-CoV/-2). B6 binding in the presence of S2P6 (red line), B6 binding in the absence of S2P6 (black line), and the control lacking the SARS-CoV/-2 stem helix peptide (gray line) are shown. (**J**) Kinetics of S2P6 binding to a panel of biotinylated betacoronavirus stem helix peptides immobilized at the surface of biolayer interferometry biosensors.

of the stem helix docks through residues F1148, L1152, Y1155, and F1156. Binding specificity is provided through backbone hydrogen bonding of residues $F1148_{SARS\text{-}CoV\text{-}2}$ and $K1149_{SARS\text{-}CoV\text{-}2}$ with CDRH3 P101 and side chain hydrogen bonding of residues $E1151_{SARS\text{-}CoV\text{-}2}$ with CDRL1 Y33 and CDRL3 S94, $D1153_{SARS\text{-}CoV\text{-}2}$ with CDRH1 Y33 side chains, as well as $Y1155_{SARS\text{-}CoV\text{-}2\ S}$ with CDRH2 S59 through a water molecule and $F1156_{SARS\text{-}CoV\text{-}2\ S}$ with CDRH2 H57, also through a water molecule (Fig. 2, C and D). The contribution of each epitope residue was validated by single-substitution scan analysis with most mutations at positions 1148, 1151 to 1153, and 1155 to 1156 abolishing S2P6 binding, which highlights the importance of these residues for mAb recognition (fig. S5A). A substitution scan analysis performed on the P34D10, P34G12, and P34E3 mAbs revealed a similar pattern of key interacting residues (fig. S5A). Residue Y1155 is conservatively substituted to $F1238_{MERS\text{-}CoV}$ or $W1237/1240_{HKU1/OC43}$, and residue D1153 is conserved in MERS-CoV and OC43 but mutated to S1235 for HKU1 (fig. S5B). The residue scan and structural results suggest that the reduced binding affinity of S2P6 for HKU1 S is at least partially a result

of the D1153 $_{SARS\text{-}CoV\text{-}2}$–S1235$_{HKU1}$ substitution, which is expected to dampen electrostatic interactions with the CDRH1 Y33 side chain hydroxyl (Fig. 2, C and D).

Although S2P6 and B6 recognize a similar epitope (fig. S4, B and C), they bind with opposite orientations of the heavy and light chains relative to the stem helix and the S2P6-bound structure resolves three additional C-terminal peptide residues (1146 to 1159) compared with the B6-bound structure (1147 to 1156) (fig. S4, B and C). Superposition of both structures based on the stem helix reveals that B6 CDRH2 would sterically clash with H1159$_{SARS\text{-}CoV\text{-}2}$, putatively explaining the broader cross-reactivity of S2P6 over B6 (fig. S4, B and C).

To further validate our structural data, we carried out viral escape mutant selection in vitro in the presence of S2P6 using a replication-competent VSV–SARS-CoV-2 S virus (*26*). After two passages, virus neutralization by S2P6 was abrogated, and deep sequencing revealed the emergence of five distinct resistance mutations—L1152F, D1153N/G/A, and F1156L, which are consistent with the structural data and substitution scan analysis (fig. S5A). Although these mutations have been detected with very low frequencies in circulating SARS-CoV-2 isolates (146 out of 1,217,814 sequences as of 30 April 2021), the subdominant immunogenicity of this cryptic site, likely because of its limited exposure, might result in low Ab pressure limiting accumulation of mutations in this epitope.

Stem helix–targeting mAbs inhibit S-mediated membrane fusion

The S stem helix forms a three-helix bundle in many prefusion cryo-EM structures of SARS-CoV-2 S and SARS-CoV S although it is not fully resolved (*2*, *3*, *11*, *27*–*29*). By contrast, the S2P6–S2M11–SARS-CoV-2 S cryo-EM structure suggests that the quaternary organization of the stem is disrupted (Fig. 2A), consistent with S2P6 binding to the hydrophobic face of the stem helix. This face is mostly buried through homo-oligomeric interactions in prefusion S and may be only transiently available for Ab binding. Although we observed S2P6 binding to postfusion SARS-CoV-2 S (fig. S1D), the epitope recognized is buried at the interface with the other two protomers of the rod-shaped trimer and therefore might become accessible as a result of conformational dynamics, as is the case for the prefusion state (fig. S4D) (*14*, *30*–*32*). On the basis of these data, we propose that S2P6 binding to S sterically interferes with the conformational changes leading to membrane fusion, as observed for B6 (*14*) and 27D9 (*15*).

To validate the inferred mechanism of S2P6-mediated broad coronavirus neutralization, we first showed that S2P6 binding did not block engagement of SARS-CoV-2 S by angiotensin-converting enzyme 2 (ACE2)—using enzyme-linked immunosorbent assay (ELISA)—as expected based on the distance of its epitope from the RBD (Fig. 3A). S2P6, however, blocked cell-cell fusion between Vero-E6 cells transfected with full-length SARS-CoV-2 S as effectively as the S2M11 mAb, which locks SARS-CoV-2 S in the closed state (*21*) (Fig. 3B). We previously described mAbs targeting RBD antigenic sites Ia (e.g., S2E12) and IIa (e.g., S2X259 or S2X35), which can mimic receptor attachment and prematurely trigger fusogenic S conformational changes (*11*, *20*, *33*). Accordingly, S2P6 at concentrations as low as 1 ng/ml abrogated the formation of syncytia mediated by S2E12 (*33*). Collectively, these results suggest that the main mechanism of S2P6 neutralization is to prevent viral entry by impeding S fusogenic rearrangements, thereby inhibiting membrane fusion (Fig. 3C).

S2P6-mediated protection in hamsters is enhanced by Fc-mediated effector functions

Functions mediated by the constant (Fc) region of Abs can contribute to in vivo protection by promoting viral clearance and antiviral immune responses (*34*–*37*). We analyzed the ability of S2P6 to trigger activation of the Fc receptors, FcγRIIa and FcγRIIIa, as well as to exert Fc effector functions in vitro. S2P6 promoted moderate dose-dependent FcγRIIa- and FcγRIIIa-mediated signaling using a luciferase reporter assay (Fig. 4A). However, S2P6 promoted robust activation of Ab-dependent cell cytotoxicity (ADCC), to levels comparable to those observed with the S309 mAb (*38*), after incubation of SARS-CoV-2 S–expressing CHO-K1 target cells with human peripheral blood mononuclear cells (PBMCs) (Fig. 4B). S2P6 also triggered measurable Ab-dependent cellular phagocytosis (ADCP) activity using cell trace violet–labeled PBMCs as phagocytic cells and

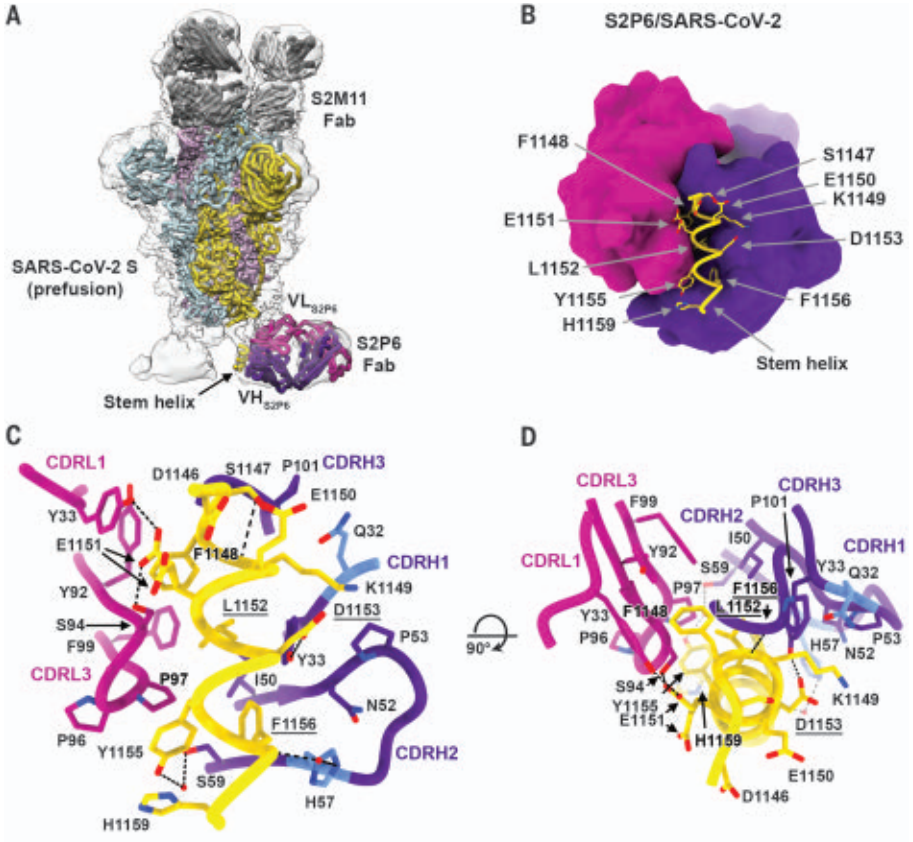


Fig. 2. Structural basis for the broad S2P6 cross-reactivity with the conserved coronavirus stem helix peptide. (**A**) Composite model of the S2P6-bound SARS-CoV-2 S cryo-EM structure and of the S2P6-bound stem helix peptide crystal structure docked in the cryo-EM map (semitransparent gray surface). SARS-CoV-2 S protomers are colored pink, cyan, and gold; the S2P6 Fab heavy and light chains are colored purple and magenta; and the S2M11 Fab heavy and light chains are colored dark and light gray, respectively. (**B**) Crystal structure of the S2P6 Fab (surface rendering) in complex with the SARS-CoV-2 S stem helix peptide (yellow ribbon with side chains rendered as sticks). (**C** and **D**) Ribbon diagram in two orthogonal orientations of the S2P6 Fab bound to the SARS-CoV-2 S stem helix peptide showing the network of interactions. Only key interface residues and the S2P6 CDR loops are shown for clarity. Residues Q32 and H57, which are mutated during affinity maturation of the S2P6 heavy chain, are colored blue. Hydrogen bonds are indicated with dashed lines. Residues substituted in the escape mutants isolated are underlined. Single-letter abbreviations for the amino acid residues are as follows: A, Ala; C, Cys; D, Asp; E, Glu; F, Phe; G, Gly; H, His; I, Ile; K, Lys; L, Leu; M, Met; N, Asn; P, Pro; Q, Gln; R, Arg; S, Ser; T, Thr; V, Val; W, Trp; and Y, Tyr.

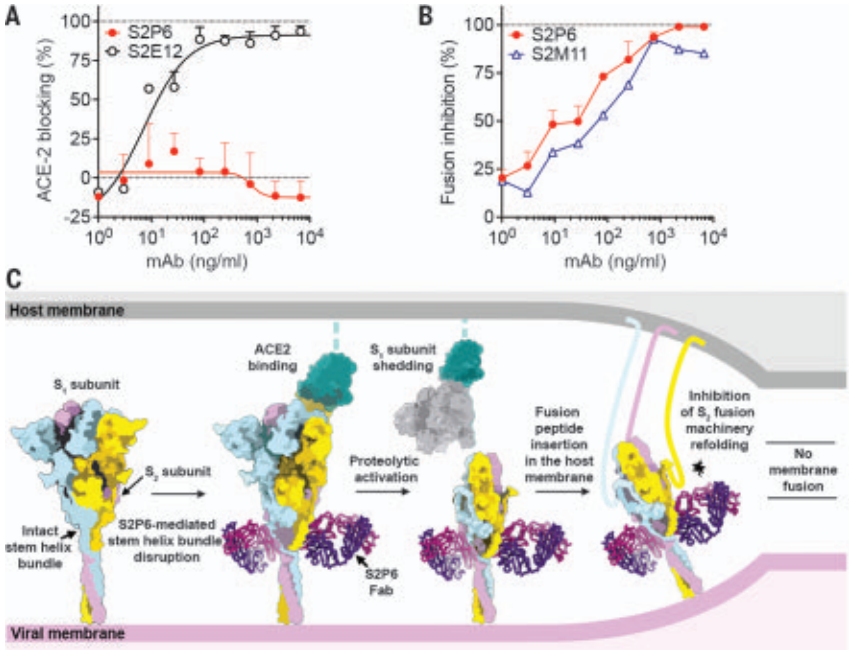


Fig. 3. S2P6 binding disrupts the stem helix bundle and sterically inhibits membrane fusion. (**A**) SARS-CoV-2 S binding to ACE2 in the presence of mAb S2P6 analyzed by ELISA. S2E12 was included as a positive control. (**B**) S2P6 inhibition of cell-cell fusion using VeroE6 cells transfected with SARS-CoV-2 S. S2M11 was included as a positive control. Inhibition of fusion values are normalized to the percentage of fusion without mAb (100%) and to that of fusion of nontransfected cells (0%). (**C**) Proposed mechanism of inhibition mediated by the S2P6 mAb. S2P6 binds to the hydrophobic core of the stem helix bundle and disrupts its quaternary structure. S2P6 binding likely prevents S_2 subunit refolding from the pre- to the postfusion state and blocks viral entry.

SARS-CoV-2 S–expressing CHO (CHO-S) as target cells (Fig. 4C). Finally, S2P6 did not promote complement-dependent cytotoxicity (CDC) (Fig. 4D), indicating that S2P6 Fc–mediated effector functions, but not CDC, might participate in viral control in vivo.

We evaluated the prophylactic activity of S2P6 against challenge with the prototypic (Wuhan-1 related) SARS-CoV-2 in a Syrian hamster model (*39*). As we previously showed that the human IgG1 Fc fragment poorly recognizes hamster FcγRs (*33*), we compared S2P6 harboring a human IgG1 constant region (Hu-S2P6) with S2P6 harboring a hamster IgG2a constant region (Hm-S2P6), the latter enabling optimal interactions with hamster FcγRs. Two different doses of Hu-S2P6 or Hm-S2P6 were administered 24 hours before intranasal SARS-CoV-2 challenge, and the lungs of the animals were assessed 4 days after infection for viral RNA load and replicating virus. Hm-S2P6 administered at 20 mg/kg reduced lung viral RNA copies and replicating viral titers by two orders of magnitude relative to a control mAb but did not exert any antiviral effect at 2 mg/kg (Fig. 4E and fig. S6). Hm-S2P6 at 20 mg/kg reduced lung viral RNA load to levels statistically significantly lower than those observed with Hu-S2P6 at 20 mg/kg, suggesting a beneficial effect of S2P6 effector functions in vivo. On the basis of the comparable S2P6 neutralization potencies toward SARS-CoV-2 VOCs observed in vitro (Fig. 1F), we assessed the protective efficacy of S2P6 in hamsters challenged with SARS-CoV-2 B.1.351 (Beta VOC). Prophylactic administration of Hu-S2P6 at 20 mg/kg reduced replicating viral titers in the lungs (but not RNA copy numbers) by ~1.5 orders of magnitude relative to the control group. Although this difference was not statistically significant, the observed efficacy against this VOC is in line with the strict conservation of the stem helix epitope in all VOCs identified to date (Fig. 4F). Collectively, these findings demonstrate that Abs targeting a highly conserved epitope in the S fusion machinery can trigger Fc-mediated ADCC and ADCP in vitro and that their in vivo antiviral activity may rely on both neutralization and effector functions.

Natural infection or vaccination predominantly elicit stem helix–directed Abs of narrow specificities

To understand how frequently stem helix–specific Abs are elicited, we analyzed plasma samples from prepandemic, COVID-19–convalescent, and COVID-19–vaccinated individuals to determine IgG binding titers to the SARS-CoV-2–SARS-CoV (SARS-CoV/-2), OC43, MERS-CoV, HKU1, HKU4, and HKU5 stem helix peptides (Fig. 5A and fig. S7). In prepandemic samples, we only observed binding to the HKU1 stem helix peptide, probably reflecting prior infection with this virus in the cohort. Stem helix–specific Abs were found at low frequencies in individuals previously infected with SARS-CoV-2 or those who had received two doses of mRNA vaccines (Fig. 5A). The highest frequencies of stem helix–specific serum Abs were observed for vaccinated individuals who were previously infected (ranging from 22 to 78% against the different stem helix peptides). Overall, these data show that plasma Ab responses to the stem helix are elicited upon SARS-CoV-2 infection or vaccination, although they are relatively rare. Evaluation of the prevalence of mAbs targeting other fusion machinery epitopes will reveal whether this trend holds true for the overall S_2 subunit or whether it is a specificity of the cryptic stem helix epitope.

Next, we investigated the frequencies of stem helix–specific memory B cells among 21 convalescent and 17 vaccinated individuals using a clonal analysis based on in vitro polyclonal stimulation (*40*) (Fig. 5, B to G, and figs. S7 to S9). In both cohorts, we observed frequencies of culture positive for stem helix–specific IgGs ranging from 0 to 2.5%, except for one individual (infected and vaccinated with a single dose of mRNA vaccine) for which 99.6% of culture supernatants were binding to the SARS-CoV/-2 stem helix (fig. S9). Most SARS-CoV-2 stem helix–specific memory B cells were cross-reactive with OC43, consistent with the high sequence identity of the stem helices of these two viruses (Fig. 5, C and F, and Fig. 1H). Abs specific for the HKU1 S stem helix were found, but they were not cross-reactive with other betacoronaviruses except for one convalescent and one vaccinated individual (Fig. 5, D and G). This analysis revealed a single example of cross-reactivity to all stem helix betacoronavirus peptides tested (Fig. 5E), whereas most other Abs show limited cross-reactivity among betacoronaviruses.

Broadly reactive betacoronavirus Abs enhance their binding affinity and cross-reactivity through somatic mutations

To define the ontogeny of the broadly reactive betacoronavirus mAbs presented here, we generated a panel of germline variants of S2P6, P34D10, P34E3, and P34G12. Two out of seven S2P6 heavy chain residues that are mutated relative to germline contribute to epitope recognition (Q32 and H57), whereas none of the five light chain mutated residues

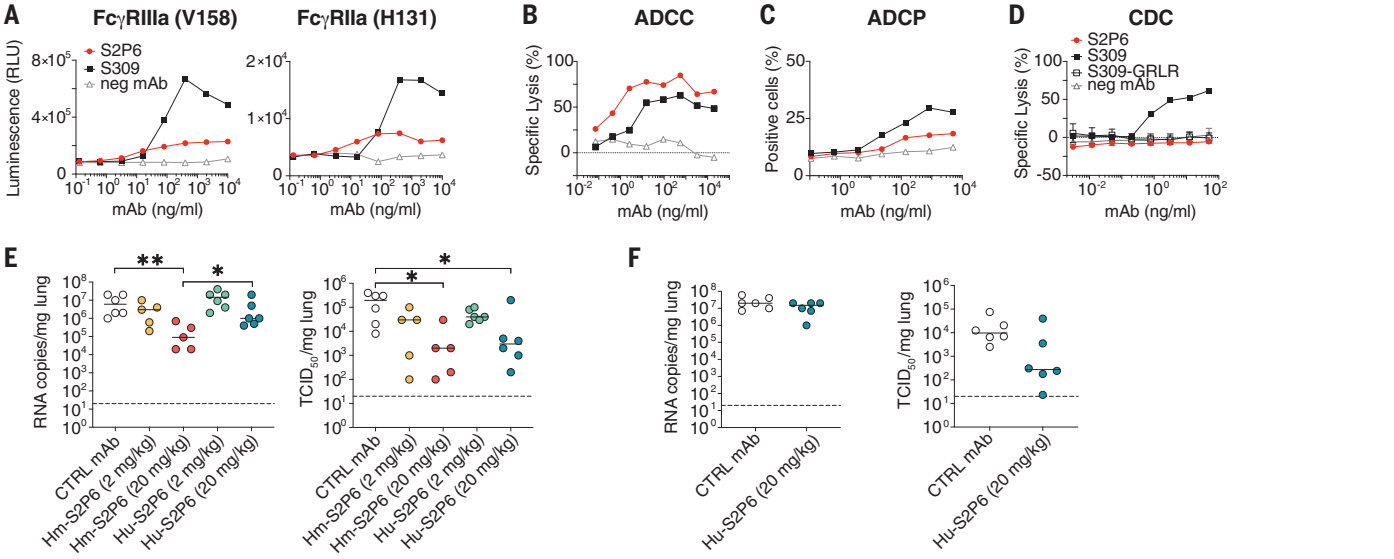


Fig. 4. S2P6 activates effector functions and reduces SARS-CoV-2 lung burden in Syrian hamsters. (**A**) NFAT (nuclear factor of activated T cells)–driven luciferase signal induced in Jurkat cells stably expressing FcγRIIIa (V158, left) or FcγRIIa (V131, right) upon S2P6 binding to full-length wild-type SARS-CoV-2 S expressed at the surface of CHO target cells. S309 is included as positive control. RLU, relative luminescence unit. (**B**) mAb-mediated ADCC using SARS-CoV-2 CHO-K1 cells (genetically engineered to stably express a HaloTag-HiBit) as target cells and PBMC as effector cells. The magnitude of natural killer cell–mediated killing is expressed as a percentage of specific lysis. (**C**) mAb-mediated ADCP using cell trace violet–labeled PBMCs as a source of phagocytic cells (monocytes) and PKH67–fluorescently labeled S-expressing CHO cells as target cells. The *y* axis indicates the percentage of monocytes double-positive for anti-CD14 (monocyte) marker and PKH67. (**D**) Lysis of SARS-CoV-2 S stably transfected CHO cells by mAbs in the presence of complement. S309 was included as positive control; S309-GRLR with diminished FcγR binding capacity and an unrelated mAb (neg mAb) were used as negative controls. (**E**) Syrian hamsters were administered with the indicated amount of S2P6 mAb harboring either a hamster (Hm-S2P6) or a human (Hu-S2P6) constant region before intranasal challenge with prototypic SARS-CoV-2 (Wuhan-1 related). An irrelevant mAb (MGH2 against *Plasmodium falciparum* CSP) at 20 mg/kg was used as negative control (CTRL) (*60*). Viral RNA loads and replicating virus titers are shown on the left and right, respectively. $TCID_{50}$, median tissue culture infectious dose. (**F**) Prophylactic administration of Hu-S2P6 at 20 mg/kg in hamsters challenged with SARS-CoV-2 B.1.351 (Beta) VOC. Viral RNA loads and replicating virus titers are shown on the left and right, respectively. **P* < 0.05; ***P* < 0.01; Mann-Whitney test.

participate in S binding (Fig. 2, C and D). To address the role of VH and VK somatic mutations, we generated a panel of S2P6 germline variants for the heavy or the light chain, or both variable regions (VH and VK). The fully germline-reverted S2P6 [unmutated common ancestor (UCA)] bound to OC43 and MERS-CoV stem helix peptides [with approximately one order of magnitude higher median effective concentration (EC_{50}) compared with that of the mature mAb] but did not bind to SARS-CoV/-2 or HKU1 stem helix peptides or spike trimers (Fig. 5H and fig. S10, A to C). Somatic mutations in VH were sufficient for high-avidity binding to SARS-CoV/-2, whereas both VH and VK mutations were required for optimal binding to HKU1. The presence of residue G103 in CDRH3 was essential for binding to all betacoronaviruses (fig. S10, A to C). These findings indicate that the S2P6 mAb likely arose in response to OC43 infection, and its specificity was broadened toward SARS-CoV-2 and HKU1 through somatic mutations selected upon natural infection with one or both of these betacoronaviruses. By contrast, analysis of UCA binding of the clonally related P34D10, P34G12, and P34E3 mAbs suggests that they were likely primed by HKU1 infection rather than OC43 infection and acquired cross-reactivity toward the other human betacoronaviruses primarily through somatic mutations in VH (Fig. 5I and fig. S10, D to F). Collectively, these findings demonstrate that broadly reactive betacoronavirus Abs may result from priming of virus-specific B cells gaining affinity and cross-reactivity through somatic mutations in response to heterotypic coronavirus exposures.

Discussion

The coronavirus S_2 subunit (fusion machinery) contains several conserved antigenic sites, including the fusion peptide and the heptad-repeat 2 regions (*41*–*46*). The recent identification of four cross-reactive mAbs targeting the stem helix in the S_2 subunit highlighted the importance of this epitope, which is conserved among betacoronavirus but not alphacoronavirus S glycoproteins (*14*–*16*, *47*), although none of these mAbs inhibit members of all three betacoronavirus subgenera. Here, we identified five stem helix–specific human mAbs cross-reacting with human and animal betacoronaviruses and showed that S2P6 broadly neutralized all sarbecoviruses, merbecoviruses, and embecoviruses pseudotypes evaluated through the inhibition of membrane fusion.

We show that an S_2 subunit–directed mAb reduces lung viral burden in hamsters challenged with SARS-CoV-2 with a key contribution of Fc-mediated effector functions, as described for some SARS-CoV-2 RBD-specific mAbs (*34*, *37*) and influenza virus hemagglutinin stem mAbs (*17*, *48*, *49*). Although this study showcases the stem helix as a target of pan-betacoronavirus Abs, the existence of other cross-reactive S_2 epitopes with neutralizing potential remains a subject of investigation. Stem helix–targeted Abs are elicited upon natural infection by endemic (OC43 or HKU1) or pandemic (SARS-CoV-2) coronaviruses as well as by COVID-19 mRNA vaccines. Similarly to the subdominance of Abs recognizing the conserved hemagglutinin stem region of influenza A viruses (*48*, *50*), stem helix–specific Abs are present at low titers in convalescent or vaccinee plasma and at low frequencies in their memory B cell repertoires, possibly as a result of limited epitope exposure. These findings along with the moderate neutralization potency of these mAbs indicate that eliciting high-enough titers of stem helix–targeted mAbs through vaccination will be a key challenge to overcome to develop pan-betacoronavirus vaccines. We propose that harnessing recent advances in computational protein design, such as epitope-focused vaccine design approaches as described for the respiratory syncytial virus fusion protein (*51*–*53*) and multivalent display as described for influenza virus (*54*–*59*) to target

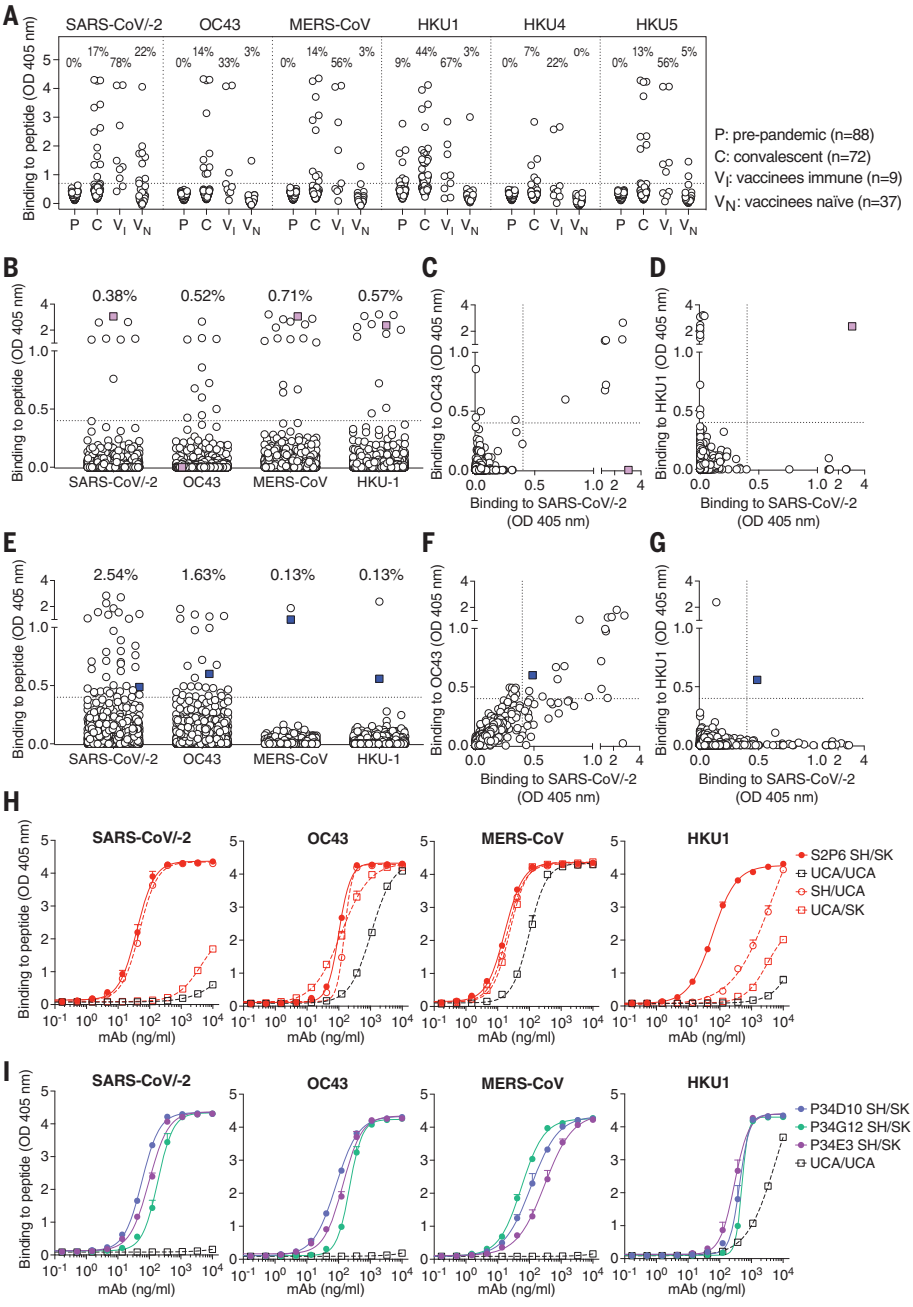


Fig. 5. Stem helix–directed Abs are rare, of narrow specificities, and enhance their binding affinity and cross-reactivity through somatic mutations. (**A**) Binding of prepandemic (P; *n* = 88), COVID-19 convalescent (C; *n* = 72), vaccinees immune (VI; *n* = 9), and vaccinees naïve (VN; *n* = 37) plasma Abs (diluted 1:10) to immobilized betacoronavirus stem helix peptides analyzed by ELISA. A cutoff of 0.7 was determined on the basis of the signal of prepandemic samples and binding to uncoated ELISA plates (horizontal dashed line). The fraction of samples for which binding above the cutoff was detected is indicated. (**B** to **G**) Analysis of memory B cell specificities for betacoronavirus stem helix peptides. Each dot represents a well containing oligoclonal B cell supernatant screened for the presence of stem helix peptide binding IgG Abs using ELISA. Samples obtained from 21 COVID-19 convalescent individuals [(B) to (D)] and 16 vaccinees [(E) to (G)]. Pairwise reactivity comparison is shown for SARS-CoV/-2 and OC43 [(C) and (F)] and SARS-CoV/-2 and HKU1 [(D) and (G)]. Cultures cross-reactive with at least three peptides are highlighted in color. A cutoff of 0.4 is indicated by a horizontal dashed line. The fraction of wells for which binding above the cutoff was detected is indicated. (**H** and **I**) Binding to stem helix peptides of S2P6 (H) harboring mature (SH/SK), fully germline-reverted (UCA/UCA), germline-reverted heavy chain paired with mature light chain (UCA/SK), mature heavy chain paired with germline-reverted light chain (SH/UCA), and of P34D10, P34G12, and P34E3 (I) harboring either mature (SH/SK) or germline-reverted (UCA/UCA) sequences.

the S stem helix or the fusion peptide regions, might enable elicitation of broad betacoronavirus immunity.

REFERENCES AND NOTES

1. M. A. Tortorici, D. Veesler, *Adv. Virus Res.* **105**, 93–116 (2019).
2. A. C. Walls *et al.*, *Cell* **181**, 281–292.e6 (2020).
3. D. Wrapp *et al.*, *Science* **367**, 1260–1263 (2020).
4. E. C. Thomson *et al.*, *Cell* **184**, 1171–1187.e20 (2021).
5. M. McCallum *et al.*, *Cell* **184**, 2332–2347.e16 (2021).
6. K. R. McCarthy *et al.*, *Science* **371**, 1139–1142 (2021).
7. B. Choi *et al.*, *N. Engl. J. Med.* **383**, 2291–2293 (2020).
8. Z. Liu *et al.*, *Cell Host Microbe* **29**, 477–488.e4 (2021).
9. Y. Weisblum *et al.*, *eLife* **9**, e61312 (2020).
10. M. McCallum *et al.*, *Science* **373**, 648–654 (2021).
11. A. C. Walls *et al.*, *Cell* **176**, 1026–1039.e15 (2019).
12. Y. Watanabe, J. D. Allen, D. Wrapp, J. S. McLellan, M. Crispin, *Science* **369**, 330–333 (2020).
13. Y. Yang *et al.*, *J. Virol.* **89**, 9119–9123 (2015).
14. M. M. Sauer *et al.*, bioRxiv 2020.12.29.424482 [Preprint] (2021). https://doi.org/10.1101/2020.12.29.424482.
15. C. Wang *et al.*, *Nat. Commun.* **12**, 1715 (2021).
16. G. Song *et al.*, *Nat. Commun.* **12**, 2938 (2021).
17. N. L. Kallewaard *et al.*, *Cell* **166**, 596–608 (2016).
18. B. F. Haynes, D. R. Burton, J. R. Mascola, *Sci. Transl. Med.* **11**, eaaz2686 (2019).
19. Z. Wang *et al.*, *Nature* **592**, 616–622 (2021).
20. L. Piccoli *et al.*, *Cell* **183**, 1024–1042.e21 (2020).
21. M. A. Tortorici *et al.*, *Science* **370**, 950–957 (2020).
22. M. Hoffmann *et al.*, *Nature* **585**, 588–590 (2020).
23. M. Hoffmann *et al.*, *Cell* **181**, 271–280.e8 (2020).
24. M. Hoffmann, H. Kleine-Weber, S. Pöhlmann, *Mol. Cell* **78**, 779–784.e5 (2020).
25. Y. Kaname *et al.*, *J. Virol.* **84**, 3210–3219 (2010).
26. J. B. Case *et al.*, *Cell Host Microbe* **28**, 475–485.e5 (2020).
27. M. Gui *et al.*, *Cell Res.* **27**, 119–129 (2017).
28. R. N. Kirchdoerfer *et al.*, *Sci. Rep.* **8**, 15701 (2018).
29. Y. Yuan *et al.*, *Nat. Commun.* **8**, 15092 (2017).
30. A. C. Walls *et al.*, *Proc. Natl. Acad. Sci. U.S.A.* **114**, 11157–11162 (2017).
31. Y. Cai *et al.*, *Science* **369**, 1586–1592 (2020).
32. X. Fan, D. Cao, L. Kong, X. Zhang, *Nat. Commun.* **11**, 3618 (2020).
33. F. A. Lempp *et al.*, bioRxiv 2021.04.03.438258 [Preprint] (2021). https://doi.org/10.1101/2021.04.03.438258.
34. A. Schäfer *et al.*, *J. Exp. Med.* **218**, e20201993 (2021).
35. S. Bournazos, T. T. Wang, J. V. Ravetch, *Microbiol. Spectr.* **4**, 4.6.20 (2016).
36. S. Bournazos, D. Corti, H. W. Virgin, J. V. Ravetch, *Nature* **588**, 485–490 (2020).
37. E. S. Winkler *et al.*, *Cell* **184**, 1804–1820.E16 (2021).
38. D. Pinto *et al.*, *Nature* **583**, 290–295 (2020).
39. R. Boudewijns *et al.*, *Nat. Commun.* **11**, 5838 (2020).
40. D. Pinna, D. Corti, D. Jarrossay, F. Sallusto, A. Lanzavecchia, *Eur. J. Immunol.* **39**, 1260–1270 (2009).
41. C. Daniel *et al.*, *J. Virol.* **67**, 1185–1194 (1993).
42. H. Zhang *et al.*, *J. Virol.* **78**, 6938–6945 (2004).
43. C. M. Poh *et al.*, *Nat. Commun.* **11**, 2806 (2020).
44. H. A. Elshabrawy, M. M. Coughlin, S. C. Baker, B. S. Prabhakar, *PLOS ONE* **7**, e50366 (2012).
45. Z. Zheng *et al.*, *Euro Surveill.* **25**, 2000291 (2020).
46. A. C. Walls *et al.*, *Nature* **531**, 114–117 (2016).
47. P. Zhou *et al.*, bioRxiv 2021.03.30.437769 [Preprint] (2021). https://doi.org/10.1101/2021.03.30.437769.
48. D. Corti *et al.*, *Science* **333**, 850–856 (2011).
49. D. J. DiLillo, G. S. Tan, P. Palese, J. V. Ravetch, *Nat. Med.* **20**, 143–151 (2014).
50. D. Corti *et al.*, *J. Clin. Invest.* **120**, 1663–1673 (2010).
51. F. Sesterhenn *et al.*, *Science* **368**, eaay5051 (2020).
52. M. L. Azoitei *et al.*, *Science* **334**, 373–376 (2011).
53. B. E. Correia *et al.*, *Nature* **507**, 201–206 (2014).
54. A. C. Walls *et al.*, *Cell* **183**, 1367–1382.e17 (2020).
55. A. C. Walls *et al.*, bioRxiv 2021.03.15.435528 [Preprint] (2021). https://doi.org/10.1101/2021.03.15.435528.
56. S. Boyoglu-Barnum *et al.*, *Nature* **592**, 623–628 (2021).
57. M. Kanekiyo *et al.*, *Nature* **499**, 102–106 (2013).
58. M. Kanekiyo *et al.*, *Nat. Immunol.* **20**, 362–372 (2019).
59. J. Marcandalli *et al.*, *Cell* **176**, 1420–1431.e17 (2019).
60. J. Tan *et al.*, *Nat. Med.* **24**, 401–407 (2018).

ACKNOWLEDGMENTS

We thank J. C. Nix for x-ray data collection, T. I. Croll for assistance in refinement of the crystal structure, A. Arvin for her insightful comments, M. Meury for help with protein production, and H. Tani (University of Toyama) for providing the reagents necessary for preparing VSV pseudotyped viruses. The authors would also like to

thank C. Castado and N. Blais (GSK Vaccines) for their help in the selection of the genetically divergent sarbecoviruses used in this study. We thank Promega Corporation for kindly providing SARS-CoV-2 CHO-K1 cells (genetically engineered to stably express a HaloTag-HiBit-tagged). **Funding:** This study was supported by the National Institute of Allergy and Infectious Diseases (DP1AI158186 and HHSN272201700059C to D.V. and U01 AI151698-01 to WCVV), a Pew Biomedical Scholars Award (D.V.), Investigators in the Pathogenesis of Infectious Disease Awards from the Burroughs Wellcome Fund (D.V.), Fast Grants (D.V.), the Swiss National Science Foundation (P400PB_183942 to M.M.S.), the University of Washington Arnold and Mabel Beckman cryo-EM center, Vir Biotechnology, and the Helmut Horten Foundation (to F.S. and the Institute for Research in Biomedicine). The project was also partially funded by the Swiss Kidney Foundation. Use of the Stanford Synchrotron Radiation Lightsource, SLAC National Accelerator Laboratory, is supported by the US Department of Energy, Office of Science, Office of Basic Energy Sciences, under contract no. DE-AC02-76SF00515. The SSRL Structural Molecular Biology Program is supported by the DOE Office of Biological and Environmental Research and by the National Institutes of Health, National Institute of General Medical Sciences (P30GM133894). The contents of this publication are solely the responsibility of the authors and do not necessarily represent the official views of NIGMS or NIH. **Author contributions:** Experiment design: D.P., M.M.S., J.S.L., M.A.T., M.S.P., H.W.V., M.B., D.C., and D.V.; Donors' recruitment and sample collection: E.C., F.B., B.G., A.Ce., P.F., P.E.C., O.G., S.C., C.G., A.R., L.P., M.S., D.V., and C.H.-D.; Antibody discovery: D.P., M.B., J.S.L., J.J., S.J., N.S., K.C., E.C., and D.C.; Antigen-specific memory B cell repertoire analysis preparation: C.S.-F., J.B., and A.Ca.; Expression and purification of proteins: A.C.W., J.E.B., and J.J.; Antibody functional experiments: D.P., M.M.S., N.C., J.S.L., M.A.T., A.C.W., F.A.L., J.No., S.B., and R.M.; Bioinformatic analysis of virus diversity and variants: J.d.I., I.B., and A.T.; Evaluation of effector functions: B.G.; SPR binding assays: L.E.R.; Neutralization assay: D.P., M.A.T., F.A.L., J.No., and M.P.H.; Escape mutants selection and sequencing: H.K., S.I., F.A.L., and J.d.I.; Effects in the hamster model and data analysis: R.A., C.F., L.C., J.Ne., E.V., and F.B.; Cryo-EM data collection, processing, and model building: M.M.S. and D.V.; Crystallization, x-ray crystallography data collection, processing, and model building: M.M.S., N.C., G.S., and D.V.; Serological assays: D.P. and R.M.; Data analysis: D.P., M.M.S., M.B., J.S.L., J.J., F.A.L., J.No., N.C., A.T., A.C.W., G.S., D.C., and D.V.; Manuscript writing: D.P., M.M.S., J.S.L., M.B., G.S., F.S., A.L., H.W.V., D.C., and D.V. **Competing interests:** D.P., N.C., M.P.H., J.No., B.G., L.E.R., J.d.I., H.K., S.I., S.J., N.S., K.C., I.B., S.B., C.S.-F., J.B., R.M., E.V., F.B., E.C., L.P., M.S.P., M.S., D.H., A.T., F.A.L., C.H.-D., A.L., G.S., H.W.V., M.B., and D.C. are employees of Vir Biotechnology and may hold shares in Vir Biotechnology. D.C., J.S.L., F.S., A.Ca., and A.L. are currently listed as inventors on multiple patent applications, which disclose the subject matter described in this manuscript. D.V. is a consultant for Vir Biotechnology Inc. The Veesler laboratory and the Sallusto laboratory have received sponsored research agreements from Vir Biotechnology Inc. The other authors declare no competing interests. **Data and materials availability:** The crystal structure of S2P6-bound SARS-CoV-2 stem helix peptide was deposited to the Protein Data Bank (PDB) with accession no. 7RNJ. The cryo-EM structure of SARS-CoV-2 spike protein bound to the S2P6 and S2M11 Fab fragments was deposited to the Electron Microscopy Data Bank with accession no. EMD-24533. Materials generated in this study will be made available on request but may require a completed materials transfer agreement signed with Vir Biotechnology or the University of Washington. This work is licensed under a Creative Commons Attribution 4.0 International (CC BY 4.0) license, which permits unrestricted use, distribution, and reproduction in any medium, provided the original work is properly cited. To view a copy of this license, visit https://creativecommons.org/licenses/by/4.0/. This license does not apply to figures/photos/artwork or other content included in the article that is credited to a third party; obtain authorization from the rights holder before using such material.

SUPPLEMENTARY MATERIALS

science.sciencemag.org/content/373/6559/1109/suppl/DC1
Materials and Methods
Figs. S1 to S10
Tables S1 and S2
References (*61*–*86*)
MDAR Reproducibility Checklist

6 May 2021; accepted 29 July 2021
Published online 3 August 2021
10.1126/science.abj3321

REPORTS

CLIMATE DYNAMICS

Linking Arctic variability and change with extreme winter weather in the United States

Judah Cohen[1,2]*, Laurie Agel[3], Mathew Barlow[3], Chaim I. Garfinkel[4], Ian White[4]

The Arctic is warming at a rate twice the global average and severe winter weather is reported to be increasing across many heavily populated mid-latitude regions, but there is no agreement on whether a physical link exists between the two phenomena. We use observational analysis to show that a lesser-known stratospheric polar vortex (SPV) disruption that involves wave reflection and stretching of the SPV is linked with extreme cold across parts of Asia and North America, including the recent February 2021 Texas cold wave, and has been increasing over the satellite era. We then use numerical modeling experiments forced with trends in autumn snow cover and Arctic sea ice to establish a physical link between Arctic change and SPV stretching and related surface impacts.

Anthropogenic global warming is projected to increase some weather extremes—for example, more heat waves and heavy precipitation events (*1*, *2*)—but not severe winter weather such as cold air outbreaks and heavy snowfalls (*3*, *4*). Yet, contrary to global climate model (GCM) projections, recent weather extremes have included an increase in cold air outbreaks and/or heavy snowfalls across the Northern Hemisphere (NH) since 1990 up to the recent past (*3*, *5*–*8*). The most recent example of extreme winter weather was the anomalous cold weather of January and February 2021 in Asia (*9*), Europe (*10*, *11*), and especially the United States (US). The US Southern Plains cold wave of February 2021 may be exceptional in the observational record for the region based on the aggregate severity of the cold intensity, cold duration, and widespread disruptive snowfall (*12*, *13*). The collapse of the Texas energy infrastructure could make it the state's costliest natural disaster, even more so than previous hurricanes (*14*) and at least twice as costly as the entire record-breaking North Atlantic 2020 hurricane season (*15*). This event has reignited the debate whether climate change contributes to more severe winter weather (*16*).

One of the more robust signatures of global warming is accelerated Arctic warming, known as Arctic amplification (AA) (*17*), which has been evident since the 1990s (*5*). AA is both a response to and accelerator of Arctic sea ice decline, with the greatest losses observed in the Barents–Kara and Chukchi–Bering Seas in the fall and winter (*8*). AA has also coincided with increasing snow fall and snow cover at high latitudes, including across Eurasia during October through January (*18*–*21*), in part due to the decline in sea ice, which increases moisture availability in the Arctic (*18*, *21*). In figs. S1 and S2, we show that Eurasian October snow cover has increased, whereas fall Arctic sea ice has decreased over the satellite and AA periods.

A hypothesis that has received much recent attention is that AA is driving winter mid-latitude cooling (*7*, *22*, *23*). One theory that links less sea ice and/or more Eurasian snow cover to severe winter weather in the mid-latitudes involves a pathway through the SPV (*5*, *24*). Less sea ice and more snow cover increase the probability of a stronger Siberian high-pressure ridge and upward atmospheric wave energy flux. Increased wave flux from the troposphere to the stratosphere can result in a sudden stratospheric warming (SSW) characterized by large rises in polar geopotential heights centered over the North Pole, often followed by an increase in NH severe winter weather (*3*). However, whether AA can result in more severe winter weather, and how, is a matter of active debate (*25*–*29*).

Kretschmer *et al.* (*30*) used a machine learning (ML) technique to demonstrate that the weakest SPV state (SSWs) are increasing in frequency, whereas the strongest SPV states are decreasing in January and February over the period of AA. In a follow-up study, the same ML technique identified a less-known SPV disruption whereby the SPV is stretched (*31*) (P4 in Fig. 1) as opposed to the well-known SSW (P5 in Fig. 1). One important difference between SSWs and SPV stretching is that the vertical component of atmospheric wave energy known as wave activity flux (WAF_z) or Eliassen Palm (EP) flux preceding SSWs converges in the polar stratosphere, resulting in

[1]Atmospheric and Environmental Research, Inc., Lexington, MA 02421, USA. [2]Department of Civil and Environmental Engineering, Massachusetts Institute of Technology, Cambridge, MA 02139, USA. [3]Department of Environmental, Earth, and Atmospheric Sciences, University of Massachusetts Lowell, Lowell, MA, USA. [4]The Hebrew University of Jerusalem, Institute of Earth Sciences, Edmond J. Safra Campus, Jerusalem, Israel.
***Corresponding author. Email: jcohen@aer.com**

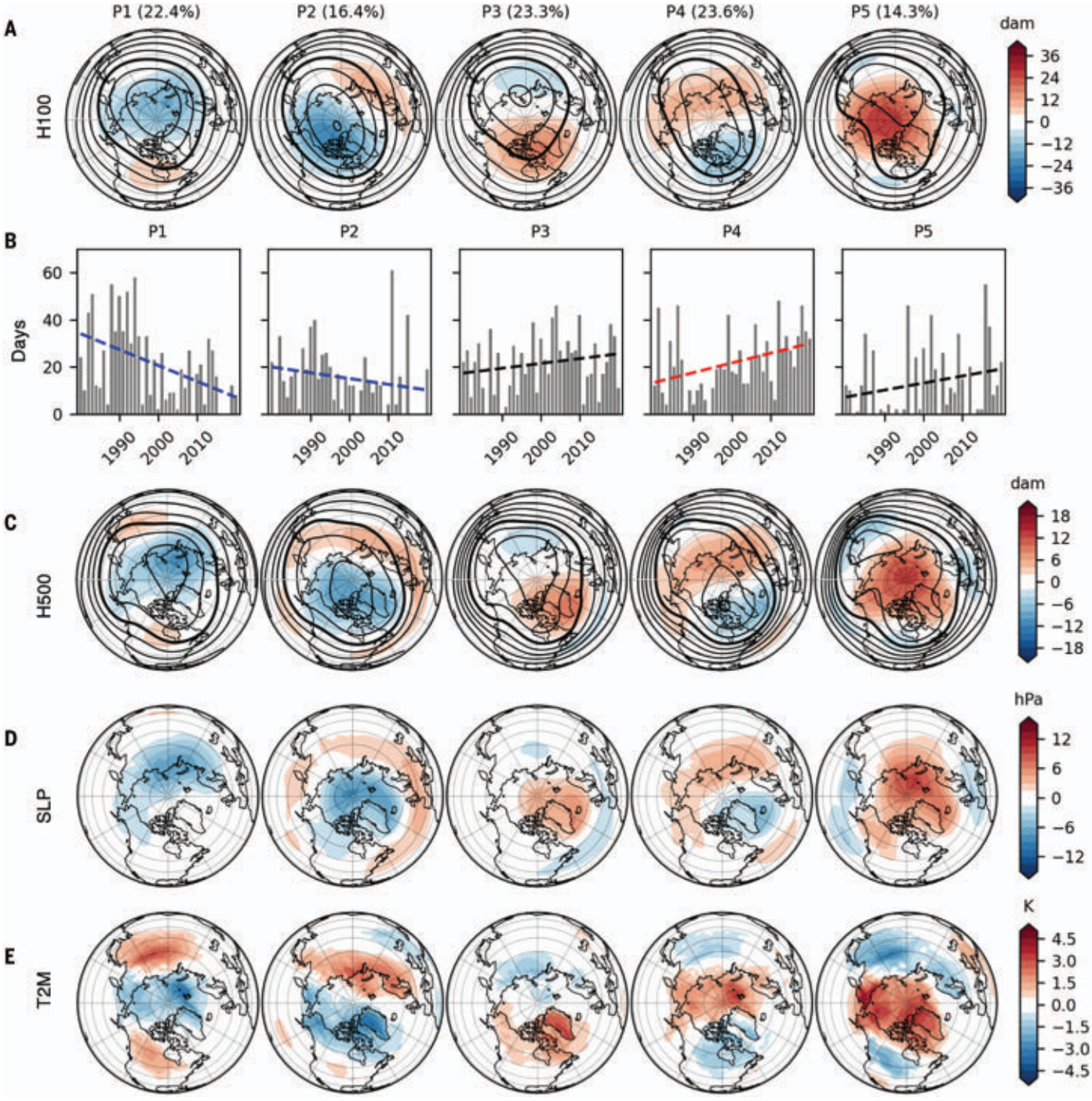


Fig. 1. Five major patterns of stratospheric polar vortex variability for the months October through December. (**A**) 100-hPa geopotential height composites [contours in 20-decameter (dam) intervals, anomalies shaded, and 1580-dam contour bolded] for pattern days P1 to P5. Percentage of days assigned to the pattern is indicated in parentheses. (**B**) Yearly frequency of (left to right) P1–P5 pattern days (gray bars), with dashed lines showing linear trend (blue if statistically significant negative trend, red if significant positive trend, and black otherwise). Statistical significance is at the 0.05 level, as determined by the Wald test with t-distribution of the test statistic. Composites for (left to right) P1–P5 pattern days of (**C**) 500-hPa geopotential heights (in decameters, with anomalies shaded and 540-dam contour bolded), (**D**) mean sea-level pressure (SLP) anomalies (hPa), and (**E**) 2-m surface temperature anomalies (K). Monthly data are for the years 1980 through 2020.

rapid warming and rising of geopotential heights in the stratosphere, whereas during SPV stretching, WAF_z is reflected from the SPV back into the troposphere (and is therefore also referred to as "reflective" events) (*32*–*34*), where it amplifies the climatological pressure ridge and trough across North America. A second important difference is that North American cold spells tend to be more extreme following SPV stretching events (*31*).

Here we expand the analysis of SPV variability and its tropospheric links to include fall and early winter, which identifies trends and links to surface snow and ice changes in the high latitudes that are consistent with surface forcing

of the SPV variability. We then use modeling experiments to establish a causal link between the surface changes and the SPV variability and its tropospheric links and, therefore, between AA and extreme mid-latitude winter weather.

We extend the ML technique of Kretschmer *et al.* (*30*, *31*) to analyze SPV variability in fall and early winter (October through December) over the reanalysis period (1980 through early 2021), shown in Fig. 1 [in fig. S3, we update the January and February analysis of Kretschmer *et al.* (*31*)]. The first two clusters (P1 and P2 in Fig. 1) show a stronger-than-normal SPV (i.e., lower geopotential heights), and the last two (P4 and P5) show a weaker-than-normal SPV (i.e., higher geopotential heights in the polar stratosphere). The stronger SPV states are experiencing a statistically significant decreasing trend in frequency, whereas the weaker SPV states are experiencing a statistically significant increasing trend, not only for January and February but also for the preceding months of October through December (fig. S4). Here we show that SPV stretching disruptions (P4) have a statistically significant increasing trend in both fall and winter, even more so than SSWs over the reanalysis period, and are increasing for the months October through February (fig. S5).

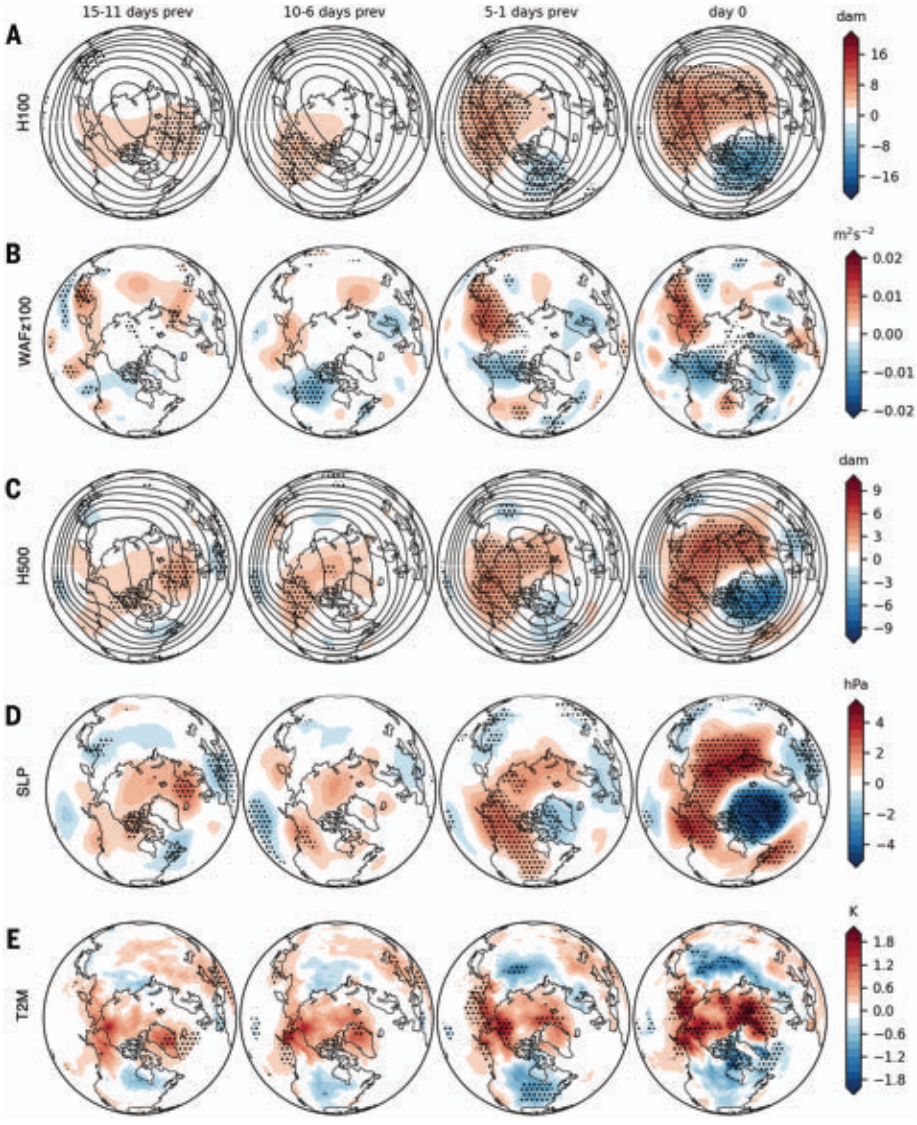


Fig. 2. Lower-stratospheric and tropospheric precursor patterns to SPV stretching events. Composite fields of (left to right) days 15 to 11, days 10 to 6, days 5–1, and day 0 before start of all P4 events for (**A**) 100-hPa geopotential height (dam, contours in 20-dam intervals, anomalies shaded), (**B**) 100-hPa vertical WAF or Plumb flux anomalies ($m^2\ s^{-2}$, positive values are upward), (**C**) 500-hPa geopotential height (dam, contours, with anomalies shaded), (**D**) mean sea-level pressure anomalies (hPa), and (**E**) 2-m surface temperature anomalies (K). P4 events are defined as one or more consecutive P4 days. Stippling indicates regions where precursor composite is statistically significant at the 0.05 level based on random sampling from a full set of days for October to December 1980 to 2020, using a sample size equal to the number of P4 events.

The concurrent surface temperature anomalies are presented in Fig. 1E. The two strong SPV states exhibit a cold Arctic–warm continent pattern and the two weak SPV states exhibit a warm Arctic–cold continent pattern. Specifically, for the two weak states, SSWs (P5) are related to warming around Greenland and Baffin Bay, whereas SPV stretching (P4) is related to Arctic warming focused in the Barents–Kara and Chukchi–Bering Seas. In the mid-latitudes, both SSWs and SPV stretching are associated with relatively cold temperatures across Northern Europe, Northern and Eastern Asia, and North America; however, during SPV stretching, North American cold temperatures are more widespread and shifted eastward. It has already been shown that SSWs are contributing to an observed cooling trend across northern Eurasia for the two winter months of January and February (*30*, *35*), but our analysis suggests that an increasing number of SPV stretching events are a cooling influence across North America.

The tropospheric precursor pattern to SSWs has been previously identified as consisting of relatively high pressure across Northern Europe and the Urals coupled with relatively low pressure across East Asia into the northern North Pacific (*30*, *36*, *37*). This anomalous dipole projects onto the climatological standing wave-1 of the NH (*36*–*38*), and through constructive interference gives rise to an enhanced WAF_z from the troposphere to the stratosphere. Although anomalous vertical wave energy flux has also been shown to precede SPV stretching disruptions (*31*), other precursor features in the tropospheric circulation to these events have not yet been examined.

The precursor patterns to SPV stretching events are shown in Fig. 2. At 100 hPa in the lower stratosphere (Fig. 2A), there are regional ridging and positive height anomalies, which begin over the North Atlantic and then migrate to the Gulf of Alaska, Alaska, Chukchi–Barents–Kara Seas, and the Urals. The ridging amplifies shortly before and up until the time of the event (day 0). In addition, prior to SPV stretching, there is a WAF_z dipole (Fig. 2B) with positive anomalies in Eastern Siberia and negative anomalies in northwest North America (similar to Kretschmer *et al.*) (*31*). Climatologically, WAF_z is upward over Siberia, reflected in the stratosphere, and then downward over Canada (*31*). The low and mid-troposphere precursor patterns (Fig. 2, C and D) project onto the climatological NH standing wave-2 (*36*, *37*). Finally, the observed precursors in surface temperature (Fig. 2E) begin as positive anomalies in the Arctic focused near Greenland and to a lesser extent in the Chukchi Sea. However, shortly before and at the time of the event, two regions of positive anomalies emerge—one over the North Atlantic side of the Arctic and a second over Alaska and

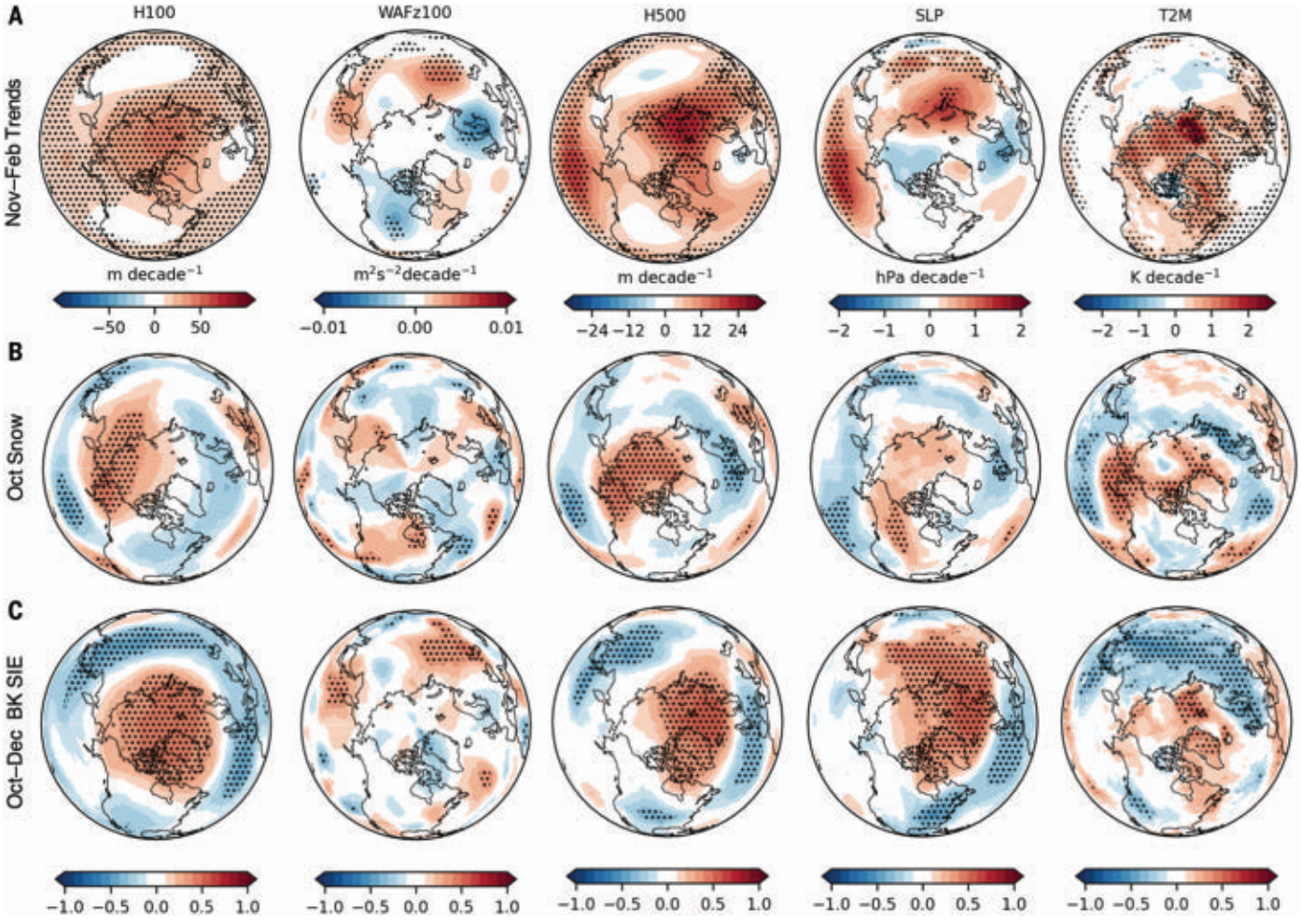


Fig. 3. Lower-stratospheric and tropospheric trends in late fall and early winter project onto SPV stretching precursors. (**A**) Trends in (left to right) 100-hPa geopotential heights (m decade^{-1}), 100-hPa vertical WAF or Plumb flux (m^2 s^{-2} decade^{-1}), 500-hPa geopotential heights (m decade^{-1}), mean sea-level pressure (hPa decade^{-1}), and 2-m surface temperature (K decade^{-1}) for the period November to February 1980 to 2021. (**B**) Correlation between detrended October Eurasian snow cover extent and same fields as in (A) but for November to January 1980 to 2021. (**C**) Correlation between detrended October to December Barents–Kara sea ice concentration and same fields as in (A) but for December to February 1980 to 2021. For all panels, stippling indicates regions with statistical significance at the 0.05 level based on the t-distribution.

Chukchi–Bering Seas region of even greater amplitude and extent, whereas negative temperature anomalies emerge first in Siberia but then also develop over North America.

Could climate change have contributed to the observed increasing trends in the SPV stretching events that force cold to extreme cold in North America and East Asia? In Fig. 3, we show the trends (1980–2021) in the late fall and winter months of the same variables used to identify the precursors to SPV stretching events. Trends in lower stratospheric WAF_z exhibit the same dipole associated with SPV stretching events, with positive trends over Siberia and negative trends over northwest North America (10 to 0 days previous; Fig. 2B). At the surface and 500-hPa mid-to-high latitudes, increasing trends in pressure and geopotential heights are centered on the Barents–Kara Seas and Urals with a secondary maximum in the Gulf of Alaska and Alaska region, which matches what is observed in the precursors to SPV stretching (15 to 0 days previous; Fig. 2, C and D). Surface temperatures have been rising most strongly in the Arctic with two maximum centers, one in the North Atlantic side of the Arctic and the other in the Chukchi–Bering Seas, similar to the observed Arctic warming prior to SPV stretching events (15 to 0 days previous; Fig. 2E). There is some weak cooling in Asia. Projections of the seasonal and monthly (October through February) SPV stretching precursors (Fig. 3A and fig. S6) onto the trends are statistically significant (figs. S7 and S8), especially relatively warm surface temperatures in the Barents–Kara and Chukchi–Bering Seas, and ridging and high pressure at 500 hPa and at the surface in the Barents–Kara Seas and Urals and to a lesser extent, the northern North Pacific.

We complete our observational analysis by correlating leading Eurasian snow cover and Arctic sea ice concentration with the lagging atmospheric fields analyzed for trends (Fig. 3, B and C; with all time series detrended). The correlations with snow cover (Fig. 3B) most closely resemble SPV stretching precursors (Fig. 2), with ridging centered near Alaska and downstream troughing over eastern North America and into the North Atlantic and Europe (the correlation between snow and SPV stretching frequency is statistically significant). By contrast, correlations with Barents–Kara sea ice (Fig. 3C) most closely resemble the observed trends, especially the pan-Arctic geopotential height rises in the lower stratosphere (100 hPa) and pressure ridging from the Urals to Greenland at 500 hPa (correlations between ice with SSW frequency and ice with SPV stretching frequency are both found to be significant),

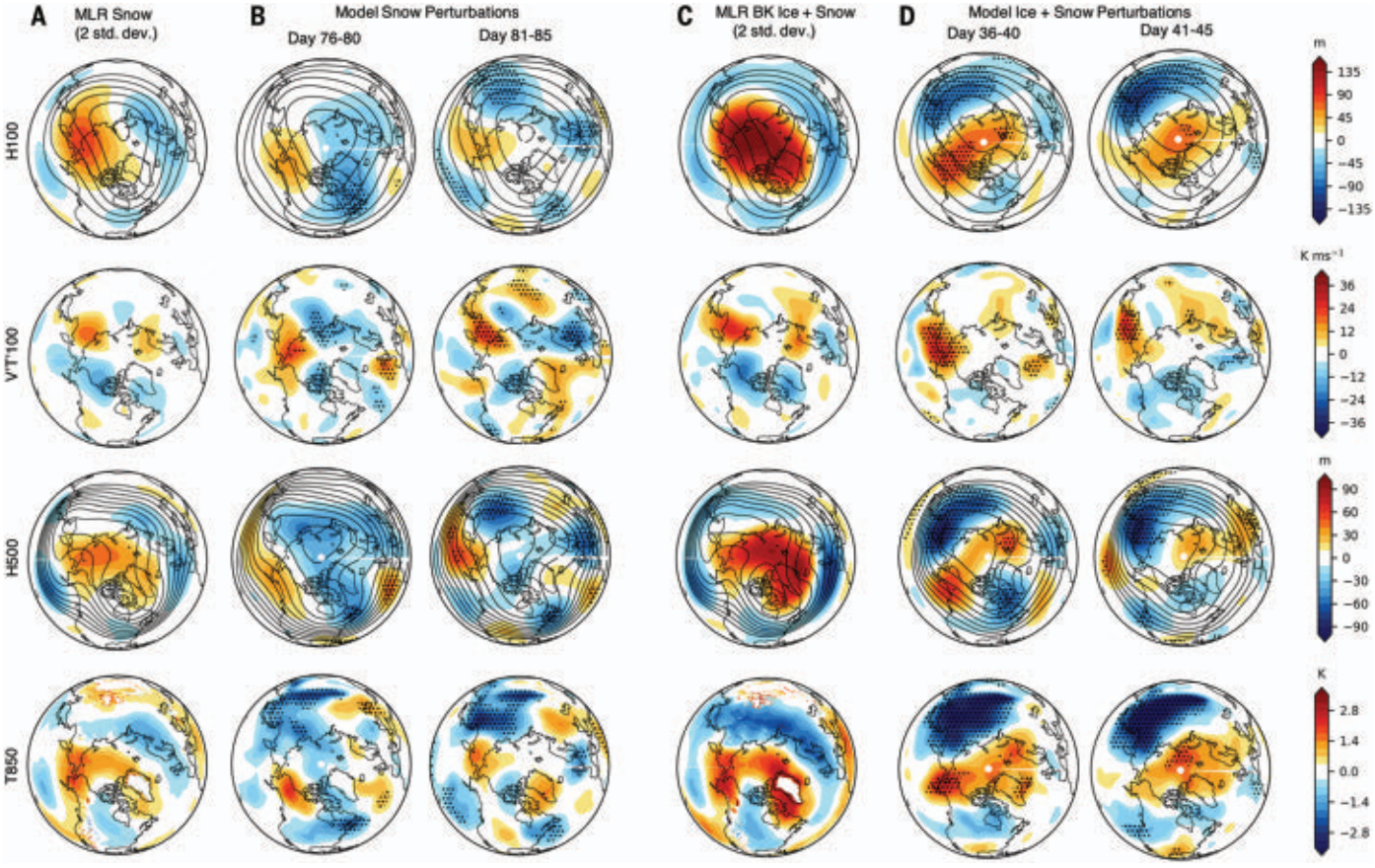


Fig. 4. The atmospheric response to a model forced with increased snow cover and sea ice loss resembles atmospheric anomalies associated with SPV stretching events. (**A**) Linear regression using observations between detrended October Eurasian snow cover extent with (top to bottom) detrended 100-hPa geopotential heights (m), 100-hPa meridional heat transport (K ms^{-1}), 500-hPa geopotential heights (m), and 850-hPa temperature (K) for December to February 1980 to 2021. (**B**) Composite difference between control run and snow forcing for (left to right) days 76 to 80 and 81 to 85 after model initialization of (top to bottom) 100-hPa geopotential height (m), 100-hPa meridional heat transport (K ms^{-1}), 500-hPa geopotential height (m), and 850-hPa temperature (K). (**C**) Multilinear regression (regression using multiple predictors) using observations between detrended October Eurasian snow cover extent and October to December Barents–Kara sea ice concentration with same fields as in (A). (**D**) Composite difference between control run and both Barents–Kara sea ice and Eurasian snow forcing for (left to right) days 36 to 40 and 41 to 45 days after model initialization of the (top to bottom) same fields as in (B). Stippling in (B) and (D) indicates regions with statistical significance at the 0.05 level based on the t-distribution. For (A to D), 100- and 500-hPa geopotential height panels also show contours of the full field.

more reminiscent of the atmospheric response to SSWs (Fig. 1C for P5). Despite the statistically significant correlations, it is a challenge to demonstrate cause and effect with observational analysis alone.

To more directly assess the physical links, we conducted numerical modeling experiments related to both increased Eurasian snow cover and reduced sea ice, using a simplified GCM. This kind of model is well-suited for isolating the atmospheric response to idealized heating perturbations (*39*) (see materials and methods).

To simulate the observed trend of more extensive October Eurasian snow cover (fig. S2), the model was forced with increased surface albedo (fig. S9). About 2 months after the forcing Is imposed, the model response shows features that resemble the circulation anomalies associated with SPV stretching events, including a stretched SPV, the lower stratospheric dipole in poleward heat transport (a good proxy for WAF_z), the mid-troposphere ridging and warm anomalies in Alaska and the Bering Sea, and troughing and cool anomalies in East Asia and eastern North America (see Fig. 4B and fig. S10B for comparison with the stretched SPV pattern from cluster analysis in Fig. 2). The simulated atmospheric response to snow cover forcing is of comparable magnitude to the atmospheric response inferred from observational analysis (Fig. 4A), though in many previous GCM snow sensitivity experiments, the simulated response is weaker (*40*).

Because Barents–Kara sea ice shows a strong observational relationship with Ural mid-tropospheric ridging and downstream East Asian troughing (Fig. 3C) that projects strongly onto the precursor pattern of SPV stretching events (Fig. 2C), we further forced the GCM with anomalous heating in the Barents–Kara Seas during October through December where ice loss is observed (figs. S2 and S9). The simulated atmospheric response to both snow and ice forcing (Fig. 4D) exhibits a pattern similar to the correlations between sea ice, with ridging and warming centered in the Barents–Kara Seas at 100, 500, and 850 hPa and troughing and cooling in East Asia in the mid-to-low troposphere (Fig. 3C). In addition, the model forced with both snow and ice anomalies includes anomalous ridging and warming in the Chukchi–Bering seas at 500 and 850 hPa and accelerates the model response to Arctic changes by about a month. The simulated atmospheric response to the combined forcing of snow and ice is of comparable magnitude but somewhat weaker than the inferred response from observational analysis but still larger than many previous GCM studies (*3*, *41*).

We also examine the regression of Eurasian snow cover (Fig. 4A) and multiple regression of snow and Barents–Kara sea ice (Fig. 4C) with the atmospheric circulation. Correlations

with snow cover exhibit anomalous ridging and warming focused on the North Pacific side of the Arctic from the surface to the lower stratosphere. Therefore, the atmospheric response to snow-cover-only forcing better matches the atmospheric anomalies associated with SPV stretching events than the atmospheric response to sea-ice-only forcing, where the anomalous ridging and warming are either focused in the Barents–Kara Seas or are pan-Arctic. However, when including both snow and ice, the atmospheric response in both observations and in the model better matches full Arctic trends, and the model atmospheric response of SPV stretching is more persistent, with anomalous troughing and relatively cold temperatures in North America persisting for more than 3 weeks (days 36 to 60; fig. S11). Both observational analysis and modeling experiments show that Chukchi–Bering sea ice loss has little impact on the SPV, consistent with previous studies (*42*); however, the tropospheric response to Chukchi–Bering sea ice loss can amplify (based on observations, fig. S12) or force anomalous Alaska ridging and warming with downstream anomalous North American troughing and cooling (fig. S13). Although Chukchi–Bering sea ice loss may not force SPV disruptions, it could amplify the tropospheric response across Asia and North America (*43*).

Finally, we examined the recent winter of 2020–2021 for stretching SPV events. We applied our clustering technique to observed 100-hPa geopotential heights in January and February 2021. Though our analysis shows that January 2021 was dominated by P5, it identifies P4 for more than 60% of the days from 29 January through 15 February. Also, in early February, WAF_z was upward over Siberia and downward over Canada, consistent with SPV stretching events, as opposed to convergence in the stratosphere (consistent with SSW events), as observed in early January prior to an SSW on 5 January (fig. S14). Though the SSW observed in January may have also contributed to the hemispheric pattern in February, our analysis supports that the historic February (approximately 6 to 21) 2021 Texas cold wave was likely the response to the SPV stretching in February, and the atmospheric circulation can be seen transitioning from circulation anomalies associated with SSWs to those associated with SPV stretching from late January through early February (fig. S15).

In this analysis, we have demonstrated that SPV stretching events have accelerated in the era of AA. Climate change in general, but Arctic change in particular, is favorable for forcing these events. In fig. S16, we provide a generalized timeline of the principal atmospheric features beginning with Ural ridging, followed by North Pacific ridging and ending with North American and East Asian cold. It is argued that warming in the Barents–Kara and Chukchi–Bering Seas favor anomalous ridging and high pressure in these regions in the troposphere (*3*, *8*, *43*). Autumn Siberian snowfall has also been increasing (*21*), favoring anomalous troughing over East Asia. This pattern of ridging in the Urals and Barents–Kara Seas region and troughing in East Asia strongly projects onto the tropospheric pattern favorable for forcing SPV stretching that often delivers extreme cold to Canada and the United States. This interpretation is supported by a GCM forced with increased Eurasian snow cover and decreased Barents–Kara sea ice, where the atmospheric response is an increase in SPV stretching events with troughing and colder temperatures across Asia and North America 1 to 2 months after the introduction of Arctic forcing. Therefore, Arctic change is likely contributing to the increasing frequency of SPV stretching events, including one just prior to the Texas cold wave of February 2021.

These results have important societal implications. First, they highlight an important type of stratosphere-troposphere coupling, SPV stretching, that has been mostly hidden in the heretofore primary focus on SSWs, even though the impact of SPV stretching events on North American temperatures can be of greater extent and magnitude (*31*). Second, the identification of the precursor pattern to stretching events can potentially extend the warning lead time of cold extremes in Asia, Canada, and the United States. Third, our analysis is informative for policy-makers. Preparing for only a decrease in severe winter weather can compound the human and economic cost when severe winter weather does occur, as exemplified during the Texas cold wave of February 2021.

REFERENCES AND NOTES

1. D. Coumou, S. Rahmstorf, *Nat. Clim. Chang.* **2**, 491–496 (2012).
2. D. Coumou, J. Lehmann, J. Beckmann, *Science* **348**, 324–327 (2015).
3. J. Cohen *et al*., *Nat. Clim. Chang.* **10**, 20–29 (2020).
4. W. S. Ashley, A. M. Haberlie, V. A. Gensini, *Nat. Clim. Chang.* **10**, 539–544 (2020).
5. J. Cohen *et al*., *Nat. Geosci.* **7**, 627–637 (2014).
6. J. Cohen, K. Pfeiffer, J. A. Francis, *Nat. Commun.* **9**, 869 (2018).
7. J. E. Overland *et al*., *J. Clim.* **28**, 7917–7932 (2015).
8. J. E. Overland *et al*., *Environ. Res. Lett.* **16**, 043002 (2021).
9. F. Zheng *et al*., *Adv. Atmos. Sci.* (2021).
10. www.euronews.com/2021/01/07/spain-records-coldest-ever-temperature-at-35-8-c
11. www.dw.com/en/german-village-logs-289-celsius-overnight-as-cold-snap-persists/a-56576765
12. https://twitter.com/capitalweather/status/1364681912728621057 and https://www.washingtonpost.com/weather/2021/02/24/texas-winter-storm-temperature-records/?arc404=true
13. J. Doss-Gollin, D. J. Farnham, U. Lall, V. Modi, *Environ. Res. Lett.* **16**, 064056 (2021).
14. https://www.texastribune.org/2021/02/25/texas-winter-storm-cost-budget/
15. https://www.accuweather.com/en/winter-weather/damages-from-feb-snowstorms-could-be-as-high-as-155b/909620
16. https://www.nytimes.com/2021/02/18/briefing/texas-blackouts-mars-rover-cuomo-new-york.html
17. M. Serreze, A. Barrett, J. Stroeve, D. Kindig, M. Holland, *Cryosphere* **3**, 11–19 (2009).
18. J. Cohen, J. Jones, J. C. Furtado, E. Tziperman, *Oceanography* **26**, 150–160 (2013).
19. M. Wegmann, M. Roher, M. Santolaria-Otín, G. Lohmann, *Earth Syst. Dyn.* **11**, 509–524 (2020).
20. Z. Lü, F. Li, Y. J. Orsolini, Y. Gao, S. He, *J. Clim.* **33**, 527–545 (2020).
21. M. Wegmann *et al*., *Environ. Res. Lett.* **10**, 054015 (2015).
22. T. Vihma, *Surv. Geophys.* **35**, 1175–1214 (2014).
23. R. L. Newson, *Nature* **241**, 39–40 (1973).
24. J. Zhang, W. Tian, M. Chipperfield, F. Xie, J. Huang, *Nat. Clim. Chang.* **6**, 1094–1099 (2016).
25. E. Kintisch, *Science* **344**, 250–253 (2014).
26. C. Gramling, *Science* **347**, 818–821 (2015).
27. J. M. Wallace, I. M. Held, D. W. J. Thompson, K. E. Trenberth, J. E. Walsh, *Science* **343**, 729–730 (2014).
28. T. G. Shepherd, *Science* **353**, 989–990 (2016).
29. R. J. Blackport, A. Screen, K. van der Wiel, R. Bintanja, *Nat. Clim. Chang.* **9**, 697–704 (2019).
30. M. Kretschmer *et al*., *Bull. Am. Meteorol. Soc.* **99**, 49–60 (2018a).
31. M. Kretschmer, J. Cohen, V. Matthias, J. Runge, D. Coumou, *Atmos. Sci.* **1**, 1–10 (2018b).
32. K. Kodera, H. Mukougawa, S. Itoh, *Geophys. Res. Lett.* **35**, L16806 (2008).
33. K. Kodera, H. Mukougawa, A. Fujii, *J. Geophys. Res. Atmos.* **118**, 8333–8345 (2013).
34. D. Nath, W. Chen, L. Wang, Y. Ma, *Adv. Atmos. Sci.* **31**, 851–862 (2014).
35. C. I. Garfinkel, S. W. Son, K. Song, V. Aquila, L. D. Oman, *Geophys. Res. Lett.* **44**, 374–382 (2017).
36. O. Martius, L. M. Polvani, H. C. Davies, *Geophys. Res. Lett.* **36**, L14806 (2009).
37. C. Garfinkel, D. Hartmann, F. Sassi, *J. Clim.* **23**, 3282–3299 (2010).
38. K. Smith, P. J. Kushner, J. Cohen, *J. Clim.* **24**, 6185–6202 (2011).
39. P. Maher *et al*., *Rev. Geophys.* **57**, 250–280 (2019).
40. G. R. Henderson, Y. Peings, J. C. Furtado, P. J. Kushner, *Nat. Clim. Chang.* **8**, 954–963 (2018).
41. M. Kretschmer, G. Zappa, T. G. Shepherd, *Weather Clim. Dynam* **1**, 715–730 (2020).
42. C. M. McKenna, T. J. Bracegirdle, E. F. Shuckburgh, P. H. Haynes, M. M. Joshi, *Geophys. Res. Lett.* **44**, (2017).
43. J.-S. Kug *et al*., *Nat. Geosci.* **8**, 759–762 (2015).
44. I. P. White, C. I. Garfinkel, M. Jucker, E. P. Gerber, ianpwhite/MiMA: MiMA: Applying stratospheric heating perturbations (MiMA-ThermalForcing-v1.0beta), Zenodo (2021); https://doi.org/10.5281/zenodo.4523199.
45. C. I. Garfinkel, I. P. White, E. P. Gerber, M. Jucker, M. Erez, *J. Clim.* **33**, 5611–5633 (2020).

ACKNOWLEDGMENTS

We thank three anonymous reviewers whose efforts resulted in a substantially improved manuscript. J.C. thanks M. Kretschmer and S. Kazuyuki, whose creativity as graduate students made this study possible. **Funding:** J.C. is supported by the National Science Foundation grant PLR-1901352. L.A. and M.B. received supported from NSF AGS-1657921 and NOAA NA20OAR4310424. C.I.G. and I.W. acknowledge the support of a European Research Council starting grant under the European Union Horizon 2020 research and innovation programme (grant agreement no. 677756). **Author contributions:** Conceptualization: J.C. Methodology: J.C., M.B., L.A., C.I.G. Investigation: J.C., M.B., L.A., C.I.G., I.W. Figures: J.C., L.A., C.I.G. Supervision: J.C. Writing – original draft: J.C. Writing – review and editing: J.C., M.B., L.A., C.I.G., I.W. **Competing interests:** None for all the authors. **Data and materials availability:** Observational analysis was performed with MERRA2: available at https://gmao.gsfc.nasa.gov/reanalysis/MERRA-2/. NOAA Snow cover extent is available at http://climate.rutgers.edu/snowcover/index.php and Arctic sea ice concentration is available at www.metoffice.gov.uk/hadobs/hadisst/. The version of MiMA used in this study can be downloaded from https://github.com/ianpwhite/MiMA/releases/tag/MiMA-ThermalForcing-v1.0beta and Zenodo (*44*). The version of MiMA used in this study follows that used in Garfinkel *et al*. (*45*) albeit with the albedo and ocean heat-flux modifications as listed in the materials and methods. MiMA v2.0 can be downloaded from https://github.com/mjucker/MiMA.

SUPPLEMENTARY MATERIALS

science.sciencemag.org/content/373/6559/1116/suppl/DC1
Materials and Methods
Figs. S1 to S16
References (*46*–*68*)

8 April 2021; accepted 3 August 2021
10.1126/science.abi9167

SUPERCONDUCTIVITY

Discovery of mesoscopic nematicity wave in iron-based superconductors

T. Shimojima[1]*†, Y. Motoyui[2]†, T. Taniuchi[2,3], C. Bareille[2,3], S. Onari[4], H. Kontani[4], M. Nakajima[5], S. Kasahara[6]‡, T. Shibauchi[7], Y. Matsuda[6], S. Shin[2,3,8]*

Nematicity is ubiquitous in the electronic phases of iron-based superconductors. The order parameter that characterizes the nematic phase has been investigated in momentum space, but its real-space arrangement remains largely unexplored. We use linear dichroism (LD) in a low-temperature laser–photoemission electron microscope to map out the nematic order parameter of nonmagentic FeSe and antiferromagnetic $BaFe_2(As_{0.87}P_{0.13})_2$. In contrast to structural domains, which have atomic-scale domain walls, the LD patterns in both materials show peculiar sinusoidal waves of electronic nematicity with wavelengths more than 1000 times as long as the unit cell. Our findings put strong constraints on the theoretical investigation of electronic nematicity.

Electronic nematicity (*1*), a spontaneous breaking of the fourfold (C_4) rotational symmetry, has been observed in high–transition temperature (T_c) superconductors, such as cuprates (*2*, *3*) and iron-based superconductors (IBSCs) (*4*, *5*). The nematicity has been suggested to be closely linked to the pseudogap state in cuprates (*6*) and the formation of Cooper pairs in IBSCs (*7*). In IBSCs, the electronic instabilities caused by spin and orbital degrees of freedom can induce lattice distortion from tetragonal to orthorhombic structure at T_s, referred to as nematic order (*8*). FeSe and $BaFe_2(As_{1-x}P_x)_2$ (AsP122) are representative of IBSCs exhibiting nematic order. The former shows nematicity without any long-range magnetic order (*9*) (Fig. 1A), whereas the latter exhibits a nematic order slightly above the antiferromagnetic (AFM) order (T_N) (*10*) (Fig. 1B).

Electronic nematicity in IBSCs is associated with the anisotropy of the in-plane band structure near the Fermi level (E_F), composed of multiple Fe 3d orbitals (*11*). As depicted in Fig. 1C, C1, the hole bands around Γ have *xz* and *yz* orbital components, which are energetically degenerate in the tetragonal state (*12*). In the nematic state, the energy level of the *xz* band (E_{xz}) is ~10 meV higher than that of the *yz* orbital (E_{yz}) at Γ (*13*–*15*), which gives rise to the orbital polarization in the electronic density of states (DOS) (Fig. 1C, C2). Anisotropy in in-plane physical properties has also been reported from the transport (*4*) and nematic susceptibility measurements (*7*, *16*), suggesting that the nematicity is electronic in origin (*8*, *17*). In real space, optical microscopy measurements (*18*–*20*) reported nematic domains of 10 to 100 μm that coincided with the locations of local strain (*19*) and orthorhombic

[1]RIKEN Center for Emergent Matter Science (CEMS), Wako 351-0198, Japan. [2]Institute for Solid State Physics (ISSP), The University of Tokyo, Kashiwa 277-8581, Japan. [3]Material Innovation Research Center (MIRC), The University of Tokyo, Kashiwa, Chiba 277-8561, Japan. [4]Department of Physics, Nagoya University, Furo-cho, Nagoya 464-8602, Japan. [5]Department of Physics, Osaka University, Toyonaka, Osaka 560-0043, Japan. [6]Department of Physics, Kyoto University, Kyoto 606-8502, Japan. [7]Department of Advanced Materials Science, The University of Tokyo, Kashiwa 277-8561, Japan. [8]Office of University Professor, The University of Tokyo, Kashiwa, Chiba 277-8581, Japan.
***Corresponding author. Email: takahiro.shimojima@riken.jp (T.S.); shin@issp.u-tokyo.ac.jp (S.S.)**
†These authors contributed equally to this work.
‡Present address: Research Institute for Interdisciplinary Science, Okayama University, 3-1-1 Tsushimanaka, Kita-ku, Okayama 700-8530, Japan.

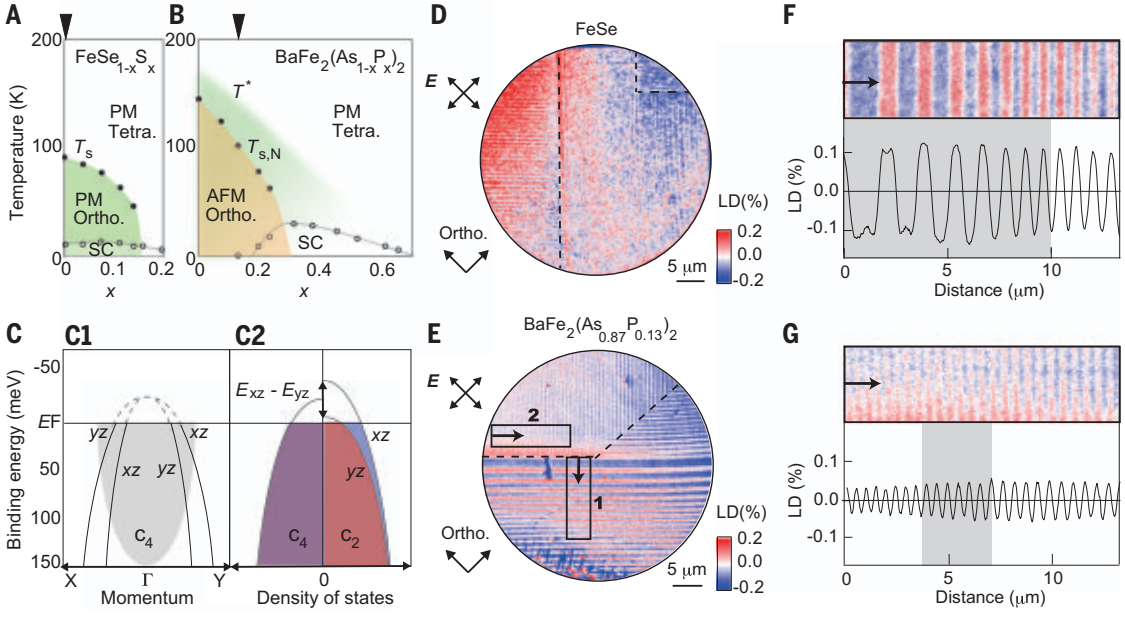


Fig. 1. Laser-based LD-PEEM in the nematic ordered state. (**A** and **B**) Phase diagrams of $FeSe_{1-x}S_x$ (*34*) and $BaFe_2(As_{1-x}P_x)_2$ (*10*) systems. Triangles indicate the compositions studied in this work. T^* indicates the temperature at which the system starts to show C_2-symmetric physical properties (*5*, *23*). PM, paramagnetic; SC, superconducting; Tetra., tetragonal; Ortho., orthorhombic. (**C**) (C1) Schematics of fourfold symmetric band structure around Γ of IBSCs (*12*). For the photoemission with low photon energy (4.66 eV), the observable energy-momentum region is limited around the Fermi level ($E_F < E < 150$ meV) and Γ (from -0.2 Å$^{-1} < k < 0.2$ Å^{-1}) as indicated by the gray area. (C2) Schematics of the partial DOS for *xz* and *yz* orbtials around Γ in the tetragonal (C_4) and nematic ordered state (C_2). (**D** and **E**) LD images obtained by the laser linearly polarized along the orthorhombic axes for FeSe at 11 K and $BaFe_2(As_{0.87}P_{0.13})_2$ at 65 K, respectively. Thick dashed lines represent the boundary at which the stripe patterns are rotated by 90°. (**F** and **G**) LD images and integrated LD signals of rectangles 1 and 2 in (E), respectively. We analyzed the integrated LD signals in the gray regions, as indicated in Fig. 2, D and E.

domains (*18*, *20*). Although these studies provided an overall picture of electronic nematicity, its spatial variation on a nanometer scale has been unclear. Here, we report a real-space visualization of the nematic order parameter on the crystal surface of FeSe and under-doped AsP122 by employing linear dichroism (LD) mapping in high-resolution laser–photoemission electron microscopy (PEEM) (*21*) down to lowest temperatures.

By employing LD in laser-PEEM, we map the amplitude of the orbital polarization between *xz* and *yz* around Γ, owing to the selection rules (*12*). The LD signal is detected by taking the difference between the PEEM images obtained by laser beams whose polarization directions are parallel and perpendicular to the orthorhombic axes. As shown in Fig. 1, D and E, the LD images clearly reveal complex stripe patterns in the paramagnetic (PM)–nematic state of FeSe and the AFM-nematic state of $BaFe_2(As_{0.87}P_{0.13})_2$, covering the entire field of view. By inspecting the LD signals integrated in the selected LD images in Fig. 1, F and G, we find characteristic spatial variations. Near the boundaries at which the stripe patterns are rotated by 90° (thick dashed lines in Fig. 1, D and E), plateaus appear at the maximum and minimum of the LD signal (left region of Fig. 1F). Away from the boundaries, the period of the signal becomes shorter, and the plateaus gradually disappear, leading to a sinusoidal wave–like profile (right region of Fig. 1F). The amplitude of the LD signal is reduced in the region where the wavelength is shorter, as shown in Fig. 1G and fig. S1 (*12*). These peculiar features are commonly observed for $BaFe_2(As_{0.87}P_{0.13})_2$ and FeSe (fig. S2) (*12*).

To understand these features, we consider two scenarios—electron density waves and nematic domain walls. The former naturally explains the sinusoidal waveform in the LD signal. However, within this picture it is difficult to understand the plateaus and the period ranging from 400 to 1300 nm (fig. S1) (*12*). By contrast,

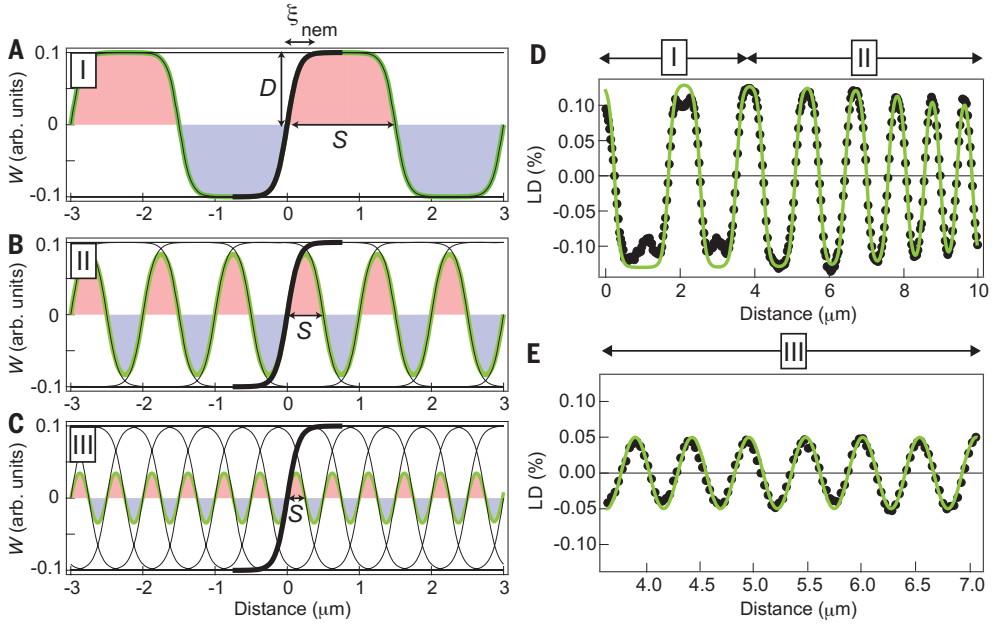


Fig. 2. Fitting analysis of the LD signals in $BaFe_2(As_{0.87}P_{0.13})_2$. (**A** to **C**) Simulations of the LD signals (green curves) based on a model that assumes a train of nematic domain walls $W(x) = D\tanh[x/2\xi_{nem}]$ (black curves) with domain-wall intervals S = 1500, 500, and 250 nm, respectively. D and ξ_{nem} are set to 0.1 and 500 nm, respectively. arb. units, arbitrary units. (**D**) Fitting analysis on the LD signal in the gray region of Fig. 1F. The green curve represents the fitting function composed of the nematic domain walls with D = 0.13, ξ_{nem} = 450 nm, and $S(x)$ ranging from 400 to 1400 nm. (**E**) The same as (D) but in the gray region of Fig. 1G. The parameters were set to D = 0.13, ξ_{nem} = 450 nm, and S = 260 nm.

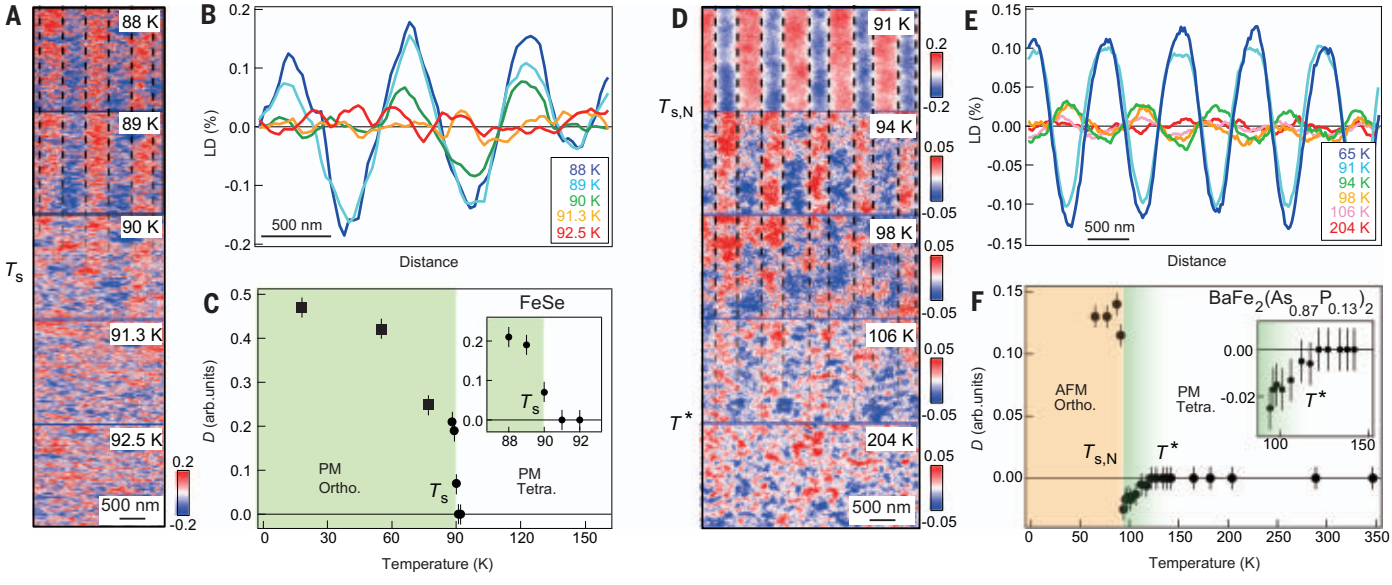


Fig. 3. Temperature dependence of the LD signal. (**A** and **B**) Temperature dependence of the LD image (A) and integrated LD signal across T_s (90 K) (B) for FeSe. Dotted lines in (A) indicate the nodal positions of the nematicity wave. (**C**) Temperature dependence of the nematic domain wall height (D) extracted from the fitting analysis. (**D** to **F**) The same as (A) to (C) but for $BaFe_2(As_{0.87}P_{0.13})_2$ ($T_{s,N}$ = 93 K).

for the latter scenario, the complex stripe patterns (Fig. 1, D and E) are naturally understood because of a resemblance to the orthorhombic twinned domains (*18*). Here, we show that this phenomenological model consistently explains the spatial variations in the waveform, period, and amplitude of the LD signals.

We assume a nematic domain wall much thicker than the typical orthorhombic twin boundary (TB) [5 nm in (*22*)]. According to the Ginzburg-Landau theory (*12*), the profile of the nematic domain wall can be expressed as $W(x) = D\tanh[x/2\xi_{nem}]$. The nematic domain wall has an intrinsic height D and coherence length ξ_{nem}, both of which are assumed to be the same on the entire crystal surface, as indicated by the thick black curves in Fig. 2, A to C. In this picture, the plateaus in the LD signal show up if the nematic domain wall interval [$S(x)$] is larger than ~$3\xi_{nem}$ (Fig. 2A, case I). As $S(x)$ decreases (~ξ_{nem}), neighboring domain walls are partially merged and then become nearly equivalent to a sinusoidal wave (Fig. 2B, case II). When $S(x)$ becomes comparable to $\xi_{nem}/2$, the LD amplitude starts to decrease while keeping the sinusoidal waveform (Fig. 2C, case III).

The LD signals in the gray areas of Fig. 1, F and G, are well fitted by the nematic domain wall model. By setting common parameters of D = 0.13 and ξ_{nem} = 450 nm, the fitting function composed of the train of nematic domain walls with $S(x)$ ranging from 400 to 1400 nm (green curve in Fig. 2D) reproduced the plateaus and sinusoidal waveform in the LD signal (fig. S3) (*12*), corresponding to case I and case II, respectively. The low-amplitude LD signal in Fig. 2E is also reproduced by the nematic domain wall model with D = 0.13, ξ_{nem} = 450 nm, and S = 260 nm (corresponding to case III). The green curve composed of the nematic domain walls in Fig. 2E is equivalent to a sinusoidal wave with the wavelength of $2S(x)$. For FeSe, the LD signals can also be well fitted by the nematic domain wall model with coherence length ξ_{nem} = 550 nm (fig. S2) (*12*). These results suggest that the observed peculiar sinusoidal LD signals (nematicity wave) can be attributed to nematic domain walls with a material-dependent mesoscopic coherence length.

Although the shape and the period of the LD signals in FeSe and $BaFe_2(As_{0.87}P_{0.13})_2$ bear a close resemblance to each other, they exhibit notable differences in their temperature (T) dependence. In FeSe, which has no AFM order, the LD signals disappear at T_s (90 K), and no discernible periodic signal is observed above T_s, as shown by the LD images (Fig. 3A) and the integrated LD signals (Fig. 3B). As depicted in Fig. 3C, D obtained from the fitting analysis (figs. S4 and S5) (*12*) rapidly increases below T_s, as expected from the evolution of the *xz*/*yz* orbital polarization at Γ detected by bulk-sensitive laser–angle-resolved photoemission spectroscopy (ARPES) (fig. S6) (*12*), which is consistent with the second-order tetragonal-to-orthorhombic phase transition (*9*). In stark contrast to FeSe, the amplitude of the LD signal for $BaFe_2(As_{0.87}P_{0.13})_2$ remains finite even above $T_{s,N}$ = 93 K. The most notable feature is that the sign of the LD signal is reversed at $T_{s,N}$, although the wavelength and its nodal positions are unchanged with T, as indicated by the dotted lines in Fig. 3D and crossing points of the LD signals in Fig. 3E. Figure 3F indicates the T evolution of D showing a characteristic T where the LD signals start to appear below $T^* \approx 120$ K. Previous experimental studies have shown that the 122 systems exhibit the signatures of the electronic nematicity even above $T_{s,N}$. The LD signal at $T_{s,N} < T < T^*$ can be attributed to the lifting of the degeneracy of the *xz*/*yz* orbital bands as probed by ARPES on $BaFe_2As_2$ (*15*) and the AsP122 system (*23*). In torque magnetometry data on $BaFe_2(As_{0.86}P_{0.14})_2$, the C_2 component appears at temperatures similar to T^* (*5*). The sign change across $T_{s,N}$ may be caused by $(\pi,0)$ band folding because of the AFM order, which induces large inequivalency in the partial DOS between *xz* and *yz* electrons (*24*). These results suggest that the LD signals in both materials reflect the electronic nematicity in bulk crystals, regardless of the presence or absence of the AFM order.

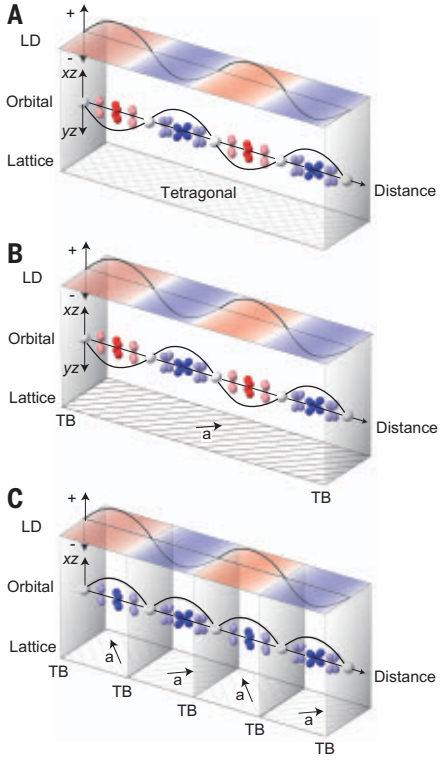


Fig. 4. Real-space scenarios for the sinusoidal LD signals. (**A**) Schematics for the sinusoidal LD signal at $T_s < T < T^*$. Blue and red orbitals represent the *xz*- and *yz*-dominated electronic states at Γ, respectively. (**B** and **C**) Same as (A) but at $T < T_s$ for the cases with and without correspondence between the locations of TBs and nodes of sinusoidal LD signal, respectively. The orthorhombic axes are rotated by 90° at the TB. *x*, *y*, and *z* are coordinates along the crystal axes of the orthorhombic setting *a*, *b*, and *c*, respectively.

A salient feature is that the LD signal of $BaFe_2(As_{0.87}P_{0.13})_2$ shows up at $T_{s,N} < T < T^*$. For an ideal tetragonal lattice, an oscillating LD signal can be interpreted as the alternation of *xz*-dominated ($E_{xz} - E_{yz} > 0$) and *yz*-dominated ($E_{xz} - E_{yz} < 0$) electronic states (Fig. 4A). In real materials, short-range orthorhombic distortion detected above T_s (*5*, *25*–*27*) might be coupled to the nematicity wave. As T decreases below T_s, orthorhombic TBs appear to relax the lattice distortion. If the TB does not locate at each node of the nematicity wave, a sinusoidal LD signal can be interpreted by the sinusoidal modulation between *xz*-dominated ($E_{xz} - E_{yz} > 0$) and *yz*-dominated ($E_{xz} - E_{yz} < 0$) electronic states within a single orthorhombic domain (Fig. 4B). This situation is compatible with the characteristic dimension of the orthorhombic domain pattern on the order of 10 μm reported from optical measurements (*18*–*20*). Within this picture, the *xz*/*yz* orbital polarization can change sign without the change in the sign of orthorhombicity, challenging our understanding of the interplay between the orbital and elastic degrees of freedom (*8*, *17*). Alternatively, we consider the scenario in which each TB corresponds to a nematic domain wall (Fig. 4C). In this case, the orbital polarization should have the same sign in the orthorhombic setting of each domain (blue orbital in Fig. 4C), given that the orthorhombic axes are rotated by 90° across the TB. We emphasize that regardless of interpretation, the observation of the mesoscopic nematicity wave suggests a nematic order parameter that exhibits high stiffness against real-space modulation and unusual decoupling from the lattice. To arrive at the correct real-space picture, experimental investigation of the orthorhombic domains with nanometer resolution will be important.

The interval of the nematic domain walls is determined by the repulsive force between each wall, which is expected to depend on the local environment. The origin of the unusually long coherence length remains unclear. The T-dependent LD signals for FeSe and $BaFe_2(As_{0.87}P_{0.13})_2$ can be reproduced by assuming a constant value of ξ_{nem} for each material, as shown in figs. S4 and S5 (*12*). These results suggest that the coherence length is not very sensitive to the band structure reconstruction at T_s and $T_{s,N}$. It is also important to discuss the influence of local strain (*12*). In the T-cycle LD-PEEM measurements in fig. S8 (*12*), once the nematic wave completely disappears by increasing T, it never appears

at the same location at low T. This is to be contrasted with the strong pinning of the nematic domain boundary (50 to 100 μm) to the local strain (*19*). There is a possibility that the present LD-PEEM is detecting the central region of the micrometer-sized nematic domains away from the local strain. The slow development of the nematic order parameter below T^* in LD-PEEM (Fig. 3F) is quite similar to the T dependence of the photo-modulation response far away from the nematic domain boundary in the optical measurements (*19*).

Although the possibility of coexistence between mesoscopic and atomic-scale electronic nematicity remains (*27*), our results open the door to experimental and microscopic theoretical investigations to address whether the nematicity wave and its fluctuations contribute to the electron pairing in IBSCs. In a wider context, mesoscopic phenomena have been found in other strongly correlated electron systems (*28*–*31*). The mesoscopic electronic modulations accompanied with hysteresis in the resistance (*32*) and colossal magnetoresistance effect (*33*) have been reported for several manganese oxides. The nematicity wave we observed may also give rise to interesting transport properties (*20*).

REFERENCES AND NOTES

1. E. Fradkin, S. A. Kivelson, M. J. Lawler, J. P. Eisenstein, A. P. Mackenzie, *Annu. Rev. Condens. Matter Phys.* **1**, 153–178 (2010).
2. V. Hinkov *et al*., *Science* **319**, 597–600 (2008).
3. A. J. Achkar *et al*., *Science* **351**, 576–578 (2016).
4. J. H. Chu *et al*., *Science* **329**, 824–826 (2010).
5. S. Kasahara *et al*., *Nature* **486**, 382–385 (2012).
6. Y. Sato *et al*., *Nat. Phys.* **13**, 1074–1078 (2017).
7. H. H. Kuo, J.-H. Chu, J. C. Palmstrom, S. A. Kivelson, I. R. Fisher, *Science* **352**, 958–962 (2016).
8. R. M. Fernandes, A. V. Chubukov, J. Schmalian, *Nat. Phys.* **10**, 97–104 (2014).
9. A. E. Böhmer *et al*., *Phys. Rev. B* **87**, 180505 (2013).
10. M. Nakajima *et al*., *J. Phys. Soc. Jpn.* **81**, 104710 (2012).
11. M. Yi *et al*., *Proc. Natl. Acad. Sci. U.S.A.* **108**, 6878–6883 (2011).
12. See supplementary materials.
13. Y. Suzuki *et al*., *Phys. Rev. B* **92**, 205117 (2015).
14. M. D. Watson, A. A. Haghighirad, L. C. Rhodes, M. Hoesch, T. K. Kim, *New J. Phys.* **19**, 103021 (2017).
15. H. Pfau *et al*., *Phys. Rev. Lett.* **123**, 066402 (2019).
16. R. M. Fernandes *et al*., *Phys. Rev. Lett.* **105**, 157003 (2010).
17. J. K. Glasbrenner *et al*., *Nat. Phys.* **11**, 953–958 (2015).
18. M. A. Tanatar *et al*., *Phys. Rev. B* **79**, 180508(R) (2009).
19. E. Thewalt *et al*., *Phys. Rev. Lett.* **121**, 027001 (2018).
20. F. Yang *et al*., *Nat. Phys.* **16**, 514–519 (2020).
21. T. Taniuchi, Y. Kotani, S. Shin, *Rev. Sci. Instrum.* **86**, 023701 (2015).
22. T. Watashige *et al*., *Phys. Rev. X* **5**, 031022 (2015).
23. T. Sonobe *et al*., *Sci. Rep.* **8**, 2169 (2018).
24. T. Shimojima *et al*., *Phys. Rev. Lett.* **104**, 057002 (2010).
25. R. Zhou, L. Y. Xing, X. C. Wang, C. Q. Jin, G.-q. Zheng, *Phys. Rev. B* **93**, 060502(R) (2016).
26. W. Wang *et al*., *Nat. Commun.* **9**, 3128 (2018).
27. B. A. Frandsen, Q. Wang, S. Wu, J. Zhao, R. J. Birgeneau, *Phys. Rev. B* **100**, 020504(R) (2019).
28. E. Dagotto, *Science* **309**, 257–262 (2005).
29. H. Lin *et al*., *Phys. Rev. Lett.* **120**, 267202 (2018).
30. M. Fratini *et al*., *Nature* **466**, 841–844 (2010).
31. I. Sosnowska, T. P. Neumaier, E. Steichele, *J. Phys. C* **15**, 4835 (1982).
32. S. Cox, J. Singleton, R. D. McDonald, A. Migliori, P. B. Littlewood, *Nat. Mater.* **7**, 25–30 (2008).
33. K. Lai *et al*., *Science* **329**, 190–193 (2010).
34. Y. Sato *et al*., *Proc. Natl. Acad. Sci. U.S.A.* **115**, 1227–1231 (2018).
35. T. Shimojima, Data for Science paper 2021 [Data set], Zenodo (2021); https://doi.org/10.5281/zenodo.4885407.

ACKNOWLEDGMENTS

Funding: This work was supported by Grants-in-Aid for Scientific Research (nos. JP18H01175, JP21H04443, JP18H05227, JP19H00649, and JP19H00651) and Innovative Areas "Quantum Liquid Crystals" (nos. JP19H05824 and JP19H05825) from the Japan Society for the Promotion of Science and by JST CREST (JPMJCR19T5).
Author contributions: S.S. conceived the project. Y.Mo. and T.T. performed the laser-PEEM measurements. T.Shim. and Y.Mo. analyzed the data. M.N. synthesized $BaFe_2(As_{0.87}P_{0.13})_2$ single crystals. S.K., T.Shib., and Y.Ma. synthesized FeSe single crystals. S.O. and H.K. provided the calculations for the band structure and PEEM signal. T.Shim. wrote the paper with input from all coauthors. **Competing interests:** The authors declare no competing interests. **Data and materials availability:** Data for this report are available at Zenodo (*35*).

SUPPLEMENTARY MATERIALS

science.sciencemag.org/content/373/6559/1122/suppl/DC1
Materials and Methods
Supplementary Text
Figs. S1 to S9
References (*36*–*40*)

4 July 2020; accepted 3 August 2021
10.1126/science.abd6701

SUPERNOVAE

A transient radio source consistent with a merger-triggered core collapse supernova

D. Z. Dong[1]*, G. Hallinan[1], E. Nakar[2], A. Y. Q. Ho[1,3,4], A. K. Hughes[5], K. Hotokezaka[6], S. T. Myers[7], K. De[1], K. P. Mooley[1,7], V. Ravi[1], A. Horesh[8], M. M. Kasliwal[1], S. R. Kulkarni[1]

A core collapse supernova occurs when exothermic fusion ceases in the core of a massive star, which is typically caused by exhaustion of nuclear fuel. Theory predicts that fusion could be interrupted earlier by merging of the star with a compact binary companion. We report a luminous radio transient, VT J121001+495647, found in the Very Large Array Sky Survey. The radio emission is consistent with supernova ejecta colliding with a dense shell of material, potentially ejected by binary interaction in the centuries before explosion. We associate the supernova with an archival x-ray transient, which implies that a relativistic jet was launched during the explosion. The combination of an early relativistic jet and late-time dense interaction is consistent with expectations for a merger-driven explosion.

Most massive stars [i.e., those more massive than eight solar masses ($M_\odot$)] are born in close binaries, within which expansion of one star during its evolution can lead to mass transfer with the companion (*1*, *2*). In some systems, the faster-evolving (more massive) star explodes as a supernova, leaving behind a compact object (neutron star or black hole) remnant in a close orbit with its companion. When the companion (second star) later expands, it transfers mass in the other direction, onto the compact object. Systems of this type with wide orbits have been observed in the Milky Way (*3*). Those with closer orbits undergo unstable mass transfer, causing the compact object to spiral into the atmosphere of the massive star, forming a common envelope binary.

During the common envelope phase, the outer atmosphere of the donor star becomes unbound, forming a dense and expanding toroidal shell around the binary (*4*). The physics of the common envelope are difficult to model. Some inspirals halt before reaching the donor's core. This process is a leading candidate for producing the close double-compact-object binaries detected by gravitational wave observatories (*5*). Other systems are expected to spiral inward until the compact object reaches the star's core. Theory predicts that some of these systems tidally disrupt the core, forming a rapidly accreting, neutrino-cooled disk (*6*). This energetic accretion is predicted to launch a jet and cause a merger-driven explosion (*6*–*8*).

We performed a systematic blind search for radio transients in the Very Large Array Sky Survey (VLASS) (*9*). We identified and followed up luminous point sources associated with galaxies closer than 200 megaparsec (Mpc) that are present in the first half-epoch (Epoch 1.1; September 2017 to February 2018) of the survey but absent from the earlier (1994–2005) Faint Images of the Radio Sky at Twenty-Centimeters (FIRST) survey (*10*, *11*). The most luminous source that we identified was VLASS transient J121001+495647 (hereafter abbreviated VT 1210+4956), located in an

[1]Division of Physics, Mathematics, and Astronomy, California Institute of Technology, Pasadena, CA 91125, USA. [2]School of Physics and Astronomy, Tel Aviv University, Tel Aviv, 69978, Israel. [3]Department of Astronomy, University of California, Berkeley, CA 94720, USA. [4]Miller Institute for Basic Research in Science, Berkeley, CA 94720, USA. [5]Department of Physics, University of Alberta, Edmonton, Alberta T6G 2E1, Canada. [6]Research Center for the Early Universe, Graduate School of Science, University of Tokyo, Bunkyo-ku Tokyo 113-033, Japan. [7]National Radio Astronomy Observatory, Socorro, NM 87801, USA. [8]Racah Institute of Physics, The Hebrew University of Jerusalem, Jerusalem, 91904, Israel.
***Corresponding author. Email: dillondong@astro.caltech.edu**

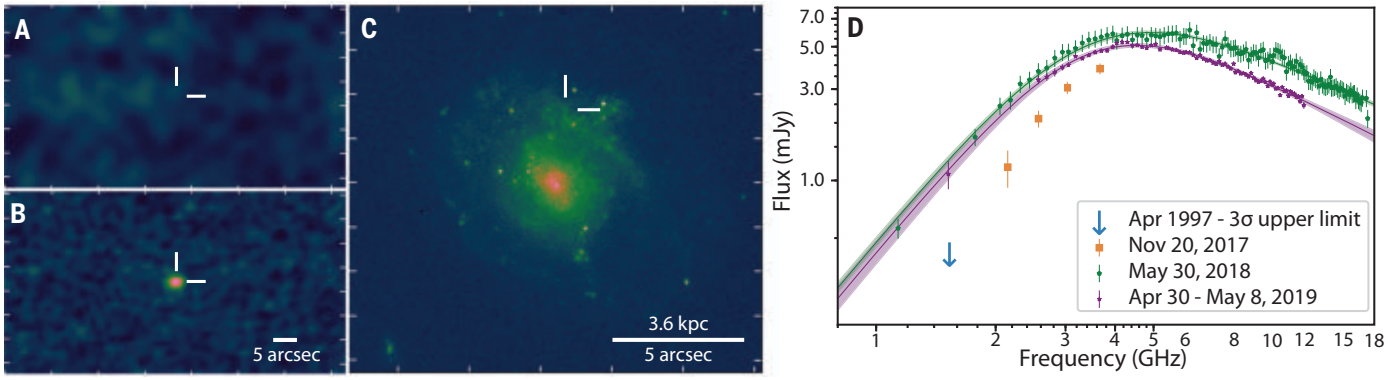


Fig. 1. The luminous radio transient VT 1210+4956. (**A**) Nondetection in the FIRST survey at 1.4 GHz, with a 3σ upper limit of 0.41 millijansky (mJy) on 17 April 1997. (**B**) Detection in VLASS at 3 GHz at 2.7 ± 0.1 (stat) ± 0.5 (sys) mJy on 20 November 2017, 20.59 years after the FIRST observation, at right ascension 12h10m01.32s, declination +49°56′47.006″ [as indicated by white crosshairs in (A) to (C)]. (**C**) Optical image of the location of VT 1210+4956 taken from the Hubble Space Telescope archive (PI: T. Schrabback). (**D**) Radio spectrum of VT 1210+4956 measured from the VLASS observation and follow-up epochs observed with the VLA, plotted with 1σ uncertainties. Follow-up epochs are fitted with a synchrotron self-absorption model (*11*).

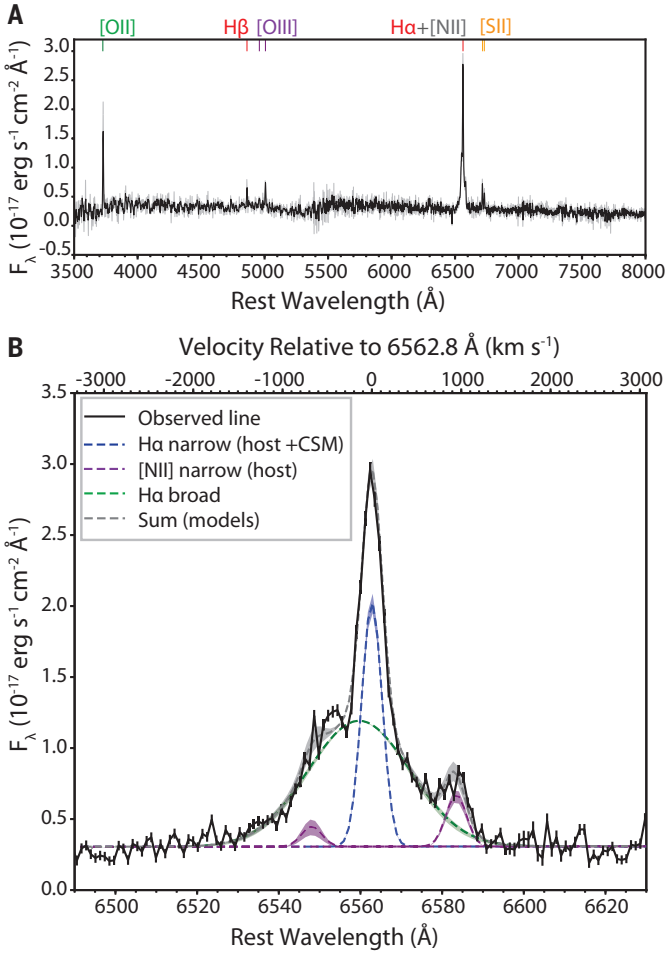


Fig. 2. Optical spectrum of VT 1210+4956. Image taken with Keck/LRIS on 13 April 2018, ~4.45 months after the detection in VLASS. (**A**) The full spectrum, including spectrally unresolved emission lines from the host galaxy. Unbinned data are shown in gray; data shown in black were smoothed with a 3-Å boxcar kernel. (**B**) Details of the Hα and [NII] part of the spectrum, with Gaussian models fitted to the lines. The narrow Hα and [NII] lines are unresolved, whereas the broad component has a full width at half maximum of 1340 ± 60 km/s. The best-fitting model parameters and their uncertainties are listed in table S1.

off-nuclear region of the dwarf star–forming galaxy SDSS J121001.38+495641.7 (Fig. 1) (*12*). This galaxy has a stellar mass of ~$10^{9.2}$ $M_\odot$, a specific star formation rate of ~0.25 $M_\odot$ Gyr^{-1} $M_\odot^{-1}$, and an abundance of elements heavier than helium (metallicity) of ~80% the solar value (*12*).

We observed two follow-up epochs with the Karl G. Jansky Very Large Array (VLA), finding a peak radio luminosity of 1.5×10^{29} erg s^{-1} Hz^{-1} at 5 GHz (Fig. 1) (*11*), 10 times more luminous than any other non-nuclear transient found in our search. We obtained an optical spectrum of the radio transient location using the Low Resolution Imaging Spectrometer on the Keck I telescope, which exhibits a hydrogen-alpha (Hα at 6563Å) emission line with luminosity $(7.3 \pm 0.3) \times 10^{38}$ erg s^{-1} and full width at half maximum of ~1340 ± 60 km s^{-1} (Fig. 2) (*11*). This emission line implies a massive, ionized outflow associated with the radio source (*13*, *14*), and its redshift $z = 0.03470 \pm 0.00003$ confirms its association with the host galaxy, which is at $z = 0.03472 \pm 0.00003$ (*12*). In addition to the broad component, we observed spectrally unresolved (narrow) emission lines consistent with a co-located star-forming region. The environment, broad line, and high radio luminosity indicate a likely association with the explosion of a massive star.

Radio emission from supernovae is powered by synchrotron emission from fast ejecta driving a shock into the ambient circumstellar medium (CSM) (*15*). The most luminous events require exceptionally fast material, such as relativistic (close to the speed of light) jets driven by central compact-object engines or interaction with a particularly dense CSM. All known supernovae with radio emission peaking at $\gtrsim 10^{29}$ erg s^{-1} Hz^{-1} are high-luminosity examples of transient classes that involve central engines (e.g., *16*–*21*). Supernovae featuring dense CSM interaction are typically more than an order of magnitude less luminous. Given the high luminosity of VT 1210+4956, we checked for early-time signatures of a central engine by searching archival optical, x-ray, and gamma-ray transient catalogs for a counterpart source (*11*). This search yielded one match: gamma-ray burst (GRB) 140814A, an unusual soft x-ray burst detected by the Monitor of All Sky X-ray Image (MAXI) instrument on the International Space Station using its Gas Slit Camera (GSC) (*22*).

GRB 140814A was detected by the GSC at 2 to 4 keV and 4 to 10 keV in a 15 ± 3 s window centered at 07:12:23 Universal Time on

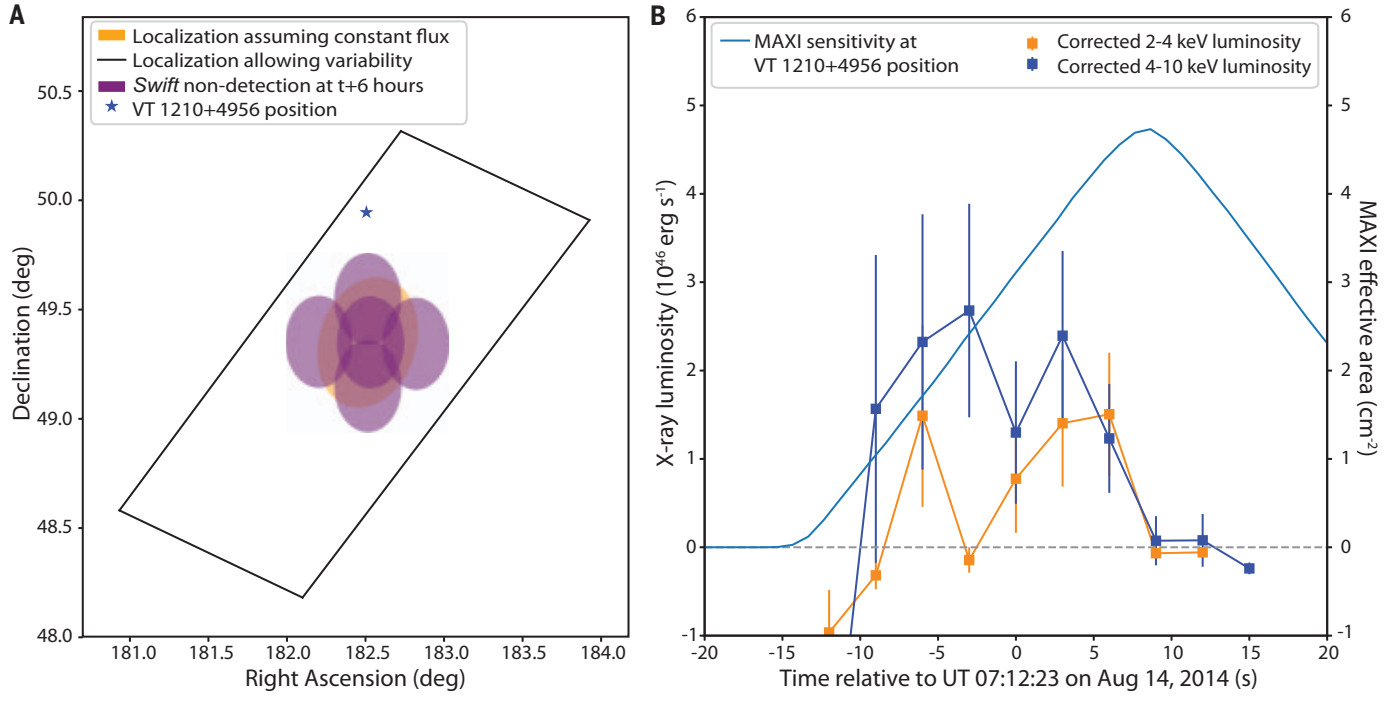


Fig. 3. The x-ray transient MAXI 140814A, which we associate with VT 1210+4956, was observed 3.268 years before VLASS detection. (**A**) Location of VT 1210+4956 compared with published MAXI localizations. Orange ellipse assumes constant flux and black rhombus allows for variability. This position is consistent within 1σ of the expectation from the light curve in (B) (*11*). The purple ellipses show fields with nondetections in Swift observations, with upper limits 60,000 times fainter than the MAXI 140814A ~6 hours after the burst (*11*). (**B**) MAXI 2- to 4-keV (orange) and 4- to 10-keV (blue) light curves, corrected for instrumental sensitivity at the location of VT 1210+4956 (*11*).

14 August 2014, with a similar flux in both bands. It was not detected in a simultaneous observation with a similar sensitivity in the GSC 10- to 20-keV band, suggesting a characteristic energy of ~5 keV. The position of VT 1210+4956 is consistent with the MAXI data and implies a short, fading burst that occurred at the beginning of the GSC's ~40-s transit (Fig. 3) (*11*). We estimate a false alarm probability for the spatial association of (1.2 to 4.8) × 10^{-3} (*11*). We performed several additional consistency checks: (i) that the shock properties of VT 1210+4956 were consistent with an explosion on the date of GRB 140814A, (ii) that the upper limits from contemporaneous optical observations did not rule out a stripped envelope supernova at the location of VT 1210+4956 and time of GRB 140814A, and (iii) that alternative classes of x-ray transients are not consistent with the observational data (*11*).

Our association of VT 1210+4956 with GRB 140814A implies that the x-ray emission had a peak 2- to 10-keV luminosity of ~4 × 10^{46} erg/s. This combination of high luminosity, short duration, and soft spectrum is unlike other x-ray transients with measured luminosities. Known transients with similar spectral peaks and durations, such as the shock breakout of supernova SN 2008D (*23*), are more than three orders of magnitude less luminous. Transients with similar luminosities, such as x-ray flashes and low-luminosity GRBs, typically maintain this luminosity for at least an order of magnitude longer duration (*24*), or peak at one or more orders of magnitude higher energy (*25*). The luminosity and duration of MAXI 140814A implies a relativistic outflow with Lorentz factor $\gamma \gtrsim 2.5$, and the characteristic energy of the photons implies a jetted geometry (*11*). Producing such a relativistic jet requires the presence of a central engine at the time of explosion.

Unlike the early relativistic jet, the radio emission detected in our follow-up epochs (observed >3 years after GRB 140814A) was powered by a low-velocity shock propagating in a dense, extended CSM. The spectral peaks of the radio spectra are caused by synchrotron self-absorption rather than by free-free absorption, suggesting that the CSM is asymmetric, observed along a lower-density line of sight (*11*). The peak luminosities and frequencies imply forward shock radii $R \sim 9 \times 10^{16}$ cm, postshock magnetic fields $B \sim 0.35$ G, and energies dissipated in the shock $U \sim 7 \times 10^{49}$ erg (*11*). The change in R between follow-up epochs implies a forward shock velocity of ~1800 km/s (*11*). This velocity, which is similar to the width of the broad Hα line, implies a high density of ~10^6 cm^{-3} for the CSM swept up in the ~1 year between follow-up epochs. This density is sufficient to allow the shocked gas to cool, on a time scale of ~1 year, from a shock-heated temperature of ~10^7 K to an ~10^4 K dense shell, cool enough to produce the Hα emission (*26*). Compared with known explosive radio transients, VT 1210+4956 has a highly energetic shock propagating at low velocity and a high CSM density at large radius (Fig. 4).

Measurements of the CSM density as a function of radius trace the rate and timing of pre-explosion mass loss. Accounting for both the cool Hα-emitting gas and the hot synchrotron-emitting gas, we found a lower limit to the total swept-up CSM mass of $\gtrsim 1\ M_\odot$ (*11*). The high density and total mass at a radius of ~10^{17} cm requires a pre-explosion mass loss rate of $\dot{M} \approx 4 \times 10^{-2}\ (v/100\ \mathrm{km\ s^{-1}})\ M_\odot\ \mathrm{year^{-1}}$, where v is the preshock CSM velocity (*11*). This is more than an order of magnitude higher than the densest observed stellar winds and requires a pre-supernova eruption (*27*). With these observed and inferred constraints on the CSM velocity, we found that the eruption occurred a few centuries before the explosion (Fig. 4) (*11*).

Similar pre-explosion eruptive mass loss has been inferred from the dense and extended CSM around a few peculiar supernovae, including SN 2014C (*28*–*30*) and SN 2001em (*31*, *32*), which both transitioned from stripped envelope (type Ib/c) to interacting (type IIn) spectral classifications. Several models have been proposed to explain the synchronization of this eruptive mass loss with core collapse, including nuclear burning instabilities (*28*, *33*), binary interaction timed coincidentally with core collapse (*28*, *30*), and merger-driven explosions (*6*, *7*, *28*). For VT 1210+4956, the

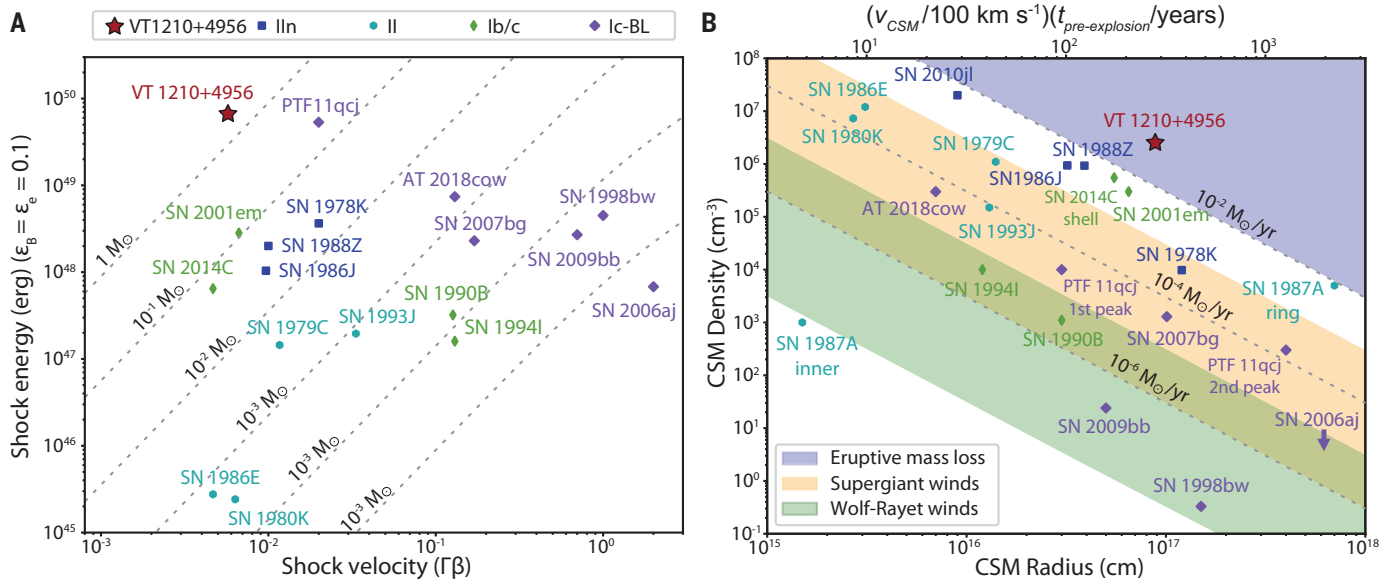


Fig. 4. Comparison of inferred shock properties for VT 1210+4956 and other luminous radio supernovae. (**A**) Shock energies derived from broadband radio spectra versus shock velocities. The dashed curves show constant shocked mass, assuming that the shock energy is equal to the kinetic energy. (**B**) CSM density versus CSM radius with values derived from optical and radio spectra. The upper axis gives the time between mass loss and explosion normalized to a CSM velocity of 100 km/s. The dotted and dashed lines indicate constant mass flow rates $\dot{M}/v$, with the color-shaded regions indicating approximate ranges of values for winds and eruptive mass loss from different types of systems (*27*). Sources are listed in table S5.

detection of a central engine allowed us to distinguish between these scenarios, and the order-of-magnitude higher radio luminosity and shock energy suggests the possibility of a different origin to SN 2014C and SN 2001em.

Nuclear burning instabilities strong enough to produce VT 1210+4956's pre-explosion mass loss rate are predicted to occur in only the final few years before core collapse (*33*), so they would produce shells that are more than an order of magnitude more compact at the time of interaction than we observed. Binary mass transfer is common in massive stars and is more consistent with the early eruptive mass loss. Approximately 70% of massive stars are found in orbits that will eventually lead to mass transfer, with an estimated third of these interactions leading to common envelope inspiral (*1*, *2*). Such interactions are predicted to drive mass loss at or above the rate inferred for VT 1210+4956 (*27*). Unlike the case in single-star models, the mass is ejected in the plane of the binary (*4*, *7*), providing a natural explanation for the inferred asymmetry of the CSM.

Binary interactions can occur at any time during the life of a star and can thus produce shells at any radius. However, the delay time between eruption and core collapse constrains the specific type of interaction. At the near solar metallicity of VT 1210+4956's host galaxy, most interactions are expected to occur while the mass donor is undergoing fusion of hydrogen or helium, ~10^4 to 10^7 years before core collapse (*34*). Interactions synchronized coincidentally within ~10^2 years of core collapse are expected to be extremely rare (*34*), although uncertainties in the rates from binary population synthesis modeling allow this to be a viable scenario for previous events such as SN 2014C (*28*, *30*).

The synchronization is more naturally explained if the interaction itself triggers the core collapse. To do so, an inspiraling object must disrupt the donor star's core. A non-compact merging body (e.g., a main sequence star) is unable to do so because it would replenish fuel in the core, producing a rejuvenated massive star (*35*). By contrast, an inspiraling neutron star or black hole is capable of tidally disrupting the core, leading to a merger-driven explosion (*6*, *7*). During the inspiral phase, the compact object is expected to eject mass from the donor star at a rate similar to our calculated value (*36*). When it reaches the core, theory predicts the formation of an accretion disk and launching of a jet (*6*, *7*). Of the models that we considered for eruptive mass loss, this scenario is most consistent with the jetted x-ray transient.

The high mass loss rate that we infer occurred centuries before explosion, much longer than the dynamical time scale of the inspiraling compact object, which may indicate that the donor star had an envelope with a steep density profile. This would be theoretically expected for a star undergoing core helium fusion, for example (*36*). A steep density profile is thought to be required for merger during the dynamical inspiral phase (*36*, *37*). Flatter density profiles would lead to full envelope ejection before merger, producing close compact object–evolved star binaries. These binaries may subsequently evolve into double compact object systems, with orbits close enough to merge within the lifetime of the Universe, and therefore contribute to gravitational wave events (*5*, *36*, *37*). Our proposed scenario for VT 1210+4956 is an alternative outcome to the formation of such systems.

On the basis of our blind search, we estimate a rate of (1 to 8) × 10^{-8} Mpc^{-3} $year^{1}$ for transients with similar 3-GHz luminosities to VT 1210+4956 (*11*). However, given the continuous distributions of stellar binary periods and mass ratios (*1*, *2*), there may be a wider range of delays between interaction and core collapse, thus producing CSM shells at smaller or larger radii. If this is the case, then these events may be more easily identified at other frequencies, so we regard this rate as a lower limit on the rate of merger-driven explosions.

REFERENCES AND NOTES

1. H. Sana *et al.*, *Science* **337**, 444–446 (2012).
2. M. Moe, R. Di Stefano, *Distribution of Binary Stars. Astrophys. J. Suppl. Ser.* **230**, 15 (2017).
3. J. Orosz *et al.*, *Astrophys. J.* **742**, 84 (2011).
4. M. MacLeod, E. C. Ostriker, J. M. Stone, *Astrophys. J.* **868**, 136 (2018).
5. T. M. Tauris *et al.*, *Astrophys. J.* **846**, 170 (2017).
6. R. A. Chevalier, *Astrophys. J.* **752**, L2 (2012).
7. S. L. Schrøder, M. MacLeod, A. Loeb, A. Vigna-Gómez, I. Mandel, *Astrophys. J.* **892**, 13 (2020).
8. N. Soker, *Mon. Not. R. Astron. Soc.* **471**, 4839–4843 (2017).
9. M. Lacy *et al.*, *Publ. Astron. Soc. Pac.* **132**, 035001 (2020).
10. R. H. Becker, R. L. White, D. J. Helfand, *Astrophys. J.* **450**, 559 (1995).
11. Materials and methods are available as supplementary materials.
12. D. S. Aguado *et al.*, *Astrophys. J. Suppl.* **240**, 23 (2019).
13. D. Milisavljevic *et al.*, *Astrophys. J.* **751**, 25 (2012).
14. K. Heng, *Publ. Astron. Soc. Aust.* **27**, 23–44 (2010).
15. R. A. Chevalier, *Astrophys. J.* **499**, 810–819 (1998).

16. A. J. van der Horst *et al*., GRB 030329: 3 years of radio afterglow monitoring*Philos. Trans. A Math Phys. Eng. Sci.* **365**, 1241–1246 (2007).
17. A. Y. Q. Ho *et al*., *Astrophys. J.* **871**, 73 (2019).
18. A. Y. Q. Ho *et al*., *Astrophys. J.* **895**, 49 (2020).
19. A. Corsi *et al*., *Astrophys. J.* **782**, 42 (2014).
20. S. R. Kulkarni *et al*., *Nature* **395**, 663–669 (1998).
21. A. M. Soderberg *et al*., *Nature* **463**, 513–515 (2010).
22. M. Serino *et al*., *Publ. Astron. Soc. Jpn.* **66**, 87 (2014).
23. A. M. Soderberg *et al*., *Nature* **453**, 469–474 (2008).
24. S. Campana *et al*., *Nature* **442**, 1008–1010 (2006).
25. G. Ghirlanda, M. G. Bernardini, G. Calderone, P. D'Avanzo, *J. High Energy Astrophys.* **7**, 81–89 (2015).
26. B. T. Draine, *Physics of the Interstellar and Intergalactic Medium* (Princeton Univ. Press, 2011).
27. N. Smith, *Annu. Rev. Astron. Astrophys.* **52**, 487–528 (2014).
28. R. Margutti *et al*., *Astrophys. J.* **835**, 140 (2017).
29. G. E. Anderson *et al*., *Mon. Not. R. Astron. Soc.* **466**, 3648–3662 (2017).
30. N. C. Sun, J. R. Maund, P. A. Crowther, *Mon. Not. R. Astron. Soc.* **497**, 5118–5135 (2020).
31. N. N. Chugai, R. A. Chevalier, *Astrophys. J.* **641**, 1051–1059 (2006).
32. P. Chandra, R. A. Chevalier, N. Chugai, D. Milisavljevic, C. Fransson, *Astrophys. J.* **902**, 55 (2020).
33. S. Wu, J. Fuller, *Astrophys. J.* **906**, 3 (2021).
34. J. Klencki, G. Nelemans, A. G. Istrate, O. Pols, *Astron. Astrophys.* **638**, A55 (2020).
35. N. Langer, *Annu. Rev. Astron. Astrophys.* **50**, 107–164 (2012).
36. R. E. Taam, E. L. Sandquist, *Annu. Rev. Astron. Astrophys.* **38**, 113–141 (2000).
37. N. Ivanova *et al*., *Astron. Astrophys. Rev.* **21**, 59 (2013).
38. D. Z. Dong, dillon-z-dong/vt1210: initial release, version 1.0, Zenodo (2021); https://doi.org/10.5281/zenodo.5136735.

ACKNOWLEDGMENTS

We thank the NRAO staff who made the VLASS possible, the VLASS Survey Science Group, J. Fuller and J. Lux for useful discussions, and the reviewers for helpful comments. Our results are based on data from the Karl G. Jansky Very Large Array, which is operated by the National Radio Astronomy Observatory (NRAO). The NRAO is a facility of the National Science Foundation operated under cooperative agreement by Associated Universities Inc. This research has made use of MAXI data provided by RIKEN, JAXA, and the MAXI team. Some of the data were obtained at the W. M. Keck Observatory, which is operated as a scientific partnership among the California Institute of Technology, the University of California, and the National Aeronautics and Space Administration. Keck Observatory was made possible by the generous financial support of the W. M. Keck Foundation. We recognize and acknowledge the cultural role and reverence that the summit of Maunakea has always had within the indigenous Hawaiian community. We are most fortunate to have the opportunity to conduct observations from this mountain. **Funding:** D.Z.D. and G.H. were supported by National Science Foundation (NSF) grant AST-1654815. G.H., D.Z.D., and A.H. were supported by the United States–Israel Binational Science Foundation (grant 2018154). A.H. also acknowledges support from the I-Core Program of the Planning and Budgeting Committee and the Israel Science Foundation and ISF grant 647/18. A.Y.Q.H. and K.D. were supported by the GROWTH project funded by the NSF under PIRE grant 1545949. A.K.H. was supported by NSERC Discovery Grants RGPIN-2016-06569 and RGPIN-2021-04001. A.Y.Q.H. was supported by the Miller Institute for Basic Research in Science at the University of California, Berkeley. K.H. was supported by JSPS Early-Career Scientists grant 20K14513. S.M. was supported by the NRAO. S.R.K. was supported by the Heising-Simons Foundation. **Author contributions:** G.H., D.Z.D., and K.P.M. designed the transient search strategy. D.Z.D. implemented the transient search pipeline, with help from A.K.H. in visual vetting and A.Y.Q.H. in matching the MAXI transient. D.Z.D., G.H., and S.T.M. obtained the radio and optical follow-up observations with the help of telescope staff at the VLA and Keck. D.Z.D. processed and analyzed the radio data with contributions from S.T.M. D.Z.D. processed and analyzed the optical data and estimated the transient rates. E.N. led the analysis of the x-ray data with help from D.Z.D. D.Z.D. and G.H. wrote the paper with contributions from E.N., K.H., and the remaining authors. **Competing interests:** The authors declare no competing interests. **Data and materials availability:** VLASS quicklook images are available at https://archive-new.nrao.edu/vlass/quicklook/. VLA follow-up observations are available from the VLA archive at https://archive.nrao.edu/ under project code 19A-422. The FIRST data were taken from https://third.ucllnl.org/cgi-bin/firstcutout. The Keck observations are available at https://koa.ipac.caltech.edu/cgi-bin/KOA/nph-KOAlogin?more with KOAIDs beginning LB.20180413. The Hubble Space Telescope image was taken from the archive https://hla.stsci.edu/ under proposal ID 13493. Our analysis and model fitting software code is available at https://github.com/Dillon-Z-Dong/VT1210 and is archived on Zenodo (*38*).

SUPPLEMENTARY MATERIALS

science.sciencemag.org/content/373/6559/1125/suppl/DC1
Materials and Methods
Supplementary Text
Tables S1 to S5
References (*39*–*94*)

15 January 2021; accepted 3 August 2021
10.1126/science.abg6037

QUANTUM GASES

Generalized hydrodynamics in strongly interacting 1D Bose gases

Neel Malvania[1]†, Yicheng Zhang[1]†, Yuan Le[1], Jerome Dubail[2], Marcos Rigol[1], David S. Weiss[1]*

The dynamics of strongly interacting many-body quantum systems are notoriously complex and difficult to simulate. A recently proposed theory called generalized hydrodynamics (GHD) promises to efficiently accomplish such simulations for nearly integrable systems. We test GHD with bundles of ultracold one-dimensional (1D) Bose gases by performing large trap quenches in both the strong and intermediate coupling regimes. We find that theory and experiment agree well over dozens of trap oscillations, for average dimensionless coupling strengths that range from 0.3 to 9.3. Our results show that GHD can accurately describe the quantum dynamics of a 1D nearly integrable experimental system even when particle numbers are low and density changes are large and fast.

In interacting many-body quantum systems, such as electrons in a metal, the low-energy properties can often be described to a good approximation in terms of quasiparticles that travel almost freely and have a finite lifetime. In integrable systems, quasiparticles provide an exact description and live forever. They allow the efficient computation of the entire energy spectrum (*1*) and simplify the study of quantum dynamics (*2*). When there is weak integrability breaking, the quasiparticle

[1]Department of Physics, The Pennsylvania State University, University Park, PA 16802, USA. [2]Université de Lorraine, CNRS, LPCT, F-54000 Nancy, France.
***Corresponding author. Email: dsweiss@phys.psu.edu**
†These authors contributed equally to this work.

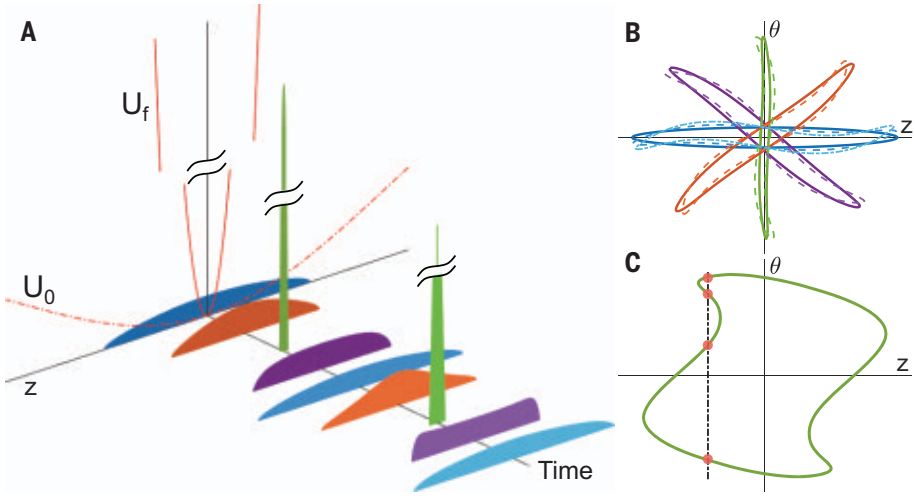


Fig. 1. GHD theory after a 100-fold trap quench. (**A**) Spatial evolution of the initially strongly coupled central 1D gas. At time $t = 0$, the trap depth, U, is increased by a factor of 100 (from the dot-dashed to the solid red lines). The colored curves are the calculated atomic density distributions at various times as the cloud collapses and expands twice. (**B**) The evolution in position (z)–rapidity (θ) space. The colors correspond to the curves in (A), with the solid lines showing the first cycle and the dashed lines showing the second cycle. (**C**) A spatially magnified view of the half-period curve in (B) (see also fig. S1). The two segments of the dashed line inside the contour depict two Fermi seas, the smaller one of which develops during the time evolution. Once a second Fermi sea forms, no existing hydrodynamic theory other than GHD can model the evolution.

picture remains useful at all energies. In many situations, a theory called generalized hydrodynamics (GHD) (*3*, *4*) drastically simplifies the study of dynamics by focusing on the evolution of the momenta of the quasiparticles, the rapidities (*5*).

GHD consists of coupled hydrodynamic equations that are based on two assumptions (*3*, *6*). First, the system is viewed as a continuum of fluid cells, each of which is spatially homogeneous, integrable, and contains many particles. Second, the time variation of local quantities is slow enough that each fluid cell is locally equilibrated to a generalized Gibbs ensemble (GGE) parameterized by its distribution of rapidities (*7*). Experimentally testing GHD is tantamount to determining how robust these two assumptions are in real quantum dynamical systems. GHD was recently tested experimentally for relatively hot, weakly interacting atoms (*8*). In this study, we use ultracold strongly and intermediately coupled atoms to study the quantum regime, which is characterized by strong entanglement and complex correlations among particles. We show that GHD describes the experimental results even when there are few particles (~10) and when there are rapid changes in the nature of the quasiparticles.

In our experiments and GHD simulations, we suddenly ramp up the axial trapping potential around a bundle of ultracold one-dimensional (1D) Bose gases and follow the evolution of the rapidity distribution as the gases successively collapse into the trap center and rebound (Fig. 1A). Our 1D Bose gases are initially close to their ground states, so they can each be described as a Fermi sea for quasiparticles (*9*). For a short time after the trap quench, they remain locally close to a zero-temperature Fermi-sea state. Such a situation could have been described before the advent of GHD using a hydrodynamic approach (*10*, *11*). However, GHD predicts (*12*, *13*) the eventual local formation of states with multiple Fermi seas (*14*), illustrated in Fig. 1, B and C, which shows an example of phase space evolution in the first two cycles after one of our trap quenches. Such local states cannot be modeled with the hydrodynamic methods that preceded GHD. The quantum dynamics considered here are extremely challenging for any other computational approach, except when dealing with few particles and short times or in the limiting cases of very weak or very strong interactions (*11*, *15*).

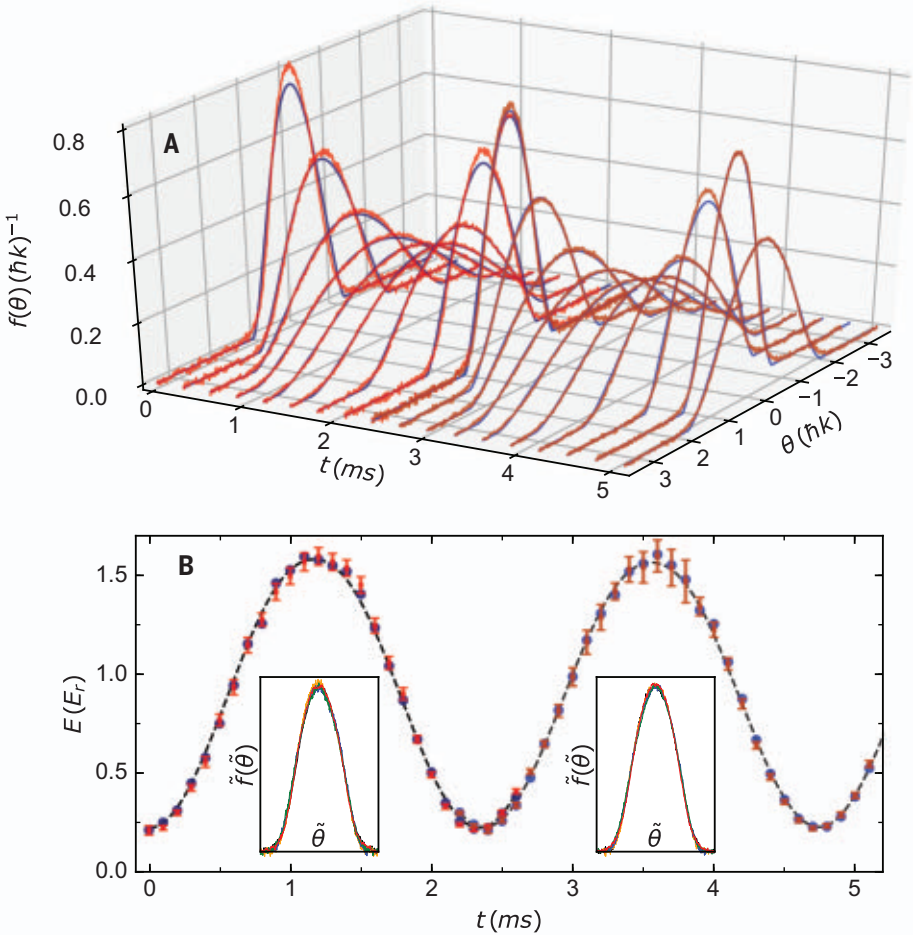


Fig. 2. Intermediate coupling (10-fold) trap quench. (**A**) Time evolution of the rapidity distribution after the trap is suddenly made 10 times deeper for 1D gases with $\bar{\gamma}_0 = 1.4$. The red curves show the experimental rapidity distributions over the course of the first two collapse cycles. The blue curves are the associated GHD theory, taking into account the measured atom number at each point (fig. S2, A and B). The slight difference in color for the two cycles denotes a 2.7% change in the trap depth associated with the slow experimental drift (*17*). (**B**) Time evolution of the rapidity energy, *E*, after the quench. The red squares are extracted from experimental distributions like those in (A) (*17*). The blue circles are for the associated GHD theory. The dashed line is the GHD theory for the average atom number. The two insets show the rescaled (to the same height and area) experimental rapidity distributions ($\tilde{f}$ versus $\tilde{\theta}$, with arbitrary units) for points throughout the first and second cycles, respectively (0, $\pi/4$, $\pi/2$, $3\pi/4$, and π phase points are black, orange, blue, green, and red, respectively). The curves are shape invariant.

To create a bundle of ultracold 1D gases from a ^{87}Rb Bose-Einstein condensate confined by a 55-μm beam waist red-detuned crossed dipole trap, we slowly turn on a 2D blue-detuned optical lattice until it is $40E_r$ deep, where $E_r = \hbar^2k^2/(2m) = 2.55 \times 10^{-30}$ J is the recoil energy defined by the lattice light wavevector, $k = 2\pi/(772\text{ nm})$, $\hbar$ is the reduced Planck's constant, and m is the atom mass (*16*). We use two different initial conditions to study gases that are initially either intermediately or strongly 1D coupled, as characterized by the dimensionless parameter $\gamma = 4.44/n_{1D}$, where n_{1D} is the local 1D density in units of inverse micrometers (*17*). To start with an intermediate (strong) weighted average of γ, $\bar{\gamma}_0 = 1.4$ (9.3), we use ~3×10^5 (~1×10^5) atoms in a $9.4E_r$ ($0.56E_r$) crossed dipole trap, so the 2D distribution of 1D gases extends across a 17-μm (22-μm) radius (figs. S2 and S3). These radii are much smaller than the 2D lattice beam waists of 420 μm, so the transverse confinement for each 1D gas is about the same. The axial trap depths, however, vary across the 1D gases by up to 14% (27%).

We measure rapidity distributions by first shutting off the axial trapping only and letting the atoms expand in 1D in a nearly flat axial potential until the momentum distributions have evolved into the rapidity distributions (*5*, *17*). Then we turn off the 2D lattice and measure the rapidity distributions via time of flight. Our previous dynamical fermionization measurement (*5*) validated this momentum-to-rapidity mapping with parameters very close to our $\bar{\gamma}_0 = 9.3$ initial condition. Because all the other initial cloud lengths are smaller, which allows for relatively more expansion in the flat potential, the mappings in this work are at least as good. We also measure momentum distributions by first suddenly turning off all the light traps. As the atoms rapidly expand transversely, atom interactions decrease rapidly and substantially (*5*). The integrated axial spatial distributions after a time of flight

reflect the 1D momentum distribution at the shutoff time. We adjust the times of flight for different measurements to maximize sensitivity and rescale the spatial distributions by the time of flight to obtain the momentum distributions.

Figure 2A shows the evolution of the rapidity distribution starting from $\bar{\gamma}_0 = 1.4$ after a quench to a ten-times-deeper trap. Our quenches are small enough to ensure that two atoms never have enough energy to get transversely excited in a collision, so the system remains 1D throughout (*18*). The weighted average total energy of the quenched state is 1.9 times the weighted average ground-state energy in the deeper trap. Over the first two cycles, the shapes of all the distributions are self-similar (Fig. 2B, insets). Figure 2B shows the evolution of the integrated energy associated with the rapidities, which is the total energy minus the trap potential energy (*17*). The squares are for the experiment (fig. S4), the dashed line shows the theory for an average number of atoms, and the circles show the theory using the measured number of atoms at each point (*17*). After the quench, the calculated average cloud size drops from 14 μm to 3 μm, and $\bar{\gamma}$ drops from 1.4 to 0.3 (fig. S5, A to J). Figure 2 clearly shows that GHD accurately describes these experiments, where the weighted average (maximum) number of atoms per 1D gas is 60 (140) and the nature of the quasiparticles changes gradually during the collapse. The onset of multiple Fermi seas for this setup occurs in the third cycle. By the 11th cycle, we experimentally observe a loss of self-similarity that is consistent with our theoretical calculations. However, by that time, an ~20% atom loss complicates the theory beyond the scope of this work (*19*) (fig. S6).

With $\bar{\gamma}_0 = 9.3$ we can measure dozens of cycles without appreciable loss and can quench to a 100-times-deeper trap. In this case, the weighted average total energy of the quenched state is 7.3 times the weighted average ground-state energy in the deeper trap. Figure 3A shows the rapidity evolution over the first two cycles. The shapes are no longer self-similar by the end of the first cycle (Fig. 3B, insets). The GHD theory agrees well with the experiment throughout. A second Fermi sea (Fig. 1C) emerges during the first collapse; GHD is essential past that point. Figure S5K shows theoretical calculations of the evolution of cloud sizes; averaged over all 1D gases, the full width at half the central density decreases by a factor of 35, from 17.5 μm to 0.5 μm. Although the cloud size of the central 1D gases remains similar to the average, sharp features appear that are suppressed by averaging. Similar sharp features appear in the rapidity distributions of single 1D gases, and these also tend to be suppressed by averaging (figs. S7 and S8).

The squares, the dashed line, and the circles in Fig. 3B show the integrated rapidity energy

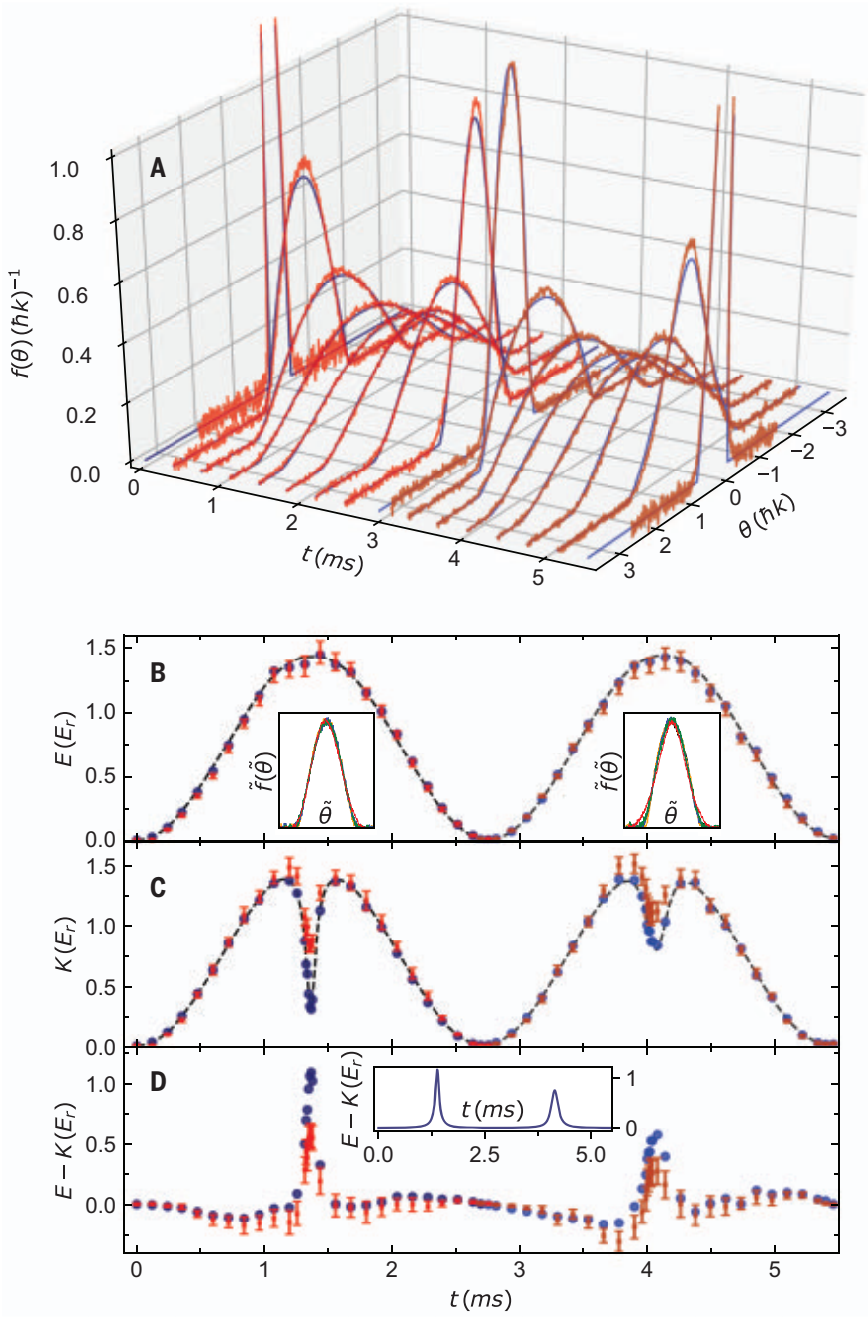


Fig. 3. Strong coupling (100-fold) trap quench. (**A**) Time evolution of the rapidity distribution after the trap is suddenly made 100 times deeper for 1D gases with $\bar{\gamma}_0 = 9.3$. The red curves show the experimental rapidity distributions over the course of the first two collapse cycles. The blue curves are the associated GHD theory, accounting for the measured atom number at each point (fig. S2, C and D). The slight difference in color for the two cycles denotes a 1% change in the trap depth due to the slow experimental drift (*17*). (**B**) Time evolution of the rapidity energy, *E*, after the quench. The red squares are extracted from experimental distributions like those in (A) (*17*). The blue circles are for the associated GHD theory. The dashed line is the GHD theory using the average atom number. The two insets show the rescaled (to the same height and area) experimental rapidity distributions for points throughout the first and second cycles, respectively (points near 0, π/4, π/2, 3π/4, and π phases are shown in black, orange, blue, green, and red, respectively). By the second cycle, the distributions are no longer self-similar. (**C**) Time evolution of the kinetic energy, *K*, after the quench, measured from the momentum distribution just as the rapidity energy is measured from the rapidity distribution. The labeling is the same as for (B), but the trap depths are slightly (<4%) different (see fig. S2, E and F, for the associated atom numbers). (**D**) Time evolution of the interaction energy after the quench. The experimental and GHD theory points are obtained from (B) and (C) by subtracting *K* from *E* at each time. The inset shows GHD theory for a constant atom number and trap depth.

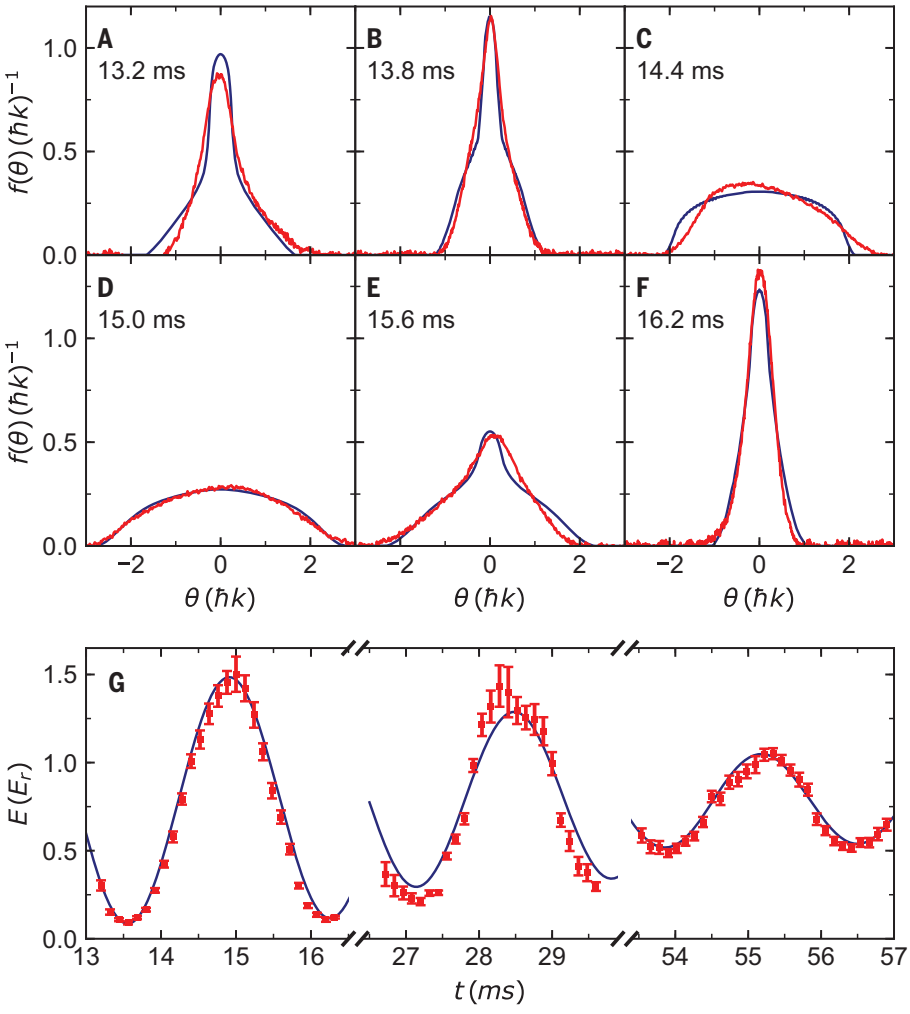


Fig. 4. Strong coupling (100-fold) trap quench at long times. (**A** to **F**) Experimental and GHD theory rapidity distributions during the sixth cycle after the 100-fold quench. The red curves show the experiment, the blue curves the associated theory. (**G**) The rapidity energy during the 6th, 11th, and 21st oscillations after the quench. For all the theory curves in this figure, we use the average number of atoms for each cycle, and the trap depth has been adjusted for each cycle so that the theory is in phase with the experiment.

as a function of time for, respectively, the experiment (fig. S4), the theory with the average atom number, and the theory with the measured atom numbers (fig. S9). The squares in Fig. 3C show the integrated kinetic energy as a function of time, determined from the measured momentum distributions. The momentum measurement near peak compression is somewhat compromised by the large interaction energy, some of which gets converted to kinetic energy early in the time of flight. There is no corresponding complication in the rapidity measurement. We extract the theoretical kinetic energy from GHD by using the Lieb-Liniger model in each GHD spatial cell to determine the interaction energy, integrating it and subtracting it from the total integrated rapidity energy (*17*). We adjust the axial trap depth in the theory to account for day-to-day experimental drifts (<4%). The dashed line in Fig. 3C shows the result for the average atom number; the circles use the measured atom numbers. Figure 3D shows the difference between the rapidity and kinetic energies as a function of time, both experimentally and theoretically (with measured atom numbers), and the inset shows the theory for a fixed atom number and trap depth.

The data in Fig. 3 test the range of validity of GHD in two distinct ways. First, the weighted average (maximum) occupancy in the 1D gases is 11 (*25*), challenging the continuum approximation. To gain confidence in this surprising result, we have compared GHD in the infinite γ limit with exact theory, which is only available in that regime (*17*). There are short wavelength features (Friedel-like oscillations) in the exact calculations for single 1D gases. For our distribution of 1D gases with different atom numbers, these features are smoothed out and the GHD theory overlaps the exact one (fig. S7). Second, during the compression, $\bar{\gamma}$ drops from 9.3 to 0.4 (fig. S5M), with the final factor-of-8 decrease occurring in the final 0.2 ms (right after the kinetic energy maximum). During this time, the ratio of interaction energy to kinetic energy increases from 0.076 to 4.2, as illustrated by the first peak in Fig. 3D. The momentum distributions in this final stage of compression change shape from fermionic to bosonic, as was shown in (*5*) using a less drastic quench. Our results validate the GHD description even in the face of rapid variations in the nature of the quasiparticles, suggesting that the system remains locally equilibrated to the GGE throughout.

We next study rapidity distributions during the sixth oscillation cycle (Fig. 4, A to F, and fig. S8). The theoretical distributions now change more noticeably during the cycle. Their distinctive shapes match the experimental curves reasonably well, except for slight experimental asymmetries caused by drifts in the gravity-canceling vertical magnetic field gradient, which lead to initial displacements of atoms from the light trap center by up to 100 nm, or 0.006 of the full width of their distribution (*17*). By the 11th cycle, finer features appear in the theory that are smeared out in the experiment (fig. S10, A to D), presumably on account of the initial atom cloud displacements and perhaps light trap asymmetry. In Fig. 4G, we show the integrated rapidity energies for cycles up to the 21st for the experiment and theory, with the period adjusted to account for small trap depth drifts (see fig. S10, E to I, for the corresponding rapidity distributions). The theory shows that there is $\lesssim$20% loss of contrast in individual 1D gases, with the additional contrast loss coming from the inhomogeneity of axial trap depths. An extensive quantity, the rapidity energy is less sensitive to minor experimental imperfections. GHD is accurate enough to describe these experiments for the available measurement times.

We have shown that GHD accurately describes the dynamics of nearly integrable 1D Bose gases, with strong and intermediate coupling, after a trap quench. We experimentally challenged GHD's two underlying assumptions, the continuum and local GGE approximations, and we did so for long evolution times. A natural next step would be to study arrays of identical 1D gases or to further study single 1D gases, where it might be possible to observe finer features in rapidity distributions and to see direct evidence of the presence of multiple Fermi seas. One could also explore GHD in spin chains (*20*) and perform similar tests on systems that are further from integrable (*21*), for example, because of

dipolar interactions in 1D gases (*22*) or dimensional crossover from 1D to 3D, a regime for which extensions to GHD have been recently explored (*23*). Looking ahead, GHD and its extensions promise to become a standard tool in the description of strongly interacting 1D quantum dynamics close to integrable points. Such points describe a wide range of experiments involving 1D ultracold gases of bosons (*24*) and fermions (*25*), as demonstrated in experiments in continuum (*26*–*28*) and lattice (*29*–*31*) systems.

REFERENCES AND NOTES

1. H. Bethe, *Z. Phys.* **71**, 205–226 (1931).
2. J.-S. Caux, F. H. L. Essler, *Phys. Rev. Lett.* **110**, 257203 (2013).
3. O. A. Castro-Alvaredo, B. Doyon, T. Yoshimura, *Phys. Rev. X* **6**, 041065 (2016).
4. B. Bertini, M. Collura, J. De Nardis, M. Fagotti, *Phys. Rev. Lett.* **117**, 207201 (2016).
5. J. M. Wilson *et al.*, *Science* **367**, 1461–1464 (2020).
6. B. Doyon, *SciPost Phys. Lect. Notes* 18 (2020).
7. M. Rigol, V. Dunjko, V. Yurovsky, M. Olshanii, *Phys. Rev. Lett.* **98**, 050405 (2007).
8. M. Schemmer, I. Bouchoule, B. Doyon, J. Dubail, *Phys. Rev. Lett.* **122**, 090601 (2019).
9. E. H. Lieb, W. Liniger, *Phys. Rev.* **130**, 1605–1616 (1963).
10. G. De Rosi, S. Stringari, *Phys. Rev. A* **94**, 063605 (2016).
11. S. Peotta, M. D. Ventra, *Phys. Rev. A* **89**, 013621 (2014).
12. B. Doyon, J. Dubail, R. Konik, T. Yoshimura, *Phys. Rev. Lett.* **119**, 195301 (2017).
13. J.-S. Caux, B. Doyon, J. Dubail, R. Konik, T. Yoshimura, *SciPost Phys.* **6**, 070 (2019).
14. T. Fokkema, I. S. Eliëns, J.-S. Caux, *Phys. Rev. A* **89**, 033637 (2014).
15. J.-S. Caux, R. M. Konik, *Phys. Rev. Lett.* **109**, 175301 (2012).
16. T. Kinoshita, T. Wenger, D. S. Weiss, *Science* **305**, 1125–1128 (2004).
17. See supplementary materials.
18. J.-F. Riou, L. A. Zundel, A. Reinhard, D. S. Weiss, *Phys. Rev. A* **90**, 033401 (2014).
19. I. Bouchoule, B. Doyon, J. Dubail, *SciPost Phys.* **9**, 044 (2020).
20. P. N. Jepsen *et al.*, *Nature* **588**, 403–407 (2020).
21. A. J. Friedman, S. Gopalakrishnan, R. Vasseur, *Phys. Rev. B* **101**, 180302 (2020).
22. Y. Tang *et al.*, *Phys. Rev. X* **8**, 021030 (2018).
23. F. Møller *et al.*, *Phys. Rev. Lett.* **126**, 090602 (2021).
24. M. A. Cazalilla, R. Citro, T. Giamarchi, E. Orignac, M. Rigol, *Rev. Mod. Phys.* **83**, 1405–1466 (2011).
25. X.-W. Guan, M. T. Batchelor, C. Lee, *Rev. Mod. Phys.* **85**, 1633–1691 (2013).
26. T. Kinoshita, T. Wenger, D. S. Weiss, *Nature* **440**, 900–903 (2006).
27. G. Pagano *et al.*, *Nat. Phys.* **10**, 198–201 (2014).
28. W. Kao, K.-Y. Li, K.-Y. Lin, S. Gopalakrishnan, B. L. Lev, *Science* **371**, 296–300 (2021).
29. B. Paredes *et al.*, *Nature* **429**, 277–281 (2004).
30. T. Fukuhara *et al.*, *Nature* **502**, 76–79 (2013).
31. M. Boll *et al.*, *Science* **353**, 1257–1260 (2016).
32. D. Weiss, N. Malvania, Y. Zhang, Y. Le, M. Rigol, Replication Data for: Generalized hydrodynamics in strongly interacting 1D Bose gases, Version 1, Harvard Dataverse (2021); https://doi.org/10.7910/dvn/xyxmyb.
33. J. Dubail, jdubail/Zero-entropy-GHD: Example of zero-entropy GHD simulation: quasi-harmonic trap quench in the one-dimensional Bose gas, Version 1, Zenodo (2021); https://doi.org/10.5281/zenodo.5094916.

ACKNOWLEDGMENTS

Funding: Supported by NSF grants PHY-2012039 (D.S.W., N.M., and Y.L.) and PHY-2012145 (Y.Z. and M.R.), and by US Army Research Office grant W911NF-16-0031-P00005 (D.S.W., N.M., and Y.L.). The computations were carried out at the Institute for Computational and Data Sciences at Penn State. **Author contributions:** N.M. and Y.L. carried out the experiments. Y.Z. carried out the theoretical calculations. D.S.W. oversaw the experimental work. J.D. and M.R. oversaw the theoretical work. All authors were involved in the analysis of the results, and all contributed to writing the paper. **Competing interests:** There are no conflicts of interests. **Data and materials availability:** The presented data (*32*) and the core theoretical code (*33*) are archived.

SUPPLEMENTARY MATERIALS

science.sciencemag.org/content/373/6559/1129/suppl/DC1
Materials and Methods
Supplementary Text
Figs. S1 to S10
References (*34*–*50*)

29 September 2020; accepted 2 August 2021
10.1126/science.abf0147

METASURFACES

Plasmonic topological metasurface by encircling an exceptional point

Qinghua Song[1], Mutasem Odeh[2], Jesús Zúñiga-Pérez[1], Boubacar Kanté[2,3], Patrice Genevet[1]*

Resonant scattering, guided mode propagation phase, and/or orientation-dependent phase retardations are the three main mechanisms used to date to conceive optical metasurfaces. Here, we introduce an additional degree of freedom to address optical phase engineering by exploiting the topological features of non-Hermitian matrices operating near their singular points. Choosing metasurface building blocks to encircle a singularity following an arbitrarily closed trajectory in parameter space, we engineered a topologically protected full 2π-phase on a specific reflected polarization channel. The ease of implementation together with its compatibility with other phase-addressing mechanisms bring topological properties into the realm of industrial applications at optical frequencies and prove that metasurface technology represents a convenient test bench to study and validate topological photonic concepts.

Metasurfaces (*1*–*6*) are artificial materials constructed with subwavelength arrays of spatially distributed nanostructures that enable versatile wavefront engineering. From a fundamental perspective, a metasurface is an open system, continuously exchanging and/or absorbing energy between the impinging field and the resonant nanostructures. Unlike closed systems, open systems experience a phase transition at the exceptional point (EP), leading to complex scattering phenomena related to optical singularities (*7*). The latter can be equivalently described in an optical system by using the scattering matrix and Hamiltonian representations (*8*–*10*). Singularities also manifest in the reflection-zero regime, perfect absorption and bound state in the continuum, giving rise to, for example, unidirectional transmission or reflection (*11*, *12*), single-mode laser operation (*13*), and extreme sensitiveness to perturbation (*14*, *15*). Tailoring light reflection, or transmission, with metasurfaces consists in addressing the values of complex coefficients by varying the nanostructure geometries. Choosing any arbitrary loop in parameter space to achieve phase distribution does not necessarily lead to full 2π-phase accumulation. Here, we show how to leverage the 2π-phase excursion that occurs on the coefficient value by encircling zeros or singularities in the complex plane. Encircling a singular point to accumulate an optical phase difference is of crucial interest for wavefront engineering, enrichening the metasurface design toolbox with an additional phase-addressing mechanism.

Previous works on metasurfaces have shown that non-Hermitian metasurfaces can operate close to an EP and have approached singularity owing to a series of individually distinct metasurfaces for which a given parameter is changed (*16*–*19*). The exploitation of the robust topological phase around the EP, referred to as the exceptional topological (ET) phase, to realize functional devices has remained elusive. The proposed ET phase is fundamentally different from the conventional Pancharatnam-Berry (PB) phase (*20*–*23*), and as a consequence, ET can be combined with other phase-addressing mechanisms, including PB, to achieve full and independent control of the polarization channels. We have demonstrated a meta-hologram by using the ET phase encircling the EP to project an image of "C" for left circular polarized (LCP) light, leaving the cross right circular polarized (RCP) channel unaffected. By combining the ET and PB phases, we decoupled the two circular polarizations (CPs) and achieved two different holographic projections with an image of "A" for LCP light and "B" for RCP light.

The plasmonic topological metasurface consists of three layers, where a dielectric layer is sandwiched between a metal ground

[1]Université Côte d'Azur, CNRS, Centre de Recherche sur l'Hétéro-Epitaxie et ses Applications, Rue Bernard Gregory, Sophia Antipolis, 06560 Valbonne, France. [2]Department of Electrical Engineering and Computer Sciences, University of California, Berkeley, CA 94720, USA. [3]Materials Sciences Division, Lawrence Berkeley National Laboratory, Berkeley, CA 94720, USA.
*Corresponding author. Email: patrice.genevet@crhea.cnrs.fr

and a metallic structured layer (Fig. 1A). The metal ground blocks all the transmission so that the metasurface works in the reflective regime. The structured layer is formed by a two-dimensional (2D) planar chiral structure array, which is composed of an "L"-shaped nanostructure, near-field coupled to a straight nanorod. To observe the EP complex-square-root topology of the eigenvalues surface, two parameters need to be varied, defining the parameter space $\boldsymbol{R} = (L_1, L_3)$, with L_1 and L_3 being the geometrical parameters shown in Fig. 1A. L_1 and L_3 were chosen because they play key roles in the y- and x-polarized resonances (fig. S9 and supplementary text S4), giving access to a full 2π reflection phase for r_{+-} [where the subscript +− represents reflected CP conversion from RCP ($|-\rangle$) to LCP ($|+\rangle$)].

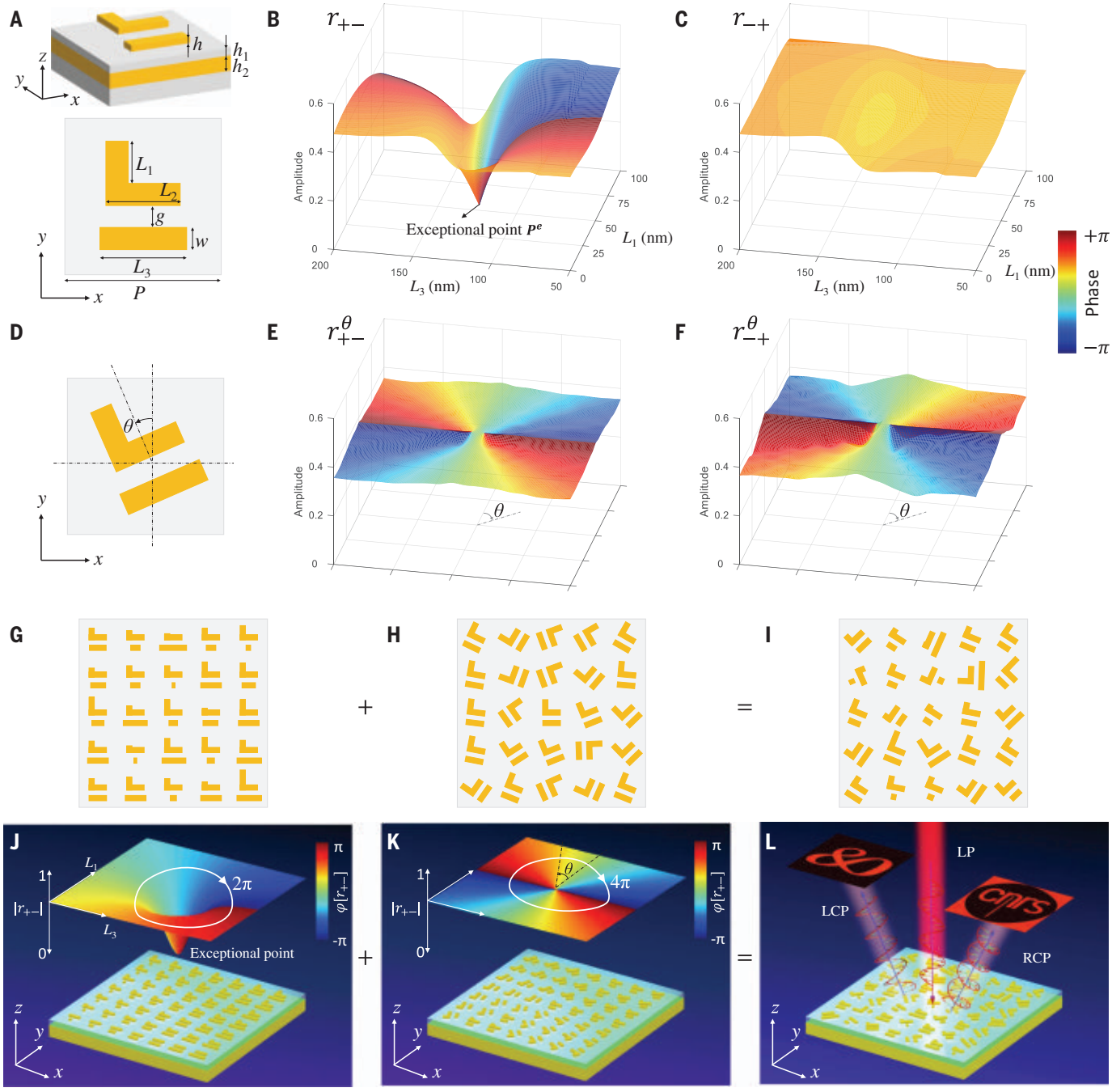


Fig. 1. Design principle of the topological metasurface. (**A**) (Top) Perspective and (bottom) top view of 2D chiral meta-atom design in reflection. The dimensions are L_2 = 140 nm, P = 300 nm, w = 50 nm, g = 70 nm, h = 30 nm, h_1 = 40 nm, and h_2 = 150 nm. (**B** and **C**) Simulated CP conversion coefficients (B) r_{+-} and (C) r_{-+} in the parameter space covered by $L_1 \in [0, 100\ \text{nm}]$ and $L_3 \in [50\ \text{nm}, 200\ \text{nm}]$. An EP is obtained at (L_1, L_3) = (52 nm, 119 nm). A vortex phase profile for r_{+-} and a topological protected 2π-phase accumulation is obtained by encircling the EP, as indicated in (B) by the full-color map coverage on the surface. (**D**) Top view of meta-atom with rotation angle of θ. (**E** and **F**) Simulated CP conversion coefficients (E) r^{θ}_{+-} and (F) r^{θ}_{-+} with $\theta \in [0, 2\pi]$. In (E) and (F), the original ET phase without rotation ($r^{0}_{\pm\mp}$) has been subtracted to display the PB phase only. The z axis in (B), (C), (E), and (F) indicates the amplitude, and the color scale indicates the phase. (**G** to **I**) The combination of (G) ET phase and (H) PB phase is designed to realize an (I) ET+PB phase metasurface. (**J** to **L**) Schematics of the design implemented for combining the (J) ET and (K) PB phase control in (L) a single ET+PB phase metasurface, able to independently control the two CP beams.

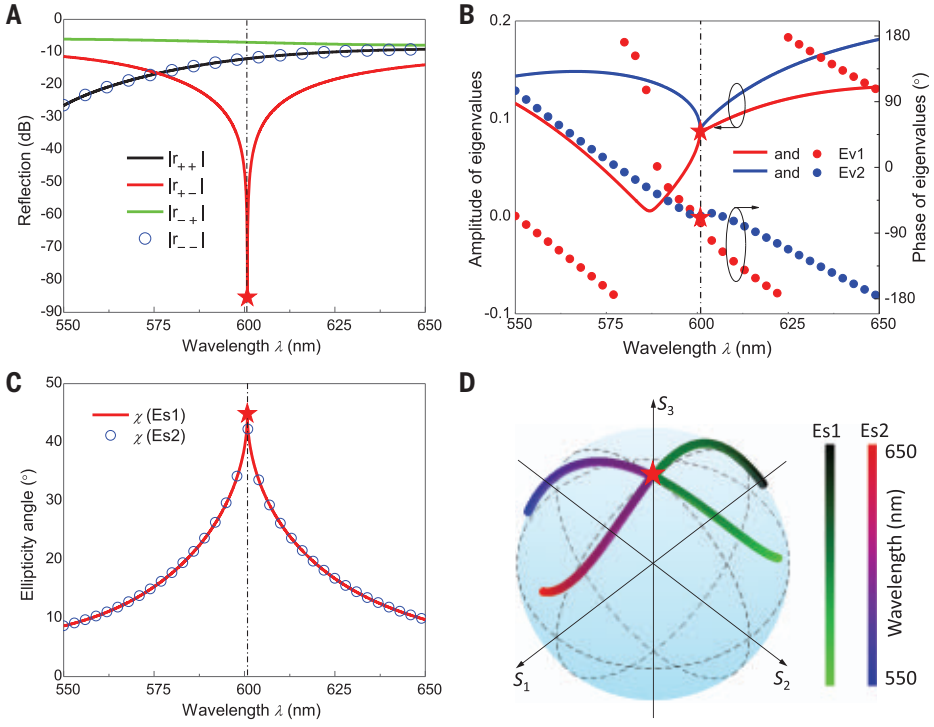


Fig. 2. Simulated reflection spectra and the corresponding eigenvalues and eigenstates. (**A**) Spectral dependence of the reflection matrix coefficients (in the circular basis). A singularity point, where $r_{+-} = 0$, is observed at $\lambda = 600$ nm. (**B**) Amplitude and phase of the reflection matrix eigenvalues. The two eigenvalues degenerate at $\lambda = 600$ nm. (**C**) Simulated ellipticity angle of the two eigenstates, which overlap and degenerate as RCP at $\lambda = 600$ nm. (**D**) Position of the eigenstates on the Poincaré sphere as a function of wavelength, which degenerate at $\lambda = 600$ nm. All of these features prove that an EP is obtained at $\lambda = 600$ nm.

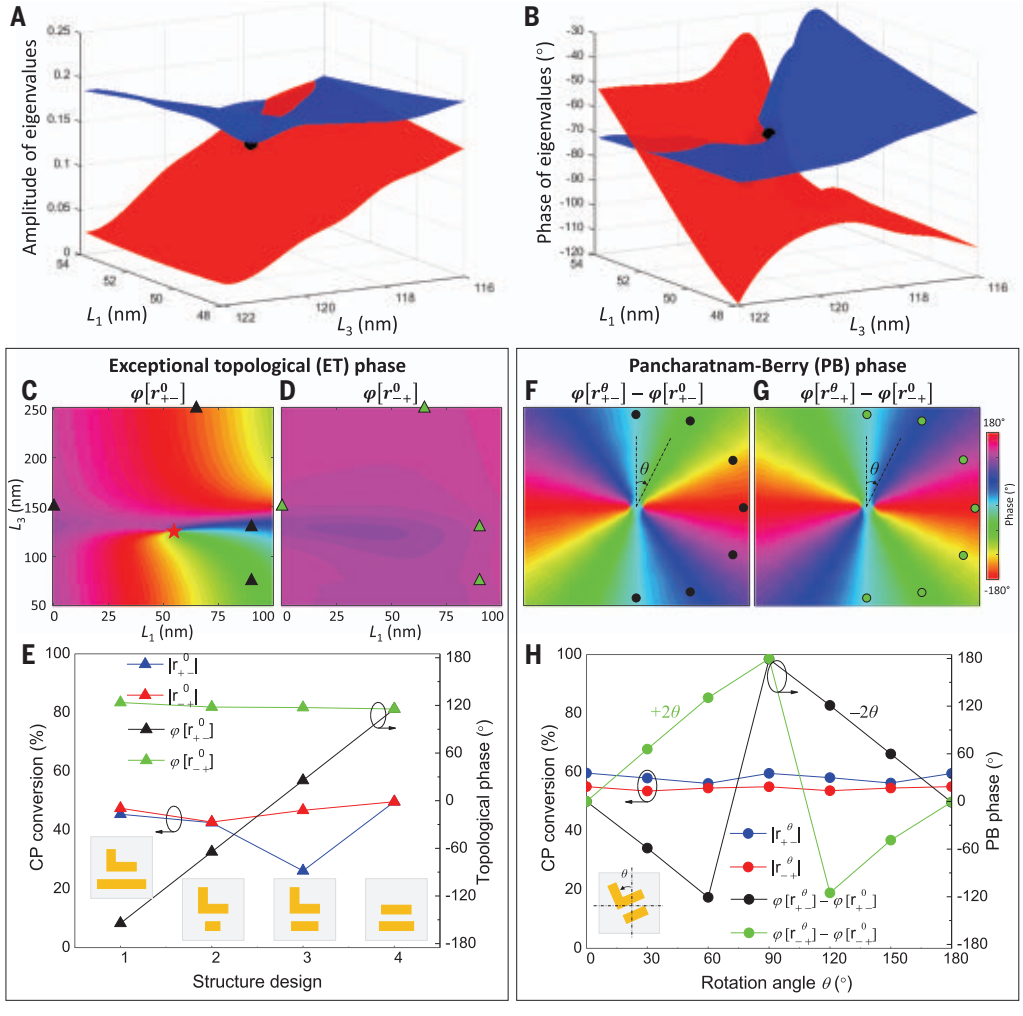


Fig. 3. Simulation results of the metasurface in the parameter space $R = (L_1, L_3)$. (**A**) Simulated amplitude and (**B**) phase of two eigenvalues at $\lambda = 600$ nm. A self-intersecting Riemann surface profile is observed. The EP is indicated with the black dot, where two eigenvalues degenerate at (L_1, L_3) = (52 nm, 119 nm). (**C**) Simulated ET phase of r^0_{+-} and (**D**) nearly constant phase of r^0_{-+}. (**E**) Four meta-atom designs are selected so that the ET phase interval is 90°, indicated with triangles in (C) and (D). (Insets) Four corresponding structure designs. (**F** and **G**) Simulated PB phase of (F) r^θ_{+-} and (G) r^θ_{-+} with (L_1, L_3) = (80 nm, 95 nm). where the presented phase has been subtracted by the original phase of $r^0_{\pm\mp}$ without rotation to display PB phase only. (**H**) Seven rotated structures are presented with rotation angle from 0° to 180° stepped by 30°, indicated with dots in (F) and (G) (figs. S11 and S14).

The EP was obtained by adjusting the nanostructure structural properties, so that both eigenstates degenerate as CP beams. If the degenerate eigenstate is RCP—that is, $\hat{r}|-\rangle = \lambda_{1,2}|-\rangle$, where $\hat{r}$ is the reflection matrix and $\lambda_1 = \lambda_2$ are two degenerate eigenvalues—then RCP input light is preserved, and the CP conversion channel from RCP to LCP vanishes—that is, $r_{+-} = 0$. A zero point or singularity point, equivalent to perfect absorption cases (*24*–*26*), is obtained for r_{+-} (Fig. 1B). The chiral response of the surface current distribution at the EP (fig. S7) is a key ingredient to achieve CP-dependent reflectivity. The induced chirality is an inherent property of the EP from a symmetric non-Hermitian Hamiltonian (*27*) and leads to an asymmetric conversion from

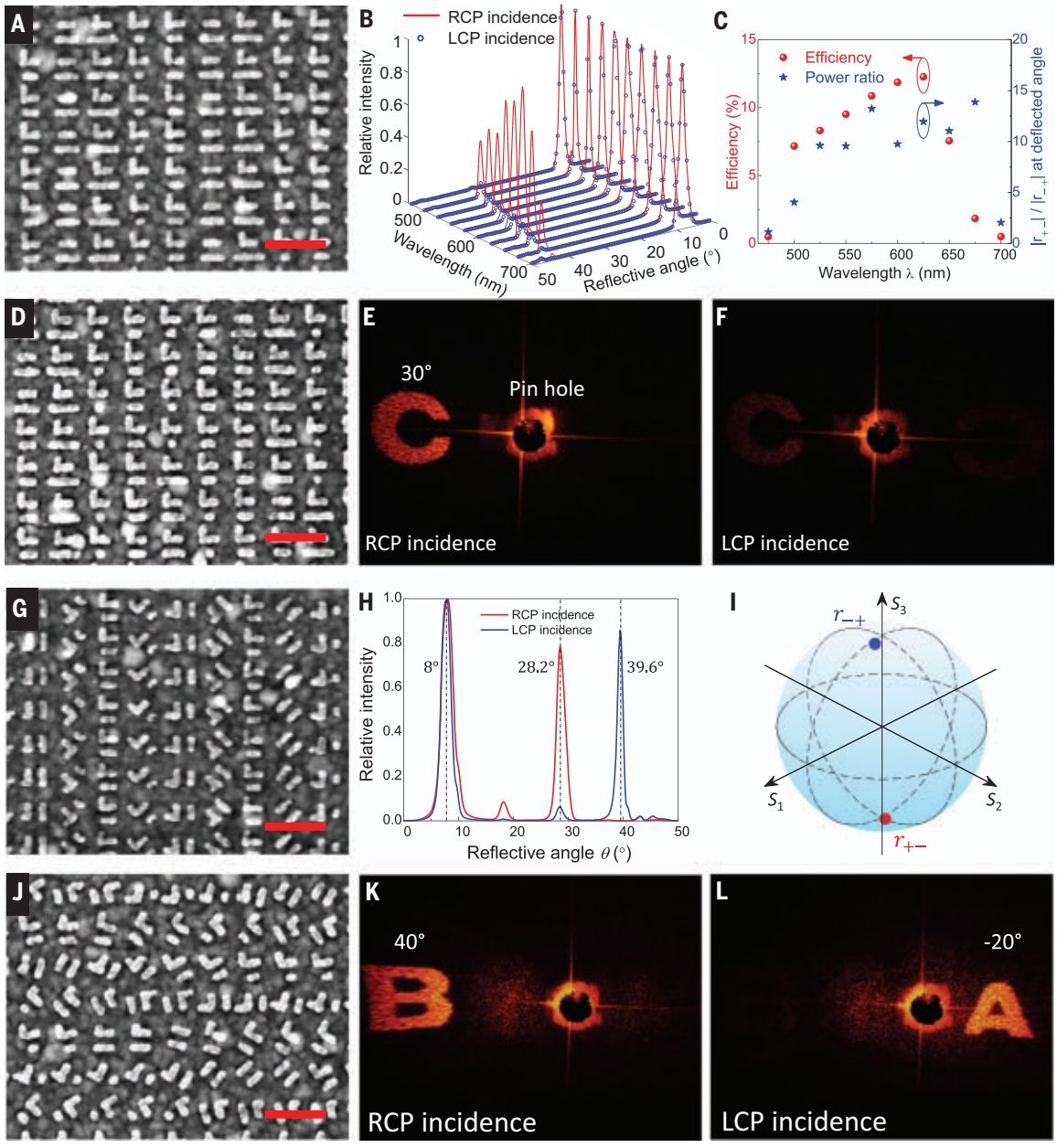


Fig. 4. Experimental results of the topological metasurface. (**A**) Fabricated nanostructures for the ET phase meta-deflector. (**B**) Measured far-field power patterns for RCP (red solid curves) and LCP (blue dotted curves) incidence on ET phase meta-deflector. The phase gradient between adjacent meta-atoms is designed as 90°. The first order of the CP-converted beam r_{+-} is deflected from 34° to ~44° when the wavelength λ varies from 500 to ~675 nm, whereas the other CP-converted beam of r_{-+} is undeflected (at the zero order of 8°). (**C**) Measured efficiency of the deflector (red dots) and measured power ratio of $|r_{+-}|/|r_{-+}|$ at the deflected angle (blue stars). (**D**) Fabricated nanostructures for an ET phase meta-hologram designed by encoding the holographic phase profile into the deflector. (**E**) A holographic image of "C" for r_{+-} is displayed at the angle of 30°, but (**F**) no image appears for r_{-+}. (**G**) Fabricated nanostructures for an ET+PB phase meta-deflector. (**H**) Measured far-field power patterns with RCP (red curve) and LCP (blue curve) incidence on ET+PB phase meta-deflector. The phase gradient between adjacent meta-atoms is designed as 60° and 90°, respectively for r_{+-} and r_{-+}. (**I**) Poincaré sphere representation of the measured polarization of r_{+-} (red dot) and r_{-+} (blue dot) at the first deflected order. (**J**) Fabricated nanostructures for an ET+PB phase meta-hologram. (**K** and **L**) Holographic images of (K) "B" for r_{+-} and (L) "A" for r_{-+} are displayed at the designed angle of 40° and −20°, respectively. All the curves in (B) and (H) are normalized with the zero order as unity. The operating wavelength in (E), (F), (H), (K), and (L) is λ = 600 nm. The incident angles of the deflectors and holograms are 8° and 0°, respectively. Scale bars, 500 nm.

one CP to the other and vice versa ($r_{+-} \neq r_{-+}$). The spectral response of only one of the two CP conversions undergoes a 2π-phase change around the EP wavelength. Because of the topological protection provided by encircling of the EP (supplementary text S1 and S2), the 2π-phase accumulation is maintained for the reflected phase map irrespective of the closed path, as long as it encircles one EP in parameter space. Given the metasurface versatility, we realized on a single component an assembly of antennas with different parameters chosen so as to move around the EP in the parameter space, thus realizing simultaneously a set of optical responses (Fig. 1, G and J). We also observed amplitude variation with singular value. The other reflective CP conversion coefficient (r_{-+}) does not present a singularity in this parameter space, resulting in almost constant phase and amplitude profiles (Fig. 1C).

The conventional PB phase works oppositely for the two reflective CP conversion beams (Fig. 1, D to F). Being fundamentally different, the ET phase is imposed on only one CP conversion and thus can be combined with the standard PB phase (supplementary text S5). As a result, the combination of ET and PB phases can be used to decouple the phase of the two CP conversion beams, leading to independent control of each polarization-converted wavefront (Fig. 1, G to L).

A spectral singularity point of r_{+-}, together with its degeneracy of the eigenvalues and eigenstates at λ = 600 nm, prove the existence of an EP (Fig. 2, red star). This behavior was further confirmed by the intersecting double Riemann surface corresponding to the reflection matrix eigenvalues (Fig. 3, A and B). Various phase and amplitude-conversion distribution choices are possible for the deflecting unit cell. We chose a simple unit cell phase coverage, considering 90° phase steps, so as to keep the distance between neighboring antennas constant, which slightly compromises the amplitude of the third structure (Fig. 3E). Seven designs of PB phase interval of 60° are also presented in Fig. 3, C to H, for combination with the ET phase.

We experimentally demonstrated an ET-phase gradient metasurface, behaving as a beam deflector and a meta-hologram. The scanning electron micrograph (SEM) of the fabricated beam deflector is shown in Fig. 4A. An asymmetric reflection of the two CP conversion beams is measured in Fig. 4B, with a maximum efficiency of 12% and power ratio around 10:1, as quantified in Fig. 4C. The spectral position of the singular design (EP antenna) evolves as a function of the antenna structural parameters (fig. S13), indicating that small nanofabrication errors can slightly shift the position of the EP and modify the expected deflection efficiencies and power ratio. To show the versatility of this wavefront phase encoding technique, we realized a meta-hologram (Fig. 4D). As expected, a holographic image of "C" is displayed for r_{+-} (Fig. 4E), but no image appears for r_{-+} (Fig. 4F).

The wealth of applications of the ET phase expands by combining it with other phase-control mechanisms. We combined ET with the widespread PB phase by simply rotating the metasurface elements (Fig. 4, G to L) to decouple the deflection angles of the two CP beams (Fig. 4, H and I). Similarly, we applied ET+PB phase encoding to project two different CP holographic images (Fig. 4, K and L).

We have demonstrated a planar chiral plasmonic metasurface that exhibits 2π topological phase accumulation in a reflection regime by choosing nanoantenna designs distributed along any arbitrarily closed parameter loop encircling the EP. We have shown that 2π-phase accumulation is imposed on only one of the CP conversion beams defined by the chirality of the encircled EP. Exploiting a linear combination of ET and PB phases, we decoupled LCP and RCP channels. Addressing phase retardation by encircling singularities of the S-matrix opens vast research opportunities for linear and nonlinear topological electromagnetic field control at optical frequencies.

REFERENCES AND NOTES

1. N. Yu *et al.*, *Science* **334**, 333–337 (2011).
2. P. Genevet *et al.*, *Nat. Nanotechnol.* **10**, 804–809 (2015).
3. A. Alù, N. Engheta, *Nat. Photonics* **2**, 307–310 (2008).
4. Q. Song *et al.*, *Nat. Commun.* **12**, 3631 (2021).
5. M. V. Gorkunov, A. A. Antonov, Y. S. Kivshar, *Phys. Rev. Lett.* **125**, 093903 (2020).
6. D. B. Haim, L. Michaeli, O. Avayu, T. Ellenbogen, *Opt. Express* **28**, 17923–17933 (2020).
7. W. D. Heiss, *J. Phys. A Math. Theor.* **45**, 444016 (2012).
8. W. R. Sweeney, C. W. Hsu, S. Rotter, A. D. Stone, *Phys. Rev. Lett.* **122**, 093901 (2019).
9. Ş. K. Özdemir, S. Rotter, F. Nori, L. Yang, *Nat. Mater.* **18**, 783–798 (2019).
10. M.-A. Miri, A. Alù, *Science* **363**, eaar7709 (2019).
11. A. Regensburger *et al.*, *Nature* **488**, 167–171 (2012).
12. Z. Lin *et al.*, *Phys. Rev. Lett.* **106**, 213901 (2011).
13. L. Feng, Z. J. Wong, R.-M. Ma, Y. Wang, X. Zhang, *Science* **346**, 972–975 (2014).
14. J.-H. Park *et al.*, *Nat. Phys.* **16**, 462–468 (2020).
15. M. C. Rechtsman, *Nature* **548**, 161–162 (2017).
16. H. Alaeian, J. A. Dionne, *Phys. Rev. A* **89**, 033829 (2014).
17. X. Wang, X. Fang, D. Mao, Y. Jing, Y. Li, *Phys. Rev. Lett.* **123**, 214302 (2019).
18. M. Lawrence *et al.*, *Phys. Rev. Lett.* **113**, 093901 (2014).
19. S. H. Park *et al.*, *Nanophotonics* **9**, 1031–1039 (2020).
20. D. Lin, P. Fan, E. Hasman, M. L. Brongersma, *Science* **345**, 298–302 (2014).
21. G. Zheng *et al.*, *Nat. Nanotechnol.* **10**, 308–312 (2015).
22. Q. Song *et al.*, *Nat. Commun.* **11**, 2651 (2020).
23. Q. Song *et al.*, *Sci. Adv.* **7**, eabe1112 (2021).
24. E. Plum, N. I. Zheludev, *Appl. Phys. Lett.* **106**, 221901 (2015).
25. X. Yang, M. Li, Y. Hou, J. Du, F. Gao, *Opt. Express* **27**, 6801–6814 (2019).
26. A. Krasnok *et al.*, *Adv. Opt. Photonics* **11**, 892–951 (2019).
27. W. D. Heiss, H. L. Harney, *Eur. Phys. J. D* **17**, 149–151 (2001).

ACKNOWLEDGMENTS

Funding: P.G. acknowledges funding from the European Union's Horizon 2020 research and innovation program (grant agreement 639109). B.K. acknowledges funding from Office of Naval Research Young Investigator Award (N00014-17-1-2671) and the Laboratory Directed Research and Development Program of Lawrence Berkeley National Laboratory under the US Department of Energy (DE-AC02-05CH11231). **Author contributions:** Q.S., J.Z.-P., and P.G. conceived the initial ideas and carried out the experiment. Q.S. designed the structure and performed the numerical calculations. M.O. and B.K. fabricated the samples. P.G. supervised the research. All authors wrote the manuscript. **Competing interests:** The authors declare no competing financial interest. **Data and materials availability:** All data needed to evaluate the conclusions in the paper are available in the main text or the supplementary materials.

SUPPLEMENTARY MATERIALS

science.sciencemag.org/content/373/6559/1133/suppl/DC1
Materials and Methods
Supplementary Text S1 to S5
Figs. S1 to S14
References (*28*, *29*)

5 May 2021; accepted 3 August 2021
10.1126/science.abj3179

PLANT SCIENCE

Florigen sequestration in cellular membranes modulates temperature-responsive flowering

Hendry Susila[1], Snježana Jurić[1,2], Lu Liu[3,4], Katarzyna Gawarecka[1], Kyung Sook Chung[1], Suhyun Jin[1], Soo-Jin Kim[1], Zeeshan Nasim[1], Geummin Youn[1], Mi Chung Suh[5], Hao Yu[3], Ji Hoon Ahn[1]*

Plants respond to temperature changes by modulating florigen activity to optimize the timing of flowering. We show that the *Arabidopsis thaliana* mobile florigen FLOWERING LOCUS T (FT) interacts with the negatively charged phospholipid phosphatidylglycerol (PG) at cellular membranes and binds the lipid bilayer. Perturbing PG biosynthesis in phloem companion cells leads to temperature-insensitive early flowering. Low temperatures facilitate FT sequestration in the cellular membrane of the companion cell, thus reducing soluble FT levels and delaying flowering. A mutant in *PHOSPHATIDYLGLYCEROLPHOSPHATE SYNTHASE 1* accumulates more soluble FT at lower temperatures and exhibits reduced temperature sensitivity. Thus, cellular membranes sequester FT through their ability to bind the phospholipid PG, and this sequestration modulates the plant's response to temperature changes.

Plants improve their ability to survive and reproduce by monitoring ambient temperatures and modulating the complex signaling cascades that regulate growth and development (*1*, *2*). In particular, plants regulate flowering by integrating various environmental cues and endogenous signals. The transition from vegetative to reproductive growth is initiated in the leaves, which perceive floral-promoting signals such

as day length. Leaf cells produce florigen, a conserved, long-distance flowering activator that is transported to the shoot apical meristem, where it activates the plant's reproductive program. Modulation of florigen transport and activity in response to changes in ambient temperature affects crop growth. In this study, we investigated how intracellular lipid membranes regulate the transport of florigen.

To determine the lipid-binding capabilities of the florigen molecule, we tested the interaction of *Arabidopsis thaliana* FLOWERING LOCUS T (FT) (*3*) with phospholipids and galactolipids. FT preferentially interacted with negatively charged phospholipids, showing the strongest interaction with phosphatidylglycerol (PG) (Fig. 1A and fig. S1, A and B). Recombinant His-FT was pulled down with PG and phosphatidylserine (PS) in vitro (fig. S1C). Testing the binding of recombinant His-tagged FT to small unilamellar vesicles (SUVs) showed that the SUVs that were composed of 100% PG efficiently sedimented FT, whereas increasing the proportion of the neutral phospholipids phosphatidylcholine (PC) and phosphatidylethanolamine (PE) reduced FT sedimentation (Fig. 1B and fig. S1, D and E). We observed preferential binding of His-FT to PG rather than PC at acidic and neutral pH conditions (Fig. 1C and fig. S1F), which correspond to the pH of most intracellular compartments (*4*). The dissociation constant (K_d) value of the FT-PG interaction was 1.6 ± 0.9 μM; we failed to obtain a K_d value for the FT-PC pair, consistent with the preferential binding of FT to PG (fig. S1G).

We then turned to protein-lipid reciprocal coimmunoprecipitation assays in *Arabidopsis* protoplasts to assess whether FT binds phospholipids in vivo. Indeed, FT fused to the fluorescent protein mTurquoise2 (FT-mTq2) interacted with PG in vivo (Fig. 1D and fig. S1H). This is consistent with the finding that FT-mTq2 colocalized with 16:0-12:0 c7-nitro-1,2,3-benzoxadiazole-PG (tNBD-PG) in protoplasts (Fig. 1E, arrows, and fig. S2). Consistent with these observations, liquid chromatography–tandem mass spectrometry (LC-MS/MS) and ultra-performance liquid chromatography–electrospray ionization–tandem mass spectrometry (UPLC-ESI-MS/MS) analyses showed that, compared with other phospholipids, more PG (especially PG 34:4 and PG 34:3) coimmunoprecipitated with FT-GFP-His in *p35S::FT:GFP:His* plants in vivo (Fig. 1, F and G and fig. S3). We also tested the phospholipid binding potential of *Arabidopsis* FT homologs by using recombinant proteins with a His tag. As shown with FT, increasing the relative amount of PE reduced sedimentation of *Arabidopsis* FT homologs with PG SUVs (fig. S4). Thus, FT and FT-related proteins prefer to bind to PG in vitro and in vivo, which contradicts a previous report (*5*). This discrepancy is likely due to differences in experimental conditions, including pH (Fig. 1C) and PG molecular species used.

We next examined the intracellular localization of FT and its behavior at intracellular membranes. We observed localization of FT in TERMINAL FLOWER 1–related vesicles (dense, 100-nm vesicles that may be associated with trafficking to the protein storage vacuole) (*6*), as well as the outer envelope of free chloroplasts (Fig. 2A), consistent with the finding that the chloroplast envelope is rich in PG (*7*), in addition to the other organelles in which FT localizes (*8*–*10*) (fig. S5A). We confirmed the localization of FT in the chloroplast outer envelope by immunogold labeling experiments (fig. S5B). The PG-binding lipopeptide daptomycin, which competitively binds to PG, reduced FT binding to the chloroplast envelope (fig. S5C). By contrast, FT showed little colocalization with the mitochondria or multivesicular bodies (i.e., prevacuolar compartments) (Fig. 2B and fig. S5D). These results suggest that FT

[1]Department of Life Sciences, Korea University, Seoul 02841, Korea. [2]Ruđer Bošković Institute, Bijenička cesta 54, 10000 Zagreb, Croatia. [3]Department of Biological Sciences and Temasek Life Sciences Laboratory, National University of Singapore, Singapore 117543, Singapore. [4]Joint Center for Single Cell Biology, School of Agriculture and Biology, Shanghai Jiao Tong University, Shanghai 200240, China. [5]Department of Life Science, Sogang University, Seoul 04107, Korea.
*Corresponding author. Email: jahn@korea.ac.kr

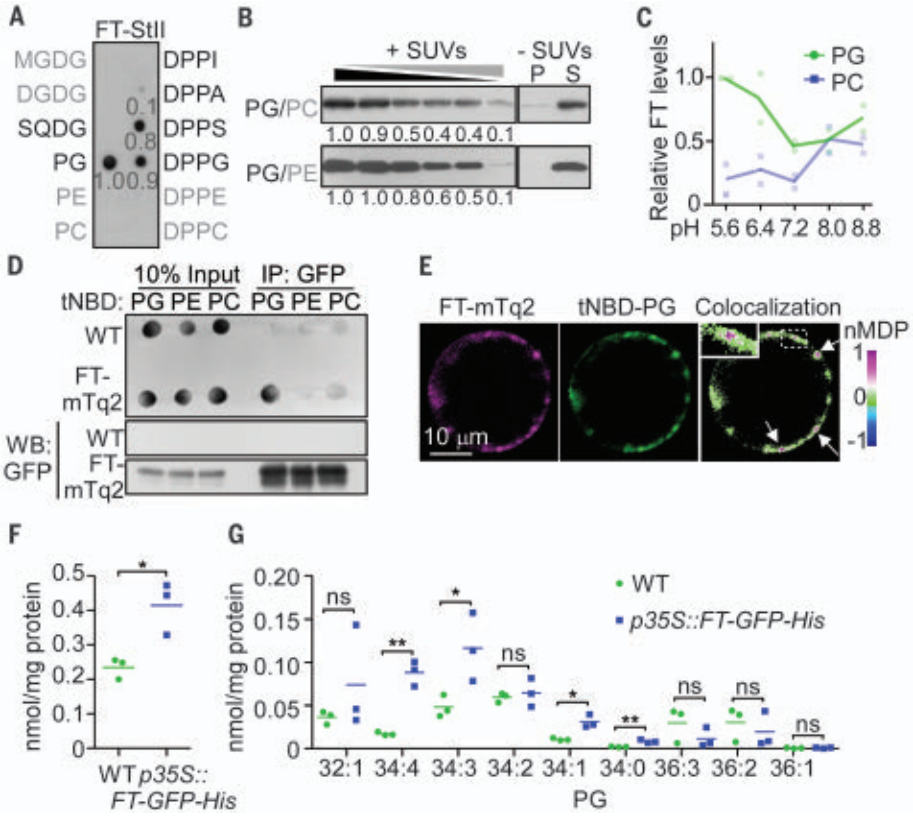


Fig. 1. Phospholipid-binding properties of FT. (**A**) Lipid overlay assay of recombinant FT fused to Strep-tag II (FT-StII) with various phospholipids and galactolipids. Black, negatively charged; gray, neutral (for further explanation and definition of abbreviations, see materials and methods). (**B**) Liposome binding assay of recombinant His-FT with different combinations of PG/PC and PG/PE SUVs. Sedimentation with 100% PG SUVs was set to 1.0. P, pellet; S, supernatant. (**C**) Relative FT levels, as detected with anti-His antibodies, from liposome binding assays using PG or PC SUVs at different pH levels. Recombinant His-FT levels with PG SUVs at pH 5.6 were set to 1.0. (**D**) In vivo protein-phospholipid coimmunoprecipitation assays using FT-mTq2 and tNBD-phospholipids in protoplasts. WT, wild type; WB, western blot; GFP, green fluorescent protein; IP, immunoprecipitation. (**E**) Colocalization of FT-mTq2 (magenta) and tNBD-PG (green) in protoplasts. Color scale, normalized mean deviation product (nMDP) from signal intensity in colocalization heatmap; arrows, colocalization spots. (**F** and **G**) Quantification of PG levels (F) and PG molecular species (G) coimmunoprecipitated by FT-GFP-His with LC-MS/MS. Asterisks represent significant differences derived from Student's *t* tests (ns, nonsignificant; *$P \leq 0.05$, **$P \leq 0.01$).

localizes to some—but not all—types of intracellular membrane compartments in vivo.

We next incubated purified thylakoids with recombinant FT to investigate how FT behaves at the PG-rich thylakoid membrane (*7*). FT was not washed away by alkaline (urea and Na_2CO_3) or chaotropic (NaCl and NaSCN) agents and was instead found in the pellet (Fig. 2C and fig. S6A), similar to the thylakoid transmembrane protein CURVATURE THYLAKOID 1A (*11*), suggesting that FT is likely buried in the membrane, similar to its putative bovine homolog (*12*). By contrast, recombinant FT proteins harboring the Arg^{119}→His (R119H) or Pro^{94}→Leu (P94L) substitutions, characteristic of the *ft-3* and *ft-6* mutants (*13*, *14*), respectively, were washed off of the membrane by alkaline and chaotropic agents, although they retained the ability to bind phospholipids (fig. S6, A to C), similar to the peripheral thylakoid protein NAD(P)H DEHYDROGENASE SUBUNIT H (*11*). The ft-3 and ft-6 proteins do not interact with the FT binding partners FD and 14-3-3 (GENERAL REGULATORY FACTOR3) (fig. S6D) (*8*, *15*), suggesting that the ft-3 and ft-6 proteins are unable to form the florigen activation complex (*15*) in the shoot apical meristem. As the R119 and P94 residues sustain the integrity of the anion binding pocket in FT (*16*), these data suggest that the conserved anion binding pocket is involved not only in the transcriptional activity of FT in the shoot apical meristem (*17*) but also in membrane binding activity.

To investigate the effects of impaired biosynthesis of PG in planta, we analyzed the flowering time of several PG biosynthesis mutants under long-day (LD) conditions. PG is synthesized mainly in the chloroplast by means of a pathway that involves several enzymes (fig. S7A). PG biosynthesis mutants (fig. S7B) (*18*–*20*), especially those lacking PHOSPHATIDYLGLYCEROLPHOSPHATE SYNTHASE 1 (PGP1) activity, flowered earlier than their parental wild type when grown at 16°C under LD conditions (Fig. 3A and table S1, experiments 1 to 5), indicating that the mutations reduced sensitivity to temperature changes and limited the extent to which lower temperatures delay flowering (Fig. 3B). We observed no flowering time phenotype for PG biosynthesis mutants grown under short-day conditions (table S1, experiments 6 and 7). Indeed, treatment with exogenous PG—but not PC and PE—delayed flowering of wild-type and *pgp1* mutants in a dose-dependent manner (table S1, experiments 8 to 13, and fig. S8).

Although the PG biosynthesis mutants flowered early, transcript levels of *FT*, *TWIN SISTER OF FT* (*TSF*), and *SUPPRESSOR OF OVEREXPRESSION OF CONSTANS 1* showed little change in these mutants relative to the wild type (fig. S9A). However, early flowering of *pgp1* mutants was suppressed by the *ft-10* and *ft-10 tsf-1* mutations (Table 1, experiments 1 and 2, and fig. S9, B and C), raising the possibility that the early flowering phenotype caused by a defect in PG biosynthesis might be associated with the regulation of FT proteins. We therefore investigated whether the loss of PGP1 alters the intracellular localization of FT. In wild-type plants grown under LD at 16°C, FT-9×myc was more abundant in the membrane fractions [P8 (nucleus, mitochondria, and chloroplast) and P100 (plasma membrane, endoplasmic reticulum, and small vesicles)], concomitant with a twofold reduction of FT in the soluble fraction (S100: cytosol and soluble proteins), when compared with plants grown at 23°C (Fig. 3C and fig. S10). However, *pgp1* mutants grown at 16°C accumulated less FT-9×myc in the membrane fractions, with FT-9×myc being enriched in the soluble fraction instead (Fig. 3C, asterisk). Further analyses showed that the sequestration of FT in the membrane of the chloroplast envelope, vesicles, and trans-Golgi network at 16°C is PG dependent (figs. S11 and S12). These findings suggest that impairment of PG biosynthesis reduces FT sequestration in intracellular membranes at low temperatures, leading to increased FT abundance in the soluble fraction and thus mimicking the FT distribution at higher temperatures. Consistent with this observation, endogenous PG levels were reduced in *pgp1* mutants at 23° and 16°C (fig. S13A). However, the levels of total PG in whole seedlings, P8, or P100 fractions were unperturbed by temperature (fig. S13, A and B). Ambient temperatures instead modulated the saturation levels of PG species (for instance, 34:4 and 36:6) (fig. S13C) (*21*). Spatial and temporal lipidomics analyses will be necessary to test the link between membrane sequestration of FT and the desaturation levels of PG species.

Our genetic analysis indicated that PG participates in the photoperiodic pathway alongside florigen. To clarify the role of PG in florigen-induced flowering, we misexpressed *FT* in companion cells of the leaf vasculature with the *SUCROSE-PROTON SYMPORTER 2* promoter (*pSUC2::FT-9×myc*) or in the shoot epidermis with the *PROTODERMAL FACTOR 1* promoter (*pPDF1::FT-9×myc*). Both transgenes suppressed late flowering of *ft-10* mutants; in particular, the *pPDF1::FT-9×myc* plants showed a strong early flowering phenotype (Table 1, experiments 3 and 4, and fig. S14A). However, only *pSUC2::FT-9×myc* plants exhibited temperature-sensitive flowering [leaf number ratio (LNR); 2.1; wild type; 2.3] (*22*), although *FT* mRNA and FT protein levels at both temperatures were similar in *pSUC2::FT-9×myc* plants (fig. S14, B and C). Introduction of *pSUC2::FT-9×myc* in the *pgp1* mutant background caused temperature-insensitive flowering (LNR: 1.5) (Fig. 3D), similar to that seen in *pgp1* mutants (LNR: 1.4). Plants expressing

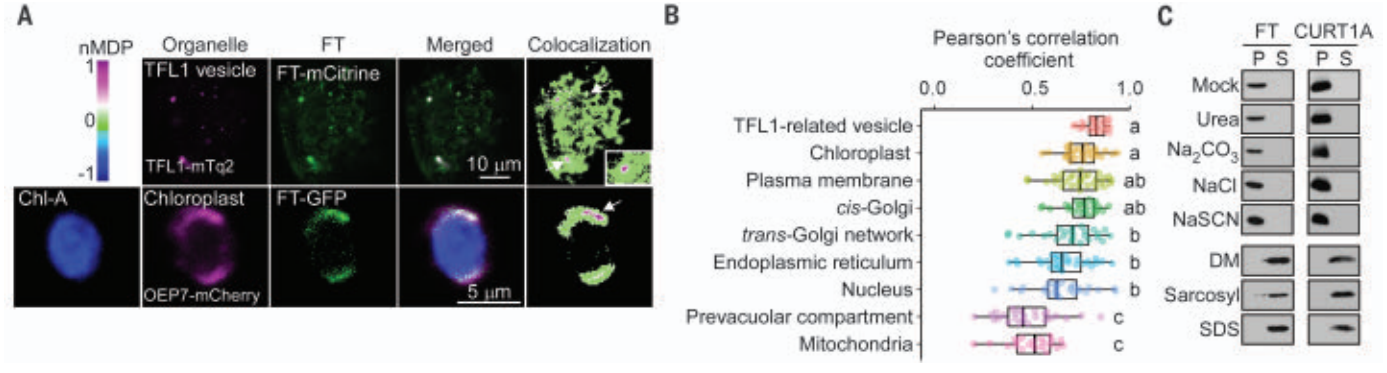


Fig. 2. FT binds the lipid bilayer of intracellular membranes. (**A**) Localization of FT-mCitrine (green) in TERMINAL FLOWER 1 (TFL1)–related vesicles (*6*) and the outer chloroplast envelope in protoplasts (mTq2-tagged membrane marker, magenta). To visualize vesicles, protoplasts were fixed with paraformaldehyde. Free chloroplasts were isolated after shearing of protoplasts to prevent a false signal from the cytosol. Color scale, nMDP from signal intensity; arrows, colocalization spots. (**B**) Quantification of colocalization of FT with intracellular membrane compartments. Different lowercase letters represent significant differences derived from a one-way analysis of variance (ANOVA) followed by Tukey's multiple comparison tests ($P \leq 0.01$). (**C**) Chemical washing experiment of His-FT binding to the thylakoid as a model membrane. CURVATURE THYLAKOID 1A (CURT1A, thylakoid transmembrane protein) was used as a control. DM, *n*-dodecyl β-D-MALTOSIDE.

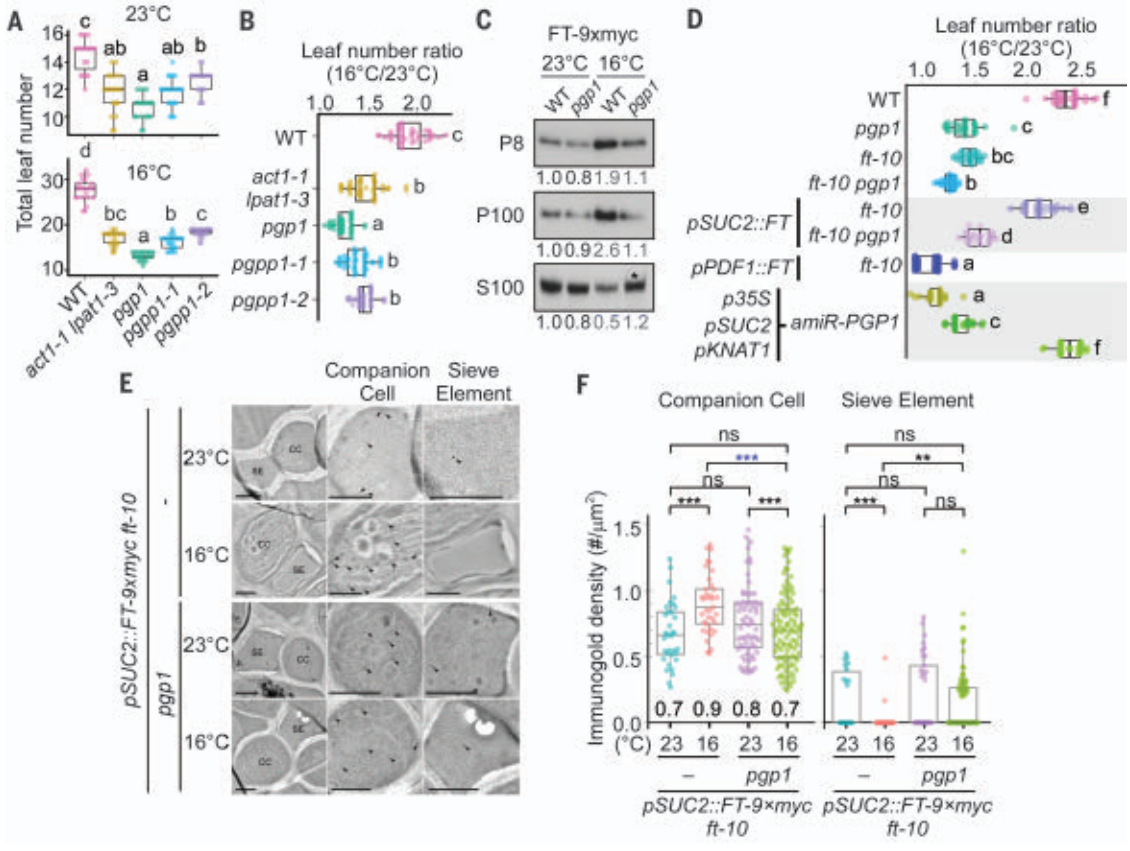


Fig. 3. Temperature and PG modulate long-distance transport of FT. (**A** and **B**) Total leaf number (A) and leaf number ratio (LNR) (B) of wild-type and PG biosynthesis mutants grown under long-day conditions. (**C**) Effect of the *pgp1* mutation on the intracellular distribution of FT in different cellular compartments of *ft-10 pSUC2::FT-9×myc* plants. (**D**) LNR of *ft-10 pgp1 pSUC2::FT-9×myc* plants and transgenic plants expressing *amiR-PGP1* under the control of different promoters. Different lowercase letters represent significant differences derived from a one-way ANOVA followed by Tukey's multiple comparison tests ($P \leq 0.01$). (**E**) Effect of the *pgp1* mutation on FT-9×myc distribution in companion cells (CC) and sieve elements (SE) in the first rosette leaf of 11-day-old *ft-10 pSUC2::FT-9×myc* seedlings, as determined by immunogold labeling. Arrowheads point to the gold particles. Scale bars, 1 μm. (**F**) Numbers of FT-9×myc immunogold particles in companion cells and sieve elements. Values are the average density of gold particles per square micrometer from at least 20 sections. Asterisks represent significant differences derived from Student's *t* tests (ns, nonsignificant; $^{**}P \leq 0.01$, $^{***}P \leq 0.001$).

FT fused with smaller tags [hemagglutinin (HA) and the 11–amino acid T7 epitope] showed similar results (table S1, experiments 14 to 16, and fig. S15) (*23*). In addition, knockdown of *PGP1* expression specifically in the leaf vasculature by artificial miRNA (amiR) technology (*24*) (*pSUC2::amiR-PGP1*) (fig. S16) resulted in early flowering at 16°C relative to the wild type (Table 1, experiments 3 and 4) and reduced temperature sensitivity (LNR: 1.3), similar to the *pgp1* mutants (Fig. 3D). However, expressing *amiR-PGP1* specifically in the shoot apical meristem from the *KNOTTED-LIKE FROM ARABIDOPSIS THALIANA* promoter (*pKNAT1::amiR-PGP1*) did not accelerate flowering (LNR: 2.2) (fig. S16). These results indicated that PG likely acts in the leaf vasculature to modulate flowering.

We then micrografted cotyledons (fig. S17A) onto *ft-10* seedlings to test the export of florigen from micrografted cotyledons. We discovered that cotyledons with the *pgp1* mutation (*pgp1 p35S::FT-GFP-His* > *ft-10*) accelerated flowering of recipient *ft-10* plants compared with cotyledons with functional PGP1 at 16°C (Table 1, experiments 5 and 6, and fig. S17, B and C). The specific ablation of chloroplasts in companion cells of the leaf vasculature using amiRNAs targeting *PLASTID TRANSCRIPTIONALLY ACTIVE 10* (*PTAC10*) or *CHLORINA42/SULFUR* (*SUL*) resulted in early flowering at 16°C with decreased LNR values (table S1, experiments 17 and 18), without affecting *FT* transcript levels (fig. S18). Together, these findings suggest that the transport of FT from the leaf is PG dependent and that PG in leaf companion cells restricts the long-distance transport of FT.

We then performed immunogold labeling to visualize the effect of PG on FT localization in the leaf vasculature. We determined that FT-9×myc is more abundant (33% increase) in the companion cells of *ft-10 pSUC2::FT-9×myc* plants grown at 16°C than at 23°C (Fig. 3, E and F). However, introduction of the *pgp1* mutation caused a 22% decrease in FT-9×myc particle density in companion cells at 16°C. Among sieve elements, we observed only 2 out of 33 sieve elements with FT-9×myc particles from *ft-10 pSUC2::FT-9×myc* plants grown at 16°C. The introduction of the *pgp1* mutation raised the frequency of FT-9×myc particles in sieve elements at 16°C (37 out of 92 sieve elements), which was thus comparable to that seen in *ft-10 pSUC2::FT-9×myc* plants at 23°C (Fig. 3F). Early flowering of *pgp1* mutants at 16°C was not suppressed by a mutation in *FT-INTERACTING PROTEIN 1* (*ftip1-1*) (table S1, experiments 19 and 20), suggesting that the transport of FT in *pgp1* mutants is mediated by an FTIP1-independent mechanism. These findings suggest that FT transport from companion cells to sieve elements occurs in a PG-dependent manner.

Our results demonstrate that FT interacts with the negatively charged phospholipid PG. Low ambient temperature promotes sequestration of FT within intracellular membranes in a PG-dependent manner, thereby restricting translocation of FT from companion cells to sieve elements to prevent precocious flowering. We propose that in addition to the FT-PC interaction in the shoot apical meristem that promotes flowering (*5*), PG-enriched membrane domains serve as docking sites for FT proteins, thus delaying flowering under unfavorable conditions such as low temperature and providing an additional layer of regulation during florigen transport. Our results further suggest that membranes sense and adapt to external temperatures and modulate the amount of membrane-bound florigen accordingly.

Table 1. Flowering times of mutants and transgenic plants. RLN, rosette leaf number; CLN, cauline leaf number; TLN, total leaf number; Stdev, standard deviation; *n*, number of plants analyzed; #, identifier of individual transgenic lines. Different lowercase letters represent significant differences derived from a one-way ANOVA followed by Tukey's multiple comparison tests ($P \leq 0.01$).

Genotype	RLN	CLN	TLN	TLN Stdev	TLN range	*n*	$P \leq 0.01$
Experiment 1 (23°C long days)							
Col-0 (wild type)	11.3	3.1	14.4	1.3	13–17	16	b
pgp1	8.4	2.0	10.4	1.4	9–12	16	a
ft-10	30.7	7.5	38.2	3.1	36–44	16	d
ft-10 pgp1	28.0	6.2	34.2	2.4	29–37	15	c
ft-10 tsf-1	46.8	13.3	60.1	2.6	55–64	10	e
ft-10 tsf-1 pgp1	46.4	11.5	57.9	2.6	53–62	11	e
Experiment 2 (16°C long days)							
Col-0 (wild type)	27.0	7.1	34.1	1.7	30–36	15	b
pgp1	11.9	2.3	14.2	1.2	11–16	16	a
ft-10	36.0	7.7	43.4	3.0	39–49	13	d
ft-10 pgp1	31.0	6.9	37.9	2.7	34–42	15	c
ft-10 tsf-1	48.6	12.3	60.9	3.6	54–66	15	e
ft-10 tsf-1 pgp1	50.4	9.9	60.3	2.9	56–64	12	e
Experiment 3 (23°C long days)							
Col-0 (wild type)	10.5	3.0	13.5	1.0	12–16	13	e
pgp1	8.5	2.1	10.6	0.8	9–12	12	cd
ft-10	28.3	5.9	34.2	2.2	31–38	12	h
ft-10 pgp1	26.1	6.1	32.2	1.6	30–36	14	g
pSUC2::FT:9xmyc ft-10	12.1	3.8	15.9	1.0	14–17	15	f
pSUC2::FT:9xmyc ft-10 pgp1	10.5	3.6	14.1	0.8	13–15	13	e
pPDF1::FT:9xmyc	4.3	1.1	5.4	0.5	5–6	15	a
35S::amiR-PGP1 #3-2	7.1	1.5	8.6	0.8	7–10	11	b
35S::amiR-PGP1 #6-1	7.3	1.7	9.0	0.7	8–10	12	bc
pSUC2::amiR-PGP1 #1-2	8.1	2.5	10.6	1.0	9–12	12	cd
pSUC2::amiR-PGP1 #2-1	9.1	2.5	11.6	0.7	10–12	13	d
pKNAT1::amiR-PGP1 #4-4	9.9	2.7	12.6	0.7	12–14	12	e
pKNAT1::amiR-PGP1 #9-6	10.1	2.9	13.0	0.8	12–14	12	e
Experiment 4 (16°C long days)							
Col-0 (wild type)	25.6	6.1	31.7	1.8	29–35	13	ef
pgp1	12.8	2.7	15.5	1.1	14–17	12	c
ft-10	40.3	9.0	49.3	2.4	45–53	13	h
ft-10 pgp1	32.8	7.6	40.4	1.7	37–42	13	g
pSUC2::FT:9xmyc ft-10	25.3	8.3	33.6	2.3	29–37	13	f
pSUC2::FT:9xmyc ft-10 pgp1	16.0	5.6	21.6	1.5	19–23	14	d
pPDF1::FT:9xmyc	5.1	0.7	5.8	0.8	5–7	17	a
35S::amiR-PGP1 #3-2	8.4	1.4	9.8	0.6	8–10	11	b
35S::amiR-PGP1 #6-1	8.6	1.6	10.2	0.6	9–11	12	b
pSUC2::amiR-PGP1 #1-2	13.5	3.5	17.0	1.1	15–19	10	c
pSUC2::amiR-PGP1 #2-1	12.6	3.1	15.7	1.4	14–18	11	c
pKNAT1::amiR-PGP1 #4-4	23.9	6.0	29.9	1.5	27–32	11	e
pKNAT1::amiR-PGP1 #9-6	23.9	5.5	29.4	1.9	26–32	11	e
Experiment 5 (23°C long days) (donor > recipient)							
ft-10 > ft-10	38.9	7.9	46.8	2.3	43–51	17	c
Col-0 (wild type) > *ft-10*	29.3	6.8	36.1	2.7	31–40	11	b
pgp1 > ft-10	27.2	7.7	34.9	1.7	32–37	10	b
35S::FT:GFP:His > ft-10	22.5	7.1	29.6	4.2	27–35	16	a
35S::FT:GFP:His pgp1 > ft-10	19.9	6.8	26.7	3.7	20–32	12	a
Experiment 6 (16°C long days) (donor > recipient)							
ft-10 > ft-10	42.1	9.6	51.7	2.6	48–55	11	d
Col-0 (wild type) > *ft-10*	35.3	7.8	43.1	3.6	37–48	12	c
pgp1 > ft-10	32.9	6.3	39.2	3.7	35–47	10	bc
35S::FT:GFP:His > ft-10	31.2	7.5	38.7	7.3	26–46	13	b
35S::FT:GFP:His pgp1 > ft-10	23.0	6.1	29.1	2.5	25–32	10	a

Because FT-like florigen proteins have conserved functions across plant species (*25*), sequestration of FT in membranes might serve as a common strategy for plants to adjust the timing of flowering in response to changing seasonal temperatures.

REFERENCES AND NOTES

1. M. Legris, C. Nieto, R. Sellaro, S. Prat, J. J. Casal, *Plant J.* **90**, 683–697 (2017).
2. H. Susila, Z. Nasim, J. H. Ahn, *Int. J. Mol. Sci.* **19**, 3196 (2018).
3. L. Corbesier *et al.*, *Science* **316**, 1030–1033 (2007).
4. J. Shen *et al.*, *Mol. Plant* **6**, 1419–1437 (2013).
5. Y. Nakamura *et al.*, *Nat. Commun.* **5**, 3553 (2014).
6. E. J. Sohn *et al.*, *Proc. Natl. Acad. Sci. U.S.A.* **104**, 18801–18806 (2007).
7. P. Moreau *et al.*, *Prog. Lipid Res.* **37**, 371–391 (1998).
8. M. Abe *et al.*, *Science* **309**, 1052–1056 (2005).
9. L. Liu, C. Li, Z. W. N. Teo, B. Zhang, H. Yu, *Plant Cell* **31**, 2475–2490 (2019).
10. L. Liu *et al.*, *PLOS Biol.* **10**, e1001313 (2012).
11. U. Armbruster *et al.*, *Plant Cell* **25**, 2661–2678 (2013).
12. B. S. Vallée *et al.*, *Eur. J. Biochem.* **268**, 5831–5841 (2001).
13. M. Koornneef, C. J. Hanhart, J. H. van der Veen, *Mol. Gen. Genet.* **229**, 57–66 (1991).
14. Y. Kobayashi, H. Kaya, K. Goto, M. Iwabuchi, T. Araki, *Science* **286**, 1960–1962 (1999).
15. K. Taoka *et al.*, *Nature* **476**, 332–335 (2011).
16. J. H. Ahn *et al.*, *EMBO J.* **25**, 605–614 (2006).
17. W. W. H. Ho, D. Weigel, *Plant Cell* **26**, 552–564 (2014).
18. H. U. Kim, P. Vijayan, A. S. Carlsson, L. Barkan, J. Browse, *Plant Physiol.* **153**, 1135–1143 (2010).
19. C. Xu *et al.*, *Plant Physiol.* **129**, 594–604 (2002).
20. Y.-C. Lin, K. Kobayashi, C.-H. Hung, H. Wada, Y. Nakamura, *Plant J.* **88**, 1022–1037 (2016).
21. Q. Li *et al.*, *Plant Cell* **27**, 86–103 (2015).
22. L. Liu, Y. Zhang, H. Yu, *J. Integr. Plant Biol.* **62**, 1385–1398 (2020).
23. C. Lee *et al.*, *Plant J.* **99**, 452–464 (2019).
24. R. Schwab, S. Ossowski, M. Riester, N. Warthmann, D. Weigel, *Plant Cell* **18**, 1121–1133 (2006).
25. S. Jin, Z. Nasim, H. Susila, J. H. Ahn, *Semin. Cell Dev. Biol.* **109**, 20–30 (2020).

ACKNOWLEDGMENTS

We are grateful to J. Browse, C. Benning, and D. Weigel for providing research materials and H. K. Song for fluorescence polarization spectroscopy experiments. We also thank S. J. Yoo, Y. J. Kim, S. M. Hong, and H. Y. Shin for technical assistance. **Funding:** This work was supported by a National Research Foundation (NRF) of Korea grant funded by the Korean government (NRF-2017R1A2B3009624 to J.H.A.) and Samsung Science and Technology Foundation (SSTF-BA1602-12 to J.H.A). This work was also supported by the Singapore National Research Foundation Investigatorship Programme (NRFNRFI2016-02 to H.Y). **Author contributions:** H.S., S.Ju., and J.H.A conceived the research direction; H.S. performed most of the experiments; S.Ju. performed preliminary analyses; L.L. and H.Y. performed immunogold transmission electron microscopy; K.G. and M.C.S. performed lipidomics analysis; K.G. performed PG feeding experiments; K.G., K.S.C., and H.S. performed cotyledon grafting; K.S.C., S.Ji., G.Y., and Z.N. generated the transgenic lines; S.-J.K. generated the untagged FT protein; H.S. and J.H.A. analyzed and interpreted data, supervised the project, and wrote the manuscript; and S.Ju., L.L., and H.Y. commented on the manuscript. **Competing interests:** The authors declare no competing interests. **Data and materials availability:** All data are available in the main text or in the supplementary materials.

SUPPLEMENTARY MATERIALS

science.sciencemag.org/content/373/6559/1137/suppl/DC1
Materials and Methods
Figs. S1 to S18
Tables S1 to S3
References (*26*–*66*)
MDAR Reproducibility Checklist

6 March 2021; accepted 7 July 2021
10.1126/science.abh4054

CORONAVIRUS

Structural basis of mismatch recognition by a SARS-CoV-2 proofreading enzyme

Chang Liu[1]*, Wei Shi[2], Scott T. Becker[3], David G. Schatz[1], Bin Liu[2]*, Yang Yang[3]*

Coronavirus 3′-to-5′ exoribonuclease (ExoN), residing in the nonstructural protein (nsp) 10–nsp14 complex, boosts replication fidelity by proofreading RNA synthesis and is critical for the virus life cycle. ExoN also recognizes and excises nucleotide analog inhibitors incorporated into the nascent RNA, undermining the effectiveness of nucleotide analog–based antivirals. Here we present cryo–electron microscopy structures of both wild-type and mutant severe acute respiratory syndrome coronavirus 2 (SARS-CoV-2) nsp10-nsp14 in complex with an RNA substrate bearing a 3′-end mismatch at resolutions ranging from 2.5 to 3.9 angstroms. The structures reveal the molecular determinants of ExoN substrate specificity and offer insight into the molecular mechanisms of mismatch correction during coronavirus RNA synthesis. Our findings provide guidance for rational design of improved anticoronavirus therapies.

Severe acute respiratory syndrome coronavirus 2 (SARS-CoV-2), the causative agent of the COVID-19 pandemic, has infected more than 160 million people and led to more than 3 million deaths worldwide (https://covid19.who.int). Although several SARS-CoV-2 vaccines are now available (*1*), there are no highly effective antiviral agents to treat the disease. One of the most important druggable targets for SARS-CoV-2 is its replication-and-transcription complex (RTC), a multisubunit machine that carries out viral genome replication and transcription and plays an essential role in the virus life cycle (*2*, *3*). Central to the coronavirus RTC is the core RNA-dependent RNA polymerase (RdRp); nonstructural protein 12 (nsp12) (*4*); and two associated accessory proteins, nsp7 and nsp8 (*5*). SARS-CoV-2 RdRp is a promising target for nucleotide analog antivirals such as remdesivir (*6*, *7*). However, the efficacy of nucleotide analog inhibitors on coronavirus RdRp is compromised by the presence of the viral nsp14 exoribonuclease (ExoN) (*8*, *9*), an RNA proofreader that is specific to coronaviruses and a few other closely related virus families of the Nidovirales order and crucial to maintain the integrity of their unusually large RNA genome (*9*–*11*). In addition, ExoNs from coronaviruses and other RNA viruses play a key role in the evasion of host immune responses by degrading the viral double-stranded RNA (dsRNA) intermediates that would otherwise be recognized by host pathogen recognition receptors (*12*–*15*).

Nsp14 is a bifunctional enzyme that harbors both 3′-to-5′ ExoN and mRNA cap guanine-N7 methyltransferase (N7-MTase) activities (*16*, *17*) (Fig. 1A). The N-terminal ExoN domain of nsp14 improves RNA synthesis fidelity by removing misincorporated nucleotides or nucleotide analogs from the nascent RNA, whereas the C-terminal N7-MTase domain is involved in the 5′ capping processes of the viral genomic and subgenomic mRNAs (*16*–*18*). The ExoN activity of nsp14 is stimulated by nsp10, which binds to the ExoN domain and helps stabilize the architecture of the ExoN active site (*18*). Previous studies of the SARS-CoV nsp10-nsp14 complex defined the nsp14 ExoN domain as a DED/EDh-type exonuclease and identified the five active-site residues through structural comparison and mutagenesis analyses (*19*). However, the molecular details of substrate binding by coronavirus nsp10-nsp14 ExoN remain unclear. In addition, how the viral ExoN recognizes and excises misincorporated nucleotides or nucleotide analog inhibitors at the 3′ end of the newly synthesized RNA is poorly understood.

To understand the substrate recognition and catalytic mechanism of SARS-CoV-2 ExoN, we constructed a hairpin RNA substrate (hereafter referred to as T35P31) that contains a template strand (T-strand, which is also the nonscissile strand for ExoN) with three initiating guanosines followed by the 32 nucleotides (nts) at the 3′ end of the SARS-CoV-2 genome [excluding the poly(A) tail] and a 31-nt product strand (P-strand, which is also the scissile strand for ExoN) ending with a cytidine-5′-monophosphate (CMP), resulting in a C-U mismatch at the 3′ end (Fig. 1C). The preformed SARS-CoV-2 nsp10-nsp14 complex digests the T35P31 RNA substrate in the presence of $MgCl_2$ (Fig. 1B). To obtain a stable nsp10-nsp14-RNA complex, we substituted $MgCl_2$ with $CaCl_2$ in the reconstitution buffer or introduced an ExoN active-site mutation, E191A, to nsp14. Both measures retained the RNA binding capability but abolished the RNA cleavage activity of the nsp10-nsp14 complex (Fig. 1B and figs. S1 and S2).

[1]Department of Immunobiology, Yale School of Medicine, New Haven, CT, USA. [2]Section of Transcription and Gene Regulation, The Hormel Institute, University of Minnesota, Austin, MN, USA. [3]Roy J. Carver Department of Biochemistry, Biophysics and Molecular Biology, Iowa State University, Ames, IA, USA.
***Corresponding author. Email: c.liu@yale.edu (C.L.); liu00794@umn.edu (B.L.); yan9yang@iastate.edu (Y.Y.)**

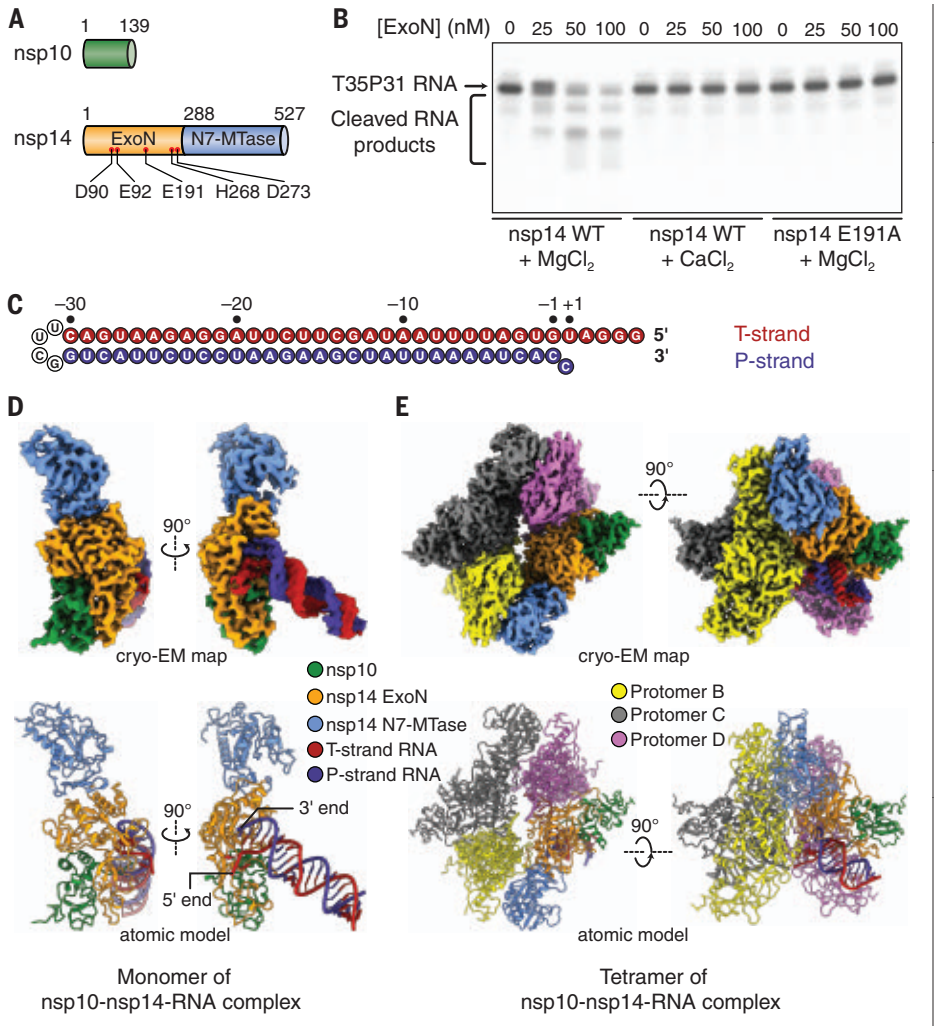


Fig. 1. Structural and functional overview of SARS-CoV-2 nsp10-nsp14-RNA complexes. (**A**) Domain organization of SARS-CoV-2 nsp10 and nsp14. Domain boundary residues are numbered. Five catalytic residues in the nsp14 ExoN domain are indicated as red dots and are labeled. (**B**) Cleavage of T35P31 RNA substrate by SARS-CoV-2 nsp10-nsp14 ExoN complex. The nanomolar concentrations of WT or E191A mutant ExoN are indicated. The RNAs were resolved by denaturing polyacrylamide gel electrophoresis (PAGE) and stained by SYBR Gold. A representative result from three biological replicates is shown. (**C**) Sequence and numbering of the T35P31 RNA substrate used in biochemical characterization and structural determination. T-strand (template strand) and P-strand (product strand) RNAs are connected by a UUCG tetraloop. (**D**) Cryo-EM map and atomic model of the monomeric form of the SARS-CoV-2 nsp10-nsp14-RNA complex. (**E**) Cryo-EM map and atomic model of the tetrameric form of the SARS-CoV-2 nsp10-nsp14-RNA complex. A, Ala; D, Asp; E, Glu; H, His.

The reconstituted nsp10-nsp14-RNA complexes were purified by size-exclusion chromatography (SEC) and analyzed by single-particle cryo–electron microscopy (cryo-EM). The final cryo-EM maps for the wild-type (WT) and mutant nsp10-nsp14-RNA complexes were refined to 3.9 Å (figs. S1 and S3) and 3.4 Å (figs. S2 and S3), respectively. With the exception of minor differences in the conformations of the RNA substrate and protein residue side chains, the two structures are almost identical, with a root mean square deviation of 0.39 Å across all protein Cα atoms (fig. S4). The ExoN active site, which is located in the nsp14 ExoN domain and supported by the N terminus of nsp10, binds the 3′ end of the RNA, separating it from the 5′ overhang (Fig. 1D). Most of the RNA helix remains freely accessible in the solvent-exposed space (Fig. 1D).

To explore the possible link between SARS-CoV-2 RdRp and ExoN, SARS-CoV-2 nsp8 was included in the reconstitution of the complex and was found to be coeluted with the nsp10-nsp14-RNA complex on the SEC column (figs. S1A and S2A). However, it did not form a stable complex with nsp10-nsp14-RNA in the cryo-EM sample and was observed in only a small fraction of the particles (fig. S2C), indicating that association of nsp8 with the nsp10-nsp14-RNA complex is weak and dynamic. Although further in silico classification of the nsp8-bound class did not yield a map with high-resolution features of nsp8, the 6-Å low-pass–filtered map showed strong extra density along the solvent exposed region of the RNA duplex (fig. S2C). When docking nsp8 from the SARS-CoV-2 RdRp complex structure (*20*) into the density as a rigid body, its N-terminal extended helices fit generally well, and its orientation relative to the RNA backbone matched that in the SARS-CoV-2 RdRp complex (*20*, *21*) (fig. S5A). The docking places the C-terminal domain of nsp8 outside of the cryo-EM density, but there is unoccupied cryo-EM density adjoining the N-terminal helices (fig. S5A), which suggests that nsp8 likely adopts a conformation that differs from when it is in the RdRp complex. This is consistent with previous structural studies, demonstrating extensive structural plasticity of nsp8 (*21*–*23*). The binding mode of nsp8 to the nsp10-nsp14-RNA complex suggests that nsp8 may help stabilize substrate binding for ExoN-mediated RNA cleavage. Indeed, an exoribonuclease activity assay shows that nsp8 enhances RNA digestion by the nsp10-nsp14 complex (fig. S5B). As a common component in both ExoN and RdRp complexes, nsp8 may play a role in RNA substrate transfer between the two enzymes. However, elucidating the detailed function of nsp8 in mismatch correction in vivo will require further investigation.

The cryo-EM sample reconstituted with the use of mutant ExoN contained a class that represents a tetrameric form of the nsp10-nsp14-RNA complex (Fig. 1E and fig. S2C). The tetramerization improved the resolution of three-dimensional (3D) reconstruction to 2.5 Å without affecting the architecture of the complex (figs. S2C and S6A). However, tetramerization of the nsp10-nsp14-RNA complex likely blocks nsp8 binding (fig. S6B). As a result, nsp8-like density is not observed along the RNA duplex in the tetramer map. Although 2D class averages from the WT nsp10-nsp14-RNA complex dataset also reveal particles that likely represent the tetrameric form of the complex (fig. S1B), the limited quantity of such particles precluded a meaningful 3D reconstruction. Unless otherwise indicated, we used the tetramer form of the nsp10-nsp14-RNA complexes for subsequent structural analyses of the ExoN active site and its interactions with RNA substrate because of its higher resolution.

Compared with the apo form of the SARS-CoV nsp10-nsp14 complex (*19*), the structure of the SARS-CoV-2 WT nsp10-nsp14-RNA complex displays local conformational changes in the α4-α5 and α2-α3 loops, resulting in a slightly narrowed RNA binding pocket (Fig. 2A).

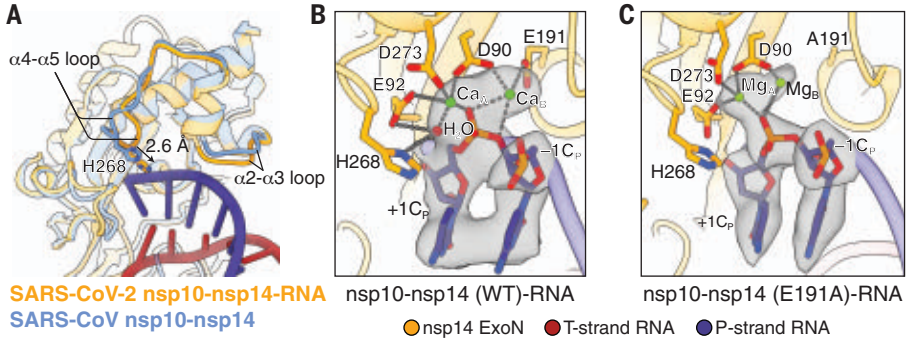


Fig. 2. Active-site conformation and catalytic mechanism of SARS-CoV-2 ExoN. (**A**) Superimposition of the SARS-CoV nsp10-nsp14 complex (blue; PDB ID 5C8U) and the SARS-CoV-2 nsp10-nsp14-RNA complex (orange) illustrates the conformational changes of the α2-α3 and α4-α5 loops and a 2.6-Å shift of H268 toward the RNA upon substrate binding. (**B**) Active-site structure of the SARS-CoV-2 nsp10-nsp14 (WT)–RNA complex. Ca^{2+} ions, green spheres; catalytic water, red sphere. Nucleotide residues in P-strand RNA are indicated with a subscript "P." +1C$_P$, −1C$_P$, the catalytic water, and two active-site metal ions are superimposed with their cryo-EM densities contoured at 10σ. (**C**) Active-site structure of the SARS-CoV-2 nsp10-nsp14 (E191A)–RNA complex. Mg^{2+} ions, green spheres. +1C$_P$, −1C$_P$, and two active-site metal ions are superimposed with their cryo-EM densities contoured at 7σ.

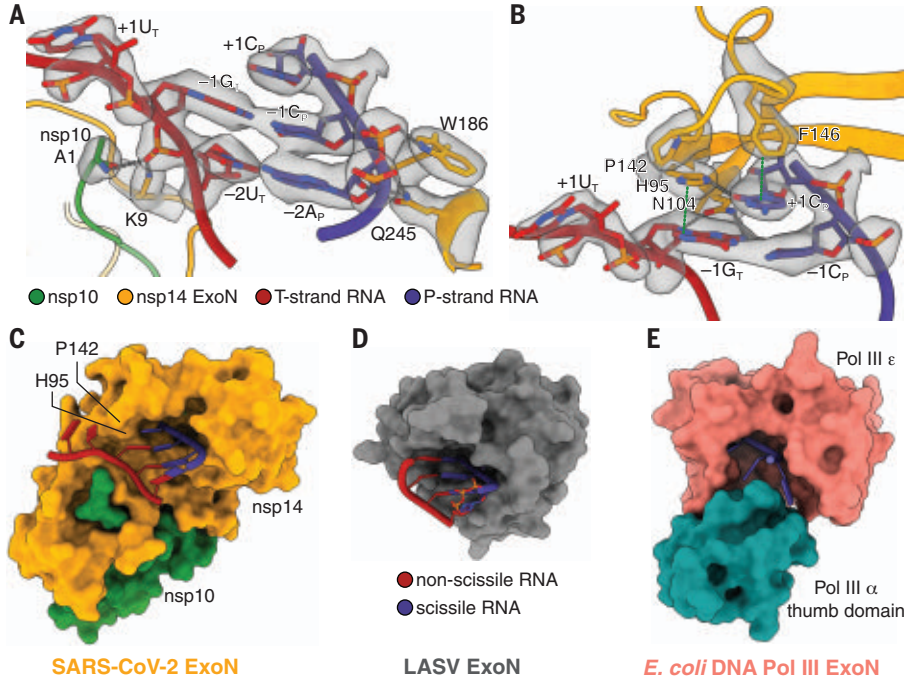


Fig. 3. Mechanism of substrate recognition by SARS-CoV-2 ExoN. (**A**) Interactions between SARS-CoV-2 nsp10-nsp14 ExoN and the T35P31 RNA backbone. Nucleotide residues in T-strand RNA are indicated with a subscript "T," whereas nucleotide residues in P-strand RNA are indicated with a subscript "P." Hydrogen bonds and salt bridges are shown as gray dotted lines. Interacting nucleotide and protein residues are superimposed with their cryo-EM densities contoured at 7σ. (**B**) Interactions between SARS-CoV-2 nsp10-nsp14 ExoN and T35P31 RNA at +1 and −1 nucleobase positions. Hydrogen bonds and salt bridges are shown as gray dotted lines. π-π stacking interactions are indicated by green dotted lines. Interacting nucleotide and protein residues are superimposed with their cryo-EM densities contoured at 7σ. (**C**) Surface representation of the SARS-CoV-2 nsp10-nsp14 ExoN substrate binding pocket shows a restricted opening on the T-strand side that prevents base-pairing at the substrate RNA +1 position. For clarity, the N7-MTase domain of nsp14 is not shown. (**D**) Surface representation of the LASV NP ExoN domain. A fully base-paired dsRNA substrate (shown in cartoon representation) is bound in the substrate binding pocket of LASV ExoN. (**E**) Surface representation of the *E. coli* DNA Pol III ExoN complex. The narrow substrate binding pocket allows the entry of ssDNA only. F, Phe; K, Lys; N, Asn; P, Pro; Q, Gln; W, Trp.

Substrate binding also leads to full assembly of the ExoN active site. Whereas apo ExoN captures only one divalent metal ion (*19*), the RNA-bound ExoN contains two metal ion binding sites in its catalytic center (Fig. 2B and fig. S7A). Metal ion A, coordinated by carboxylate oxygens of D90, E92, and D273, activates a water molecule for nucleophilic attack. Metal ion B is coordinated by D90 and E191 and stabilizes the O3′ leaving group of −1C$_P$ (nucleotide numbering shown in Fig. 1C) (Fig. 2B and fig. S7A). In the E191A mutant nsp10-nsp14-RNA complex, metal ion B is poorly coordinated, owing to the absence of the E191 side-chain carboxylate and is out of the coordination distance from the O3′ leaving group of −1C$_P$ (Fig. 2C and fig. S7B). The fifth catalytic residue, H268, which functions as a general base and deprotonates the catalytic water during the phosphoryl-transfer reaction (*24*, *25*) (Fig. 2B and fig. S7A), is located in the nsp14 α4-α5 loop and shifts 2.6 Å toward the scissile phosphate, completing the active site in the presence of the RNA substrate (Fig. 2A).

The nucleoprotein (NP) of Lassa virus (LASV) in the Arenaviridae family represents the only other group of ExoNs found in RNA viruses (*14*, *15*, *26*). Although the coronavirus nsp14 and arenavirus NPs have evolved divergent additional domains to address different functions (*15*), the overall fold and active-site conformation of their ExoN domains are similar (fig. S7, C and D). The primary difference is that D466 of the LASV NP undertakes the role of E191 in nsp14 to coordinate metal ion B, presumably through an intermediate water molecule, owing to its shorter side chain (fig. S7D).

The shallow SARS-CoV-2 ExoN substrate binding pocket encompasses only base pairs −1 and −2 of the dsRNA, interacting with the RNA backbone through the A1 of nsp10 and K9, W186, and Q245 in nsp14 (Fig. 3A). At the 3′ end of the dsRNA substrate, nsp14 separates the mismatched C-U pair and flips +1U$_T$ out of the RNA double helix (Fig. 3, A and B). As a result, binding in the SARS-CoV-2 ExoN active site is a dsRNA with a 1-nt 3′ overhang comprising +1C$_P$ (Fig. 3, A and B), a substrate structure different from that observed in other RNA virus and proofreading DED/EDh exonucleases (*26*–*28*) and from that previously predicted for SARS-CoV ExoN (*8*, *18*). The substrate specificity of SARS-CoV-2 ExoN is contributed by many interactions between nsp14 and the RNA substrate (Fig. 3, A and B). F146 at the bottom of the SARS-CoV-2 ExoN substrate binding pocket stacks against the 3′-end unpaired +1C$_P$. N104 inserts into the minor groove of the dsRNA and establishes two hydrogen bonds with the nucleobase and 2′-OH group of −1G$_T$, respectively. H95, which is approximately coplanar with the unpaired +1C$_P$, is hydrogen-bonded with the cytidine base and stacks against −1G$_T$ (Fig. 3B). The ability of

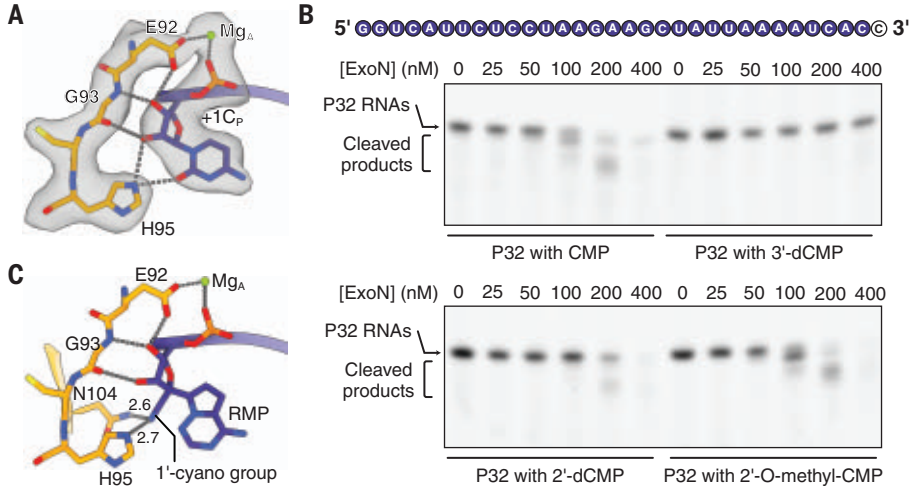


Fig. 4. Structural insights into antiviral design. (**A**) Interactions between SARS-CoV-2 nsp10-nsp14 ExoN and the 3′-end nucleotide mediated by its 2′- and 3′-OH groups. Mg^{2+} ion, green sphere. Hydrogen bonds are shown as gray dotted lines. $+1C_P$ and its interacting protein residues are superimposed with cryo-EM densities contoured at 7σ. (**B**) Cleavage of various P32 ssRNA substrates by the SARS-CoV-2 nsp10-nsp14 complex. The 3′-end CMP that bears different modifications at its 2′- or 3′-OH groups is shown as a black letter in a white circle. The nanomolar concentrations of ExoN are indicated. The RNAs were resolved by denaturing PAGE and stained by SYBR Gold. A representative result from three biological replicates is shown. (**C**) Predicted interactions between SARS-CoV-2 nsp10-nsp14 ExoN and RMP, which is modeled at the 3′-end +1 position of P-strand RNA. G, Gly.

H95 to act as both hydrogen bond donor and acceptor probably allows it to accommodate all four types of nucleotides, explaining the relative insensitivity of nsp14 to substrate sequence (*18*). Digestion of dsRNA substrates by SARS-CoV-2 ExoN may slow at a C-G base pair, owing to the higher energy required to break this base pair. Additionally, P142, situated at the rim of the ExoN RNA binding pocket, works together with H95 to restrict the depth of the substrate binding pocket on the T-strand side and likely forces the strand separation of the RNA substrate 3′-end C-U mismatched pair (Fig. 3, B and C). The lower energy needed for separating a mismatched base pair could explain the preference of coronavirus ExoN for a dsRNA substrate with a 3′-end mismatch instead of a perfectly matched substrate (*18*). By contrast, the LASV ExoN RNA binding pocket has a slightly deeper opening on the nonscissile strand side and therefore is able to accommodate a fully base-paired dsRNA substrate (*26*) (Fig. 3D). This is consistent with its role as a dsRNA-degrading immune suppressor rather than an RNA synthesis proofreader (*14*, *15*). At the other end of the spectrum are DNA polymerase–associated proofreading ExoNs, such as the *Escherichia coli* DNA polymerase III (Pol III) ε subunit. This subunit has a much narrower DNA binding pocket, partially because of its tight association with the Pol III α subunit, and can fit only a single-stranded DNA substrate (*27*) (Fig. 3E). All of the RNA-contacting residues in nsp14 are highly conserved among different coronavirus genera (fig. S8), indicating a shared RNA substrate recognition mechanism of coronavirus ExoN.

As a 3′-to-5′ exoribonuclease, SARS-CoV-2 nsp10-nsp14 specifically recognizes the 2′- and 3′-OH groups of the 3′-end nucleotide. The 2′-OH of $+1C_P$ forms two hydrogen bonds with H95 and the carbonyl oxygen of G93, respectively, whereas the 3′-OH of the nucleotide is hydrogen bonded with the G93 main-chain nitrogen and catalytic residue E92 (Fig. 4A). To examine the effects of the 2′- and 3′-OH groups of the 3′-end nucleotide on RNA cleavage efficiency by SARS-CoV-2 ExoN, we performed exonuclease assays using 32-nt single-stranded RNA (ssRNA) substrates (referred to as P32 RNAs) ending with either a standard ribonucleotide or a nucleotide with modifications at the 2′ or 3′ position (Fig. 4B). SARS-CoV-2 nsp10-nsp14 efficiently cleaves the unmodified ssRNA, although significantly higher enzyme concentrations are needed to obtain cleavage comparable to that achieved on a dsRNA substrate with the same P-strand sequence (fig. S9). This is likely due to the weaker binding of ssRNA to SARS-CoV-2 ExoN, resulting from the loss of protein-RNA interactions on the T-strand side (Fig. 3, A and B). The ability of ExoN to accept both ssRNA and dsRNA substrates suggests two possible modes of mismatch correction in vivo. ExoN may bind to and cleave the 3′-end single-stranded region of P-strand RNA, which resulted from RdRp backtracking, as proposed by previous studies (*21*, *29*). Alternatively, dsRNA substrates that contain a 3′-end mismatch may dissociate from RdRp and are subsequently recognized by ExoN for mismatch excision.

Removing the 2′- or 3′-OH groups of the 3′-end nucleotide either reduces or almost abolishes nucleolytic degradation by SARS-CoV-2 ExoN within the range of tested enzyme concentrations (Fig. 4B), consistent with the previous findings on SARS-CoV ExoN (*18*) and reflecting the key roles of 2′- and 3′-oxygens in coronavirus ExoN catalysis. On the other hand, 2′-O-methylation of the 3′-end cytidine does not substantially affect the substrate cleavage by SARS-CoV-2 nsp10-nsp14 (Fig. 4B), likely because some interactions between the 2′-oxygen and nsp14 are retained.

Remdesivir is the only US Food and Drug Administration–approved nucleotide analog antiviral to treat COVID-19. To assess whether remdesivir can be effectively excised by SARS-CoV-2 ExoN, we modeled the incorporated form of the inhibitor, remdesivir monophosphate (RMP), at the +1 position of the P-strand (Fig. 4C). The modeled RMP maintains most of the favorable interactions formed between nsp14 and the 3′-end CMP. In addition, the 1′-cyano group of RMP, the determinant of its delayed RdRp stalling activity (*6*, *7*), snugly fits in the space between H95 and N104 and forms hydrogen bonds with the side-chain nitrogen atoms from the two residues (Fig. 4C). These observations indicate that product RNA containing RMP could be a substrate for coronavirus ExoN, consistent with the findings that RNA terminated with RMP does not display substantial resistance to ExoN excision (*30*) and that coronaviruses lacking ExoN proofreading activity are significantly more sensitive to remdesivir (*31*).

Our study offers insights into the mechanism of mismatch correction during SARS-CoV-2 RNA synthesis and reveals the structural features in the substrate that are essential for ExoN recognition and catalysis, providing a basis for structural-guided design of specific and potent ExoN inhibitors. Coadministration of such ExoN inhibitors with nucleotide analog–based viral RdRp antivirals could constitute a more effective treatment for COVID-19. Additionally, our study sheds light on the development of ExoN-resistant nucleotide analog inhibitors. In particular, we show that a free 3′-OH of the RNA substrate is critical for exonucleolytic degradation by ExoN. It has been shown that 3′-deoxy ribonucleotides can be efficiently incorporated into nascent RNA by RdRp from other positive-strand RNA viruses, such as hepatitis C virus and poliovirus, and can subsequently block RNA extension (*32*, *33*). Therefore, 3′-deoxy nucleotide analogs can potentially act as effective coronavirus RdRp chain terminators that also resist ExoN excision. Nonetheless, modifications at other positions on the ribose ring also merit further exploration.

REFERENCES AND NOTES

1. A. Mullard, *Nat. Rev. Drug Discov.* **20**, 8 (2021).
2. J. Ziebuhr, *Curr. Top. Microbiol. Immunol.* **287**, 57–94 (2005).
3. I. Sola, F. Almazán, S. Zúñiga, L. Enjuanes, *Annu. Rev. Virol.* **2**, 265–288 (2015).
4. A. J. te Velthuis, J. J. Arnold, C. E. Cameron, S. H. van den Worm, E. J. Snijder, *Nucleic Acids Res.* **38**, 203–214 (2010).
5. Y. Gao *et al.*, *Science* **368**, 779–782 (2020).
6. G. Kokic *et al.*, *Nat. Commun.* **12**, 279 (2021).
7. J. P. K. Bravo, T. L. Dangerfield, D. W. Taylor, K. A. Johnson, *Mol. Cell* **81**, 1548–1552.e4 (2021).
8. F. Ferron *et al.*, *Proc. Natl. Acad. Sci. U.S.A.* **115**, E162–E171 (2018).
9. F. Robson *et al.*, *Mol. Cell* **79**, 710–727 (2020).
10. A. E. Gorbalenya, L. Enjuanes, J. Ziebuhr, E. J. Snijder, *Virus Res.* **117**, 17–37 (2006).
11. N. S. Ogando *et al.*, *J. Virol.* **94**, e01246-20 (2020).
12. M. Becares *et al.*, *J. Virol.* **90**, 5399–5414 (2016).
13. J. B. Case *et al.*, *J. Virol.* **92**, e01531-17 (2017).
14. K. M. Hastie, C. R. Kimberlin, M. A. Zandonatti, I. J. MacRae, E. O. Saphire, *Proc. Natl. Acad. Sci. U.S.A.* **108**, 2396–2401 (2011).
15. X. Qi *et al.*, *Nature* **468**, 779–783 (2010).
16. E. Minskaia *et al.*, *Proc. Natl. Acad. Sci. U.S.A.* **103**, 5108–5113 (2006).
17. Y. Chen *et al.*, *Proc. Natl. Acad. Sci. U.S.A.* **106**, 3484–3489 (2009).
18. M. Bouvet *et al.*, *Proc. Natl. Acad. Sci. U.S.A.* **109**, 9372–9377 (2012).
19. Y. Ma *et al.*, *Proc. Natl. Acad. Sci. U.S.A.* **112**, 9436–9441 (2015).
20. H. S. Hillen *et al.*, *Nature* **584**, 154–156 (2020).
21. J. Chen *et al.*, *Cell* **182**, 1560–1573.e13 (2020).
22. Y. Zhai *et al.*, *Nat. Struct. Mol. Biol.* **12**, 980–986 (2005).
23. Y. Xiao *et al.*, *J. Virol.* **86**, 4444–4454 (2012).
24. Y. Zuo, M. P. Deutscher, *Nucleic Acids Res.* **29**, 1017–1026 (2001).
25. S. Hamdan, P. D. Carr, S. E. Brown, D. L. Ollis, N. E. Dixon, *Structure* **10**, 535–546 (2002).
26. X. Jiang *et al.*, *J. Biol. Chem.* **288**, 16949–16959 (2013).
27. R. Fernandez-Leiro *et al.*, *Nat. Struct. Mol. Biol.* **24**, 140–143 (2017).
28. L. S. Beese, V. Derbyshire, T. A. Steitz, *Science* **260**, 352–355 (1993).
29. B. Malone *et al.*, *Proc. Natl. Acad. Sci. U.S.A.* **118**, e2102516118 (2021).
30. S. Jockusch *et al.*, *Sci. Rep.* **10**, 16577 (2020).
31. M. L. Agostini *et al.*, *mBio* **9**, e00221-18 (2018).
32. J. Shim, G. Larson, V. Lai, S. Naim, J. Z. Wu, *Antiviral Res.* **58**, 243–251 (2003).
33. G. Campagnola, P. Gong, O. B. Peersen, *Antiviral Res.* **91**, 241–251 (2011).

ACKNOWLEDGMENTS

We thank S. Wu for help with cryo-EM data collection at the Yale Titan Krios cryo-EM facility. We particularly thank R. Breaker at Yale University for his support during the early phases of this work. **Funding:** This work was supported by NVIDIA GPU Grant Program (C.L.); the start-up funding granted to B.L. from The Hormel Institute, University of Minnesota; and the start-up funding granted to Y.Y. from Iowa State University. **Author contributions:** Y.Y. and C.L. conceived and designed the experiments. Y.Y. performed the biochemical characterizations. Y.Y., B.L., and W.S. prepared the cryo-EM samples and collected cryo-EM data. Y.Y., C.L., and B.L. processed the cryo-EM data. C.L. and Y.Y. performed model building and structural analyses. Y.Y. and C.L. wrote the manuscript, with input from S.T.B., D.G.S., and B.L. **Competing interests:** The authors declare no competing interests. **Data and materials availability:** Atomic coordinates of three structures determined in this study have been deposited in the Protein Data Bank with accession codes 7N0B [SARS-CoV-2 nsp10-nsp14 (WT)–RNA complex], 7N0C [SARS-CoV-2 nsp10-nsp14 (E191A)–RNA complex, monomer], and 7N0D [SARS-CoV-2 nsp10-nsp14 (E191A)–RNA complex, tetramer]. The cryo-EM maps have been deposited in the Electron Microscopy Data Bank with accession number EMD-24102 [SARS-CoV-2 nsp10-nsp14 (WT)–RNA complex], EMD-24103 [SARS-CoV-2 nsp10-nsp14 (E191A)–RNA complex, monomer], and EMD-24104 [SARS-CoV-2 nsp10-nsp14 (E191A)–RNA complex, tetramer]. Materials are available from Y.Y. upon request and may require a material transfer agreement.

This work is licensed under a Creative Commons Attribution 4.0 International (CC BY 4.0) license, which permits unrestricted use, distribution, and reproduction in any medium, provided the original work is properly cited. To view a copy of this license, visit https://creativecommons.org/licenses/by/4.0/. This license does not apply to figures/photos/artwork or other content included in the article that is credited to a third party; obtain authorization from the rights holder before using such material.

SUPPLEMENTARY MATERIALS

science.sciencemag.org/content/373/6559/1142/suppl/DC1
Materials and Methods
Figs. S1 to S9
Table S1
References (*34*–*47*)
MDAR Reproducibility Checklist

9 April 2021; accepted 20 July 2021
Published online 27 July 2021
10.1126/science.abi9310

CRISPR TECHNOLOGY

MIC-Drop: A platform for large-scale in vivo CRISPR screens

Saba Parvez[1], Chelsea Herdman[2], Manu Beerens[3], Korak Chakraborti[1], Zachary P. Harmer[1]†, Jing-Ruey J. Yeh[4], Calum A. MacRae[3], H. Joseph Yost[2], Randall T. Peterson[1]*

CRISPR-Cas9 can be scaled up for large-scale screens in cultured cells, but CRISPR screens in animals have been challenging because generating, validating, and keeping track of large numbers of mutant animals is prohibitive. Here, we introduce Multiplexed Intermixed CRISPR Droplets (MIC-Drop), a platform combining droplet microfluidics, single-needle en masse CRISPR ribonucleoprotein injections, and DNA barcoding to enable large-scale functional genetic screens in zebrafish. The platform can efficiently identify genes responsible for morphological or behavioral phenotypes. In one application, we showed that MIC-Drop could identify small-molecule targets. Furthermore, in a MIC-Drop screen of 188 poorly characterized genes, we discovered several genes important for cardiac development and function. With the potential to scale to thousands of genes, MIC-Drop enables genome-scale reverse genetic screens in model organisms.

Historically, large-scale genetic screens in zebrafish have used forward genetic techniques such as chemical or insertional mutagenesis (fig. S1A) (*1*, *2*). These screens have proven invaluable in identifying key pathways regulating vertebrate development (*3*–*5*) and behavior (*6*, *7*). Although impressive in scale, forward genetic techniques are time and labor intensive, requiring years to link a desired phenotype with the genotype. Reverse genetics approaches such as CRISPR have the potential to circumvent some of the issues of forward genetics but are severely limited in throughput (*8*, *9*). Targeting genes of interest is typically done one gene at a time, designing individual guide RNAs (gRNA), injecting Cas9-gRNA ribonucleoprotein (RNP) complexes, and maintaining, propagating, and genotyping groups of fish, all of which require extensive time, labor, and space. The largest such screen to date targeted 128 genes in zebrafish (*10*, *11*). Recent studies using multiplexed gRNAs to generate biallelic F_0 mutants that successfully phenocopy germline mutant phenotypes are a welcome step but have not been scaled up for genome-wide CRISPR screens (*10*, *12*–*17*).

We have developed a platform, Multiplexed Intermixed CRISPR Droplets (MIC-Drop), for performing large-scale reverse genetic screens in zebrafish (Fig. 1A). The platform uses microfluidics to generate nanoliter-sized droplets, each containing Cas9, multiplexed gRNAs targeting a gene of interest, and a unique barcode associated with each target gene. Droplets targeting hundreds to thousands of different genes are intermixed together and injected into zebrafish embryos from a single needle (movie S1). Embryos are raised en masse, and then those exhibiting the phenotype(s) of interest are isolated and the identities of the perturbed genes are rapidly uncovered by retrieving and sequencing the barcodes. The ability to inject all intermixed droplets from a single needle circumvents the laborious and wasteful process of filling a separate needle for each gene targeted. The ability to identify perturbed genes by retrieving barcodes circumvents the need to raise each injected animal separately or deconvolute the mutated gene through genome sequencing.

After testing different surfactant-oil combinations, we identified a particular combination of fluorinated oil and a fluorosurfactant as optimal for droplet generation using a repurposed Bio-Rad QX-200 droplet generator

[1]Department of Pharmacology and Toxicology, University of Utah, Salt Lake City, UT, USA. [2]Department of Neurobiology and Molecular Medicine Program, University of Utah School of Medicine, Salt Lake City, UT, USA. [3]Department of Cardiovascular Medicine, Genetics and Network Medicine, Brigham and Women's Hospital and Harvard Medical School, Boston, MA, USA. [4]Cardiovascular Research Center, Massachusetts General Hospital and Harvard Medical School, Boston, MA, USA.
***Corresponding author. Email: randall.peterson@pharm.utah.edu**
†Present address: Cellular and Molecular Biology, University of Wisconsin-Madison, Madison, WI, USA.

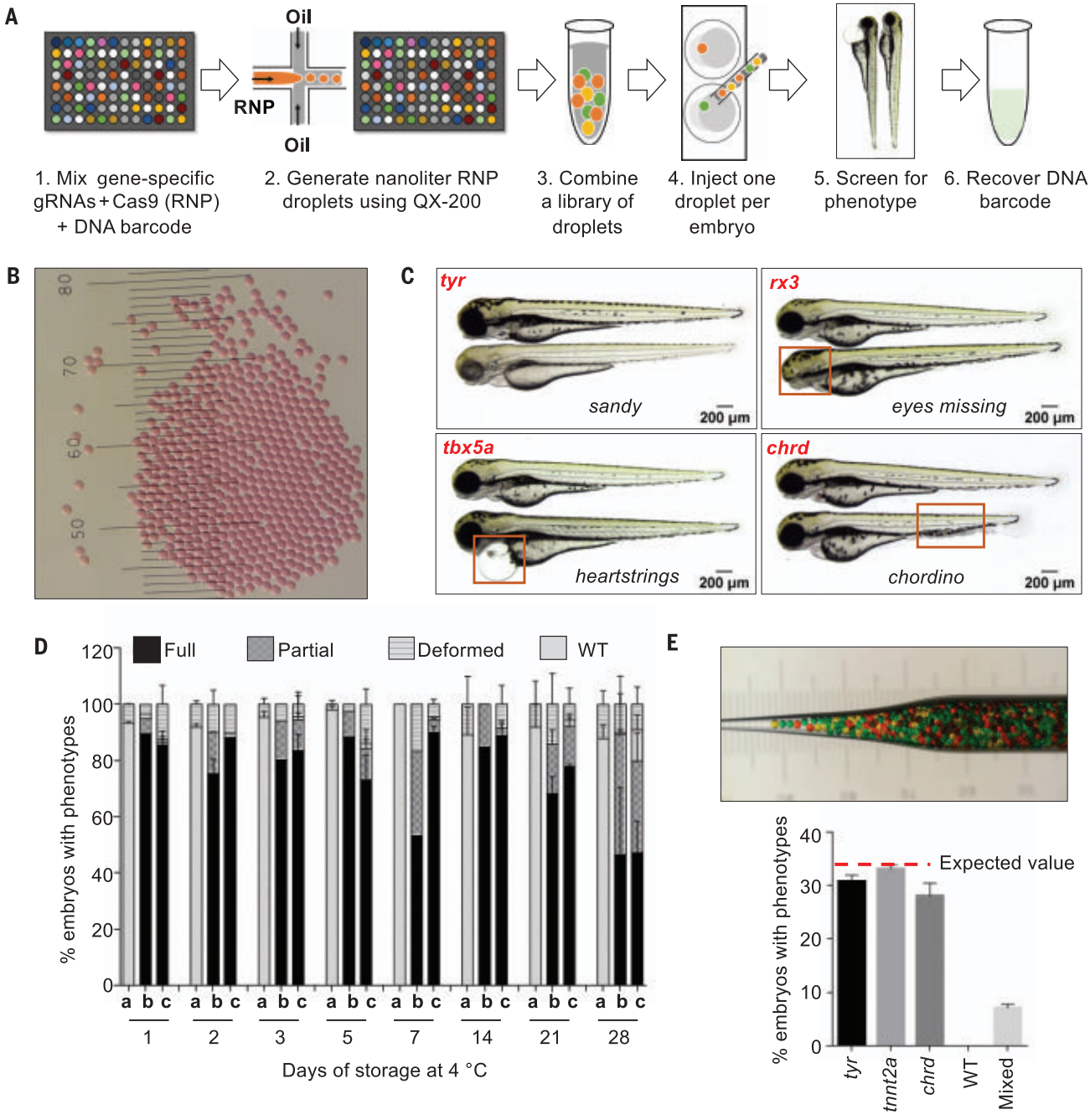


Fig. 1. MIC-Drop enables high-throughput CRISPR screens in zebrafish. (**A**) Workflow of the MIC-Drop platform. A microfluidics device generates nanoliter-sized droplets, each containing RNPs targeting a gene of interest and a unique DNA barcode associated with the gene. Droplets targeting multiple genes are intermixed, loaded into a single injection needle, and injected serially into one-cell zebrafish embryos. Embryos showing phenotypes of interest are isolated and the causative genotype is identified by retrieving and sequencing the barcode. (**B**) Droplets are uniform in size. Distance between bars is 0.1 mm. (**C**) Injection of droplets containing RNPs targeting *tyr*, *rx3*, *tbx5a*, and *chrd* genes recapitulates known mutant phenotypes in F_0, highlighted by red boxes. (**D**) RNP-containing droplets are nontoxic and stable for prolonged storage, retaining activity for at least 28 days of storage at 4°C. (a) Uninjected; (b) traditional RNP injection; and (c) MIC-Drop injection. Day 1: (a) *N* = 118, (b) *N* = 79, (c) *N* = 134; day 2: (a) *N* = 116, (b) *N* = 68, (c) *N* = 59; day 3: (a) *N* = 120, (b) *N* = 88, (c) *N* = 87; day 5: (a) *N* = 129, (b) *N* = 78, (c) *N* = 95; day 7: (a) *N* = 105, (b) *N* = 102, (c) *N* = 107; day 14: (a) *N* = 94, (b) *N* = 53, (c) *N* = 77; day 21: (a) *N* = 123, (b) *N* = 100, (c) *N* = 32; and day 28: (a) *N* = 114, (b) *N* = 100, (c) *N* = 94. (**E**) Single-needle injection of intermixed droplets targeting three different genes (*tyr*, *tnnt2a*, and *chrd*) and subsequent phenotyping showing even representation of each droplet, with most of the embryos exhibiting only one of the three expected phenotypes; none (0%) was wild type. *N* = 230 total sequenced from three separate injections. Inset: Hundreds of artificially colored droplets (used as proxies for droplets targeting different genes) do not fuse when transferred to an injection needle.

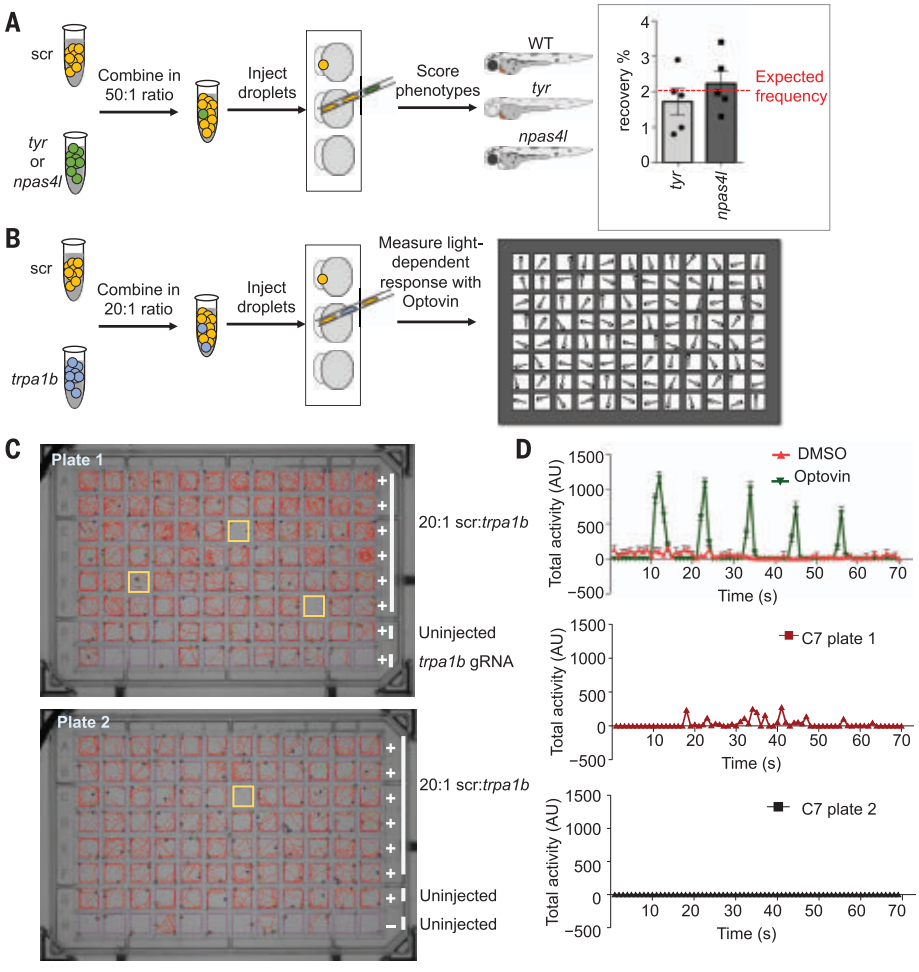


Fig. 2. MIC-Drop enables large-scale phenotypic screens and small-molecule target identification. (**A** and **B**) Schematic of a spike-in phenotypic (A) and behavioral (B) screen to test the robustness of the MIC-Drop platform. (A) For the phenotypic screen, droplets targeting either *tyr* or *npas4l* were intermixed with droplets containing nontargeting scrambled gRNAs (scr) in a 1:50 ratio. After single-needle droplet injection, the percentage of embryos showing *sandy* or *cloche* phenotypes was scored. Inset: The *sandy* and *cloche* phenotypes were recovered at a frequency of ~2%, which is the expected frequency from a 1:50 ratio mixture. (B) Similar to (A) except droplets targeting *trpa1b* were intermixed with scr droplets in a 1:20 ratio. After injection, embryos were arrayed in a multiwell plate, treated with optovin, and assayed for light-dependent motor response. (**C** and **D**) Tracking (C) and quantitation (D) of zebrafish movement showing that embryos injected with droplets targeting *trpa1b* are refractory to optovin- and light-induced motion response.

(for more details, see the supplementary text and materials and methods). The droplets generated were uniform and ~100 μm in diameter (Fig. 1B). Each droplet contained four gRNAs targeting a gene of interest. We found that using four gRNAs per gene recapitulated the phenotypes of homozygous mutants in F_0 embryos with high penetrance (fig. S1, B to D, and table S1). Injection of four gRNAs targeting *tyr*, *tnnt2a*, *tbx5a*, *rx3*, *npas4l*, *chrd*, *tbx16*, and *fgf24* resulted in highly efficient biallelic mutagenesis (fig. S2, A and B) and the expected *sandy* (lack of pigmentation), *silent heart*, *heartstrings*, *eyes missing*, *cloche*, *chordino* (tissue ventralization), *spadetail*, and *ikarus* (lack of pectoral fins) mutant phenotypes, respectively, in 70 to 100% of the F_0 embryos. No substantial toxicity was observed in embryos injected with MIC-Drop except for the low level of nonspecific morphological defects typical of traditional RNP injection (Fig. 1, C and D, and figs. S1E and S3, A and B). Droplets were stable during prolonged storage and showed high phenotypic penetrance even after a month of storage at 4°C (Fig. 1D). Additionally, after generating and injecting a mini-library of MIC-Drops, with each droplet targeting any one of three to eight different genes, we found that most embryos exhibited a unique phenotype, demonstrating successful injection of a single droplet per embryo (Fig. 1E and fig. S3, C and D). The frequency of each phenotype was close to the expected value, indicating proportionate representation of each droplet within a mixed pool. Finally, the injected DNA barcodes could be recovered at least up to 7 days post fertilization (dpf) (fig. S3E). Retrieval and sequencing of the barcode from the injected embryos revealed a high genotype-phenotype correlation. Although we used single-guide RNA DNA templates as the basis of the barcodes here, other barcoding strategies may be feasible (see the supplementary text).

Next, we tested whether MIC-Drop could identify genes responsible for a particular phenotype from a list of candidate genes (Fig. 2A). We spiked droplets targeting the *tyr* or *npas4l* genes into a larger pool of droplets containing scrambled gRNAs such that the *tyr* or *npas4l* MIC-drops each represented 2% of the total. Hundreds of embryos were injected with the intermixed droplets, and the frequency of *sandy* and *cloche* phenotypes among the injected embryos was assessed. We observed frequencies of 1.7 ± 0.8% and 2.2 ± 0.8% for the *sandy* and *cloche* phenotypes, respectively (Fig. 2A, inset), comparable to the theoretical expected frequency of 2%, indicating that MIC-Drop screens are sensitive and may be a useful platform for a variety of applications requiring identification of genotype-phenotype relationships in vertebrates on a large scale.

Identifying the protein targets of small molecules remains one of the major challenges in chemical biology and pharmacology (*18*, *19*). We hypothesized that MIC-Drop could be used to identify the targets of small molecules that result in complex behavioral phenotypes in the zebrafish. As proof of principle, we used optovin, a small-molecule agonist of the *trpa1b* channel that allows photoactivatable behavioral modifications in zebrafish (*20*). We spiked droplets targeting the *trpa1b* channel into a collection of droplets containing scrambled gRNAs in a 1:20 ratio (Fig. 2B). Droplet-injected embryos were arrayed into 96-well plates, treated with optovin, and exposed to violet light flashes while simultaneously recording embryo movement. Treatment of wild-type zebrafish embryos with optovin resulted in a light-dependent

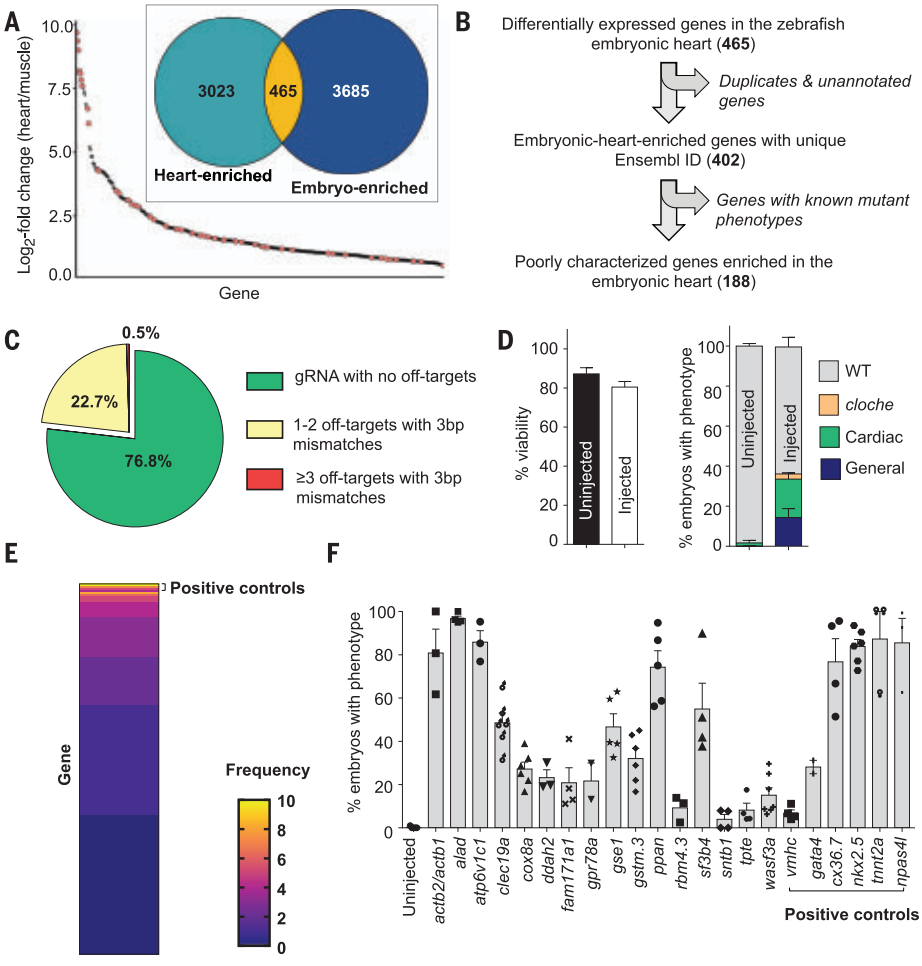


Fig. 3. A genetic screen to identify new regulators of cardiovascular development. (**A**) A publicly available dataset was used to populate a list of candidate genes enriched in the embryonic zebrafish heart. About 14% of the genes (orange dots) have reported cardiac phenotypes in ZFIN, suggesting enrichment of genes important in heart development. (**B**) Filtering to remove genes with known mutant phenotypes yielded 188 poorly characterized genes potentially important for cardiovascular development in zebrafish. (**C**) gRNA sequences with fewer off-targets were prioritized. (**D**) MIC-Drop screen of the 188 candidate genes and subsequent phenotyping showing no significant differences in viability between uninjected and droplet-injected embryos by 3 dpf. Left: uninjected, *N* = 1801, injected, *N* = 2502; right: uninjected, *N* = 1571, injected, *N* = 2013. Embryos with gross morphological defects at 3 dpf (~15%) were removed and the barcodes of those with cardiac defects were sequenced. Droplets targeting *npas4l* were spiked-in at a 2% proportion as a positive control. (**E**) Barcode sequencing of embryos displaying any cardiac phenotype (e.g., looping defect, chamber dysmorphogenesis, valve defect, arrhythmia, etc.) yields "hit" candidates. Heat map shows the observed frequency of each barcode. As positive controls, barcodes for *tnnt2a*, *nkx2.5*, and *npas4l* are enriched in the set of embryos exhibiting any visible cardiac phenotype. Genes with barcode frequency of ≥4 (binomial probability ≤ 0.05) or with consistent cardiac phenotypes were considered for secondary validation. (**F**) Secondary validation by direct RNP injection corroborated the screening results and identified 12 new genes, the loss of which resulted in cardiac phenotypes in at least 20% of F_0 embryos. WT, *N* = 238; *actb2/actb1*, *N* = 124; *alad*, *N* = 137; *atp6v1c1*, *N* = 135; *clec19a*, *N* = 182; *cox8a*, *N* = 130; *ddah2*, *N* = 126; *fam171a1*, *N* = 259; *gpr78a*, *N* = 186; *gse1*, *N* = 266; *gstm.3*, *N* = 199; *ppan*, *N* = 304; *rbm4.3*, *N* = 153; *sf3b4*, *N* = 307; *sntb1*, *N* = 107; *tpte*, *N* = 209; *wasf3a/b*, *N* = 130; *vmhc*, *N* = 107; *gata4*, *N* = 106; *cx36.7*, *N* = 147; *nkx2.5*, *N* = 186; *tnnt2a*, *N* = 124; and *npas4l*, *N* = 103.

motor response (fig. S4, A to C, and movie S2). Embryos that showed reduced or no movement in the assay were isolated and their barcodes sequenced for genotype verification. We found that 2 to 3% of embryos showed a complete loss of photoinduced motion (Fig. 2B and fig. S4D). Barcode sequencing revealed that 100% of the unresponsive embryos were of the *trpa1b* genotype. An additional ~2% of the embryos showed a photoinduced motor response despite being of the *trp1ab* genotype, likely because of incomplete loss of *trpa1b* function (fig. S4D). Thus, we were able to use the MIC-Drop platform to identify the target of optovin from among a library of nontarget candidates.

We envisioned that MIC-Drop could be used to rapidly perform large-scale, reverse genetic screens to uncover genes responsible for important phenotypes such as developmental defects in the cardiovascular system. Congenital heart disease is the most common form of birth defect in humans, affecting nearly 1% of all live births (*21*). Genetic factors play a strong causal role in the development of congenital heart disease, but a comprehensive understanding of all of the genes responsible is still lacking. We used publicly available RNA-sequencing datasets to curate a list of 188 poorly characterized genes that are enriched in the zebrafish embryonic heart tissue relative to skeletal muscle (Fig. 3, A and B; fig. S5, A and B; and tables S2 to S4) (*22*, *23*) and postulated that these genes might be important in vertebrate heart development. We generated a library containing MIC-Drops for all 188 genes plus several control genes (Fig. 3C and table S5). When two ohnologs of a gene were identified, two gRNAs for each ohnolog were combined in a single droplet. Morphological phenotyping of zebrafish embryos at 48 to 72 hours postfertilization after MIC-Drop injection identified 16 new genes, the loss of which resulted in a variety of specific cardiac or blood phenotypes (Fig. 3, D and E, and table S5). Secondary validation of these "hits" corroborated the findings of the initial screen, with 12 of 16 genes showing phenotypic penetrance in >20% of F_0 embryos (Fig. 3E). The screen identified gene mutations responsible for a range of phenotypes, including one mutation (*alad*) causing porphyria, two mutations (*gstm.3* and *atp6v1c1*) causing arrhythmia, and seven mutations (*actb2*, *clec19a*, *gse1*, *ppan*, *sf3b4*, *cox8a*, and *ddah2*) causing abnormal cardiac development, including defects in ventricular morphogenesis, cardiac looping, and formation of the atrioventricular valve and cardiac jelly.

Several reports have demonstrated that F_0 "crispant" phenotypes reliably reflect loss of target gene function, but nonspecific or off-target phenotypes are theoretically possible (see the supplementary text). To ensure that the phenotypes that we observed were caused by on-target gene knockout, we performed phenotype rescue with mRNA injection. *alad* crispants showed a complete loss of hemoglobin synthesis, which was rescued by injection of *alad* mRNA (Fig. 4A and fig. S6A), indicating a role for *alad* in erythropoiesis.

Voltage mapping of the *gstm.3* and *atp6v1c1* crispants showed slowed atrial and ventricular

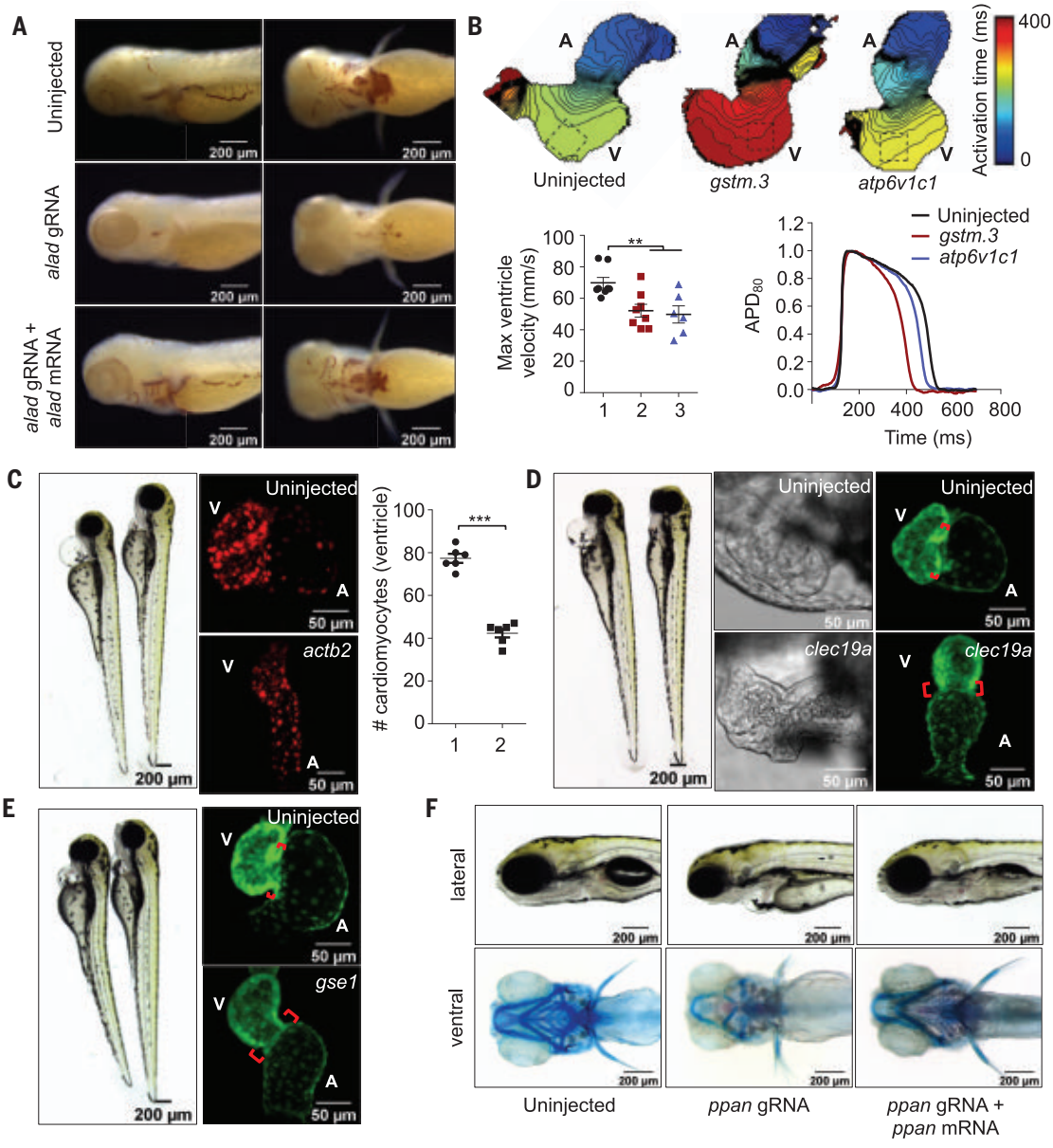


Fig. 4. CRISPR screen using MIC-Drop identifies new genes responsible for cardiovascular development. (**A**) *o*-dianisidine staining showing that loss of *alad* results in porphyria, which can be rescued by coinjection of *alad* mRNA. (**B**) Loss of *gstm.3* or *atp6v1c1* results in abnormal cardiac electrophysiology. Isochronal maps and action potential measurements reveal reduced conduction velocities and shorter ventricular action potential duration in the *gstm.3* and *atp6v1c1* crispants relative to uninjected controls. 1: Uninjected; 2: *gstm.3* crispants; 3: *atp6v1c1* crispants. Data are presented as mean ± SEM (**$P \leq 0.01$; ***$P \leq 0.001$). (**C** to **F**) Loss of *actb2* (C), *clec19a* (D), *gse1* (E), and *ppan* (F) result in distinct cardiac malformations. *actb2* crispants have a small ventricle with reduced number of ventricular cardiomyocytes. 1: Control; 2: *actb2*-targeting gRNAs (C). Loss of *clec19a* and *gse1* result in abnormal morphogenesis and an extended atrioventricular canal relative to wild-type embryos [(D) and (E)]. Alcian blue staining of *ppan* crispants showing abnormal jaw and skull development, which was rescued by *ppan* mRNA injection. The embryos also display cardiac edema and a silent ventricle (F).

conductions and altered action potential duration (Fig. 4B and fig. S6B). We identified *atp6v1c1b* as the ohnolog responsible for the ventricular arrhythmia phenotype (fig. S6C). GSTM3 was recently identified as a risk factor in Brugada syndrome with increased susceptibility to sudden cardiac death (*24*). Germline *gstm.3* zebrafish mutants exhibited ventricular arrhythmia, corroborating our results observed in MIC-Drop crispants. Loss of function of several genes resulted in cardiac development defects. β-actin (*actb1* and *actb2*) crispants showed cardiac edema; a small, silent ventricle with reduced cardiomyocytes; leaky blood vessels; and gross craniofacial defects (Fig. 4C and movie S3). Loss of *actb2* alone was sufficient to recapitulate the cardiac phenotypes without the gross morphological defects, suggesting that *actb2* and *actb1* have nonoverlapping roles (Fig. 4C and fig. S6, D and E). *clec19a*, a c-type lectin protein with unknown functions, was found to be important for the normal development of cardiac jelly and the atrioventricular valve in 3 dpf zebrafish embryos (Fig. 4D and movie S4). Additionally, *cox8a*, a component of the mitochondrial electron transport chain, and *ddah2*, an arginine-metabolizing enzyme, were shown to be important for normal cardiac looping and ventricular morphogenesis (fig. S7A). Finally, three other genes with limited annotation of their functions were identified as being important in heart development. Loss of *ppan*, *gse1*, and *sf3b4* resulted in cardiac abnormalities along with other development defects such as malformed cartilage in the jaw and pharyngeal arches (*ppan*), bent trunk (*gse1* and *sf3b4*), and craniofacial defects (*sf3b4*) causing embryonic lethality (Fig. 4, E and F; fig. S7B; and movies S5 and S6). Phenotypes associated with *actb2*, *ppan*, and *sf3b4* MIC-Drops were also rescued by coinjection of *actb2*, *ppan*, and *sf3b4* mRNAs (Fig. 4F and figs. S6 and S7), suggesting that the phenotypes are caused by loss of function of the targeted genes. Therefore, MIC-Drop enabled a highly efficient reverse-genetic CRISPR screen in an intact vertebrate, leading to the discovery of several genes that contribute to diverse aspects of cardiac development or function.

In conclusion, we have developed a microfluidics-based platform for large-scale

CRISPR screens in a vertebrate. CRISPR screens have previously been performed in cultured cells (*25*, *26*), but genome editing in vertebrates has primarily been done one gene at a time. The few small-scale CRISPR screens reported in vertebrates were enabled by brute force scaling of single-gene methods for generating, tracking, and analyzing individual genes, with little economy of scale (*10*, *11*, *27*). By intermixing droplets targeting many genes and incorporating a barcode for retrospective target identification, the MIC-Drop platform enables zebrafish to be injected, housed, and analyzed en masse, with rapid identification of the target genes in individuals exhibiting phenotypes of interest. The pilot screen reported here quickly discovered several genes important for cardiovascular development and function. This screen of 188 genes was completed efficiently by a single investigator and could readily be scaled to thousands of genes or even to full genome scale (see the supplementary text). Moreover, MIC-Drop is versatile and can conceivably be used, not just for gene knockout, but also for other screens such as CRISPR activation and inactivation screens, screens that mutate promoter or regulatory elements to create "transcript-less" mutants (*28*), and functional screens of noncoding genetic elements (see the supplementary text). Finally, the platform could be adapted for use in other model organisms, including *Xenopus* and mouse embryos, in which F_0 crispants are shown to recapitulate known germline mutant phenotypes (*29*, *30*), and likely also in other model organisms amenable to microinjection, such as sea urchins, fruit flies, and nematodes. Thus, the MIC-Drop platform enables in vivo vertebrate CRISPR experiments to be performed with the speed, efficiency, and scale previously available only to in vitro systems.

REFERENCES AND NOTES

1. E. E. Patton, L. I. Zon, *Nat. Rev. Genet.* **2**, 956–966 (2001).
2. A. Amsterdam *et al.*, *Proc. Natl. Acad. Sci. U.S.A.* **101**, 12792–12797 (2004).
3. W. Driever *et al.*, *Development* **123**, 37–46 (1996).
4. P. Haffter *et al.*, *Development* **123**, 1–36 (1996).
5. B. M. Weinstein *et al.*, *Development* **123**, 303–309 (1996).
6. M. Sison, J. Cawker, C. Buske, R. Gerlai, *Lab Anim. (NY)* **35**, 33–39 (2006).
7. R. A. Jain *et al.*, *Curr. Biol.* **28**, 1357–1369.e5 (2018).
8. W. Y. Hwang *et al.*, *Nat. Biotechnol.* **31**, 227–229 (2013).
9. M. Jinek *et al.*, *Science* **337**, 816–821 (2012).
10. W. Pei *et al.*, *NPJ Regen. Med.* **3**, 11 (2018).
11. G. K. Varshney *et al.*, *Genome Res.* **25**, 1030–1042 (2015).
12. F. Kroll *et al.*, *eLife* **10**, e59683 (2021).
13. A. N. Shah, C. F. Davey, A. C. Whitebirch, A. C. Miller, C. B. Moens, *Nat. Methods* **12**, 535–540 (2015).
14. K. Hoshijima *et al.*, *Dev. Cell* **51**, 645–657.e4 (2019).
15. J. A. Gagnon *et al.*, *PLOS ONE* **9**, e98186 (2014).
16. A. Burger *et al.*, *Development* **143**, 2025–2037 (2016).
17. R. S. Wu *et al.*, *Dev. Cell* **46**, 112–125.e4 (2018).
18. M. Jost, J. S. Weissman, *ACS Chem. Biol.* **13**, 366–375 (2018).
19. C. Fellmann, B. G. Gowen, P. C. Lin, J. A. Doudna, J. E. Corn, *Nat. Rev. Drug Discov.* **16**, 89–100 (2017).
20. D. Kokel *et al.*, *Nat. Chem. Biol.* **9**, 257–263 (2013).
21. S. Zaidi, M. Brueckner, *Circ. Res.* **120**, 923–940 (2017).
22. L. Wang, X. Ma, X. Xu, Y. Zhang, *Sci. Rep.* **7**, 1250 (2017).
23. Y. H. Shih *et al.*, *Circ. Cardiovasc. Genet.* **8**, 261–269 (2015).
24. J. J. Juang *et al.*, *EBioMedicine* **57**, 102843 (2020).
25. T. Wang, J. J. Wei, D. M. Sabatini, E. S. Lander, *Science* **343**, 80–84 (2014).
26. O. Shalem *et al.*, *Science* **343**, 84–87 (2014).
27. W. Tang *et al.*, *iScience* **23**, 100942 (2020).
28. M. A. El-Brolosy *et al.*, *Nature* **568**, 193–197 (2019).
29. I. L. Blitz, J. Biesinger, X. Xie, K. W. Y. Cho, *Genesis* **51**, 827–834 (2013).
30. H. Wang *et al.*,*Cell* **153**, 910–918 (2013).
31. C. Herdman, Code for: MIC-Drop: A platform for large-scale in vivo CRISPR screens, Version 1.0, Zenodo (2021). https://doi.org/10.5281/zenodo.5154537.

ACKNOWLEDGMENTS

We thank A. Serrano for assistance in imaging, B. Bisgrove for advice on phenotyping and for providing a list of candidate cardiac development genes, B. Demarest for advice on RNA-sequencing data analysis, and members of the Peterson laboratory for their insights and critical feedback at all stages of the project. We also acknowledge the Centralized Zebrafish Animal Resource (CZAR) for providing zebrafish husbandry and microinjection equipment. **Funding:** This work was supported by the NIH (grant 5R01GM134069-02 to R.T.P. and J.J.Y., grant UM1 HL098160 to H.J.Y., NINDS grant U54-NS079201 to C.A.M., and OD grant R24OD017870 to C.A.M.) and by the American Heart Association (postdoctoral fellowship 827636 to S.P.).

Author contributions: S.P. and R.T.P contributed to conception and design, collection, analysis, and interpretation of the data, and manuscript writing. J.J.Y. contributed to conceptualization and experimental design. C.H. and H.J.Y. performed RNA-sequencing data analysis. M.B. and C.A.M. performed and interpreted cardiac voltage-mapping experiments. K.C. and Z.P.H. provided help with testing and optimizing the MIC-Drop platform. All authors contributed to the writing and review of the manuscript. **Competing interests:** S.P., J.J.Y., and R.T.P. have applied for a patent covering the technology described herein. R.T.P. has received honoraria (NIH) and expert testimony fees (Sterne Kessler/University of California) for work related to CRISPR technology. **Data and materials availability:** All data are available in the main text or the supplementary materials. All RNA-sequencing data are available on Gene Expression Omnibus under project accession no. GSE85416. Code for the analysis, including processed data, is available on Zenodo (*31*). Reagents will be made available upon request to the corresponding author.

SUPPLEMENTARY MATERIALS

science.sciencemag.org/content/373/6559/1146/suppl/DC1
Materials and Methods
Supplementary Text
Figs. S1 to S7
Reference (*32*)
MDAR Reproducibility Checklist
Tables S1 to S5
Movies S1 to S6

7 April 2021; accepted 3 August 2021
10.1126/science.abi8870

STRUCTURAL BIOLOGY

Three-megadalton complex of methanogenic electron-bifurcating and CO_2-fixing enzymes

Tomohiro Watanabe[1]†‡, Olivia Pfeil-Gardiner[2]†, Jörg Kahnt[3], Jürgen Koch[1], Seigo Shima[1]*, Bonnie J. Murphy[2]*

The first reaction of the methanogenic pathway from carbon dioxide (CO_2) is the reduction and condensation of CO_2 to formyl-methanofuran, catalyzed by formyl-methanofuran dehydrogenase (Fmd). Strongly reducing electrons for this reaction are generated by heterodisulfide reductase (Hdr) in complex with hydrogenase or formate dehydrogenase (Fdh) using a flavin-based electron-bifurcation mechanism. Here, we report enzymological and structural characterizations of Fdh-Hdr-Fmd complexes from *Methanospirillum hungatei*. The complexes catalyze this reaction using electrons from formate and the reduced form of the electron carrier F_{420}. Conformational changes in HdrA mediate electron bifurcation, and polyferredoxin FmdF directly transfers electrons to the CO_2 reduction site, as evidenced by methanofuran-dependent flavin-based electron bifurcation even without free ferredoxin, a diffusible electron carrier between Hdr and Fmd. Conservation of Hdr and Fmd structures suggests that this complex is common among hydrogenotrophic methanogens.

Methane is a potent greenhouse gas produced mainly by methanogenic archaea (*1*). In the hydrogenotrophic methanogenic pathway, CO_2 is reduced and then condensed to a C_1-carrier methanofuran to form formyl-methanofuran (*2*). These reactions are catalyzed by the molybdenum-containing formyl-methanofuran dehydrogenase, FmdABCDFG, or its tungsten isoform, FwdABCDFG (*3*, *4*). Electrons for CO_2 reduction are provided by methyl viologen–reducing hydrogenase (MvhAG) (*5*–*7*) or formate dehydrogenase (FdhAB) (*8*–*11*) in complex with heterodisulfide reductase (HdrABC), which carries out flavin-based electron bifurcation (FBEB) (*5*). In this process, the energy in a pair of electrons is split, giving rise to a strongly reducing electron for CO_2 fixation and a weakly reducing electron for reduction of the heterodisulfide of coenzyme M and coenzyme B

[1]Microbial Protein Structure Group, Max Planck Institute for Terrestrial Microbiology, 35043 Marburg, Germany. [2]Redox and Metalloprotein Research Group, Max Planck Institute of Biophysics, 60438 Frankfurt am Main, Germany. [3]Core Facility for Mass Spectrometry and Proteomics, Max Planck Institute for Terrestrial Microbiology, 35043 Marburg, Germany.
***Corresponding author. Email: shima@mpi-marburg.mpg.de (S.S.); bonnie.murphy@biophys.mpg.de (B.J.M.)**
†These authors contributed equally to this work.
‡Present address: Institute of Low Temperature Science, Hokkaido University, 060-0819 Sapporo, Japan.

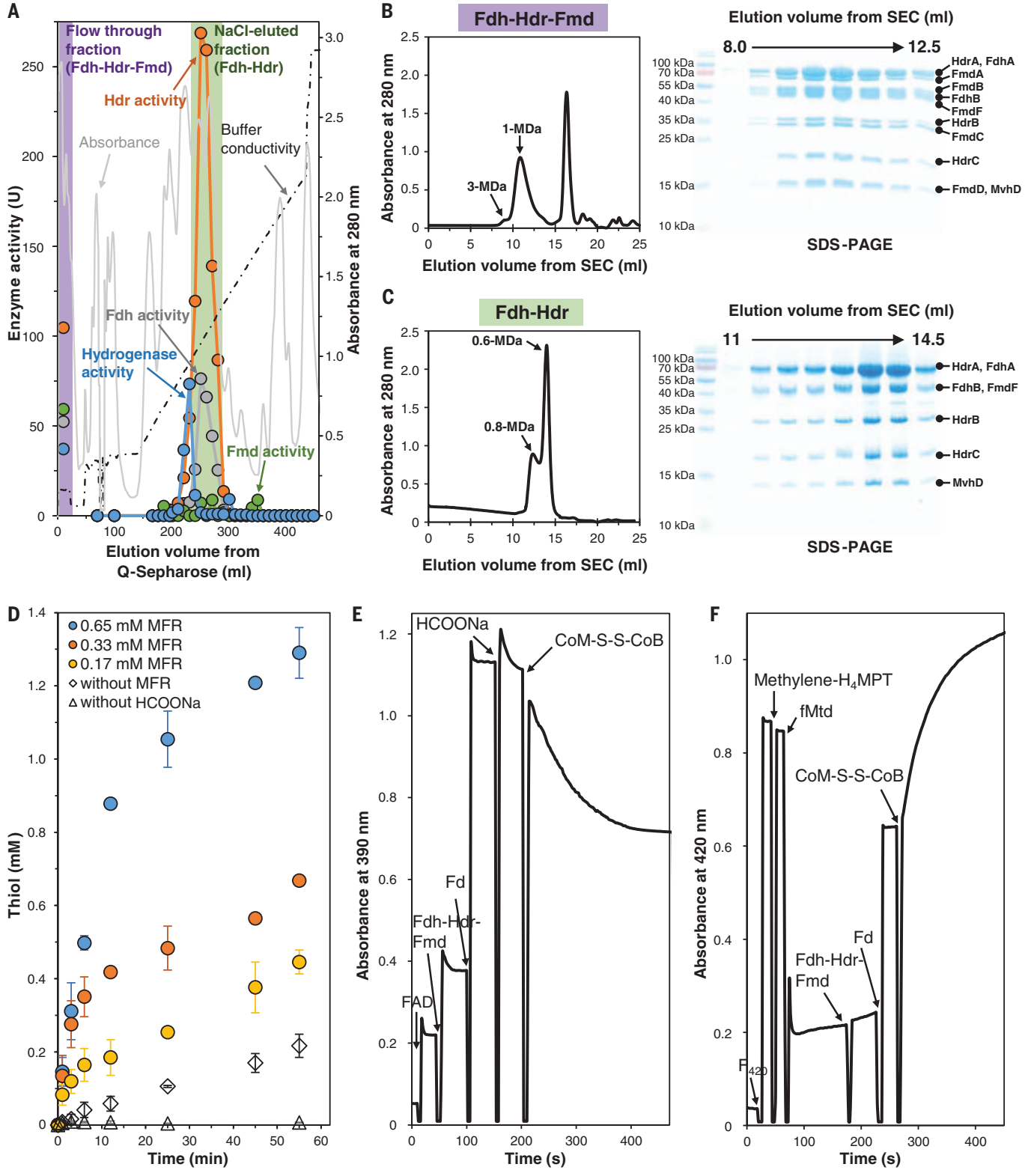


Fig. 1. Purification and characterization of the enzyme complexes from *M. hungatei*. (**A**) Q Sepharose chromatography. (**B**) SEC profile and SDS–polyacrylamide gel electrophoresis (PAGE) of the Fdh-Hdr-Fmd complex purified from the flow-through fraction of Q Sepharose [purple shaded area in (A)]. (**C**) SEC profile and SDS-PAGE of the Fdh-Hdr complex purified from the NaCl-eluted fraction of Q Sepharose [green shaded area in (A)]. (**D**) Electron-bifurcating reduction of CO_2 to formyl-methanofuran (formyl-MFR) with formate as electron donor and CoM-S-S-CoB as co-oxidant (reaction 10 in table S3). (**E**) Electron-bifurcating reduction of ferredoxin from *C. pasteurianum* (Fd) and CoM-S-S-CoB with formate (reaction 6). The decrease of absorbance at 390 nm indicates the reduction of Fd. (**F**) Electron-bifurcating reduction of ferredoxin and CoM-S-S-CoB with $F_{420}H_2$ (reaction 8). The increase of absorbance at 420 nm indicates oxidation of $F_{420}H_2$. fMtd, F_{420}-dependent methylene-H_4MPT dehydrogenase from *Archaeoglobus fulgidus*; H_4MPT, tetrahydromethanopterin. (D to F) Reactions with the Fdh-Hdr-Fmd complex.

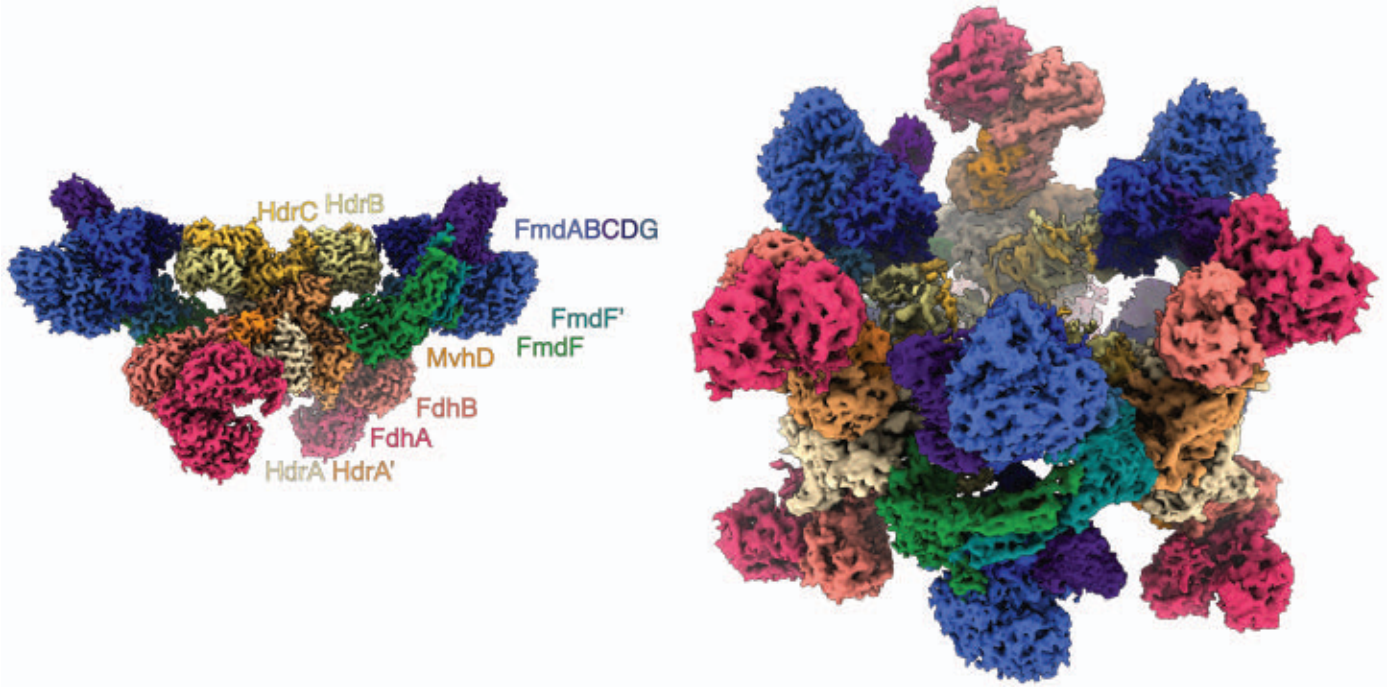


Fig. 2. Composite cryo-EM maps of the dimeric (left) and hexameric (right) Fdh-Hdr-Fmd complex. Polyferredoxin FmdF (green and teal) connects HdrA subunits in the hexameric structure. The hexameric model, viewed along the threefold axis of symmetry, is shown in fig. S20.

(CoM-S-S-CoB), a co-oxidant that is regenerated by the methane formation reaction [for reviews, see (*12*, *13*)]. The structure of an Hdr complex, Mvh-Hdr from *Methanothermococcus thermolithotrophicus*, suggested that conformational changes would be required for electron bifurcation (*6*).

A generally accepted scheme of hydrogenotrophic methanogenesis features Mvh-Hdr or Fdh-Hdr, and Fmd or Fwd as independent complexes, which are linked by electron transfer by a diffusible ferredoxin (*1*, *11*, *14*). However, members of the class Methanomicrobia, including *Methanospirillum hungatei*, encode all or some Fmd genes in the Hdr gene cluster (fig. S1). Liu *et al.* predicted from the genetic context that Mvh, Hdr, and Fwd in *Methanocella conradii* form a large enzyme complex (*15*). This hypothesis was partially supported by pull-down assays that indicated the presence of transient complexes of Fdh-Hdr-Fwd and Mvh-Hdr-Fwd in *Methanococcus maripaludis* and Fdh-Hdr-Fwd in *Methanoculleus thermophilus* (*9*–*11*), although these complexes were not stable to size exclusion chromatography (SEC) and the whole complexes were not enzymatically characterized.

Here, we report the purification and characterization of a massive (3 MDa) complex of the electron-bifurcating Fdh-Hdr together with the CO_2-reducing Fmd from *M. hungatei* (the Fdh-Hdr-Fmd hexamer), as well as dimeric Fdh-Hdr-Fmd and Fdh-Hdr subcomplexes. Fdh-Hdr-Fmd complexes catalyze FBEB reactions by using electrons from formate or the reduced form of F_{420} ($F_{420}H_2$) without external ferredoxin. Cryogenic electron microscopy (cryo-EM) of the complexes indicates the direct connection of the redox active sites through a polyferredoxin subunit FmdF to couple FBEB with CO_2 fixation. Conformational changes within the HdrA subunit provide a conformationally gated pathway for electrons to and from the bifurcating flavin adenine dinucleotide (FAD).

We purified an enzyme complex that catalyzes Hdr, Fdh, and Fmd reactions by three chromatography steps and subcomplexes that exhibit Hdr and Fdh activities by four chromatography steps from *M. hungatei* cells (Fig. 1, supplementary text, and tables S1 and S2). We determined the enzymatic activities and molecular properties of the Fdh-Hdr-Fmd and Fdh-Hdr complexes (Fig. 1, D to F; supplementary text; fig. S2; and table S3). Mass spectrometry (MS) revealed that the Fdh-Hdr-Fmd complex eluted from SEC primarily as a 1-MDa dimer of subunits FdhAB-MvhD-HdrABC-FmdABCDFG (Fig. 1B and table S4). The Fdh-Hdr complexes were isolated as two oligomeric states, which contained FdhAB-MvhD-HdrABC-FmdF (Fig. 1C and table S4). We detected two of five isoenzymes of FdhA and FdhB in all complexes (table S4).

Samples were anaerobically prepared for analysis by cryo-EM (fig. S3). Imaging the dimeric fraction of Fdh-Hdr-Fmd (Fig. 1B) and initial image processing gave rise to two-dimensional (2D) classes with similarity to a crystal structure of Mvh-Hdr of *M. thermolithotrophicus* (*6*). Three-dimensional (3D) refinement with C_2 symmetry provided a 2.6 Å–resolution map of the HdrABC dimeric core (excluding N- and C-terminal domains of HdrA), whereas symmetry expansion and focused classifications and refinements gave subregions at 3- to 3.6-Å resolution (Fig. 2, figs. S4 to S6, table S5, and movie S1) (*16*). The density for approximately half of FdhA is poorly resolved, which suggests that the subunit is partially unfolded, in line with a low occupancy of molybdenum (table S6). Two isoforms of FdhA and FdhB were detected by MS, but we were unable to separate these by 3D image classification. We have therefore modeled the most abundant isoforms, FdhA3 and FdhB3. The dimeric Fdh-Hdr-Fmd structure reveals that FdhAB and HdrABC are connected via MvhD in a manner similar to that of Mvh-Hdr of *M. thermolithotrophicus* (*6*) and that a polyferredoxin FmdF bridges HdrABC and FmdABCDG (Fig. 2).

A minority of 2D classes from the dimeric fraction correspond to a larger structure, which was enriched in the reproducibly observed higher molecular mass shoulder region of the SEC peak (Fig. 1B). After 2D classification and 3D refinement, a 4.4 Å–resolution map of the hexameric complex was obtained, corresponding to D_3-symmetric organization of three dimeric complexes, in which homodimers of the polyferredoxin FmdF bridge the $Hdr(ABC)_2$ and $Fmd(ABCDG)_2$ units (Fig. 2, movie S2, and fig. S7). Symmetry expansion and focused

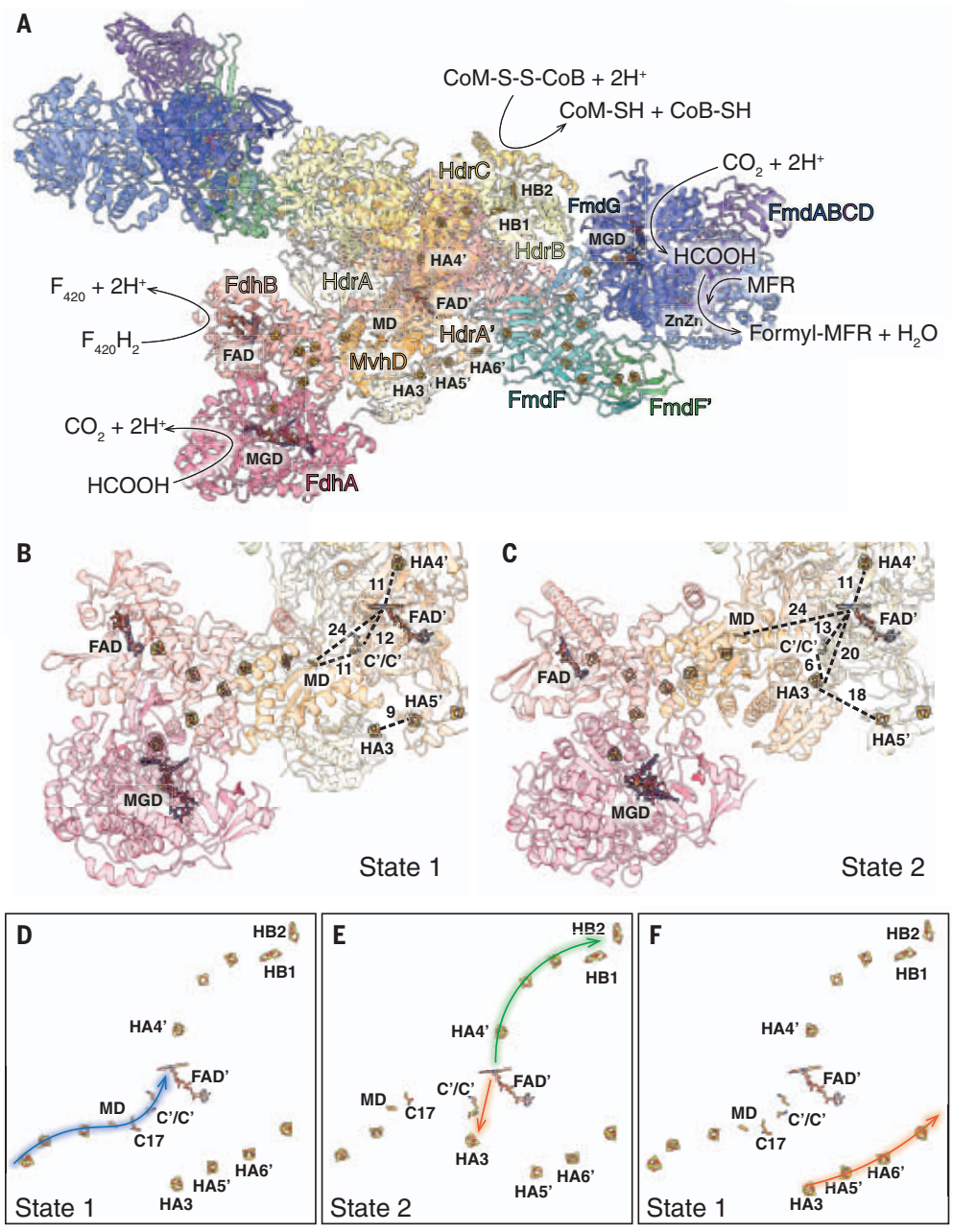


Fig. 3. Proposed electron transfer pathways within the Fdh-Hdr-Fmd complex. (**A**) Formate is oxidized to CO_2 at the molybdopterin (MGD) site in FdhA; alternatively, $F_{420}H_2$ is oxidized at the FAD site in FdhB (see also fig. S14). Electrons from formate or $F_{420}H_2$ are transferred by a series of [4Fe-4S] clusters to reach the [2Fe-2S] cluster of MvhD (MD). The active-site cofactors—MGD in FdhA and FmdB, FAD in FdhB and HdrA, noncubane [4Fe-4S] clusters (HB1 and HB2) in HdrB, dinuclear zinc center (ZnZn) in FmdA, and the cubane [4Fe-4S] clusters—are depicted with stick models. (**B** and **C**) State 1 (B) and state 2 (C) conformations of the Fdh-Hdr-Fmd complex differ by a rotation of the mobile arm consisting of FdhA, FdhB, MvhD, and the N- and C-terminal domains of HdrA. Dashed lines indicate distances, in angstroms, between cofactors. C′/C′ shows the $Cys^{198'}$/$Cys^{201'}$ pair of HdrA′. (**D**) In state 1, MD approaches the bifurcating FAD′ of HdrA′, which would allow electron transfer by an unknown mechanism, possibly involving Cys^{17} of MvhD and $Cys^{198'}$ and $Cys^{201'}$ of HdrA (blue line). (**E**) Rotation of the mobile arm brings the complex into state 2. A weakly reducing electron is transferred from the fully reduced FAD′ to the noncubane [4Fe-4S] clusters of HdrB (HB1 and HB2) via cluster HA4′ for reduction of CoM-S-S-CoB (green line). The strongly reducing electron is transferred from the FAD′ semiquinone to the isolated cluster HA3, which acts as an electron shuttle (red line). (**F**) Conformational change back to state 1 brings HA3 back within rapid electron transfer distance of cluster HA5′ of HdrA′, thereby forming a conductive pathway to the CO_2-reducing site of the Fmd module (red line).

refinements gave maps of FmdABCDG at 3.4-Å resolution, FdhAB-Mvh at 3.7-Å resolution, and the HdrABC core at 3.4-Å resolution (figs. S5, S8, and S9). An identical interaction of HdrA with FmdF forms the basis of complexation in the dimer and the hexamer, except that we observe only partial occupancy of FmdABCDFG at its binding site on HdrA in the dimeric complex (fig. S4). The dimeric complex map shows a weak density for additional subunits outside of the dimeric core (fig. S10), including an intertwined homodimer of FmdF, similar to the dimeric FwdF from *Methanothermobacter wolfeii* (*3*). This would not be expected for a physiological dimer, which would show a single FmdF chain bound to each of the equivalent binding sites of two HdrA. Given that HdrA and FmdF both form homodimers, only the hexameric organization allows all FmdF dimers to interact with two HdrA and vice versa (fig. S7), suggesting that the hexameric form is a physiological form, whereas the dimer may result from incomplete assembly or breakdown of the hexamer.

The HdrABC modules in the dimer and hexamer show a fold highly similar to that of Mvh-Hdr of *M. thermolithotrophicus* (fig. S11, A and B). The electron-bifurcating FAD is fully occupied in HdrA, and the residues forming the FAD-binding pocket are conserved (fig. S12). HdrB contains two noncubane [4Fe-4S] clusters, which form the active site for the reduction of CoM-S-S-CoB (fig. S13) (*6*). In the hexameric structure of Fdh-Hdr-Fmd, the fold and quaternary structure of dimers of FmdABCDFG are very similar to those of FwdABCDFG of *M. wolfeii* (fig. S11, C and D) (*3*).

Our structures show the electron transfer chain from formate via molybdopterin in FdhA to the FBEB-catalyzing HdrA (Fig. 3A). FdhB contains a partially solvent-exposed FAD molecule that forms a likely F_{420}-binding site, which shows a fold similar to that of the FAD-containing site of F_{420}-reducing hydrogenase (Frh) (fig. S14) (*17*). The electron transfer chains from FdhB FAD and the FdhA active site converge at an unpredicted [4Fe-4S] cluster with ligation from one histidine and three

cysteine residues (fig. S15), and the [4Fe-4S] clusters in FdhAB form a conductive pathway with distances below 14 Å. Accordingly, our assays demonstrate that the Fdh-Hdr-Fmd and Fdh-Hdr complexes can catalyze FBEB using the electrons from formate or $F_{420}H_2$ (Fig. 1, D to F; table S3; and fig. S2). $F_{420}H_2$ is generated in vivo by H_2-dependent reduction by Frh. We detected Frh activity in the cell extract of *M. hungatei* (Fig. 1A). Our data demonstrate how *M. hungatei* can use both formate and, indirectly, H_2 as electron donors for CO_2 fixation, even though the *M. hungatei* genome does not encode an Hdr-associated hydrogenase (Mvh) (fig. S16). An $F_{420}H_2$-dependent FBEB reaction in Fdh-Hdr confers metabolic flexibility in methanogen species using both Fdh-Hdr and Mvh-Hdr; an *M. maripaludis* mutant lacking the Mvh homologs Vhu and Vhc grows on H_2 and CO_2, and this growth depends on Frh activity (*10*) , for which our work provides an explanation. $F_{420}H_2$-dependent Hdr activity has been observed in a membrane fraction of *Methanococcus voltae* (*18*) and in the heterologously produced $Hdr(ABC)_2$ complex from *Methanosarcina acetivorans* (*19*); however, the contribution of the Fdh module for the F_{420}-dependent Hdr activity was not reported.

Symmetric global refinement of the dimeric and hexameric Fdh-Hdr-Fmd complexes results in well-resolved density for the HdrABC core but smeared density for the subcomplex containing the N- and C-terminal domains of HdrA together with MvhD, FdhA, and FdhB, which we refer to as the "mobile arm." Focused classification gave two well-resolved conformational states for both the dimeric and hexameric datasets, differing by a rotation of around 40°, creating displacements of up to 3.3 nm (Fig. 3, B and C). The movement of the mobile arm pivots around a point near Pro^{141} and Pro^{590} in the two-strand connection between the central thioredoxin reductase domain, N-terminal domain, and C-terminal ferredoxin domain of HdrA (fig. S17). One conformation, here termed "state 1," brings the [2Fe-2S] cluster of MvhD [MD; naming consistent with (*6*)] close to the bifurcating FAD′ of HdrA′ (prime symbol indicates the alternate protomer). In this state, a conserved cysteine pair $Cys^{198\prime}$/$Cys^{201\prime}$ of HdrA′ is located between the two cofactors, 11 Å from MD and 12 Å from FAD′ (Fig. 3B). A conserved nonligating cysteine of MvhD (Cys^{17} in *M. hungatei*) lies between cluster MD and the $Cys^{198\prime}$/$Cys^{201\prime}$ pair; the distance between the thiol groups of Cys^{17} and $Cys^{201\prime}$ is 5 Å (fig. S18). Cys^{17}, the MD-ligating Cys^{68}, and Cys^{201} are replaced by selenocysteine in some species, which often indicates a special functional importance. The second well-resolved conformation of the mobile arm, "state 2" (Fig. 3C), much more closely resembles the previously published crystal structures of Mvh-Hdr of *M. thermolithotrophicus* (*6*). In state 2, the [4Fe-4S] cluster HA3 of the N-terminal domain of HdrA is near (6 Å) the conserved $Cys^{198\prime}$/$Cys^{201\prime}$ pair and 20 Å from FAD′. The crystal structure shows that the distance between FAD′ and HA3 can be narrowed (<15 Å) in HdrA of *M. thermolithotrophicus* (*6*). Our map densities suggest that $Cys^{198\prime}$/$Cys^{201\prime}$ form a disulfide bond in state 2, but not in state 1 (fig. S19).

A proposed electron transfer pathway is summarized in Fig. 3, D to F, and movie S3. In state 1, electrons from formate or $F_{420}H_2$ (H_2 in the related Mvh-Hdr complexes) travel via the electron relay to the [2Fe-2S] cluster MD and from there are predicted to transfer to the bifurcating FAD′ of HdrA′ (Fig. 3D) (*6*, *13*). The distance between MD and FAD′ of HdrA′ (24 Å) is too far for direct electron transfer. Moreover, the crossed potentials of the flavin require a mechanism that bypasses the high-energy radical state in the reductive direction (*13*). Thus, a further conformational change is likely required to mediate electron transfer from MD to FAD′. The localization of the conserved $Cys^{198\prime}$/$Cys^{201\prime}$ pair and Cys^{17} suggests a contribution of the thiol groups for the electron transfer, although further studies will be needed to clarify the mechanism. With a transition to state 2, a weakly reducing electron can be transferred from the fully reduced FAD′ via HA4′ to the Hdr site (HB1 and HB2), and a strongly reducing electron derived from FBEB can be transferred from the FAD′ semiquinone to HA3, which acts as an electron shuttle (Fig. 3E). As the complex returns to state 1, HA3 transfers an electron to HA5′ of the inserted ferredoxin domain of HdrA, which is within electron transfer distance (9 Å) (Fig. 3B). From HA5′, the electron passes via HA6′ to FmdF and further to molybdopterin in FmdBD via FmdG (Fig. 3F and movie S3). The interdimer electron transfers provide a rationale for the importance of HdrA dimerization. In the proposed scheme, an electron passes through the MD and HA3 clusters of the same mobile arm, which allows a single conformational change of the mobile arm to gate electron flow to and away from the FAD.

The purified Fdh-Hdr-Fmd complex catalyzes methanofuran-dependent CoM-S-S-CoB reduction by using formate as an electron donor in the absence of free ferredoxin (Fig. 1D), which indicates that the Fdh, Hdr, and Fmd active sites are electronically connected through the electron-bifurcating HdrA subunit. The Fdh-Hdr-Fmd and Fdh-Hdr complexes also catalyze the electron-bifurcating reduction of external ferredoxin (2[4Fe-4S] ferredoxin from *Clostridium pasteurianum*) and CoM-S-S-CoB using formate or $F_{420}H_2$ as electron donor (Fig. 1, E and F, and table S3). Interaction with soluble ferredoxin is physiologically important to use electrons from ferredoxin reduced by membrane-bound hydrogenase (Eha/Ehb) for anaplerotic CO_2 fixation (fig. S16) (*20*, *21*).

The structures of *M. thermolithotrophicus* Mvh-Hdr [Protein Data Bank (PDB) ID 5ODH] (*6*) and *M. wolfeii* Fwd (PDB ID: 5T61) (*3*) can be superposed on our hexameric complex without leading to clashes (fig. S20). In light of the notable structural conservation, we propose that the hexameric electron-bifurcating, CO_2-reducing complex is a common structure in hydrogenotrophic methanogens without cytochromes. The apparent instability of the complex to dissociation (*10*, *11*) may explain why Mvh-Hdr, Fdh-Hdr, and Fwd complexes are often purified separately. Our proposal is supported by the previous observation of co–pull-down of Hdr and Fwd complexes in other methanogens (*9*–*11*). FwdABCDFG of *M. wolfeii* forms a tetrameric "hourglass" complex, with an additional [4Fe-4S] cluster at the dimer-dimer interface of FmdF (figs. S21 and S22). Combining the "hourglass" and hexameric modes of multimerization does not lead to clashes. The complexation of electron-bifurcating and CO_2-reducing reactions, which allows direct electron transfer (fig. S16), may be important to avoid the loss of strongly reducing electrons and support the low–energy gain methanogenic metabolism in natural environments.

REFERENCES AND NOTES

1. R. K. Thauer, A.-K. Kaster, H. Seedorf, W. Buckel, R. Hedderich, *Nat. Rev. Microbiol.* **6**, 579–591 (2008).
2. S. Shima, G. Huang, T. Wagner, U. Ermler, *Annu. Rev. Microbiol.* **74**, 713–733 (2020).
3. T. Wagner, U. Ermler, S. Shima, *Science* **354**, 114–117 (2016).
4. R. A. Schmitz, S. P. Albracht, R. K. Thauer, *Eur. J. Biochem.* **209**, 1013–1018 (1992).
5. A.-K. Kaster, J. Moll, K. Parey, R. K. Thauer, *Proc. Natl. Acad. Sci. U.S.A.* **108**, 2981–2986 (2011).
6. T. Wagner, J. Koch, U. Ermler, S. Shima, *Science* **357**, 699–703 (2017).
7. E. Setzke, R. Hedderich, S. Heiden, R. K. Thauer, *Eur. J. Biochem.* **220**, 139–148 (1994).
8. R. D. Milton, J. C. Ruth, J. S. Deutzmann, A. M. Spormann, *Biochemistry* **57**, 4848–4857 (2018).
9. K. C. Costa *et al.*, *Proc. Natl. Acad. Sci. U.S.A.* **107**, 11050–11055 (2010).
10. K. C. Costa, T. J. Lie, Q. Xia, J. A. Leigh, *J. Bacteriol.* **195**, 5160–5165 (2013).
11. M. F. Abdul Halim, L. A. Day, K. C. Costa, *Appl. Environ. Microbiol.* **87**, e02698-20 (2020).
12. W. Buckel, R. K. Thauer, *Front. Microbiol.* **9**, 401 (2018).
13. W. Buckel, R. K. Thauer, *Chem. Rev.* **118**, 3862–3886 (2018).
14. P. N. Evans *et al.*, *Nat. Rev. Microbiol.* **17**, 219–232 (2019).
15. P. Liu, Y. Yang, Z. Lü, Y. Lu, *Appl. Environ. Microbiol.* **80**, 4668–4676 (2014).
16. D. Liebschner *et al.*, *Acta Crystallogr. D Struct. Biol.* **75**, 861–877 (2019).
17. S. Vitt *et al.*, *J. Mol. Biol.* **426**, 2813–2826 (2014).
18. J. Brodersen, G. Gottschalk, U. Deppenmeier, *Arch. Microbiol.* **171**, 115–121 (1999).
19. Z. Yan, M. Wang, J. G. Ferry, *mBio* **8**, e02285-16 (2017).
20. T. J. Lie *et al.*, *Proc. Natl. Acad. Sci. U.S.A.* **109**, 15473–15478 (2012).
21. R. K. Thauer *et al.*, *Annu. Rev. Biochem.* **79**, 507–536 (2010).

ACKNOWLEDGMENTS

We thank A. Seubert for inductively coupled plasma MS analysis. We thank R. K. Thauer for helpful suggestions. We thank U. Ermler, D. Mills, S. Vitt, and S. Prinz for support with anaerobic plunge freezing and the Central Electron Microscopy Facility, Max Planck Institute of Biophysics, Frankfurt. **Funding:** This work is supported by the Max Planck Society (to S.S. and B.J.M.) and Deutsche

Forschungsgemeinschaft (SH 87/1-1 to S.S.) and fellowships from the Alexander von Humboldt Foundation and Japan Society for the Promotion of Science (T.W.). **Author contributions:** S.S. directed the biochemistry and enzymology. T.W. cultured cells, purified the enzyme complexes, and performed biochemical assays and analysis. J.Ka. performed mass spectrometry analysis. J.Ko. synthesized CoM-S-S-CoB. T.W. and B.J.M. prepared cryo-EM samples. O.P.-G. and B.J.M. performed cryo-EM imaging and analysis and built and refined atomic models. T.W., O.P.-G., S.S., and B.J.M. analyzed models, prepared figures and movies, and wrote the manuscript in consultation with all other authors.

Competing interests: The authors declare no competing interests.
Data and materials availability: Atomic models have been deposited in the PDB under accession numbers 7BKC (dimer), 7BKB (hexamer), 7BKD (mobile arm state 1), and 7BKE (mobile arm state 2). Maps and half-maps have been deposited in the EMDB under accession numbers 12196 to 12212. All other data are presented in the main text or supplementary material.

SUPPLEMENTARY MATERIALS

science.sciencemag.org/content/373/6559/1151/suppl/DC1
Materials and Methods
Supplementary Text
Figs. S1 to S22
Tables S1 to S8
References (*22*–*44*)
MDAR Reproducibility Checklist
Movies S1 to S3

29 January 2021; accepted 30 July 2021
10.1126/science.abg5550

NEUROSCIENCE

The integrated stress response contributes to tRNA synthetase–associated peripheral neuropathy

E. L. Spaulding[1,2]†, T. J. Hines[1], P. Bais[1], A. L. D. Tadenev[1], R. Schneider[1], D. Jewett[1], B. Pattavina[1], S. L. Pratt[1,3], K. H. Morelli[1,2]‡, M. G. Stum[1]§, D. P. Hill[1], C. Gobet[4], M. Pipis[5], M. M. Reilly[5], M. J. Jennings[6], R. Horvath[6], Y. Bai[7], M. E. Shy[7], B. Alvarez-Castelao[8]¶, E. M. Schuman[8], L. P. Bogdanik[1], E. Storkebaum[9], R. W. Burgess[1,2,3]*

Dominant mutations in ubiquitously expressed transfer RNA (tRNA) synthetase genes cause axonal peripheral neuropathy, accounting for at least six forms of Charcot-Marie-Tooth (CMT) disease. Genetic evidence in mouse and *Drosophila* models suggests a gain-of-function mechanism. In this study, we used in vivo, cell type–specific transcriptional and translational profiling to show that mutant tRNA synthetases activate the integrated stress response (ISR) through the sensor kinase GCN2 (general control nonderepressible 2). The chronic activation of the ISR contributed to the pathophysiology, and genetic deletion or pharmacological inhibition of *Gcn2* alleviated the peripheral neuropathy. The activation of GCN2 suggests that the aberrant activity of the mutant tRNA synthetases is still related to translation and that inhibiting GCN2 or the ISR may represent a therapeutic strategy in CMT.

In humans, dominant mutations in at least six aminoacyl-tRNA synthetases (AARSs) cause the specific degeneration of peripheral motor and sensory axons (*1*, *2*). A shared underlying mechanism is possible (*3*), and mouse studies support a neomorphic activity of mutant AARSs (*4*–*6*). Impaired translation is attractive as a candidate disease mechanism. Overexpression of mutant glycyl- or tyrosyl-tRNA synthetase (encoded by the genes *GARS* or *YARS*, respectively) in *Drosophila* causes decreased translation, independent of their normal tRNA charging activity (*7*). However, whether decreased translation is an effect of a neomorphic activity or secondary to cell stress and whether cell stress contributes to disease have not been investigated.

To evaluate translation in vivo, we performed fluorescent noncanonical amino acid tagging (*8*, *9*) in motor neurons of two mouse models of Charcot-Marie-Tooth (CMT) disease type 2D (CMT2D), caused by dominant mutations in *Gars* (figs. S1 and S2) (*4*, *10*). Translation is impaired in motor neurons in both models. In pre–disease onset mice, impairments in translation were present and correlated with onset of neurodegeneration (fig. S2). Translation was not impaired in the liver or heart of mutant *Gars* mice using puromycin labeling (fig. S2).

To further examine changes in transcription and translation in motor neurons, we performed RiboTagging using *Chat-Cre* to activate the system in cholinergic neurons (*11*). We validated this system using spinal cord samples from wild-type mice by confirming an enrichment of known motor neuron markers and depletion of non-neuronal genes (fig. S3), as well as up-regulation of known markers of axotomy such as *Sprr1a*, *Atf3*, and *Npy* (*12*–*14*) after unilateral sciatic nerve injury (fig. S3 and data S1).

We next compared ribosome-associated mRNA from $Gars^{+/+}$ spinal cord with that from spinal cord of the CMT2D mouse models $Gars^{C201R/+}$ or $Gars^{P278KY/+}$. $Gars^{C201R/+}$ motor neurons contain 1976 up-regulated and 126 down-regulated transcripts, and $Gars^{P278KY/+}$ motor neurons contain 603 up-regulated and 233 down-regulated transcripts (Fig. 1, A to C). Many of the same highly up-regulated transcripts—including fibroblast growth factor 21 (*Fgf21*), growth differentiation factor 15 (*Gdf15*), and corneodesmosin (*Cdsn*)—were found in both genotypes. We also performed RNA sequencing (RNA-seq) from whole spinal cord in mutant *Gars* mice, including a third humanized CMT2D model, $Gars^{\Delta ETAQ/+}$ (*6*). Up-regulated transcripts were similar between RiboTagging and whole–spinal cord RNA-seq experiments and among all three mouse models (Fig. 1, D and E; Jaccard similarity indices 0.12 to 0.16, $p < 0.002$ across RNA-seq experiments). The up-regulated transcripts in mutant *Gars* datasets did not overlap with those up-regulated after sciatic nerve injury or with results from a *mitofusin-2* mouse model of CMT disease type 2A (*15*). Only one differentially expressed gene in the $Gars^{C201R/+}$ whole spinal cord overlapped with results from an equivalent experiment in a mouse model of *Ighmbp2*-associated spinal muscular atrophy (*16*). We also performed RiboTagging and RNA-seq from pre–disease onset mutant *Gars* mice and found early up-regulation of a subset of the same transcripts (fig. S3). Ingenuity pathway analysis (IPA) of up-regulated genes indicated forms of cell stress and activation of the integrated stress response (ISR) (Fig. 1F). The ISR-associated transcription factor *Atf4* and several known ATF4 targets were among the up-regulated transcripts in our RiboTagging data (Fig. 1C). We confirmed activation of the ISR using immunolabeling of phospho-eIF2α (phosphorylated eukaryotic translation initiation factor 2α), which was increased in all three *Gars* alleles and was specific to a subset of spinal motor neurons (Fig. 1, G and H, and fig. S4). These data indicate that the ISR is activated in spinal motor neurons, that this up-regulation occurs before overt neuropathy symptoms, and that this is seen in three *Gars* alleles.

[1]The Jackson Laboratory, Bar Harbor, ME 04609, USA. [2]Graduate School of Biomedical Science and Engineering, University of Maine, Orono, ME 04469, USA. [3]Neuroscience Program, Graduate School of Biomedical Sciences, Tufts University, Boston, MA 02111, USA. [4]School of Life Sciences, Ecole Polytechnique Fédérale de Lausanne (EPFL), CH-1015 Lausanne, Switzerland. [5]MRC Centre for Neuromuscular Diseases, Department of Neuromuscular Diseases, UCL Queen Square Institute of Neurology, London, UK. [6]Department of Clinical Neuroscience, University of Cambridge, Cambridge, UK. [7]Department of Neurology, Carver College of Medicine, University of Iowa, Iowa City, IA 52242, USA. [8]Max Planck Institute for Brain Research, Frankfurt, Germany. [9]Department of Molecular Neurobiology, Donders Institute for Brain, Cognition and Behaviour and Faculty of Science, Radboud University, Nijmegen, Netherlands.
***Corresponding author. Email: robert.burgess@jax.org**
†Present address: Mount Desert Island Biological Laboratory, Bar Harbor, ME 04609, USA. ‡Present address: Cellular and Molecular Medicine, University of California, San Diego, La Jolla, CA 92093, USA. §Present address: ClearH2O Inc., Portland, ME 04101, USA. ¶Present address: Department of Biochemistry, Veterinary School, University Complutense of Madrid, Madrid, Spain.

To address the cell-type specificity within the spinal cord, we examined five of the top up-regulated ATF4 target genes using RNAscope in situ hybridization. *Chat* was used as a marker of motor neurons, which include *Spp1*-positive alpha motor neurons (~70%), and *Spp1*-negative gamma motor neurons (~30%) (Fig. 2A) (*17*, *18*). Robust and specific up-regulation of all five transcripts was confirmed in *Chat*-positive cells in the ventral horn in mutant *Gars* motor neurons (Fig. 2, B to D, and fig. S5). About 70% of *Gars*$^{P278KY/+}$ motor neurons expressed the ATF4 target genes (Fig. 2E and fig. S5). ISR activation was selective to alpha motor neurons because *Spp1*-positive cells were also *Fgf21*-postive, whereas *Fgf21*-negative cells were *Spp1*-negative (Fig. 2, F to H).

We next examined a related mouse model of dominant intermediate CMT type C that carries a disease-associated knockin mutation in tyrosyl-tRNA synthetase, *Yars*^{E196K} (*19*) (fig. S6). We identified activation of the ISR in alpha motor neurons in this model at 7 months of age by phospho-eIF2α labeling and by in situ hybridization for the same five ATF4 target genes. This was observed in *Yars*$^{E196K/E196K}$ mice and, to a lesser extent, in *Yars*$^{E196K/+}$ mice (fig. S7). Whole–spinal cord RNA-seq also indicated that ATF4 target genes were up-regulated in *Yars*$^{E196K/E196K}$ mice (fig. S8; Jaccard similarity index 0.064, $p < 0.002$, *Yars*$^{E196K/E196K}$ with the union of *Gars* gene lists), although the signal visible in *Yars*$^{E196K/+}$ motor neurons by in situ hybridization was not detectable, which was confirmed by quantitative reverse transcription polymerase chain reaction (qRT-PCR) (fig. S8).

Peripheral sensory neurons were examined for ISR activation by probing for up-regulation of the ATF4 target genes in lumbar dorsal root ganglia (DRG; fig. S9). Robust up-regulation of *Fgf21* was observed in a subset of mutant *Gars* DRG neurons, especially medium-large neurons, colabeled with neurofilament heavy chain (*Nefh*) (*20*). We included parvalbumin (*Pvalb*) as an additional marker (*21*), and subsets of both mechanosensitive (*Nefh*$^+$, *Pvalb*$^-$) and proprioceptive (*Nefh*$^+$, *Pvalb*$^+$) sensory neurons expressed *Fgf21* (fig. S9). Thus, the ISR was activated specifically in alpha motor neurons and in a subset of sensory neurons.

The ISR is activated by four discrete kinases, all of which phosphorylate eIF2α to suppress cap-dependent translation and activate ATF4 target gene expression (*22*). ISR activation through the sensor kinase GCN2 (general control nonderepressible 2) is observed with impairments in translation and ribosome stalling (*23*, *24*). We tested for the involvement of GCN2 by breeding *Gars*$^{P278KY/+}$ mice into a *Gcn2* knockout (KO) background (*Gcn2*$^{KO/KO}$). The *Gars*$^{P278KY/+}$ mice have a disease onset at ~2 weeks of age and actively lose motor and

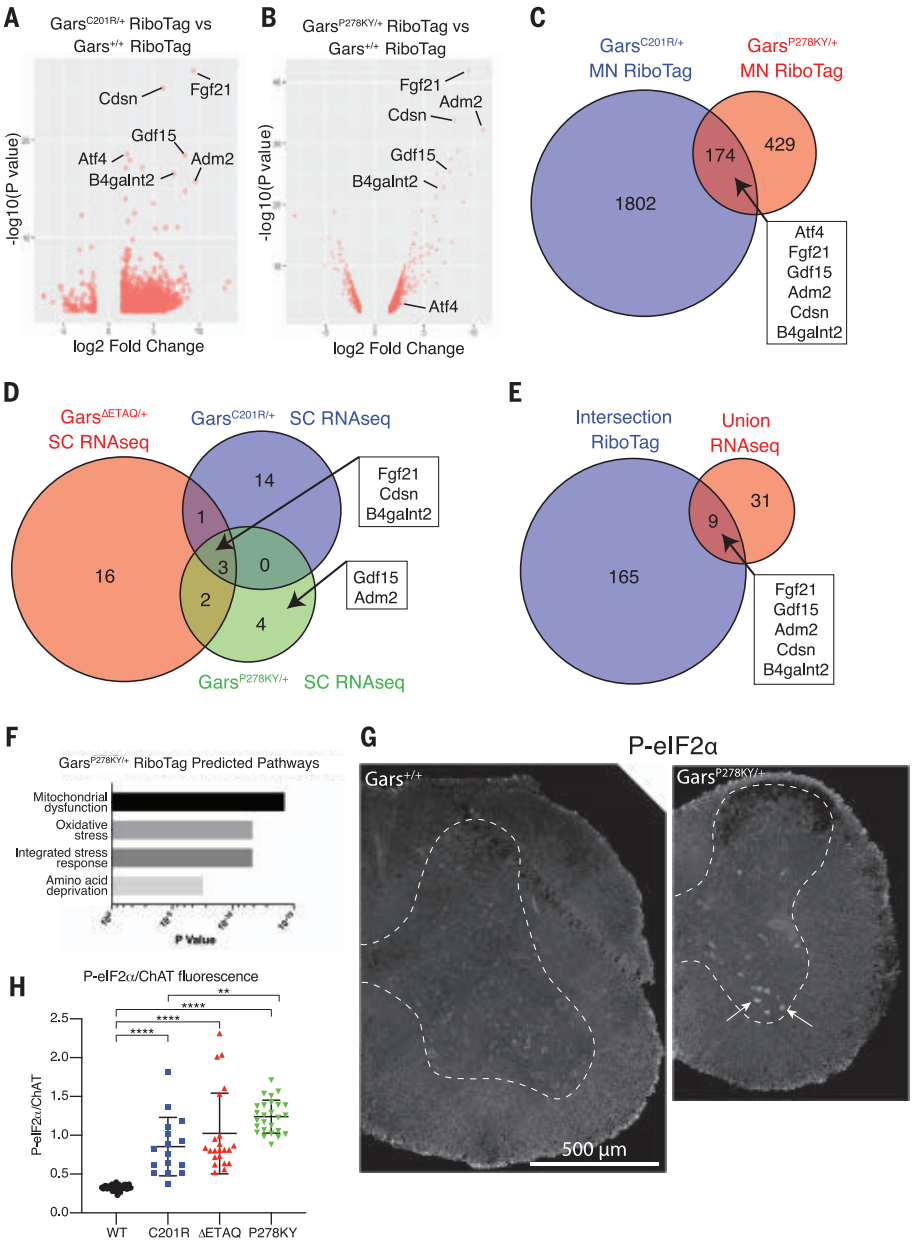


Fig. 1. Differential gene expression in *Gars*-CMT2D mice. (**A**) Compared with *Gars*$^{+/+}$ motor neurons, 1976 up- and 126 down-regulated ribosome-associated mRNAs were found in *Gars*$^{C201R/+}$ motor neurons. (**B**) Compared with *Gars*$^{+/+}$ motor neurons, 603 up- and 233 down-regulated ribosome-associated mRNAs were found in *Gars*$^{P278KY/+}$ motor neurons. (**C**) Between *Gars*$^{C201R/+}$ and *Gars*$^{P278KY/+}$ motor neurons, 174 up-regulated genes were found in common; six genes relevant to subsequent studies are noted. MN, motor neuron. (**D**) The intersections of up-regulated gene lists from whole–spinal cord RNA-seq in three different dominant alleles of *Gars*. SC, spinal cord. (**E**) The up-regulated genes shared in RiboTagging data overlap the union up-regulated gene list from whole–spinal cord RNA-seq. (**F**) IPA of up-regulated ribosome-associated mRNAs with log fold change (FC) ≥ 1.5 and false discovery rate (FDR) < 0.05 in *Gars*$^{P278KY/+}$ motor neurons. (**G**) Activation of the ISR was confirmed with immunolabeling of phospho-eIF2α, which was found specifically in ventral horn motor neurons (arrows) in *Gars*$^{P278KY/+}$ mutant spinal cord (right panel). The dashed lines indicate the boundary of white matter and gray matter. The scale bar is the same for both images. (**H**) The ratio of phospho-eIF2α labeling intensity to that of the motor neuron marker ChAT is increased in motor neurons expressing any of the three alleles of *Gars* and in *Gars*$^{P278KY/+}$ motor neurons compared with *Gars*$^{C201R/+}$ motor neurons. Points represent individual motor neurons; $n = 3$ mice per genotype. Horizontal bars represent mean ± SD. $^{**}p < 0.01$; $^{****}p < 0.0001$ by one-way analysis of variance (ANOVA) with Tukey's multiple comparisons. For (A) and (B), volcano plots show transcripts with log FC > |1.5|; $p < 0.05$. $n = 4$ to 6 mice [in (A) to (C)] or 6 mice [three males, three females in (D)] per genotype at 8 weeks of age.

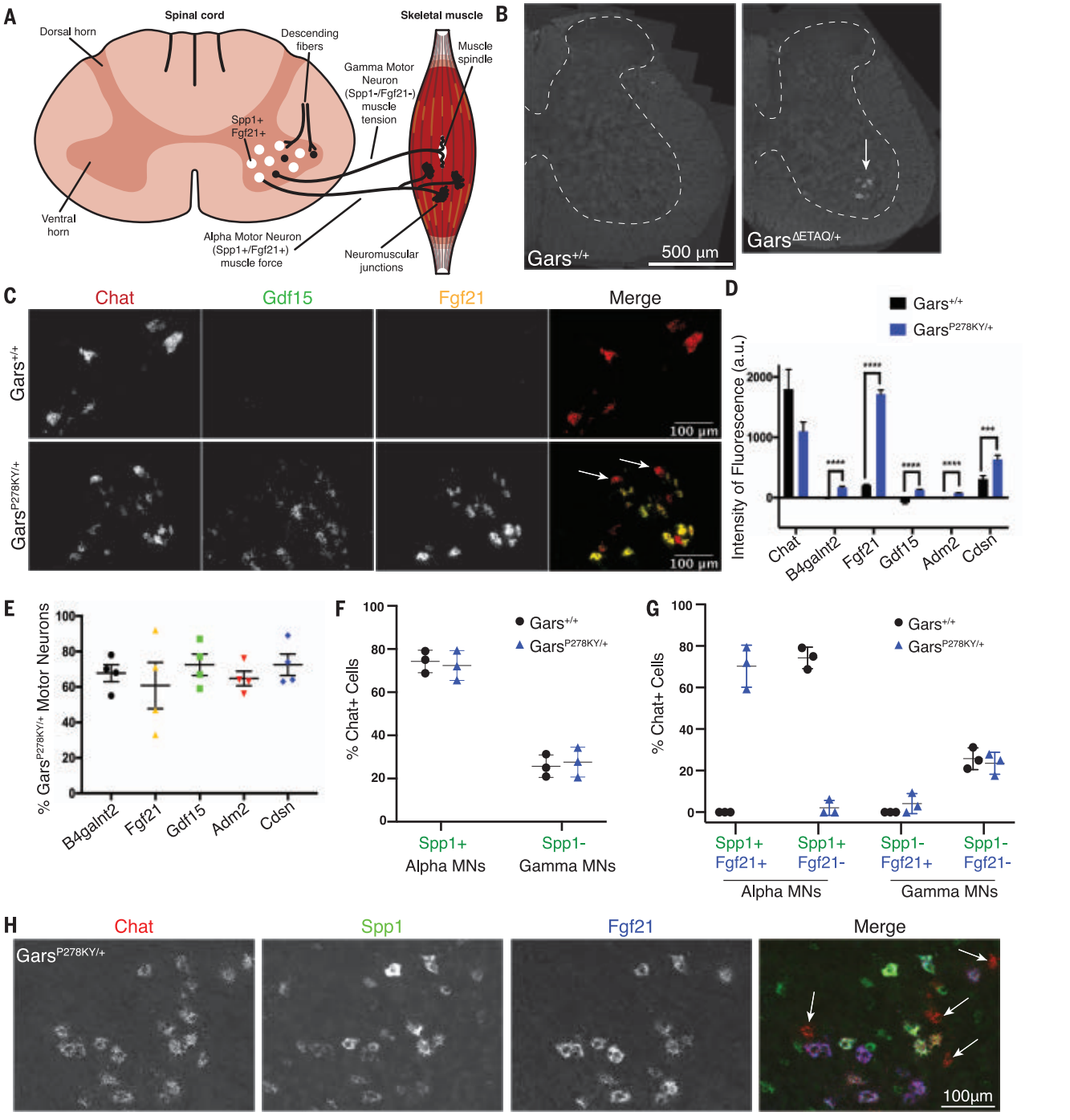


Fig. 2. ATF4 target gene expression is restricted to alpha motor neurons within mutant *Gars* spinal cord. (**A**) Motor neurons in the ventral horn of the spinal cord include alpha (*Spp1*-positive) and gamma (*Spp1*-negative) populations, but only *Spp1*-positive cells express *Fgf21* in mutant mice. (**B**) RNAscope in situ hybridization (ISH) showed up-regulation of the ATF4 target gene *Fgf21* in a subset of ventral horn motor neurons in $Gars^{\Delta ETAQ/+}$ mice (arrow). The scale bar is the same for both images. (**C**) ISH in spinal cord of $Gars^{P278KY/+}$ mice, with *Chat* (red), *Gdf15* (green), and *Fgf21* (yellow). Some *Chat*-positive mutant *Gars* motor neurons do not show expression of disease-related transcripts (arrows). All images use the same scale bars as in the right panels. (**D**) Quantification of background-subtracted ISH fluorescence intensity. ***$p < 0.001$; ****$p < 0.0001$ (two-tailed Student's *t* test; $n = 4$ mice per genotype at 8 weeks of age). Error bars represent SD. a.u., arbitrary units. (**E**) Percentage of $Gars^{P278KY/+}$ motor neurons that expressed the five disease-associated transcripts. (**F**) RNAscope ISH in spinal cord with *Chat* and *Spp1* revealed the same percentage of alpha and gamma motor neurons in mutant mice. (**G** and **H**) Only *Spp1*-positive alpha motor neurons in mutant spinal cords express *Fgf21*. Arrows in (H) point to cells labeled with *Chat* that do not express *Spp1* or *Fgf21*; all images use the same scale bar as in the right panel. In (F) to (H), $n = 3$ mice per genotype at 8 weeks of age; in (E) to (G), horizontal bars represent mean ± SD.

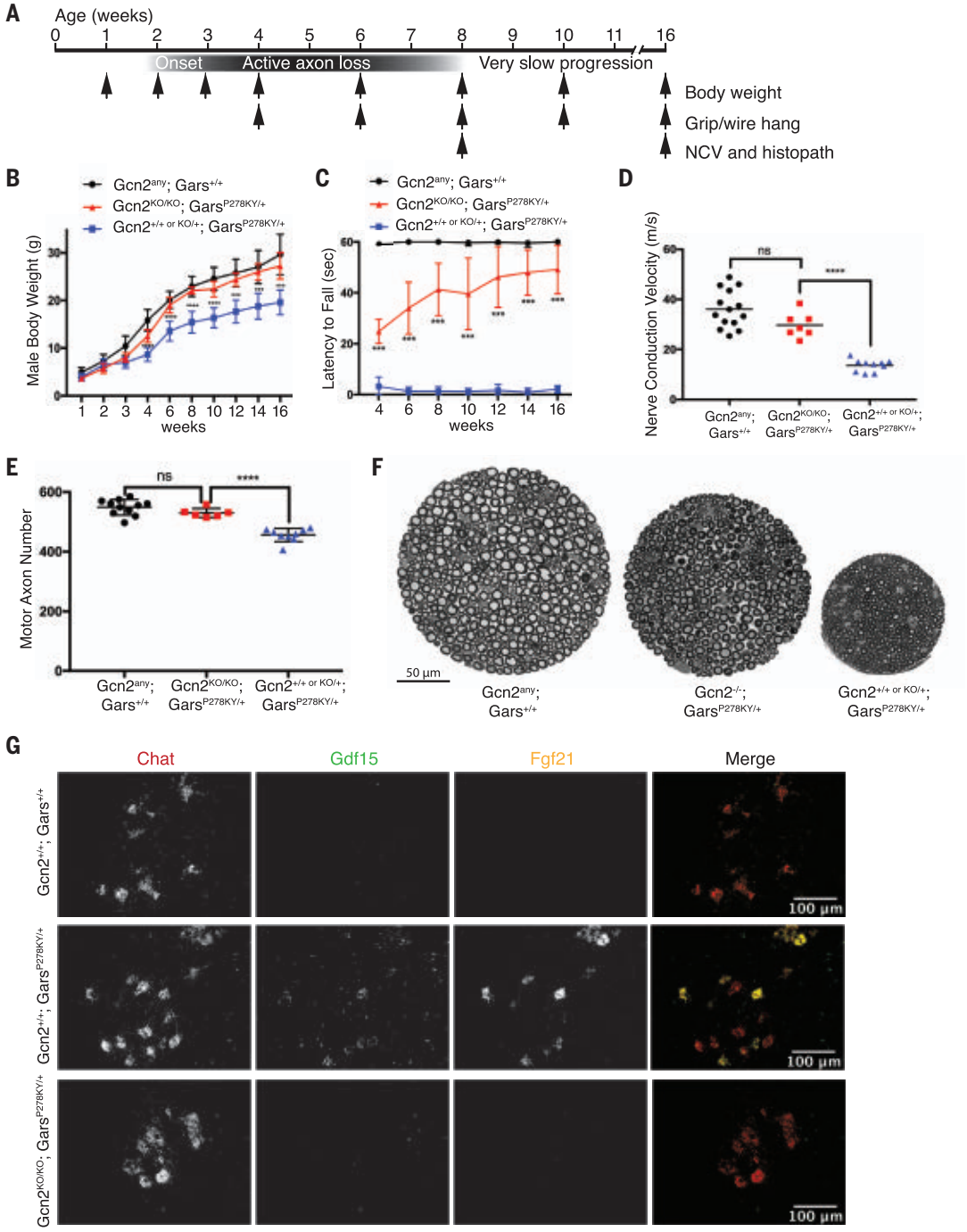


Fig. 3. Deletion of *Gcn2* alleviates the *Gars*$^{P278KY/+}$ phenotype. (**A**) *Gars*$^{P278KY/+}$ mice have a neuromuscular phenotype by 2 weeks of age and actively lose peripheral axons until ~8 weeks of age, after which the phenotype progresses very slowly. (**B**) Body weight of male *Gcn2*$^{KO/KO}$;*Gars*$^{P278KY/+}$ mice is significantly greater than that of *Gcn2*$^{+/+}$;*Gars*$^{P278KY/+}$ or *Gcn2*$^{+/KO}$;*Gars*$^{P278KY/+}$ mice (one-way ANOVA); *Gcn2*^{any} denotes the +/+, +/KO, or KO/KO genotype). Error bars represent SD. (**C**) *Gcn2*$^{KO/KO}$;*Gars*$^{P278KY/+}$ mice have increased latency to fall from an inverted wire grid (one-way ANOVA). The test is stopped after 60 s, and the mean of three trials is reported for each day. Body weight and wire-hang analyses were performed with 18 to 22 mice per grouped genotype. Error bars represent SD. (**D**) Motor nerve conduction velocity of the sciatic nerve is increased in *Gcn2*$^{KO/KO}$;*Gars*$^{P278KY/+}$ mice compared with *Gcn2*$^{+/+}$; *Gars*$^{P278KY/+}$ or *Gcn2*$^{+/-}$;*Gars*$^{P278KY/+}$ mice and is no longer different from that of *Gars*$^{+/+}$ mice regardless of *Gcn2* genotype (one-way ANOVA). (**E**) The average number of motor axons in the femoral nerve of 16-week-old *Gcn2*$^{KO/KO}$; *Gars*$^{P278KY/+}$ mice is greater than that of *Gcn2*$^{+/+}$;*Gars*$^{P278KY/+}$ or *Gcn2*$^{+/-}$; *Gars*$^{P278KY/+}$ mice. *Gcn2*$^{KO/KO}$;*Gars*$^{P278KY/+}$ axon counts are no longer different from those of *Gars*$^{+/+}$ mice regardless of *Gcn2* genotype (one-way ANOVA). (**F**) The motor branch of the femoral nerve in *Gcn2*$^{KO/KO}$;*Gars*$^{P278KY/+}$ mice is intermediate in size compared with that of *Gars*$^{+/+}$ mice and *Gcn2*$^{+/+}$; *Gars*$^{P278KY/+}$ or *Gcn2*$^{+/-}$;*Gars*$^{P278KY/+}$ mice. (**G**) *Gcn2*$^{+/+}$;*Gars*$^{+/+}$ motor neurons show no expression of ATF4 target genes *Gdf15* (green) or *Fgf21* (yellow), whereas *Gcn2*$^{+/+}$;*Gars*$^{P278KY/+}$ motor neurons show robust up-regulation. ATF4 target gene expression is eliminated in *Gcn2*$^{KO/KO}$;*Gars*$^{P278KY/+}$ motor neurons. All images use the same scale bars as in the right panels. For (D) and (E), data points represent individual mice of both sexes; horizontal bars represent the mean (D) or mean ± SD (E). For (B) to (E), ns is not significant, ***$p < 0.001$, and ****$p < 0.0001$.

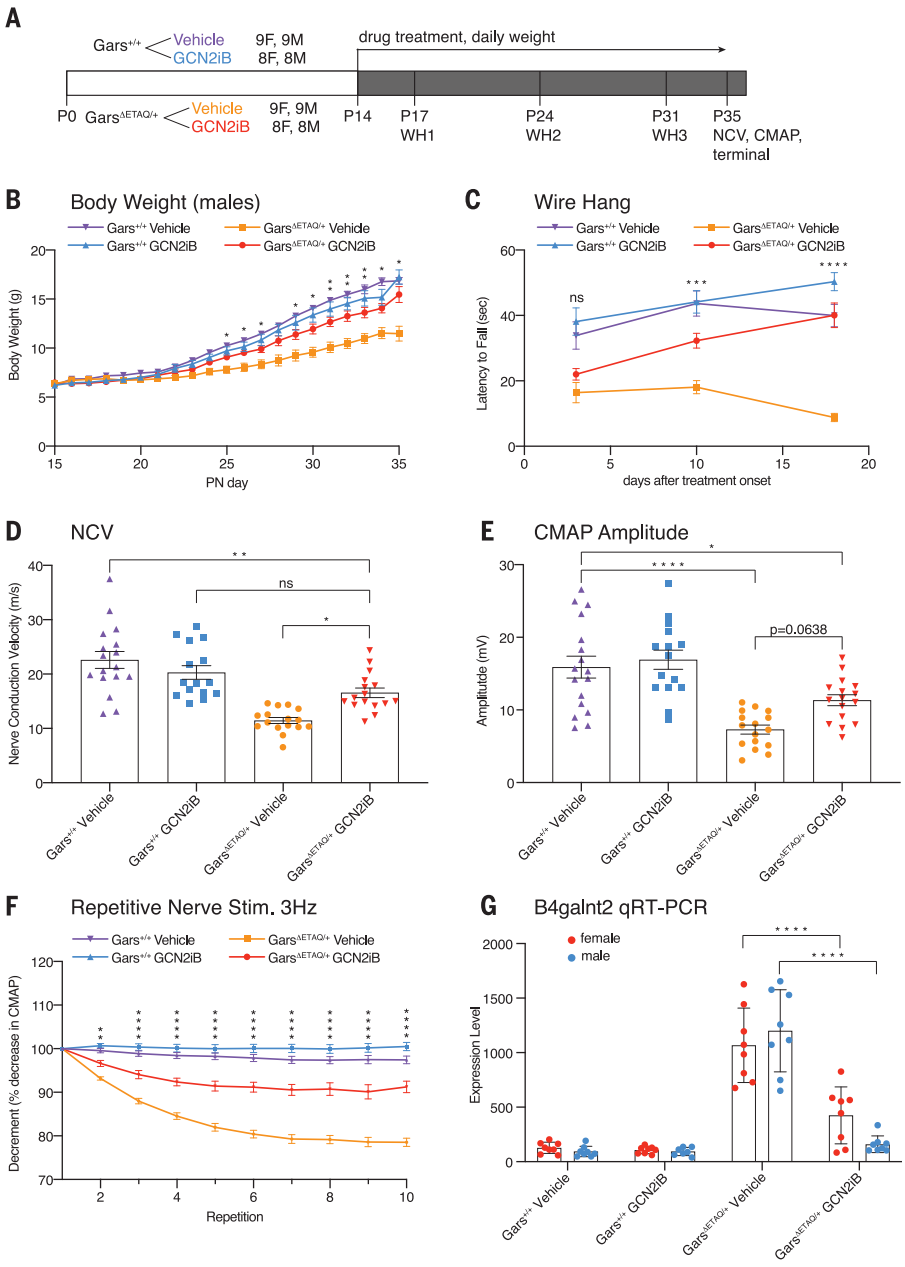


Fig. 4. Pharmacological inhibition of GCN2 is efficacious. (**A**) Study design. Cohorts of *Gars*$^{\Delta ETAQ/+}$ or littermate control (*Gars*$^{+/+}$) mice were treated with GCN2iB or vehicle starting at 2 weeks of age for 3 weeks; eight or nine mice per sex per genotype per treatment group were enrolled. F, female; M, male; P, postnatal day; WH, wire hang. (**B**) GCN2iB improved body weight in *Gars*$^{\Delta ETAQ/+}$ male mice. (**C**) GCN2iB improved strength and endurance in the wire-hang test. (**D**) GCN2iB improved sciatic motor NCV in *Gars*$^{\Delta ETAQ/+}$ mice, although values were still reduced compared with those of controls. (**E**) CMAP amplitude was not significantly improved over vehicle-treated mutant mice. (**F**) The decrement in CMAP amplitude after bouts of repetitive nerve stimulation was alleviated in *Gars*$^{\Delta ETAQ/+}$ mice with GCN2iB treatment. Data from male and female mice are pooled in (C) to (F), although improvement was generally greater in males. (**G**) Expression of the ATF4 target gene *B4galnt2* was reduced with GCN2iB treatment; effects were greater in males. Statistical analysis: (B), (C), (F), and (G) were tested with two-way ANOVA and correction for multiple comparisons; (D) and (E) were tested with one-way ANOVA and correction for multiple comparisons. Asterisks in (B), (C), and (F) indicate significance between GCN2iB-treated and vehicle-treated *Gars*$^{\Delta ETAQ/+}$ mice as well as the pairwise comparisons noted in (D), (E), and (G). For (B) to (G), error bars represent standard error [(B), (C), and (F)] and standard deviation [(D), (E), and (G)]; ns is not significant, *$p < 0.05$, **$p < 0.01$, ***$p < 0.001$, and ****$p < 0.0001$.

sensory axons until about 2 months of age, followed by very slow progression (Fig. 3A) (*4*). We assayed body weight, grip strength, and endurance using a wire-hang test and performed neurophysiology and histopathological examination in a cohort of mice aged to 8 weeks and in a second cohort aged to 16 weeks. The homozygous removal of *Gcn2* markedly alleviated neuropathy in *Gars*$^{P278KY/+}$ mice. The neuropathy started, but the progression was prevented, not merely delayed, as demonstrated by the improvement in phenotypes at 8 weeks of age (fig. S10), which was even greater by 16 weeks (Fig. 3, B to F, and fig. S11). At 16 weeks of age, body weights and motor performance of mutant *Gars* mice lacking GCN2 (*Gcn2*$^{KO/KO}$;*Gars*$^{P278KY/+}$) were nearly restored to *Gars*$^{+/+}$ levels. *Gcn2*$^{KO/KO}$;*Gars*$^{P278KY/+}$ mice also had improved sciatic motor nerve conduction velocity (NCV), no significant motor axon loss, larger diameter motor axons, and less denervation at the neuromuscular junction (NMJ) compared with mutant *Gars* mice expressing GCN2 (*Gcn2*$^{+/+}$;*Gars*$^{P278KY/+}$ or *Gcn2*$^{+/KO}$;*Gars*$^{P278KY/+}$). There was no expression of ATF4 target genes in motor neurons of *Gcn2*$^{KO/KO}$;*Gars*$^{P278KY/+}$ mice by in situ hybridization or RNA-seq (Fig. 3G and fig. S11). Upon removal of *Gcn2*, only 85 genes were differentially expressed between *Gars*$^{+/+}$ and *Gars*$^{P278KY/+}$ mice (fig. S11 and data S1), which no longer included the ATF4 target genes and included many pseudogenes. IPA suggested that these 85 genes show a translation signature. Thus, genetic deletion of *Gcn2* alleviates the ISR and neuropathy.

In a more translational experiment, we treated *Gars*$^{\Delta ETAQ/+}$ mutant and littermate control mice with a GCN2 inhibitor (GCN2iB) (*25*). Treatment began at disease onset at 2 weeks of age and continued for 3 weeks (Fig. 4A). GCN2iB improved body weight, motor performance, and sciatic nerve conduction velocity, although improvement in compound muscle action potential (CMAP) amplitude did not reach significance (Fig. 4, B to E). A decrement in CMAP amplitude with repetitive nerve stimulation, indicative of synaptic transmission problems at the NMJ (*26*), was also improved (Fig. 4F). The effects of GCN2iB were seen in both sexes but were of

greater magnitude in males (fig. S12). GCN2iB effectively reduced ISR activation, which was assayed by phospho-eIF2α labeling and by qRT-PCR for ATF4 target genes (Fig. 4G and fig. S13), with a larger effect observed in males than in females.

We tested for the presence of the secreted ATF4 targets FGF21 and GDF15 in the blood of neuropathy patients with mutations in *GARS*, alanyl-ARS (*AARS*), *YARS*, and tryptophanyl-ARS (*WARS*). Mutant *Gars* mice have increased levels of FGF21 in blood (fig. S14). Neuropathy patients had highly variable levels of FGF21; however, GDF15 was significantly increased in both tRNA synthetase patients and in CMT disease type 1A patients. The cellular source of the circulating GDF15 is unknown, but it may serve as a biomarker of neuropathy.

Our findings indicate that neuropathy-causing mutations in AARSs activate the ISR through GCN2 in alpha motor neurons and a subset of sensory neurons and that inhibiting GCN2 may be an effective therapeutic strategy. The activation of GCN2 may be explained by translation defects downstream of the sequestration of tRNAs by the mutant synthetases (*27*). However, the highly specific activation of the ISR remains puzzling and is not explained by codon bias, because we did not find evidence of this in motor neuron RiboTagging data (fig. S15). Furthermore, we cannot distinguish whether the ISR exacerbates neuropathy through a defect in translation that is compounded by eIF2α phosphorylation, which further decreases translation, or whether expression of ATF4 target genes in peripheral neurons is deleterious. However, the residual phenotype is very mild when the ISR is blocked.

REFERENCES AND NOTES

1. E. Storkebaum, *BioEssays* **38**, 818–829 (2016).
2. A. Antonellis, E. D. Green, *Annu. Rev. Genomics Hum. Genet.* **9**, 87–107 (2008).
3. N. Wei, Q. Zhang, X. L. Yang, *J. Biol. Chem.* **294**, 5321–5339 (2019).
4. K. L. Seburn, L. A. Nangle, G. A. Cox, P. Schimmel, R. W. Burgess, *Neuron* **51**, 715–726 (2006).
5. W. W. Motley *et al*., *PLOS Genet.* **7**, e1002399 (2011).
6. K. H. Morelli *et al*., *J. Clin. Invest.* **129**, 5568–5583 (2019).
7. S. Niehues *et al*., *Nat. Commun.* **6**, 7520 (2015).
8. D. C. Dieterich *et al*., *Nat. Protoc.* **2**, 532–540 (2007).
9. B. Alvarez-Castelao *et al*., *Nat. Biotechnol.* **35**, 1196–1201 (2017).
10. F. Achilli *et al*., *Dis. Model. Mech.* **2**, 359–373 (2009).
11. E. Sanz *et al*., *Proc. Natl. Acad. Sci. U.S.A.* **106**, 13939–13944 (2009).
12. M. L. Starkey *et al*., *J. Comp. Neurol.* **513**, 51–68 (2009).
13. H. Lindå, M. K. Sköld, T. Ochsmann, *Front. Neurol.* **2**, 30 (2011).
14. X. Zhang, B. Meister, R. Elde, V. M. Verge, T. Hökfelt, *Eur. J. Neurosci.* **5**, 1510–1519 (1993).
15. Y. Zhou *et al*., *J. Clin. Invest.* **129**, 1756–1771 (2019).
16. G. A. Cox, C. L. Mahaffey, W. N. Frankel, *Neuron* **21**, 1327–1337 (1998).
17. N. Stifani, *Front. Cell. Neurosci.* **8**, 293 (2014).
18. H. Misawa *et al*., *J. Neurosci. Res.* **90**, 732–742 (2012).
19. A. Jordanova *et al*., *Nat. Genet.* **38**, 197–202 (2006).
20. G. L. Ferri *et al*., *Brain Res.* **515**, 331–335 (1990).
21. C. E. Le Pichon, A. T. Chesler, *Front. Neuroanat.* **8**, 21 (2014).
22. K. Pakos-Zebrucka *et al*., *EMBO Rep.* **17**, 1374–1395 (2016).
23. R. Ishimura, G. Nagy, I. Dotu, J. H. Chuang, S. L. Ackerman, *eLife* **5**, e14295 (2016).
24. A. J. Inglis *et al*., *Proc. Natl. Acad. Sci. U.S.A.* **116**, 4946–4954 (2019).
25. A. Nakamura *et al*., *Proc. Natl. Acad. Sci. U.S.A.* **115**, E7776–E7785 (2018).
26. E. L. Spaulding *et al*., *J. Neurosci.* **36**, 3254–3267 (2016).
27. A. Zuko *et al*., *Science* **373**, 1161–1166 (2021).
28. Sequencing data have been deposited in the Gene Expression Omnibus under GEO accession number GSE145006.
29. Codon usage analysis is available at https://github.com/cgob/codon_usage/.

ACKNOWLEDGMENTS

We thank the patients who participated in this study, as well as the Scientific Services at the Jackson Laboratory and A. Rossor and G. Cox for input and assistance. **Funding:** R.W.B. was supported by the National Institutes of Health (NIH) (R37 NS054154, R01 NS113583, and U54 OD020351) and the Paul E. Kelly Foundation. E.L.S. was supported by NIH F31 NS100328. M.E.S. and M.M.R. were supported by NIH U54 NS065712-08. M.M.R. is also supported by the National Institute for Health Research (NIHR) University College London Hospitals Biomedical Research Centre. E.M.S. received funding from the European Research Council (ERC) under the European Union's Horizon 2020 research and innovation program (no. 743216). E.S. was supported by the Muscular Dystrophy Association (MDA479773); the EU Joint Programme – Neurodegenerative Disease Research [JPND; ZonMW 733051075 (TransNeuro) and ZonMW 733051073 (LocalNMD)]; an ERC consolidator grant (ERC-2017-COG 770244); and the Radala Foundation for ALS Research. R.H. is a Wellcome Trust Investigator (109915/Z/15/Z) and is supported by the Medical Research Council (UK) (MR/N025431/1 and MR/V009346/1); the ERC (309548); the Wellcome Trust Pathfinder Scheme (201064/Z/16/Z); the Newton Fund (MR/N027302/1); the Evelyn Trust (19/14); the Lily Foundation; an MRC strategic award to establish an International Centre for Genomic Medicine in Neuromuscular Diseases (ICGNMD) (MR/S005021/1); and the NIHR Cambridge Biomedical Research Centre (BRC-1215-20014). The views expressed are those of the authors and not necessarily those of the NIHR or the Department of Health and Social Care. **Author contributions:** E.L.S., R.S., D.J., B.P., and L.P.B. performed in vivo experiments; P.B. and D.P.H. analyzed transcriptome data; T.J.H., A.L.D.T., and S.L.P. performed ISR activation studies; K.H.M. and M.G.S. generated mouse models; C.G. performed codon usage analysis; M.P., M.M.R., M.J.J., R.H., Y.B., and M.E.S. provided patient samples and analyses; B.A.-C. and E.M.S. provided mice before publication; E.L.S., E.S., and R.W.B. oversaw experimental design and data analysis; and E.L.S. and R.W.B. wrote the manuscript with input from all authors. **Competing interests:** R.W.B. is on the scientific board of the Hereditary Neuropathy Foundation; R.W.B., M.R., and M.E.S. are on the scientific board of the Charcot-Marie-Tooth Association. E.L.S. and R.W.B. are co-inventors on the pending patent "GCN2 inhibitors to treat peripheral neuropathy." **Data and materials availability:** Animal models, reagents, and protocols are available upon request; the $Gars^{C201R}$ mice were generated in Harwell, UK. Data are presented here and in the supplementary materials. Sequencing data are available through the GEO database (*28*). Code for codon usage analysis is available at https://github.com/cgob/codon_usage/ (*29*).

SUPPLEMENTARY MATERIALS

science.sciencemag.org/content/373/6559/1156/suppl/DC1
Materials and Methods
Figs. S1 to S15
References (*30*–*44*)
MDAR Reproducibility Checklist
Data S1

17 February 2020; resubmitted 10 April 2021
Accepted 16 July 2021
10.1126/science.abb3414

NEUROSCIENCE

tRNA overexpression rescues peripheral neuropathy caused by mutations in tRNA synthetase

Amila Zuko[1]†, Moushami Mallik[1,2]†, Robin Thompson[3], Emily L. Spaulding[4,5]‡, Anne R. Wienand[1], Marije Been[1], Abigail L. D. Tadenev[4], Nick van Bakel[1], Céline Sijlmans[1], Leonardo A. Santos[3], Julia Bussmann[2], Marica Catinozzi[1,2], Sarada Das[3], Divita Kulshrestha[1,2], Robert W. Burgess[4,5], Zoya Ignatova[3], Erik Storkebaum[1,2]*

Heterozygous mutations in six transfer RNA (tRNA) synthetase genes cause Charcot-Marie-Tooth (CMT) peripheral neuropathy. CMT mutant tRNA synthetases inhibit protein synthesis by an unknown mechanism. We found that CMT mutant glycyl-tRNA synthetases bound $tRNA^{Gly}$ but failed to release it, resulting in $tRNA^{Gly}$ sequestration. This sequestration potentially depleted the cellular $tRNA^{Gly}$ pool, leading to insufficient glycyl-$tRNA^{Gly}$ supply to the ribosome. Accordingly, we found ribosome stalling at glycine codons and activation of the integrated stress response (ISR) in affected motor neurons. Moreover, transgenic overexpression of $tRNA^{Gly}$ rescued protein synthesis, peripheral neuropathy, and ISR activation in *Drosophila* and mouse CMT disease type 2D (CMT2D) models. Conversely, inactivation of the ribosome rescue factor GTPBP2 exacerbated peripheral neuropathy. Our findings suggest a molecular mechanism for CMT2D, and elevating $tRNA^{Gly}$ levels may thus have therapeutic potential.

Heterozygous mutations in six genes encoding cytoplasmic aminoacyl-tRNA synthetases (AARSs) cause axonal and intermediate forms of Charcot-Marie-Tooth (CMT) peripheral neuropathy (*1*–*3*). AARSs are ubiquitously expressed enzymes that covalently attach amino acids to their cognate tRNAs (tRNA aminoacylation) (*4*, *5*). Aminoacylated tRNAs are used by the ribosome for mRNA translation (*6*). Interestingly, some CMT AARS mutations do not affect aminoacylation activity (*7*–*11*), indicating that loss of aminoacylation activity is not a prerequisite for disease causality. Rather, a gain-of-toxic-function mechanism may underlie CMT associated with glycyl-tRNA synthetase (GlyRS) mutations [CMT disease type 2D (CMT2D)] (*9*, *12*). In vivo cell type–specific visualization of newly synthesized proteins in *Drosophila* (*13*) by fluorescent noncanonical amino acid tagging (FUNCAT)

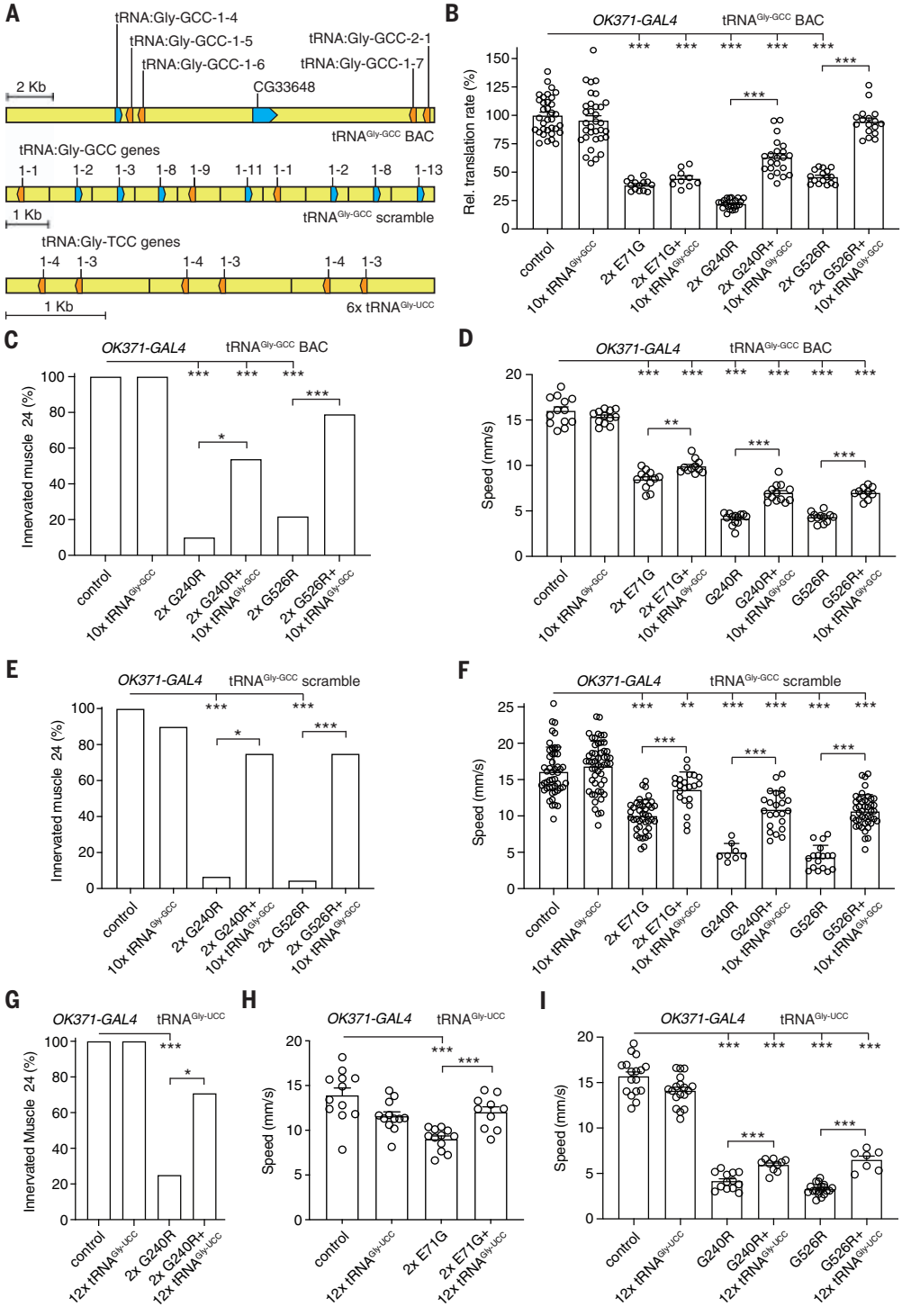


Fig. 1. tRNA^{Gly} overexpression rescues inhibition of protein synthesis and peripheral neuropathy phenotypes in *Drosophila* CMT2D models. (**A**) Schematic of the transgenes used for tRNA$^{Gly-GCC}$ or tRNA$^{Gly-UCC}$ overexpression. (**B**) Relative translation rate as determined by FUNCAT in motor neurons (*OK371-GAL4*) of larvae expressing E71G, G240R, or G526R GlyRS (2x indicates two transgene copies), in the presence or absence of the tRNA$^{Gly-GCC}$ BAC transgene (10xtRNA$^{Gly-GCC}$). n = 10 to 34 animals per genotype; ***P < 0.001 by Kruskal-Wallis test. Single-letter abbreviations for the amino acid residues are as follows: A, Ala; C, Cys; D, Asp; E, Glu; F, Phe; G, Gly; H, His; I, Ile; K, Lys; L, Leu; M, Met; N, Asn; P, Pro; Q, Gln; R, Arg; S, Ser; T, Thr; V, Val; W, Trp; and Y, Tyr. (**C**, **E**, and **G**) Percentage of larvae with innervated muscle 24. GlyRS transgenes were expressed in motor neurons (*OK371-GAL4*), in the presence or absence of 10xtRNA$^{Gly-GCC}$ BAC (C), 10xtRNA$^{Gly-GCC}$ scramble (E), or 12xtRNA$^{Gly-UCC}$ (G). n = 19 to 26 (C), 8 to 22 (E), and 12 to 27 (G) animals per genotype; *P < 0.05; ***P < 0.005 by Fisher's exact test with Bonferroni correction. (**D**, **F**, **H**, and **I**) Negative geotaxis climbing speed of 7-day-old female flies expressing GlyRS transgenes in motor neurons (*OK371-GAL4*), in the presence or absence of 10xtRNA$^{Gly-GCC}$ BAC (D), 10xtRNA$^{Gly-GCC}$ scramble (F), or 12xtRNA$^{Gly-UCC}$ [(H) and (I)]. n = 11 to 13 (D), 8 to 52 (F), and 7 to 19 [(H) and (I)] groups of 10 flies per genotype; **P < 0.01; ***P < 0.005 by two-way analysis of variance (ANOVA) (D) or Brown-Forsythe and Welch ANOVA [(F), (H), and (I)]. Controls in (B) to (I) are driver-only. Graphs represent mean ± SEM.

(*14*) revealed that each of six GlyRS or tyrosyl-tRNA synthetase (TyrRS) mutants substantially inhibited global protein synthesis in motor and sensory neurons (*9*), implicating impaired mRNA translation in CMT AARS.

In this study, we investigated the molecular mechanism by which CMT mutant GlyRS variants inhibit translation. Manipulation of upstream regulatory pathways or translation initiation did not rescue inhibition of translation (fig. S1), suggesting that CMT mutant GlyRS may interfere with translation elongation. We thus evaluated the effect of tRNA^{Gly} overexpression by generating *Drosophila* carrying a bacterial artificial chromosome (BAC)

[1]Department of Molecular Neurobiology, Donders Institute for Brain, Cognition and Behaviour and Faculty of Science, Radboud University, Nijmegen, Netherlands. [2]Molecular Neurogenetics Laboratory, Max Planck Institute for Molecular Biomedicine, Münster, Germany. [3]Biochemistry and Molecular Biology, Department of Chemistry, University of Hamburg, Hamburg, Germany. [4]The Jackson Laboratory, Bar Harbor, ME, USA. [5]Graduate School of Biomedical Sciences and Engineering, University of Maine, Orono, ME, USA.
***Corresponding author. Email: erik.storkebaum@donders.ru.nl**
†These authors contributed equally to this work.
‡Present address: Mount Desert Island Biological Laboratory, Bar Harbor, ME, USA.

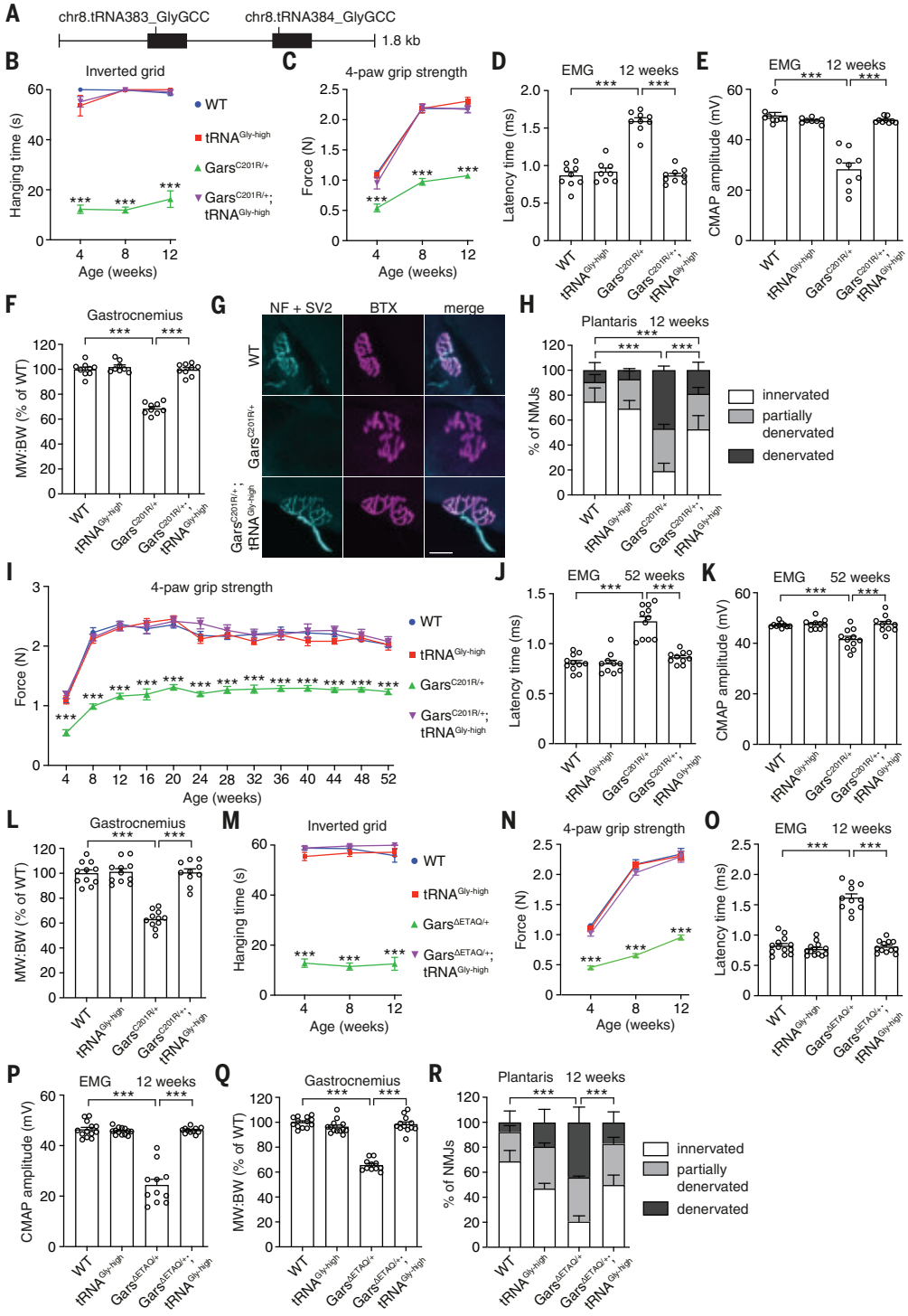
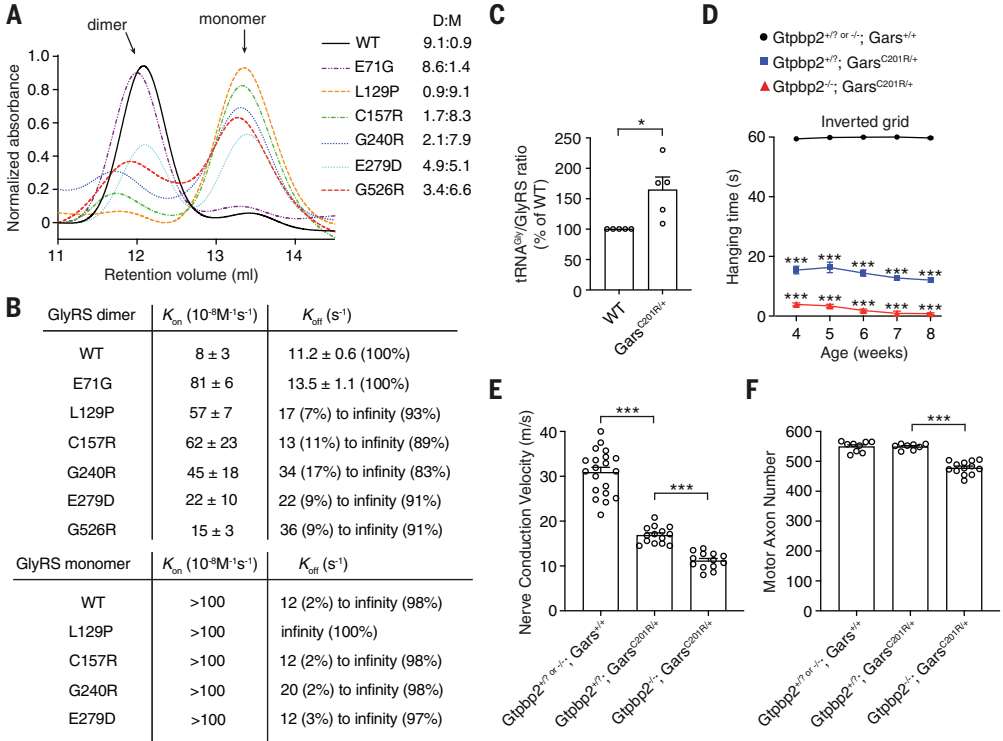


Fig. 2. tRNA$^{Gly\text{-}GCC}$ overexpression rescues peripheral neuropathy in CMT2D mouse models. (**A**) Schematic of the genomic fragment used for generation of tRNA$^{Gly\text{-}GCC}$ transgenic mice. (**B** and **M**) Hanging time in the inverted grid test of male *Gars*$^{C201R/+}$ × tRNA$^{Gly\text{-}high}$ (B) or *Gars*$^{\Delta ETAQ/+}$ × tRNA$^{Gly\text{-}high}$ (M) mice. *n* = 8 or 9 (B) and 11 to 13 (M) mice per genotype; ***P < 0.0001 by one-sample *t* test and two-tailed unpaired *t* test with Bonferroni correction per time point. (**C**, **I**, and **N**) Four-paw grip strength as measured by dynamometer. *n* = 8 or 9 (C), 10 or 11 (I), and 11 to 13 (N) mice per genotype; ***P < 0.001 by two-way ANOVA with Tukey's multiple comparisons test per time point [(C) and (I)] or Brown-Forsythe and Welch ANOVA (N). (**D**, **E**, **J**, **K**, **O**, and **P**) Electromyography (EMG) at 12 [(D), (E), (O), and (P)] or 52 [(J) and (K)] weeks of age. [(D, (J), and (O)] Latency time between sciatic nerve stimulation at sciatic notch level and detection of a compound muscle action potential (CMAP) in the gastrocnemius muscle. *n* = 8 or 9 (D), 10 or 11 (J), and 11 to 13 (O) mice per genotype; ***P < 0.0001 by two-way ANOVA with Tukey's multiple comparisons test (D) or Brown-Forsythe and Welch ANOVA [(J) and (O)]. [(E), (K), and (P)] CMAP amplitude in the gastrocnemius muscle. *n* = 8 or 9 (E), 10 or 11 (K), and 11 to 13 (P) mice per genotype; ***P < 0.0005 by Brown-Forsythe and Welch ANOVA [(E) and (P)] or two-way ANOVA with Tukey's multiple comparisons test (K). (**F**, **L**, and **Q**) Ratio of muscle weight to body weight (MW:BW, shown as % of WT) of the gastrocnemius at 12 [(F) and (Q)] or 52 (L) weeks of age. *n* = 8 or 9 (F), 10 or 11 (L), and 11 to 13 (Q) mice per genotype; ***P < 0.0001 by two-way ANOVA with Tukey's multiple comparisons test. (**G**, **H**, and **R**) Representative images (G) and quantification [(H) and (R)] of NMJ innervation status in plantaris muscle. In (G), neurofilament (NF) and SV2 label presynaptic nerve endings, while TRITC-conjugated bungarotoxin (BTX) labels postsynaptic acetylcholine receptors. *n* = 5 mice per genotype; ***P < 0.005 by Fisher's exact test with Bonferroni correction. Scale bar, 25 μm. Graphs represent mean ± SEM.

transgene containing five tRNA^{Gly} genes with GCC anticodon (tRNA$^{Gly\text{-}GCC}$) (Fig. 1A). Flies with 10 or 20 additional tRNA$^{Gly\text{-}GCC}$ gene copies displayed ~13 and ~25% higher tRNA$^{Gly\text{-}GCC}$ levels than wild type (WT), respectively (fig. S2, A and B). The 10xtRNA$^{Gly\text{-}GCC}$ transgene partially rescued the translation defect (Fig. 1B and fig. S3A), and peripheral neuropathy–like phenotypes induced by three CMT mutant GlyRS proteins [E71G (Glu^{71}→Gly), G240R, and G526R] (*9*) (table S1), including larval muscle denervation (Fig. 1C and fig. S3F), developmental lethality (fig. S3, B to E), adult motor deficits (Fig. 1D), sensory neuron morphology defects (fig. S3, G and H), and reduced life span (fig. S3I). In general, phenotypic rescue was more pronounced for G240R and G526R than for E71G. tRNA$^{Gly\text{-}GCC}$ overexpression did not alter GlyRS protein levels (fig. S4), nor did it rescue peripheral neuropathy phenotypes induced by CMT mutant TyrRS (fig. S5), indicating that only the cognate tRNA can rescue. Transgenic lines containing 10 different tRNA$^{Gly\text{-}GCC}$ genes (Fig. 1A, "tRNA$^{Gly\text{-}GCC}$ scramble") induced a more pronounced dosage-dependent increase in tRNA$^{Gly\text{-}GCC}$ levels than did the BAC transgene (~30% for 10xtRNA$^{Gly\text{-}GCC}$)



GlyRS dimer	K_{on} ($10^{-8}M^{-1}s^{-1}$)	K_{off} (s^{-1})
WT	8 ± 3	11.2 ± 0.6 (100%)
E71G	81 ± 6	13.5 ± 1.1 (100%)
L129P	57 ± 7	17 (7%) to infinity (93%)
C157R	62 ± 23	13 (11%) to infinity (89%)
G240R	45 ± 18	34 (17%) to infinity (83%)
E279D	22 ± 10	22 (9%) to infinity (91%)
G526R	15 ± 3	36 (9%) to infinity (91%)
GlyRS monomer	**K_{on} ($10^{-8}M^{-1}s^{-1}$)**	**K_{off} (s^{-1})**
WT	>100	12 (2%) to infinity (98%)
L129P	>100	infinity (100%)
C157R	>100	12 (2%) to infinity (98%)
G240R	>100	20 (2%) to infinity (98%)
E279D	>100	12 (3%) to infinity (97%)
G526R	>100	25 (3%) to infinity (97%)

Fig. 3. tRNA^{Gly} sequestration by CMT mutant GlyRS induces ribosome stalling. (**A**) Size-exclusion chromatography of purified recombinant human GlyRS proteins. D:M, dimer-to-monomer ratio. (**B**) K_{on} and K_{off} values of tRNA$^{Gly\text{-}GCC}$ binding and release, respectively, to dimer and monomer forms of the indicated GlyRS variants. The percentage in parentheses denotes the frequency of a measured value. (**C**) Quantification of tRNA^{Gly} bound to GlyRS in tRNA^{Gly}-GlyRS complexes immunoprecipitated from whole brains of *Gars*$^{C201R/+}$ and WT littermate control mice. tRNA^{Gly}/GlyRS ratio of WT is set as 100%; $n = 5$ independent experiments; $^{*}P < 0.05$ by one-sample t test. (**D**) Hanging time in the inverted grid test of male *Gtpbp2*$^{+/?\text{ or }-/-}$; *Gars*$^{+/+}$ (control), *Gtpbp2*$^{+/?}$;*Gars*$^{C201R/+}$, and *Gtpbp2*$^{-/-}$;*Gars*$^{C201R/+}$ littermate mice at 4, 5, 6, 7, and 8 weeks of age. $n = 15$ to 28 mice per genotype group; $^{***}P < 0.0005$ by one-sample t test and two-tailed unpaired t test with Bonferroni correction per time point. (**E**) Nerve conduction velocity of the sciatic nerve at 8 weeks of age. $n = 13$ to 20 mice per genotype group; $^{***}P < 0.0001$ by Brown-Forsythe and Welch ANOVA. (**F**) Axon number in the motor branch of the femoral nerve at 8 weeks of age. $n = 8$ to 13 per genotype group; $^{***}P < 0.0001$ by one-way ANOVA with Tukey's multiple comparisons test. Graphs represent mean ± SEM.

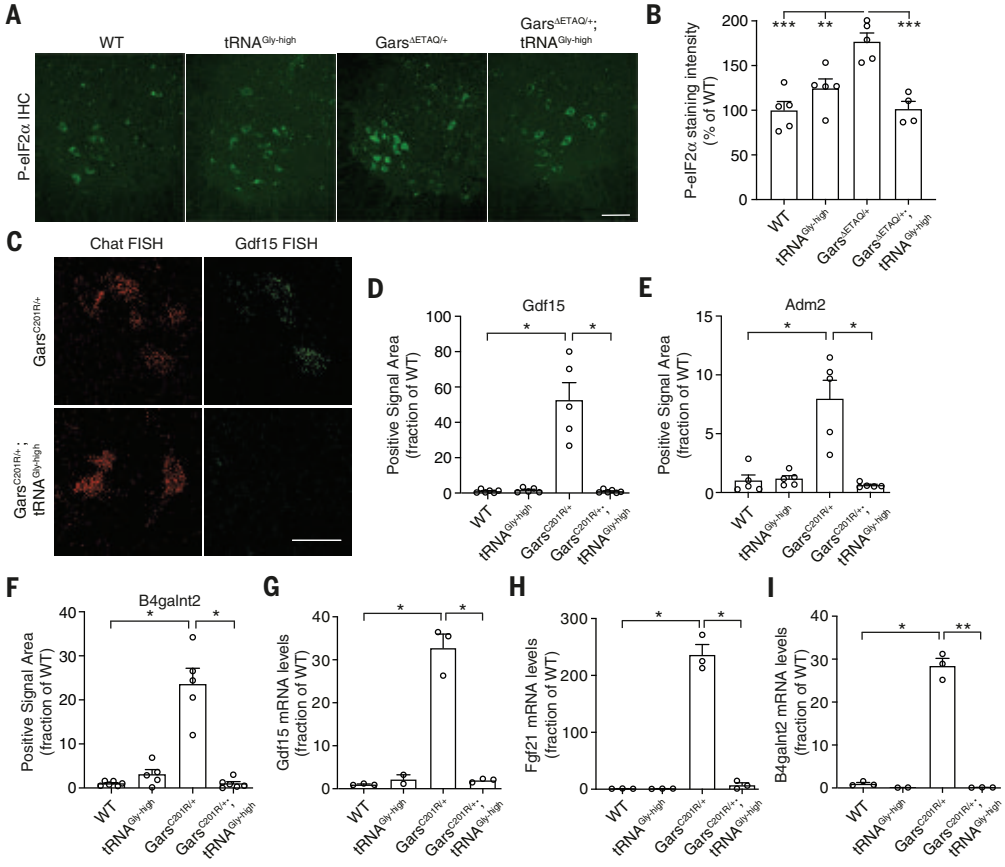


Fig. 4. tRNA$^{Gly\text{-}GCC}$ overexpression prevents ISR activation in CMT2D mouse models. (**A** and **B**) Representative images (A) and quantification (B) of immunostaining intensity of phosphorylated eIF2α (P-eIF2α) in motor neuron cell bodies in the spinal cord ventral horn of *Gars*$^{\Delta ETAQ/+}$ × tRNA$^{Gly\text{-}high}$ mice. IHC, immunohistochemistry. Scale bar, 100 μm. $n = 4$ or 5 mice per genotype; $^{**}P < 0.01$, $^{***}P < 0.0005$ by two-way ANOVA with Tukey's multiple comparisons test. (**C** to **F**) Representative images (C) and quantification of fluorescent in situ hybridization (FISH) for ATF4 target genes *Gdf15* (D), *Adm2* (E), and *B4galnt2* (F). Scale bar, 50 μm. $n = 5$ to 6 mice per genotype; $^{*}P < 0.05$ by two-tailed Welch's t test with Bonferroni correction. (**G** to **I**) mRNA levels of ATF4 target genes *Gdf15* (G), *Fgf21* (H), and *B4galnt2* (I) in spinal cord of *Gars*$^{C201R/+}$ × tRNA$^{Gly\text{-}high}$ mice. $n = 3$ mice per genotype; $^{*}P < 0.05$, $^{**}P < 0.01$ by Brown-Forsythe and Welch ANOVA. Graphs represent mean ± SEM.

(fig. S2, C and D) as well as a more substantial rescue of muscle denervation and motor performance (Fig. 1, E and F). Thus, the degree of rescue correlated with $tRNA^{Gly\text{-}GCC}$ overexpression level.

We next generated transgenic lines overexpressing the other $tRNA^{Gly}$ isoacceptor, $tRNA^{Gly\text{-}UCC}$ (Fig. 1A). 12xt$RNA^{Gly\text{-}UCC}$ flies displayed ~75% higher $tRNA^{Gly\text{-}UCC}$ levels (fig. S6, A and B) than WT. For E71G and G240R, $tRNA^{Gly\text{-}UCC}$ overexpression partially rescued developmental lethality (fig. S6, C to F), muscle denervation (Fig. 1G), motor deficits (Fig. 1, H and I), and life span (fig. S6I). For G526R, $tRNA^{Gly\text{-}UCC}$ overexpression partially rescued motor performance (Fig. 1I) but aggravated sensory neuron morphology defects (fig. S6, G and H) and further reduced life span (fig. S6I). Thus, for E71G and G240R, both $tRNA^{Gly\text{-}GCC}$ and $tRNA^{Gly\text{-}UCC}$ partially rescued peripheral neuropathy phenotypes, while for G526R, the rescue was isoacceptor specific.

To strengthen the potential relevance for human CMT2D, we evaluated the effect of $tRNA^{Gly\text{-}GCC}$ overexpression in CMT2D mouse models. We generated transgenic mice with ~27 ($tRNA^{Gly\text{-}high}$) or two ($tRNA^{Gly\text{-}low}$) copies of a genomic transgene containing two $tRNA^{Gly\text{-}GCC}$ genes (Fig. 2A and fig. S7A). In spinal cord (SC), tibialis anterior muscle, and sciatic nerve of $tRNA^{Gly\text{-}high}$ mice, $tRNA^{Gly\text{-}GCC}$ levels were ~90 to 150% higher compared to WT (fig. S7, B to G). Targeted locus amplification (TLA) revealed integration of all transgene copies in *Stk38* (serine/threonine kinase 38) on chromosome 17, with an ~7-kb deletion at the integration site, deleting exons 8 through 12 of *Stk38* (fig. S8). In both male and female $Gars^{C201R/+}$ mice (*15*) of 3 to 6 weeks of age, $tRNA^{Gly\text{-}GCC}$ overexpression fully rescued the reduced body weight (fig. S9, A and B) and motor deficits (fig. S9, C to F). Reduced nerve conduction velocity (NCV) and compound muscle action potential (CMAP) amplitude in $Gars^{C201R/+}$ mice were also fully rescued (fig. S9, G to J). Thus, increasing $tRNA^{Gly\text{-}GCC}$ levels completely prevented peripheral neuropathy in $Gars^{C201R/+}$ mice without affecting *Gars* mRNA and GlyRS protein levels (fig. S10).

Follow-up of an independent cohort of $Gars^{C201R/+}$ × $tRNA^{Gly\text{-}high}$ mice from 4 to 12 weeks of age confirmed full rescue of motor performance (Fig. 2, B and C) and neuromuscular transmission (Fig. 2, D and E). At 12 weeks of age, $tRNA^{Gly\text{-}GCC}$ overexpression fully rescued the reduced gastrocnemius muscle weight (Fig. 2F) and substantially mitigated muscle denervation (Fig. 2, G and H). The rescuing effect persisted until 1 year of age in another cohort of $Gars^{C201R/+}$ × $tRNA^{Gly\text{-}high}$ mice. Body weight and motor performance were fully rescued from 4 to 52 weeks of age (Fig. 2I and fig. S9, K and L), as were NCV, CMAP amplitude, and gastrocnemius muscle weight (Fig. 2, J to L). Thus, $tRNA^{Gly\text{-}GCC}$ overexpression completely prevents peripheral neuropathy in $Gars^{C201R/+}$ mice.

Finally, we crossed $tRNA^{Gly\text{-}high}$ mice to another CMT2D mouse model carrying a patient mutation (245-248_delETAQ) in the mouse *Gars* gene (*16*). At 4, 8, and 12 weeks of age, $tRNA^{Gly\text{-}GCC}$ overexpression fully rescued motor deficits, reduced NCV and CMAP amplitude, reduced gastrocnemius weight, and muscle denervation (Fig. 2, M to R). In $tRNA^{Gly\text{-}low}$ mice, the $tRNA^{Gly\text{-}GCC}$ level was not altered (fig. S11). $Gars^{C201R/+}$;$tRNA^{Gly\text{-}low}$ mice were indistinguishable from $Gars^{C201R/+}$ mice for all parameters evaluated (fig. S12), showing that $tRNA^{Gly\text{-}GCC}$ overexpression, and not the mere presence of the transgene, is responsible for phenotypic rescue.

We next explored the molecular mechanism underlying the rescue of CMT2D phenotypes by $tRNA^{Gly}$ overexpression. We hypothesized that CMT mutant GlyRSs may exhibit altered kinetics of $tRNA^{Gly}$ binding and release. Size-exclusion chromatography of various purified human GlyRS variants revealed that WT and E71G migrated predominantly as dimers, whereas L129P, C157R (equivalent to mouse C201R), G240R, E279D, and G526R partitioned between the monomer and dimer forms (Fig. 3A). All CMT mutant GlyRS dimers bound $tRNA^{Gly\text{-}GCC}$ (K_{on}, association rate constant) with one-half to one-tenth the affinity of WT dimers (Fig. 3B). L129P, C157R, G240R, E279D, and G526R dimers displayed markedly slower $tRNA^{Gly\text{-}GCC}$ release (K_{off}, dissociation rate constant), with >80% of traces showing no $tRNA^{Gly\text{-}GCC}$ release (Fig. 3B). In contrast, E71G dimers displayed $tRNA^{Gly\text{-}GCC}$ release kinetics comparable to WT. L129P, C157R, G240R, E279D, and G526R monomers bound $tRNA^{Gly\text{-}GCC}$ with very low affinity, but once bound, the $tRNA^{Gly\text{-}GCC}$ release was markedly inhibited (Fig. 3B). The $tRNA^{Gly\text{-}UCC}$ isoacceptor displayed similar binding and release kinetics to GlyRS dimers and monomers (table S2). The slow $tRNA^{Gly}$ release by CMT mutant GlyRS dimers and monomers suggests that mutant GlyRSs sequester a large fraction of cellular $tRNA^{Gly}$ and thus deplete it for translation. To provide in vivo evidence for $tRNA^{Gly}$ sequestration, we immunoprecipitated GlyRS from brains of $Gars^{C201R/+}$ and WT littermate mice and quantified the amount of $tRNA^{Gly}$ bound to GlyRS. The $tRNA^{Gly}$ amount was ~65% larger in $Gars^{C201R/+}$ than in WT (Fig. 3C and fig. S13A), indicating stronger $tRNA^{Gly}$ association with GlyRS-C201R.

Because $tRNA^{Gly}$ sequestration may lead to ribosome stalling at Gly codons, we performed ribosome profiling on SC extracts of $Gars^{C201R/+}$ and WT littermate mice, revealing that Gly codons are more frequently found in the ribosomal A site in $Gars^{C201R/+}$ SC relative to WT (a cumulative increase of 79%) (fig. S13B). Prolonged ribosome dwelling at codons is resolved by "ribosome rescue" pathways (*17*–*19*), and because Gly codons are frequent, ribosome stalling in CMT2D may deplete ribosome rescue factors, and inactivation of a rescue factor may aggravate the phenotype of CMT2D mice. Indeed, inactivation of *Gtpbp2*, encoding the ribosome rescue factor GTPBP2 (guanosine triphosphate binding protein 2), does not induce peripheral neuropathy by itself (*20*) but substantially enhanced peripheral neuropathy in $Gars^{C201R/+}$ mice (Fig. 3, D to F, and fig. S14, A and B). Thus, ribosome stalling causally contributes to CMT2D pathogenesis.

Because stalled ribosomes may activate the integrated stress response (ISR) through general control nonderepressible 2 (GCN2) (*21*–*23*), and ISR activation was implicated in CMT2D (*24*), we evaluated ISR induction in CMT2D mice intercrossed with $tRNA^{Gly\text{-}high}$ mice. $tRNA^{Gly\text{-}GCC}$ overexpression fully rescued increased phosphorylated eukaryotic initiation factor 2α (eIF2α) immunostaining intensity (~75% higher than in WT) in spinal motor neurons of $Gars^{\Delta ETAQ/+}$ mice (Fig. 4, A and B) as well as the strong induction of activating transcription factor 4 (ATF4) target genes *Gdf15*, *Adm2*, *B4galnt2*, and *Fgf21* in motor neurons of $Gars^{C201R/+}$ mice (Fig. 4, C to I). Thus, $tRNA^{Gly\text{-}GCC}$ overexpression abrogates ISR activation in CMT2D mice, indicating that depletion of the cellular $tRNA^{Gly}$ pool and consequent ribosome stalling is upstream of ISR activation. When *Gtpbp2* is inactivated in $Gars^{C201R/+}$ mice, the percentage of motor neurons showing ISR activation does not change, nor do additional cell types show ISR activation, despite widespread *Gtpbp2* expression in SC (fig. S15). This suggests that $tRNA^{Gly}$ levels are only below a critical threshold in affected motor and sensory neurons, leading to ribosome stalling selectively in these cell types. This may explain the relatively modest increase in ribosome dwelling at Gly codons in $Gars^{C201R/+}$ SC (fig. S13B).

Our data propose a detailed molecular mechanism underlying CMT2D (fig. S16). Beyond the seven CMT2D mutations studied here, this mechanism may apply to additional CMT mutant GlyRS proteins, because 14 of 25 reported CMT2D mutations result in net addition of positive charge (table S3), which could alter binding and release kinetics of the negatively charged $tRNA^{Gly}$. Similarly, most CMT-causing mutations in TyrRS and AlaRS also result in net addition of positive charge (table S4). Finally, our data indicate that increasing $tRNA^{Gly}$ level may constitute a therapeutic approach for CMT2D.

REFERENCES AND NOTES

1. M. E. Kuo, A. Antonellis, *Trends Genet.* **36**, 105–117 (2020).
2. N. Wei, Q. Zhang, X. L. Yang, *J. Biol. Chem.* **294**, 5321–5339 (2019).
3. E. Storkebaum, *BioEssays* **38**, 818–829 (2016).
4. P. Schimmel, *Annu. Rev. Biochem.* **56**, 125–158 (1987).

5. M. Ibba, D. Soll, *Annu. Rev. Biochem.* **69**, 617–650 (2000).
6. N. Sonenberg, A. G. Hinnebusch, *Cell* **136**, 731–745 (2009).
7. A. Antonellis *et al*., *J. Neurosci.* **26**, 10397–10406 (2006).
8. L. A. Nangle, W. Zhang, W. Xie, X. L. Yang, P. Schimmel, *Proc. Natl. Acad. Sci. U.S.A.* **104**, 11239–11244 (2007).
9. S. Niehues *et al*., *Nat. Commun.* **6**, 7520 (2015).
10. E. Storkebaum *et al*., *Proc. Natl. Acad. Sci. U.S.A.* **106**, 11782–11787 (2009).
11. C. A. Froelich, E. A. First, *Biochemistry* **50**, 7132–7145 (2011).
12. W. W. Motley *et al*., *PLOS Genet.* **7**, e1002399 (2011).
13. I. Erdmann *et al*., *Nat. Commun.* **6**, 7521 (2015).
14. D. C. Dieterich *et al*., *Nat. Neurosci.* **13**, 897–905 (2010).
15. F. Achilli *et al*., *Dis. Model. Mech.* **2**, 359–373 (2009).
16. K. H. Morelli *et al*., *J. Clin. Invest.* **129**, 5568–5583 (2019).
17. A. P. Schuller, R. Green, *Nat. Rev. Mol. Cell Biol.* **19**, 526–541 (2018).
18. M. Graille, B. Séraphin, *Nat. Rev. Mol. Cell Biol.* **13**, 727–735 (2012).
19. C. A. P. Joazeiro, *Annu. Rev. Cell Dev. Biol.* **33**, 343–368 (2017).
20. R. Ishimura *et al*., *Science* **345**, 455–459 (2014).
21. A. J. Inglis *et al*., *Proc. Natl. Acad. Sci. U.S.A.* **116**, 4946–4954 (2019).
22. H. P. Harding *et al*., *eLife* **8**, e50149 (2019).
23. C. C. Wu, A. Peterson, B. Zinshteyn, S. Regot, R. Green, *Cell* **182**, 404–416.e14 (2020).
24. E. L. Spaulding *et al*., *Science* **373**, 1156–1161 (2021).

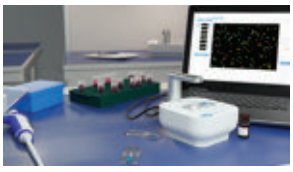
ACKNOWLEDGMENTS

We thank X.-L. Yang for GlyRS expression plasmids and the General Instruments Facility (Faculty of Science, Radboud University) for advice on image acquisition and analysis. **Funding:** This work was supported by the Max Planck Society, the Donders Center for Neuroscience, the Muscular Dystrophy Association (MDA479773), the EU Joint Programme–Neurodegenerative Disease Research [JPND; ZonMW 733051075 (TransNeuro) and ZonMW 733051073 (LocalNMD)], the Radala Foundation, and an ERC consolidator grant (ERC-2017-COG 770244) to E.S., Deutsche Forschungsgemeinschaft (DFG, IG73/14-2) to Z.I., and NIH grants to R.W.B. (R01 NS054154 and U54 OD020351). **Author contributions:** A.Z., M.M., R.T., E.L.S., A.R.W., M.B., A.L.D.T., N.v.B., C.S., L.A.S., J.B., M.C., S.D., D.K., Z.I., and E.S. performed experiments and analyzed data. R.W.B., Z.I., and E.S. supervised the work. E.S. conceptualized and coordinated the work. R.W.B., Z.I., and E.S. acquired funding. E.S. wrote the paper, with contributions from A.Z., M.M., E.L.S., and A.R.W. and with feedback from all authors. **Competing interests:** Patent application 2024840 (tRNA delivery as a therapeutic approach for CMT AARS) with E.S. as inventor was submitted to the Netherlands Patent Agency. E.L.S. and R.W.B. have a pending patent application "GCN2 inhibitors for treating peripheral neuropathy." R.W.B. is a member of the scientific advisory boards of the Charcot-Marie-Tooth Association and the Hereditary Neuropathy Foundation. **Data and materials availability:** The ribosome profiling data are in the Gene Expression Omnibus (accession number GSE160584). $tRNA^{Gly}$ transgenic mice are available under a material transfer agreement.

SUPPLEMENTARY MATERIALS

science.sciencemag.org/content/373/6559/1161/suppl/DC1
Materials and Methods
Figs. S1 to S16
Tables S1 to S8
References (*25*–*92*)
MDAR Reproducibility Checklist

17 February 2020; resubmitted 2 April 2021
Accepted 16 July 2021
10.1126/science.abb3356



Cell Counter

CytoSMART Exact FL is an automated dual fluorescence cell counter with an expanded field of view and unmatched resolution and magnification power. Using an advanced complementary metal-oxide semiconductor (CMOS)-based optical system and an image-analysis software powered by artificial intelligence, CytoSMART Exact FL calculates the exact number of cells in a sample and provides reliable assessment of key cellular parameters, including cell viability and transfection efficiency. The unit's increased magnification and high resolution offer an unprecedented level of detail, enabling the user to distinguish between whole cells and cell debris and count even the smallest of mammalian cells [e.g., chimeric antigen receptor T (CAR-T) cells, stem cells, peripheral blood mononuclear cells (PBMCs), or splenocytes].

CytoSMART

For info: +1-908-392-5985
cytosmart.com

Multi-Organ Microphysiological System

CN Bio announces the launch of its new PhysioMimix organ-on-a-chip (OOC) Multi-Organ Microphysiological System (MPS). The next-generation platform combines CN Bio's in vitro 3D liver model with a range of other organs to more accurately recapitulate the multi-organ and systemic effects observed in humans. The PhysioMimix OOC Multi-Organ MPS can be used to decrease the risk of clinical-trial failures due to cross-species translational differences, and can be used in the development of new human-specific modalities for which animal models are unsuited. The company's advanced 3D liver model can be easily and reliably interconnected with other organs (such as gut, lung, or kidney) to provide a human in vitro alternative to animal or in silico first-pass absorption, distribution, metabolism, and excretion (ADME) studies, to elicit a deeper human-specific mechanistic understanding of disease states and to identify reactive metabolite-driven toxicity or multi-organ toxicity. Furthermore, in vitro to in vivo clinical predictions can be extrapolated using physiologically based pharmacokinetics (PBPK) mathematical models. For existing PhysioMimix users, an upgrade path is available.

CN Bio

For info: +44-(0)-1223-737941
cn-bio.com/physiomimixooc

Electronic Laboratory Notebook

Dotmatics Ltd. introduces eln.online, a quick-start version of its electronic laboratory notebook (ELN). Establishing lab and IT infrastructure, including electronic notebooks, is essential in the startup plan for new research companies. As a multitenant, software as a service (SaaS) offering, the software can be easily established, minimizing IT overheads and maximizing return on investment. eln.online enables the search and capture of a wide variety of experimental data in a secure, cloud-based notebook, thereby facilitating effective collaboration between multiple scientists within or between organizations. It also ensures that organizations secure and protect their internet protocol from an early stage, which is crucial for future licensing, partnering, and mergers and acquisitions plans. As an efficient alternative to spreadsheets, eln.online provides a standard template to capture an unlimited amount of diverse discovery experiments as well as an additional template designed specifically for medicinal and synthetic chemistry projects.

Dotmatics Ltd.

For info: +44-(0)-1279-654-123
www.dotmatics.com

Bioprinter

The combination of a two-photon 3D-printer with an innovative hydrogel-based bioink allows the direct printing of 3D structures containing living cells at both the meso- and microscale. Developed by UpNano, the NanoOne Bio is a printer based on the successful NanoOne range of laser-powered two-photon 3D-printers, which are able to build structures across 12 orders of magnitude. The new hydrogel has been developed with Xpect-INX, a Belgian spinoff foundation specializing in the production of biocompatible materials for the 3D-(bio-)printing industry. It is the only commercially available resin that allows embedding living cells straight from a culture plate within highly precise 3D-printed structures for biological applications. 2D cell cultures have been the standard in pharmaceutical preclinical R&D and biomedical research for many decades. So far, building complex, highly precise 3D structures with embedded living cells has been hampered by lack of suitable materials and printing systems. But thanks to the joint development of a novel hydrogel-based bioink by Xpect INX and UpNano, in combination with UpNano's new printing model, this endeavor has now become reality.

UpNano

For info: +43-(0)-1-890-16-52
www.upnano.at

Single-Cell Analyzer

Chromium X makes single-cell analysis easy, reliable, and scalable thanks to its proprietary Next GEM technology. The key to this technology is the ability to generate hundreds of thousands of single-cell partitions, each containing an identifying barcode for downstream analysis. Combined with an innovative reagent delivery system and turnkey software analysis tools, this system enables the discovery of previously inaccessible biological information. In addition, it features fully integrated, automated system support in the 10x Genomics Cloud, complete with temperature control and improved access to support. Flexible enough to fit into any lab, Chromium X can analyze hundreds to hundreds of thousands of cells in a single run, making million-cell studies routine. It can easily handle a range of projects, from pilot studies to the highest-throughput analysis. Chromium Single Cell products can capture molecular readouts of cell activity in multiple dimensions, including gene expression, chromatin accessibility, cell-surface proteins, immune clonotype, antigen specificity, and CRISPR perturbation screens.

10x Genomics

For info: +1-800-709-1208
www.10xgenomics.com/chromium-x

Electronically submit your new product description or product literature information! Go to www.sciencemag.org/about/new-products-section for more information.

Newly offered instrumentation, apparatus, and laboratory materials of interest to researchers in all disciplines in academic, industrial, and governmental organizations are featured in this space. Emphasis is given to purpose, chief characteristics, and availability of products and materials. Endorsement by *Science* or AAAS of any products or materials mentioned is not implied. Additional information may be obtained from the manufacturer or supplier.

ScienceCareers online @sciencecareers.org

ScienceCareers
FROM THE JOURNAL SCIENCE AAAS

Confused about your next career move?

Download Free Career Advice Booklets!

ScienceCareers.org/booklets





INDIANA UNIVERSITY
BLOOMINGTON

Tenure-Track Faculty Position in Plant Biology
Genome, Cell, and Developmental
Biology (GCDB) Program
Department of Biology, College of Arts and Sciences
https://biology.indiana.edu/index.html

The Biology Department at Indiana University invites applications for a tenure-track Assistant Professor position, beginning in fall 2022, in the broad area of plant growth and development. We seek candidates using molecular, cellular, biochemical and/or genetic approaches to understand developmental and/or physiological processes at a mechanistic level.

IU Bloomington provides state-of-the-art facilities for genomics and bioinformatics, light and electron microscopy, flow cytometry, structural biology, protein analysis, and molecular biology, in addition to generous greenhouse, field and growth chamber space. Our faculty are expected to establish and maintain well-funded research programs and participate in both undergraduate and graduate education. See https://biology.indiana.edu/graduate/genome-cell-development/index.html for more information about the GCDB program.

Bloomington is a culturally diverse, family-friendly city with a vibrant arts and entertainment scene, including theatre, art-house cinema, music, dance and comedy offerings as well as wide-ranging restaurant and food options, including multiple farmers' markets. We are located among the hills, lakes, and forested landscape of south-central Indiana, providing extensive opportunities for outdoor activities including hiking, camping, water sports and cycling (http://www.visitbloomington.com/).

Applicants should hold a Ph.D. or equivalent degree and have relevant postdoctoral experience with a strong record of research accomplishments. Applicants should submit a cover letter, CV, research statement, a 1-2 page statement on fostering diversity, equity, and inclusion in and out of the classroom, and a list of three references with contact information using the submission link at http://indiana.peopleadmin.com/postings/11311. Please address inquires to Jennifer Tarter jenjones@indiana.edu; 812-856-3984. **Applications received by November 1, 2021** will be assured of full consideration.

The College of Arts and Sciences is committed to building and supporting a diverse, inclusive, and equitable community of students and scholars. Indiana University is an equal employment and affirmative action employer and a provider of ADA services. All qualified applicants will receive consideration for employment without regard to age, ethnicity, color, race, religion, sex, sexual orientation, gender identity or expression, genetic information, marital status, national origin, disability status or protected veteran status.

Shenzhen Institute of Advanced Technology
Chinese Academy of Sciences



Established in partnership between the Chinese Academy of Sciences and the Shenzhen Municipal Government, the Shenzhen Institute of Advanced Technology (SIAT) is a newly-created university with an objective to become the world's preeminent institute for emerging science and engineering programs. SIAT is equipped with state-of-art teaching and research facilities and is dedicated to cultivating international, visionary, and interdisciplinary talents while delivering research support to pursue innovation-driven development.

SIAT is located in Shenzhen, also known as the "Silicon Valley of China," a modern, clean, and green city, well-known for its stunning architecture, vibrant economy, and its status as a leading global technology hub. SIAT is seeking applications for faculty positions of all ranks in the following academic programs: Computer Science and Engineering, Bioinformatics, Robotics, Life Sciences, Material Science and Engineering, Biomedical Engineering, Pharmaceutical Sciences, Synthetic Biology, Neurosciences, etc. SIAT seeks individuals with a strong record of scholarship who possess the ability to develop and lead high-quality teaching and research programs. SIAT offers a comprehensive benefits package and is committed to faculty success throughout the academic career trajectory, providing support for ambitious and world-class research projects and innovative, interactive teaching methods.

Further information:
http://english.siat.cas.cn/DP/Va/



Science 2020
TOP EMPLOYER

Who's the top employer for 2020?

Science Careers' annual survey reveals the top companies in biotech & pharma voted on by *Science* readers.

Read the article and employer profiles at sciencecareers.org/topemployers

By **A. Rani Elwy**

Writing my way through

Earlier this year, a physician emailed me to thank me for an essay I wrote. I couldn't believe he was reaching out—after all, 18 years had passed since it was published. But he had found the piece—my first narrative medicine essay, about my experience parenting a son with a complex medical disorder—in a drawer he was cleaning out as he prepared to retire. He had tracked me down to share how important such essays were to him during his years caring for patients. I was touched—and reminded of how important these pieces were to my own professional and personal journey.

During my son's first year of life, we knew something wasn't right. He was inconsolable most of the time. He couldn't roll over or sit up on his own. He held objects very close to his face, as if he could not see them. (It turns out, he couldn't.) At the urging of a physical therapist, my husband and I started on the long path of genetic counseling and testing. At the same time, I was working as a postdoctoral fellow in a 2-year program that was meant to lead to a position as an independent investigator. In my work, I was examining health care organization, delivery, and outcomes—and it turned out I was spending my personal time thinking about many of these same issues.



"Good writing happens when one has a story to tell."

Some of my research mentors wondered how I would ever achieve research independence when my personal life was so chaotic, but I was determined to make my career path work. I attended scientific conferences, but I often got called home early because of my son's health. Desperate to meet grant deadlines and get my research published, I wrote from my son's hospital room in the intensive care unit, especially in the early morning hours when the physicians and nurses didn't need my attention.

Yet the words that kept coming to me were not about my research, but about my lived experience as a parent of a medically complex child. I remembered what a former colleague once told me: Good writing happens when one has a story to tell. The story I wanted to tell, I realized, was about the frustration, heartache, and disappointment of the diagnostic process; my gratitude for the many dedicated health care providers who were just as determined as we were to find answers; and the tremendous love, respect, and wonder I felt for my son, undergoing a host of procedures and tests, my daughter, whose young life was not normal in any way, and my husband, an unyielding partner in this medical maze. I also needed to share my feelings of inadequacy as a mother and a researcher, and my frustration with the systems that were meant to support our family but often did not.

At the time, major medical journals were beginning to publish narrative pieces. I submitted my first essay, hopeful that it might make a difference for others—and demonstrate some productivity during this time, even if it wasn't traditional research output. But I was also nervous about the potential exposure. I was surprised and thrilled when it was accepted for publication, and readers' empathetic, constructive responses alleviated my concerns about sharing my family's story.

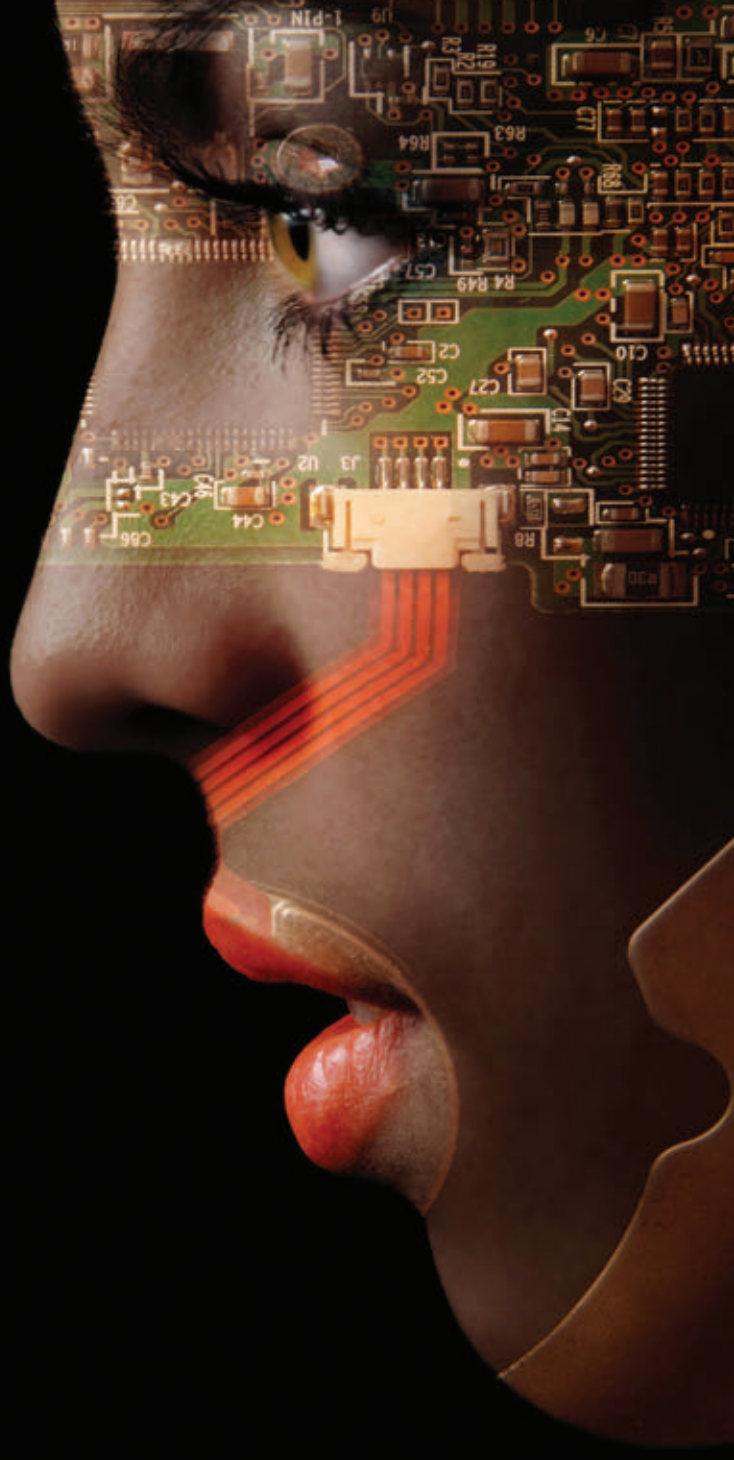
Over the following years, I somehow made it to investigator. Our youngest daughter was born; our son was diagnosed with Schwartz-Jampel syndrome, a rare, genetic neuromuscular disorder; and I took 5 months away from my research to help him get the support services he needed. Through it all, the narrative essays continued to flow. Writing about our extended family of health care providers and the need for family mental health services within pediatric care settings was highly cathartic, and reading strangers' responses was equally therapeutic.

Honing my writing through narrative medicine also helped me pen more compelling grant proposals by telling better stories. In the year after returning to my career, I wrote my first funded proposals, to study the impact of traumatic health care events on providers, patients, and families, and to examine why patients do or don't seek help for depression. I probably would not have taken these directions with my research if the topics had not been such a prominent part of my life. But I realized that there didn't need to be a divide between my personal pain and the passions that fueled my research. Instead, I could envision and craft a life that satisfied my needs for my research, my family, and myself. ■

A. Rani Elwy is a professor at Brown University and a health services researcher at VA Bedford Healthcare System.

ILLUSTRATION: ROBERT NEUBECKER

Share **Your Robotics Research** with the **World**.



Shaping the future of robotics with high impact research!

As a multidisciplinary online-only journal, *Science Robotics* publishes original, peer-reviewed, research articles that advance the field of robotics. The journal provides a central forum for communication of new ideas, general principles, and original developments in research and applications of robotics for all environments.

Submit your research today. Learn more at: **robotics.sciencemag.org**

Twitter: @SciRobotics
Facebook: @ScienceRobotics

Science Robotics
AAAS



REVEALING THE NEXT BREAKTHROUGH IN IMMUNOLOGY

APPLY NOW FOR THE $30,000 GRAND PRIZE

APPLICATIONS DUE: OCTOBER 1, 2021

The Michelson Philanthropies & ***Science*** Prize for Immunology recognizes research that will have a significant impact on vaccine and immunotherapy development. Together with AAAS/***Science***, Michelson Philanthropies awards breakthrough research from the past three years. The applications are judged on innovation and potential impact.

With these prizes, scientists (35 and younger) have the opportunity to advance their research projects, are provided with a renowned platform in ***Science*** to publish their work and connect them with other innovators through the Michelson Prizes alumni network.

Young researchers from a wide range of disciplines are encouraged to apply.

APPLY TODAY:
www.sciencemag.org/michelson

MICHELSON PHILANTHROPIES & Science
PRIZE FOR IMMUNOLOGY